HIGH SPATIAL AND SPECTRAL QUALITY DIODE-LASER-BASED PUMP SOURCES FOR SOLID-STATE LASERS AND OPTICAL PARAMETRIC OSCILLATORS

Ian D. Lindsay

A Thesis Submitted for the Degree of PhD
at the
University of St Andrews

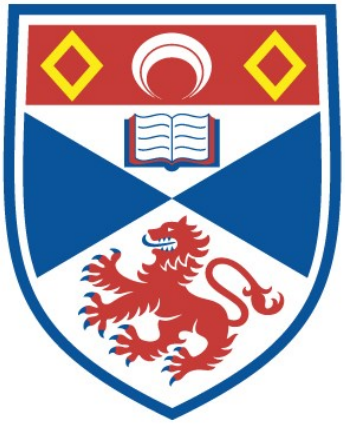

1999

High Spatial and Spectral Quality Diode-Laser-Based Pump Sources for Solid-State Lasers and Optical Parametric Oscillators.

Ian D. Lindsay, BSc., MSc.

J.F. Allen Physics Research Laboratories,
School of Physics and Astronomy,
University of St Andrews,
Fife, Scotland.

A thesis submitted to the University of St Andrews in application for the degree of Doctor of Philosophy.

July 1999.

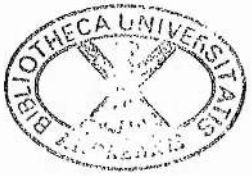

(i) I, Ian David Lindsay, hereby certify that this thesis, which is approximately 93,000 words in length, has been written by me, that it is the record of work carried out by me and that it has not been submitted in any previous application for a higher degree.

July 15th 1999 Signature of candidate:

(ii) I was admitted as a research student in October 1994 and as a candidate for the degree of Doctor of Philosophy in October 1995; the higher study for which this is a record was carried out in the University of St Andrews between 1994 and 1999.

(iii) I hereby certify that the candidate has fulfilled the conditions of the Resolution and Regulations appropriate for the degree of Doctor of Philosophy in the University of St Andrews and that the candidate is qualified to submit this thesis in application for that degree.

July 15th 1999 Signature of supervisor:

In submitting this thesis to the University of St Andrews I understand that I am giving permission for it to be made available for use in accordance with the regulations of the University Library for the time being in force, subject to any copyright vested in the work not being affected thereby. I also understand that the title and abstract will be published, and that a copy of the work may be made and supplied to any bona fide library or research worker.

July 15th 1999 Signature of candidate:

Abstract.

In this thesis the use of high spatial- and spectral-quality diode-laser pump sources for solid-state lasers and continuous-wave optical parametric oscillators (cw OPOs) is investigated. While diode lasers are potentially attractive, compact, low-cost pump sources for solid-state lasers and cw OPOs, the difficulty in obtaining moderate output powers, while retaining high spatial beam quality and spectral purity, often limits the potential of such lasers in these applications.

Techniques for obtaining high-power, high spatial- and spectral-quality output from diode lasers are reviewed and the design, development and characterisation of an injection-locked broad-area diode-laser system is described. This system produced output powers of ≈400mW in a near-diffraction-limited beam ($M^2 \approx 1.3$) and with a spectral width of <30MHz.

The injection-locked system was used as the pump source for a quasi-three-level 946-nm Nd:YAG laser. End-pumped solid-state lasers of this type can offer potentially efficient, low-threshold operation if a near-diffraction limited pump source is used allowing optimal overlap with the laser mode. A model, including pump beam quality effects, is developed for such lasers and used to highlight the advantages of a near-diffraction-limited pump source, especially in the case of the 946-nm Nd:YAG transition which suffers from low gain and significant reabsorption losses. A 946-nm Nd:YAG laser pumped by the injection-locked system is described, yielding cw output powers up to 120mW with a 46% slope efficiency, performance comparable to Ti:sapphire- or dye-laser pumping, and 27ns Q-switched pulses having peak powers of 180W. 50W, 20ns pulses at 473nm were obtained by second-harmonic generation in $KNbO_3$.

The performance and relative merits of various cw OPO configurations, in the context of diode-laser pumping, are discussed and the development of a doubly-resonant OPO (DRO) based on periodically-poled lithium niobate is described. When pumped by the injection-locked system, this device showed a threshold of 25mW and tuning of the outputs over 1.15- 1.25μm at the signal and 2.3-2.65μm at the idler was obtained by variation of crystal temperature, PPLN grating period and pump

wavelength. When pumping with a 100mW single-mode diode laser, a 15mW OPO threshold was observed while retaining a similar tuning range. This represented the first demonstration of a cw DRO directly pumped by a single-mode diode laser. The achievement of such spectral coverage while pumping with this source points to the potential of such systems as compact, tunable sources in the near- to mid-infrared.

Contents

1. Introduction. **6**

1.1 Background. 6

1.2 Scope of work presented in this thesis. 9

1.3 Relevant chronology. 11

1.4 References. 19

2. Diode Laser Pumping of Solid State Lasers. **28**

2.1 Introduction. 28

2.2 Quasi-Three-Level Lasers. 32

2.3 Modelling of longitudinally pumped solid state lasers. 33

2.3.1 Development of theoretical model. 33

2.3.2 Threshold of four-level and quasi-three-level systems. 46

2.3.3 Above-threshold behaviour and slope efficiency. 51

2.3.4 Diffraction effects and pump beam quality. 58

2.3.5 Optimisation of quasi-three-level laser parameters. 63

2.4 Conclusions. 68

2.5 References. 70

3. Nonlinear Optical Frequency Conversion and Optical Parametric Oscillators. **76**

3.1 Introduction. 76

3.2 Theoretical basis of nonlinear optics. 81

3.2.1 Nonlinear susceptibility and the origin of nonlinear optical processes. 82
3.2.2 Coupled wave-equation treatment of nonlinear frequency conversion. 88
3.2.3 The Manley-Rowe relations. 92
3.2.4 Nonlinear optics with Gaussian beams. 95
3.2.5 Optical parametric gain. 99
3.2.6 Generated second harmonic power. 100

3.3 Phase-matching of nonlinear optical processes. 102
3.3.1 Birefringent phase matching. 106
3.3.1.1 Calculation of phase-matching angle. 108
3.3.1.2 Calculation of effective nonlinear coefficient. 117
3.3.1.3 Walk-off in birefringent phase matching. 118
3.3.2 Quasi-phase-matching. 122
3.3.3 Comparison of phase matching methods. 130
3.3.4 Phase-matching acceptance bandwidths. 132

3.4 Optical parametric oscillators. 136
3.4.1 Parametric oscillator threshold. 136
3.4.1.1 Triply-resonant OPO. 142
3.4.1.2 Doubly-resonant OPO. 144
3.4.1.3 Singly-resonant OPO. 147
3.4.2 Above threshold behaviour. 150
3.4.2.1 Doubly-resonant OPOs. 152
3.4.2.2 Singly-resonant OPOs. 153
3.4.3 Tuning and stability considerations. 155
3.4.3.1 Singly-resonant OPOs. 156
3.4.3.2 Doubly-resonant OPOs. 160

3.5 Nonlinear optics with focused Gaussian beams. 176

3.6 Pump source requirements. 181

3.7 Conclusions. 185

3.8 References. 188

4. High-Power, High-Quality Diode-Laser-Based Pump Sources. 202

4.1 Introduction. 202

4.2 Optically-injected diode laser systems. 210

4.2.1 Travelling-wave amplifiers. 210

4.2.2 Monolithic Master-Oscillator/Power Amplifiers. 218

4.2.3 Injection-Locked High-Power Diode Lasers. 220

4.3 Modelling of injection-locked broad-area diode lasers. 226

4.4 Conclusions. 240

4.5 References. 241

5. Injection-Locked Broad-Area Diode Laser System: Design and Characterisation. 252

5.1 Introduction. 252

5.2 Characterisation of diode lasers. 252

5.2.1 Single-mode master laser. 252

5.2.2 High-power broad-area laser. 260

5.3 Optical system design. 264

5.4 Experimental implementation. 280

5.5 Operating characteristics. 288

5.6 Conclusions. 294

5.7 References. 297

6. Injection-Locked Broad-Area Diode Laser Pumped 946-nm Nd:YAG Laser. **298**

6.1 Introduction. 298

6.2 CW operation. 298

6.2.1 System design and projected performance. 298

6.2.2 Results and discussion. 304

6.3 Q-switched operation. 309

6.4 Second harmonic generation. 315

6.5 Conclusions. 320

6.6 References. 323

7. Diode-Laser Pumped Doubly-Resonant Optical Parametric Oscillator. **325**

7.1 Introduction. 325

7.2 System design. 325

7.2.1 PPLN design. 326

7.2.2 Mirrors and cavity configuration. 331

7.2.3 Threshold calculations. 336

7.2.4 Stability calculations. 340

7.3 Experimental results. 344

7.3.1 Injection-locked broad-area diode laser pumping. 344

7.3.2 Single-mode diode laser pumping. 350

7.3.3 Active cavity length control. 354

7.4 Conclusions. 362

7.5 References. 365

8. Conclusions. 367

8.1 References. 374

A1. Spatial Beam Quality and M^2. 377

A1.1 Propagation of non-diffraction-limited beams. 377

A1.2 Measurement of beam radius and M^2. 381

A1.3 References. 385

A2. Publications and Conference Proceedings. 386

A2.1 Publications. 386

A2.2 Conference proceedings. 386

Acknowledgements. 388

1. Introduction.

1.1 Background.

The pumping of optical parametric oscillators (OPOs) and solid-state lasers with semiconductor-diode-laser based sources has a number of attractions. The high efficiency and small physical dimensions of diode lasers enable efficient, compact, all-solid-state devices to be constructed. The wide range of operating wavelengths for which diode lasers can be constructed allows pump-wavelength requirements to be met for many solid-state laser materials and OPO configurations while the tunability of individual diodes enables optimisation of pump absorption in solid-state lasers and tuning of output wavelengths in OPOs. Finally, the fact that they are mass-produced results in diode lasers generally being considerably less expensive than equivalent laser systems based on other technologies.

Despite these attractive features, the inherent performance limitations of diode lasers have, in many cases, proved restrictive in these pumping applications. Chief among these limitations is the problem of obtaining high output powers while maintaining a high degree of spatial and spectral quality. The ideal pump source, in the majority of applications, would have an output which was spatially diffraction-limited while being spectrally narrow, exhibiting single longitudinal-mode operation. In the case of diode lasers based on the AlGaAs material system, which form the basis of all the work described in this thesis, the maximum power density tolerable at the facet before catastrophic damage occurs is of the order of 10^6 Wcm^{-2} [1,2]. Given that typical diode lasers have fact dimensions of a few μm^2 this damage restriction clearly limits the output power to a few 10s of mW. While the maximum output power can be increased by broadening the active region in the plane of the semiconductor junction, thus increasing the facet area, this results in multiple transverse mode operation of the device and an output which is many times above the diffraction limit

in this direction. Such devices are also, in general, spectrally broad emitting on multiple transverse and longitudinal modes over, typically, a few nanometers.

The need for optical confinement in the plane of the junction, a so-called narrow-stripe geometry, if predictable transverse mode structures and, ultimately, single-transverse-mode operation are to be achieved, has long been recognised [3,4,5].Combined with similar confinement of the current, this was also instrumental in achieving low-threshold operation. This confinement has been achieved using a variety of techniques over the years including gain guiding [6], buried-heterostructure construction [7] and growth over a channelled substrate [8]. Nevertheless, the restrictions imposed by facet damage remain and, although output powers of several hundred mW have been demonstrated in isolated cases [9,10], commercially available narrow-stripe single-mode diode lasers are currently limited to output powers of ≈100mW. Although considerably higher output powers are available from diode lasers, these are only achieved by broadening the active area resulting in far from diffraction-limited performance.

Diode lasers have proved highly successful as pump sources for solid state lasers [11,12] with the operating wavelengths available from AlGaAs based diodes being particularly suited to the pumping of Nd^{3+}-doped gain media. It is important, however, when discussing the effects of pump beam quality, to distinguish between the two pump geometries commonly used in solid-state lasers. Solid-state lasers pumped by flashlamps, and the earliest examples of diode-pumped solid-state lasers, utilised a transverse pumping geometry allowing a number of pump sources to be arranged around the gain medium, pumping in a direction normal to the axis of the laser. The pump power can, however, be coupled into the laser mode with considerably higher efficiency by pumping longitudinally along the axis of the laser in an end-pumped geometry. This results in an improvement in the overlap between the pump and laser modes, leading to higher efficiency and improved transverse-mode control.

The relatively high brightness available from high-power diode laser sources has proved valuable in many end-pumped solid-state lasers. However, the poor beam quality available from these devices, when compared to other types of laser, often

prevents the full potential of the end-pumped geometry for high-efficiency, low-threshold operation from being exploited, as a large laser mode must generally be used to maintain overlap with the non-diffraction-limited pump beam. To demonstrate low-threshold, high-efficiency operation it would, therefore, be desirable to obtain high output powers in a near-diffraction-limited beam from a diode-laser-based pump source. This is particularly true in the case of quasi-three-level lasers (lasers based on transitions having a significant lower-level population), where any increase in the laser mode volume results in increased reabsorption losses, raising the threshold and reducing the efficiency [13].

In the case of OPOs the requirements are more stringent still. A diffraction-limited pump beam, while desirable in the case of solid-state lasers, is generally essential in the case of OPOs. For reasonably low threshold pump powers, continuous-wave OPOs generally require near-confocal focusing, and therefore small mode waists, in relatively long crystals (10s of mm) over the length of which overlap between pump and OPO modes must be maintained. It is also generally necessary, in the case of cw OPOs, to resonate several different wavelengths simultaneously in doubly-resonant (DRO) or pump resonant devices if thresholds less than $\approx$1W are required. This places stringent requirements on the frequency stability of the pump source, essentially demanding a stable single-longitudinal-mode output, if stable operation of the OPO is to be maintained [14]. If these requirements can be met, diode-laser-pumped cw OPOs have the potential to be compact and efficient sources of tunable radiation in the important near-mid infrared region of the spectrum and several such devices have been demonstrated [15,16].

The field of cw OPOs has been transformed, within the timescale of the work presented in this thesis, by the widespread availability of quasi-phase-matched nonlinear optical materials, in particular periodically-poled lithium niobate (PPLN). These materials offer significantly higher effective nonlinear coefficients than conventional birefringently phase-matched materials, resulting in reduced OPO thresholds. Thus, they particularly lend themselves to the development of cw OPOs pumped by diode lasers and have allowed the demonstration of an extremely low-threshold diode-pumped doubly-resonant OPO [17] as well as a singly-resonant

device with a threshold low enough to allow pumping by a diode-amplifier system [18].

The problem of obtaining diffraction-limited, single-longitudinal-mode performance at high output powers from diode lasers has been approached in a number of ways with varying degrees of success. Early attempts to produce phased arrays of individual single-mode emitters [19,20] were largely unsuccessful, although further development of similar devices has led to significant near-diffraction-limited output powers [21,22]. The use of various schemes which amplify the diffraction-limited output of a low-power single-mode diode laser has been more successful. These have included resonant amplification by standard broad-area diode lasers (usually termed injection-locking) [23,24], broad-area travelling-wave amplifiers [25,26] and tapered travelling-wave amplifiers [27,28]. This last method has resulted in the highest output powers from a near-diffraction-limited diode-laser source to date, of 5.25W [28], although commercial devices of this type are limited to ≈500mW. Tapered amplifiers monolithically integrated with single-mode master lasers [29] have become commercially available in recent years although, like commercially available tapered amplifiers, they remain considerably more costly than conventional diode lasers. The most recent development in this field has been the angled-grating distributed-feedback laser or α-DFB, which uses an angled gain stripe and Bragg-grating in a broad-area device to give single-mode diffraction-limited performance [30,31]. A 500mW device based on this technology is commercially available.

1.2 Scope of work presented in this thesis.

The work presented in this thesis covers three fields. The first of these is the development and characterisation of a diode-laser-based pump source having a single-longitudinal-mode, near-diffraction-limited output of several hundred mW. Secondly, the end-pumping of quasi-three-level solid-state lasers is discussed and the use of the injection-locked diode pump source in such an application is demonstrated by the pumping of a 946-nm Nd:YAG laser. Finally, the operation of cw OPOs is considered and such a device is demonstrated, pumped both by the previously developed source and a single-mode diode laser.

The remainder of this thesis is broadly divided into background theory and experimental sections. In chapter 2 the theoretical background to the operation of end-pumped quasi-three-level lasers is developed. Particular attention is paid to the optimisation of the end-pumped geometry and the effects of pump beam quality on the operation of such lasers. A model for the end-pumping of the 946-nm Nd:YAG laser is developed, allowing the performance of the system investigated experimentally to be predicted. Chapter 3 sets out the basic principles of nonlinear optics which lead on to the operational theory of optical parametric oscillators, including threshold and stability. The stability criteria of DROs are discussed in some detail due to their relevance to the experimental work described later. The relative merits of the various OPO configurations are compared in the context of diode pumping. Having determined the requirements placed on a pump source by end-pumped solid-state lasers and OPOs in the two proceeding chapters, chapter 4 discusses the various methods used to achieve these pump-source requirements with diode lasers. The chosen technique, injection-locking of a broad-area diode laser, is described in detail and theoretical modelling used to demonstrate some of the properties of such a system. Each of these three chapters also contains a more detailed introduction to their respective field than the brief discussion of section 1.1.

Of the experimental work, the design, construction and characterisation of the injection-locked broad-area diode laser system is described in chapter 5. The design and operation of a quasi-three-level 946-nm Nd:YAG laser pumped by the injection-locked system is described in chapter 6. The results of cw, Q-switched and frequency-doubled operation of this laser are presented and these results are discussed in the context of the pump source used and compared to those obtained with alternative sources. Chapter 7 details the construction and characterisation of a doubly-resonant OPO based on PPLN. The operational characteristics of the DRO are investigated when pumped by the injection-locked system and directly by a low-power single-mode diode laser. The threshold and tuning behaviour and electronic stabilisation of the DRO are described. Finally, the work carried out is summarised and conclusions drawn in chapter 8. Possible directions for future work in the fields investigated are also discussed.

1.3 Relevant chronology.

To give a picture of the way in which the three fields of relevance to this thesis have developed, some of the key historical results of interest are presented here in chronological order. Note that this table is by no means exhaustive for each field and the results mentioned are generally those most directly relevant to the themes of this thesis. In particular, the references to diode-laser-pumped solid-state lasers generally concentrate on end-pumped and quasi-three-level systems. Unless stated otherwise, Nd:YAG laser references are for 1.064μm operation.

Year	Fields of relevance: Diode-laser-pumped solid-state lasers	Continuous-wave optical parametric oscillators	High-quality diode-laser-based pump sources	Comments	Refs.
1962			•	First demonstration of diode lasers (GaAs and GaAsP) pulsed operation at cryogenic temperatures.	[32,33]
1964	•			First demonstration of a diode-laser pumped solid-state laser. $CaF_2:U^{3+}$ gain medium.	[34]
1964	•			Demonstration of first Nd:YAG laser (lamp pumped).	[35]
1965		•		First demonstration of optical parametric oscillation in near-degenerate $LiNbO_3$ DRO pumped by SHG of Q-switched 1.06μm Nd:$CaWO_4$ laser.	[36]
1967			•	Stripe geometry used to control diode laser transverse modes (pulsed operation at cryogenic temperatures).	[3]
1968	•			First diode-laser pumped Nd:YAG laser demonstrated (pulsed operation, diode laser operated at 170K).	[37]
1968		•		First demonstration of cw OPO. Degenerate DRO using $Ba_2NaNb_5O_{15}$ pumped at 0.532μm. 45mW threshold.	[38]
1968		•		Non-degenerate, visible-signal cw OPO. $LiNbO_3$ DRO pumped by 0.5145μm Ar-ion laser. 410mW threshold.	[39]

Year	Fields of relevance				Refs.
	Diode-laser-pumped solid-state lasers				
		Continuous-wave optical parametric oscillators			
			High-quality diode-laser-based pump sources		
				Comments	
1969	•			Pulsed Nd:YAG laser operation at 946-nm and doubling to 473nm demonstrated. Flashlamp pumping, Nd:YAG cooled to ≈-40°C.	[40]
1969		•		Non-degenerate ring-cavity DRO pumped by 0.5145μm Ar-ion laser. 150mW threshold. Ring geometry gave improved efficiency and stability (no back-conversion).	[41]
1969	•			First cw Nd:YAG laser pumped by a diode source (used GaAsP LEDs at 77K rather than diode lasers).	[42]
1969			•	Single-heterostructure GaAs-AlGaAs diode laser operated at room temperature (pulsed operation).	[43]
1970			•	Room temperature pulsed operation of double-heterostructure GaAs-AlGaAs diode laser.	[44]
1970			•	Room-temperature cw operation of double-heterostructure diode lasers.	[45,46]
1971			•	Room temperature cw operation of current-confining stripe geometry double-heterostructure diode laser	[47]
1971	•			CW operation of a diode (LED) pumped Nd:YAG laser with diodes and laser crystal at room temperature.	[48]
1972			•	Proton-bombardment used to define conductive stripe in stripe-geometry diode laser.	[6]
1972	•			End-pumped operation of an Nd:YAG laser pumped by a GaAs diode laser. Pulsed operation, diode laser cryogenically cooled.	[49]
1973		•		Study of stability of cw DROs highlights need for stable pump frequency / DRO cavity length. Near degenerate $Ba_2NaNb_5O_{15}$ DRO pumped at 0.532μm and 0.5145μm shows single-mode operation and 3mW threshold.	[14]
1974			•	Buried-heterostructure GaAs-AlGaAs diode laser shows low-threshold room-temperature TEM_{00} operation.	[7]
1976	•			Room-temperature, cw operation Nd:YAG laser end-pumped by an AlGaAs superluminescent diode.	[50]

Year	Fields of relevance: Diode-laser-pumped solid-state lasers	Continuous-wave optical parametric oscillators	High-quality diode-laser-based pump sources	Comments	Refs.
1977			•	Channelled-substrate planar diode-laser structure gives transverse mode control with simple fabrication.	[51]
1978			•	Room-temperature operation of GaAs-AlGaAs quantum-well diode lasers grown by MOCVD.	[52]
1978	•			Room temperature, cw operation at of 941-nm laser in Nd:CAMGAR. End pumping by argon-ion laser.	[53]
1979			•	Gain-guided 5-stripe diode laser array produces 100mW/facet with low divergence.	[19]
1983			•	Output power of 2.6W per facet obtained from 40-stripe gain-guided diode-laser array.	[54]
1984			•	Stable (non-diffraction-limited) far field up to 250mW pulsed output power obtained from ten-element index-guided diode laser array.	[55]
1985	•			First Nd:YAG laser end-pumped by a diode laser. AlGaAs diode laser pump source, all room-temperature operation, 2.3mW threshold, 25% slope efficiency.	[56]
1985			•	105mW near diffraction-limited output from injection-locked 10-element gain-guided array for 3mW input.	[23]
1986			•	100mW near diffraction-limited cw output from single-pass broad-area travelling-wave diode-laser amplifier for 1.7mW input from single-mode diode laser.	[57]
1986		•		Degenerate triply-resonant OPO using MgO:$LiNbO_3$ pumped at 0.532μm used for investigation of squeezed states of light.	[58]
1987	•			Highly stable monolithic Nd:YAG ring resonator axially pumped by 200mW diode-laser array.	[59]
1987	•			946-nm Nd:YAG laser end-pumped at room temperature by dye laser. 11.5mW threshold, 11% slope efficiency.	[13]

Year	Fields of relevance: Diode-laser-pumped solid-state lasers	Continuous-wave optical parametric oscillators	High-quality diode-laser-based pump sources	Comments	Refs.
1987	•			CW diode-laser end-pumping of room-temperature 946-nm Nd:YAG laser. 10mW threshold, 16% slope efficiency close to threshold.	[60]
1987	•			CW operation and intracavity doubling of 946-nm Nd:YAG laser end-pumped by diode-laser arrays. ≈25mW threshold and 40% slope efficiency.	[61]
1987			•	510mW near diffraction-limited output from injection-locked 40-element gain-guided array for 11mW input.	[24]
1987		•		Type-II near-degenerate KTP DRO pumped by 0.528μm Ar-ion laser with 100mW threshold used to investigate squeezed states of light.	[62]
1987		•		Near-degenerate type-II KTP DRO pumped by stabilised 0.528μm Ar-ion laser. 80mW threshold. Active stabilisation of DRO cavity used.	[63]
1988			•	200mW output with ≈70% in single, near-diffraction-limited lobe obtained from ten-element index-guided diode laser array.	[64]
1988			•	400mW near-diffraction-limited output for ≈10mW input from injection-locked broad-area diode laser.	[65]
1989	•			3.1mW blue light generated by intracavity doubling in $KNbO_3$ of 946-nm Nd:YAG laser end-pumped by broad-area AlGaAs diode laser.	[66]
1989	•	•		Monolithic near-degenerate ring DRO pumped at 0.532μm by SHG of diode-pumped Nd:YAG laser. 12mW threshold and stable single-mode operation.	[67]
1990			•	500mW output power demonstrated from commercial, nominally-100mW single-mode diode laser.	[68]
1991			•	2.5W cw near diffraction-limited output from pulsed double-pass broad-area travelling-wave diode amplifier for ≈100mW Ti:sapphire laser input.	[69]

Year	Fields of relevance				
	Diode-laser-pumped solid-state lasers				
		Continuous-wave optical parametric oscillators			
			High-quality diode-laser-based pump sources		
				Comments	Refs.
1992	•			Q-switched operation of 946-nm Nd:YAG laser pumped by diode-laser array.	[70]
1992	•			7.6W cw TEM_{00} output and 46% slope efficiency from Nd:YAG laser end-pumped by fibre-coupled diode lasers.	[71]
1992			•	3.3W cw diffraction-limited output from single-pass broad-area diode amplifier for 400mW Ti:sapphire input.	[25]
1992			•	21W near-diffraction-limited output from single-pass diode amplifier for 500mW Ti:sapphire input (pulsed).	[26]
1992			•	2W cw diffraction-limited output from tapered diode-amplifier for 25mW single-mode-diode input.	[27]
1992			•	1.1W cw diffraction-limited output from monolithic integrated diode master-oscillator/tapered amplifier.	[29]
1993	•			60W cw TEM_{00} output with 26% efficiency obtained from Nd:YAG laser end pumped by multiple diode modules.	[72]
1993			•	5.25W cw near diffraction-limited output from tapered diode-amplifier for 200mW Ti:sapphire input.	[28]
1993			•	3W cw diffraction-limited output from monolithic diode master-oscillator/tapered amplifier (InGaAs).	[73]
1993		•		First cw SRO demonstrated. Type-II near-degenerate KTP device pumped at 0.532μm. 1.4W threshold.	[74]
1993			•	600mW single transverse and longitudinal-mode output from index-guided, triple-quantum-well diode laser.	[10]
1993			•	1W cw output with 1.7×diffraction-limited central lobe from 20-element antiguided array.	[22]
1993		•		Semi-monolithic type-II KTP near-degenerate DRO pumped by 0.531μm Kr-ion laser. 22mW threshold, stabilised single-mode operation and signal-idler heterodyne locking demonstrated.	[75]
1994	•			Stabilised operation of laser-diode-array pumped 946-nm Nd:YAG laser and two-stage doubling to 473nm and 237nm.	[76]

Year	Fields of relevance				
	Diode-laser-pumped solid-state lasers				
		Continuous-wave optical parametric oscillators			
			High-quality diode-laser-based pump sources		
				Comments	Refs.
1994	•		•	640mW near diffraction-limited output from injection-locked 20-element diode-laser array. Used to pump Nd:$LaSc_3(BO_3)_4$ microchip laser.	[77]
1994		•		Type-II LBO cw DRO pumped by 364nm Ar-ion laser. Split cavity used to obtain continuous signal-idler tuning with fixed pump frequency.	[78]
1994		•		Type-I LBO cw DRO pumped by Ti:sapphire laser demonstrates broad tuning through tuning of pump.	[79]
1994		•		Pump-enhanced (pump and idler resonant) SRO with 1W external threshold using type-II LBO pumped by 0.514μm Ar-ion laser.	[80]
1995		•		Near-degenerate type-II KTP DRO pumped at 0.523mm by SHG of diode-pumped Nd:YLF laser. Single-mode operation and continuous tuning by simultaneous control of DRO cavity length and pump frequency.	[81]
1995		•	•	Near-degenerate doubly-resonant PPLN DRO pumped by 980-nm monolithic diode master-oscillator/tapered amplifier. 61mW threshold observed.	[82]
1995		•	•	Triply-resonant type-II KTP OPO with 6mW threshold pumped by single-mode diode laser and injection-locked diode-laser array.	[83,15]
1995		•	•	Pump-enhanced (pump and idler resonant) type-II KTP SRO with 50mW threshold pumped by single-mode diode laser and injection-locked diode-laser array.	[15]
1995	•		•	305mW cw, 1.4×diffraction-limited, 670-nm output for 15mW input from injection-locked broad-area diode laser. Used to pump single-mode cw Cr^{3+}:LiSAF laser.	[84]
1996	•		•	300mW near diffraction-limited output from self injection-locked 670nm broad-area diode laser used to pump femtosecond Cr^{3+}:LiSAF laser.	[85]

Year	Fields of relevance: Diode-laser-pumped solid-state lasers	Continuous-wave optical parametric oscillators	High-quality diode-laser-based pump sources	Comments	Refs.
1996			•	1W single-mode diffraction-limited output from angled-grating DFB (α-DFB) diode laser.	[30]
1996		•		CW SRO based on PPLN pumped by multimode diode-pumped Nd:YAG laser. 2.6-4.5W threshold.	[86]
1996	•			3W output with ≈33% slope efficiency obtained from end-pumped 946-nm Nd:YAG laser pumped by beam-shaped diode-laser bar.	[87]
1996	•			6W with ≈43% efficiency obtained from Nd:YAG laser end-pumped by beam-shaped multiple diode-laser bar.	[88]
1996		•		Linear and ring-cavity PPLN SROs pumped by Nd:YAG laser. Thresholds as low as 2.9W and 3.3W. Idler output powers as high as 3.6W.	[89]
1997		•		CW KTP SRO located within Ti:sapphire laser cavity. 4W external threshold, near-optimum down conversion.	[90]
1997			•	10W output from 40-element antiguided array with 60% of power in 2×diffraction-limited central lobe (pulsed).	[21]
1997			•	2.2W cw diffraction-limited output from monolithic diode master-oscillator/tapered amplifier.	[91]
1997	•		•	≈500mW diffraction-limited output at 672-nm from tapered diode amplifier for ≈25mW input. Used to pump Kerr-lens mode-locked Cr:LiSAF laser.	[92]
1997			•	5W cw diffraction-limited output from InGaAs tapered diode-amplifier for ≈165mW input from grating-tuned tapered-amplifier master-oscillator.	[93]
1997	•			500mW output at 473nm obtained by external resonant doubling of output of diode-pumped monolithic-ring 946-nm Nd:YAG laser.	[94]
1997		•	•	Pump-enhanced (signal/idler resonant) RTA SRO pumped by diode-laser tapered amplifier system.	[16]
1997		•		PPLN pump-enhanced SRO pumped by diode-pumped Nd:YAG laser. 260mW threshold and stable, single-mode operation.	[95]

Year	Fields of relevance				
	Diode-laser-pumped solid-state lasers				
		Continuous-wave optical parametric oscillators			
			High-quality diode-laser-based pump sources		
				Comments	Refs.
1998		•		Type-I $MgO:LiNbO_3$ DRO pumped at 0.532μm by SHG of diode-pumped Nd:YAG laser. Long-term stable operation and tuning by use of FM-sideband locking.	[96]
1998		•		PPLN SRO pumped by Nd:YAG laser. OPO and sum-frequency mixing stages in single PPLN crystal to produce 2.5W cw at 0.629μm.	[97]
1998		•		Near-degenerate Type-II KTP DRO pumped at 0.532μm by SHG of diode-pumped Nd:YAG laser. 7mW threshold, long-term single-mode operation, signal-idler beat signal locked to external reference.	[98]
1998		•	•	Pump-enhanced (pump/signal resonant) PPLT SRO with 360mW threshold pumped by 925-nm InGaAs diode tapered-amplifier.	[99]
1998		•		Long-term (18h) single-mode operation of type-I near degenerate $MgO:LiNbO_3$ DRO by use of FM-locking.	[100]
1998	•		•	48% cw slope-efficiency from 946-nm Nd:YAG laser pumped by injection-locked broad-area diode laser.	[101]
1998		•	•	Singly-resonant cw PPLN OPO with 800mW threshold pumped by diode tapered-amplifier system.	[18]
1998		•	•	PPLN DRO with 16mW threshold pumped by injection-locked broad-area diode laser and single-mode diode.	[17]
1998		•		CW PPLN SRO intracavity to diode-pumped Nd:YVO_4 laser. 310mW external threshold, 70mW idler output.	[102]

1.4 References.

1 C.H. Henry, P.M. Petroff, R.A. Logan and F.R. Merritt, "Catastrophic damage of $Al_xGa_{1-x}As$ double-heterostructure laser material," J. Appl. Phys. **50**, 3721-3732 (1979).

2 K. Wakao, N. Takagi, K. Shima, K. Hanamitsu, K.-I. Hori and M. Takusagawa, "Catastrophic degradation level of visible and infrared GaAlAs lasers," Appl. Phys. Lett. **41**, 1113-1115 (1982).

3 J.C. Dyment, "Hermite-Gaussian mode patterns in GaAs junction lasers," Appl. Phys. Lett. **10**, 84-86 (1967).

4 T.H. Zachos, "Gaussian beams from GaAs junctions," Appl. Phys. Lett. **12**, 318-320 (1968).

5 S. Wang, C.-Y. Chen, A. S.-H. Liao and L. Figueroa, "Control of mode behaviour in semiconductor lasers," IEEE J. Quantum Electron. **QE-17**, 453-468 (1981).

6 J.C. Dyment, L.A. D'Asaro, J.C. North, B.I. Miller and J.E. Ripper, "Proton-bombardment formation of stripe-geometry heterostructure lasers for 300 K CW operation," Proc. IEEE 60, 726-728 (1972).

7 T. Tsukada, "GaAs-$Ga_{1-x}Al_xAs$ buried-heterostructure injection lasers," J. Appl. Phys. **45**, 4899-4906 (1974).

8 K. Aiki, M. Nakamura, T. Kuroda, J. Umeda, R. Ito, N. Chinone and M. Maeda, "Transverse mode stabilized $Al_xGa_{1-x}As$ injection lasers with channeled-substrate-planar structure," IEEE J. Quantum Electron. **QE-14**, 89-94 (1978).

9 H. Jaeckel, G.-L. Bona, P. Buchmann, H.P. Meier, P. Vettiger, W.J. Kozlovsky and W. Lenth, "Very high-power (425mW) AlGaAs SQW-GRINSCH ridge laser with frequency-doubled output (41mW at 428 nm)," IEEE J. Quantum Electron **27**, 1560-1567 (1991).

10 O. Imafuji, T. Takayama, H. Sugiura, M. Yuri, H. Naito, M. Kume and K. Itoh, "600 mW single-mode GaAlAs triple-quantum-well laser with a new index-guided structure," IEEE J. Quantum Electron. **29**, 1889-1894 (1993).

11 T.Y. Fan and R.L. Byer, "Diode laser-pumped solid-state lasers," IEEE J. Quantum Electron. **24**, 895-912, (1988).

12 D.W. Hughes and J.R.M. Barr, "Laser diode pumped solid state lasers," J. Phys. D: Appl. Phys. **25**, 563-586, (1992).

13 T.Y. Fan and R.L. Byer, "Modeling and cw operation of a quasi-three-level 946nm Nd:YAG laser," IEEE J. Quantum. Electr. QE-23, 605-612, (1987).

14 R.G. Smith, "A study of factors affecting the performance of a continuously-pumped doubly-resonant optical parametric oscillator," IEEE J. Quantum Electron. **QE-9**, 530-541 (1973).

15 M. Scheidt, B. Beier, R. Knappe, K.J. Boller and R. Wallenstein, "Diode-laser-pumped continuous-wave KTP optical parametric oscillator," J. Opt. Soc. Am. B **12**, 2087-2094 (1995).

16 M. Scheidt, B. Beier, K.J. Boller and R. Wallenstein, "Frequency-stable operation of a diode-pumped continuous-wave $RbTiOAsO_4$ optical parametric oscillator," Opt. Lett. **22**, 1287-1289 (1997).

17 I.D. Lindsay, G.A. Turnbull, M.H. Dunn and M. Ebrahimzadeh, "Doubly-resonant continuous-wave optical parametric oscillator pumped by a single-mode diode laser," Opt. Lett. **23**, 1889-1891 (1998).

18 M.E. Klein, D.-H. Lee, J.-P. Meyn, B. Beier, K.-J. Boller and R. Wallenstein, "Diode-pumped continuous-wave optical parametric oscillator," Post-deadline paper CPD1.12, Conference on Lasers and Electro-Optics-Europe September 1998, OSA Technical Digest Series 1998, Optical Society of America, Washington.

19 D.R. Scifres, R.D. Burnham and W. Streifer, "Phase-locked semiconductor laser array," Appl. Phys. Lett. **33**, 1015-1017 (1979).

20 D.R. Scifres, R.D. Burnham, C. Lindström, W. Streifer and T.L. Paoli, "Phase-locked (GaAl)As laser emitting 1.5 W CW per mirror," Appl. Phys. Lett. **42**, 645-647 (1983).

21 H. Yang, L.J. Mawst, M. Nesnidal, J. Lopez, A. Bhattacharya and D. Botez, "10 W near-diffraction-limited peak pulsed power from Al-free, 0.98μm-emitting phase-locked antiguided arrays," Electron. Lett. **33**, 136-137 (1997).

22 C. Zmudzinski, D. Botez, L.J. Mawst, C. Tu and L. Frantz, "Coherent 1W continuous wave operation of large-aperture resonant arrays of antiguided diode lasers," Appl. Phys. Lett. **62**, 2914-2916 (1993).

23 L. Goldberg, H.F. Taylor, J.F. Weller and D.R. Scifres, "Injection-locking of coupled-stripe diode laser arrays," Appl. Phys. Lett. **46**, 236-238 (1985).

24 L. Goldberg and J.F. Weller, Appl. Phys. Lett. **50**, "Injection locking and single-mode fibre coupling of a 40-element laser diode array," 1713-1715 (1987).

25 L. Goldberg, D. Mehuys and D.C. Hall, "3.3W CW diffraction limited broad area semiconductor amplifier," Electron Lett. **28**, 1082-1084 (1992).

26 L. Goldberg and D. Mehuys, "21W broad area near-diffraction-limited semiconductor amplifier," Appl. Phys. Lett. **61**, 633-635 (1992).

27 D. Mehuys, D.F. Welch and L. Goldberg, "2.0W CW, diffraction-limited tapered amplifier with diode injection," Electron. Lett. **28**, 1944-1946 (1992)

28 D. Mehuys, L. Goldberg and D.F. Welch, "5.25-W near-diffraction-limited tapered-stripe semiconductor optical amplifier," IEEE Photon. Technol. Lett. **5**, 1179-1182 (1993).

29 D.F. Welch, R. Parke, D. Mehuys, A. Hardy, R. Lang, S. O'Brien and S. Scifres, "1.1W CW, diffraction-limited operation of a monolithically integrated flared-amplifier master oscillator power amplifier," Electron. Lett. **28**, 2011-2013 (1992)

30 S.D. DeMars, K.M. Dzurko, R.J. Lang, D.F. Welch, D.R. Scifres and A. Hardy, "Angled-grating distributed feedback laser with 1W cw single-mode diffraction-limited output at 980 nm," Conference on Lasers and Electro-Optics 1996, OSA 1996 Technical Digest Series volume 9, p. 77, Optical Society of America, Washington (1996).

31 R.J. Lang, K. Dzurko, A.A. Hardy, S. Demars, A. Schoenfelder and D.F. Welch, "Theory of grating-confined broad-area lasers," IEEE J. Quantum Electron. **34**, 2196-2210 (1998).

32 R.N. Hall, G.E. Fenner, J.D. Kingsley, T.J. Soltys and R.O. Carlson, "Coherent Light Emission from GaAs Junctions," Phys. Rev. Lett. **9**, 366-368, (1962).

33 N. Holonyak Jr. and S.F. Bevacqua, "Coherent (visible) light emission from $Ga(As_{1-x}P_s)$ junctions," Appl. Phys. Lett. **1**, 82-83, (1962).

34 R.J. Keyes and T.M. Quist, "Injection luminescent pumping of $CaF_2:U^{3+}$ with GaAs diode lasers," Appl. Phys. Lett. **4**, 50-52, (1964).

35 J.E. Geusic, H.M. Marcos and L.G. Van Uitert, "Laser oscillations in Nd-doped yttrium aluminum, yttrium gallium and gadolinium garnets," Appl. Phys. Lett. **4**, 182-184, (1964).

36 J.A. Giordmaine and R.C. Miller, "Tunable coherent parametric oscillation in $LiNbO_3$ at optical frequencies," Phys. Rev. Lett. **14**, 973-976 (1965).

37 M. Ross, "YAG laser operation by semiconductor laser pumping," Proc. IEEE **56**, 196-197, (1968).

38 R.G. Smith, J.E. Geusic, H.J. Levinstein, J.J. Rubin, S. Singh and L.G. Van Uitert, "Continuous optical parametric oscillator in $Ba_2NaNb_5O_{15}$," Appl. Phys. Lett. **12**, 308-309 (1968).

39 R.L. Byer, M.K. Oshman, J.F. Young and S.E Harris, "Visible cw parametric oscillator," Appl. Phys. Lett. **13**, 109-111 (1968).

40 R.W. Wallace and S.E. Harris, "Oscillation and doubling of the 0.946-μ line in Nd^{3+}:YAG," Appl. Phys. Lett. **15**, 111-112, (1969).

41 R.L. Byer, A. Kovrigin and J.F. Young, "A cw ring-cavity parametric oscillator," Appl. Phys. Lett. **15**, 136-137 (1969).

42 R.B. Allen and S.J. Scalise, "Continuous operation of a YAlG:Nd laser by injection luminescent pumping," Appl. Phys.Lett. **14**, 188-190, (1969).

43 I. Hayashi, M.B. Panish and P.W. Foy, "A low-threshold room-temperature injection laser," IEEE J. Quantum Electron. **5**, 211-212, (1969).

44 M.B. Panish, I. Hayashi and S. Sumski, "Double-heterostructure injection lasers with room temperature thresholds as low as 2300 A/cm2," Appl. Phys. Lett. **16**, 326-327, (1970).

45 Zh.I. Alferov, V.M. Andreev, D.Z. Garbuzov, Yu.V. Zhilyaev, E.P. Morozov, E.L. Portnoi and V.G. Trofim, "Effect of the heterostructure parameters on the laser threshold current and the realisation of continuous generation at room temperature," Fiz. Tekn. Polupr. **4**, 1826, (1970). [English translation, Soviet Physics - Semiconductors **4**, 1573, (1971).]

46 I. Hayashi, M.B. Panish, P.W. Foy and S. Sumski, "Junction lasers which operate continuously at room temperature," Appl. Phys. Lett. **17**, 109-111, (1970).

47 J.E. Ripper, J.C. Dyment, L.A. D'Asaro and T.L. Paoli, "Stripe-geometry double heterostructure junction lasers: mode structure and cw operation above room temperature," Appl. Phys. Lett. **18**, 155-157 (1971).

48 F.W. Ostermayer, Jr., R.B. Allen and E.G. Dierschke, "Room temperature cw operation of a $GaAs_{1-x}P_x$ diode-pumped YAG:Nd laser," Appl. Phys. Lett. **19**, 289-292, (1971).

49 L.J. Rosenkrantz, "GaAs diode-pumped Nd:YAG laser," J. Appl. Phys. **43**, 4603-4605, (1972).

50 K. Washio, K. Iwamoto, K. Inoue, I. Hino, s. Matsumoto and F. Saito, "Room-temperature cw operation of an efficient miniaturized Nd:YAG laser end-pumped by a superluminescent diode," Appl. Phys. Lett. **29**, 720-722, (1976).

51 K. Aiki, M. Nakamura, T. Kuroda and J. Umeda, "Channeled-substrate planar structure (AlGa)As injection lasers," Appl. Phys. Lett. **30**, 649-651 (1977).

52 R.D. Dupuis and P.D. Dapkus, "Room-temperature laser operation of quantum-well $Ga_{(1-x)}Al_xAs$-GaAs laser diodes grown by metalorganic chemical vapor deposition," Appl. Phys. Lett. **32**, 295-297, (1978).

53 M. Birnbaum, A.W. Tucker and C.L. Fincher, "cw room-temperature laser operation of Nd:CAMGAR at 0.941 and 1.059 μ," J. Appl. Phys. 49, 2984-2985 (1978).

54 D.R. Scifres, C. Lindström, R.D. Burnham, W. Streifer and T.L. Paoli, "Phase-locked (GaAl)As laser diode emitting 2.6 W CW from a single mirror," Electron. Lett. **19**, 169-171 (1983).

55 Y. Twu, A. Dienes, S. Wang and J.R. Whinnery, "High power coupled ridge waveguide semiconductor laser arrays," Appl. Phys. Lett. **45**, 709-711 (1984).

56 B. Zhou, T.J. Kane, G.J. Dixon and R.L. Byer, "Efficient, frequency-stable laser-diode-pumped Nd:YAG laser," Opt. Lett. **10**, 62-64, (1985).

57 J.R. Andrews, "Traveling-wave amplifier made from a laser diode array," Appl. Phys. Lett. **48**, 1331-1333 (1986).

58 L.-A. Wu, H.J. Kimble, J.L. Hall and H. Wu, "Generation of squeezed states by parametric down conversion," Phys. Rev. Lett. **57**, 2520-2523 (1986).

59 T.J. Kane, A.C. Nilsson and R.L. Byer, "Frequency stability and offset locking of a laser-diode-pumped Nd:YAG monolithic nonplanar ring oscillator," Opt. Lett. **12**, 175-177, (1987).

60 T.Y. Fan and R.L. Byer, "Continuous-wave operation of a room-temperature, diode-laser-pumped, 946-nm Nd:YAG laser," Opt. Lett. **12**, 809-811, (1987).

61 W.P. Risk and W. Lenth, "Room-temperature, continuous-wave, 946-nm Nd:YAG laser pumped by laser-diode arrays and intracavity frequency doubling to 473nm," Opt. Lett. **12**, 993-995, (1987).

62 S. Reynaud, C. Fabre and E. Giacobino, "Quantum fluctuations in a two-mode parametric oscillator," J. Opt. Soc. Am. B **4**, 1520-1524 (1987).

63 A. Heidmann, R.J. Horowicz, S. Reynaud, E. Giacobino and C. Fabre, "Observation of quantum noise reduction on twin laser beams," Phys. Rev. Lett. 59, 2555-2557 (1987).

64 D. Botez, L. Mawst, P. Hayashida, G. Peterson and T.J. Roth, "High-power, diffraction-limited-beam operation from phase-locked diode-laser arrays of closely spaced "leaky" waveguides (antiguides)," Appl. Phys. Lett. **53**, 464-466 (1988).

65 L. Goldberg and M.K. Chun, "Injection-locking characteristics of a 1 W broad stripe laser diode," Appl. Phys. Lett. **53**, 1900-1902 (1988).

66 W.P. Risk, R. Pon and W. Lenth, "Diode laser pumped blue-light source at 473nm using intracavity frequency doubling of a 946 nm Nd:YAG laser," Appl. Phys. Lett. **54**, 1625-1627, (1989).

67 C.D. Nabors, R.C. Eckardt, W.J. Kozlovsky and R.L. Byer, "Efficient, single-axial-mode operation of a monolithic MgO:$LiNbO_3$ optical parametric oscillator," Opt. Lett. **14**, 1134-1136 (1989).

68 D. Welch, R. Craig, W Streifer and D. Scifres, "High reliability, high power, single mode laser diodes," Electron. Lett. **26**, 1481-1483 (1990).

69 L. Goldberg and J.F. Weller, "Broad-area high-power semiconductor optical amplifier," Appl. Phys. Lett. **58**, 1357-1359 (1991).

70 J. Hong, B.D. Sinclair, W. Sibbett and M.H. Dunn, "Frequency-doubled and Q-switched 946-nm Nd:YAG laser pumped by a diode-laser array," Appl. Opt. **31**, 1318-1321, (1992).

71 Y. Kaneda, M. Oka, H. Masuda and S. Kubota, "7.6W of continuous-wave radiation in a TEM00 mode from a laser-diode end-pumped Nd:YAG laser," Opt. Lett. **14**, 1003-1005, (1992).

72 S.C. Tidwell, J.F. Seamans and M.S. Bowers, "Highly efficient 60-W TEM_{00} cw diode-end-pumped Nd:YAG laser," Opt. Lett. **18**, 116-118, (1993).

73 R. Parke, D.F. Welch, S. O'Brien, R. Lang, "3.0-W cw diffraction-limited performance from a monolithically integrated master oscillator power amplifier," Talk CTu14, Conference on Lasers and Electro-Optics 1993, OSA 1993 Technical Digest Series, Optical Society of America, Washington (1993).

74 S.T. Yang, R.C. Eckardt and R.L. Byer, "Continuous-wave singly-resonant optical parametric oscillator pumped by a single-frequency resonantly doubled Nd:YAG laser," Opt. Lett. **18**, 971-973 (1993).

75 D. Lee and N.C. Wong, "Stabilization and tuning of a doubly resonant optical parametric oscillator," J. Opt. Soc. Am. B **10**, 1659-1667 (1993).

76 G. Hollemann, E. Peik and H. Walther, "Frequency-stabilized diode-pumped Nd:YAG laser at 946 nm with harmonics at 473nm and 237 nm," Opt. Lett. **19**, 192-194, (1994).

77 B. Beier, J.-P. Meyn, R. Knappe, K.-J. Boller, G. Huber and R. Wallenstein," A 180 mW Nd:$LaSc_3(BO_3)_4$ single-frequency TEM_{00} microchip laser pumped by an injection-locked diode-laser array," Appl. Phys. B **58**, 381-388 (1994).

78 F.G. Colville, M.J. Padgett and M.H. Dunn, "Continuous-wave, dual-cavity, doubly-resonant, optical parametric oscillator," Appl. Phys. Lett. **64**, 1490-1492 (1994).

79 F.G. Colville, M. Ebrahimzadeh, W. Sibbett and M.H. Dunn, "Continuous-wave LiB_3O_5 optical parametric oscillator pumped by a tunable Ti:sapphire laser," Appl. Phys. Lett. **64**, 1765-1767 (1994).

80 G. Robertson, M.J. Padgett and M.H. Dunn, "Continuous-wave, singly resonant pump-enhanced type II LiB_3O_5 optical parametric oscillator," Opt. Lett. **19**, 1735-1737 (1994).

81 A.J. Henderson, M.J. Padgett, J. Zhang, W. Sibbett and M.H. Dunn, "Continuous frequency tuning of a cw optical parametric oscillator through tuning of its pump source," Opt. Lett. **20**, 1029-1031 (1995).

82 L.E. Myers, R.C. Eckardt, M.M. Fejer and R.L. Byer, "CW diode-pumped optical parametric oscillator in bulk periodically poled LiNbO3," Advanced Solid State Lasers, February 1995, paper PD9, OSA Technical Digest Series 1995, Optical Society of America (Washington), 1995.

L.E. Myers, R.C. Eckardt, M.M. Fejer and R.L. Byer, "CW diode-pumped optical parametric oscillator in bulk periodically poled LiNbO3," Electron. Lett. 31, 1869-1870 (1995).

83 M. Scheidt, B. Beier, K.J. Boller and R. Wallenstein, "Diode-laser-pumped cw optical parametric oscillators of KTP," Conference on Lasers and Electro-Optics, May 1995, OSA Technical Digest Series 1995 vol. **15**, Optical Society of America, Washington.

84 R. Knappe, K.-J. Boller and R. Wallenstein, "Single-mode continuous-wave Cr^{3+}:LiSAF ring laser pumped by an injection-locked 670-nm broad-area diode laser," Opt. Lett. **20**, 1988-1990 (1995).

85 D. Burns, M.P. Critten and W. Sibbett, "Low-threshold diode-pumped femtosecond Cr^{3+}:$LiSrAlF_6$ laser," Opt. Lett. **21**, 477-479 (1996).

86 W.R. Bosenberg, A. Drobshoff, J.I. Alexander, L.E. Myers and R.L. Byer, "Continuous-wave singly-resonant optical parametric oscillator based on periodically poled $LiNbO_3$," Opt. Lett. **21**, 713-715 (1996).

87 W.A. Clarkson, R. Koch and D.C. Hanna, "Room-temperature diode-bar-pumped Nd:YAG laser at 946nm," Opt. Lett. **21**, 737-739, (1996).

88 W.A. Clarkson and D.C. Hanna, "Efficient Nd:YAG laser end pumped by a 20-W diode-laser bar," Opt. Lett. **21**, 869-871, (1996).

89 W.R. Bosenberg, A. Drobshoff, J.I. Alexander, L.E. Myers and R.L. Byer, "93% pump depletion, 3.5-W continuous-wave, singly resonant optical parametric oscillator," Opt. Lett. **21**, 1336-1338 (1996).

90 F.G. Colville, M.H. Dunn and M. Ebrahimzadeh, "Continuous-wave, singly resonant, intracavity parametric oscillator," Opt. Lett. **22**, 75-77 (1997).

91 S. O'Brien, R. Lang, R. Parke, J. Major, D.F. Welch and D. Mehuys, "2.2-W continuous-wave diffraction-limited monolithically integrated master oscillator power amplifier at 854 nm," IEEE Photon. Tech. Lett. **9**, 440-442 (1997).

92 A. Robertson, R. Knappe and R. Wallenstein, "Kerr-lens mode-locked Cr:LiSAF femtosecond laser pumped by the diffraction-limited output of a 672-nm diode-laser master-oscillator power-amplifier system," J. Opt. Soc. Am. B **14**, 672-675 (1997).

93 S. O'Brien, A. Schoenfelder and R.J. Lang, "5-W diffraction-limited InGaAs broad-area flared amplifier at 970 nm," IEEE Photon. Technol. Lett. **9**, 1217-1219 (1997).

94 M. Bode, I. Freitag, A. Tünnermann and H. Welling, "Frequency-tunable 500mW continuous-wave all-solid-state single-frequency source in the blue spectral region," Opt. Lett. **22**, 1220-1222, (1997).

95 K. Schneider, P. Kramper, S. Schiller and J. Mlynek, "Toward an optical synthesizer: a single-frequency parametric oscillator using periodically poled $LiNbO_3$," Opt. Lett. **22**, 1293-1295 (1997).

96 M. Bode, P.K. Lam, I. Freitag, A. Tünnermann, H.-A. Bachor and H. Welling, "Continuously-tunable doubly-resonant optical parametric oscillator," Opt. Comm. **148**, 117-121 (1998).

97 W.R. Bosenberg, J.I. Alexander, L.E. Myers and R.W. Wallace, "2.5-W, continuous-wave, 629-nm solid-state laser source," Opt. Lett. **23**, 207-209 (1998).

98 T. Ikegami, S. Slyusarev, T. Kurosu, Y. Fukuyama and S. Ohshima, "Characteristics of a cw monolithic $KTiOPO_4$ optical parametric oscillator," Appl. Phys. B **66**, 719-725 (1998).

99 M.E. Klein, D.-H. Lee, J.-P. Meynm B. Beier, K.-J. Boller and R. Wallenstein, "Diode-pumped continuous-wave widely tunably optical parametric oscillator based on periodically poled lithium tantalate," Opt. Lett. **23**, 831-833 (1998).

100 R. Al-Tahtamouni, K. Bencheikh, R. Storz, K. Schneider, M. Lang, J. Mlynek and S. Schiller, "Long-term stable operation and absolute frequency stabilization of a doubly-resonant parametric oscillator," Appl. Phys. B **66**, 733-739 (1998).

101 I.D. Lindsay and M. Ebrahimzadeh, "Efficient continuous-wave and Q-switched operation of a 946-nm Nd:YAG laser pumped by an injection-locked broad-area diode laser," Appl. Opt. **37**, 3961-3970 (1998).

102 D.J.M. Stothard, M. Ebrahimzadeh and M.H. Dunn, "Low-pump-threshold, continuous-wave singly resonant optical parametric oscillator," Opt. Lett. **23**, 1895-1897 (1998).

2. Diode Laser Pumping of Solid State Lasers.

2.1 Introduction.

The potential of diode lasers as pump sources for solid-state lasers has been widely recognised since shortly after the demonstration of the first diode lasers [1,2], when fluorescence in a solid-state laser medium (Nd^{3+}:$CaWO_4$) excited by the recombination radiation emitted from a GaAs junction was observed for the first time [3]. The authors noted the potential implications of their results for the development of efficient miniature lasers and the demonstration of the first diode laser pumped solid-state laser [4] rapidly followed. Although this device utilised the material CaF_2:U^{3+} (uranium doped calcium fluoride) the authors noted the particular suitability of this pumping technique for use with Nd^{3+} based lasers due to the strongly absorbing pump bands this ion exhibits in the region of 800nm, corresponding well with the emission range of diode lasers fabricated from GaAs based materials. They also pointed out that, by controlling the composition of the semiconductor materials used, laser diodes could be tuned to absorption maxima resulting in more efficient pumping and reduced heat dissipation compared to lamp pumped systems.

The first (lamp pumped) Nd:YAG laser was demonstrated shortly after this [5] and YAG rapidly became the host material of choice for Nd based, lamp pumped systems. In 1968 the first diode laser pumped Nd:YAG laser was demonstrated by Ross [6] who also pointed out several advantages of using laser diodes as pump sources for solid state lasers rather than making use of their output directly. These included the potential for energy storage in the solid-state laser medium, allowing high peak powers to be achieved in pulsed modes of operation and the improved spatial and spectral quality of solid-state lasers over laser diodes. The first demonstration of continuous diode-pumped operation, using LEDs rather than laser

diodes, followed soon after this [7]. Much subsequent diode pumped solid state laser development was carried out using this material.

These early demonstrations were all carried out with the pump diodes, laser rod or both cooled to cryogenic temperatures. This was done to improve the efficiency of the diodes, reduce the threshold of the laser, tune the diode emission to a wavelength which was absorbed strongly in the gain medium, or for a combination of these reasons. In the case of the first cw, diode-pumped Nd:YAG laser [7], the pump source was GaAsP LEDs operated at 77K and emitting at ≈808nm to coincide with the strongest absorption band in Nd:YAG. It was pointed out that simple compositional changes to the semiconductor material would enable this wavelength to be achieved at room temperature, and diode technology soon progressed to the stage where room-temperature pumping with LEDs at this wavelength was possible in a cw device [8].

All these early diode pumped solid-state lasers were pumped in a transverse geometry which allowed the output of many diode lasers or LEDs to be concentrated into the gain medium. While this allowed the total pump power available to be increased, the coupling of pump light into the laser mode volume was not particularly efficient due to the limited spatial overlap between the two. This geometry also limited the extent to which such lasers could be miniaturised as the diameter of the laser rod had to be comparable to the absorption length of the pump light to ensure the majority of the pump power was deposited in the gain medium. Better overlap between the pump and laser modes, and therefore higher efficiencies and lower thresholds, can be achieved in an axial or end-pumped geometry where the pump light propagates colinearly with the laser light along the axis of the laser rod. The disadvantage of this geometry is the limit on the number of diodes that can be used, however for low power operation it has many advantages. A pulsed Nd:YAG laser pumped in this geometry by a GaAs laser diode was first demonstrated in 1972 [9] and progress was made toward room temperature devices pumped by single LEDs [10,11]. Room temperature end-pumped cw operation was ultimately demonstrated pumping with a superluminescent diode [12] and a single LED [13] in the mid-1970s.

It is interesting to look at the reasons why the authors of [12] chose to use a superluminescent diode (SLD) as the pump source. This is essentially a device very similar to a diode laser but with feedback suppressed and therefore producing a high brightness, but incoherent, output by amplified spontaneous emission. They point out that, "...narrower beam divergence and higher spectral radiance of the SLD ... lead to a higher [efficiency] than when the domed LED is used." They also state that, "Laser diode use was abandoned, though higher overall efficiency is expected, because the laser diode in high-power cw operation is more susceptible to catastrophic damage than the SLD." Clearly, the higher spatial and spectral brightness of a laser diode when compared to an LED were recognised as extremely important for the development of efficient, low-threshold diode-pumped solid-state lasers, especially in an end-pumped geometry, but laser diode technology was not sufficiently developed at this stage to enable reliable long-term operation at relatively high powers. The superluminescent diode thus represented the best available compromise.

Until this stage (the late 1970s) the development of efficient laser diodes having significant output powers and long term reliability at room temperature had been a major limiting factor in the development of diode-pumped solid-state lasers. Most early work on diode-pumped solid state lasers was carried out with simple homojunction devices requiring cryogenic cooling. The development of single [14,15] and double [16] heterostructure devices in GaAs-AlGaAs lead to room temperature cw operation of a laser diode in 1970 [17,18]. Steady improvements in reliability throughout the 1970s [19,20] resulted in double-heterostructure devices having a projected mean time to failure at room temperature of greater than 100 years by 1977 [21]. Further improvements in efficiency and reliability came from the refinement of epitaxial growth techniques, in particular metalorganic chemical vapour deposition (MOCVD) [22,23] which was suited to large-scale production and allowed the fabrication of complex multilayered structures, including practical quantum-well devices [24], in GaAs-AlGaAs. The combination of a number of diode laser emitters in a coupled array [25] enabled significantly higher output powers than were possible from a solitary, narrow emitter, laser diode to be achieved in a small emitting area while retaining a stable far-field pattern, thus providing a route to very

high brightness, high power sources [26]. Integration of many devices on a single substrate [27] allowed the dense packing of large numbers of individual diode lasers, providing high power density pump sources [28].

As a result of these developments, in the early- to mid-1980s reliable room temperature laser diodes tuned to emit at wavelengths coincident with the strongest pump bands of Nd:YAG and other solid state gain media, and having output powers in the range of hundreds of milliwatts to several watts achieved widespread commercial availability. A tremendous upsurge in diode-pumped solid-state laser research took place and research activity in the field has continued at a high level to the present day. The potential of diode laser pumped solid state lasers for compact simplicity and stable, low-threshold, efficient operation was demonstrated by the first laser diode end-pumped Nd:YAG laser [29]. Highly stable, narrow linewidth devices have been developed [30] where the use of diode rather than lamp-based pumps avoids much pump-born and environmental noise. Extremely compact single-mode devices have also been demonstrated [31]. Advances in end-pumping techniques have resulted in efficient, high power cw devices using novel pumping geometries [32], fibre delivery [33], and beam-shaping methods [34]. Side-pumping has delivered both high power cw devices [35] and high energy pulsed systems [36,37] to rival those pumped by flashlamps. The potential of diode-pumped solid-state lasers for reliability and robustness is now such that a wide range of commercial devices are on the market and in routine everyday use.

Although this historical overview of the field has been necessarily brief and largely limited to developments of direct relevance to the work described in this thesis, a number of extensive review articles exist covering the development of laser diode pumped solid state lasers [38,39,40] and laser diode pump sources [41,42] and the reader is directed to these for further information.

2.2 Quasi-Three-Level Lasers.

A class of laser which has particularly benefited from diode pumping is that generally described as quasi-three-level. Unlike the more common four-level systems, in the quasi three level case the lower laser level is sufficiently close to the ground state that it has a significant population at room temperature resulting in reabsorption losses at the laser wavelength and thus in increased threshold and reduced efficiency compared to a four-level laser having otherwise identical characteristics. In this case, the ability of laser diodes in an end-pumped configuration to provide high pump power densities and efficient coupling of pump power into the laser mode can allow efficient low-threshold laser operation at room temperature. The high coupling efficiency available through laser diode end pumping, both spatially and spectrally, also reduces the dissipation of excess heat in the gain medium, thus avoiding excessive increase in the thermal population of the lower laser level.

Such transitions for which diode pumping has been demonstrated include those at $\approx$1.6μm in Er^{3+} [43], $\approx$2.0μm in Tm^{3+} [44] and $\approx$0.94μm in Nd^{3+}[45]. Interest has been shown in this last transition, between the $^4F_{3/2} \rightarrow {}^4I_{9/2}$ levels of the Nd^{3+} ion, in recent years as a potential source of blue light through second harmonic generation. Although lasers operating on this transition had been demonstrated under lamp pumping [46,47] they were generally inefficient and required cryogenic cooling to achieve threshold. Room-temperature cw operation was achieved in the host CAMGAR ($CaY_2Mg_2Ge_3O_{12}$) by end-pumping with an argon-ion laser [48] but operation in Nd:YAG was not possible due the inability to suppress the significantly stronger 1.064μm transition. The close coupling between pump and laser mode afforded by a Nd^{3+} doped fibre laser pumped by a dye laser allowed efficient low-threshold cw operation at room temperature [49]. Dye-laser end pumping was also demonstrated in a bulk device [50], rapidly followed by laser diode pumping [45, 51]. Subsequent demonstrations have included intracavity doubling [52,53,54] and stabilised operation [55,56], generation of cw output powers of several watts [57] and diode-pumped Q-switched operation [58].

2.3 Modelling of longitudinally pumped solid state lasers.

We now develop an analytical model for the study of longitudinally pumped solid-state lasers. The model described here includes the possibility of a significant population in the lower laser level and thus reabsorption of the laser radiation in the gain medium. This makes it applicable to four-level (by setting the reabsorption losses to zero) or quasi-three-level systems. The model will enable some of the differences between these two systems to be investigated, the effects of beam quality and focusing to be studied, and performance predictions made for the practical investigation of a 946-nm Nd:YAG laser described later in this thesis.

2.3.1 Development of theoretical model.

Modelling of end-pumped lasers having a significant thermal population in the lower laser level was first carried out by Fan and Byer [50] and later extended by Risk [59] to allow a more thorough investigation of the effects of pump focusing, and the first part of the model developed here is essentially based on these two works, although other similar treatments have been published [60].

The energy level system under consideration is assumed to be similar to that shown in Fig. 2-1. The laser transition is considered to take place between two energy levels, *a* and *b*, which exist within manifolds of several energy levels, 1 and 2, respectively. This is a simplified model of the situation which typically exists when a rare-earth atom is doped into a crystalline host, such as Nd in YAG, where the energy levels within a manifold are Stark split by the crystal field. The actual energy level structure associated with the three most commonly used Nd:YAG transitions is shown in Fig. 2-2.

It can be seen that in the case of the 946-nm transition, the upper manifold, equivalent to that designated 2 in our schematic model, is the $^4F_{3/2}$ and the upper laser level, equivalent to *b* in the model, is the lowest Stark level within this manifold, the R_1. Similarly the lower manifold, designated 1 in the model, represents the $^4I_{9/2}$ manifold and the lower laser level, *a*, the Z_5 Stark level. The designations of the Stark levels use a commonly employed notation where the manifolds are labelled

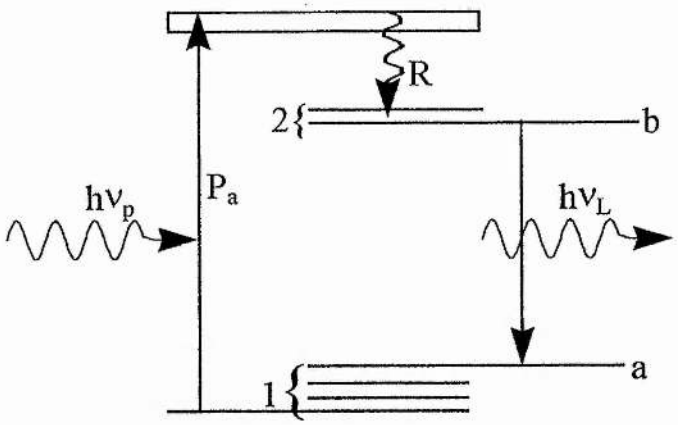

Fig. 2-1 Schematic energy level system used in theoretical model. P_a: excitation rate into pumping bands, R: excitation rate into upper laser manifold, 1: lower laser manifold, a: lower laser level, 2: upper laser manifold, b: upper laser level.

Z,Y,X,..R and the Stark levels within a manifold are numbered from that having the lowest energy upwards [61].

It is assumed that the populations of the energy levels within these manifolds are in thermal equilibrium and can thus be described by a Boltzmann distribution. This assumption relies on there being fast relaxation between the levels in the manifold. The phonon spectrum of Nd:YAG has a range of frequencies with an upper limit of around 850-860 cm^{-1} [62]. Since non-radiative transitions, such as those between levels in a manifold, are generally due to phonon interactions it can be assumed that those having energies less than or similar to the upper limit of the phonon energy will generally have a high probability of occuring. It can be seen from Fig. 2-2 that the energy levels within all the manifolds of interest meet this requirement and, indeed, the intra-manifold transitions typically occur on a time scale of 10^{-8}s or less [62].

This being the case, the relative population of a particular energy level, *j*, which is in thermal equilibrium with a number of other levels (such as within a manifold) is given by its relative Boltzmann occupation probability:

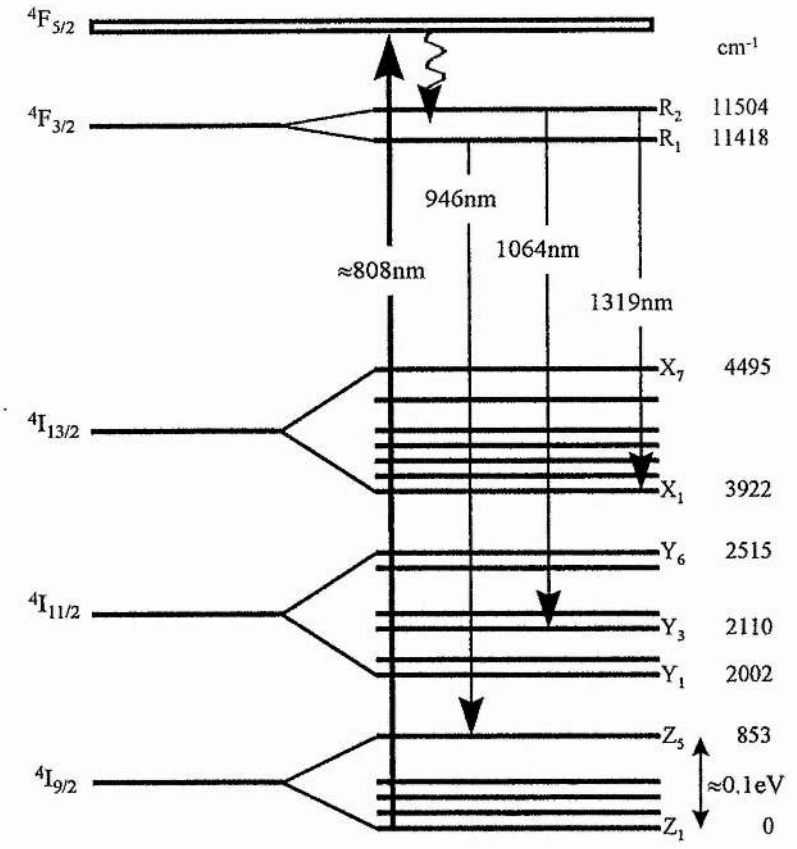

Fig. 2-2 Energy level structure associated with common laser transitions in Nd:YAG (energy level spacings not shown to scale).

$$f_j = \frac{g_j \exp\left(\frac{-h(\nu_j - \nu_0)}{kT}\right)}{\sum_i g_i \exp\left(\frac{-h(\nu_i - \nu_0)}{kT}\right)} \qquad (2\text{-}1)$$

where g_j, g_i are the degeneracies of the states j and i, $h(\nu_j - \nu_0)$ and $h(\nu_i - \nu_0)$ are their energies relative to that of the lowest level of the group in thermal equilibrium and the summation is over all the energy levels in this group. In the case of Nd:YAG each level has a degeneracy of 2 and thus g_j and g_i cancel in practice.

Thus, the populations of the upper and lower laser levels, N_b and N_a respectively, are given by:

$$N_b = f_b N_2 \tag{2-2a}$$

$$N_a = f_a N_1 \tag{2-2b}$$

where N_2 and N_1 are the upper and lower manifold populations.

To include the effects of overlap between the pump and laser modes, it is necessary to define functions describing the spatial distribution of the laser mode intensity and of the gain within the gain medium. A hemispherical cavity is assumed with both the pump and the laser modes being Gaussian TEM_{00} and having their waists at the end of the gain medium which forms the plane mirror of the cavity and through which the pump beam enters. The pump beam and laser mode are assumed to be coaxial and, at this stage, the effects of diffraction are ignored (their inclusion is discussed later on) so the radius of both beams is assumed to be constant within the gain medium. It is also assumed that the lengths of the gain medium and the cavity are identical and that the upper laser level population has the same spatial distribution as the pump beam

Considering the pump beam first, the non-normalised power distribution in the crystal is given by:

$$R_p(r,z) = \exp(-\alpha z)\exp\left(-\frac{2r^2}{w_p^2}\right) \tag{2-3}$$

where w_p is the pump waist radius and α is the pump absorption coefficient in the laser crystal.

Integrating this expression over all transverse space and the length of the crystal gives the result:

$$\int_0^{\infty}\int_0^{2\pi}\int_0^{L} R_p(r,z)\,r\,dr\,d\theta\,dz = \frac{\pi w_p^2}{2\alpha}\left(1-\exp(-\alpha L)\right) \tag{2-4}$$

where L is the length of the crystal. Thus, the pump intensity distribution normalised over the laser crystal is given by:

$$r_p(r,z) = \frac{2\alpha}{\pi w_p^2\left[1-\exp(-\alpha L)\right]}\exp\left(-\frac{2r^2}{w_p^2}\right)\exp(-\alpha z) \tag{2-5}$$

Similarly the normalised intensity distribution of the TEM_{00} laser mode is given by:

$$s_0(r,z) = \frac{2}{\pi w_L^2 L}\exp\left(-\frac{2r^2}{w_L^2}\right) \tag{2-6}$$

where w_L is the waist radius of the laser mode and it is assumed that the intensity does not vary longitudinally.

In the steady state, at or below threshold, the population of the upper laser manifold can be described by the rate equation:

$$\frac{dN_2(r,z)}{dt} = \frac{-N_2(r,z)}{\tau} + Rr_p(r,z) = 0 \tag{2-7}$$

where τ is the fluorescence lifetime of the levels in the upper manifold and R is the excitation rate into the upper manifold, related to the absorbed pump power, P_a, by:

$$R = \frac{\eta_p P_a}{h\nu_p} \tag{2-8}$$

where η_p is the pumping efficiency into the upper manifold.

The round-trip gain is given by the expression:

$$G = \iiint 2L\sigma\, s_0(r,z)\Delta N(r,z)dV \tag{2-9}$$

where the integration is over the volume of the laser crystal and the inclusion of the spatial dependencies of the laser mode and the population inversion allows the

effects of their overlap to be included. The stimulated emission cross section, σ, and the absorption cross section for the laser transition are here assumed to be the same, although there is evidence that the stimulated emission cross section is up to 25% larger than the absorption [63]. The density of the inversion between the upper and lower laser levels is given by:

$$\Delta N(r,z) = N_b(r,z) - N_a(r,z) \tag{2-10}$$

or, from (2-2):

$$\Delta N = f_b N_2 - f_a N_1 \tag{2-11}$$

Assuming that the total population is distributed only among the levels of the upper and lower manifolds, i.e. that:

$$N_0 = N_1 + N_2 \tag{2-12}$$

where N_0 is the doping concentration, (2-11) becomes:

$$\Delta N = (f_b + f_a)N_2 - f_a N_0 \tag{2-13}$$

Determining N_2 in the steady-state case at threshold from (2-7) and using (2-8), we can rewrite (2-13) as:

$$\Delta N(r,z) = \eta_p (f_b + f_a) P_a r_p(r,z) \frac{\tau}{h\nu_p} - f_a N_0 \tag{2-14}$$

At threshold, the round-trip gain must be equal to the round-trip loss, δ. Thus, from (2-9) and (2-14):

$$\iiint 2L\sigma s_0(r,z) \left[\eta_p (f_b + f_a) P_{a,th} r_p(r,z) \frac{\tau}{h\nu_p} - f_a N_0 \right] dV = \delta \tag{2-15}$$

where $P_{a,th}$ is the absorbed pump power at threshold. The loss figure δ includes all losses apart from the reabsorption loss due to the thermal population of the lower laser level and can be defined as:

$$\delta = \delta_e + 2\alpha_i L \tag{2-16}$$

where α_i represents length-dependent losses intrinsic to the laser crystal such as scattering and absorption by impurities and δ_e represents extrinsic losses. This can be broken down further into output coupling losses, δ_{oc}, and parasitic losses such as and reflection at interfaces, δ_p, that is:

$$\delta_e = \delta_{oc} + \delta_p \tag{2-17}$$

The reabsorption loss can be considered as an additional loss mechanism by introducing the substitution:

$$\alpha_l = \sigma f_a N_0 \tag{2-18}$$

Making this substitution, and remembering that (2-6) results in the integral of $s_0(r,z)$ over the laser crystal volume being unity, (2-15) can be rewritten as:

$$P_{a,th} \iiint s_0(r,z) r_p(r,z) dV = \frac{h\nu_p}{2L\eta_p \sigma (f_b + f_a)\tau} (\delta + 2\alpha_l L) \tag{2-19}$$

Finally, substituting (2-5) and (2-6) and evaluating the integral gives:

$$P_{a,th} = \frac{\pi h \nu_p}{4\eta_p \sigma (f_b + f_a)\tau} (w_L^2 + w_p^2)(\delta + 2\alpha_l L) \tag{2-20}$$

It should be remembered that this expression gives the absorbed pump power at threshold. The corresponding threshold in terms of pump power entering the gain medium is related to this by the expression:

$$P_{th} = \frac{P_{a,th}}{1 - \exp(-\alpha L)} \tag{2-21}$$

Above threshold, in the steady state condition, the rate equations describing the populations of the upper and lower laser levels take the form:

$$\frac{dN_b(r,z)}{dt} = f_b R r_p(r,z) - f_b \frac{N_2(r,z) - N_2^0}{\tau} - \frac{f_b c\sigma\left(N_b(r,z) - N_a(r,z)\right)}{n} S s_0(r,z) = 0 \tag{2-22a}$$

$$\frac{dN_a(r,z)}{dt} = -f_a R r_p(r,z) + f_a \frac{N_2(r,z) - N_2^0}{\tau} + \frac{f_a c\sigma\left(N_b(r,z) - N_a(r,z)\right)}{n} S s_0(r,z) = 0 \tag{2-22b}$$

where N_2^0 is the unpumped upper laser manifold population in thermal equilibrium and S is the cavity photon number. The three terms in the main body of both equations represent pumping from the lower to the upper manifold, spontaneous emission from the upper to the lower manifold and stimulated emission from the upper to the lower laser level, respectively. Using (2-12), equation (2-22b) can be rewritten as:

$$\frac{dN_a(r,z)}{dt} = -f_a R r_p(r,z) - f_a \frac{N_1(r,z) - N_1^0}{\tau} + \frac{f_a c\sigma\left(N_b(r,z) - N_a(r,z)\right)}{n} S s_0(r,z) = 0 \tag{2-22c}$$

This now allows a rate equation describing the population inversion between the two laser levels to be obtained by subtracting (2-22c) from (2-22a) to give:

$$\frac{d\Delta N(r,z)}{dt} = R r_p(r,z)\left(f_b + f_a\right) - \frac{\Delta N(r,z) - \Delta N^0}{\tau} - \frac{\left(f_b + f_a\right) c\sigma \Delta N(r,z)}{n} S s_0(r,z) = 0 \tag{2-23}$$

The thermal-equilibrium population inversion in the absence of pumping is defined as:

$$\Delta N^0 = -f_a N_0 \tag{2-24}$$

where it is assumed that in the unpumped case the entire population resides in the ground-state manifold.

The above-threshold steady-state rate equation describing the cavity photon number is:

$$\frac{dS}{dt} = \frac{c\sigma}{n}\iiint \Delta N(r,z) S\, s_0(r,z) dV - \frac{c\delta}{2nL} S = 0 \tag{2-25}$$

The inversion can be obtained by solving (2-23) for ΔN and allowing this to be substituted in (2-25) to give an expression relating the pump rate and the cavity photon number:

$$\begin{aligned}\frac{\delta}{2\sigma L} = \left(f_b + f_a\right) R\tau \iiint \frac{r_p(r,z)\, s_0(r,z)}{1 + \dfrac{(f_b + f_a)c\sigma\tau}{n} S s_0(r,z)} dV \\ + \Delta N^0 \iiint \frac{s_0(r,z)}{1 + \dfrac{(f_b + f_a)c\sigma\tau}{n} S s_0(r,z)} dV\end{aligned} \tag{2-26}$$

It can be seen that this expression simplifies to that for threshold, (2-19), when S=0, as would be expected.

While (2-26) can be solved wholly analytically in the case of Gaussian pump beams and integer values of w_L/w_p^2 [50], it is more useful for the purposes of general calculations to simplify the expression as far as possible and obtain a form for which relatively straightforward numerical solutions can be found. Making the substitutions for $r_p(r,z)$ and $s_0(r,z)$ using (2-5) and (2-6) and evaluating the second integral completely and the first as far as possible gives the expression:

$$\frac{\delta}{2\sigma L}=\left(f_b+f_a\right)R\tau\int_0^{\infty}\frac{\exp\left[-2r^2\left(\frac{1}{w_p^2}+\frac{1}{w_L^2}\right)\right]}{1+\frac{2\left(f_b+f_a\right)c\sigma\tau S}{n\pi w_L^2 L}\exp\left(-\frac{2r^2}{w_L^2}\right)}rdr$$

$$+\Delta N^0\frac{\pi Lnw_L^2}{2\left(f_b+f_a\right)c\sigma\tau S}\ln\left[1+\frac{2\left(f_b+f_a\right)c\sigma\tau S}{\pi Lnw_L^2}\right] \tag{2-27}$$

Expressing R in terms of input pump power and ΔN^0 in terms of the reabsorption loss, α_l, via (2-18) and (2-24), an expression relating cavity photon number to input pump power is obtained:

$$\frac{P\left[1-\exp(-\alpha L)\right]\eta_p}{h\nu_P}=\left[\frac{\delta}{2L}+\alpha_l\frac{S_o}{2S}\ln\left(1+\frac{2S}{S_o}\right)\right]\frac{\pi w_P^2 L}{2\sigma\left(f_b+f_a\right)\tau}$$

$$\times\left[\int_0^{\infty}\frac{\exp\left(-x\left(1+\frac{w_L^2}{w_P^2}\right)\right)}{1+2\frac{S}{S_o}\exp(-x)}dx\right]^{-1} \tag{2-28}$$

where the substitutions:

$$x=\frac{2r^2}{w_L^2} \tag{2-29}$$

$$S_0=\frac{n\pi w_L^2 L}{\left(f_b+f_a\right)c\sigma\tau} \tag{2-30}$$

have been made. S_0 can be considered to be the saturation cavity photon number i.e. that which results in the rate at which photons are emitted by stimulated emission being equal to the spontaneous emission rate. Again, it can be seen that (2-28) simplifies to (2-20) when S=0.

The output power is related to the cavity photon number, S, by the expression:

$$P_{out} = \frac{STch\nu_L}{2L_{cav}} \tag{2-31}$$

where T is the output coupler transmission, ν_L is the frequency of the laser light and L_{cav} is the laser cavity length.

As mentioned earlier, when the normalised mode distributions were defined, it has been assumed that the cavity length and the crystal length are identical, i.e. that $L_{cav}=nL$ where n is the refractive index of the laser medium. This does not prevent the model developed here being used for any cavity length as long as the crystal length is used as the cavity length both in the mode distribution defined in (2-6) and in the output expression (2-31). Use of the actual cavity length in both definitions would result in a proportional increase in the cavity photon number, S, obtained from the rate-equation analysis and thus in the same output power from (2-31) as in the case of assumed equality of cavity and crystal length. However, normalising both the pump and laser modes over the crystal length simplifies the calculation of the overlap integral and is thus the approach used here.

Having developed the basis for theoretical modelling of an end-pumped solid-state laser, we can now go on to investigate some aspects of the calculated behaviour comparing the performance of quasi-three-level to four-level systems having otherwise similar properties and, specifically, that of the 946-nm transition in Nd:YAG to the more familiar one at 1064 nm. To do this, the values for various parameters used in the modelling must first be defined for both transitions.

Beginning with the intrinsic material properties, the Nd^{3+} ion concentration is taken to be the typical value for Nd:YAG of 1.1% atomic, giving a doping concentration by volume of $N_0=1.518 \times 10^{20}$ cm^{-3}. The fluorescence lifetime of the $^4F_{3/2}$ manifold is taken as $\tau = 230\mu s$[64] and the stimulated-emission cross sections for the 946-nm and 1064-nm transitions are taken to be $\sigma_{946} = 4.0\times10^{-20}$ cm^2 and $\sigma_{1064} = 65\times10^{-20}$ cm^2, respectively [65]. In calculating the fractional populations of the upper laser levels for the two laser transitions, it is important to remember that the 946-nm transition occurs from the R_1 level of the $^4F_{3/2}$ manifold, while the 1064-nm transition occurs from the R_2 level. From the energy levels shown in Fig. 2-2 and

applying (2-1) fractional populations for the levels in the $^4F_{3/2}$ manifold, and therefore for the upper levels of the to laser transitions, of $f_{b,946} = 0.602$ and $f_{b,1064} = 0.398$ at 300 K are obtained. A number of authors [39,64] define an effective stimulated emission cross section as the product of the transition cross section and the fractional population of the upper laser level namely:

$$\sigma_{eff} = \sigma f_b \tag{2-32}$$

and use this in calculations rather than stating the cross section and upper-level fractional population explicitly. From the values above, we obtain $\sigma_{eff,946} = 2.4\times10^{-20}$ cm^2 and $\sigma_{eff,1064} = 25.9\times10^{-20}$ cm^2.

When considering the fractional populations of the lower laser levels, most treatments assume the entire lower-level population resides in the ground-state ($^4I_{9/2}$) manifold and that there is rapid relaxation from the $^4I_{11/2}$ manifold into the $^4I_{9/2}$. This results in the fractional lower-laser-level population for the 946-nm transition being calculated using (2-1), with the summation taken across the five levels of the $^4I_{9/2}$ manifold, and that for the 1064-nm transition being zero, as would be expected for a 4-level laser. For consistency of treatment, however, the two lower manifolds should be assumed to be in thermal equilibrium and the summation of (2-1) taken across the eleven levels for both transitions. In practice this makes very little difference to the final result, yielding values of $f_{a,946} = 0.0078$ and $f_{a,1064} = 1.87\times10^{-5}$ at 300 K and thus allowing the fractional population for the 1064-nm transition to be assumed to be zero for all practical purposes. Having calculated the fractional populations of the lower laser levels, we can now use these values, along with the doping level given earlier, in (2-24) to determine the unpumped population inversions for the two transitions as $\Delta N_{0,946} = -1.184\times10^{18}$ cm^{-3} and $\Delta N_{0,1064} = -2.839\times10^{15}$ cm^{-3}. Making use of the stimulated-emission cross sections given earlier and, as previously mentioned, assuming equality of stimulated-emission and absorption cross section in both cases, the use of (2-18) allows the reabsorption loss coefficients to be calculated as $\alpha_{l,946} = 0.0474$ cm^{-1} and $\alpha_{l,1064} = 0.0018$ cm^{-1}.

The strong $^4I_{9/2} \rightarrow {}^4F_{5/2}$ absorption band in Nd:YAG corresponds to a pump wavelength of 808.5nm. With the pump source tuned to have its peak emission at

Parameter.	Symbol.	Value.	
		$^4F_{3/2}\rightarrow{}^4I_{9/2}$ (946-nm) transition.	$^4F_{3/2}\rightarrow{}^4I_{11/2}$ (1064-nm) transition.
Nd^{3+} ion concentration (1.1 at.% doping).	N_0	1.518×10^{20} cm^{-3}	
Upper state manifold fluorescence lifetime.	τ	230μs	
Absorption/stimulated emission cross section.	σ	4×10^{-20} cm^2	65×10^{-20} cm^2
Fractional population of upper laser level (300K).	f_b	0.602	0.398
Fractional population of lower laser level (300K).	f_a	0.0078	1.87×10^{-5}
Effective cross section (300K).	σ_{eff}	2.4×10^{-20} cm^2	25.9×10^{-20} cm^2
Unpumped population inversion (300K).	ΔN_0	-1.184×10^{18} cm^{-3}	-2.839×10^{15} cm^{-3}
Reabsorption coefficient (300K).	α_l	0.0474 cm^{-1}	0.0018 cm^{-1}
Distributed crystal losses.	α_i	0.002 cm^{-1}	
Pump absorption coefficient (λ_p=808.5nm).	α	5-12 cm^{-1}	
Pumping efficiency.	η_p	1	
Refractive index.	n	1.82	

Table 2-1 Parameters used in the modelling of end-pumped Nd:YAG lasers.

this wavelength, the pump absorption coefficient, α, is dependent on the degree of spectral overlap between the pump emission and the absorption bandwidth and, therefore, on the spectral bandwidth of the pump source. The peak absorption coefficient is typically quoted as 12 cm^{-1} [65], however experimental values for 1.1 at.% doped material range from 9.5 cm^{-1} for an infra-red dye laser pump to 5.2cm^{-1} in the case of laser diode array pumping [51]. It is, therefore, instructive to calculate the laser performance for various pump absorption coefficients, allowing the effect of the spectral quality of the pump to be gauged. Finally, the crystal scattering losses were taken to be α_i = 0.002 cm^{-1} [64], the pumping efficiency was assumed to be η_p=1 [64] and the refractive index n=1.82 [65]. The various parameters used in the modelling are summarised in Table 2-1.

2.3.2 Threshold of four-level and quasi-three-level systems.

When considering the laser threshold, it can be seen from (2-20) and (2-21) that in the quasi three level case there will exist an optimum length of crystal which achieves the best compromise between effective absorption of the incident pump light and minimising the reabsorption loss occurring over the length of the crystal. From (2-20) and (2-21) the expression:

$$\frac{1}{\alpha \exp(-\alpha L)} - L - \frac{\delta_e}{2(\alpha_t + \alpha_l)} - \frac{1}{\alpha} = 0 \qquad (2\text{-}33)$$

is obtained which, when solved for L, gives the optimum crystal length for minimum threshold. This effect can be seen in Fig. 2-3 where the threshold is plotted as a function of crystal length for the 946nm transition at 0K and 300K, and the 1064nm transition at 300K, with the values of f_b, f_a and α_l being calculated for these

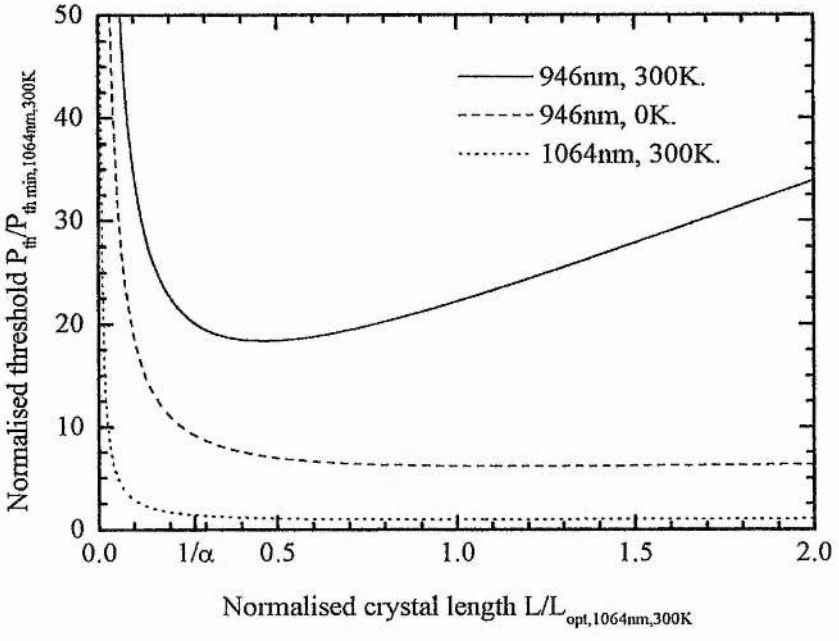

Fig. 2-3 Variation of normalised threshold pump power with laser crystal length for 946-nm transition at 300K and 0K, and 1064-nm transition at 0K (δ_e=2%, w_p=w_l=20μm, α=8cm^{-1}).

temperatures. The round-trip extrinsic losses were set to δ_e=2%, the waist radii of the pump and laser modes to w_p=w_l=20μm and the pump absorption coefficient to α=8cm^{-1}. All other parameters took the values specified in Table 2-1, and the plotted values have been normalised to the optimum values for the 1064-nm transition at 300K.

The existence of an optimum crystal length in the case of the 946-nm laser at 300K is immediately apparent as is the change in the behaviour of the 946-nm laser when cooled to 0K. In this case, the thermal population of the lower laser level, and therefore the reabsorption loss, becomes zero and the laser is now a four-level system showing essentially the same behaviour as the 1064-nm laser at 300K. In these two four-level cases, the minimum threshold is obtained for crystal lengths a few times the pump-light absorption length (marked 1/α in Fig. 2-3). For crystals longer than this optimum length the threshold shows only an almost imperceptible increase due to the distributed crystal losses α_i, and, in the 1064-nm case, to the small reabsorption loss which can be seen from Table 2-1 to be of a similar magnitude. The difference in the final threshold value for the two four-level cases is due to the difference in the cross section of the two transitions, the ratio of these threshold values being the same as that of the effective cross section of the 1064-nm transition at 300K to the cross section of the 946-nm transition and having a value of 6.48.

In contrast to the four-level transitions, the quasi-three-level case of the 946-nm laser at 300K shows a rapid increase in threshold as the crystal length is increased beyond its optimum value and, even with the crystal length optimised, the threshold is significantly larger than in the four-level case for the same transition. It can therefore be seen from Fig. 2-3 that there are two factors, the reabsorption loss and the reduced stimulated-emission cross section, which diminish the suitability of the 946-nm transition for low-threshold room-temperature operation when compared to the 1064-nm transition.

When considering the effects of temperature on the threshold of the two transitions, it is important to consider not only the population of the lower laser level, which results in reabsorption loss, but also that of the upper laser level. It can be seen from

Fig. 2-2 that the 946-nm transition occurs from the lower, R_1, level of the $^4F_{3/2}$ manifold, while the 1064-nm transition occurs from the upper, R_2, level. Clearly this will result in the fractional population of the upper laser level f_b, and therefore the effective emission cross section σ_{eff}, increasing for the 946-nm transition as the temperature is reduced, while falling for the 1064-nm transition. It would therefore be expected that, in the absence of reabsorption effects from the lower laser level, the threshold for the 946-nm transition would fall and that for the 1064-nm transition would increase as the temperature were reduced.

The optimum crystal length, obtained from (2-33), and resulting minimum threshold are plotted as a function of temperature for both the 946-nm and 1064-nm transitions in Fig. 2-4 where the temperature dependence of both the upper and lower level fractional populations have been included. Again, both quantities have been

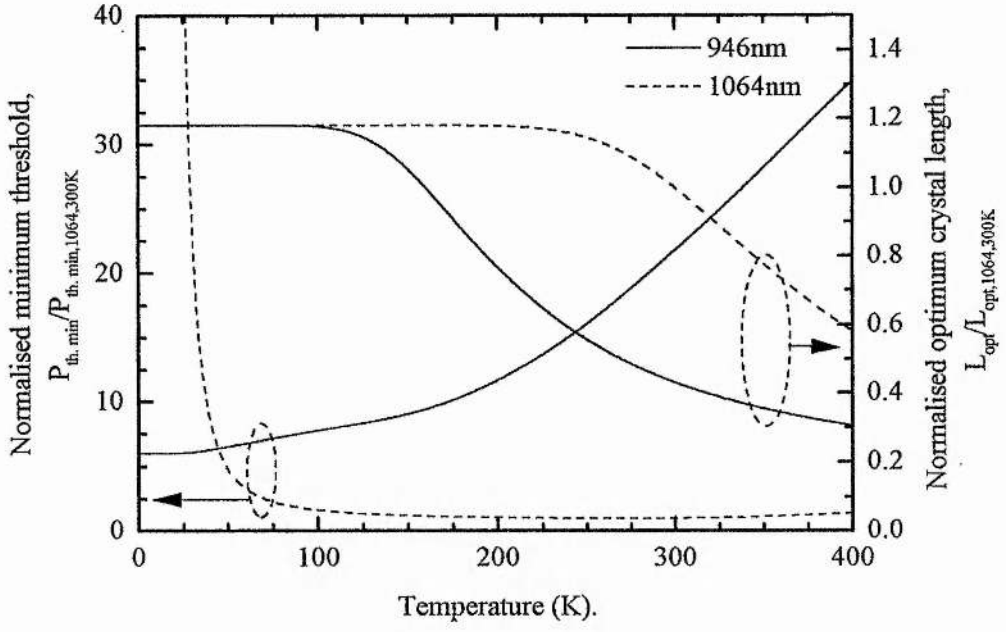

Fig. 2-4 Variation of normalised minimum threshold pump power and optimum crystal length with temperature for the 946-nm and 1064-nm transitions with effects of temperature change on upper level populations included (δ_e=2%, w_p=w_l=20μm, α=8cm^{-1}).

normalised to their values for the 1064-nm transition at 300K. The minimum threshold for the 946-nm transition can be seen to show a rapid increase with temperature while that for the 1064-nm transition increases slightly at higher temperatures. At temperatures below 100K, the minimum threshold for the 1064-nm transition increases rapidly as expected.

The optimum length is seen to shorten with temperature above 100K in the case of the 946-nm transition, and 250K in the 1064-nm case, due to the increasing reabsorption losses. Below these temperatures the optimum lengths remain virtually constant indicating that further reduction in temperature does not significantly reduce the population of the lower laser level and therefore the reabsorption loss. The changes in minimum threshold below these temperatures are, therefore, due to changes in the population of the upper laser levels alone.

Since the differences between quasi-three-level and four-level lasers are due to the lower laser level population alone, it is useful to ignore the effects of temperature change on the upper level populations when discussing these differences. This is done in Fig. 2-5 which shows essentially the same calculations as Fig. 2-4 but with the upper level fractional populations fixed at their 300K values. It is clear that reabsorption losses due to thermal population of the lower level have very little effect on the threshold of the four-level 1064-nm laser over practical temperature ranges, while the quasi-three-level 946-nm laser threshold shows a strong temperature dependence due to such effects. It can also be seen that at 300K the threshold of the 946-nm laser would be expected to be around twenty times that of an otherwise similar 1064-nm laser.

It should be pointed out that in practice the threshold behaviour of 1064-nm lasers with temperature is somewhat different from that described in Fig. 2-4. The 1064-nm gain band in Nd:YAG actually consists of two overlapping transitions [66]. The $R_2 \rightarrow Y_3$ transition at 1064.1nm is generally dominant and has been considered in isolation here. The $R_1 \rightarrow Y_2$ transition at 1064.5nm has a significantly smaller cross section of 1.2×10^{-20} cm^2 [65] and ions in the R_1 level usually transfer thermally into the R_2 level before participating in laser action via the $R_2 \rightarrow Y_3$ transition [64]. At reduced temperatures, however, the fractional population of the R_1 level becomes

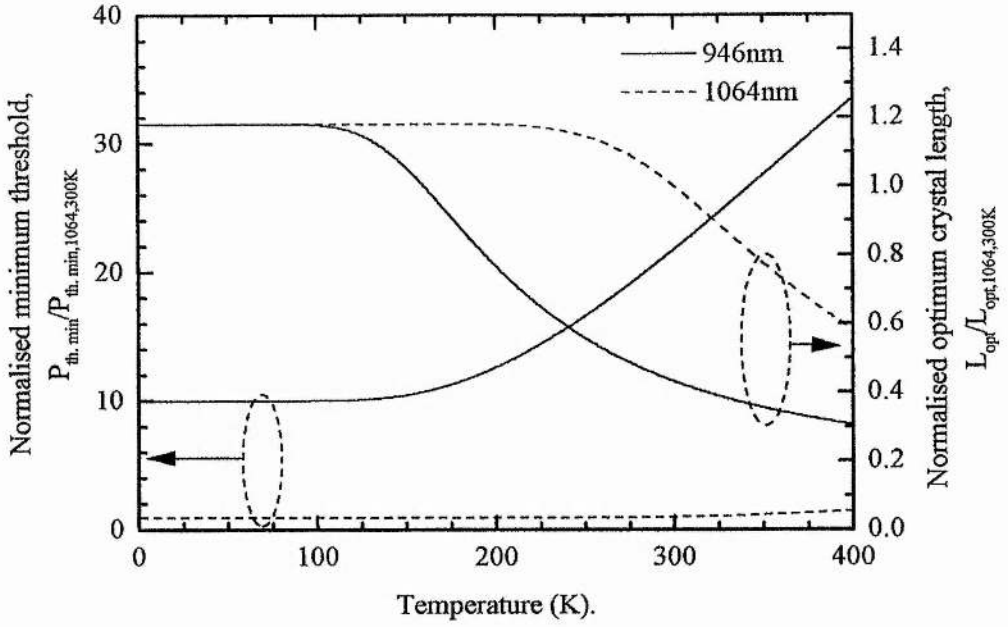

Fig. 2-5 Variation of normalised minimum threshold pump power and optimum crystal length with temperature for the 946-nm and 1064-nm transitions with upper level populations fixed at 300K values (δ_e=2%, w_p=w_l=20μm, α=8cm^{-1}).

significantly larger than that of the R_2 and the effective cross sections of the two transitions become the same at around 75K. Below this temperature the threshold for 1064-nm laser operation would be expected to be determined by the $R_1 \rightarrow Y_2$ transition.

In practical 1064-nm lasers the situation is further complicated by the presence of the $R_1 \rightarrow Y_1$ transition at 1061nm which has a cross section of around 50% that of the $R_2 \rightarrow Y_3$ transition [67]. The effective cross sections of these two transitions become equal at 229K and below this temperature such lasers tend to operate at 1061nm.

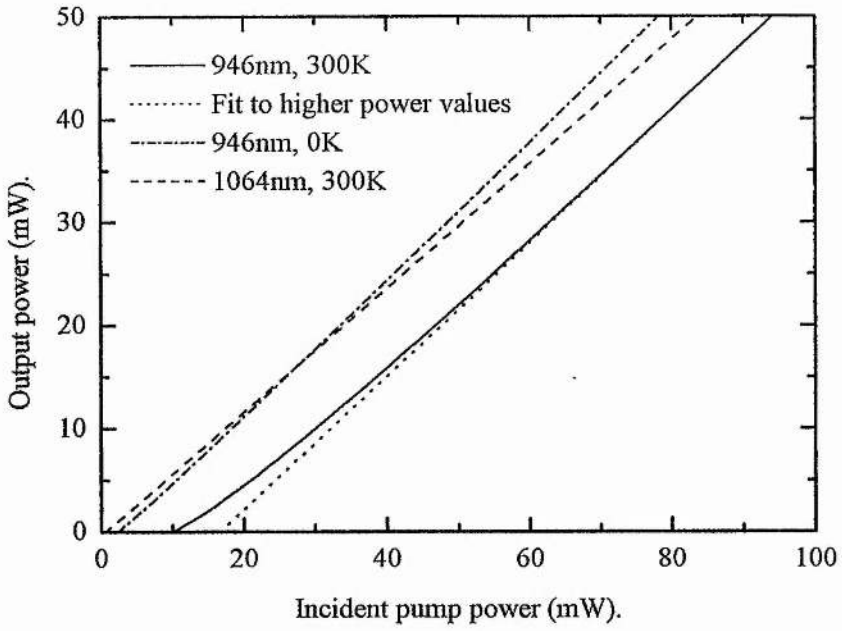

Fig. 2-6 Variation of laser output power with pump power for 946-nm and 1064-nm lasers (δ_e=1% output coupling, w_p=w_l=20μm, L=2mm, α=8cm^{-1}).

2.3.3 Above-threshold behaviour and slope efficiency.

The comparative above-threshold behaviour of 946-nm and 1064-nm lasers is illustrated in Fig. 2-6. Here the variation of laser output power is shown for 946-nm lasers at 0K and 300K and a 1064-nm laser at 300K with other parameters otherwise identical (1% output coupling, 20μm pump and laser mode radii, 2mm long crystal and 8cm^{-1} pump absorption coefficient). As would be expected from the discussion above the 1064-nm transition has the lowest threshold, around one fifth of that of the 946-nm transition at 0K, due to its significantly larger cross section and the room-temperature threshold for the 946-nm transition is significantly larger than that at 0K.

Looking at the slope efficiencies above threshold, it can be seen that the 1064-nm laser has a lower efficiency than the 946-nm laser at 0K. This is due to the larger

quantum defect in the 1064-nm case. In the quasi-three-level case of the 946-nm laser at 300K, the slope efficiency is much lower close to threshold than at higher pump powers where it approaches that of the four-level case of the same transition at 0K. This behaviour would be expected from examination of (2-28), where it can be seen that the reabsorption behaves as a saturable loss, tending to zero for large cavity photon numbers.

The effects of reabsorption loss on slope efficiency were discussed by Fan and Byer [50] who solved expressions similar to (2-27) and (2-28) analytically for certain values of w_L/w_P. They showed that while the reabsorption loss is significant close to threshold, the efficiency is similar to that of the four level case when operating well above threshold or when the reabsorption loss is small compared to the other, non-saturable, losses such as output coupling.

A more detailed study was carried out by Risk [59] who, by solving expressions similar to (2-27) and (2-28) numerically for arbitrary values of w_L/w_P, was also able to model these effects. Additionally, he was able to discuss the influence of the pump mode size on slope efficiency in lasers exhibiting reabsorption loss which is a particularly important consideration in the context of the work presented here.

While it is clear from (2-20) that the threshold can be reduced by making the pump and laser mode waists, w_P and w_L, as small as possible, the effects of their relative size on slope efficiency, and therefore output power, are not so readily apparent from (2-28). Fig. 2-7 shows the slope efficiency, calculated numerically from (2-28), as a function of the ratio of pump mode radius to laser mode radius with S/S_0, the ratio of the cavity photon number to the saturation photon number, as a parameter for a range of values of $2\alpha_l/\delta$, the ratio of the reabsorption loss to the fixed cavity losses. In all cases, the slope efficiency is normalised to the value obtained with zero reabsorption loss and a relative pump mode radius of zero (on-axis pumping).

Considering first Fig. 2-7(a), which represents the case of zero reabsorption loss, and therefore a four-level system, several important features can be seen. Firstly, it is clear that for all levels of cavity photon number the slope efficiency falls rapidly for values of w_P/w_L greater than unity. Clearly this is expected as, in these cases, the

pump mode is larger than the laser mode and therefore sections of the gain medium are being pumped which do not contribute to the laser output.

It can also be seen that the point at which the slope efficiency starts to fall off tends to smaller relative mode waists for lower cavity photon numbers. This is due to the laser mode distribution, as defined in (2-6), having its largest value on axis resulting in a higher stimulated emission rate, and therefore more efficient coupling of pump

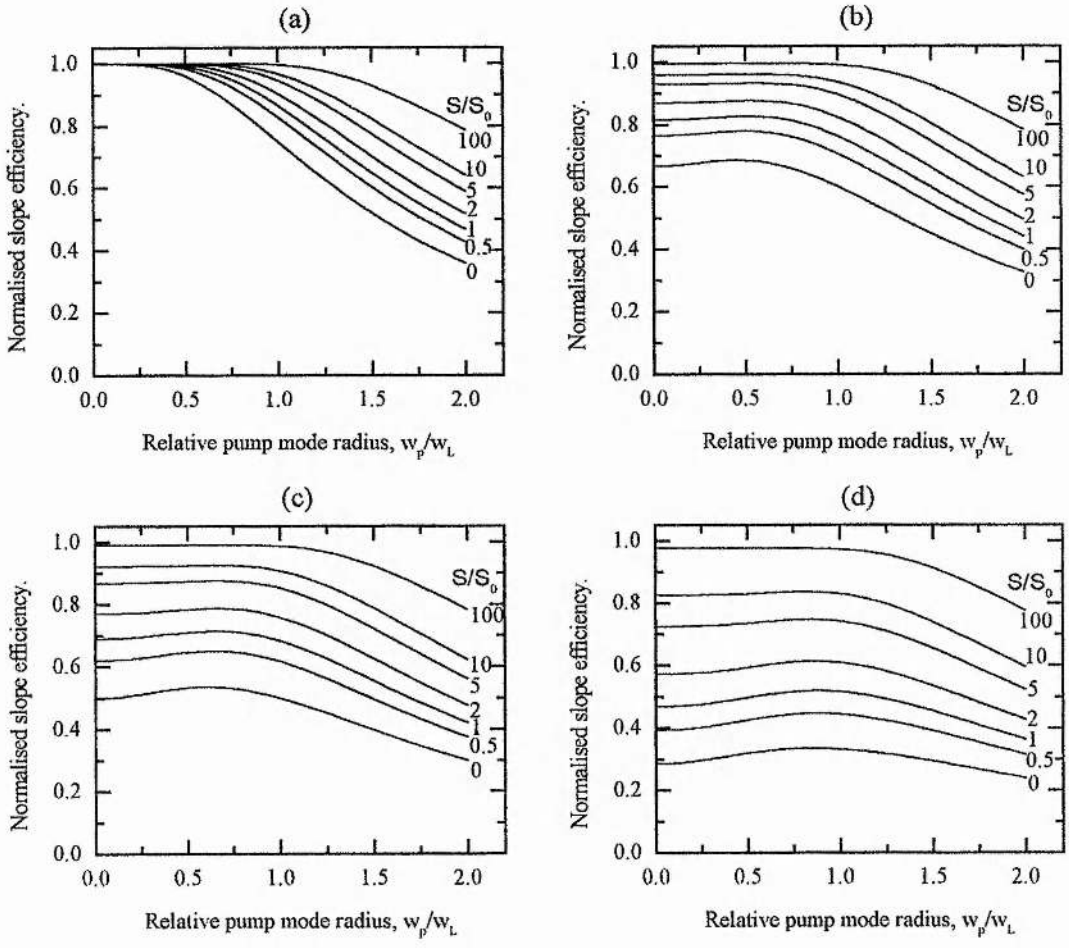

Fig. 2-7 Calculated variation of normalised slope efficiency with relative pump mode radius, for a fixed w_L, with relative cavity photon number S/S_0 as a parameter, for different relative reabsorption losses: $\frac{2\alpha_l L}{\delta} = 0$ (a), 1 (b), 2 (c), 5 (d). (After [59]).

energy into the laser mode, than in the wings of the distribution where more of the pumped population decays by spontaneous emission. For larger cavity photon numbers the distance from the axis at which the spontaneous emission rate becomes significant compared to the stimulated emission rate is greater, allowing high efficiency to be maintained for larger pump mode radii. Thus, it can be concluded that in the case of a four-level laser the highest efficiency is obtained by pumping as small a volume as possible along the laser mode axis.

When considering the cases of significant reabsorption loss shown in Fig. 2-7(b)-(d) two differences from the case of zero reabsorption loss are immediately apparent. Firstly, the efficiency falls as the cavity photon number is reduced. In contrast to the case of zero reabsorption loss, this happens even for on-axis pumping ($w_P/w_L=0$). This occurs due to the reabsorption loss being saturable, as was shown in Fig. 2-6. Thus, the overall losses are lower for large cavity photon numbers and the efficiency is accordingly higher.

The second clear difference between the cases of significant reabsorption loss and no reabsorption loss is that the maximum efficiency does not necessarily occur for on-axis pumping ($w_P/w_L=0$). This can also be explained in terms of the nature of the reabsorption loss. It is apparent from (2-18) and (2-24) that the reabsorption loss is analogous to a negative gain produced by a negative population inversion. Any given section of the gain medium must, therefore, be pumped sufficiently hard to overcome this negative inversion before the laser mode sees a net gain on passage through it, as opposed to a net loss. In the four-level case shown in Fig. 2-7(a) pumping a small volume close to the axis of the laser mode results in high efficiency, as described above, while the unpumped remainder of the laser mode volume is essentially transparent exhibiting neither gain nor loss.

In the quasi-three-level examples of Fig. 2-7(b)-(d) this is no longer the case. Any unpumped regions of the laser mode volume in the gain medium will have a negative population inversion, and therefore will be lossy, reducing the overall efficiency. There exists, therefore, an optimum value of relative pump mode radius which results in the best compromise between the increased efficiency obtained by on-axis pumping and the reduced efficiency resulting from leaving off-axis sections of the

laser mode volume unpumped. It can be seen from Fig. 2-7 that the larger the reabsorption loss the more pronounced this effect will be and the larger the optimum pump mode radius for maximum efficiency. It can also be seen that for large cavity photon numbers the effect is not observed due to saturation of the reabsorption loss. In all cases, however, it is clear that an increased reabsorption loss will result in a reduction in efficiency.

The calculated results of Fig. 2-7 are presented in a slightly different format in Fig. 2-8. Here the slope efficiency is plotted against the pump power relative to threshold, with the relative pump mode radius as a parameter, for a range of levels of reabsorption loss. Again, the slope efficiencies have been normalised to that for zero reabsorption loss and on-axis pumping. It can, again, be seen that as the reabsorption loss increases the optimum pump mode radius also increases (although it is not generally desirable to have $w_P/w_L>1$) and that higher relative pump powers (and therefore higher cavity photon numbers) result in higher efficiencies and less of a variation of efficiency with pump mode radius.

It is clear that there appear to be two conflicting requirements placed on the pump mode radius when attempting to obtain the maximum efficiency in the presence of reabsorption loss. While it is desirable to have a certain, non-minimal, pump mode radius to avoid unpumped regions of the laser mode volume, it is also desirable to pump the laser as far above threshold as possible. For a given pump power this means that reducing the threshold will result in increased efficiency. From (2-20), it is clear that the threshold can be reduced by making the pump mode waist smaller, an opposing requirement to the first one.

In deciding which of these effect is the most significant, it is important to remember that the data shown in Fig. 2-8 is plotted against the pump power relative to the threshold value for each pump mode radius. To present these results in a form more relevant to practical situations, when a given pump power is generally available, Fig. 2-9 shows the same data plotted against the pump power relative to the threshold value for the case of on-axis pumping. It is immediately apparent that, for a given available pump power, the reduction in threshold, and consequent increase in cavity photon number and therefore efficiency, is a much stronger effect than the reduction

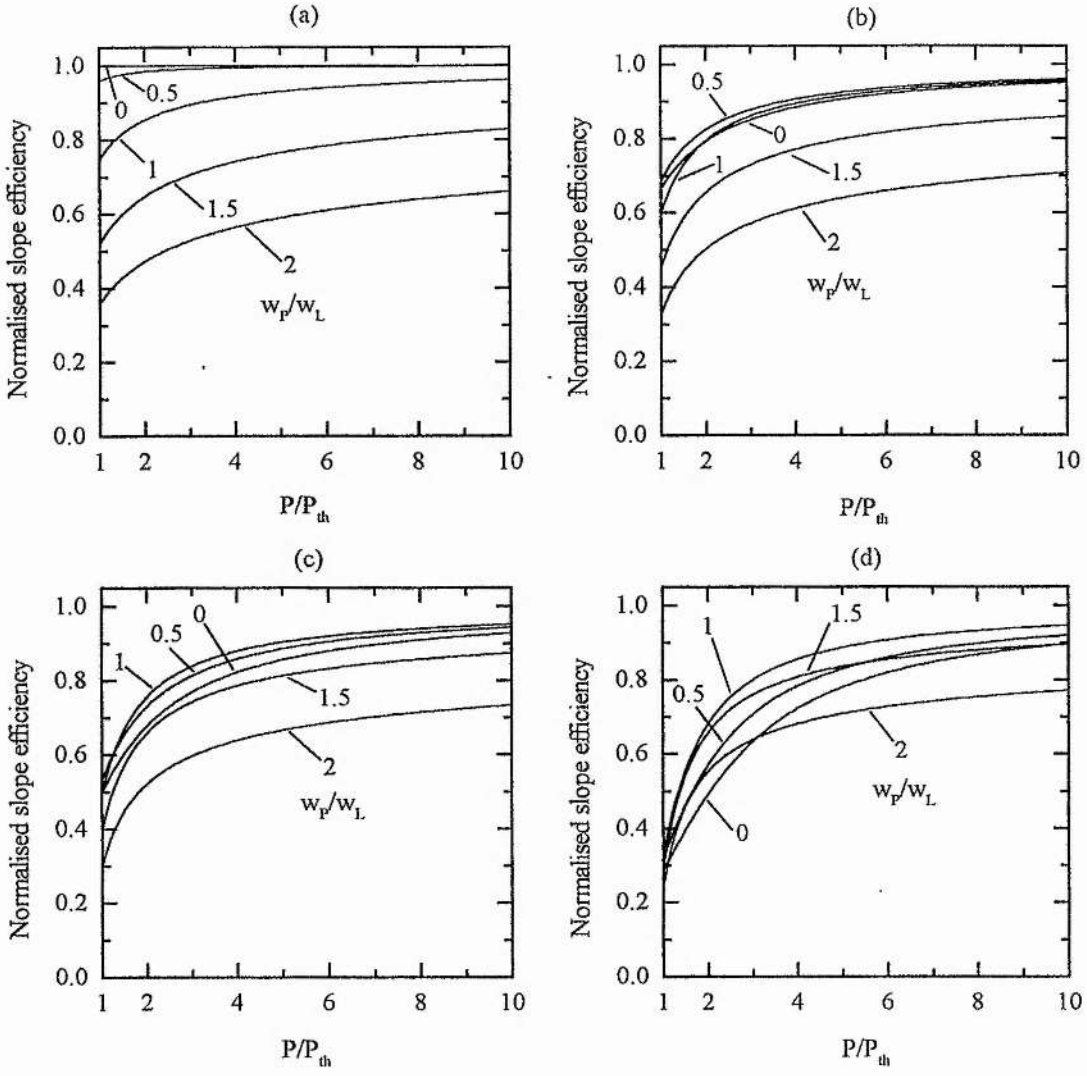

Fig. 2-8 Calculated variation of normalised slope efficiency with relative pump power, with relative pump mode radius w_P/w_L, for a fixed w_L, as a parameter, for different relative reabsorption losses: $\frac{2\alpha_l L}{\delta} = 0$ (a), 1 (b), 2 (c), 5 (d). (After [59]).

in efficiency due to increased absorption in the wings of the laser mode distribution when using a small pump mode radius.

Although increased reabsorption loss results in the efficiency of the w_P/w_L=0 case becoming similar to that for w_P/w_L=1, it is clear that in the quasi-three-level, as in the

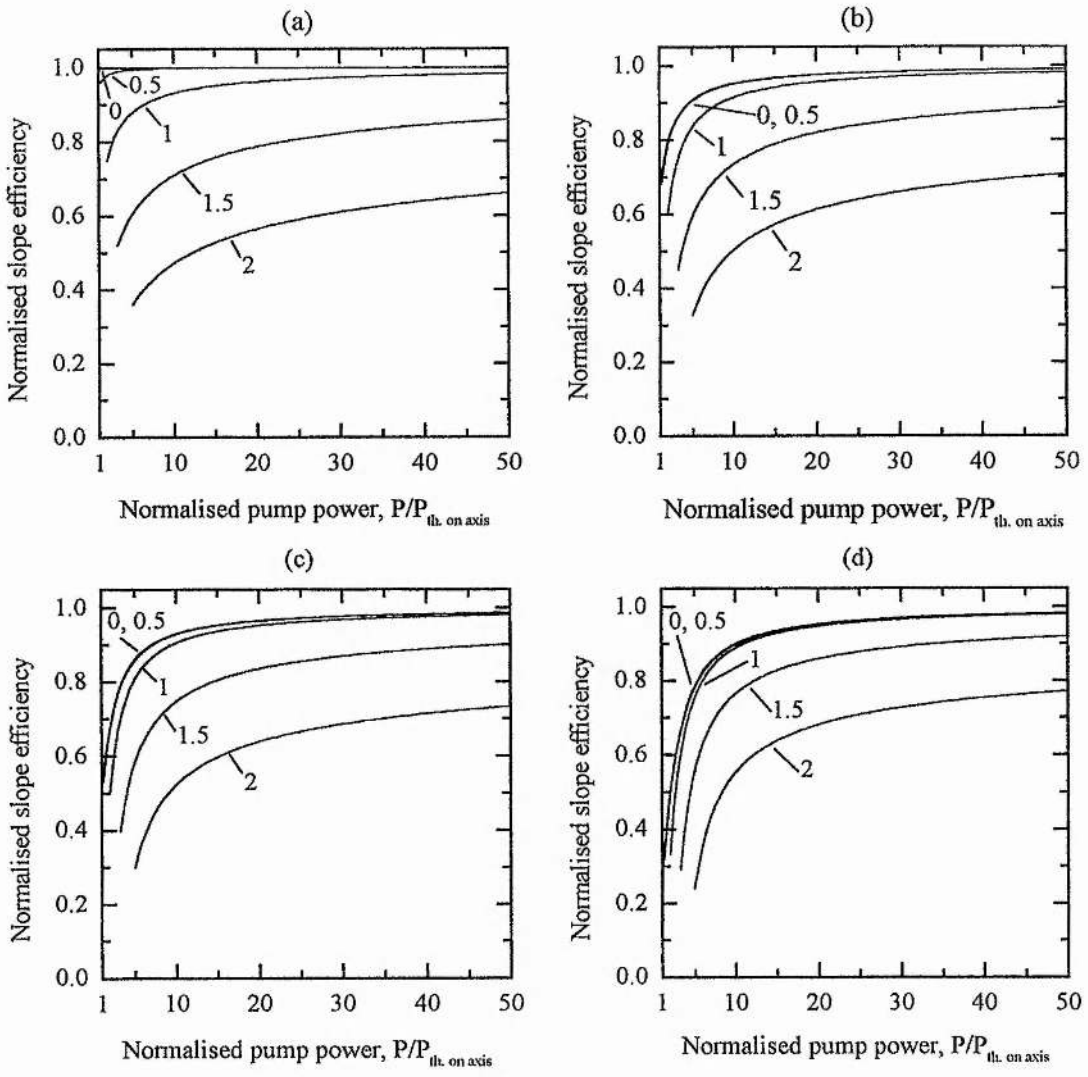

Fig. 2-9 Calculated variation of normalised slope efficiency with pump power relative to the on-axis threshold, with relative pump mode radius w_P/w_L, for a fixed w_L, as a parameter, for different relative reabsorption losses: $\frac{2\alpha_l L}{\delta} = 0$ (a), 1 (b), 2 (c), 5 (d).

four-level, case the best efficiency and lowest threshold, and therefore the maximum output power, are obtained by making w_P as small as possible.

It is also important to bear in mind that since, as Fig. 2-9 shows, it is advantageous to reduce the threshold when attempting to increase the efficiency, improved efficiency

will also be obtained by reducing the laser mode radius. Clearly, too small a laser mode radius will result in w_P/w_L becoming large and a consequent fall in efficiency.

On the other hand, too large a laser mode radius will result in an increase in laser threshold also reducing the efficiency and the pump power available above threshold. It should be noted at this point that the values of w_P/w_L shown in Fig. 2-7 to Fig. 2-9 are defined for fixed values of w_L. Thus, the increase in efficiency achieved by reducing w_P/w_L in Fig. 2-9 is due to a reduction in w_P rather than an increase in w_L.

It can be concluded, therefore, that the best efficiency for a given laser mode size will be obtained with the smallest possible pump mode. Further reductions in threshold and increases in efficiency will be obtained by reducing the laser mode size to similar dimensions, i.e. making it as small as possible without reducing it to the point where significant pump power falls outside the laser mode volume.

To put some of these results in a more practical context it is worth pointing out that, given the value of α_l in Table 2-1, the overall reabsorption loss for a 946-nm Nd:YAG laser at room temperature with a 2mm long crystal can be calculated as 1.9%.

2.3.4 Diffraction effects and pump beam quality.

A significant limitation on the model as described so far is that, like most similar approaches published [50,59], it does not include the effects of diffraction of the pump beam or laser mode within the gain medium. While this leads to some unphysical results, such as the optimum value for w_P and w_L being zero in some cases, the overall predictions of the two models are not seriously affected in most cases, as long as these limitations are born in mind. Ignoring diffraction does, however, become a more serious problem when small mode radii are used which, as we have seen, will generally be the case when low-threshold, high-efficiency operation is required. Neglecting diffraction effects also limits the ease with which the effects of pump beam quality, often an important consideration in the case of diode lasers, can be included. So far the pump beam has been assumed to be a

diffraction limited Gaussian. Clearly the use of a non-diffraction limited pump beam will, to some extent, affect the mode overlaps achieved with given values of w_P/w_L.

The inclusion of diffraction effects and influence of pump beam quality on the performance of end-pumped lasers has been discussed by a number of authors [68,69,70,71]. Here we use a simple approach [72] to include the effects of diffraction and pump-beam quality in the modelling of laser performance and optimisation of pumping geometry, and use these results to illustrate the advantages of a diffraction limited pump source. A more complete treatment, taking a very similar approach, has also been published which allows for elliptical pump beams and also allows determination of the optimum beam waist location [73].

Diffraction effects can be simply included in the expressions derived above by using the average values of the pump and laser mode radii taken over the length of the gain medium, in place of w_P and w_L. This average value is obtained by integrating the beam radius over the length of the gain medium and dividing by this length. For a beam waist radius w_o at one end of a length L of gain medium, this results in the expression [74]:

$$\overline{w}^2 = w_o^2 + \frac{1}{3}\left(\frac{M^2\lambda L}{\pi n w_o}\right)^2 \qquad (2\text{-}34)$$

where λ is the wavelength of the light, n is the refractive index of the gain medium and the factor M^2 has been introduced to allow for non-diffraction-limited beams. It has been suggested that more accurate results are obtained, in the case of the pump beam, by averaging over a numerically calculated effective length which depends on the pump beam divergence and the absorption coefficient of the pump light in the gain medium [70]. For the purposes of this discussion, however, we continue to make the simplification of averaging over the length of the gain medium.

If the average radii (strictly, the root mean square radii) of the laser and pump modes, calculated using (2-34), are $\overline{w}_L$ and $\overline{w}_P$, respectively, then we can apply the same conclusions reached in the previous section regarding relative and optimum values of w_L and w_P in the absence of diffraction to the average values $\overline{w}_L$ and $\overline{w}_P$.

These can then be used to optimise the actual waist radii, w_L and w_P, with diffraction and pump beam quality taken into account. The corresponding average mode radii $\overline{w}_L$ and $\overline{w}_P$ can then be used in equations (2-20) and (2-28), in place of w_L and w_P, to predict performance in the presence of diffraction effects and non-diffraction-limited pump beams.

By differentiating (2-34), the optimum value of w_o to obtain the minimum value of $\overline{w}$, $\overline{w}_{\min}$, can be shown to be

$$w_{o,opt} = \left(\frac{1}{\sqrt{3}}\frac{M^2\lambda L}{\pi n}\right)^{\frac{1}{2}} \tag{2-35}$$

From (2-34), this then gives the minimum attainable average mode radius for a given M^2, λ and L:

$$\overline{w}_{\min} = \left(\frac{2}{\sqrt{3}}\frac{M^2\lambda L}{\pi n}\right)^{\frac{1}{2}} = \sqrt{2}\, w_{o,opt} \tag{2-36}$$

From (2-20), it can be seen that it is desirable to minimise the average laser mode radius, $\overline{w}_L$, to reduce the threshold. The laser mode waist radius to achieve this, $w_{L,opt}$, can be calculated from (2-35) and the minimum average laser mode radius in the gain medium, $\overline{w}_{L,\min}$, from (2-36). In both cases, it is assumed that the laser mode is always diffraction-limited and therefore has an M^2 value of 1. Although not necessarily the values that will give best performance in practice, $w_{L,opt}$ and $\overline{w}_{L,\min}$ represent the smallest achievable laser mode size and therefore, from (2-20), will result in minimum threshold for a given pump beam geometry. As such, $w_{L,opt}$ and $\overline{w}_{L,\min}$ are useful normalisation values when looking at the behaviour of non-diffraction-limited pump beams. The ratio of the average pump beam radius to the minimum average laser mode radius in the gain medium can be shown, using (2-34) and (2-36) to be:

$$\frac{\overline{w}_p}{\overline{w}_{L,\min}} = \frac{1}{\sqrt{2}}\left(a^2 + \frac{1}{a^2}\frac{\left(M_P^2\lambda_P\right)^2}{\lambda_L^2}\right)^{\frac{1}{2}} \tag{2-37}$$

which is independent of crystal length, and where M_P^2 is the pump beam quality factor and the ratio of pump beam waist to optimum laser mode waist is given by:

$$a = \frac{w_P}{w_{L,opt}} \tag{2-38}$$

In writing (2-37), we have made the simplifying assumption that the refractive indices at the pump and laser wavelengths are the same.

The ratio $\overline{w}_p / \overline{w}_{L,\min}$ is plotted against a in Fig. 2-10 for λ_L=946nm and λ_P=808nm and a range of values of M_P^2. It can be seen that the $M_P^2 = 1$ curve has its minimum value when a=0.9. This point represents the geometry giving the lowest possible threshold as $\overline{w}_L$ and $\overline{w}_P$ are at their minimum, diffraction limited, values. Thus, there is nothing to be gained in terms of reducing the average pump mode radius, and therefore the threshold, by focusing the pump beam tighter than this. For pump beams having higher values of M_P^2 it can be seen that the minimum possible average mode radius, and the beam waist radius for which this occurs, both increase as would be expected. It is also clear that even small increases in the M^2 value of the pump beam will result in a minimum average pump beam radius attainable with that M^2 value, $\overline{w}_{P,\min}$, that is larger than that of the minimum average radius of the diffraction limited laser mode, $\overline{w}_{L,\min}$.

It is useful at this stage to return to our earlier finding that for a given pump power and laser mode the maximum output will be achieved by minimising the ratio w_P/w_L. Obviously, this translates into minimising $\overline{w}_p / \overline{w}_L$ when taking account of diffraction. In the case of a diffraction limited pump beam, it is clear from (2-20) that the lowest threshold will be obtained by using pump and laser waist radii of $w_{P,opt}$ and $w_{L,opt}$, respectively, as defined by (2-35), which give the minimum possible average pump and laser mode radii. This will also result in the highest output power

at a given pump power as it represents the minimum possible value of $\overline{w}_p / \overline{w}_L$, for this optimum laser mode waist, as shown in Fig. 2-10 and mentioned above.

In the case of non diffraction limited pump beams, it can be seem from (2-20) that, again, the lowest threshold will be obtained by using pump and laser mode waists of $w_{P,opt}$ and $w_{L,opt}$, respectively, as this corresponds to minimum average pump and laser mode waists, $\overline{w}_{P,\min}$ and $\overline{w}_{L,\min}$. However, as pointed out above, Fig. 2-10 shows that increasing M_P^2 rapidly results in values for $\overline{w}_{P,\min} / \overline{w}_{L,\min}$ greater than unity. Once this becomes the case, the slope efficiency will rapidly fall as an increasing fraction of the pump light falls outside the laser mode. Clearly, this can be rectified by increasing $\overline{w}_L$, but only at the expense of a higher threshold.

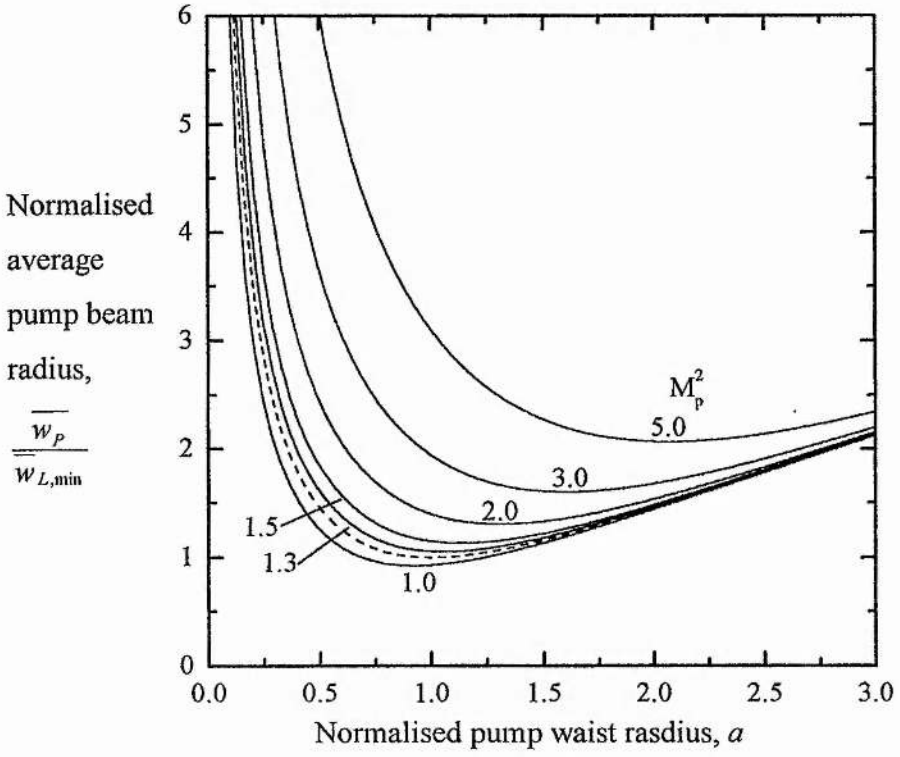

Fig. 2-10 Ratio of average pump-beam radius $\overline{w}_P$ to minimum average laser-mode radius $\overline{w}_{L,\min}$ versus $a = w_P / w_{L,opt}$ for a range of values of pump-beam quality factor M_P^2 and λ_P=808nm and λ_L=946nm. Dashed curve is for $\lambda_P = \lambda_L$ and $M_P^2 = 1$.

For a given pump power and beam quality, the highest output power will still be achieved with a pump mode waist of $w_{P,opt}$ which gives the minimum average pump radius, $\overline{w}_{P,\min}$, for this value of M_P^2. There will, however, be an optimum value of w_L, and therefore of $\overline{w}_L$, which achieves the best compromise between increased threshold and reduced slope efficiency and thus maximises the laser output. The exact value of w_L for which this occurs will depend on a number of factors, in particular the pump power above threshold and the round trip loss. It can be exactly determined by finding the value of $\overline{w}_L$ which, when used in (2-28) with an average pump beam radius of $\overline{w}_{P,\min}$, maximises the intra-cavity photon number S for a given pump power P. This value will generally not be the same as $w_{L,opt}$ which results in minimum threshold.

It is apparent from the above discussion that for a pump source with a given M^2, a practical strategy for optimising laser output is to first focus the pump beam to a waist of the optimum radius, $w_{P,opt}$, given by (2-35) and then adjust the laser mode radius to obtain maximum output. Clearly then, to obtain both low threshold and high efficiency it is desirable to use a pump source which is as close to diffraction limited as possible.

2.3.5 Optimisation of quasi-three-level laser parameters.

In most practical situations a maximum pump power is available and optimisation of the laser aims to maximise the output power for this pump power. In the case of a four level laser, for a given geometry, this is simply a case of optimising the output coupling to find that transmission which achieves the best compromise between increasing the threshold, thus reducing the intracavity power for a given pump power, and increasing the fraction of this intracavity power which is usefully coupled out. The calculation of this optimum output coupling level is fairly straightforward [75]. In the quasi-three-level case the situation is somewhat more complex.

As was shown earlier, an optimum crystal length exists for achieving minimum threshold which allows the best compromise between increasing the absorbed pump power and increasing the reabsorption loss. It is clear that such an optimum length

will also exist for obtaining maximum output above threshold and, due to the saturable nature of the reabsorption loss, this length will depend on the intracavity power and therefore the level of output coupling. Conversely, the optimum level of output coupling will depend on the crystal length for the similar reasons. As a result, both the crystal length and output coupling must be optimised simultaneously.

This is most easily done by plotting the output power for a given pump power against both crystal length and output coupling, as shown in Fig. 2-11. It is clear that the optimum level of output coupling varies with the crystal length and vice-versa, and also that the optimum crystal length above threshold is generally not the same as that for minimum threshold. It can also be seen that the optimum crystal length increases for higher pump powers, as the effects of the reabsorption loss become less significant due to its saturation as the intracavity power increases.

It is interesting to look at the effects of relative mode sizes in a similar way. As discussed earlier, it is always beneficial to make the average pump mode radius, and therefore the mode volume, as small as possible. However, the optimum laser mode volume relative to this was not so readily apparent. Fig. 2-12 shows the laser output power variation with crystal length and output coupling at a fixed pump power and with the pump mode size set to the optimum value for a range of relative average laser mode radii. In the case of $\overline{w}_L = 0.5\overline{w}_P$, the laser is seen to be above threshold for the whole of the range plotted, but the maximum output power is considerably lower than in the other cases. This would be expected from the previous discussion where it was seen that a small laser mode radius results in a low threshold, but a laser mode radius smaller than that of the pump leads to poor efficiency.

The converse is true in the case of $\overline{w}_L = 2\overline{w}_P$ where the maximum output power is slightly higher but the range over which the laser is above threshold is significantly reduced. Again, from the above discussion, it is apparent that the small relative pump mode radius results in increased efficiency but, as this is achieved by increasing the laser mode radius, the threshold also increases and the overall increase in output power is negligible. The highest output powers are obtained with $\overline{w}_L = \overline{w}_P$, indicating that the optimum laser mode radius is that which gives an average mode radius equal to that of the pump mode.

Performance departs from that in the optimal case quite rapidly either side of this value.

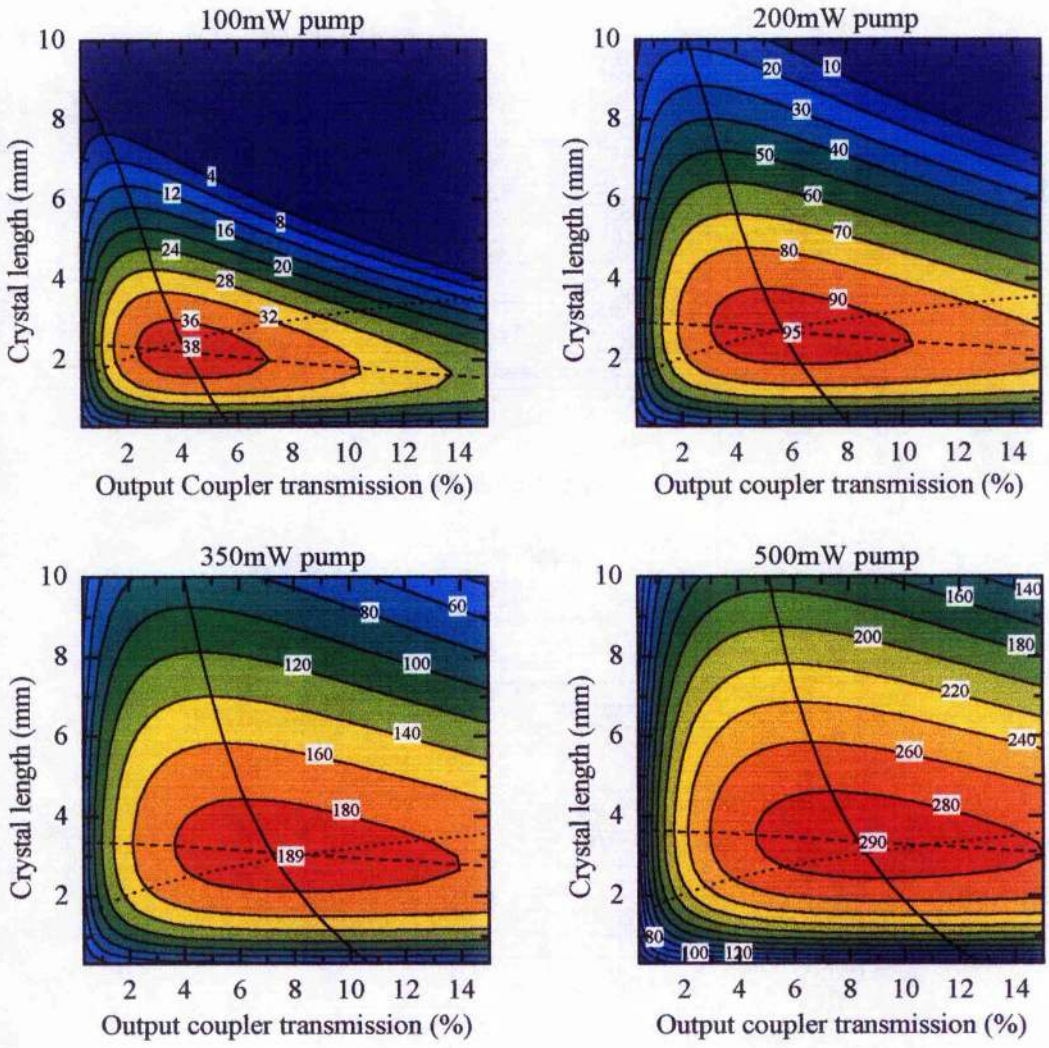

Fig. 2-11 Variation of 946-nm Nd:YAG laser output power (mW) at 300K with crystal length and output coupler transmission for various incident pump powers. Other paramterers: $w_P = w_{P,opt}$, $M_P^2 = 1$, $\overline{w}_L = \overline{w}_P$, parasitic extrinsic losses δ_p=1%, and α=8cm^{-1}.

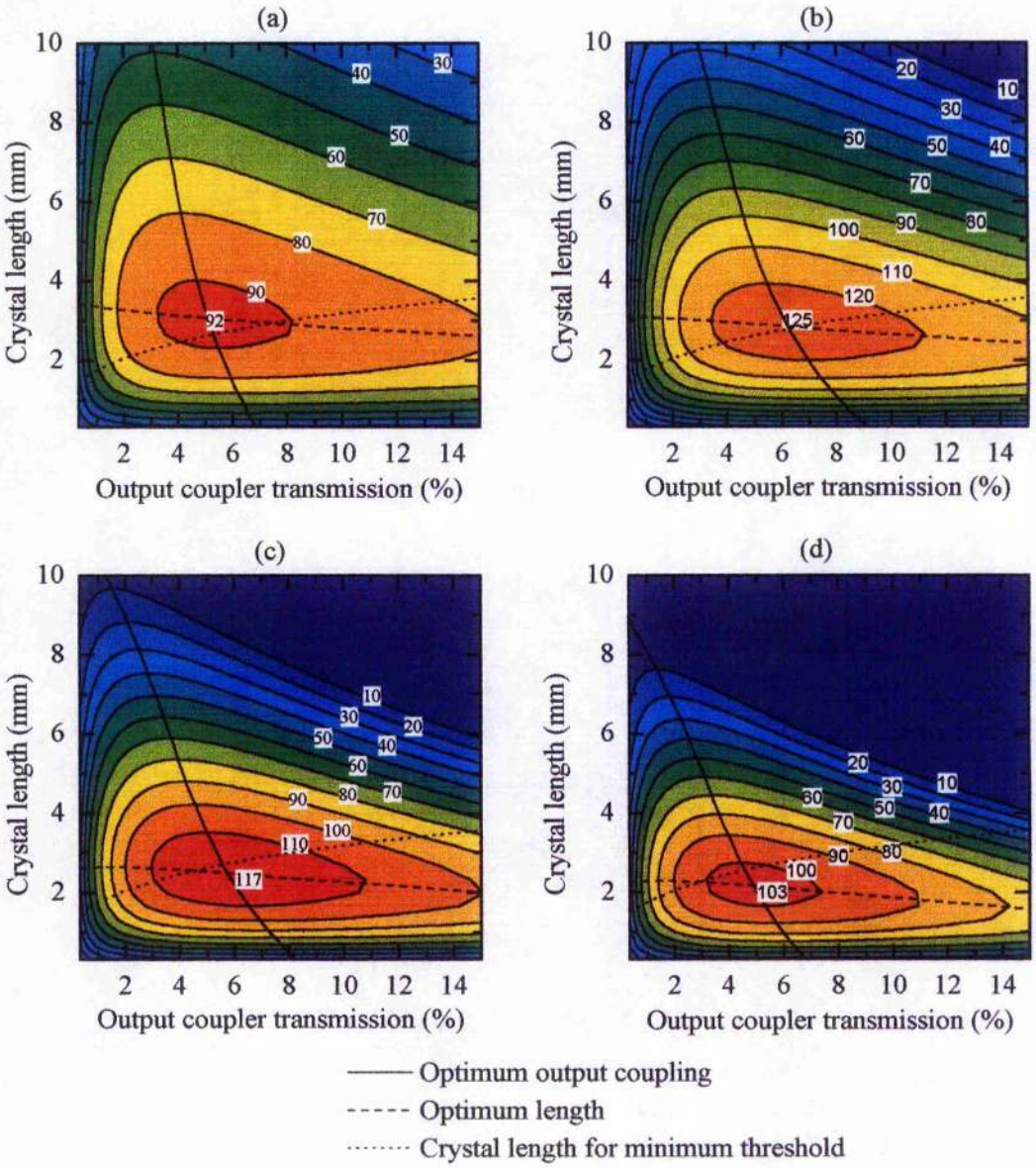

Fig. 2-12 Variation of 946-nm Nd:YAG laser output power (mW) at 300K with crystal length and output coupler transmission for various average laser mode radii: (a) $\overline{w}_L = 0.5\overline{w}_P$, (b) $\overline{w}_L = \overline{w}_P$, (c) $\overline{w}_L = 1.5\overline{w}_P$, (d) $\overline{w}_L = 2\overline{w}_P$ Other paramterers: w_P=$w_{P,opt}$, $M_P^2 = 1$, parasitic extrinsic losses δp=1%, and α=8cm^{-1} incident pump power 250mW.

Finally, the consequences of using a non-diffraction-limited pump source are illustrated in Fig. 2-13. Here, the pump mode waist is set to the optimum value for its M^2 parameter and the crystal length, and the laser mode is set to give the same

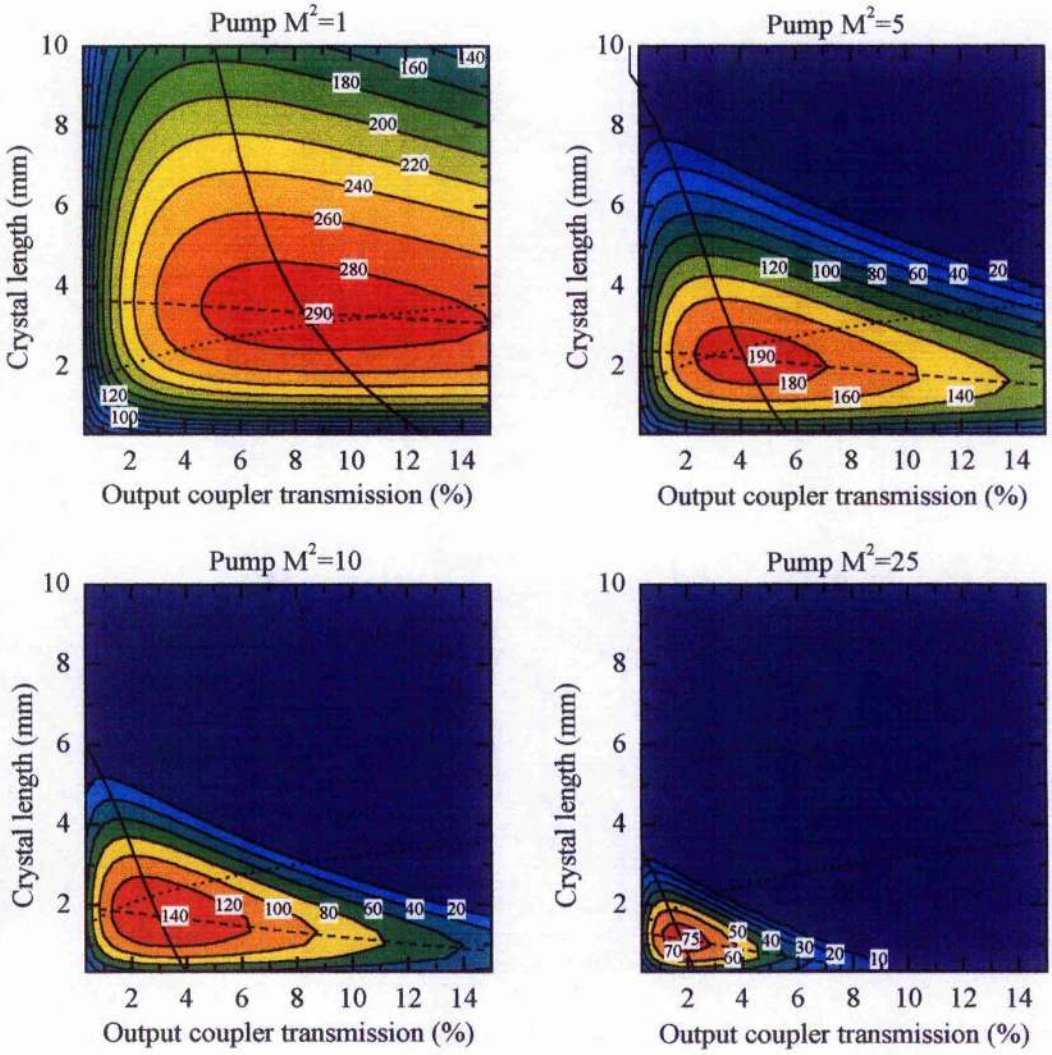

Fig. 2-13 Variation of 946-nm Nd:YAG laser output power (mW) at 300K with crystal length and output coupler transmission for various pump M^2 values. Other parameters; $w_P=w_{P,opt}$, $\overline{w}_L = \overline{w}_P$, parasitic extrinsic losses δp=1%, α=8cm^{-1}, incident pump power: 500mW.

average radius as the pump mode. The reduction in output power resulting from using a pump source with $M^2>1$ is clearly apparent.

It was shown in Fig. 2-10 that increasing the pump M^2 rapidly resulted in significant increases in the minimum obtainable average radius of the pump mode and therefore an increase in threshold. It has also been shown that unless the laser mode radius is increased to maintain a similar average value to the pump mode radius the efficiency is reduced. Thus, as the pump M^2, and therefore average mode radius, increases, the laser mode radius must also increase resulting in a further rise in the threshold. This can be clearly seen in Fig. 2-13 where the range over which the laser is above threshold rapidly falls with increasing M^2 and the maximum output power is significantly reduced as a result of the increased threshold. The maximum power obtained using a diffraction limited pump source ($M^2=1$) is almost three times that obtained with a source having $M^2=25$, a typical value, in the junction plane, for broad-area laser diodes with output powers of a few watts.

2.4 Conclusions.

The results of the modelling described in this chapter, particularly Fig. 2-7 - Fig. 2-9, have shown that quasi-three-level lasers can approach the efficiency of, otherwise equivalent, four-level systems as long as they are pumped high enough above threshold to largely saturate the reabsorption loss. However, as the reabsorption loss acts to increase the threshold, as shown in Fig. 2-5, it is important to try to find other strategies to minimise the threshold if high efficiency operation is required. In the case of the 946-nm Nd:YAG laser operating at room temperature this becomes even more important due to the low stimulated-emission cross section.

Equation (2-20) shows that the threshold can be reduced by reducing the pump and laser mode radii, while Fig. 2-9 shows that having a pump mode radius larger than that of the laser mode results in poor efficiency. When considering the effects of diffraction, these results can be applied to the average mode radii and it is clear from Fig. 2-10 that the smallest value attainable for this in the case of the pump is limited by the pump beam quality. It is, therefore, clear that when attempting to reduce

threshold it is important to have a pump source as close to diffraction limited as possible. This not only allows the average pump mode radius to be reduced, thus lowering the threshold, but also allows the laser mode radius to be reduced, in a similar way, without compromising efficiency by pumping regions outside the laser mode volume.

Other factors which can be used to reduce threshold are the temperature of the Nd:YAG crystal, reduction of which results in a reduced reabsorption loss, and the spectral width of the pump, narrowing of which improves the efficiency with which pump light is absorbed by the laser gain medium.

Thus, the characteristics of the pump beam which can significantly affect the laser threshold and efficiency are the beam quality, or M^2 value, and the spectral quality, or linewidth. Unfortunately, in the case of diode laser pump sources, these two parameters, while significantly better than incoherent pump sources, are generally worse than other laser pump sources. This is especially true in the case of laser diodes having output powers of more than around 100mW. Many of the other properties of laser diodes make them highly attractive as pump sources, so it would be desirable to also achieve high spatial and spectral quality with high powers from these devices.

2.5 References.

1 R.N. Hall, G.E. Fenner, J.D. Kingsley, T.J. Soltys and R.O. Carlson, "Coherent Light Emission from GaAs Junctions," Phys. Rev. Lett. **9**, 366-368, (1962).

2 N. Holonyak Jr. and S.F. Bevacqua, "Coherent (visible) light emission from $Ga(As_{1-x}P_s)$ junctions," Appl. Phys. Lett. **1**, 82-83, (1962).

3 R. Newman, "Excitation of Nd^{3+} fluorescence in $CaWO_4$ by recombination radiation in GaAs," J. Appl. Phys. **34**, 473, (1963).

4 R.J. Keyes and T.M. Quist, "Injection luminescent pumping of $CaF_2:U^{3+}$ with GaAs diode lasers," Appl. Phys. Lett. **4**, 50-52, (1964).

5 J.E. Geusic, H.M. Marcos and L.G. Van Uitert, "Laser oscillations in Nd-doped yttrium aluminum, yttrium gallium and gadolinium garnets," Appl. Phys. Lett. **4**, 182-184, (1964).

6 M. Ross, "Yag laser operation by semiconductor laser pumping," Proc. IEEE **56**, 196-197, (1968).

7 R.B. Allen and S.J. Scalise, "Continuous operation of a YAlG:Nd laser by injection luminescent pumping," Appl. Phys.Lett. **14**, 188-190, (1969).

8 F.W. Ostermayer, Jr., R.B. Allen and E.G. Dierschke, "Room temperature cw operation of a $GaAs_{1-x}P_x$ diode-pumped YAG:Nd laser," Appl. Phys. Lett. **19**, 289-292, (1971).

9 L.J. Rosenkrantz, "GaAs diode-pumped Nd:YAG laser," J. Appl. Phys. **43**, 4603-4605, (1972).

10 R.B. Chesler and D.A. Draegert, "Miniature diode-pumped Nd:YAlG lasers," Appl. Phys. Lett. **23**, 235-236, (1973).

11 D.A. Draegert, "Single-diode end-pumped Nd:YAG laser," IEEE J. Quantum Electron. **QE-9**, 1146-1149, (1973).

12 K. Washio, K. Iwamoto, K. Inoue, I. Hino, s. Matsumoto and F. Saito, "Room-temperature cw operation of an efficient miniaturized Nd:YAG laser end-pumped by a superluminescent diode," Appl. Phys. Lett. **29**, 720-722, (1976).

13 F.W. Ostermayer, Jr., "LED end-pumped Nd:YAG lasers," IEEE J. Quantum Electron. **QE-13**, 1-6, (1977).

14 I. Hayashi, M.B. Panish and P.W. Foy, "A low-threshold room-temperature injection laser," IEEE J. Quantum Electron. **5**, 211-212, (1969).

15 I. Hayashi and M.B. Panish, "GaAs-$Ga_xAl_{1-x}As$ heterostructure injection lasers which exhibit low thresholds at room temperature," J. Appl. Phys. **41**, 150-163, (1970).

16 M.B. Panish, I. Hayashi and S. Sumski, "Double-heterostructure injection lasers with room temperature thresholds as low as 2300 A/cm^2," Appl. Phys. Lett. **16**, 326-327, (1970).

17 Zh.I. Alferov, V.M. Andreev, D.Z. Garbuzov, Yu.V. Zhilyaev, E.P. Morozov, E.L. Portnoi and V.G. Trofim, "Effect of the heterostructure parameters on the laser threshold current and the realisation of continuous generation at room temperature," Fiz. Tekn. Polupr. **4**, 1826, (1970). [English translation, Soviet Physics - Semiconductors **4**, 1573, (1971).]

18 I. Hayashi, M.B. Panish, P.W. Foy and S. Sumski, "Junction lasers which operate continuously at room temperature," Appl. Phys. Lett. **17**, 109-111, (1970).

19 R.L. Hartman, J.C. Dyment, C.J. Hwang and M. Kuhn, "Continuous operation of GaAs-$Ga_{1-x}Al_xAs$ double-heterostructure lasers with 30°C half-lives exceeding 1000h," Appl. Phys. Lett. **23**, 181-183, (1973).

20 W.B. Joyce, R.W. Dixon and R.L. Hartman, "Statistical characterization of the lifetimes of continuously operated (Al,Ga)As double-heterostructure lasers," Appl. Phys. Lett. **28**, 684-686, (1976).

21 R.L. Hartman, N.E. Schumaker and R.W. Dixon, "Continuously operated (Al,Ga)As double-heterostructure lasers with 70°C lifetimes as long as two years," Appl. Phys. Lett. **31**, 756-759, (1977).

22 R.D. Dupuis and P.D. Dapkus, "Room-temperature operation of $Ga_{(1-x)}Al_xAs$/GaAs double-heterostructure lasers grown by metalorganic chemical vapor deposition," Appl. Phys. Lett. **31**, 466-468, (1977).

23 R.D. Dupuis and P.D. Dapkus, "$Ga_{(1-x)}Al_xAs$/ $Ga_{(1-y)}Al_yAs$ double-heterostructure room-temperature lasers grown by metalorganic chemical vapor deposition," Appl. Phys. Lett. **31**, 839-841, (1978).

24 R.D. Dupuis and P.D. Dapkus, "Room-temperature laser operation of quantum-well $Ga_{(1-x)}Al_xAs$-GaAs laser diodes grown by metalorganic chemical vapor deposition," Appl. Phys. Lett. **32**, 295-297, (1978).

25 D.R. Scifres, R.D. Burnham and W. Streifer, "Phase-locked semiconductor laser array," Appl. Phys. Lett. **33**, 1015-1017, (1979).

26 D.R. Scifres, R.D. Burnham, C. Lindström, W. Streifer and T.L. Paoli, "Phase-locked (GaAl)As laser emitting 1.5W cw per mirror," Appl. Phys. Lett. **42**, 645-647, (1983).

27 M. Sakamoto, G.L. Harnagel, D.F. Welch, C.R. Lennon, W. Streifer, H. Kung and D.R. Scifres, "12.5-W continuous-wave monolithic laser-diode arrays," Opt. Lett. **13**, 378-379, (1988).

28 M. Sakamoto, J.G. Endriz and D.R. Scifres, "120W cw output power from monolithic AlGaAs (800nm) laser diode array mounted on diamond heatsink," Electron. Lett. **28**, 197-199, (1992).

29 B. Zhou, T.J. Kane, G.J. Dixon and R.L. Byer, "Efficient, frequency-stable laser-diode-pumped Nd:YAG laser," Opt. Lett. **10**, 62-64, (1985).

30 T.J. Kane, A.C. Nilsson and R.L. Byer, "Frequency stability and offset locking of a laser-diode-pumped Nd:YAG monolithic nonplanar ring oscillator," Opt. Lett. **12**, 175-177, (1987).

31 J.J. Zayhowski and A. Mooradian, "Single-frequency microchip Nd lasers," Opt. Lett. **14**, 24-26, (1989).

32 S.C. Tidwell, J.F. Seamans and M.S. Bowers, "Highly efficient 60-W TEM_{00} cw diode-end-pumped Nd:YAG laser," Opt. Lett. **18**, 116-118, (1993).

33 Y. Kaneda, M. Oka, H. Masuda and S. Kubota, "7.6W of continuous-wave radiation in a TEM_{00} mode from a laser-diode end-pumped Nd:YAG laser," Opt. Lett. **14**, 1003-1005, (1992).

34 W.A. Clarkson and D.C. Hanna, "Efficient Nd:YAG laser end pumped by a 20-W diode-laser bar," Opt. Lett. **21**, 869-871, (1996).

35 D. Golla, S. Knoke, W. Schöne, G. Ernst, M. Bode, A. Tünnermann and H. Welling, "300-W cw diode-laser side-pumped Nd:YAG rod laser," Opt. Lett. **20**, 1148-1150, (1995).

36 J.J. Kasinski, W. Hughes, D. DiBiase, P. Bournes and R. Burnham, "One joule output from a diode-array-pumped Nd:YAG laser with side-pumped rod geometry," IEEE J. Quantum Electr. **28**, 977-985, (1992).

37 L.E. Holder, C. Kennedy, L. Long and G. Dubé, "One joule per Q-switched pulse diode-pumped laser," IEEE J. Quantum Electr. **28**, 986-991, (1992).

38 R.L. Byer, "Diode laser-pumped solid state lasers," Science **239**, 742-747, (1988).

39 T.Y. Fan and R.L. Byer, "Diode laser-pumped solid-state lasers," IEEE J. Quantum Electron. **24**, 895-912, (1988).

40 D.W. Hughes and J.R.M. Barr, "Laser diode pumped solid state lasers," J. Phys. D: Appl. Phys. **25**, 563-586, (1992).

41 W. Streifer, D.R. Scifres, G.L. Harnagel, D.F. Welch, J. Berger and M. Sakamoto, "Advances in diode laser pumps," IEEE J. Quantum Electron. **24**, 883-894, (1988).

42 J.G. Endriz, M. Vakili, G.S. Browder, M. DeVito, J.M. Haden, G.L. Harnagel, W.E. Plano, M. Sakamoto, D.F. Welch, S. Willing, D.P. Worland and H.C. Yao, "High power diode laser arrays," IEEE J. Quantum Electr. **28**, 952-965, (1992).

43 T. Schweizer, T. Jensen, E. Heumann and G. Huber, "Spectroscopic properties and diode pumped 2.6μm laser performance in Yb-codoped Er:$Y_3Al_5O_{12}$ and Er:Y_2SiO_5," Opt. Comm. **118**, 557-561 (1995).

44 T. Yokozawa and H. Hara, "Laser-diode end-pumped Tm^{3+}:YAG eye-safe laser," Appl. Opt. **35**, 1424-1426 (1996).

45 T.Y. Fan and R.L. Byer, "Continuous-wave operation of a room-temperature, diode-laser-pumped, 946-nm Nd:YAG laser," Opt. Lett. **12**, 809-811, (1987).

46 L.F. Johnson and R.A. Thomas, "Maser oscillations at 0.9 and 1.35 microns in $CaWO_4$:Nd^{3+}," Phys. Rev. **131**, 2038-2040, (1963).

47 R.W. Wallace and S.E. Harris, "Oscillation and doubling of the 0.946-μ line in Nd^{3+}:YAG," Appl. Phys. Lett. **15**, 111-112, (1969).

48 M. Birnbaum, A.W. Tucker and C.L. Fincher, "cw room-temperature laser operation of Nd:CAMGAR at 0.941 and 1.059 μ," J. Appl. Phys. **49**, 2984-2985 (1978).

49 I.P. Alcock, A.I. Ferguson, D.C. Hanna and A.C. Tropper, "Continuous-wave oscillation of a monomode neodymium-doped fibre laser at 0.9mm on the $^4F_{3/2} \rightarrow {}^4I_{9/2}$ transition," Opt. Comm. **58**, 405-408, (1986).

50 T.Y. Fan and R.L. Byer, "Modeling and cw operation of a quasi-three-level 946nm Nd:YAG laser," IEEE J. Quantum. Electr. **QE-23**, 605-612, (1987).

51 W.P. Risk and W. Lenth, "Room-temperature, continuous-wave, 946-nm Nd:YAG laser pumped by laser-diode arrays and intracavity frequency doubling to 473nm," Opt. Lett. **12**, 993-995, (1987).

52 G.J. Dixon, Z.M. Zhang, R.S.F. Chang and N. Djeu, "Efficient blue emission from an intracavity-doubled 946-nm Nd:YAG laser," Opt. Lett. **13**, 137-139, (1988).

53 W.P. Risk, R. Pon and W. Lenth, "Diode laser pumped blue-light source at 473nm using intracavity frequency doubling of a 946 nm Nd:YAG laser," Appl. Phys. Lett. **54**, 1625-1627, (1989).

54 A. Harada, Y, Nihei, Y, Okazaki and H. Hyuga, "Intracavity frequency doubling of a diode-pumped 946-nm Nd:YAG laser with bulk periodically poled MgO-$LiNbO_3$," Opt. Lett. **22**, 805-807, (1997).

55 G. Hollemann, E. Peik and H. Walther, "Frequency-stabilized diode-pumped Nd:YAG laser at 946 nm with harmonics at 473nm and 237 nm," Opt. Lett. **19**, 192-194, (1994).

56 M. Bode, I. Freitag, A. Tünnermann and H. Welling, "Frequency-tuneable 500mW continuous-wave all-solid-state single-frequency source in the blue spectral region," Opt. Lett. **22**, 1220-1222, (1997).

57 W.A. Clarkson, R. Koch and D.C. Hanna, "Room-temperature diode-bar-pumped Nd:YAG laser at 946nm," Opt. Lett. **21**, 737-739, (1996).

58 J. Hong, B.D. Sinclair, W. Sibbett and M.H. Dunn, "Frequency-doubled and Q-switched 946-nm Nd:YAG laser pumped by a diode-laser array," Appl. Opt. **31**, 1318-1321, (1992).

59 W.P. Risk, "Modeling of longitudinally pumped solid-state lasers exhibiting reabsorption losses," J. Opt. Soc. Am. B **5**, 1412-1423 (1988).

60 R.J. Beach, "CW theory of quasi-three-level end-pumped laser oscillators," Opt. Comm. **123**, 385-393, (1996).

61 S. Singh, R.G. Smith and L.G. Van Uitert, "Stimulated-emission cross section and fluorescent quantum efficiency of Nd3+ in yttrium aluminum garnet at room temperature," Phys. Rev. B **10**, 2566-2572, (1974).

62 G.M. Zverev, Yu. D. Golyaev, E.A. Shalaev and A.A. Shokin, "Neodymium activated Yttrium-Aluminium-Garnet (YAG:Nd) Lasers," J. Sov. Laser Research **8**, 189-282, (1987).

63 B.F. Aull and H.P. Jenssen, "Vibronic interactions in Nd:YAG resulting in nonreciprocity of absorption and stimulated emission cross section," IEEE J. Quantum Electron. **QE-18**, 925, (1992).

64 W. Koechner, "Solid-State Laser Engineering" (third edition), Springer-Verlag, Berlin, (1992).

65 J.J. Zayhowski and J. Harrison, "Minature Solid-State Lasers," in Handbook of Photonics, CRC Press, New York, 1997.

66 T. Kushida, H.M. Marcos and J.E. Geusic, "Laser transition cross section and fluorescence branching ratio for Nd3+ in Yttrium Aluminium Garnet," Phys. Rev. **167**, 289-291, (1968).

67 M. Birnbaum and C.F. Klein, "Stimulated emission cross section at 1.061μm in Nd:YAG," J. Appl. Phys. **44**, 2928-2930, (1973).

68 D.G. Hall, R.J. Smith and R.R. Rice, "Pump-size effects in Nd:YAG lasers," Appl. Opt. **19**, 3041-3043, (1980).

69 T.Y. Fan and A. Sanchez, "Pump source requirements for end-pumped lasers," IEEE J. Quantum. Electron. **26**, 311-316, (1990).

70 P. Laporta and M. Brussard, "Design criteria for mode size optimization in diode-pumped solid-state lasers," IEEE J. Quantum Electron. **27**, 2319-2326 (1991).

71 Y.F. Chen, T.S. Liao, C.F. Kao, T.M. Huang, K.H. Lin and S.C. Wang, "Optimization of fibre-coupled laser-diode end-pumped lasers: influence of pump-beam quality," IEEE J. Quantum Electron. **32**, 2010-2016, (1996).

72 I.D. Lindsay and M. Ebrahimzadeh, "Efficient continuous-wave and Q-switched operation of a 946-nm Nd:YAG laser pumped by an injection-locked broad-area diode laser," Appl. Opt. **37**, 3961-3970 (1998).

73 "Minimum averaged area of asymmetric multimode pumping beam," J.K. Jabczynski, Opt. Comm. **140**, 1-5 (1997).

74 M.J.F. Digonnet and C.J. Gaeta, "Theoretical analysis of optical fibre laser amplifiers and oscillators," Appl. Opt. **24**, 333-342 (1985).

75 A.E. Siegman, "Lasers," University Science Books, Mill Valley, California, USA (1986).

3. Nonlinear Optical Frequency Conversion and Optical Parametric Oscillators.

3.1 Introduction.

The demonstration of the laser made available, for the first time, a light source yielding the intensities necessary to observe nonlinear optical frequency mixing in dielectric media and made possible the first experimental demonstration of optical second harmonic generation (SHG) in 1961 [1]. It was soon realised that the efficiency of such processes could be vastly enhanced by ensuring that the interacting waves travelled through the nonlinear medium with matched phase velocities. This was achieved, by exploiting the natural birefringence of the optically anisotropic materials used, the following year [2,3] which also saw the classic treatment laying down the theoretical foundations of the field [4].

The obvious attraction of nonlinear optical frequency conversion as a means of extending the spectral coverage of conventional laser sources motivated further experimental demonstrations including intracavity second harmonic generation [5] as well as parametric oscillation [6] and difference-frequency mixing [7]. Theoretical treatment was also extended [8,9,10]. The development of new materials [11] and sources, particularly neodymium based lasers [5,12,13], accelerated research in the field and nonlinear processes and devices were soon being widely studied [11,14,20]. As a result, harmonic generation continued to be used to extend the range of both pulsed [15,16] and continuous-wave [17,18] laser sources throughout the 1970s.

Following the first demonstration of an optical parametric oscillator (OPO) [6], a pulsed device, a continuous-wave (cw) device was also demonstrated [19]. While other frequency mixing techniques were limited in their tuning range by the

tunability of the laser sources used, OPOs had the obvious appeal of allowing broad tunability from a single, fixed-wavelength pump source and considerable research activity took place in the early stages of their development [20,21,22,23]. The early devices mentioned above used cavities which resonated both parametrically generated waves in an attempt to reduce the threshold pump power. However, those investigating these devices, and other early workers in the field [24,25], noted that this double-resonance requirement resulted in high degree of instability in output power and wavelength. Despite this, a number of other continuous-wave devices, based on doubly-resonant cavities, were demonstrated around this time [26,27,28]. The discovery that Q-switched lasers could provide sufficient peak powers to achieve threshold in singly-resonant OPOs [29], which do not suffer from the same instability problems as doubly-resonant devices, moved interest in the direction of pulsed, singly-resonant devices [30,13]. This resulted in the enthusiastic development of such devices, their commercial availability as early as 1970 [31] and their use in a number of practical applications [32,33].

By contrast, after initial optimism [21], continuous wave OPOs were somewhat neglected as singly-resonant OPO (SRO) thresholds were beyond the reach of continuous-wave laser powers. As a result, doubly-resonant OPOs (DROs), with their attendant stability problems, had to be used for continuous-wave operation. A ground-breaking study by Smith [34] of the factors affecting the stability of DROs identified the need for a stable, single-frequency, effectively isolated pump source and careful control of the DRO cavity length. Given these conditions, it was shown that stable, single-frequency operation of the DRO could be obtained with thresholds as low as 3mW. Despite this, very little effort was expended on the study of cw-OPOs during the 1970s.

The development and availability of a new generation of materials [35,36,37,38] led to a resurgence of interest in nonlinear optics during the 1980s. In addition, advances in the diode pumping of solid state lasers occurring around the same time [39,40] resulted in two highly complementary technologies, with nonlinear optical processes being used to convert the, mainly near-infrared, output of compact efficient diode-pumped solid state lasers to other spectral regions. In particular, the use of diode-

pumped neodymium-based lasers in conjunction with nonlinear materials such as potassium titanyl phosphate (KTP) has allowed high-power green light generation in both pulsed [41,42] and continuous [43,44,45] systems. Cascading of conversion processes has allowed the extension of harmonic generation by Nd lasers into the ultraviolet [46,47].

The widespread use of diode-pumped solid state lasers had largely been instigated by advances in the technology of AlGaAs based diode lasers, resulting in reliable operation over long lifetimes at increased power levels compared to earlier devices. This also prompted developments in the direct use of diode lasers for nonlinear optical frequency conversion. The nonlinear material potassium niobate ($KNbO_3$) was found to be particularly suitable for doubling laser radiation in the region of 800 nm produced by AlGaAs diode lasers. Although early experiments used single-pass doubling to generate second-harmonic powers below 1mW with very low efficiencies [48], it was soon found that much higher efficiencies could be obtained by the use of a resonant enhancement cavity [49,50]. This technique has continued to be used to generate increasingly high second harmonic powers [51,52,53,54] and in a recent demonstration 1W of second harmonic light was generated by the resonant doubling of a high-power diode laser amplifier [55]. In a number of cases, sufficient second-harmonic power has been generated for further resonant doubling to be used to produce ultraviolet light [53,56]

The 1980s also saw a renewal of interest in continuous-wave optical parametric oscillators due to their potential as sources of squeezed states of light arising from the fact that such a device generates photons in correlated pairs [57]. It is, however, interesting to note that many such experiments have made use of optical parametric amplifiers (OPAs) or below-threshold DROs, as the required quantum correlation properties are obtained without the problems normally associated with maintaining stable operation in an above-threshold DRO [58,59,60]. Nevertheless, similar experiments have been carried out using above-threshold DROs and TROs [61,62,63] with stabilised pump sources and servo cavity-length control techniques or monolithic cavities, for stability.

The same advances in materials and pump-source development, described above, which benefited frequency upconversion, also advanced the development of continuous-wave OPOs. Stable, single-mode operation of a DRO pumped by the second harmonic of a diode-laser-pumped Nd:YAG laser was demonstrated [64] and stable, narrow-linewidth operation of a similar system pumped by an injection-locked lamp-pumped Nd:YAG laser was also achieved [65]. Such a system was also used, with a diode-pumped monolithic Nd:YAG ring laser, to investigate the stability and tuning properties of the DRO [66] and, shortly after, stabilisation, tuning and signal-idler heterodyne locking to an external reference were demonstrated [67]. Since these results a number of experimental demonstration of stable and/or smoothly tuneable continuous-wave OPOs have been carried out [68,69,70,71,72].

Another approach to stable operation which was made possible through developments in pump sources and nonlinear materials was the continuous-wave operation of a singly-resonant OPO. The first cw SRO was demonstrated in 1993 with a threshold of 1.4W [73] and several similar devices have since followed [74,75,76]. All these devices were operated external to the laser cavity resulting in external thresholds of the order of 1W or more. An alternative approach that has been demonstrated in recent years is to locate the nonlinear crystal inside the pump laser cavity allowing the OPO to be pumped by the high internal circulating field [77]. A number of such devices have been demonstrated [78,79,80], retaining many of the advantages of SROs without such high external pump power requirements. External pump power thresholds as low as 310mW have been achieved by this method [81]. These various developments have recently resulted in the commercial availability of several continuous-wave SROs [82].

Like frequency upconversion, the direct pumping of OPOs by diode lasers has also been widely demonstrated in recent years. Doubly resonant and pump-enhanced OPOs have been pumped by diode laser systems using techniques such as master oscillator/power amplifiers [83] and injection-locking [84] to obtain high powers with high spatial and spectral quality from the laser diodes [85,86,87]. In addition, single-mode laser diodes have been used to pump triply-resonant [84], pump

enhanced [84] and doubly-resonant [88] OPOs and a singly-resonant OPO has been demonstrated with a tapered diode-amplifier pump source [89].

The most important recent development to have a large-scale impact on nonlinear optics research has been the widespread availability of quasi-phase-matched materials, particularly periodically-poled lithium niobate (PPLN). These provide an alternative phase matching method to birefringent techniques which allows access to the highest nonlinear coefficients of the material [90]. As a result, significant improvements have been brought about in the performance of frequency mixing processes [91] and, particularly, of OPOs [92,93].

The many recent developments in nonlinear optical frequency mixing and optical parametric oscillators has made them more attractive solutions for practical applications. The wide tunability of OPOs has long been recognised as a potentially useful spectroscopic tool, and pulsed OPOs have been used in such applications for some time [32,33,94]. More recently, continuous OPOs have started to be used in spectroscopic applications [95,96]. Also, difference-frequency mixing has, in recent years, been found to be a particularly useful route to developing compact sources in the 3-μm region for the detection of atmospheric trace gases with a high degree of sensitivity [97,98,99].

In addition to squeezed light generation, mentioned above, another application which makes use of the special properties of nonlinear optical frequency mixing processes is that of optical frequency standards. Since energy is always conserved in nonlinear frequency conversion, accurate knowledge of two of the interacting frequencies allows the third to also be accurately determined. This property can prove useful in comparing optical standards which are widely separated in frequency and linking these to known radio-frequency standards [100,101]. In particular, the advent of high-precision frequency standards based on trapped atoms and ions [102] has led to a requirement to compare such standards to other trapped-atom references and to known microwave reference frequencies [103]. Various schemes have been proposed and demonstrated using OPOs to compare optical and radio frequency standards [104,105,106] and to generate "combs" of many known frequency markers [107].

Moreover, nonlinear frequency-mixing processes are routinely used with lasers in optical frequency chains [102,108,109].

Although the above review has been fairly brief, it can be seen that the field of continuous-wave nonlinear optics is probably more active currently than it has ever been. The remainder of this chapter will provide an overview of the theoretical basis of nonlinear optical interactions, phase-matching in nonlinear optical processes and the behaviour of continuous-wave optical parametric oscillators. The demands such devices place on pump sources will be discussed at the end of the chapter.

3.2 Theoretical basis of nonlinear optics.

In the case of the classical optical processes associated with light propagating in a dielectric medium, the relationship between the polarisation field in the medium and the incident optical electric field is considered to be linear, i.e.

$$\mathbf{P}(\mathbf{r},t) = \varepsilon_0 \chi \mathbf{E}(\mathbf{r},t) \tag{3-1}$$

where ε_0 is the permittivity of free space and χ is the susceptibility of the material. This results in effects such as refraction and reflection at boundaries. In the case of intense applied fields, such as those obtained from a laser, the electrons in the medium experience displacing forces comparable in magnitude to the intra-atomic forces they are subject to within the material. This results in the linearity of equation (3-1) breaking down and, in an analogous way to the breakdown of Hooke's law under large displacements, higher order terms must be considered. Under these conditions, equation (3-1) can be expanded as:

$$\mathbf{P}(\mathbf{r},t) = \varepsilon_0\left(\chi^{(1)}\mathbf{E}(\mathbf{r},t) + \chi^{(2)}\mathbf{E}^2(\mathbf{r},t) + \chi^{(3)}\mathbf{E}^3(\mathbf{r},t) + \ldots\right) \tag{3-2}$$

Here we discuss how the consideration of these higher order terms, in particular that involving $\chi^{(2)}$, can lead to processes resulting in the frequency conversion of laser light within a suitable, usually crystalline, medium. These processes have been widely discussed by a number of authors, the original treatment being that of

Armstrong et al. [4]. A rather more accessible treatment was made by Boyd and Kleinman [10] which also extended to focused beams rather than plane waves. Treatments based on, or similar to, that of [10] have been presented by a number of authors [11,14,110] and it is on such treatments that the discussion here is based. The one important difference is that the work presented here uses the m.k.s./S.I. definition of susceptibility according to (3-2), resulting in $\chi^{(2)}$ having units of mV^{-1}, rather than the c.g.s definition used by [10,11,14,110] which results $\chi^{(2)}$ having units of cm per stat. volt, or e.s.u.

3.2.1 Nonlinear susceptibility and the origin of nonlinear optical processes.

Of the nonlinear terms in equation (3-2), the $\chi^{(2)}$ term is of most relevance to the work described here, although $\chi^{(3)}$ processes, particularly self-focussing (Kerr lensing) and four-wave mixing are often utilised experimentally. Beyond $\chi^{(3)}$, the nonlinear susceptibility becomes very small in most media and very high intensities are generally required to observe such processes.

If we consider only the second-order term of equation (3-2) alone, the nonlinear polarisation can be written as:

$$\mathbf{P}^{(2)}(\mathbf{r},t) = \varepsilon_0 \chi^{(2)} \mathbf{E}^2(\mathbf{r},t) \tag{3-3}$$

To make use of this interaction, a material must be used which lacks inversion symmetry as $\chi^{(2)}$ vanishes in centrosymmetric crystals.

If $\mathbf{E}(\mathbf{r},t)$ is considered to be the resultant of a range of Fourier components, it can be described by:

$$\mathbf{E}(\mathbf{r},t) = \int_{-\infty}^{\infty} \mathbf{E}(\mathbf{r},\omega) e^{-i\omega t} d\omega \tag{3-4}$$

In the case of n discrete components, this integral can be reduced to:

$$\mathbf{E}(\mathbf{r},t)=\sum_{n}\frac{1}{2}\left[\mathbf{E}_n(\mathbf{r})e^{-i\omega_n t}+c.c.\right] \tag{3-5}$$

where the factor of 1/2 and the complex conjugate are introduced to account for the fact that the integral of (3-5) is over positive and negative frequency components and that $\mathbf{E}(\mathbf{r},t)$ must always be real to represent a physical field. Since second-order frequency conversion processes can be described generally as the mixing of waves at two frequencies to generate a third, it is helpful to consider the case where $\mathbf{E}(\mathbf{r},t)$ consists of two components at frequencies ω_1 and ω_2 having amplitudes $\mathbf{E}_1$ and $\mathbf{E}_2$, respectively:

$$\mathbf{E}(\mathbf{r},t)=\frac{1}{2}\left[\mathbf{E}_1(\mathbf{r})e^{-i\omega_1 t}+\mathbf{E}_2(\mathbf{r})e^{-i\omega_2 t}+c.c.\right] \tag{3-6}$$

In this case the squared resultant amplitude term of (3-3) can be expanded as:

$$\begin{aligned}\mathbf{E}^2(r,t)=\frac{1}{4}\Big[&\mathbf{E}_1^2(\mathbf{r})e^{-i2\omega_1 t}+\mathbf{E}_2^2(\mathbf{r})e^{-i2\omega_2 t}\\&+2\mathbf{E}_1(\mathbf{r})\mathbf{E}_2(\mathbf{r})e^{-i(\omega_1+\omega_2)t}\\&+2\mathbf{E}_1(\mathbf{r})\mathbf{E}_2^*(\mathbf{r})e^{-i(\omega_1-\omega_2)t}\\&+\mathbf{E}_1(\mathbf{r})\mathbf{E}_1^*(\mathbf{r})+\mathbf{E}_2(r)\mathbf{E}_2^*(\mathbf{r})\\&+c.c.\Big]\end{aligned} \tag{3-7}$$

If the second-order nonlinear polarisation is defined in a similar way to the applied field in (3-5), i.e.

$$\mathbf{P}^{(2)}(r,t)=\frac{1}{2}\left[\mathbf{P}(\mathbf{r})e^{-i\omega t}+c.c.\right]=\frac{1}{2}\left[\mathbf{P}(\mathbf{r},t)+\mathbf{P}^*(\mathbf{r},t)\right] \tag{3-8}$$

then the complex second-order nonlinear polarisation, from (3-3) and (3-7), becomes:

$$\begin{aligned}\mathbf{P}(\mathbf{r},t) = \frac{1}{2}\varepsilon_0\chi^{(2)}\Big[&\mathbf{E}_1^2(\mathbf{r})e^{-i2\omega_1 t} + \mathbf{E}_2^2(\mathbf{r})e^{-i2\omega_2 t} \\ &+ 2\mathbf{E}_1(\mathbf{r})\mathbf{E}_2(\mathbf{r})e^{-i(\omega_1+\omega_2)t} \\ &+ 2\mathbf{E}_1(\mathbf{r})\mathbf{E}_2^*(\mathbf{r})e^{-i(\omega_1-\omega_2)t} \\ &+ \mathbf{E}_1(\mathbf{r})\mathbf{E}_1^*(\mathbf{r}) + \mathbf{E}_2(\mathbf{r})\mathbf{E}_2^*(\mathbf{r})\Big]\end{aligned} \tag{3-9}$$

Examination of the various terms on the right hand side of the expression shows components at double the frequency of each of the original components, at the sum of their frequencies and at the difference of their frequencies. These terms represent the processes of second harmonic generation, sum frequency mixing and difference frequency mixing, respectively. Two time-invariant terms are also present, proportional to the squares of the amplitudes, corresponding to the process of optical rectification which results in a d.c. field across the crystal.

For any given three-wave mixing process energy must be conserved, so the relationship:

$$\omega_3 = \omega_1 + \omega_2 \tag{3-10}$$

will always hold, where ω_3 conventionally identifies the highest frequency component participating in the process and ω_1 the lowest. In this case, the terms of (3-9) not relating to the process of interest can be ignored and, as the frequencies of all three components are known, the terms describing the temporal variations of the fields can also be assumed. As a result, the processes of sum-frequency mixing, difference-frequency mixing and second-harmonic generation can be described, respectively, from the appropriate terms in (3-9), by:

$$\mathbf{P}_3(\mathbf{r}) = \varepsilon_0\chi^{(2)}(-\omega_3,\omega_1,\omega_2)\big[\mathbf{E}_1(\mathbf{r})\mathbf{E}_2(\mathbf{r})\big] \tag{3-11 a}$$

$$\mathbf{P}_2(\mathbf{r}) = \varepsilon_0\chi^{(2)}(-\omega_2,-\omega_1,\omega_3)\big[\mathbf{E}_3(\mathbf{r})\mathbf{E}_1^*(\mathbf{r})\big] \tag{3-11 b}$$

$$\mathbf{P}_2(\mathbf{r}) = \frac{1}{2}\varepsilon_0\chi^{(2)}(-\omega_2,\omega_1,\omega_1)\big[\mathbf{E}_1^2(\mathbf{r})\big] \tag{3-11 c}$$

where the ω_3 term has been dropped in the case of second-harmonic generation and ω_2 has become the highest frequency. Note that the possibility of dispersion in the susceptibility has been allowed for in equations (3-11).

In addition to their functional dependence on **r**, describing the spatial variation in their magnitude and therefore in the amplitude of the waves they describe, **P** and **E** are vectors as they also describe the polarisation directions of their respective waves. Given that, in general, the medium in which the interaction is takes place will be anisotropic the susceptibility will be described by a tensor and equations (3-11) can be written:

$$P_3(\mathbf{r})_i = \varepsilon_0 \sum_{j,k} \chi^{(2)}(-\omega_3, \omega_1, \omega_2)_{ijk} E_1(\mathbf{r})_j E_2(\mathbf{r})_k \qquad \text{(3-12 a)}$$

$$P_2(\mathbf{r})_i = \varepsilon_0 \sum_{j,k} \chi^{(2)}(-\omega_2, -\omega_1, \omega_3)_{ijk} E_3(\mathbf{r})_j E_1^*(\mathbf{r})_k \qquad \text{(3-12 b)}$$

$$P_2(\mathbf{r})_i = \frac{1}{2} \varepsilon_0 \sum_{j,k} \chi^{(2)}(-\omega_2, \omega_1, \omega_1)_{ijk} E_1(r)_j E_1(r)_k \qquad \text{(3-12 c)}$$

where the indices i,j,k take values X,Y,Z corresponding to the crystalline piezoelectric axes, which share the same frame of reference as the nonlinear optical coefficients, resulting in the summation being over all axis directions. In making the summations as shown above, it is assumed that the susceptibility obeys two symmetry conditions. The first of these is that of Armstrong et al. [4] which states that $\chi^{(2)}$ is invariant with permutations in frequencies $\omega_1,\omega_2,\omega_3$ as long as the indices i,j,k are simultaneously permuted in the same way. The second symmetry condition is that of Kleinman [111] which extends the first to state that, in the case of a lossless medium, the indices i,j,k can be permuted without permuting the frequencies and, therefore, that $\chi^{(2)}$ is the same for all combinations of the three given frequencies.

Equations (3-12) can be expressed in a more compact form by returning P and E to vector form, expressing $\chi^{(2)}$ as a tensor, and using dyadic notation where summation over all axis directions is implicit:

$$\mathbf{P}_3(\mathbf{r}) = \varepsilon_0 \chi^{(2)}(-\omega_3, \omega_1, \omega_2) : \mathbf{E}_1(\mathbf{r})\mathbf{E}_2(\mathbf{r}) \tag{3-13 a}$$

$$\mathbf{P}_2(\mathbf{r}) = \varepsilon_0 \chi^{(2)}(-\omega_2, -\omega_1, \omega_3) : \mathbf{E}_3(\mathbf{r})\mathbf{E}_1^*(\mathbf{r}) \tag{3-13 b}$$

$$\mathbf{P}_2(\mathbf{r}) = \frac{1}{2}\varepsilon_0 \chi^{(2)}(-\omega_2, \omega_1, \omega_1) : \mathbf{E}_1(r)\mathbf{E}_1(r) \tag{3-13 c}$$

It can be seen that in the case of second-harmonic generation a factor of 1/2 is present which does not occur in the case of sum- or difference-frequency mixing. This can be seen to result from substituting a single-frequency incident field into equation (3-9), either as a single component ($\mathbf{E}_1(\mathbf{r})=\mathbf{E}_0(\mathbf{r})$, $\mathbf{E}_2(\mathbf{r})=0$) or splitting the same field into two components ($\mathbf{E}_1(\mathbf{r}) = \frac{1}{2}\mathbf{E}_0(\mathbf{r}), \mathbf{E}_2(\mathbf{r}) = \frac{1}{2}\mathbf{E}_0(\mathbf{r})$). Since second-harmonic generation is the method usually used to characterise the susceptibility of a material, the quantity $\frac{1}{2}\chi^{(2)}$ is measured and thus defines the nonlinear coefficient **d**:

$$\mathbf{d} = \frac{1}{2}\chi^{(2)} \tag{3-14}$$

which is used almost exclusively in practical calculations relating to nonlinear optics. Clearly **d** will also be a tensor which, it can be seen from (3-12), will have 27 elements when expressed fully. However, application of Kleinman symmetry results in no physical significance being attached to permutation of the second and third indices *j* and *k*. This allows a reduced notation to be employed where *j,k* is replaced by a single index, *l*, as shown in Table 3-1, enabling **d** to be expressed by a 3×6 matrix.

j,k	X,X	Y,Y	Z,Z	Y,Z Z,Y	X,Z Z,X	X,Y Y,X
l	1	2	3	4	5	6

Table 3-1 Contracted index notation used in definition of **d** matrix. X,Y,Z are piezoelectric axis directions.

Defining the incident field as a column vector on which the **d** matrix operates allows the nonlinear polarisation to be calculated in terms of its components along the crystalline axes as (for example in the case of difference-frequency mixing):

$$\begin{pmatrix} P_2(\mathbf{r})_X \\ P_2(\mathbf{r})_Y \\ P_2(\mathbf{r})_Z \end{pmatrix} = 2\varepsilon_0 \begin{pmatrix} d_{11} & d_{12} & d_{13} & d_{14} & d_{15} & d_{16} \\ d_{21} & d_{22} & d_{23} & d_{24} & d_{25} & d_{26} \\ d_{31} & d_{32} & d_{33} & d_{34} & d_{35} & d_{36} \end{pmatrix} \begin{pmatrix} E_3(\mathbf{r})_X E_1^*(\mathbf{r})_X \\ E_3(\mathbf{r})_Y E_1^*(\mathbf{r})_Y \\ E_3(\mathbf{r})_Z E_1^*(\mathbf{r})_Z \\ E_3(\mathbf{r})_Y E_1^*(\mathbf{r})_Z + E_3(\mathbf{r})_Z E_1^*(\mathbf{r})_Y \\ E_3(\mathbf{r})_X E_1^*(\mathbf{r})_Z + E_3(\mathbf{r})_Z E_1^*(\mathbf{r})_X \\ E_3(\mathbf{r})_X E_1^*(\mathbf{r})_Y + E_3(\mathbf{r})_Y E_1^*(\mathbf{r})_X \end{pmatrix} \tag{3-15}$$

A similar expression describes sum-frequency mixing which, in the case of second-harmonic generation, reduces to:

$$\begin{pmatrix} P_2(\mathbf{r})_X \\ P_2(\mathbf{r})_Y \\ P_2(\mathbf{r})_Z \end{pmatrix} = \varepsilon_0 \begin{pmatrix} d_{11} & d_{12} & d_{13} & d_{14} & d_{15} & d_{16} \\ d_{21} & d_{22} & d_{23} & d_{24} & d_{25} & d_{26} \\ d_{31} & d_{32} & d_{33} & d_{34} & d_{35} & d_{36} \end{pmatrix} \begin{pmatrix} E_1^2(\mathbf{r})_X \\ E_1^2(\mathbf{r})_Y \\ E_1^2(\mathbf{r})_Z \\ 2E_1(\mathbf{r})_Y E_1(\mathbf{r})_Z \\ 2E_1(\mathbf{r})_X E_1(\mathbf{r})_Z \\ 2E_1(\mathbf{r})_X E_1(\mathbf{r})_Y \end{pmatrix} \tag{3-16}$$

The number of independent elements in the **d** tensor can be further reduced by applying Kleinman's symmetry which dictates that, for example, $d_{12}=d_{122}=d_{212}=d_{26}$. By systematic application of this argument it can be shown that:

$$\mathbf{d} = \begin{pmatrix} d_{11} & d_{12} & d_{13} & d_{14} & d_{15} & d_{16} \\ d_{16} & d_{22} & d_{23} & d_{24} & d_{14} & d_{12} \\ d_{15} & d_{24} & d_{33} & d_{23} & d_{13} & d_{14} \end{pmatrix} \tag{3-17}$$

The number of independent, non-zero elements can be reduced still further by symmetry arguments for each crystal class [112] based on those for the piezoelectric tensor [113] with which the nonlinear susceptibility shares symmetry.

While a tensor is required to fully describe **d**, in most practical situations the polarisation directions of the interacting waves are known. This enables the projections of the field polarisation directions on the crystalline axes to be calculated and multiplied, as weighting factors, by the relevant **d** tensor components. These weighted components are then added together to yield an effective nonlinear coefficient, d_{eff}, which can be used with the scalar amplitudes of the interacting waves. The calculation of d_{eff} for the various uniaxial crystal classes has been described, and the results tabulated, by a number of sources [11,114]. This results in the expressions for sum- and difference-frequency mixing and second harmonic generation:

$$P_{\omega_1+\omega_2}(\mathbf{r}) = 2\varepsilon_0 d_{eff} E_{\omega_1}(\mathbf{r}) E_{\omega_2}(\mathbf{r}) \tag{3-18 a}$$

$$P_{\omega_3-\omega_1}(\mathbf{r}) = 2\varepsilon_0 d_{eff} E_{\omega_3}(\mathbf{r}) E^*_{\omega_1}(\mathbf{r}) \tag{3-18 b}$$

$$P_{2\omega}(\mathbf{r}) = \varepsilon_0 d_{eff} E^2_{\omega}(\mathbf{r}) \tag{3-18 c}$$

where P and E are the scalar amplitudes, along their polarisation directions, of the relevant waves and the frequency relationships have been stated explicitly for clarity.

3.2.2 Coupled wave-equation treatment of nonlinear frequency conversion.

The above discussion has shown how electromagnetic waves of given frequencies can induce a response at other frequencies in an appropriate medium. We now go on to look at how this induced response results in the generation of new waves at these other frequencies and how power is transferred between the interacting waves. The starting point is Maxwell's equations in a medium:

$$\nabla \cdot \mathbf{D} = \rho \tag{3-19 a}$$

$$\nabla \times \mathbf{E} + \dot{\mathbf{B}} = 0 \tag{3-19 b}$$

$$\nabla \cdot \mathbf{B} = 0 \tag{3-19 c}$$

$$\nabla \times \mathbf{H} - \dot{\mathbf{D}} = \mathbf{J} \tag{3-19 d}$$

The nonlinear polarisation is included by remembering that the displacement field **D** is defined by:

$$\mathbf{D} = \left(\varepsilon_0 \mathbf{E} + \mathbf{P}\right) \tag{3-20}$$

The definition of **P** given by (3-2) allows the separation of the linear and nonlinear susceptibility using the definition of the relative permittivity of the material:

$$\varepsilon_r = \left(1 + \chi^{(1)}\right) \tag{3-21}$$

Further simplifications can be made by assuming that the material is non-magnetic and that there are no free charges or free currents (i.e. the material is lossless) implying, respectively:

$$\mathbf{B} = \mu_0 \mathbf{H} \tag{3-22}$$

$$\rho = 0 \tag{3-23}$$

$$\mathbf{J} = 0 \tag{3-24}$$

Maxwell's equations can then be rewritten as:

$$\nabla \cdot \left(\varepsilon_0 \varepsilon_r \mathbf{E} + \mathbf{P}^{(NL)}\right) = 0 \tag{3-25 a}$$

$$\nabla \times \mathbf{E} = -\frac{\partial}{\partial t}(\mu_0 \mathbf{H}) \tag{3-25 b}$$

$$\nabla \cdot \mathbf{B} = 0 \tag{3-25 c}$$

$$\nabla \times \mathbf{H} = \frac{\partial}{\partial t}(\varepsilon_0 \varepsilon_r \mathbf{E} + \mathbf{P}^{(NL)}) \tag{3-25 d}$$

Following the standard derivation of Maxwell's equation for electromagnetic waves the curl is taken of both sides of (3-25 b) and (3-25 d) is substituted into the resulting equation. Making use of the identity $\nabla \times \nabla \times \mathbf{E} = \nabla(\nabla \cdot \mathbf{E}) - \nabla^2 \mathbf{E}$ and setting

$\nabla \cdot \mathbf{E} = 0$ which, from (3-25 a), is generally true, gives the nonlinear electromagnetic wave equation:

$$\nabla^2 \mathbf{E} = \mu_0 \left(\varepsilon_0 \varepsilon_r \frac{\partial^2 \mathbf{E}}{\partial t^2} + \frac{\partial^2 \mathbf{P}^{(NL)}}{\partial t^2} \right) \tag{3-26}$$

At this point the problem is simplified by considering only unbounded plane waves propagating along the z-axis. Equation (3-26) can then be rewritten:

$$\frac{\partial^2 \mathbf{E}(z,t)}{\partial z^2} = \mu_0 \varepsilon_0 \varepsilon_r \frac{\partial^2 \mathbf{E}(z,t)}{\partial t^2} + \mu_0 \frac{\partial^2 \mathbf{P}^{(NL)}(z,t)}{\partial t^2} \tag{3-27}$$

and in the case of a second-order three-wave interaction $\mathbf{E}$ is then defined as:

$$\mathbf{E}(z,t) = \frac{1}{2}\left[\mathbf{E}_1(z) e^{i(k_1 z - \omega_1 t)} + \mathbf{E}_2(z) e^{i(k_2 z - \omega_2 t)} + \mathbf{E}_3(z) e^{i(k_3 z - \omega_3 t)} + c.c. \right] \tag{3-28}$$

Using the definitions of (3-18 a, b) the complex amplitudes of the polarisations at the three interacting frequencies can be written:

$$P_1^{(NL)}(z,t) = 2\varepsilon_0 d_{eff} E_3(z) E_2^*(z) e^{i\left[(k_3 - k_2)z - (\omega_3 - \omega_2)t\right]} \tag{3-29 a}$$

$$P_2^{(NL)}(z,t) = 2\varepsilon_0 d_{eff} E_3(z) E_1^*(z) e^{i\left[(k_3 - k_1)z - (\omega_3 - \omega_1)t\right]} \tag{3-29 b}$$

$$P_3^{(NL)}(z,t) = 2\varepsilon_0 d_{eff} E_1(z) E_2(z) e^{i\left[(k_1 + k_2)z - (\omega_1 + \omega_2)t\right]} \tag{3-29 c}$$

where, as previously, the use of the effective nonlinear coefficient allows scalar amplitudes to be used.

Considering terms which result in waves at each frequency in turn now allows the interaction of the three waves to be described. Starting with sum-frequency mixing terms, i.e. those which result in waves with frequency ω_3, (3-28) becomes:

$$\frac{\partial^2}{\partial z^2}\left[E_3(z)e^{i(k_3 z-\omega_3 t)}\right]=\mu_0\varepsilon_0\varepsilon_r\frac{\partial^2}{\partial t^2}\left[E_3(z)e^{i(k_3 z-\omega_3 t)}\right]$$
$$+\mu_0\frac{\partial^2}{\partial t^2}\left[2\varepsilon_0 d_{eff}E_1(z)E_2(z)e^{i\left[(k_1+k_2)z-(\omega_1+\omega_2)t\right]}\right] \quad (3\text{-}30)$$

Determining the three derivative terms gives:

$$\frac{\partial^2}{\partial z^2}\left[E_3(z)e^{i(k_3 z-\omega_3 t)}\right]=\left[\frac{d^2E_3(z)}{dz^2}+2ik_3\frac{dE_3(z)}{dz}-k_3^2E_3(z)\right]e^{i(k_3 z-\omega_3 t)} \quad (3\text{-}31\text{ a})$$

$$\frac{\partial^2}{\partial t^2}\left[E_3(z)e^{i(k_3 z-\omega_3 t)}\right]=-\omega_3^2E_3(z)e^{i(k_3 z-\omega_3 t)} \quad (3\text{-}31\text{ b})$$

$$\frac{\partial^2}{\partial t^2}\left[2\varepsilon_0 d_{eff}E_1(z)E_2(z)e^{i\left[(k_1+k_2)z-(\omega_1+\omega_2)t\right]}\right]=-\left(\omega_1+\omega_2\right)^2 2\varepsilon_0 d_{eff}E_1(z)E_2(z)e^{i\left[(k_1+k_2)z-(\omega_1+\omega_2)t\right]} \quad (3\text{-}31\text{ c})$$

It is now assumed that the change in amplitude occurring over propagation distances comparable to a wavelength is small. This can be expressed as:

$$\frac{d^2E_3(z)}{dz^2}<<k_3\frac{dE_3(z)}{dz} \quad (3\text{-}32)$$

This allows the second derivative term on the right hand side of (3-31 a) to be assumed to be zero - an assumption usually described as slowly varying envelope approximation [4]. (3-30) can then be written:

$$2ik_3\frac{dE_3}{dz}e^{i(k_3 z-\omega_3 t)}=\left[k_3^2E_3(z)-\mu_0\varepsilon_r\varepsilon_0\omega_3^2E_3(z)\right]e^{i(k_3 z-\omega_3 t)}$$
$$-\mu_0\varepsilon_0\left(\omega_1+\omega_2\right)^2 2d_{eff}E_1(z)E_2(z)e^{i\left[(k_1+k_2)z-(\omega_1+\omega_2)t\right]} \quad (3\text{-}33)$$

Using the substitutions $c=\frac{1}{\sqrt{\varepsilon_0\mu_0}}$, $n^2=\varepsilon_r$ and $k_3=\frac{n\omega_3}{c}$ and eliminating the temporal dependence so that only the variation in amplitude with propagation distance is described, we obtain:

$$\frac{dE_3(z)}{dz} = -i\frac{\omega_3}{n_3 c} d_{eff} E_1(z) E_2(z) e^{i(k_1+k_2-k_3)z} \tag{3-34}$$

Similar expressions can be arrived at for waves at frequencies ω_2 and ω_1. Using the definition:

$$\Delta k = k_3 - k_2 - k_1 \tag{3-35}$$

these expressions can be rewritten:

$$\frac{dE_1(z)}{dz} = i\frac{\omega_1}{n_1 c} d_{eff} E_3(z) E_2^*(z) e^{i\Delta kz} \tag{3-36 a}$$

$$\frac{dE_2(z)}{dz} = i\frac{\omega_2}{n_2 c} d_{eff} E_3(z) E_1^*(z) e^{i\Delta kz} \tag{3-36 b}$$

$$\frac{dE_3(z)}{dz} = i\frac{\omega_3}{n_3 c} d_{eff} E_1(z) E_2(z) e^{-i\Delta kz} \tag{3-36 c}$$

These are the coupled amplitude equations describing general three-wave mixing processes. In the case of second-harmonic generation, the polarisation expression of (3-18 c) results in the coupled amplitude equations:

$$\frac{dE_\omega(z)}{dz} = i\frac{\omega}{n_\omega c} d_{eff} E_{2\omega}(z) E_\omega^*(z) e^{i\Delta kz} \tag{3-37 a}$$

$$\frac{dE_{2\omega}(z)}{dz} = i\frac{2\omega}{2n_{2\omega} c} d_{eff} E_\omega^2(z) e^{-i\Delta kz} \tag{3-37 b}$$

It can be seen from equations (3-36) and (3-37) that energy is transferred between the waves as they propagate through the crystal their amplitudes being coupled through the nonlinear coefficient.

3.2.3 The Manley-Rowe relations.

The intensity associated with an electromagnetic wave is given in terms of the wave amplitude, E, by:

$$I_i = \frac{1}{2}\sqrt{\frac{\varepsilon_0}{\mu_0}} n_i |E_i|^2 = \frac{1}{2}\varepsilon_0 c n_i |E_i|^2 \tag{3-38}$$

It is useful to define a new field variable, A, such that:

$$A_i = \sqrt{\frac{n_i}{\omega_i}} E_i \tag{3-39}$$

This results in $|A_i|^2$ being proportional the photon flux at frequency ω_i. From (3-38) this results in the intensity being related to A by:

$$I_i = \frac{1}{2}\sqrt{\frac{\varepsilon_0}{\mu_0}} \omega_i |A_i|^2 \tag{3-40}$$

Rewriting the coupled wave equations for three-wave mixing in terms of the new field variable gives:

$$\frac{dA_1(z)}{dz} = iKA_3(z)A_2^*(z)e^{i\Delta kz} \tag{3-41 a}$$

$$\frac{dA_2(z)}{dz} = iKA_3(z)A_1^*(z)e^{i\Delta kz} \tag{3-41 b}$$

$$\frac{dA_3(z)}{dz} = iKA_1(z)A_2(z)e^{-i\Delta kz} \tag{3-41 c}$$

where the definition:

$$K = \frac{d_{eff}}{c}\left(\frac{\omega_1\omega_2\omega_3}{n_1 n_2 n_3}\right)^{\frac{1}{2}} \tag{3-42}$$

has been used. Multiplying equations (3-41 a-c) by A_1^*, A_2^*, A_3^*, respectively, gives:

$$\frac{d|A_1|^2(z)}{dz} = iKA_3(z)A_2^*(z)A_1^*(z)e^{i\Delta kz} \tag{3-43 a}$$

$$\frac{d|A_2|^2(z)}{dz} = iKA_3(z)A_1^*(z)A_2^*(z)e^{i\Delta kz} \tag{3-43 b}$$

$$\begin{aligned}\frac{d|A_3|^2(z)}{dz} &= iKA_1(z)A_2(z)A_3^*(z)e^{-i\Delta kz} \\ &= -iKA_3(z)A_1^*(z)A_2^*(z)e^{i\Delta kz}\end{aligned} \tag{3-43 c}$$

It can be seen from (3-43) that the relationship:

$$\frac{d|A_1|^2(z)}{dz} = \frac{d|A_2|^2(z)}{dz} = -\frac{d|A_3|^2(z)}{dz} \tag{3-44}$$

or, in terms of intensities:

$$\frac{d}{dz}\left(\frac{I_1}{\omega_1}\right) = \frac{d}{dz}\left(\frac{I_2}{\omega_2}\right) = -\frac{d}{dz}\left(\frac{I_3}{\omega_3}\right) \tag{3-45}$$

holds. Expressions having the form of (3-44) and (3-45) are known as the Manley-Rowe relations and can be interpreted as showing that the destruction of one photon at ω_3 results in the generation of one photon each at ω_1 and ω_2, respectively. If the total intensity is defined as:

$$I_T = I_1 + I_2 + I_3 \tag{3-46}$$

Using this definition, (3-40) and the fact that $\omega_3=\omega_2+\omega_1$, equations (3-43) show that:

$$\frac{dI_T}{dz} = \frac{dI_1}{dz} + \frac{dI_2}{dz} + \frac{dI_3}{dz} = 0 \tag{3-47}$$

in other words the total intensity is conserved.

Carrying out a similar analysis to that given above for second harmonic generation, as described by equations (3-37), gives:

$$\frac{d}{dz}\left(\frac{I_{2\omega}}{2\omega}\right) = -\frac{1}{2}\frac{d}{dz}\left(\frac{I_{\omega}}{\omega}\right) \tag{3-48}$$

indicating the creation of a photon at 2ω is accompanied by the destruction of two photons at ω.

The Manley-Rowe relations show that power is transferred between the propagating waves as they travel through the nonlinear medium. It can be seen from equations (3-43) that the direction of this power transfer (i.e. which of the waves will grow in amplitude and which will decrease) is determined by the relative phases of the waves.

3.2.4 Nonlinear optics with Gaussian beams.

The discussion so far has been confined to the case of plane waves of infinite extent. In most practical situations, however, Gaussian beams with finite waist radii will be used. We now go on to discuss how the Gaussian profile of the interacting waves and, importantly, their relative waist dimensions affects the nonlinear interaction and how this can be included in the coupled wave equations. The analysis will, however, be confined at this stage to the case of Gaussian beams in the near-field approximation, i.e. it will be assumed that the nonlinear interaction takes place over a distance less than confocal parameters of the interacting beams and the waist radii can therefore be assumed constant over the interaction length.

The mixing of two waves ω_1 and ω_2 having waists w_1 and w_2 results in a driving polarisation at the resultant frequency ω_3 having a waist of $\overline{w}_3$ which is defined by [8]:

$$\frac{1}{\overline{w}_3^2} = \frac{1}{w_1^2} + \frac{1}{w_2^2} \tag{3-49}$$

This waist is not necessarily the same as that at ω_1 defined by other criteria such as the geometry of a resonant cavity and designated w_3. The coupled-wave equations (3-36) can be rewritten in the case of Gaussian beams as:

$$\frac{d\overline{E}_{0,1}(z)}{dz}e^{-\frac{r^2}{\overline{w}_1^2}} = i\frac{\omega_1}{n_1 c}d_{eff}E_{0,3}(z)e^{-\frac{r^2}{w_3^2}}E^*_{0,2}(z)e^{-\frac{r^2}{w_2^2}}e^{i\Delta kz} \tag{3-50 a}$$

$$\frac{d\overline{E}_{0,2}(z)}{dz}e^{-\frac{r^2}{\overline{w}_2^2}} = i\frac{\omega_2}{n_2 c}d_{eff}E_{0,3}(z)e^{-\frac{r^2}{w_3^2}}E^*_{0,1}(z)e^{-\frac{r^2}{w_1^2}}e^{i\Delta kz} \tag{3-50 b}$$

$$\frac{d\overline{E}_{0,3}(z)}{dz}e^{-\frac{r^2}{\overline{w}_3^2}} = i\frac{\omega_3}{n_3 c}d_{eff}E_{0,1}(z)e^{-\frac{r^2}{w_1^2}}E_{0,2}(z)e^{-\frac{r^2}{w_2^2}}e^{-i\Delta kz} \tag{3-50 c}$$

where E_0 represent the on-axis field amplitudes of the Gaussian distributions and $\overline{E}$ the polarisation-driven field amplitudes. To calculate the degree of coupling between the polarisation-driven fields $\overline{E}$ and the fields E defined by resonator geometry or incident beam dimensions, overlap integrals must be calculated which, when normalised to that for exactly overlapping beams, result in a coupling factor [22]:

$$g = \frac{\int_0^\infty e^{-\frac{r^2}{\overline{w}^2}}e^{-\frac{r^2}{w^2}}r\,dr}{\int_0^\infty e^{-\frac{r^2}{w^2}}e^{-\frac{r^2}{w^2}}r\,dr} \tag{3-51}$$

From (3-51) and (3-49) the coupling factors for the three interacting waves can be defined as:

$$g_1 = 2\left(\frac{w_2^2 w_3^2}{w_1^2 w_2^2 + w_1^2 w_3^2 + w_2^2 w_3^2}\right) \tag{3-52 a}$$

$$g_2 = 2\left(\frac{w_1^2 w_3^2}{w_1^2 w_2^2 + w_1^2 w_3^2 + w_2^2 w_3^2}\right) \tag{3-52 b}$$

$$g_3 = 2\left(\frac{w_1^2 w_2^2}{w_1^2 w_2^2 + w_1^2 w_3^2 + w_2^2 w_3^2}\right) \tag{3-52 c}$$

In cases where the beam waist is defined by the generated field, such as non-resonant sum or difference frequency generation, $\overline{w} = w$ and g=1. When coupling into

resonant cavity modes of incident beams, generally g<1. The coupled-wave equations can thus be rewritten in terms of the Gaussian peak field amplitudes as:

$$\frac{dE_{0,1}(z)}{dz} = i\frac{\omega_1}{n_1 c} d_{eff} g_1 E_{0,3}(z) E^*_{0,2}(z) e^{i\Delta kz} \tag{3-53 a}$$

$$\frac{dE_{0,2}(z)}{dz} = i\frac{\omega_2}{n_2 c} d_{eff} g_2 E_{0,3}(z) E^*_{0,1}(z) e^{i\Delta kz} \tag{3-53 b}$$

$$\frac{dE_{0,3}(z)}{dz} = i\frac{\omega_3}{n_3 c} d_{eff} g_3 E_{0,1}(z) E_{0,2}(z) e^{-i\Delta kz} \tag{3-53 c}$$

The total power associated with a particular wave can be defined in terms of the peak Gaussian amplitudes used in (3-53) by making use of (3-38) and integrating the squared Gaussian amplitude distribution over all space to give:

$$\begin{aligned} P &= \frac{1}{2}\varepsilon_0 nc\left|E_0\right|^2\left(\frac{1}{2}\pi w_0^2\right) \\ &= I_0\left(\frac{1}{2}\pi w_0^2\right) \end{aligned} \tag{3-54}$$

where I_0 is the peak intensity and the term in brackets represents an effective area for the beam. This allows the definition of a new field variable α [115] where:

$$\begin{aligned} \alpha_j(z) &= \left(\frac{n_j c\varepsilon_0 \pi w_j^2}{4\hbar\omega_j}\right)^{\frac{1}{2}} E_{0,j}(z) \qquad j = 1,2 \\ \alpha_3(z) &= i\left(\frac{n_3 c\varepsilon_0 \pi w_3^2}{4\hbar\omega_3}\right)^{\frac{1}{2}} E_{0,3}(z) \end{aligned} \tag{3-55}$$

These definitions result in $|\alpha|^2$ being equal to the total photon flow in the beam. Rewriting the coupled Gaussian wave equations of (3-53) in terms of this new variable gives:

$$\frac{d\alpha_1(z)}{dz} = 2\kappa\alpha_3(z)\alpha_2^*(z)e^{i\Delta kz} \tag{3-56 a}$$

$$\frac{d\alpha_2(z)}{dz} = 2\kappa\alpha_3(z)\alpha_1^*(z)e^{i\Delta kz} \tag{3-56 b}$$

$$\frac{d\alpha_3(z)}{dz} = -2\kappa\alpha_1(z)\alpha_2(z)e^{-i\Delta kz} \tag{3-56 c}$$

where:

$$\kappa = 2d_{eff}\, m\left(\frac{\hbar\omega_1\omega_2\omega_3}{n_1n_2n_3c^3\varepsilon_0\pi}\right)^{\frac{1}{2}} \tag{3-57}$$

$$m = \left(\frac{w_1w_2w_3}{w_1^2w_2^2 + w_1^2w_3^2 + w_2^2w_3^2}\right) \tag{3-58}$$

A similar analysis can be carried out, starting from equations (3-37), for second harmonic generation. If single-pass second harmonic generation, unconstrained by a resonator, is assumed the second-harmonic waist is defined by that of the driving polarisation, thus:

$$\frac{1}{w_{2\omega}^2} = \frac{1}{\overline{w}_{2\omega}^2} = \frac{2}{w_\omega^2}$$
$$\therefore w_{2\omega} = \frac{w_\omega}{\sqrt{2}} \tag{3-59}$$

The resulting coupled-wave equations are:

$$\frac{d\alpha_\omega(z)}{dz} = 2\kappa\alpha_{2\omega}(z)\alpha_\omega^*(z)e^{i\Delta kz} \tag{3-60 a}$$

$$\frac{d\alpha_{2\omega}(z)}{dz} = -\kappa\alpha_\omega^2(z)e^{-i\Delta kz} \tag{3-60 b}$$

where κ is as defined in (3-57) with the additional definitions:

$$
\begin{aligned}
w_1 &= w_2 = w_\omega & w_3 &= w_{2\omega} = \frac{w_\omega}{\sqrt{2}} \\
\omega_1 &= \omega_2 = \omega & \omega_3 &= 2\omega \\
n_1 &= n_2 = n_\omega & n_3 &= n_{2\omega} \\
& \Delta k = k_{2\omega} - 2k_\omega
\end{aligned}
\tag{3-61}
$$

3.2.5 Optical parametric gain.

Having seen from equations (3-56) how power can be transferred between three interacting waves, we now go on to show how this can result in amplification of waves passing through the nonlinear medium. Starting with equations (3-56) we assume that the expressions of the fields can be expanded as a power series of z, and that only the zeroth-order term need be considered [115]. This effectively means that the changes in amplitude of the fields as they pass through the crystal are assumed to be much smaller than the amplitudes of the fields themselves which is a good approximation of the steady-state situation in an OPO. This assumption is equivalent, in the case of the pump, to assuming zero depletion which is a common assumption in many analyses [11,22,23,110]. This allows us to set $\alpha_j(z)=\alpha_j(0)$ in equations (3-56) and therefore allows us to write (taking α_1 as an example):

$$
\alpha_1(L) - \alpha_1(0) = 2\kappa\alpha_3(0)\alpha_2^*(0)\int_0^L e^{i\Delta kz}dz \tag{3-62}
$$

The integration of (3-62) can be simply performed to give, after some rearrangement:

$$
\alpha_1(L) = \alpha_1(0) + 2\kappa L\,\mathrm{sinc}\left(\frac{\Delta kL}{2}\right)e^{i\frac{\Delta kL}{2}}\alpha_3(0)\alpha_2^*(0) \tag{3-63}
$$

similar manipulation of the expressions in α_2 and α_3 leads to the equations:

$$
\alpha_1(L) = \alpha_1(0) + 2\Gamma\alpha_3(0)\alpha_2^*(0) \tag{3-64 a}
$$

$$
\alpha_2(L) = \alpha_2(0) + 2\Gamma\alpha_3(0)\alpha_1^*(0) \tag{3-64 b}
$$

$$\alpha_3(L) = \alpha_3(0) - 2\Gamma^* \alpha_1(0)\alpha_2(0) \qquad \text{(3-64 c)}$$

where the definition:

$$\Gamma = \kappa L \operatorname{sinc}\left(\frac{\Delta kL}{2}\right) e^{i\frac{\Delta kL}{2}} \qquad \text{(3-65)}$$

has been used.

It can be seen that these equations imply gain for α_1 and α_2 with a corresponding depletion at α_3. It should, however, be remembered that α_3 includes a factor of i, i.e. $\alpha_3 = i|\alpha_3|$. Since our original definition of the form of the propagating waves (3-6) results in a negative temporal phase, this factor of i, equivalent to one of $+\pi/2$, corresponds to a $\pi/2$ phase lag relative to the driving polarisation. Multiplying equations (3-64) through by i (i.e. changing the sign of the phase difference) results in a set of equations that imply depletion of α_1 and α_2 and gain at α_3, i.e. back-conversion. Thus, the dependence of the direction of power transfer on the relative phases of the waves is implicitly contained in equations (3-64).

3.2.6 Generated second harmonic power.

The generated second-harmonic power can be calculated by a similar method to that used above for the parametric gain. In this case, however, we shall consider single-pass SHG with an undepleted pump. Thus, starting with equations (3-60), we assume that $\alpha_\omega(x)=\alpha_\omega(0)$ and that $\alpha_{2\omega}(0)=0$. This results in an expression for the second-harmonic amplitude:

$$\alpha_{2\omega}(L) = -\kappa\alpha_\omega^2(0)\int_0^L e^{-i\Delta kz}dz \qquad \text{(3-66)}$$

Performing the integration results in the expression:

$$\begin{aligned}\alpha_{2\omega}(L) &= -\kappa\alpha_{\omega}^{2}(0)L\,\mathrm{sinc}\left(\frac{\Delta kL}{2}\right)e^{-i\frac{\Delta kL}{2}} \\ &= -\Gamma^{*}\alpha_{\omega}^{2}(0)\end{aligned} \tag{3-67}$$

where Γ is as defined in (3-65). Again, although the equation appears to imply depletion rather than growth this is a result of our definition of $\alpha_{2\omega}$ and, as before, multiplying through by i to introduce the correct phase relation between the waves results in an increasing $\alpha_{2\omega}$:

$$\left|\alpha_{2\omega}\right|(l) = i\Gamma^{*}\alpha_{\omega}^{2}(0) \tag{3-68}$$

If we multiply this equation by its complex conjugate to obtain an expression in terms of photon flows, $\left|\alpha_{j}\right|^{2}$, we obtain:

$$\left|\alpha_{2\omega}\right|^{2}(L) = \kappa^{2}L^{2}\left|\alpha_{\omega}\right|^{4}(0)\,\mathrm{sinc}^{2}\left(\frac{\Delta kL}{2}\right) \tag{3-69}$$

Making use of the definitions (3-54), (3-55), (3-57), (3-59) and (3-61) this expression can be rewritten in terms of powers to give an efficiency:

$$\eta_{0,SHG} = \frac{P_{2\omega}}{P_{\omega}} = \frac{2d_{eff}^{2}\omega^{2}L^{2}}{n_{\omega}^{2}n_{2\omega}c^{3}\varepsilon_{0}}\frac{P_{\omega}}{\pi w_{\omega}^{2}}\mathrm{sinc}^{2}\left(\frac{\Delta kL}{2}\right) \tag{3-70}$$

which is the standard result for single-pass second harmonic generation in the case of an undepleted pump [112]. If pump depletion is taken into account, the efficiency can be expressed in terms of (3-70) as [112]:

$$\eta_{SHG} = \tanh^{2}\left(\eta_{0,SHG}\right)^{\frac{1}{2}} \tag{3-71}$$

3.3 Phase-matching of nonlinear optical processes.

It can be seen that equation (3-70) includes the factor:

$$\mathrm{sinc}^2\left(\frac{\Delta kL}{2}\right) \tag{3-72}$$

and from the definition of Γ in (3-65) it can be seen that this factor will appear in the power expressions for all the nonlinear interactions discussed. Clearly this factor will be maximised when Δk=0 (i.e. the process is phase-matched) and, from the definition of Δk of equation (3-35), it can be seen that this will occur when:

$$k_3 = k_1 + k_2 \tag{3-73 a}$$

$$k_{2\omega} = 2k_{\omega} \tag{3-73 b}$$

in the cases of parametric generation and SHG, respectively. This can be interpreted as implying that the strength of the nonlinear interaction will be maximised when momentum is conserved. If there is a phase mismatch, i.e. $\Delta k \neq 0$, it can be seen that (3-72) will be periodic in l with a period of $2\pi/\Delta k$. This results in a coherence length, after which the generated power reaches a maximum, defined as:

$$l_c = \frac{\pi}{\Delta k} \tag{3-74}$$

From the definition of k, the phase matching conditions of equations (3-73) can be rewritten:

$$n_3\omega_3 = n_1\omega_1 + n_2\omega_2 \tag{3-75 a}$$

$$n_{2\omega}2\omega = 2n_{\omega}\omega \tag{3-75 b}$$

Clearly, if the refractive index of the material is the same at the frequencies of all the interacting waves then the process will be phase matched. It can also be seen that in the case of non-degenerate parametric generation $(\omega_1 \neq \omega_2)$, the process can be phase matched by selecting appropriate, different, values of n_1, n_2 and n_3, such that (3-75 a)

is satisfied. However, the refractive indices will usually have different values determined by the material dispersion and thus the interaction will not, in general, be phase-matched.

The effects of a phase-mismatch can be seen in Fig. 3-1 calculated for the case of second harmonic generation (although essentially identical results could be calculated for other nonlinear optical processes), where the intensity and phase of the second harmonic, calculated from (3-68) and (3-69), are shown as a function of distance through the crystal. It has been assumed that the initial amplitude of the second harmonic is zero. As a result, both the phase-matched and the non-phase-matched second harmonic waves adopt the same phase as the driven field at the

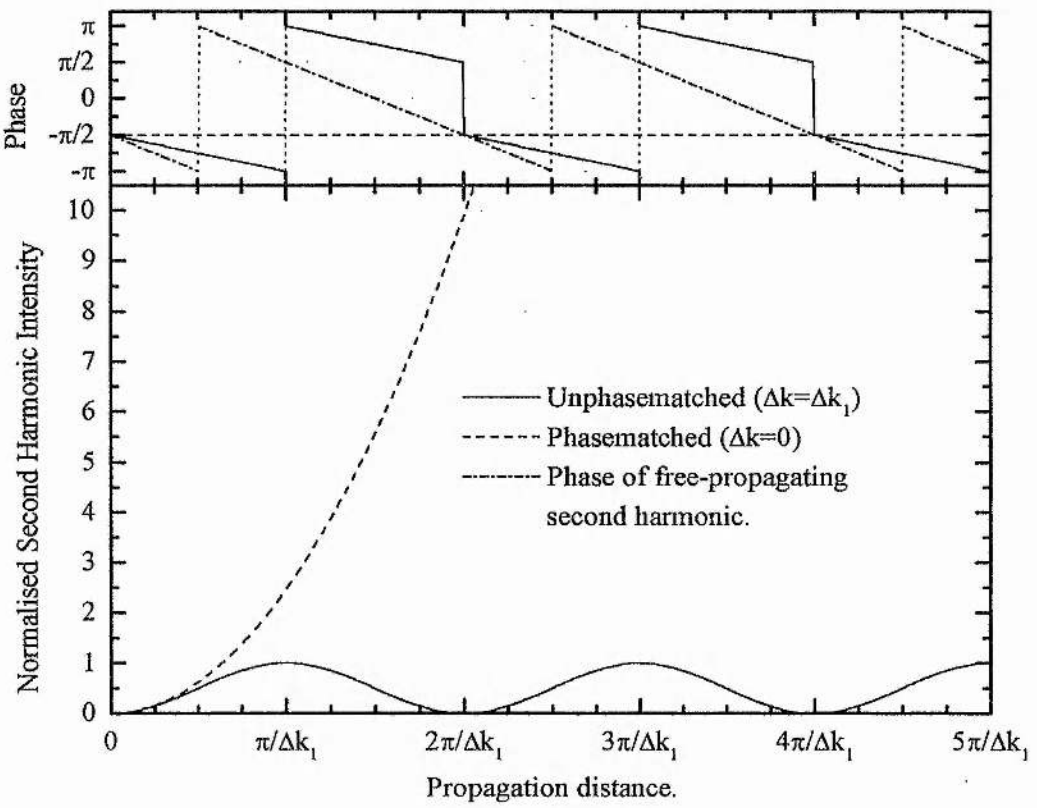

Fig. 3-1 Intensity and phase of phase-matched and non phase-matched second harmonic with propagation distance. All phases are measured relative to the polarisation at the second harmonic.

second harmonic, i.e. a $\pi/2$ lag relative to the polarisation. In the phase-matched case the propagating second harmonic remains in phase with the driven field as it travels through the crystal. As a result, further contributions from the driven field always add in phase with the propagating second harmonic wave and its intensity increases quadratically.

It can be seen, however, that the phase of the non-phase-matched wave is not constant relative to the driven field but lags by an increasing amount as the wave propagates. At one coherence length the propagating second harmonic wave lags the driven wave by $\pi/2$ in phase and beyond this point further contributions from the driven field add to the propagating wave destructively, causing its intensity to decay back to zero after it has propagated two coherence lengths. At this point, it again adopts the phase of the driven field and repeats the process.

It is interesting to compare the rate of phase change of the non phase-matched wave to that of a freely-propagating wave at the second-harmonic frequency, i.e. one that has the same phase mismatch but is not interacting with the polarisation induced in the material by the fundamental. Any relative phase change in such a wave is solely due to the dispersion of the material. It can be seen from Fig. 3-1 that this wave changes its phase relative to the polarisation at twice the rate of the wave which is interacting with the driven field. This difference occurs because two processes affect the phase of the generated second harmonic. In addition to the phase shift due to the material dispersion experienced by the free-propagating wave, the out-of-phase contributions from the driven second harmonic field also influence the phase of the propagating wave. It can be seen from Fig. 3-1 that the phase of this contribution always adds in the opposite direction to that due to the dispersion, thus reducing the overall rate of phase change compared to that of the free-propagating wave.

The effects of varying phase-mismatch are shown in Fig. 3-2. Here the normalised second-harmonic intensity generated in a crystal of length l is plotted for a range of phase-mismatch values yielding the sinc^2 function of (3-72). Again, identical results would be obtained for parametric generation. It can be seen that for a phase mismatch of π/l, i.e. in a situation where the coherence length is equal to the crystal length, the generated intensity is reduced by a factor of $(2/\pi)^2$ from the perfectly

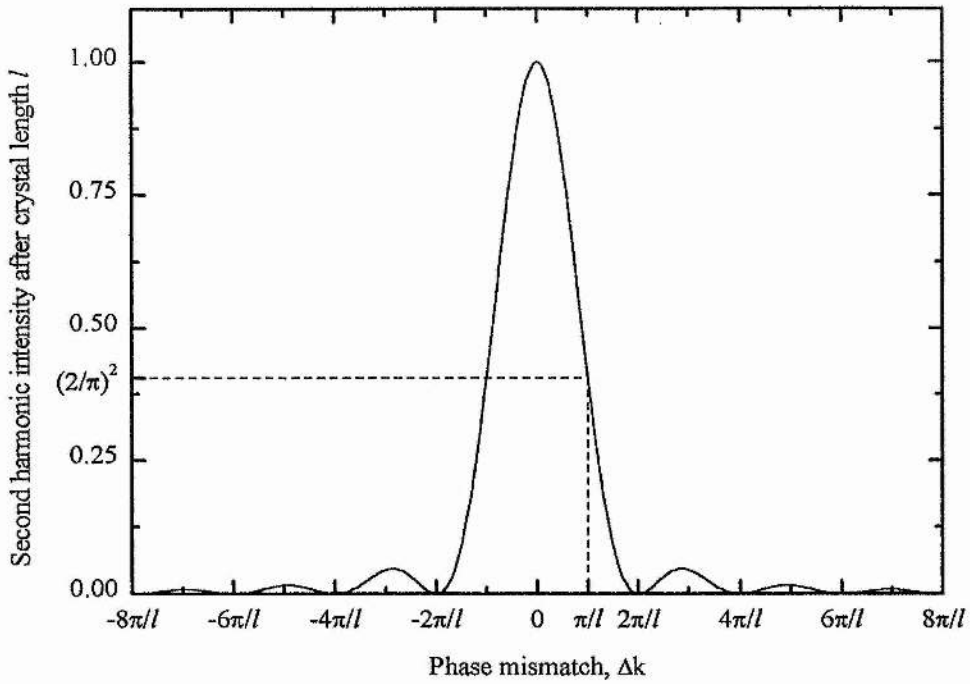

Fig. 3-2 Effect on normalised second-harmonic intensity of varying phase mismatch for a fixed crystal length, L.

phase-matched case, thus the amplitude is reduced by $(2/\pi)$. Fig. 3-2 clearly shows that as the crystal length is increased, which is desirable to increase the intensity generated by the nonlinear interaction, the magnitude of phase-mismatch which can be tolerated rapidly falls.

It is apparent from Fig. 3-1 and Fig. 3-2 that unless the phase-mismatch, which will generally occur in the nonlinear interaction of interest, can somehow be corrected the resultant intensity will never be more than that achieved after one coherence length, resulting in low conversion efficiencies. This was, in fact, the case in the first experimental demonstration of a nonlinear optical interaction [1]. Two methods are generally used to phase-match nonlinear optical interactions. Birefringent phase-matching makes use of the variation of refractive index with polarisation inherent in most materials used in nonlinear optics to achieve the appropriate combination of refractive indices for equations (3-75) to be satisfied. Quasi-phase-matching makes use of a modulation of the material properties to periodically correct the phase of the

driven field, ensuring that it always contributes constructively to the propagating wave.

3.3.1 Birefringent phase matching.

Birefringent phase-matching was the first technique successfully applied to the problem [2, 3]. The technique makes use of the fact that many materials used in nonlinear optics have anisotropic refractive indices, i.e. the refractive index at a given wavelength depends of the propagation direction of the light and on its polarisation.

The refractive indices, at a given wavelength, of an anisotropic crystal can be characterised by the refractive indices for waves polarised along the principal dielectric axes x, y, z, namely n_x, n_y and n_z (the principle refractive indices) at that wavelength. Their relationship can be visualised using the index ellipsoid, a three-dimensional surface defined by:

$$\frac{x^2}{n_x^2}+\frac{y^2}{n_y^2}+\frac{z^2}{n_z^2}=1 \tag{3-76}$$

In the simplest anisotropic case, that of a uniaxial crystal, two of the principal indices are equal, i.e.

$$n_x = n_y \neq n_z \tag{3-77}$$

The index ellipsoid corresponding to this situation, with $n_x=n_y>n_z$ (described as a negative uniaxial crystal), is shown in Fig. 3-3. It can be seen that for a given propagation direction, defined by k, the wave will be polarised in a plane normal to this direction. The region of this plane bounded by the ellipsoid, shown shaded in Fig. 3-3, is generally an ellipse with major and minor axis lengths equal to the refractive index for the two orthogonal polarisations of a wave travelling in the direction defined by k.

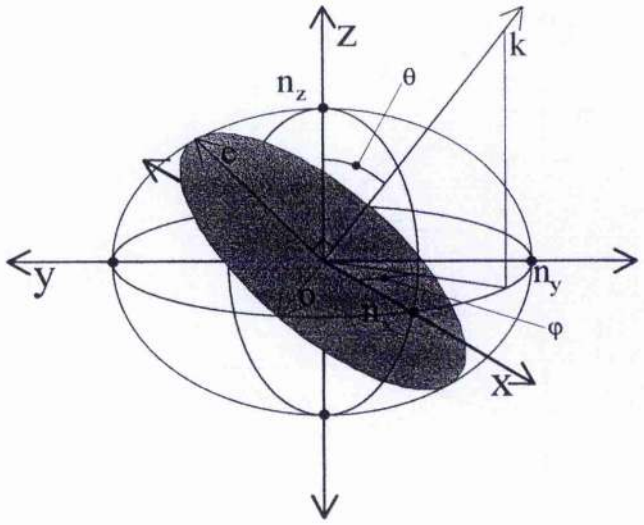

Fig. 3-3 Index ellipsoid for a negative-uniaxial cryastal ($n_x=n_y>n_z$). x, y and z are the principle dielectric axes, n_x, n_y, n_z the principle refractive indices and k is the propagation direction. The shaded plane represents the polarisation ellipse with o and e the ordinary and extraordinary polarisations respectively.

It can be seen that in the uniaxial case the refractive index for a wave polarised normal to the z-axis (the ordinary or o-wave marked o in Fig. 3-3) will be invariant with propagation direction having a value of $n_o=n_x=n_y$ for all values of θ. However, that polarised in the plane of the z-axis (the extraordinary or e-wave marked e in Fig. 3-3) will change as the polar angle, θ, varies taking values between $n_e=n_z$, when $\theta=90^\circ$, and n_o when $\theta=0^\circ$. When the wave is propagating parallel to the z-axis the o-wave and e-wave will both be polarised in the x-y plane, the polarisation ellipse will become circular and the refractive index will be invariant with polarisation direction. The propagation direction for which this occurs is designated as the optical axis and falls along one of the principal dielectric axes in the uniaxial case.

3.3.1.1 Calculation of phase-matching angle.

To determine the correct propagation direction for a phase-matched interaction in this case, a diagram such as that shown in Fig. 3-4 is used. Here, taking SHG as an example, the refractive indices for the ordinary an extraordinary waves are plotted on a polar diagram as a function of polar angle θ for both the fundamental and the second harmonic. Except in regions of anomalous dispersion, the refractive index for a given polarisation will always be larger at the second harmonic than at the fundamental. Thus, the refractive index at the two wavelengths will never be the same if they both have the same polarisation. If, however, the fundamental is polarised ordinarily and the second harmonic extraordinarily, then as long as $n_{o,\omega}>n_{e,2\omega}$, a propagation direction will exist where the two refractive indices are equal. This direction will be at a polar angle θ_{pm} from the optic axis as shown in Fig. 3-4.

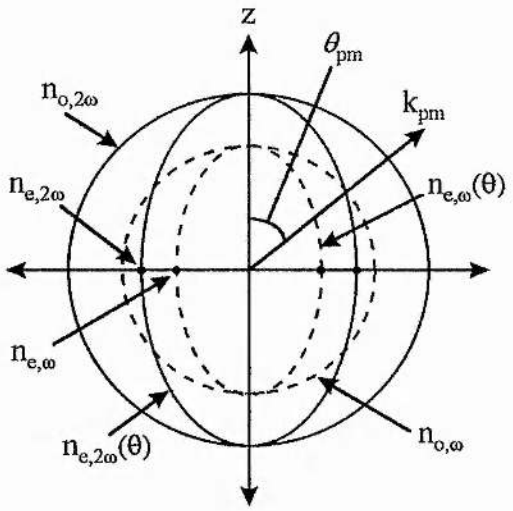

Fig. 3-4 Phase matching diagram for second harmonic generation in a negative uniaxial crystal. k_{pm} indicates the phase-matched propogation direction, θ_{pm} the phase-matching polar angle measured from the optic axis. n_o, $n_e(\theta)$ and n_e represent the ordinary and extraordinary refractive indices and the extraordinary index when polarised along the optic axis, respectively.

Given that the elliptical variation of the extraordinary index with propagation direction is given by:

$$\frac{1}{n_e^2(\theta)} = \frac{\cos^2\theta}{n_o^2} + \frac{\sin^2\theta}{n_e^2} \tag{3-78}$$

It can be seen from Fig. 3-4 that the phase-matching angle, θ_{pm}, will be given by:

$$\sin^2\theta_{pm} = \frac{(n_{o,\omega})^{-2} - (n_{o,2\omega})^{-2}}{(n_{e,2\omega})^{-2} - (n_{o,2\omega})^{-2}} \tag{3-79}$$

It can be seen that in this situation the second harmonic must always be extraordinarily polarised to phase match the interaction. The other potential situation in a uniaxial crystal is that where $n_x=n_y<n_z$, i.e. $n_e>n_o$ (a positive uniaxial crystal). The phase-matching diagram in this case is shown in Fig. 3-5. Here it can be seen that the second harmonic must be ordinarily polarised, and $n_{e,\omega}>n_{o,2\omega}$ for phase-matching to be achieved. The phase-matching angle is calculated in the same way as

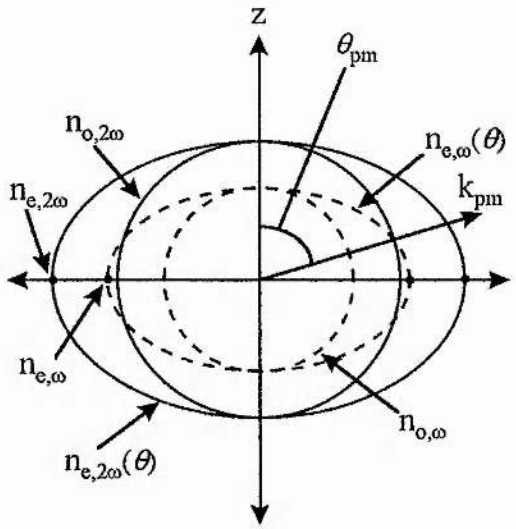

Fig. 3-5 Phase matching diagram for second harmonic generation in a positive uniaxial crystal. Labelling is as for Fig. 3-4.

the negative uniaxial case resulting in an expression similar to (3-79), but with the subscripts ω and 2ω transposed in the terms on the right-hand-side.

Both the cases described above assume that only one polarisation exists at the fundamental frequency and that the second harmonic is polarised orthogonally to this, a situation described as type-I phase matching. The alternative situation where the fundamental contains two different polarisations is described as type-II phase matching. These definitions, in fact, extend to all nonlinear optical interactions with the situation where the two interacting waves of lower frequency have the same polarisation being described as type-I and that where the two low-frequency waves have orthogonal polarisations being described as type-II.

The more general case of a material where $n_x \neq n_y \neq n_z$ describes a biaxial crystal of which a uniaxial crystal is actually a special case. While the refractive indices of biaxial crystals can also be represented by an index ellipsoid similar to that shown in Fig. 3-3, it is clearly not possible to reduce this to a single-plane diagram such as Fig. 3-4 and Fig. 3-5, as it is in the case of uniaxial crystals. This is due to the refractive index varying not only with the polar angle θ, but also with the azimuthal angle φ shown in Fig. 3-3.

In many cases, however, propagation is only considered in the principal planes. If this restriction is made, the variation of refractive index with polarisation and propagation direction can be represented by a three-dimensional locus diagram, as shown in Fig. 3-6. These diagrams represent the variation of refractive index with propagation direction and polarisation, for propagation within one octant of the index ellipsoid. It is clear that in the biaxial case the optical axis will lie in the same plane as the polarisations having the largest and smallest refractive indices (the x-z plane in Fig. 3-6) and normal to the polarisation direction having the intermediate refractive index (the y-axis in Fig. 3-6). The optic axis will be at an angle Ω from the polar (z) axis in this plane such that the projections of n_x and n_z yield a resultant refractive index equal to n_y. It can also be seen that the other optic axis will lie in the same plane in the opposite octant at an angle $-\Omega$ from the z-axis. The angle Ω can be shown to be given by:

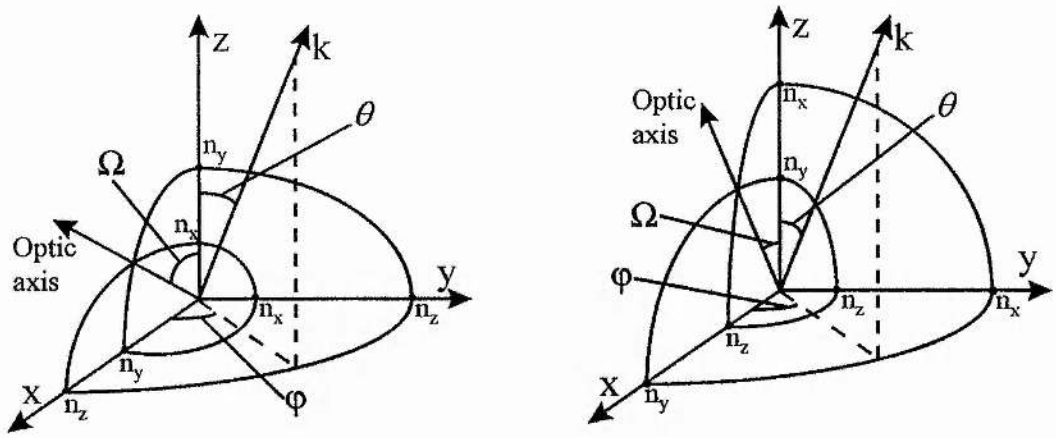

(a) $n_x<n_y<n_z$ (b) $n_x>n_y>n_z$

Fig. 3-6 Refractive index variation with propagation direction and polarisation in biaxial crystals for (a) $n_x<n_y<n_z$ and (b) $n_x>n_y>n_z$ where n_x,n_y,n_z are the refractive indices for waves polarised along the principle axes. θ and φ represent the polar and azimuthal angles respectively and Ω represents the angle between the optic axes and the z-axis.

$$\sin\Omega = \left[\frac{(n_y)^{-2}-(n_x)^{-2}}{(n_z)^{-2}-(n_x)^{-2}}\right]^{\frac{1}{2}} = \left[\frac{n_z^2(n_x^2-n_y^2)}{n_y^2(n_x^2-n_z^2)}\right]^{\frac{1}{2}} \qquad (3\text{-}80)$$

Clearly Ω will vary with wavelength, but the average values of Ω allow biaxial crystals to be categorised as positive-biaxial ($\Omega_{av} \leq 45^o$) and negative-biaxial ($\Omega_{av} > 45^o$) [116].

Calculation of phase-matching angles is rather more complex in the biaxial case than for uniaxial crystals and the first thorough treatment was made by Hobden [117]. The situation is greatly simplified, however, by considering propagation only in the principal planes. Such a calculation is best illustrated by an example. Potassium Niobate ($KNbO_3$) is a biaxial crystal which exhibits high nonlinear coefficients and is of relevance to some of the work described in this thesis. We start by defining the

axis systems used in the description of the various crystal properties of interest. The area of axis definition in nonlinear optics is notorious for inconsistency and confusion, so careful definitions are important.

The only totally unambiguous method of axis identification is to use the crystalline lattice parameters. With the crystalline axes defined as a,b,c, the lattice parameters have dimensions a_0=5.6896Å, b_0=3.9692Å, c_0=5.7256Å. This definition results in the refractive indices for polarisations along the axes having the relationship $n_b > n_a > n_c$ [118,119]. The crystalline axes a,b,c correspond to the principal dielectric axes y,z,x, respectively, and to piezoelectric axes X,Y,Z and d-tensor axes 1,2,3 [119,116]. It should be noted that these definitions, while extensively used in the literature, do not comply with standardised reporting frames which have $b_0 > a_0 > c_0$ and a,b,c corresponding to principal dielectric axes -y,x,z, piezo-electric axes Y,Z,X and d-tensor axes 1,3,2 [116]. These two definitions are summarised in Table 3-2.

Commonly used literature definition [118,119] ($n_b > n_a > n_c$).			
Crystallographic axes.	a	b	c
Lattice parameter.	a_0=5.6896Å	b_0=3.9692Å	c_0=5.7256Å
Principle dielectric axes.	y	z	x
Piezoelectric axes.	X	Y	Z
d-tensor axes.	1	2	3
IEEE/ANSI standard definition [116] ($n_c > n_a > n_b$).			
Crystallographic axes.	a	c	b
Lattice parameter.	a_0=5.6896Å	c_0=3.9692Å	b_0=5.7256Å
Principle dielectric axes.	y	x	z
Piezoelectric axes.	Y	Z	X
d-tensor axes.	1	3	2

Table 3-2 Axis definitions in potassium niobate according to both the definitions commonly used in literature and the IEEE/ANSI standard definitions. The former definitions are used throughout this text.

The first set of definitions (those commonly adopted in the literature) are used throughout this text. Having made these definitions, we can now draw a refractive-index diagram such as those shown in Fig. 3-6. This can be seen in Fig. 3-7.

Remembering that we are restricting the problem to propagation in the principal planes, and considering only type-I phase matching, it can be seen that there are two possible phase-matching geometries. The first of these has the fundamental polarised in the y-z (a-b) plane and the second harmonic polarised along the x- (c-) axis, while the second has the fundamental polarised along the z- (b-) axis with the second harmonic polarised in the x-y (c-a) plane.

Considering the first geometry, clearly second-harmonic generation can be phase matched in this case if:

$$n_z(\omega) > n_x(2\omega) > n_y(\omega) \tag{3-81}$$

To determine the phase-matching range, the variation of the refractive indices for waves polarised along the three axes with wavelength must be considered. These values are calculated from Sellmeier equations [118] and are shown in Fig. 3-8 for a

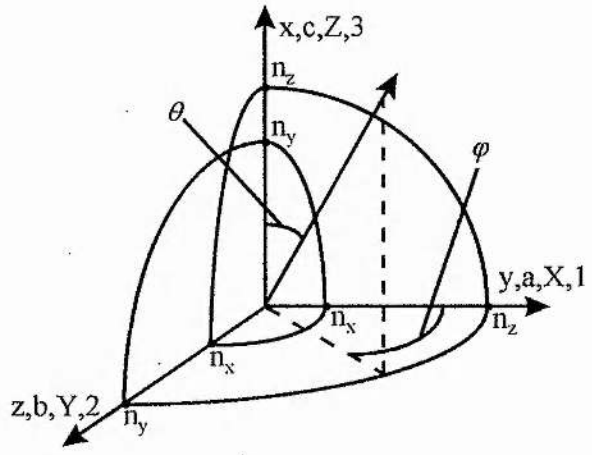

Fig. 3-7 Axis definitions and variation of refractive index with polarisation and propagation direction in potassium niobate.

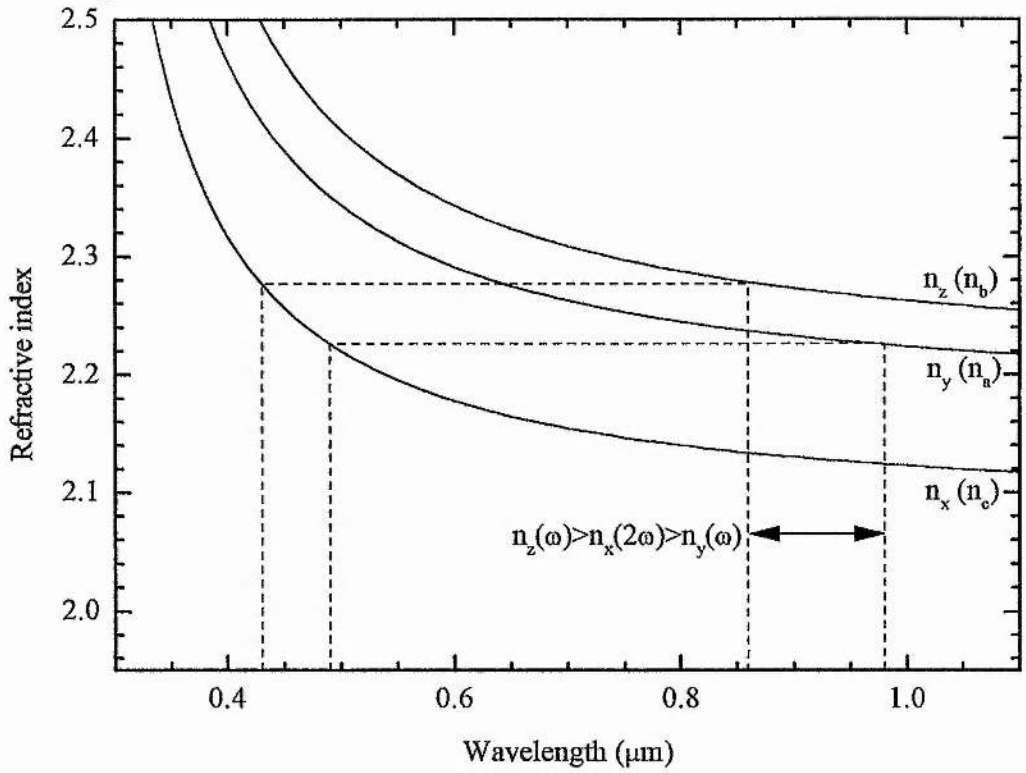

Fig. 3-8 Refractive indices of potassium niobate at a temperature of 295K [118] and phase-matching range for type-I SHG with second harmonic polarised along x-axis and fundamental polarised in y-z plane.

temperature of 295K. Also shown is the range over which (3-81) is satisfied. It can be seen that second-harmonic generation can be phase-matched in this geometry for fundamental wavelengths between 857nm and 982nm. Having determined a suitable phase-matching geometry, and the wavelength range for which it occurs, the calculation can be reduced to a simple two-dimensional problem similar to the case for a uniaxial crystal.

It can be seen that, in this phase-matching configuration, the refractive index at the second harmonic will be fixed at $n_x(2\omega)$ as the crystal is rotated in the y-z plane, while that of the fundamental varies from $n_z(\omega)$ to $n_y(\omega)$. Clearly this situation is similar to that of the positive uniaxial crystal shown in Fig. 3-5 and can be

represented in a similar phase-matching diagram, as shown in Fig. 3-9. It can be seen that the phase-matching angle φ_{pm}, measured from the y- (a-) axis, will be given by:

$$\cos^2 \varphi_{pm} = \frac{(n_{x,2\omega})^{-2} - (n_{y,\omega})^{-2}}{(n_{z,\omega})^{-2} - (n_{y,\omega})^{-2}} \tag{3-82}$$

Considering the other phase-matching configuration having the fundamental polarised along the z- (b-) axis with the second harmonic polarised in the x-y (c-a) plane, phase matching will be possible if:

$$n_y(2\omega) > n_z(\omega) > n_x(2\omega) \tag{3-83}$$

The fundamental range over which this occurs can be seen from Fig. 3-10 to be 857nm to 4.85μm. In this case the two-dimensional phase-matching diagram is as shown in Fig. 3-11, and the phase-matching angle is given by:

$$\sin^2 \theta_{pm} = \frac{(n_{z,\omega})^{-2} - (n_{y,2\omega})^{-2}}{(n_{x,2\omega})^{-2} - (n_{y,2\omega})^{-2}} \tag{3-84}$$

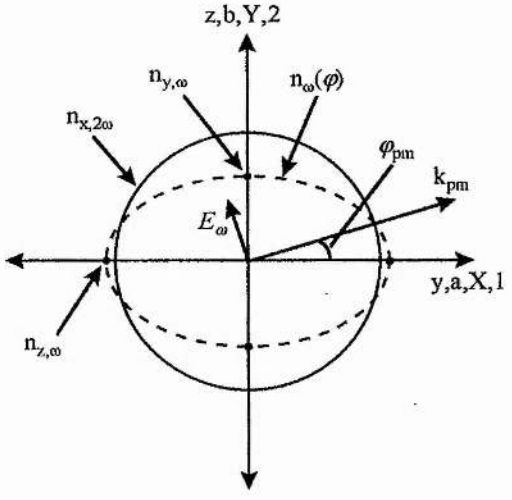

Fig. 3-9 Phase-matching diagram for type-I SHG in potassium niobate with second harmonic polarised along x-axis and fundamental polarised in y-z plane.

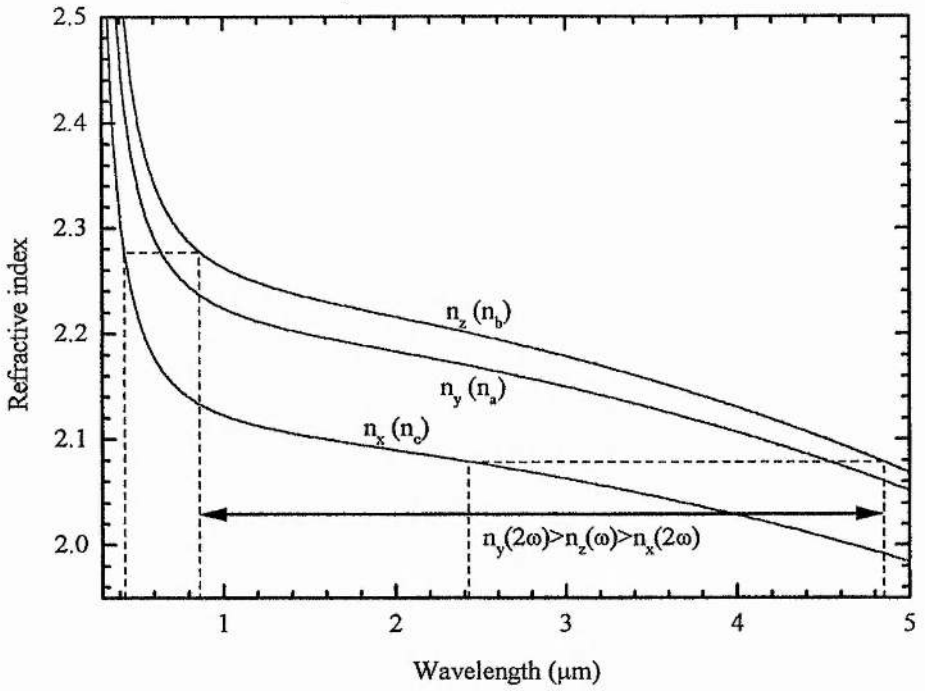

Fig. 3-10 Refractive indices of potassium niobate at a temperature of 295K [118] and phase-matching range for type-I SHG with fundamental polarised along z-axis and second harmonic polarised in x-y plane.

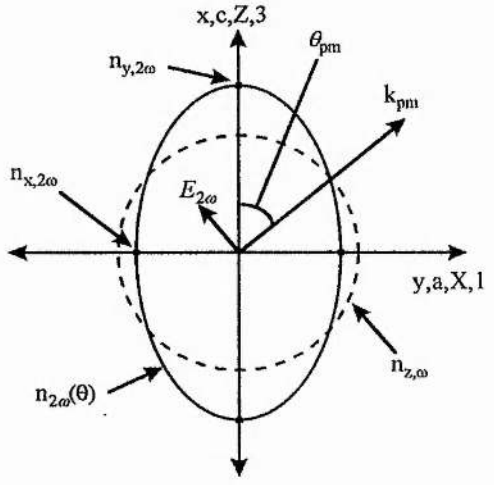

Fig. 3-11 Phase-matching diagram for type-I SHG in potassium niobate with fundamental polarised along z-axis and second harmonic polarised in x-y plane.

3.3.1.2 Calculation of effective nonlinear coefficient.

As mentioned earlier in this chapter, when the polarisation directions of the interacting waves are known an effective nonlinear coefficient, d_{eff}, is usually calculated from the projections of the polarisations on the interacting waves onto the d-tensor axes. We now look at an example of such a calculation for the two phase-matching configurations described above in potassium niobate.

Consider the first phase-matching configuration as illustrated in Fig. 3-9. Since the electric field direction of the fundamental, E_{ω}, lies in the y-z (a-b, X-Y) plane normal to the propagation direction, k, it can be seen that the fundamental will induce polarisation at the second harmonic along the piezoelectric Z- (x-, c-) axis via two components: the projection of E_{ω} on the X- (a-,y-) axis coupling through the d_{31} coefficient and the projection of E_{ω} on the Y- (b-, z-) coupling through the d_{32} coefficient. The components of the fundamental field along the X (a,y) and Y (b,z) axes are:

$$E_{\omega,X} = E_{\omega} \sin\phi \tag{3-85 a}$$

$$E_{\omega,Y} = E_{\omega} \cos\phi \tag{3-85 b}$$

Equation (3-18 c) can thus be rewritten:

$$P_{2\omega,Z} = \varepsilon_0 \left[d_{31} \left(E_{\omega} \sin\phi \right)^2 + d_{32} \left(E_{\omega} \cos\phi \right)^2 \right] \tag{3-86}$$

Thus, in this geometry:

$$d_{eff} = d_{31} \sin^2\phi + d_{32} \cos^2\phi \tag{3-87}$$

In the second configuration, illustrated in Fig. 3-11, it can be seen that the polarisation along the direction of the second-harmonic field, $E_{2\omega}$, will consist of components along the piezoelectric X- and Z- axes. Thus, in this configuration:

$$P_{2\omega} = P_{2\omega,Z} \sin\theta + P_{2\omega,X} \cos\theta \tag{3-88}$$

As the fundamental is polarised along the Y- (b-, z-) axis, the polarisation components in the Z-X (x-y, c-a) plane will be given by:

$$P_{2\omega,Z} = \varepsilon_0 d_{32} E_\omega^2 \tag{3-89 a}$$

$$P_{2\omega,X} = \varepsilon_0 d_{12} E_\omega^2 \tag{3-89 b}$$

However, in potassium niobate, the d_{12} coefficient is zero, thus there is no polarisation component along the piezoelectric X-axis in this case. Equation (3-88) thus becomes:

$$P_{2\omega} = \varepsilon_0 d_{32} E_\omega^2 \sin\theta \tag{3-90}$$

So in this geometry:

$$d_{eff} = d_{32} \sin\theta \tag{3-91}$$

Although these examples of d_{eff} calculations have been relatively simple, the same principle is used to calculate d_{eff} in any phase-matching geometry. In the most general case the projections of the driving fields (or fundamental in the case of SHG) onto the piezoelectric axes X,Y and Z form a 6×1 matrix, which is used in expressions such as (3-15) and (3-16). Calculating the projections of the resultant polarisation components onto the driven field then results in a generalised d_{eff} expression [116]. The results of such calculations have been tabulated for uniaxial [11,114] and many biaxial [120,121,122] crystal classes.

3.3.1.3 Walk-off in birefringent phase matching.

From (3-27) it can be seen that the linear part of the wave equation indicates transverse waves propagating along **k**, with wave fronts parallel to ε_r**E** or **D**. Thus, the displacement field direction, **D**, is normal to the wave propagation direction defined by **k**. Since **D**=ε_r**E**, it can be seen that in a medium with anisotropic refractive index (a birefringent medium) where ε_r is not a scalar, **D** and **E** can have

different directions. The Poynting vector, which gives the magnitude and direction of energy flow in an electromagnetic wave, is defined by:

$$\mathbf{S} = \mathbf{E} \times \mathbf{H} \tag{3-92}$$

and thus lies in the same plane as **E**, **D** and **k**, in a direction perpendicular to **E**. It is therefore clear that when **D** and **E** are in the same direction, **S** and **k** will also be parallel and the energy flow in the wave will be along the propagation direction. However, if **D** and **E** are in different directions energy will be transferred in a different direction to that in which the wave is propagating.

It can be shown that in the index-ellipsoid representation, the Poynting vector is always directed normal to the index surface at the point where it is intersected by the wave-propagation vector [123]. Clearly this means that for a polarisation which has a constant refractive index (the ordinary polarisation in a uniaxial crystal), the energy flow will always be in the propagation direction. However, if the refractive index varies with propagation direction (the extraordinary polarisation), the energy flow and propagation directions will be different. This is illustrated in Fig. 3-12, where k represents the propagation direction, s_o and s_e represent the Poynting-vector directions for the ordinary and extraordinary waves, respectively, and ρ is the walk-off angle between the Poynting-vector direction and propagation direction for the extraordinary wave.

Since birefringent phase-matching requires at least one of the interacting waves to be extraordinarily polarised, it is apparent that, generally, there will be walk-off between the interacting waves, which will limit the distance over which the interaction can occur. In the most general case of a wave propagating in an arbitrary direction through the crystal, the walk-off angle, ρ, between the Poynting vector and the propagation direction is given by [124]:

$$\tan\rho = n^2\left[\left(\frac{k_x}{n^{-2}-n_x^{-2}}\right)^2+\left(\frac{k_y}{n^{-2}-n_y^{-2}}\right)^2+\left(\frac{k_z}{n^{-2}-n_z^{-2}}\right)^2\right]^{-\frac{1}{2}} \tag{3-93}$$

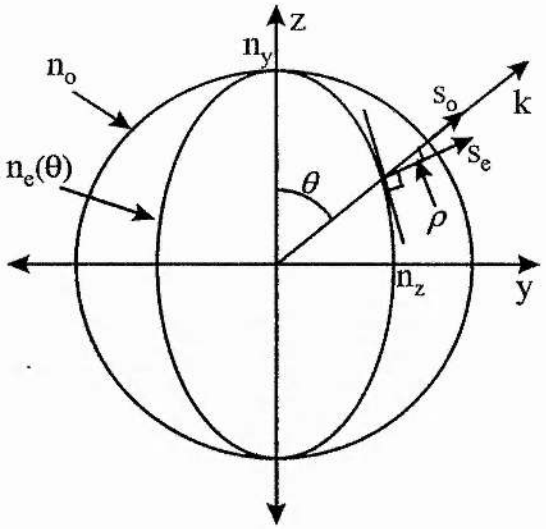

Fig. 3-12 Poynting-vector walk-off in a birefringent crystal. s_o and s_e represent the Poynting-vector direction for the ordinary and extraordinary rays, respectively, and ρ is the walk-off angle for the extraordinary ray.

where k_x, k_y, k_z are the unit vectors of the components of the wave vector along the principal dielectric axes, n_x, n_y, n_z are the refractive indices for polarisations along these axes and n is the refractive index for the propagating wave along the direction of k.

In the most general case, all the interacting waves will undergo walk-off from their common propagation direction and the walk-off between the waves will be a combination of these walk-off angles. This will result in walk-off occuring in two different planes by differing amounts. In the case of a uniaxial crystal or propagation in one of the principal planes of a biaxial crystal, however, the situation is considerably simplified. These situations all have phase-matching diagrams similar to those in Fig. 3-4 and Fig. 3-5, so, walk off will only occur for the extraordinarily polarised wave, resulting in the walk-off angle between the waves being equal to the walk-off angle for the extraordinary wave, as can be seen from Fig. 3-12. Furthermore, as propagation is in one of the principal dielectric planes, (3-93) can be

simplified. Using the situation shown in Fig. 3-12 as an example, the simplified expression is:

$$\tan\rho = \left(n_e(\theta)\right)^2\left[\left(\frac{\sin\theta}{\left(n_e(\theta)\right)^{-2} - n_y^{-2}}\right)^2 + \left(\frac{\cos\theta}{\left(n_e(\theta)\right)^{-2} - n_z^{-2}}\right)^2\right]^{\frac{1}{2}} \tag{3-94}$$

where $n_e(\theta)$ is determined using an expression similar to (3-78).

If propagation is along one of the principal dielectric axes, then clearly there will be no walk-off. It can also be seen from Fig. 3-4 and Fig. 3-5 that in this case the phase-matching angle will be less sensitive to changes in refractive index (such as might be induced by changes in temperature or wavelength) and, conversely, that phase matching will be maintained over a greater angular range than for off-axis propagation. This situation, where the phase-matching angle is 0° or 90°, is described as non-critical phase-matching. Propagation between two axes is described as critical phase-matching and is more sensitive both to Poynting-vector walk-off and the other changes described above than the non-critical case.

Obviously non-critical phase-matching is the more desirable situation, but requires that the refractive indices of the interacting waves along one of the principal axes satisfy the phase-matching condition (3-75). Returning to our previous example of SHG in potassium niobate using the first phase-matching scheme discussed, it can be seen that the phase matching will be non-critical when $n_x(2\omega)=n_z(\omega)$ ($n_c(2\omega)=n_b(\omega)$) or $n_x(2\omega)=n_y(\omega)$ ($n_c(2\omega)=n_a(\omega)$). From Fig. 3-8, it can be seen that this occurs for fundamental wavelengths of 857 and 982 nm at room temperature.

Second harmonic generation can be non-critically phase-matched for other fundamental wavelengths by varying the temperature of the crystal. The fundamental wavelength which is critically phase-matched for type-I second-harmonic generation in potassium niobate with the fundamental polarised in the y-z (a-b, X-Y) plane (the first configuration discussed above) is given by [119]:

$$\lambda_{ncpm} = a_1 T + a_2 T^2 + a_0 \tag{3-95}$$

In this expression λ_{ncpm} is the fundamental wavelength and T is the temperautre in degrees Celsius. The coefficients have the values a_0=976.04nm, a_1=0.253 nm/°C and a_2=1.146×10^{-3} nm/°C^2 for φ=90° (propagation along the y- (a-, X-) axis). For propagation along the z- (b-, Y-) axis, the coefficients take values of a_0=850.40 nm, a_1=0.294 nm/°C and a_2=1.234×10^{-3} nm/°C^2. The variation with temperature of the non-critical fundamental wavelengths, calculated using (3-95), is shown in Fig. 3-13.

3.3.2 Quasi-phase-matching.

Returning to Fig. 3-1, it can be seen that birefringent phase matching, as described above, will achieve the ideal situation of Δk=0, resulting in continuous quadratic

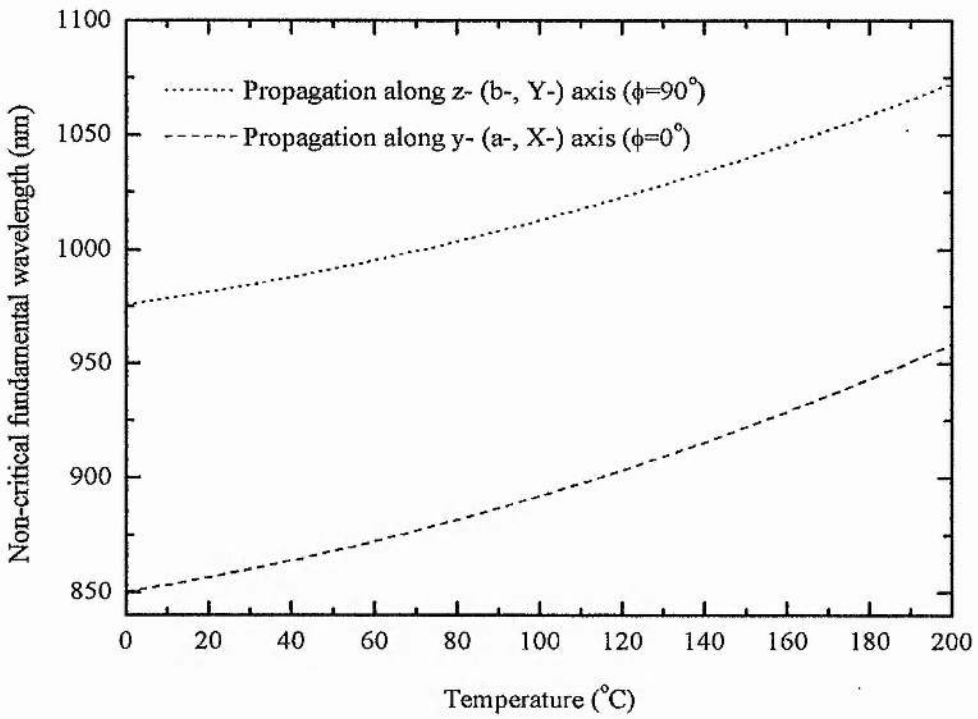

Fig. 3-13 Temperature variation of non-critically phase-matched fundamental wavelengths for type-I second harmonic generation in potassium niobate with the fundamental polarised in the y-z (a-b, X-Y) plane.

growth of the power in the generated wave. It can also be seen from Fig. 3-1 that phase matching has fixed the phase of the propagating second harmonic at a constant lag of $\pi/2$ relative to the polarisation and therefore always in phase with the driven field. Thus, the driven field always contributes constructively to the propagating wave. Looking at the un-phase-matched wave in Fig. 3-1, it can be seen that growth also occurs, but only up to the first coherence length. Beyond this point, the phase difference between the propagating and driven fields, due to dispersion, is greater than $\pi/2$ and the contributions of the driven field add destructively to the propagating field, reducing its amplitude to zero by the second coherence length.

Clearly, if the phase of the driven field were shifted by $\pi/2$ after the first coherence length its contributions to the propagating wave would still be constructive and the amplitude of the propagating wave would continue to grow. In fact, if the phase of the driven field were to change by π every coherence length it would always have a phase difference of less than $\pi/2$ from the propagating wave and would therefore always contribute constructively.Periodically modifying the phase of the driven field in this way is known as quasi-phase-matching (QPM).

This phase reversal of the driven field can be achieved by successive total-internal reflections [125] or, more commonly, by reversing the sign of the nonlinear coefficient, d, with the appropriate period, a technique usually termed periodic poling [90]. Methods of achieving this sign reversal of d have included the use of crystals with rotationally-twinned planes [126], or laminated structures of discrete crystals [127,128,129]. The period of the reversal for interactions in the visible and near-infrared regions is usually of the order of a few tens of microns or less. As a result, it proved difficult to fabricate structures using this technique having periods less than many coherence lengths [128], and the relative technological simplicity of birefringent phase-matching techniques proved more attractive . At longer wavelengths, the periods required are larger and this allowed single-coherence-length sections to be fabricated for the frequency doubling of carbon-dioxide laser radiation [127].

Smaller periods, of the order of a coherence length, were obtained by modulating the growth conditions of the crystal [130,131,132], post-growth selective heat-treatment

[133,134] and electron-beam writing [135]. In general, however, these techniques suffered from complexity and/or an inability to produce consistent periodic structures over extended crystal lengths. Yamada et al. showed that the use of modern lithographic techniques allowed accurate electrodes to be deposited on lithium niobate crystals enabling simple, room-temperature, electric-field poling to be used to produce periodic domain inversions [136]. This approach had the advantage that electrodes could be applied to relatively large areas and the poling carried out with a single voltage pulse resulting in a degree of reproducibility and accuracy, in theory, limited mainly by the quality of the lithography. This technique was further refined by the use of liquid electrodes [137] and has since become a commercial method of routinely producing quasi-phase-matched lithium niobate crystals of up to 50mm in length [92,93]. The technique has also been applied to other materials including KTP [138,139], lithium tantalate [140,141] and RTA [80].

The results of quasi-phase-matching a nonlinear optical process are shown in Fig. 3-14. Again, these calculations have been made for second-harmonic generation but similar results could be obtained for any second-order nonlinear optical process. There are several interesting features to note in Fig. 3-14. As would be expected, the growth in intensity in the quasi-phase-matched case is slower than that for the perfectly phase-matched interaction. It can be seen that the quasi-phase-matched second-harmonic power actually oscillates around that generated by a perfectly phase-matched interaction, having a $2/\pi$ reduction in amplitude compared to that of the perfectly phase-matched case with the same effective nonlinear coefficient. This would be expected from examination of Fig. 3-2, where it can be seen that the intensity generated after one coherence length in the phase-mismatched case is $(2/\pi)^2$ of that generated after the same length with $\Delta k=0$.

The phase of the quasi-phase-matched second harmonic can be seen to initially behave in a similar way to that of the non-phase-matched wave in Fig. 3-1 until the first phase-inversion point for the driven field. Beyond this point, it behaves in a similar way to that of the freely propagating wave plotted in Fig. 3-1, showing small deviations from this phase variation which become increasingly less significant with propagation distance.

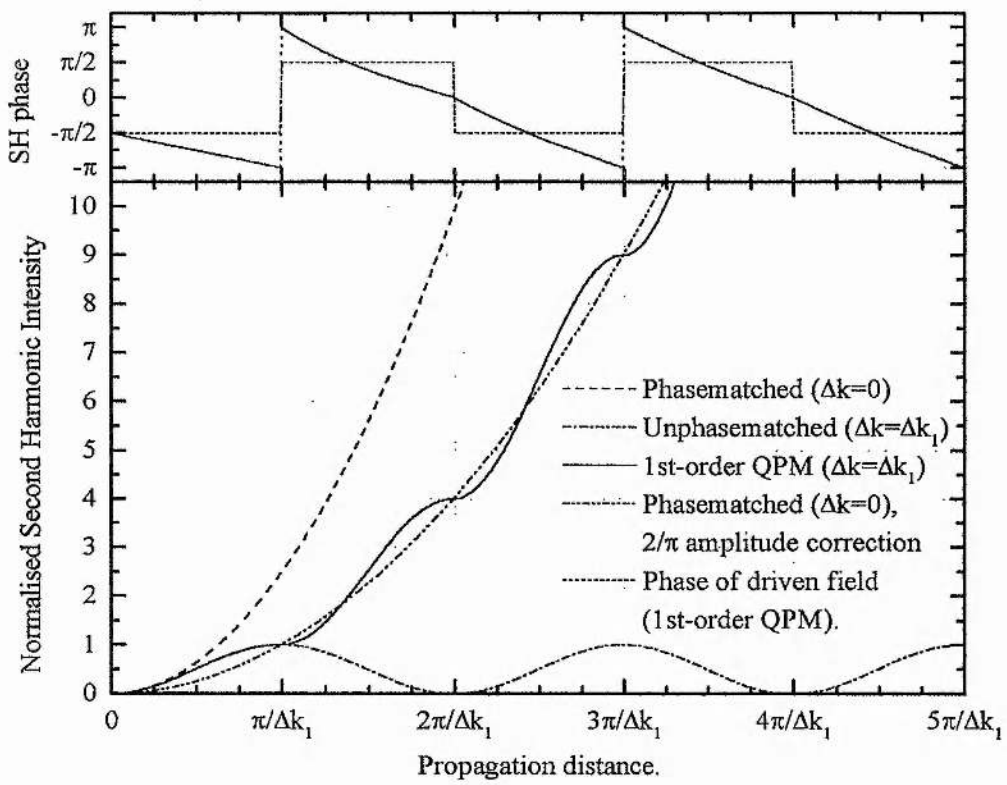

Fig. 3-14 Intensity and phase variations with propagation distance for first-order quasi-phase-matched second harmonic generation. All phases are measured relative to the polarisation at the second harmonic.

As previously discussed, the relative phase of the un-phase-matched wave changes at half the rate of a freely propagating wave with the same phase mismatch. This is due to the out-of-phase contributions from the driven field producing a phase shift in the opposite direction to that due to dispersion. In the quasi-phase-matched case, however, it can be seen that after the first phase inversion the phase contributions from the driven field are alternately in the same and in the opposite direction to the shift due to dispersion. The overall phase variation thus averages to that produced by dispersion alone (i.e. that of the freely-propagating wave) with small variations produced by the driven-field contributions. These variations become less significant as the amplitude of the propagating second harmonic grows to become much larger than the amplitude of the contribution at any given point. Thus, the phase variation

of the quasi-phase-matched wave rapidly approaches that of the freely propagating wave.

Theoretical treatments of QPM have been carried out by a number of authors [142,143,144,145,146], and most recently by Fejer et al. [91] on whose work the following discussion is based. Starting with a general form of the differential equations of (3-36) and (3-37):

$$\frac{dE_3}{dz} = \kappa d(z) e^{-i\Delta kz} \tag{3-96}$$

where $d(z)$ describes the spatially-varying nonlinear coefficient:

$$\kappa = \frac{i\omega E_1 E_2}{n_2 c} \tag{3-97}$$

and Δk is as defined in (3-35). Integrating (3-96) gives the generated field after a distance l:

$$E_3(L) = \kappa \int_0^L d(z) e^{-i\Delta kz} dz \tag{3-98}$$

Thus, if Δk=0, the result:

$$E_3(L) = \kappa d_{eff} L \tag{3-99}$$

is obtained. The form of (3-98) clearly lends itself to a Fourier transform treatment. If a normalised spatially-varying nonlinear coefficient, $g(z)$, is defined as:

$$g(z) = \frac{d(z)}{d_{eff}} \tag{3-100}$$

where $-1 \le g(z) \le 1$, then (3-98) can be rewritten:

$$E_3(L) = \kappa d_{eff} L G(\Delta k) \tag{3-101}$$

where:

$$G(\Delta k) = \frac{1}{L}\int_0^L g(z)e^{-i\Delta kz}dz \tag{3-102}$$

is a mismatch-space function being the Fourier transform of g(z) and, as can be seen by comparing (3-101) to (3-99), represents the reduction in the effective nonlinear coefficient over the perfectly phase-matched case.

If g(z) is a periodic function with a spatial period Λ, it can be defined:

$$g(z) = \sum_{m=-\infty}^{\infty} G_m e^{iK_m z} \tag{3-103}$$

i.e. as a Fourier series where the mth harmonic has the wave-vector K_m defined by:

$$K_m = \frac{2\pi m}{\Lambda} \tag{3-104}$$

The integral expression (3-102) then becomes:

$$G(\Delta k) = \frac{1}{L}\sum_{m=-\infty}^{\infty}\left(G_m\int_0^L e^{-i\Delta k_Q z}dz\right) \tag{3-105}$$

where:

$$\Delta k_Q = \Delta k - K_m = k_3 - k_2 - k_1 - \frac{2\pi m}{\Lambda} \tag{3-106}$$

Evaluating the integral in (3-105) results in the expression:

$$G(\Delta k) = \frac{1}{L}\sum_{m=-\infty}^{\infty}\left(LG_m e^{-i\frac{\Delta k_Q L}{2}}\operatorname{sinc}\left(\frac{\Delta k_Q L}{2}\right)\right) \tag{3-107}$$

Clearly, for large l, terms in the summation where $\Delta k_Q \neq 0$ can generally be ignored if a term where $\Delta k_Q \approx 0$ exists, as the sinc expression will approach unity for this term while approaching zero for the other terms. From the definition of Δk_Q in (3-106), it can be seen that this means only one value of m needs to be considered and (3-101) becomes:

$$E_3(L) = e^{-i\frac{\Delta k_Q L}{2}} \kappa d_Q L \operatorname{sinc}\left(\frac{\Delta k_Q L}{2}\right) \tag{3-108}$$

where:

$$d_Q = d_{eff} G_m \tag{3-109}$$

If the normalised spatial variation of the nonlinear coefficient g(z) is assumed to be a rectangular wave having values of ±1 and a spatial period Λ with positive sections of length l_+ and a duty cycle D given by:

$$D = \frac{l_+}{\Lambda} \tag{3-110}$$

the Fourier coefficient of the mth harmonic is given by [147]:

$$G_m = \frac{2}{\pi m} \sin(\pi m D) \tag{3-111}$$

In the case of a 50% duty cycle, which is the optimum for odd-order QPM, as the sign of the nonlinear coefficient changes every m coherence lengths (see Fig. 3-14), (3-111) simplifies to give (from (3-109)):

$$d_Q = \frac{2 d_{eff}}{\pi m} \tag{3-112}$$

This results in a $2/\pi m$ reduction in the effective nonlinear coefficient, agreeing with the result discussed earlier and illustrated in Fig. 3-14 for first-order QPM. The same

reduction (with m=3) can be seen in Fig. 3-15 where third-order QPM of second-harmonic generation is illustrated.

It can be seen by comparing (3-108) to (3-64) and (3-68) that a quasi-phase-matched nonlinear optical interaction can be analysed using all the expressions developed in section 3.2 by simply replacing Δk and d_{eff} with Δk_Q and d_Q, as defined in (3-106) and (3-112).

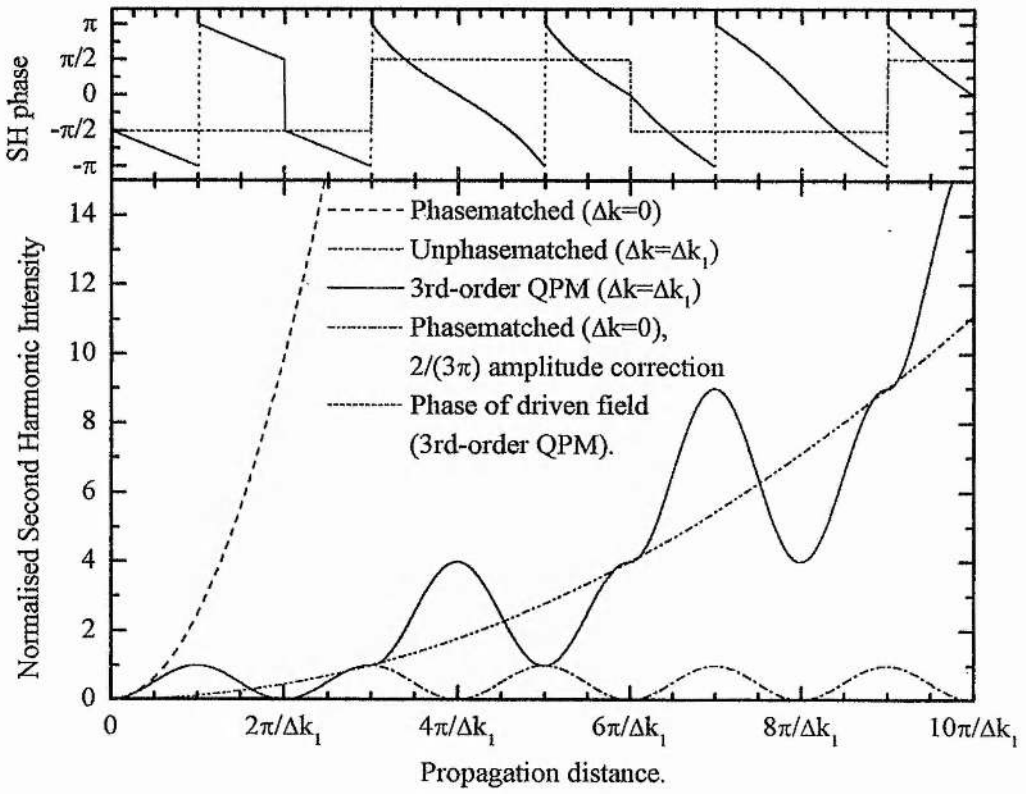

Fig. 3-15 Intensity and phase variations with propagation distance for third-order quasi-phase-matched second harmonic generation. All phases are measured relative to the polarisation at the second harmonic.

3.3.3 Comparison of phase matching methods.

Having described the two principal methods of phase-matching in nonlinear-optical interactions, it is useful to compare the merits of both on a number of important criteria.

From (3-106) it can be seen that a major advantage of QPM over birefringent methods is that one of the phase-matching parameters is completely controllable. While the interacting wavelengths and refractive indices, and therefore the wave vectors k, can be varied to some extent, the values they can adopt are not arbitrary being determined by the material properties and the wavelengths required for the desired interaction. Since these are the only variable parameters in the birefringent case, many interactions cannot be phase matched in a given material. In the case of QPM, however, the grating period, Λ, can adopt any arbitrary value. Thus, in a given material, any interaction can, in principle, be phase-matched. Although practical limitations exist, such as the transparency range of the material and the minimum period which can be achieved in the poling process, this flexibility results in a much greater range of phase-matchable interactions than in the birefringent case. A further advantage that this arbitrary control offers is the possibility of engineering the phase-matching for specialised applications. Examples of this include obtaining phase-matching profiles differing from the standard sinc^2 case [91], allowing continuously variable quasi-phase-matching [148], and phase-matching multiple nonlinear optical processes within a single crystal [76,149].

When comparing the magnitude of the effective nonlinear coefficient for the two methods, (3-112) would appear to indicate that the price paid for this flexibility in phase-matching is a reduction in the effective nonlinear coefficient. It should be remembered, however, that in birefringent phase-matching the effective nonlinear coefficient is determined by that propagation direction and combination of polarisations which will result in the interaction being phase-matched. This generally does not maximise the effective nonlinear coefficient as, in the birefringent case, orthogonal polarisations must always exist while the highest d coefficients are often those for parallel polarisations. In quasi-phase-matching however the propagation and polarisation directions can be selected to maximise the effective nonlinear

coefficient and the grating period then chosen to phase-match the interaction under these conditions.

Lithium niobate is a good example of this. While this is currently by far the most commonly used material for quasi-phase-matching, it was also one of the earliest materials used for birefringent phase-matching. While most QPM in lithium niobate makes use of the d_{33} coefficient at around 30 pmV^{-1}, this can clearly not be used in birefringent phase-matching as it involves all the interacting waves being polarised along the piezoelectric Z-axis. The first optical parametric oscillator [6] was based on birefringently-phase-matched lithium niobate utilising the d_{31} coefficient at around 6 pmV^{-1}. It is clear that even with the $2/\pi$ reduction resulting from first-order quasi-phase-matching the effective nonlinear coefficient will be over three times larger than that in this birefringent case.

Since quasi-phase-matching can, in principle, phase-match an interaction for waves propagating in an arbitrary direction by selection of the correct grating period, it is always possible to have the interacting waves propagating along one of the principal dielectric axes and therefore obtain zero Poynting vector walk-off. In fact, for the majority of crystals, polarisation along one of the piezoelectric axes to obtain the maximum effective nonlinear coefficient also results in polarisation along one of the principal dielectric axes and therefore in zero walk off. Thus, quasi-phase-matching gives all the benefits of non-critical birefringent phase-matching, allowing long interaction lengths to be combined with the high nonlinear coefficients available.

In addition to the above advantages, quasi-phase-matching can be used where birefringent phase-matching cannot. In materials which have isotropic refractive index properties, birefringent phase-matching is clearly impossible. Quasi-phase-matching, however, can be achieved and this has allowed the isotropic materials with high nonlinear coefficients to be utilised in a number of cases [127,150].

Quasi-phase-matching has also allowed temperature tuning to be used in materials which show very little tuning with temperature under birefringent phase-matching [139]. This is possible because QPM requires only that the refractive index changes with temperature, thus changing the effective grating period, for temperature tuning

to occur. In the birefringent case the dispersion, i.e. the relative refractive index at the interacting wavelengths, must vary with temperature for tuning to take place. While the second effect can be very small in some materials, the first effect is strongly present in the majority of materials used in nonlinear optics.

While all the above advantages make quasi-phase-matched materials very attractive for many applications in nonlinear optics, there are still some cases where birefringent materials are more suitable. The majority of quasi-phase-matched materials currently used are structured by electric-field poling. This technique can, however, only be applied to ferroelectric materials. Although other domain-reversal techniques have been used [127,131], they are significantly less developed than electric-field poling or are applicable only to long-wavelength regions and non-ferroelectric materials are still generally birefringently phase-matched.

Electric-field poling, also, can only generally be applied to crystals which are relatively thin in the direction in which the field is applied. Apertures of E-field poled crystals are typically only 0.5-1 mm in this direction. Although larger apertures have been obtained by diffusion bonding several crystals together [151], these materials can generally not be used where large apertures are required. Poled crystals can also be unsuitable in situations where the crystal is performing another function in addition to nonlinear frequency conversion, which would be interfered with by periodic domain reversal, such as electrooptic modulation. In such cases, a single-domain crystal is required and birefringent phase-matching must therefore be used.

3.3.4 Phase-matching acceptance bandwidths.

Clearly, changes in any parameter which affects the values of the wave propagation vectors, k, of the interacting waves and therefore the phase mismatch Δk, will have an impact on the efficiency of any nonlinear optical process. The main parameters which have this effect are the wavelengths of the interacting waves, the temperature (which affects the refractive index in all cases) and the propagation direction (which affects the refractive index for extraordinarily polarised light). Clearly, as all these parameters affect Δk, Fig. 3-2 could have wavelength, temperature or propagation

direction as the x-axis parameter. The most commonly used definition of the acceptance bandwidth for a given parameter is that range of values over which $-\pi/L \leq \Delta k \leq \pi/L$. It can be seen from Fig. 3-2 that the efficiency of the nonlinear optical process falls to $(2/\pi)^2$ or approximately 0.4 of its phase-matched value at the limits of this range. We shall consider here the problem of calculating these acceptance bandwidths in the case of a collinear interaction which simplifies the more general treatment allowing different propagation directions [152].

The function for the wave-vector mismatch, Δk, is expanded as a Taylor series:

$$\Delta k = \Delta k_0 + \left.\frac{\partial \Delta k}{\partial \zeta}\right|_{\zeta_0} \delta\zeta + \frac{1}{2}\left.\frac{\partial^2 \Delta k}{\partial \zeta^2}\right|_{\zeta_0} \delta\zeta^2 + \ldots \tag{3-113}$$

where ζ is the parameter for which the acceptance bandwidth is to be calculated and Δk_0 is the phase mismatch at the value about which the expansion takes place. The derivatives are calculated for $\zeta=\zeta_0$, where ζ_0 is the value of ζ for $\Delta k=\Delta k_0$. As the phase-matching acceptance bandwidth is calculated about the point of ideal phase matching, in most cases $\Delta k_0=0$ and the acceptance bandwidth is then defined by:

$$\left.\frac{\partial \Delta k}{\partial \zeta}\right|_{\zeta_{PM}} \delta\zeta + \frac{1}{2}\left.\frac{\partial^2 \Delta k}{\partial \zeta^2}\right|_{\zeta_{PM}} \delta\zeta^2 + \ldots = \pm\frac{\pi}{L} \tag{3-114}$$

The full acceptance bandwidth is thus given by:

$$\Delta\zeta = 2\delta\zeta \tag{3-115}$$

To calculate the wavelength acceptance bandwidth for a generalised three-wave interaction, ζ is set equal to λ_2 and λ_1 is assumed to be fixed. The wave-vector mismatch and energy conservation relations are rewritten:

$$\Delta k = 2\pi\left[\frac{n_3}{\lambda_3} - \frac{n_2}{\lambda_2} - \frac{n_1}{\lambda_1}\right] \tag{3-116}$$

$$\frac{1}{\lambda_3}=\frac{1}{\lambda_2}+\frac{1}{\lambda_1} \tag{3-117}$$

resulting in the first derivative being given by:

$$\frac{\partial \Delta k}{\partial \lambda_2}=2\pi\left[\left.\frac{\partial n_3}{\partial \lambda_3}\right|_{\lambda_3}\frac{\lambda_3}{\lambda_2^2}-\frac{n_3}{\lambda_2^2}-\left.\frac{\partial n_2}{\partial \lambda_2}\right|_{\lambda_2}\frac{1}{\lambda_2}+\frac{n_2}{\lambda_2^2}\right] \tag{3-118}$$

where n_2, n_3, λ_2, λ_3 are the values at perfect phase matching and the derivatives are calculated at these wavelength values from the Sellmeier equations. In the majority of cases, the first-derivative will dominate the expansion and the second-derivative term can thus be ignored. In this case, from (3-114) and (3-115), the wavelength acceptance bandwidth is seen to be given by:

$$\Delta\lambda_2=\frac{1}{L}\left[\left.\frac{\partial n_3}{\partial \lambda_3}\right|_{\lambda_3}\frac{\lambda_3}{\lambda_2^2}-\frac{n_3}{\lambda_2^2}-\left.\frac{\partial n_2}{\partial \lambda_2}\right|_{\lambda_2}\frac{1}{\lambda_2}+\frac{n_2}{\lambda_2^2}\right]^{-1}. \tag{3-119}$$

In the case of second-harmonic generation, (3-116) further simplifies to:

$$\Delta k=\frac{4\pi}{\lambda}\left(n_{2\omega}-n_{\omega}\right) \tag{3-120}$$

resulting in an acceptance bandwidth for the fundamental given by:

$$\Delta\lambda_{\omega}=\frac{\lambda_{\omega}}{2L}\left[\frac{1}{2}\left.\frac{\partial n_{2\omega}}{\partial \lambda}\right|_{\lambda_{2\omega}}-\left.\frac{\partial n_{\omega}}{\partial \lambda}\right|_{\lambda_{\omega}}-\frac{1}{\lambda_{\omega}}\left(n_{2\omega}-n_{\omega}\right)\right]^{-1} \tag{3-121}$$

A similar calculation can be carried out to determine the temperature acceptance bandwidth, again ignoring derivatives higher than the first in (3-114), giving temperature acceptance bandwidth:

$$\Delta T=\frac{1}{L}\left[\frac{1}{\lambda_3}\left.\frac{\partial n_3}{\partial T}\right|_{T_0}-\frac{1}{\lambda_2}\left.\frac{\partial n_2}{\partial T}\right|_{T_0}-\frac{1}{\lambda_1}\left.\frac{\partial n_1}{\partial T}\right|_{T_0}\right]^{-1}. \tag{3-122}$$

In the case of angular acceptance, the situation is slightly more complex. Firstly, the derivative of the refractive index with respect to angle depends on the polarisation. Restricting the problem to uniaxial crystals or biaxial crystals in the principal planes, it is clear that the derivatives for an ordinary-polarised wave will be zero. For an extraordinary-polarised wave, the derivatives can be calculated from (3-78) to be:

$$\frac{\partial n_e(\theta)}{\partial \theta} = 4\left(\frac{\cos^2\theta}{n_o^2} + \frac{\sin^2\theta}{n_e^2}\right)^{-3} \cos\theta \sin\theta \left(\frac{1}{n_o^2} - \frac{1}{n_e^2}\right) \tag{3-123 a}$$

$$\frac{\partial^2 n_e(\theta)}{\partial \theta^2} = \frac{4\left(\frac{1}{n_o^2} - \frac{1}{n_e^2}\right)}{\left(\frac{\cos^2\theta}{n_o^2} + \frac{\sin^2\theta}{n_e^2}\right)^3} \left[\frac{6\cos^2\theta \sin^2\theta}{\left(\frac{\cos^2\theta}{n_o^2} + \frac{\sin^2\theta}{n_e^2}\right)} \left(\frac{1}{n_o^2} - \frac{1}{n_e^2}\right) + \left(\cos^2\theta - \sin^2\theta\right) \right] \tag{3-123 b}$$

It can be seen that in the case of non-critical phase-matching ($\theta = 0$ or $\pi/2$) the first derivative will be zero and thus the second derivative must be used in the calculation of the angular acceptance bandwidth. In the case of critical phase-matching, where the first-order term dominates, the angular acceptance bandwidth can be seen to be given by:

$$\Delta\theta = \frac{\pi}{2L}\left(\frac{\cos^2\theta}{n_o^2} + \frac{\sin^2\theta}{n_e^2}\right)^3 \left(\cos\theta \sin\theta \left(\frac{1}{n_o^2} - \frac{1}{n_e^2}\right)\right)^{-1} \tag{3-124}$$

For non-critical phase-matching (3-123 b) considerably simplifies to give:

$$\Delta\theta_{\theta=0} = \left(\frac{n_o^3}{2\pi\sqrt{L}}\left(\frac{1}{n_o^2} - \frac{1}{n_e^2}\right)\right)^{-\frac{1}{2}} \tag{3-125 a}$$

$$\Delta\theta_{\theta=\pi/2} = \left(\frac{n_e^3}{2\pi\sqrt{L}}\left(\frac{1}{n_o^2} - \frac{1}{n_e^2}\right)\right)^{-\frac{1}{2}} \tag{3-125 b}$$

in the cases of $\theta=0$ and $\theta=\pi/2$, respectively. While the angular acceptance bandwidth indicates the tolerance to changes in the beam direction, it is, more importantly, also

a measure of the tolerance to the spread of propagation directions within a beam, i.e. how tightly the beam can be focused without compromising the phase matching.

The calculation of the angular acceptance bandwidth in the case of quasi-phase-matching is slightly more complex than in the birefringent case as the projection of the grating vector on the wave vectors must be calculated for a given angle. This effect influences the bandwidth in addition to any change in refractive index with propagation direction. The calculation of phase-matching bandwidths in this case has been treated by Fejer et al. [91].

3.4 Optical parametric oscillators.

It can be seen from equations (3-64) that with a large pump field at λ_3, a very small field at one of the parametrically generated wavelengths λ_1 or λ_2 will result in the generation of a significant field at the other parametrically generated wavelength. As a result, placing the nonlinear material in a cavity resonant at one or both of the parametrically generated wavelengths can, in an analogy to the gain medium in a laser cavity, provide gain at these wavelengths. Thus, given sufficient pump power, the circulating parametric power in the cavity can build up, resulting in conversion of power at the pump wavelength to significant power levels at the parametrically generated wavelengths, the signal and idler. This is the underlying concept of the optical parametric oscillator (OPO).

3.4.1 Parametric oscillator threshold.

To calculate the pump power required for parametric oscillation an approach similar to that adopted by Debuisschert et al. [115] is used with some modifications [153]. The cavity is assumed to have the form shown in Fig. 3-16. The nonlinear crystal, of length L, is taken to be at one end of the cavity which has a total length $L+l$. The whole cavity is assumed to be lossless with the exception of the input/output mirror where all the losses for the cavity are lumped. These are defined as follows:

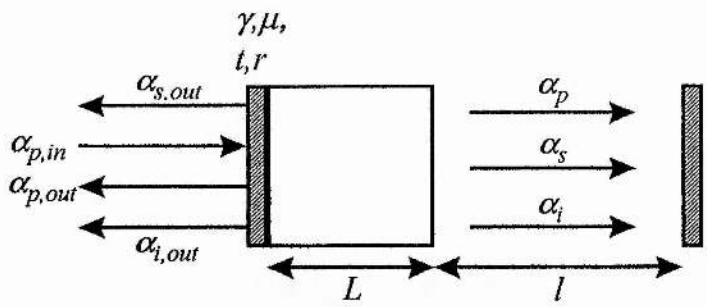

Fig. 3-16 Schematic representation of optical parametric oscillator. α_p, α_s and α_i are pump, signal and idler fields respectively. L is the crystal length, l is the cavity length excluding the crystal. All losses are lumped at one mirror having amplitude transmission t and reflection r, with output coupling losses γ and residual losses μ.

The mirror transmission losses are denoted by a loss coefficient γ_j where j=p,s,i denoting pump, signal or idler. Parasitic losses, additional to output coupling, are denoted by the coefficient μ_j. The total loss coefficient can thus be defined:

$$\gamma_j' = \gamma_j + \mu_j \tag{3-126}$$

In the case of small losses, this results in the round-trip amplitude loss, transmission and reflection coefficients being defined, respectively:

$$\ell_j = \sqrt{2\gamma_j'} \tag{3-127 a}$$

$$t_j = \sqrt{2\gamma_j} \tag{3-127 b}$$

$$r_j = 1-\gamma_j' \tag{3-127 c}$$

These are squared to give the round-trip power losses:

$$\mathcal{L}_j = 2\gamma_j' \tag{3-128 a}$$

$$T_j = 2\gamma_j \tag{3-128 b}$$

$$R_j = (1-\gamma_j')^2 \tag{3-128 c}$$

Thus, as small losses are assumed:

$$R_j + \mathcal{L}_j = 1 \tag{3-129}$$

or, in the case of output coupling being the only loss:

$$R_j + T_j = 1 \tag{3-130}$$

It can be seen from (3-128 a) that the single-pass power loss is given by γ_j'. Thus, the rate at which photons of frequency ω_j are lost from the cavity due to all loss mechanisms is given by:

$$\left|a_{j,loss}\right|^2 = 2\gamma_j'\left|\alpha_j\right|^2 \tag{3-131}$$

Similarly the rate at which photons are usefully output coupled is given by:

$$\left|a_{j,out}\right|^2 = 2\gamma_j\left|\alpha_j\right|^2 \tag{3-132}$$

It is often helpful to define the losses in terms of cavity finesse as this quantity is relatively easy to measure experimentally. This results in the definition [154]:

$$\mathcal{F}_j = \frac{\pi}{\gamma_j'} \tag{3-133}$$

The round-trip phase shift for one of the resonant waves is defined by:

$$\begin{aligned}\phi_j &= 2\frac{\omega_j}{c}\left(n_j L + l\right) + \delta_j + \delta_j' \\ &= \frac{2\pi\nu_j}{FSR_j}\end{aligned} \tag{3-134}$$

Where δ_j, δ_j' are the phase shifts introduced by reflection at the mirrors and FSR_j is the free spectral range of the cavity at the relevant wavelength defined as:

$$FSR_j = \frac{c}{2\left(n_j L + l\right)} \tag{3-135}$$

If it is assumed that all the resonant waves have frequencies close to cavity modes, the so called quasi-resonant approximation, (3-134) can be rewritten:

$$\phi_j = 2p_j\pi + \delta\phi_j + \delta_j + \delta_j' \qquad (p_j = 1,2,3\ldots \quad \delta\phi_j << 2\pi) \tag{3-136}$$

allowing the detuning from resonance to be defined:

$$\delta\phi_j = 2\frac{\Delta\omega_j}{c}\left(n_j L + l\right) = \frac{2\pi\Delta\nu_j}{FSR_j} \tag{3-137}$$

Since detuning from perfect resonance will effectively increase the cavity losses, it is useful to define a relative detuning:

$$\Delta_j = \frac{\delta\phi_j}{\gamma_j'} \tag{3-138}$$

The resultant phase-mismatch introduced between the resonant waves on reflection at one of the mirrors can be defined as:

$$\theta' = \delta_s' + \delta_i' - \delta_p' \tag{3-139}$$

Comparing (3-139) to (3-35) it can be seen that combination of the dispersion phase-mismatch, Δk, and the mirror phase-mismatch, θ', can result in an overall phase-mismatch of zero. Thus, in the presence of mirror phase shifts, Δk=0 is not generally the optimum value for the dispersion phase-mismatch.

Balancing the gain at each of the interacting waves, as given by (3-64), with the losses over one round trip gives the set of equations:

$$\alpha_p\left(1-r_p e^{i\phi_p}\right) = -2\Gamma^* \alpha_s \alpha_i e^{i\phi_p}\left(r_p + r_s r_i e^{i\theta' - i\Delta kL}\right) + t_p \alpha_p^{in} \tag{3-140 a}$$

$$\alpha_s\left(1-r_s e^{i\phi_s}\right) = 2\Gamma \alpha_p \alpha_i^* e^{i\phi_s}\left(r_s + r_p r_i e^{-i\theta' + i\Delta kL}\right) \tag{3-140 b}$$

$$\alpha_i\left(1-r_i e^{i\phi_i}\right) = 2\Gamma \alpha_p \alpha_s^* e^{i\phi_i}\left(r_i + r_p r_s e^{-i\theta' + i\Delta kL}\right) \tag{3-140 c}$$

where the first term in the brackets describes the gain due to the forward propagating interaction and the second term describes that due to the backward propagating interaction, after reflection. Assuming $r_j=(1-\gamma_j') \approx 1$ and defining a new gain coefficient, Γ', such that:

$$\begin{aligned} \Gamma' &= \Gamma\left(1+e^{i\Delta kL - i\theta'}\right) \\ &= \kappa L \operatorname{sinc}\left(\frac{\Delta kL}{2}\right) e^{i\frac{\Delta kL}{2}}\left(1+e^{i\Delta kL - i\theta'}\right) \end{aligned} \tag{3-141}$$

equations (3-140) can be rewritten, making the quasi-resonant approximation and using (3-138):

$$\alpha_p \gamma_p'\left(1-i\Delta_p\right) = -2\Gamma'^* \alpha_s \alpha_i + \sqrt{2\gamma_p}\alpha_p^{in} \tag{3-142 a}$$

$$\alpha_s \gamma_s'\left(1-i\Delta_s\right) = 2\Gamma'^* \alpha_p \alpha_i^* \tag{3-142 b}$$

$$\alpha_i \gamma_i'\left(1-i\Delta_i\right) = 2\Gamma'^* \alpha_p \alpha_s^* \tag{3-142 c}$$

It can be seen from (3-57) that κ includes the effects of overlap between the pump, signal and idler in the form of the spatial coupling parameter m defined in (3-58). It is useful to see how this parameter can be optimised to minimise OPO threshold as, unlike the case of single-pass SHG, the beam waists in an OPO are defined by the resonator geometry. It can be seen from (3-49) that for given signal and idler waists, w_s and w_i, the optimum value for the pump waist is given by:

$$\frac{1}{w_p^2} = \frac{1}{w_s^2} + \frac{1}{w_i^2} \tag{3-143}$$

which results in the maximum value of m, optimised for these signal and idler dimensions, being:

$$m_{\max} = \frac{1}{2}\left(w_s^2 + w_i^2\right)^{-\frac{1}{2}} \tag{3-144}$$

Since we are considering beams having a Gaussian profile but neglecting the effects of divergence, the smallest beam waists for a given crystal length L are defined by the confocal focusing condition:

$$w_j^2 = \frac{\lambda_j L}{2\pi n_j} = \frac{cL}{2\pi n_j \nu_j} \tag{3-145}$$

Under these conditions, the maximum spatial coupling parameter of (3-44) becomes:

$$\begin{aligned} m_{conf} &= \left[\frac{2cL}{\pi}\left(\frac{1}{n_s\nu_s} + \frac{1}{n_i\nu_i}\right)\right]^{-\frac{1}{2}} \\ &= \left[\frac{2L}{\pi}\left(\frac{\lambda_s}{n_s} + \frac{\lambda_i}{n_i}\right)\right]^{-\frac{1}{2}} \end{aligned} \tag{3-146}$$

Rather than include the signal and idler wavelengths or frequencies explicitly, it is often helpful to define a parameter, δ, describing how far from degeneracy the OPO is being operated:

$$\begin{aligned} \delta &= \frac{2\nu_s - \nu_p}{\nu_p} = \frac{2\omega_s - \omega_p}{\omega_p} \\ &= \frac{\nu_p - 2\nu_i}{\nu_p} = \frac{\omega_p - 2\omega_i}{\omega_p} \end{aligned} \tag{3-147}$$

Thus, at degeneracy δ=0. It can be seen that this results in the signal and idler frequencies being expressed in terms of the degeneracy factor as:

$$\begin{aligned} \nu_s &= \frac{1}{2}\left(\nu_p\delta - \nu_p\right) \qquad \omega_s = \frac{1}{2}\left(\omega_p\delta - \omega_p\right) \\ \nu_i &= \frac{1}{2}\left(\nu_p - \nu_p\delta\right) \qquad \omega_i = \frac{1}{2}\left(\omega_p - \omega_p\delta\right) \end{aligned} \tag{3-148}$$

This allows the coupling factor, κ, of (3-57) to be expressed as:

$$\kappa = d_{eff}m\left(\frac{\hbar\omega_p^3\left(1-\delta^2\right)}{4n_pn_sn_ic^3\varepsilon_0\pi}\right)^{\frac{1}{2}} = d_{eff}m\left(\frac{4\pi h\nu_p^3\left(1-\delta^2\right)}{n_pn_sn_ic^3\varepsilon_0}\right)^{\frac{1}{2}} \tag{3-149}$$

Thus, in the case of confocal focussing as described in (3-154) and making the simplifying assumption that, for the purposes of beam waist calculations, n_p=n_s=n_i=n the optimised coupling factor is given by:

$$\kappa_{conf}^2 = d_{eff}^2\,\frac{\pi^2\nu_p^3\left(1-\delta^2\right)^2}{2L\varepsilon_0c^4n^2}\left(h\nu_p\right) \tag{3-150}$$

3.4.1.1 Triply-resonant OPO.

Considering first the case of a cavity where the pump, signal and idler are all resonated, the triply-resonant OPO (TRO), (3-142 b) is multiplied by the complex conjugate of (3-142 c) giving the expression:

$$\gamma_s'\gamma_i'\left(1-i\Delta_s\right)\left(1+i\Delta_i\right) = 4\left|\Gamma'\right|^2\left|\alpha_p\right|^2 \tag{3-151}$$

Considering the imaginary part of the expression, it can be seen that:

$$\Delta_s = \Delta_i = \Delta \tag{3-152}$$

i.e. the relative detunings at the signal and idler are the same. This restriction is a feature of all doubly- and triply-resonant OPOs and can be understood by calculating the rate at which photons are lost from the cavity at the signal and idler. Multiplying (3-142 b) by α_s^* and (3-142 c) by α_i^*, then using (3-133), yields:

$$\left|\alpha_{s,loss}\right|^2\left(1-i\Delta_s\right)=\left|\alpha_{i,loss}\right|^2\left(1-i\Delta_i\right) \tag{3-153}$$

Clearly, under steady-state conditions, if the rates at which signal and idler photons are lost from the cavity are to be equal, then (3-152) must hold. This, clearly, must be the case as signal and idler photons are generated at the same rate in the nonlinear material.

Given (3-152), equation (3-151) can be rewritten:

$$\left|\alpha_p\right|^2=\frac{\gamma_s'\gamma_i'\left(1+\Delta^2\right)}{4\left|\Gamma'\right|^2} \tag{3-154}$$

giving the one-way pump-photon flow within the cavity. Note that this expression implies that the intra-cavity pump power clamps at the threshold level. The external threshold pump power can be obtained from equation (3-142 a) by setting α_s and α_i to zero giving:

$$\left|\alpha_p^{in}\right|_{th}^2=\frac{\gamma_p'^2\gamma_s'\gamma_i'}{8\left|\Gamma'\right|^2\gamma_p}\left(1+\Delta^2\right)\left(1+\Delta_p^2\right) \tag{3-155}$$

When the pump is on exact resonance, $\Delta^2=0$ and a maximum pump enhancement factor can be defined [154]:

$$E_{p,\max}=\frac{2\gamma_p\mathcal{F}_p^2}{\pi^2} \tag{3-156}$$

If the other waves are also on exact resonance (i.e. $\Delta=0$) then, using (3-141), (3-156) can be rewritten:

$$\left|\alpha_p^{in}\right|_{th}^2=\frac{\pi^2}{16\kappa^2l^2\mathcal{F}_s\mathcal{F}_i}\frac{1}{E_{p,\max}}\operatorname{sinc}^2\left(\frac{\Delta kl}{2}\right)\left(\cos^2\left(\frac{\Delta kl}{2}-\frac{\theta'}{2}\right)\right)^{-1} \tag{3-157}$$

It can be seen that the phase-matching term now depends on θ' in addition to Δk, resulting in the optimum value of Δk only being zero when θ' is also zero, as mentioned earlier. In this case, the threshold for optimum phase matching is:

$$\left|\alpha_p^{in}\right|^2_{th,o} = \frac{\pi^2}{16\kappa^2 l^2 \mathcal{F}_s \mathcal{F}_i} \frac{1}{E_{p,\max}} \tag{3-158}$$

In the case of optimised confocal focusing and perfect detunings (i.e. zero overall phase mismatch), this expression becomes:

$$\left|\alpha_p^{in}\right|^2_{th,\min} = \frac{n^2 \varepsilon_0 c^4}{8 d_{eff}^2 L \nu_p^3 \left(1-\delta^2\right)^2 \mathcal{F}_s \mathcal{F}_i} \frac{1}{E_{p,\max}} \frac{1}{h\nu_p}$$

$$\therefore P_{p,th,\min}^{in} = \frac{n^2 \varepsilon_0 c^4}{8 d_{eff}^2 L \nu_p^3 \left(1-\delta^2\right)^2 \mathcal{F}_s \mathcal{F}_i} \frac{1}{E_{p,\max}} \tag{3-159}$$

3.4.1.2 Doubly-resonant OPO.

Doubly-resonant OPOs (DROs), in which the signal and idler are resonated in a high finesse cavity while the pump is non-resonant, are widely utilised for continuous-wave operation. We consider here two situations. In the first, both mirrors are highly transmitting at the pump wavelength, causing the pump to make a single pass through the cavity. In the second situation the non-input mirror has significant reflectivity at the pump wavelength resulting in the pump making a double pass through the cavity. This second arrangement can result in a significantly reduced threshold without imposing the restrictions of pump resonance [155].

The derivation of the threshold proceeds as for the TRO, except that in (3-140) r_p is not automatically assumed to be unity while r_s and r_i are. In this case, the equivalent expression to (3-141) giving the double-pass gain coefficient is:

$$\Gamma'_{DP} = \kappa L \operatorname{sinc}\left(\frac{\Delta kL}{2}\right) e^{i\frac{\Delta kL}{2}} \left(1 + e^{i\Delta kL - i\theta'}\right)$$
$$\therefore \left|\Gamma'_{DP}\right|^2 = \kappa^2 L^2 \operatorname{sinc}^2\left(\frac{\Delta kL}{2}\right)\left(1 + r_p^2 + 2r_p \cos\left(\Delta kL - \theta'\right)\right) \tag{3-160}$$

From (3-155), and remembering that with a non-resonant pump $\left|\alpha_p^{in}\right|^2 = \left|\alpha_p\right|^2$, the threshold expression is found to be:

$$\left|\alpha_p^{in}\right|_{th}^2 = \frac{\pi^2}{4\kappa^2 L^2 \mathcal{F}_s \mathcal{F}_i} \frac{1}{\operatorname{sinc}^2\left(\frac{\Delta kL}{2}\right)} \frac{1}{1 + r_p^2 + 2r_p \cos\left(\Delta kL - \theta'\right)} \left(1 + \Delta^2\right) \tag{3-161}$$

The result for a single-pass pump can now be obtained by setting r_p=0 to give:

$$\left|\alpha_p^{in}\right|_{th}^2 = \frac{\pi^2}{4\kappa^2 L^2 \mathcal{F}_s \mathcal{F}_i} \frac{1}{\operatorname{sinc}^2\left(\frac{\Delta kL}{2}\right)} \left(1 + \Delta^2\right) \tag{3-162}$$

In the case of zero overall phase-mismatch this reduces to:

$$\left|\alpha_p^{in}\right|_{th,o}^2 = \frac{\pi^2}{4\kappa^2 L^2 \mathcal{F}_s \mathcal{F}_i} \tag{3-163}$$

Rearranging (3-163) in terms of pump power gives:

$$P_{p,th,o}^{in} = \frac{\gamma_s' \gamma_i' \pi n_p n_s n_i \varepsilon_0 c^3}{4L^2 \omega_s \omega_i \chi_{eff}^2} \frac{1}{m^2} \tag{3-164}$$

agreeing with expressions obtained by others [22]. In the case of zero overall phase-mismatch and confocal focusing (3-162) becomes:

$$\left|\alpha_p^{in}\right|^2_{th,\min} = \frac{n^2\varepsilon_0 c^4}{2d_{eff}^2 L\nu_p^3\left(1-\delta^2\right)^2\mathcal{F}_s\mathcal{F}_i}\frac{1}{h\nu_p}$$

$$\therefore P^{in}_{p,th,\min} = \frac{n^2\varepsilon_0 c^4}{2d_{eff}^2 L\nu_p^3\left(1-\delta^2\right)^2\mathcal{F}_s\mathcal{F}_i} \tag{3-165}$$

Returning to (3-161) and considering the case of non-zero r_p, it can be seen that this expression is the same as that for a single-pass DRO with an additional reduction factor R_{dp} given by:

$$R_{dp} = \frac{1}{\operatorname{sinc}^2\left(\frac{\Delta kL}{2}\right)}\frac{1}{1+r_p^2+2r_p\cos\left(\Delta kL-\theta'\right)} \tag{3-166}$$

The phase-mismatch ΔkL will always assume a value to minimise the threshold for a given value of θ'. However, this minimum value will depend on the exact values of r_p and the reflection phase-mismatch θ'. The reduction factor R_{dp}, effectively the ratio of DRO threshold with a double-pass pump to the single-pass case, is plotted as a function of phase-mismatch ΔkL for a range of amplitude reflectivities and reflection phase-mismatch values in Fig. 3-17. It can be seen that the double-pass threshold is always less than that for a single-pass pump when the amplitude reflectivity is greater than 0.35, corresponding to a power reflectivity of greater than 0.12.

In the ideal case of r_p=1 and Δk=θ'=0 the maximum value of R_{dp}=4 is obtained and the threshold expression of (3-161) becomes:

$$\left|\alpha_p^{in}\right|^2_{th,o} = \frac{\pi^2}{16\kappa^2 L^2\mathcal{F}_s\mathcal{F}_i} \tag{3-167}$$

giving a maximum reduction in the threshold to one quarter that of the single-pass case.

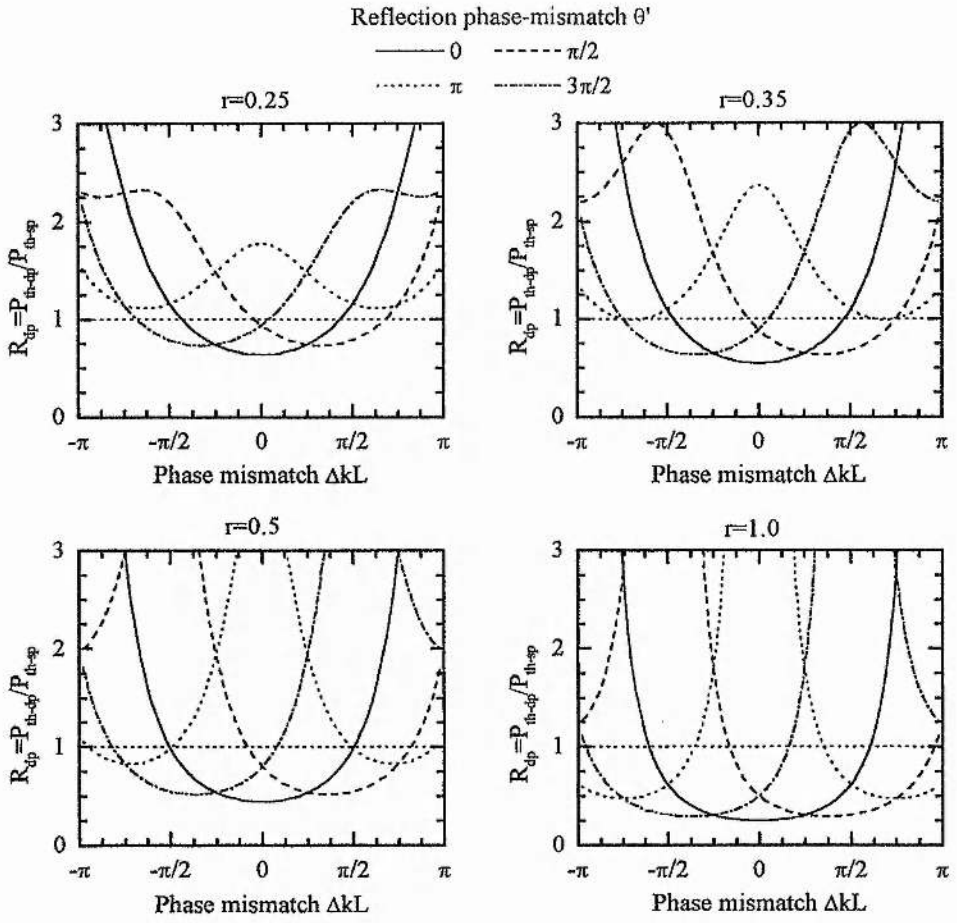

Fig. 3-17 Variation of DRO threshold with double-pass pump, relative to single pass threshold, with phase-mismatch for various values of amplitude reflectivity, r, and reflection phase-mismatch, θ'.

3.4.1.3 Singly-resonant OPO.

The final configuration to be considered is the singly-resonant OPO (SRO) in which one of the parametrically generated waves is resonant in a high-finesse cavity. Variations on this configuration include additionally resonating the pump (usually described as a pump-enhanced SRO [156]) and double passing the non-resonant parametric wave or the pump, or both.

Consider first the case of an SRO with the pump and non-resonant wave both single-passed. In the case of the idler being the resonant wave, (3-142 c) describes the idler. However, as gain and loss are not balanced for the non-resonant wave, (3-142 b) cannot be applied to the signal. If all the signal power generated on a single pass through the crystal is coupled out of the cavity after this single pass, (3-64 b) can be used to determine the signal power by setting $\alpha_2(0)=\alpha_s(0)=0$. Since the signal amplitude scales linearly with length, the average signal power, $\alpha_s(L)/2$, can be used. Thus, from (3-64 b) and (3-142 b) the pair of equations:

$$\alpha_s = \Gamma' \alpha_p \alpha_i^* \tag{3-168 a}$$

$$\alpha_i \gamma_i' \left(1 - i\Delta_i\right) = 2\Gamma' \alpha_p \alpha_s^* \tag{3-168 b}$$

are obtained. Multiplying (3-168 b) by the complex conjugate of (3-168 a) gives:

$$\gamma_i' \left(1 - i\Delta_i\right) = 2|\Gamma'|^2 \left|\alpha_p\right|^2 \tag{3-169}$$

Proceeding as before, the imaginary part of this expression yields:

$$\Delta_i = 0 \tag{3-170}$$

showing that, in the case of the SRO, the resonant wave always corresponds exactly with a resonant cavity mode. Given this result, (3-169) becomes:

$$\left|\alpha_p\right|_{th}^2 = \frac{\pi}{2\mathcal{F}_i |\Gamma'|^2} \tag{3-171}$$

Thus, in the case of optimum phase-matching:

$$\left|\alpha_p^{in}\right|_{th,o}^2 = \frac{\pi}{2\kappa^2 L^2 \mathcal{F}_i}$$

$$\therefore P_{p,th,o}^{in} = \frac{\gamma_i' \pi n_p n_s n_i \varepsilon_0 c^3}{2\omega_s \omega_i \chi_{eff}^2 L^2} \frac{1}{m^2} \tag{3-172}$$

in agreement with [22]. In the case of confocal focusing, the minimum threshold expression obtained is:

$$\left|\alpha_p^{in}\right|^2_{th,\min} = \frac{n_p^2 \varepsilon_0 c^4}{\pi L d_{eff}^2 \left(1-\delta^2\right)^2 \nu_p^3 \mathcal{F}_i} \frac{1}{h\nu_p}$$

$$\therefore P^{in}_{p,th,\min} = \frac{n_p^2 \varepsilon_0 c^4}{\pi L d_{eff}^2 \left(1-\delta^2\right)^2 \nu_p^3 \mathcal{F}_i} \tag{3-173}$$

If the pump is double passed, while the non-resonant parametric wave (the signal in this case) remains single-pass, it can be seen that, by a similar approach to that for the DRO with double-pass pump, a reduction factor of $(1+r_p^2)$ is obtained [155] and the threshold becomes:

$$\left|\alpha_p^{in}\right|^2_{th} = \frac{\pi}{2\kappa^2 L^2 \mathcal{F}_i} \frac{1}{1+r_p^2} \frac{1}{\operatorname{sinc}^2\left(\frac{\Delta kL}{2}\right)} \tag{3-174}$$

Thus, in the ideal case of r_p=1, the threshold is half that of the SRO with a single-pass pump. It is interesting to note that in this case there is no reflection dephasing factor and the minimum threshold is still obtained for Δk=0. This is due to the fact that the signal is still single pass and can assume any phase appropriate to compensate for phase shifts between the pump and idler on reflection. In the case of a double-passed pump and signal, the reduction factor must take account of the reflection dephasing and, if the signal reflectivity is unity, becomes the same as that for the DRO [157], resulting in the threshold expression:

$$\left|\alpha_p^{in}\right|^2_{th} = \frac{\pi}{2\kappa^2 L^2 \mathcal{F}_i} \frac{1}{1+r_p^2+2r_p\cos\left(\Delta kL-\theta'\right)} \frac{1}{\operatorname{sinc}^2\left(\frac{\Delta kL}{2}\right)} \tag{3-175}$$

As with the DRO, it can be seen that the threshold can be reduced by a maximum factor of four compared to that of the simple SRO.

Finally we consider the case of the pump-enhanced SRO where, in addition to one of the parametric waves, the pump is resonated in the cavity. Such systems have been used in a number of cases as an alternative to DROs in situations where a low threshold is required [69,84,158]. Clearly, the internal pump-power threshold will be the same as the incident threshold of the SRO with a double-pass pump and $r_p \approx 1$. The external threshold is thus given by:

$$\left|\alpha_p^{in}\right|_{th}^2 = \frac{\pi}{4\kappa^2 L^2 \mathcal{F}_i} \frac{1}{E_{p,\max}} \frac{1}{\operatorname{sinc}^2\left(\frac{\Delta kL}{2}\right)} \tag{3-176}$$

3.4.2 Above threshold behaviour.

Optical parametric oscillators are potentially highly efficient devices for the nonlinear frequency conversion of optical radiation. The efficiency with which this conversion takes place for an OPO above threshold is discussed here. It is useful to define a pumping ratio, σ, which is a measure of how far above threshold the OPO is being pumped:

$$\sigma = \frac{\left|\alpha_p^{in}\right|^2}{\left|\alpha_p^{in}\right|_{th,o}^2} \tag{3-177}$$

The external efficiency can be defined in terms of pump, signal and idler powers or photon flows. If the internal powers at the signal and idler are P_s and P_i then an internal efficiency can be defined:

$$\eta_{\text{int}} = \frac{P_s + P_i}{P_p^{in}} \tag{3-178}$$

The output powers are given by the product of the internal power and the ratio of the useful output coupling to the total losses allowing the conversion efficiencies for the signal and idler to be defined:

$$\eta_{j,ext} = \frac{P_j^{out}}{P_p^{in}} = \frac{T_j}{\mathcal{L}_j}\frac{\omega_j}{\omega_p}\eta_{\text{int}} \qquad (j = s,i) \tag{3-179}$$

where T_j and $\mathcal{L}_j$ are as defined in (3-128). The overall external efficiency is thus given by:

$$\eta_{ext} = \frac{P_s^{out} + P_i^{out}}{P_p^{in}} = \left[\frac{T_s}{\mathcal{L}_s}\frac{\omega_s}{\omega_p} + \frac{T_i}{\mathcal{L}_i}\frac{\omega_i}{\omega_p}\right]\eta_{\text{int}} \tag{3-180}$$

Defining the efficiency in terms of photon flows, from (3-179) one obtains:

$$\eta_{j,ph,ext} = \frac{\left|\alpha_j^{out}\right|^2}{\left|\alpha_p^{in}\right|^2} = \frac{T_j}{\mathcal{L}_j}\eta_{\text{int}} \qquad (j = s,i) \tag{3-181}$$

Thus the overall photon conversion efficiency is given by:

$$\eta_{ph,ext} = \frac{\left|\alpha_s^{out}\right|^2 + \left|\alpha_i^{out}\right|^2}{\left|\alpha_p^{in}\right|^2} = \left[\frac{T_s}{\mathcal{L}_s} + \frac{T_i}{\mathcal{L}_i}\right]\eta_{\text{int}} \tag{3-182}$$

or, in terms of finesses and output losses:

$$\eta_{ph,ext} = \left(\frac{\gamma_s\mathcal{F}_s + \gamma_i\mathcal{F}_i}{\pi}\right)\eta_{\text{int}} \tag{3-183}$$

It can be seen that where all the losses are due to output coupling, (3-180) and (3-183) become:

$$\eta_{ext,\max} = \eta_{\text{int}} \tag{3-184 a}$$

$$\eta_{ph,ext,\max} = 2\eta_{\text{int}} \tag{3-184 b}$$

Thus, the photon conversion efficiency is twice the power conversion efficiency. This would be expected as one pump photon produces one signal and one idler photon whose total energy is equal to that at the pump.

3.4.2.1 Doubly-resonant OPOs.

The case of a DRO with single-pass pump was first considered by Siegman [159]. The internal efficiency is given by:

$$\eta_{\text{int}} = \frac{2}{\sigma}\left(\sqrt{\sigma} - 1\right) \tag{3-185}$$

resulting in the external efficiencies being given by:

$$\eta_{ext} = \left(\frac{\gamma_s \mathcal{F}_s \omega_s + \gamma_i \mathcal{F}_i \omega_i}{\pi \omega_p}\right)\frac{2}{\sigma}\left(\sqrt{\sigma} - 1\right) \tag{3-186 a}$$

$$\eta_{ph,ext} = \left(\frac{\gamma_s \mathcal{F}_s + \gamma_i \mathcal{F}_i}{\pi}\right)\frac{2}{\sigma}\left(\sqrt{\sigma} - 1\right) \tag{3-186 b}$$

It can be seen that the efficiency is maximised when σ=4, resulting in a 50% power conversion efficiency. In the case where the pump is double-passed the internal efficiency is given by [155,160]:

$$\eta_{\text{int}} = \frac{2}{\sigma}\left(\sqrt{\sigma} - 1\right)\left(\frac{1 + r_p^2 + 2r_p \cos\left(\theta' + \Delta kL\right)}{1 + r_p \cos\left(\theta' + \Delta kL\right)}\right) \tag{3-187}$$

In the case of optimum dephasing, this results in the efficiency expressions:

$$\eta_{ext} = \left(\frac{\gamma_s \mathcal{F}_s \omega_s + \gamma_i \mathcal{F}_i \omega_i}{\pi \omega_p}\right)\frac{2}{\sigma}\left(\sqrt{\sigma} - 1\right)\left(1 + r_p\right) \tag{3-188 a}$$

$$\eta_{ph,ext} = \left(\frac{\gamma_s \mathcal{F}_s + \gamma_i \mathcal{F}_i}{\pi}\right)\frac{2}{\sigma}\left(\sqrt{\sigma} - 1\right)\left(1 + r_p\right) \tag{3-188 b}$$

It can be seen that, if r_p=1, the maximum power conversion efficiency, obtained with σ=4, is now 100%. Since the efficiencies are defined in terms of pump powers relative to threshold, equations (3-188) can also be applied to triply-resonant OPOs.

As mentioned in section 3.4.1.1, the intra-cavity pump power in the case of the TRO and transmitted pump power for the DRO clamp at the threshold value. This effect formed the basis of the optical power limiter proposed by Siegman [159] who also discussed the efficiency of parametric devices in terms of the downconverted, transmitted and "reflected" pump powers. The "reflected" wave, sometimes described as a power-dependent reflection, is actually a result of parametric upconversion by the backward-travelling signal and idler in the single-pass-pump DRO. This wave is generated in anti-phase with the incoming pump and therefore acts to reduce its amplitude, resulting in pump depletion. It is this effect which limits the efficiency of the DRO to 50% in the single-pass-pump case. In fact, at optimum efficiency for such devices (four times above threshold), 50% of the input pump power is converted to signal and idler, 25% is transmitted through the device and 25% is "reflected".

In the double-pass case the return pass of the pump, travelling with the signal and idler, prevents this back conversion and the efficiency is able to reach 100% [155,160]. Similar results are obtained in the case of a ring cavity, where the signal and idler are unidirectional and only pass through the nonlinear crystal in the same direction as the single-pass pump [27,22].

3.4.2.2 Singly-resonant OPOs.

Conversion efficiency in singly-resonant OPOs was first discussed by Kreuzer [30] and has since been treated by a number of other authors [20,22,23]. The transmitted pump power and internal signal and idler powers, respectively, are given by:

$$\frac{P_p^{tr}}{P_p^{in}} = \cos^2(\beta L) + \left(\frac{\Delta k}{2\beta}\right)^2 \sin^2(\beta L) \qquad \text{(3-189 a)}$$

$$\frac{P_s}{P_p^{in}} = \frac{\omega_s}{\omega_p}\left[1 - \left(\frac{\Delta k}{2\beta}\right)^2\right]\sin^2(\beta L) \qquad \text{(3-189 b)}$$

$$\frac{P_i}{P_p^{in}} = \frac{\omega_i}{\omega_p}\left[1 - \left(\frac{\Delta k}{2\beta}\right)^2\right]\sin^2(\beta L) \qquad \text{(3-189 c)}$$

where:

$$\frac{\sin^2(\beta L)}{(\beta L)^2} = \frac{P_p^{th}}{P_p^{in}} \operatorname{sinc}^2\left(\frac{\Delta k L}{2}\right) \tag{3-190}$$

It can be seen from (3-189) that in terms of photon flows:

$$\frac{|\alpha_s|^2}{|\alpha_p^{in}|^2} = \frac{|\alpha_i|^2}{|\alpha_p^{in}|^2} = \left[1-\left(\frac{\Delta k}{2\beta}\right)^2\right]\sin^2(\beta L) = \eta_{\text{int}} \tag{3-191}$$

Clearly this efficiency will be maximised, to be unity, when Δk=0 and βL=π/2. From (3-190), it can be seen that this implies:

$$\sigma = \left(\frac{\pi}{2}\right)^2 \tag{3-192}$$

Assuming the idler to be the resonant wave, the external photon efficiencies are related to the internal values by:

$$\eta_{ph,ext,s} = \eta_{\text{int}} \tag{3-193 a}$$

$$\eta_{ph,ext,i} = \frac{\gamma_i \mathcal{F}_i}{\pi}\eta_{\text{int}} \tag{3-193 b}$$

The overall external photon efficiency is thus given by:

$$\eta_{ph,ext} = \left(1+\frac{\gamma_i \mathcal{F}_i}{\pi}\right)\left[1-\left(\frac{\Delta k}{2\beta}\right)^2\right]\sin^2(\beta L) \tag{3-194}$$

Clearly, when all the idler losses are in the form of useful output coupling, and (3-192) is valid, (3-194) gives a value of 2 implying a external power efficiency of 100%. The effects of a double-passed pump on SRO efficiency have also been

investigated and shown to greatly increase the range of pump powers over which the efficiency is close to 100% [155].

3.4.3 Tuning and stability considerations.

A number of factors determine the spectral properties of optical parametric oscillators, including the phase-matching conditions, cavity-resonance restrictions and energy-conservation requirements. These frequency selection processes are also intimately linked to the power stability of the OPO output.

The primary wavelength selection process for an OPO is the requirement of phase matching:

$$|\Delta k| = \left|k_p - k_s - k_i\right| \leq \frac{\pi}{L} \tag{3-195}$$

where in the case of quasi-phase-matching an additional factor K_m, representing the mth-order grating wave-vector, would be included as in (3-106). Clearly, this defines a phase-matching bandwidth over which gain is available at the parametrically generated wavelengths. This bandwidth can be considered as similar to the gain bandwidth of a laser transition with the important advantage that the centre wavelength can be varied, in some cases over quite large ranges, by varying the pump wavelength [161], crystal angle, crystal temperature or, in the case of quasi-phase-matching, the grating period [148], as discussed in section 3.3. Tuning can also be carried out electro-optically [66], although the tuning range using this method is typically much smaller than that obtained with the other methods, and electro-optic tuning is usually reserved for fast frequency control over small ranges.

Within the phase-matching bandwidth, the next frequency selection criterion is that the frequency of the resonant wave or waves must correspond to a resonant cavity mode. In addition to this limitation, the parametrically generated waves must fulfil the third requirement satisfying energy conservation. These two requirements can be summarised by the expressions:

$$\nu_p = \nu_s + \nu_i \tag{3-196}$$

$$\nu_j - pFSR_j \leq \frac{\Delta\nu_{c,j}}{2} \qquad (j = s,i \quad p = \text{integer}) \tag{3-197}$$

where $\Delta\nu_{c,j}$ is the cavity-mode linewidth for the wave of interest. Thus, (3-197) implies that the frequency of the resonant parametric wave (or waves) must fall within the linewidth of a cavity mode. For a fixed frequency, the free spectral range (FSR) is given by (3-135), with the refractive index being calculated at this frequency from Sellmeier equations. When considering tuning behaviour and stability, it is more useful to use an expression for cavity FSR which allows small detunings, of the order of a FSRs, from the centre frequency at which the refractive index is calculated while taking account of the effects of dispersion. Assuming the detuning, $\Delta\nu_j$, is small compared to the centre frequency, $\nu_{0,j}$, and the dispersion can be approximated, over this range, to a linear variation described by the derivative at the centre frequency the FSR can be described by:

$$FSR_j = \frac{\left(\dfrac{c}{2\left(n_{0,j}L + l\right)}\right)}{\left(1 + \dfrac{\left.\dfrac{dn_j}{d\nu_j}\right|_{\nu_j=\nu_{0,j}} L\,\Delta\nu_j}{n_{0,j}L + l}\right)} \tag{3-198}$$

which simplifies to (3-135) in the cases of zero dispersion or zero detuning.

3.4.3.1 Singly-resonant OPOs.

Clearly, the simplest case is that of the SRO in which the resonant wave will adopt the frequency of the cavity mode closest to the maximum of the phase-matching bandwidth. Since the non-resonant wave (the signal if we continue with the example used in threshold calculations) is free to adopt any frequency satisfying (3-196), the frequency stability of the resonant wave (the idler) is determined by the stability of the OPO cavity. Any fluctuations in the pump frequency, as long as they result in

shifts in the phase-matching maximum of less than half a FSR at the idler, result in shifts in the idler frequency which changes to maintain (3-196), while the signal frequency remains fixed. Changes in the pump frequency resulting in the phase-matching maximum shifting by half a FSR cause the idler to hop to the next resonant cavity mode. For small frequency changes, the rate at which the phase-matching centre frequency tunes with pump frequency is given, for the signal and idler, respectively, by [162]:

$$\frac{\Delta\nu_{s,pm}}{\Delta\nu_p} = \frac{\left.\frac{\partial k_p}{\partial \nu_p}\right|_{\nu_{p,0}} - \left.\frac{\partial k_i}{\partial \nu_i}\right|_{\nu_{i,0}}}{\left.\frac{\partial k_s}{\partial \nu_s}\right|_{\nu_{s,0}} - \left.\frac{\partial k_i}{\partial \nu_i}\right|_{\nu_{i,0}}} = 1 - \frac{\Delta\nu_{i,pm}}{\Delta\nu_p} \qquad \text{(3-199 a)}$$

$$\frac{\Delta\nu_{i,pm}}{\Delta\nu_p} = \frac{\left.\frac{\partial k_p}{\partial \nu_p}\right|_{\nu_{p,0}} - \left.\frac{\partial k_s}{\partial \nu_s}\right|_{\nu_{s,0}}}{\left.\frac{\partial k_i}{\partial \nu_i}\right|_{\nu_{i,0}} - \left.\frac{\partial k_s}{\partial \nu_s}\right|_{\nu_{s,0}}} = 1 - \frac{\Delta\nu_{s,pm}}{\Delta\nu_p} \qquad \text{(3-199 b)}$$

where:

$$\left.\frac{\partial k_j}{\partial \nu_j}\right|_{\nu_{j,0}} = \frac{2\pi}{c}\left(\nu_{j,0}\left.\frac{\partial n_j}{\partial \nu_j}\right|_{\nu_{j,0}} + n_{j,0}\right) \qquad \text{(3-200)}$$

the derivative being evaluated at zero frequency change. As discussed above, this change for the resonant (idler) frequency can be plus or minus half a FSR. The maximum pump tuning range is thus:

$$\left|\Delta\nu_{p,\max}\right| = \frac{\left.\frac{\partial k_i}{\partial \nu_i}\right|_{\nu_{i,0}} - \left.\frac{\partial k_s}{\partial \nu_s}\right|_{\nu_{s,0}}}{\left.\frac{\partial k_p}{\partial \nu_p}\right|_{\nu_{p,0}} - \left.\frac{\partial k_s}{\partial \nu_s}\right|_{\nu_{s,0}}} FSR_i \qquad \text{(3-201)}$$

It can be seen from (3-199) that this results in a maximum mode-hop-free idler tuning range of:

$$\left|\Delta\nu_{i,\max}\right| = \left(\frac{\Delta\nu_p}{\Delta\nu_i} - 1\right) FSR_i \tag{3-202}$$

The relative insensitivity of the resonant frequency to pump-frequency fluctuations allows an SRO to produce a single-frequency resonant wave from a multiple-longitudinal-mode pump source, the multi-mode properties of the pump being transferred to the idler [74,75,77].

Tuning of the resonant idler frequency for a fixed pump frequency can be obtained by varying the cavity length. As discussed above, the maximum tuning range will be plus or minus half of one FSR, or one FSR in total. Due to energy conservation, this tuning range will also translate, in the opposite direction, to the idler:

$$\left|\Delta\nu_{i,\max}\right| = \left|\Delta\nu_{s,\max}\right| = FSR_i \tag{3-203}$$

The actual frequency shift within this tuning range caused by a change in cavity length, Δl, is given by:

$$\Delta\nu_i = -\Delta\nu_s = -\frac{\nu_i}{n_i L + l}\Delta l \tag{3-204}$$

In the case of a pump-enhanced SRO, the requirement of pump resonance is added to the above tuning characteristics. Clearly, for a fixed pump wavelength, the tuning range obtained by varying the cavity length will be limited by the range over which the pump is sufficiently close to resonance for the OPO to remain above threshold. This will effectively be defined by the cavity linewidth at the pump frequency and will be much smaller than the range defined in (3-203) for the single-pass pump. Pump-enhanced OPOs are more commonly used with a pump source having some degree of tunability and the cavity servo-locked to keep the pump on resonance [69,84]. In this case, the change in pump wavelength will produce a shift the phase-matching centre as described by (3-199) and change in cavity length to maintain

pump resonance will produce a change in the resonant frequency which can be calculated from (3-204) to be:

$$\Delta\nu_i = \frac{\nu_{i,0}FSR_i}{\nu_{p,0}FSR_p}\Delta\nu_p \tag{3-205}$$

As with the simple SRO, a mode hop will occur if the phase-matching centre frequency moves more than half a FSR from the resonant parametric frequency. In this case, however, the resonant idler frequency is also changing. If it is assumed that the resonant idler frequency is initially coincident with the phase-matching centre frequency, the mode hop will clearly occur when the difference between the change in the phase-matching centre frequency and the change in the resonant frequency reaches half a FSR i.e. when:

$$\Delta\nu_{i,pm} - \Delta\nu_i = \pm\frac{FSR_i}{2} \tag{3-206}$$

From (3-205) and (3-199 b), this results in a maximum pump tuning range of:

$$\left|\Delta\nu_{p,\max}\right| = FSR_i\left(\frac{\left.\frac{\partial k_p}{\partial\nu_p}\right|_{\nu_{p,0}} - \left.\frac{\partial k_s}{\partial\nu_s}\right|_{\nu_{s,0}}}{\left.\frac{\partial k_i}{\partial\nu_i}\right|_{\nu_{i,0}} - \left.\frac{\partial k_s}{\partial\nu_s}\right|_{\nu_{s,0}}} - \frac{\nu_{i,0}FSR_i}{\nu_{p,0}FSR_p}\right)^{-1} \tag{3-207}$$

resulting in a maximum mode-hop-free idler tuning range from (3-205) of:

$$\left|\Delta\nu_{i,\max}\right| = FSR_i\left(\frac{\nu_{p,0}FSR_p}{\nu_{i,0}FSR_i}\frac{\left.\frac{\partial k_p}{\partial\nu_p}\right|_{\nu_{p,0}} - \left.\frac{\partial k_s}{\partial\nu_s}\right|_{\nu_{s,0}}}{\left.\frac{\partial k_i}{\partial\nu_i}\right|_{\nu_{i,0}} - \left.\frac{\partial k_s}{\partial\nu_s}\right|_{\nu_{s,0}}} - 1\right)^{-1} \tag{3-208}$$

Clearly, if the phase-matching centre frequency changes in the same direction as the resonant frequency, the pump-tuning range of the pump-enhanced SRO will be

greater than that of the simple SRO with a fixed cavity length, while if the frequency changes are in opposite directions the tuning range will be reduced. The fact that the cavity length of a pump-enhanced SRO is locked to the pump frequency can result in high frequency stability for the parametrically-generated waves, if a stable pump source is used [69].

3.4.3.2 Doubly-resonant OPOs.

In the case of doubly-resonant OPOs the restriction of simultaneous signal and idler resonance is added to the requirements of energy conservation and phase-matching which determine the spectral characteristics of the SRO. The requirement that the sum of the signal and idler frequencies must be equal to the pump frequency, while both being resonant modes of the cavity, can result in complex tuning behaviour and large fluctuations in output power [66,67,68,34]. This effect was observed in the first demonstration of a continuous-wave OPO [19] and the first comprehensive study was carried out by Smith [34]. It is commonly illustrated using a diagram such as that shown in Fig. 3-18 of the type first used by Giordmaine and Miller [24].

Cavity modes of the signal and idler are plotted on two scales which have a common point at the degeneracy frequency. The signal scale increases in frequency from left

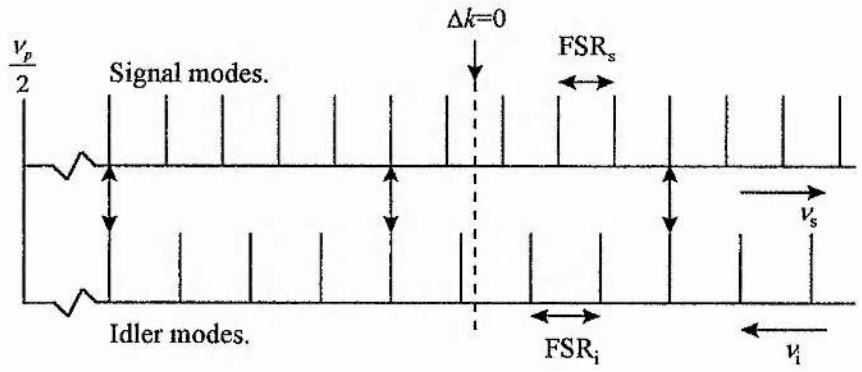

Fig. 3-18 Energy-conservation and double-resonance requirements in a DRO. Dashed line indicates point of optimum phase-matching. Vertical arrows indicate mode pairs satisfying energy conservation.

to right while the idler scale decreases in frequency at the same rate. Thus, any pair of points on the two scales which are in vertical alignment represent a pair of frequencies which conserve energy for the given pump frequency. Clearly any pair of cavity modes which are in vertical alignment represent satisfaction of both the double-resonance and energy-conservation requirements. The cavity modes of the signal and idler generally have different FSRs due to dispersion and thus only come into alignment at intervals a number of FSRs apart. The frequency interval over which this occurs is usually referred to as the cluster spacing. Changes in cavity length or pump frequency result in the two combs of modes moving across each other in opposite directions, causing new mode pairs to come into alignment indicating a change in the signal and idler frequencies.

Fig. 3-18 is a greatly simplified representation of the situation and there are a number of important additional considerations in practice. The number of FSRs between clusters is generally much larger than shown in Fig. 3-18 and the cavity modes have a finite width. This results in several mode pairs close to each cluster spacing having some degree of overlap, this being greatest at the cluster centre. Also, it is assumed in Fig. 3-18 that the FSRs of the signal and idler do not vary with frequency and as a result one cluster is indistinguishable from the next. In practice, there is generally a slight variation in FSR with frequency as a result of dispersion. This causes the point at which modes align to vary slightly from one cluster to the next and can result in a mode pair in one cluster exhibiting better overlap than the equivalent mode pair in adjacent clusters. Finally, the gain and loss factors will tend to vary with frequency. In particular, the magnitude of the phase-matching function will vary across the comb of modes. As shown in Fig. 3-18, the mode-pair closest to the phase-matching centre will always be the one on which the DRO operates. However, the above considerations can result in a mode pair further away from optimum phase matching having better overlap causing the DRO to operate here despite the larger phase-mismatch.

With the above considerations taken into account, the tuning behaviour of the DRO can be illustrated. When the cavity length or pump frequency change, resulting in the signal and idler modes moving across each other as described earlier, three possible

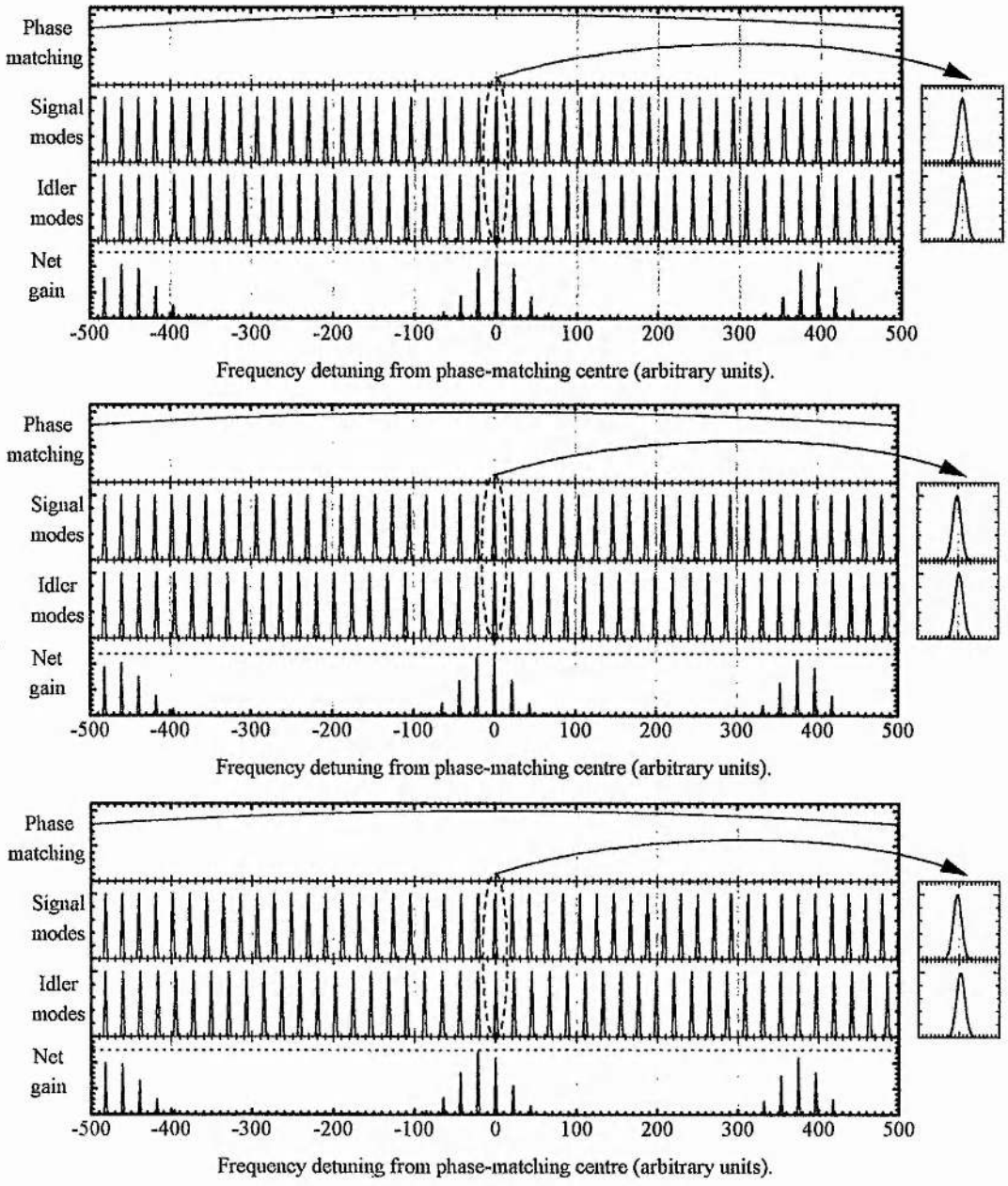

Fig. 3-19 Illustration of mode hopping in a doubly-resonant OPO. Net gain is determined by the product of the phase-matching, signal-mode and idler-mode functions. Detuning of initial signal and idler modes from phase-matching centre increases from top to bottom.

events can occur. Firstly, the pair of modes next to the current pair can move into alignment resulting in a change of one FSR in the signal and idler frequencies. This is a described as a mode hop and is illustrated in Fig. 3-19.

The phase-matching function and signal and idler mode functions are plotted against frequency. These three functions are then multiplied together to give a net-gain function which will be largest for the mode pair having the lowest threshold. Initially, in the top diagram, the pair of signal and idler modes lying at the phase-matching centre have the best overlap and the OPO thus operates on these two modes. The second diagram shows the situation after the two mode combs have shifted slightly due to a change in cavity length or pump frequency. It can be seen that the mode pair having the highest net gain in the previous diagram now has a similar net gain to the adjacent mode pair. As the detuning from the initial situation increases further, the net gain for the next mode pair becomes greater than that for the initial mode pair and the OPO will now hop to this new operating point causing the signal and idler frequencies to change by their respective free spectral ranges.

The second possible tuning event is illustrated in Fig. 3-20. Here the difference in the FSRs at the signal and idler is greater than in the case of Fig. 3-19, resulting in the cluster spacing being reduced and the clusters adjacent to the central one suffering a smaller reduction in net gain due to the increased phase-mismatch. Again, the initial upper diagram shows the two modes at the phase-matching centre having optimum overlap and thus defining the operating point of the DRO. In this case, however, as tuning occurs and the mode combs slide over each other, the next mode pair to attain the highest net gain is in a cluster adjacent to the central one. Further tuning results in the mode-pair adjacent to the original one coming into alignment and the OPO thus hops back to the central cluster, operating on the mode pair adjacent to the one on which it started. Clearly, in this situation the fluctuations in frequency at the signal and idler will be considerably larger than in the previous case of a simple in-cluster mode-hop. It can be seen from Fig. 3-19 and Fig. 3-20 that relatively small changes in cavity length or pump frequency can result in much larger changes in the DRO output frequencies.

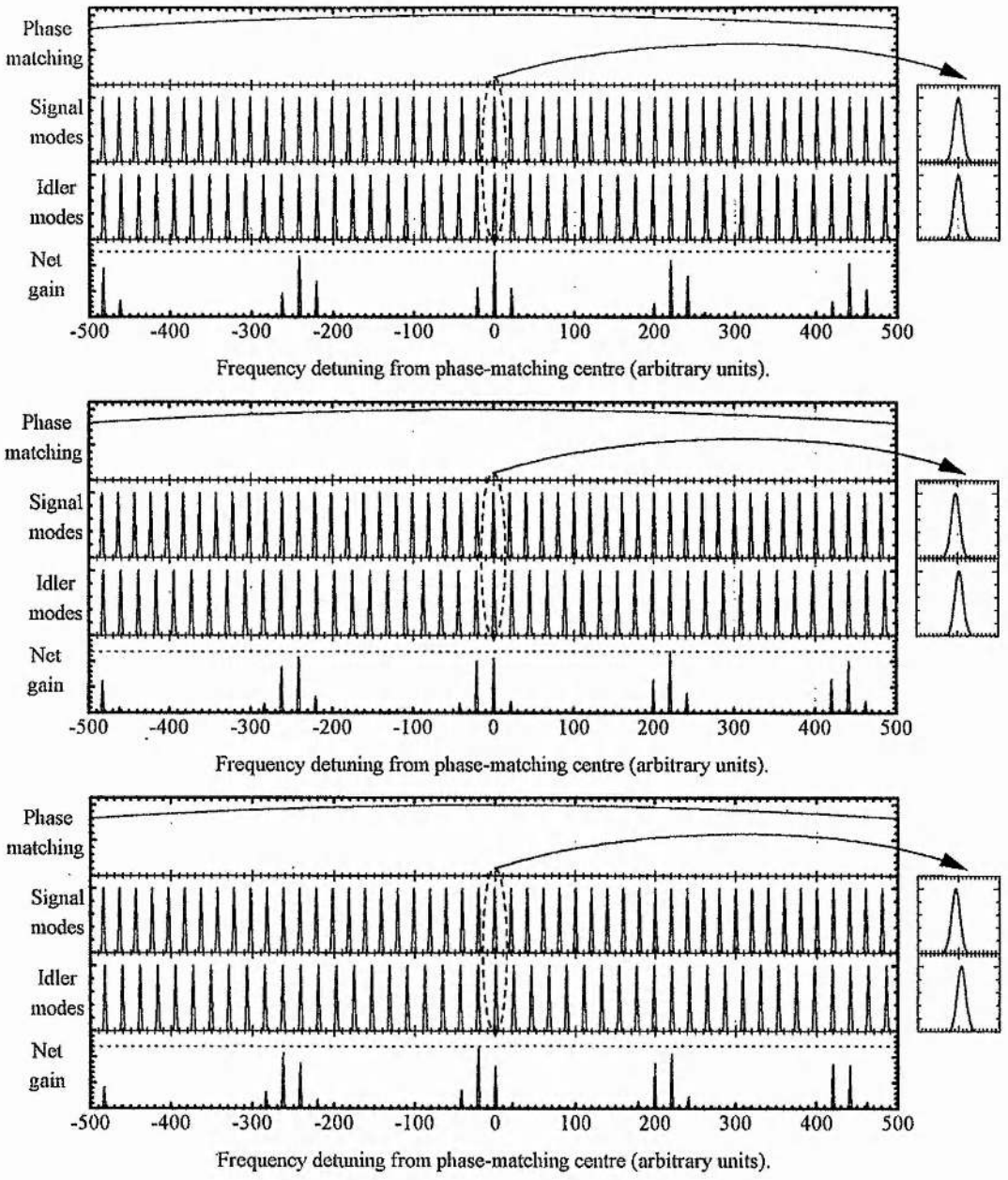

Fig. 3-20 Illustration of cluster hopping in a doubly-resonant OPO. Net gain is determined by the product of the phase-matching, signal-mode and idler-mode functions. Detuning of initial signal and idler modes from phase-matching centre increases from top to bottom.

The third situation, which can occur between mode or cluster hops, is where no mode pairs are sufficiently coincident for the DRO to reach threshold. In this case, the DRO ceases to operate until a mode pair come into sufficiently close alignment

for threshold to be attained. Clearly, this case will result in large fluctuations in output power as the DRO switches on and off. In fact, as the degree of phase-mismatch and losses will tend to vary with frequency, resulting in a threshold variation, the mode- and cluster-hopping processes described above will tend to result in fluctuations in output power in addition to the discontinuous fluctuations in frequency already mentioned. This high sensitivity of DROs to small fluctuations in pump frequency or effective cavity length, which can result in high levels of frequency and output-power instability, has in the past limited their utility for practical applications. However, it is often desirable to take advantage of the low threshold exhibited by doubly-resonant OPOs and as a result much effort has gone into modelling their stability requirements and tuning behaviour, and devising methods to control these parameters.

The tuning and stability behaviour of DROs has been investigated, theoretically and experimentally, by a number of workers [23,34,66,67,68,163]. The discussion here is mainly based on [68,163] and assumes that short-range dispersion effects are small compared to other parameters influencing the tuning behaviour, allowing the derivative term in the denominator of (3-198) to be ignored. This simplification is valid for most situations with the exception of a DRO operating close to degeneracy and having the same polarisation for signal and idler (i.e. type-I birefringent phase matching or most typical quasi-phase-matching geometries). In this case FSRs at the signal and idler are almost identical and the local dispersion is far more significant in determining the operating point. The analysis in this case is considerably more complex and has been considered in [66].

As mentioned earlier, the degree of overlap between signal and idler cavity modes is the most important factor in determining on which mode pair the DRO will operate. Two pairs of signal and idler modes are shown in Fig. 3-21, which is essentially an enlarged version of Fig. 3-19 and Fig. 3-20. The signal and idler free spectral ranges are FSR_s and FSR_i, respectively, and the cavity modes have full-widths at half-maximum of $\Delta\nu_{c,s}$ and $\Delta\nu_{c,i}$. These are related to the free spectral ranges and finesses by:

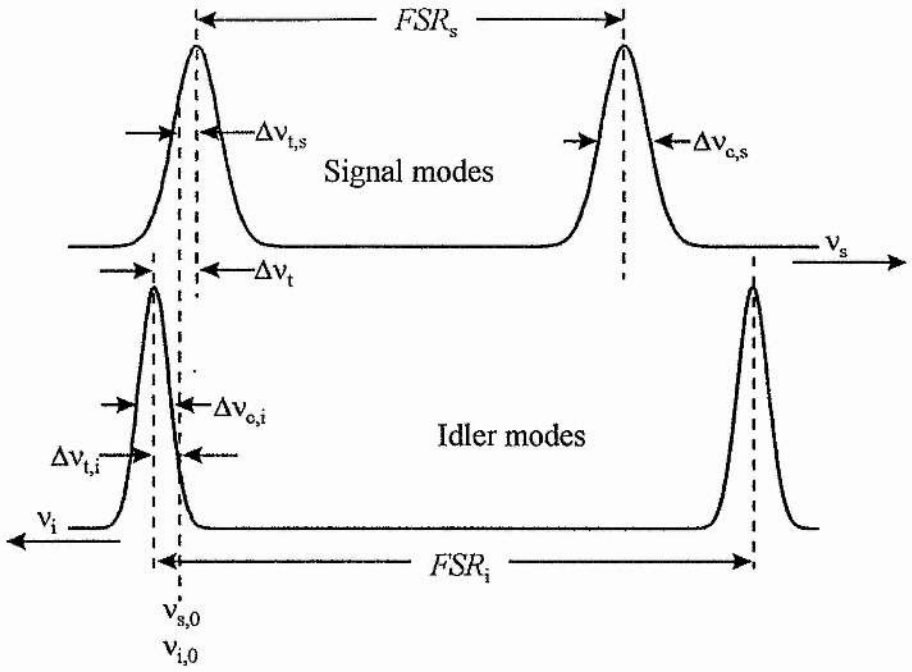

Fig. 3-21 Signal and idler cavity mode parameters used in the calculation of tuning and stability effects.

$$\Delta\nu_{c,j} = \frac{FSR_j}{\mathcal{F}_j} \qquad (j = s,i) \tag{3-209}$$

It is assumed that the two left-hand modes in Fig. 3-21 are initially in perfect coincidence, having frequencies $\nu_{s,0}$ and $\nu_{i,0}$, but have been detuned from these values by frequency shifts $\Delta\nu_{t,s}$ and $\Delta\nu_{t,i}$, giving an overall detuning factor $\Delta\nu_t$ of:

$$\Delta\nu_t = \Delta\nu_{t,s} + \Delta\nu_{t,i} \tag{3-210}$$

which is assumed to be much smaller than the free spectral ranges. Since the combined change in the signal and idler frequencies must be equal to any change in the pump frequency, if energy is to be conserved, $\Delta\nu_t$ can be defined in terms of any pump-frequency variation as:

$$\Delta\nu_t = \Delta\nu_p \tag{3-211}$$

It is also useful to define a parameter giving the difference in free spectral range between the signal and idler:

$$\Delta FSR = \left| FSR_s - FSR_i \right| \tag{3-212}$$

Modification of (3-204) to the case where both signal and idler are constrained to be cavity resonances gives an expression for the change in signal and idler frequencies with cavity length:

$$\begin{aligned} \Delta \nu_j &= -\frac{\nu_j}{n_i L + l} \Delta l \\ &= -\frac{2\nu_j FSR_j}{c} \Delta l \qquad (j = s,i) \end{aligned} \tag{3-213}$$

It can be seen from Fig. 3-21 that a detuning, $\Delta\nu_t$, equal to the difference in free spectral ranges, ΔFSR, will result in the operating point hopping to the next adjacent signal-idler mode pair. From (3-210) and (3-213), the change in length for this to occur can be seen to be given by:

$$\Delta l_{hop} = \frac{c}{2\nu_p} \frac{\Delta FSR}{FSR_{av}} \tag{3-214}$$

where the use of an average free spectral range given by:

$$FSR_{av} = \frac{FSR_s + FSR_i}{2} \tag{3-215}$$

is valid if the difference between the free spectral ranges is small compared to the free spectral ranges themselves. Similarly, since the total frequency change must be equal to any frequency change in the pump, the change in pump frequency to cause a mode hop-is given by:

$$\Delta \nu_{p,hop} = \Delta FSR \tag{3-216}$$

In addition to the mode-hopping behaviour, it is important to determine the maximum detuning that the OPO can tolerate while remaining above threshold. If this maximum detuning is denoted as the stability range and defined as that over which the overlap point between the signal and idler modes is within the full-width at half-maximum of both, then the total frequency change, $\Delta\nu_t$, defining this range is seen to be given by:

$$\begin{aligned}\Delta\nu_{t,stab} &= \pm\frac{1}{2}\left(\Delta\nu_{c,s}+\Delta\nu_{c,i}\right)\\ &= \frac{FSR_s}{2\mathcal{F}_s}+\frac{FSR_i}{2\mathcal{F}_i}\end{aligned} \tag{3-217}$$

From (3-137), (3-138) and (3-152), (3-210) can be rewritten:

$$\Delta\nu_t = \Delta\frac{FSR_s\mathcal{F}_i+FSR_i\mathcal{F}_s}{2\mathcal{F}_s\mathcal{F}_i} \tag{3-218}$$

allowing the threshold expression for a single-pass-pump DRO, (3-162), to be rewritten:

$$\left|\alpha_p^{in}\right|^2_{th} = \frac{\pi^2}{4\kappa^2L^2\mathcal{F}_s\mathcal{F}_i}\frac{1}{\operatorname{sinc}^2\left(\frac{\Delta kL}{2}\right)}\left[1+\left(\frac{2\Delta\nu_t\mathcal{F}_s\mathcal{F}_i}{FSR_s\mathcal{F}_i+FSR_i\mathcal{F}_s}\right)^2\right] \tag{3-219}$$

It can thus be seen that a detuning of $\Delta\nu=\Delta\nu_{t,stab}$ results in a doubling of the threshold and the limits of the stability range are defined as the points where the threshold reaches twice its minimum value.

Considering first the effects of cavity-length variation, (3-213) and (3-217) give:

$$\Delta l_{stab} = \pm\frac{c}{4\nu_p}\left(\frac{1}{\mathcal{F}_s}+\frac{1}{\mathcal{F}_i}\right) \tag{3-220}$$

where (3-215) has again been used. In terms of pump frequency variation, (3-210), (3-211) and (3-217) give:

$$\Delta\nu_{p,stab} = \pm\frac{FSR_{av}}{2}\left(\frac{1}{\mathcal{F}_s}+\frac{1}{\mathcal{F}_i}\right) \tag{3-221}$$

When considering tuning ranges, it can be seen that (3-220) and (3-221) result in far smaller variations in pump frequency or cavity length, with the other parameter fixed, than those for the SRO. However, from (3-210) and (3-211) it can be seen that the pump frequency can be changed to match the change in signal and idler frequency and maintain the double-resonance condition. The required pump frequency change can be seen, from (3-213), to be:

$$\Delta\nu_p = -\Delta l\left(\frac{2\nu_p FSR_{av}}{c}\right) \tag{3-222}$$

where, again, (3-215) has been used. This technique has been utilised to obtain large continuous tuning ranges from DROs [164]. It is also possible to obtain continuous tuning from a DRO with a fixed-frequency pump source, but in this case a split-cavity design must be used allowing independent control of the signal and idler free spectral ranges [165].

It is interesting to note that because both signal and idler are constrained to be modes of the cavity, neither is free to maintain energy conservation by changing its frequency to compensating for changes in the other. As a result, if the pump frequency is fixed, the signal and idler frequencies can only change by undergoing a mode hop as described above. For small changes in the cavity length that are less than Δl_{stab}, as defined above, the DRO will produce outputs at signal and idler frequencies which remain fixed to the first order. Only the threshold, and therefore the output power, will vary as the overlap between the signal and idler cavity modes changes with cavity length. Thus, the DRO adopts the frequency-stability characteristics of the pump source and has output frequencies which are relatively insensitive to small changes in cavity length. This is in contrast to the case of the SRO where changes in cavity length translate directly to changes in the output

frequencies. In a similar way, the linewidths of the DRO outputs are restricted to that of the pump, whereas in the SRO they are determined by the linewidth of the cavity at the resonant wavelength. The double-resonance condition can also be used to provide a high degree of frequency selectivity, enabling the DRO to be restricted to a single signal-idler mode pair relatively easily. This fact, in conjunction with those described above, has been used to implement a stable, spectrally-pure source which can be continuously tuned over large frequency ranges [95] and despite their complex tuning behaviour it has been shown that, with careful control of pump frequency and cavity length, DROs can exhibit high degrees of long-term spectral stability and single-mode tuning [71,72,166].

It must be remembered that the expressions for mode-hop and stability ranges derived above only apply within one (usually the central) cluster. As the effects of dispersion over the frequency ranges between clusters have not been taken into account, these expressions do not make any predictions about cluster-hopping behaviour. Clearly, in the analysis used above if the stability detunings, $\Delta\nu_{stab}$ and Δl_{stab}, are similar to or greater than those for a mode-hop, $\Delta\nu_{hop}$ and Δl_{hop}, then the DRO would be expected to remain above threshold as the cavity length or pump frequency changed, simply changing its output frequency. On the other hand, if $\Delta\nu_{stab}$ and Δl_{stab} are significantly smaller than $\Delta\nu_{hop}$ and Δl_{hop} then the DRO would be expected to switch on and off as the pump frequency or cavity length varies, producing a series of discrete output intervals, each operating on the next consecutive signal-idler mode pair.

However, the possibility exists in both cases that between moving from one mode pair to the next within the central cluster, whether this occurs continuously or with a below-threshold region in between, a pair of modes in another cluster will achieve better overlap than any in the central cluster and have a lower threshold as a result. In this case the DRO will cluster hop and operate within this new cluster, or indeed others, until the lowest threshold is again achieved by a mode pair in the original cluster.

Predictions about this type of behaviour are more easily made using a numerical modelling technique [167]. Clearly, the second and third terms of (3-219)

representing the phase-mismatch and cavity-resonance detuning, respectively, are both affected by changes in the signal and idler frequencies induced by cavity-length or pump-frequency changes and thus such changes can influence the threshold. These terms can be used to calculate the pump-power thresholds for all the lowest-threshold modes close to the point of optimum phase matching as a function of a detuning parameter such as cavity length or pump frequency. Thus, for any degree of detuning, the mode pair having the lowest threshold, and therefore on which the DRO will operate, can be readily identified as can the change in the tuning parameters necessary to move to another mode pair.

The parameters of an experimentally demonstrated DRO can be used as the basis for calculations with this modelling technique to illustrate some important aspects of DRO behaviour. The DRO under consideration [168] was based on the nonlinear optical material lithium triborate (LBO) and used type-I birefringent phase matching close to frequency degeneracy, resulting in very similar FSRs for the signal and idler. To illustrate the effect the FSR difference we shall also consider an otherwise identical system but utilising type-II phase-matching close to degeneracy and thus having a significant difference in the free spectral ranges.

The parameters used for modelling the two systems are summarised in Table 3-3. The crystal temperatures of 178°C and 20°C correspond to non-critical phase matching in the type-I and type-II cases, respectively. The principal dielectric axes along which the waves are polarised in these two cases are, for the $p \rightarrow s+i$ interaction, $y \rightarrow z+z$ and $y \rightarrow x+y$, respectively. This results in the refractive index values given in Table 3-3, which are calculated from room-temperature Sellmeier equations [169] with temperature dependence included by the extrapolation of observed temperature dependencies below 100°C [170]. In addition to the nominal cavity length, two cavity length adjustments are used for each phase-matching geometry. These are added to the nominal cavity length to give an actual unperturbed cavity length around which the cavity length is varied in the modelling. These adjustments are necessary to allow the exact position of mode-pair clusters to be controlled relative to the phase-matching bandwidth. The round-trip power losses at the signal and idler are assumed to be approximately 1.2% in both cases, resulting in

	Type-I	Type-II
Pump wavelength	0.5145 μm	0.5145 μm
Signal wavelength	0.9250 μm	0.947 μm
Idler wavelength	1.1594 μm	1.1265 μm
Crystal temperature	178 °C	20 °C
Pump refractive index, n_p	1.6053	1.5797
Signal refractive index, n_s (Δk=0)	1.6074	1.5924
Idler refractive index, n_i (Δk=0)	1.6028	1.5646
Nominal cavity length (L+l)	33 mm	33 mm
Crystal length (L)	20 mm	20 mm
Cavity length adjustments (Δl)	-180 nm, -310 nm	-70 nm, -150 nm
Cavity finesse at signal/idler	≈520	≈520
FSR_s (Δk=0)	3.3202 GHz	3.3424 GHz
FSR_i (Δk=0)	3.3270 GHz	3.3843 GHz
$\frac{FSR_i}{FSR_s}$ (Δk=0)	1.002	1.013

Table 3-3 Summary of parameters used in modelling mode-selection behaviour of LBO DROs.

cavity finesses of 520. The simple free spectral ranges (i.e. ignoring dispersion) calculated at the centre of the phase-matching bandwidth, can be seen to have a considerably larger difference for the type-II case than the type-I.

The results of the modelling in the type-I case are shown in Fig. 3-22 for two different cavity length adjustments from the nominal length. In the upper diagram, a length adjustment of -180nm results in two clusters of signal-idler mode pairs lying either side of the phase-matching centre frequency. As the cavity length is varied the individual mode-pair which is in best alignment changes, resulting in the DRO hopping between clusters. Similar behaviour is obtained from the equivalent change in pump frequency (calculated from (3-222)) for a fixed cavity length. As the mode clusters are approximately equally spaced around the phase-matching centre, the thresholds for modes in both clusters are approximately the same, resulting in little change in threshold as the cavity length is varied.

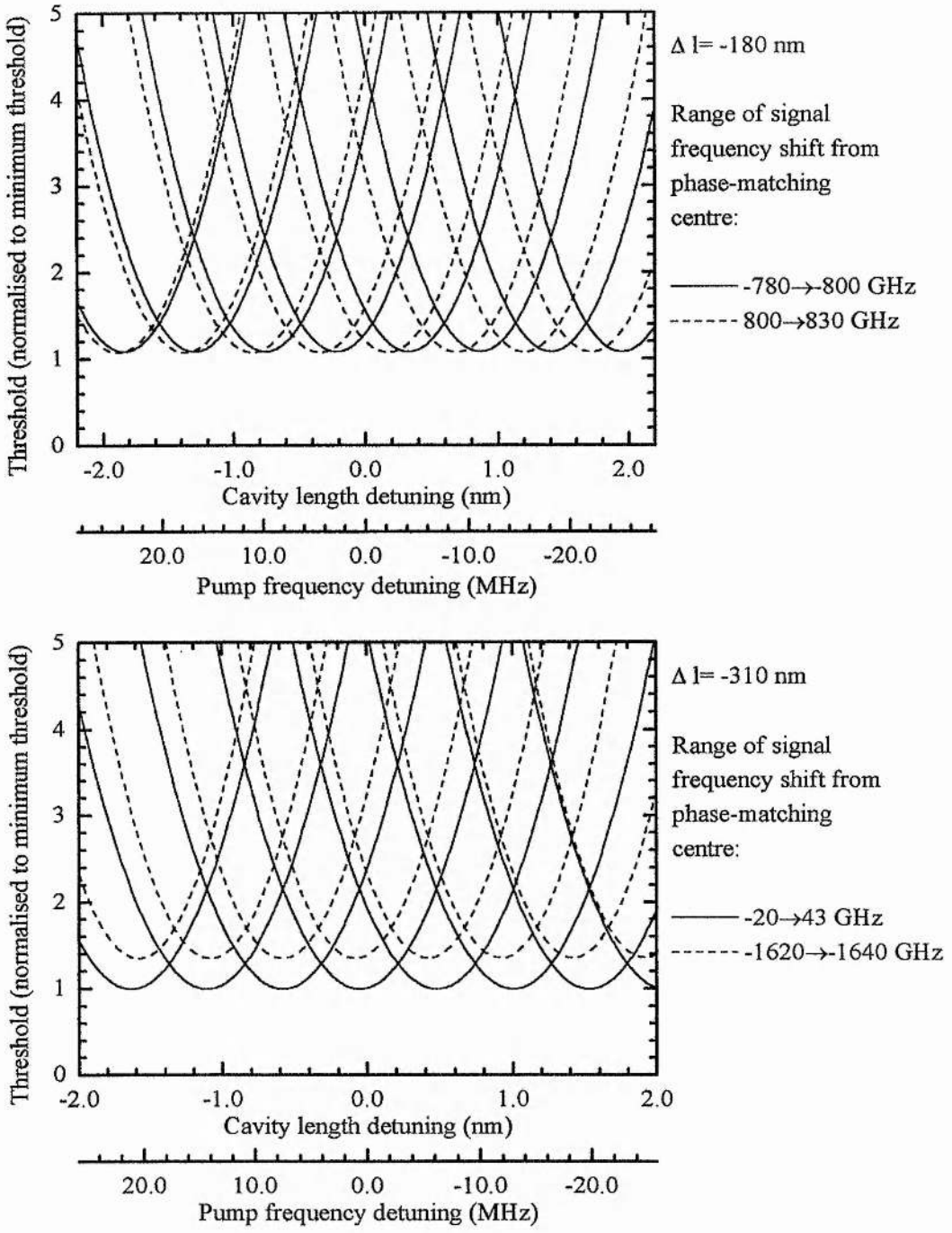

Fig. 3-22 Calculated results of variation of lowest mode-pair thresholds with cavity-length and pump-frequency detuning for type-I phase-matching in LBO. Upper graph is calculated for a cavity length adjustment of -180nm from the nominal length, lower graph is for an adjustment of -310nm.

It can be seen from the magnitudes of the frequency shifts that such a mode-hop will result in a change in signal frequency of around 1.6 THz.

The lower diagram shows the results obtained for a cavity length adjustment of -310nm. In this case, one of the clusters lies exactly at the phase-matching centre causing the DRO to hop between adjacent mode pairs in this cluster as the cavity length or pump frequency is varied. The next adjacent cluster is at too large a frequency shift from the phase-matching centre to have a lower threshold than the central cluster and thus the DRO never operates on these mode pairs.

The equivalent results for the type-II case are shown in Fig. 3-23. It is immediately apparent that the cavity-length and pump-frequency changes required to cause the DRO to mode hop are much larger than in the type-I case. It can also be seen from the frequency-shift values that the cluster spacing is much smaller. These two results are due to the larger difference in the free spectral ranges of the signal and idler, as pointed out in the qualitative discussion of mode- and cluster-hopping earlier. As a result, there is a much larger modulation of the threshold (and therefore of the output power), causing the indivdual mode-pair coincidences to be better defined as the cavity length varies, than in the type-I case. Indeed, if the OPO were pumped less than around 9 times above the minimum threshold, it would switch off between mode-pair coincidences.

In the upper diagram, a cavity length adjustment of -70 nm from the nominal length results in a pair of clusters falling either side of the optimum-phase-match point in frequency, with one cluster being slightly closer to optimum phase match than the other. It can be seen that, again, this allows the DRO to cluster hop as the cavity length or pump frequency is varied. With the length adjustment set to -150 nm, it can be seen in the lower diagram that the mode coincidences of the secondary cluster only occur where a pair of modes in the central cluster are also in coincidence. Thus, the DRO only operates on the central cluster and simply hops between adjacent mode pairs as the cavity length or pump frequency are varied.

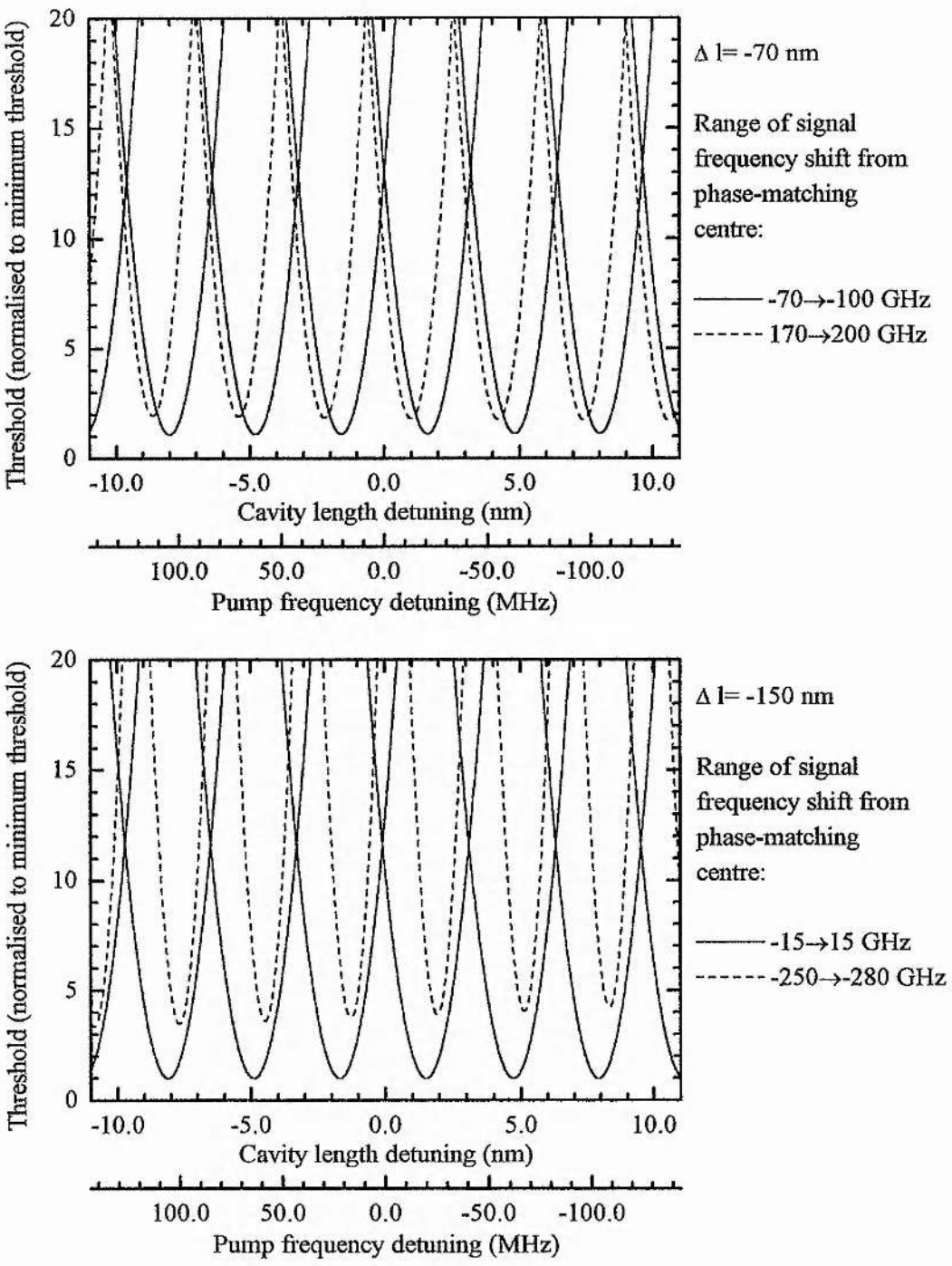

Fig. 3-23 Calculated results of variation of lowest mode-pair thresholds with cavity-length and pump-frequency detuning for type-II phase-matching in LBO. Upper graph is calculated for a cavity length adjustment of -70 nm from the nominal length, lower graph is for an adjustment of -150 nm.

When comparing the tuning behaviour of the type-I and type-II phase-matched DROs close to degeneracy, it is clear from the above modelling that the type-II device will be more tolerant to perturbations in cavity length and pump frequency without mode hopping. The type-II system also has the advantage that the mode-pair coincidences are well separated as the cavity length or pump frequency are varied which will result in a series of well-defined output maxima. This is of particular importance in the case of certain servo-locking techniques used to maintain single mode-pair operation by adjusting the cavity length to compensate for changes in pump frequency, especially those using a side-of-fringe technique [68,164]. However, servo stabilisation of a type-I DRO has been demonstrated through the use of more sophisticated FM locking techniques and/or high finesse cavities [65,71,72].

Obviously, the problems associated with type-I phase matching will be less serious well away from degeneracy, where material dispersion will result in a larger difference in free spectral ranges. It is interesting to note that quasi-phase-matched materials, in which all three waves have the same polarisation, will exhibit the same behaviour as type-I birefringent materials in this context and this may limit the extent to which they can form the basis of stabilised DROs operating close to degeneracy.

3.5 Nonlinear optics with focused Gaussian beams.

The effects of focusing in an OPO were discussed earlier and it was assumed that the optimum beam waist was that which resulted in a confocal parameter equal to the crystal length. The spatial coupling factor in this case was defined in (3-146) and a similar result could be obtained for second-harmonic generation. This conclusion arises as a result of our assumption throughout this chapter that the interacting beams maintain essentially constant dimensions in the nonlinear crystal and diffraction can be ignored. Clearly, in practice, this will not strictly be the case if beams are focused into the crystal. The effects of diffraction on nonlinear optical interactions with focused Gaussian beams have been treated theoretically [10,171,172] and investigated experimentally [173]. The results derived in [10], which include the

effects of both focussing and Poynting-vector walkoff, are widely made use of and are summarised, without proof, here.

Two new parameters are defined to include the effects of focusing and walk off in the focused case. A focusing parameter is defined as the ratio of the crystal length to the confocal parameter of the beam:

$$\xi = \frac{L}{b_0} = \frac{\lambda_0 L}{2\pi n_0 w_0^2} \tag{3-223}$$

where w_0 is the beam waist radius in the crystal. The parameters w_0, λ_0, n_0 are the values at degeneracy and ξ is assumed to be the same for all the interacting waves. This approximation is valid in the case SHG and DROs with optimal mode matching of the pump beam according to (3-49). The walk-off parameter is defined as:

$$B = \frac{1}{2}\rho\left(Lk_0\right)^{\frac{1}{2}} \tag{3-224}$$

where ρ is the walk-off angle in radians, as defined in (3-93), and k_0 is measured in the material. The expression for generated second-harmonic power in the case of an undepleted pump and optimum phase matching is given by [10,22]:

$$\frac{P_{2\omega}}{P_\omega} = \frac{2d_{eff}^2\omega^2}{n_\omega^2 n_{2\omega} c^3 \varepsilon_0 \pi} P_\omega L k_\omega h_m(B,\xi) \tag{3-225}$$

where the function $h_m(B,\xi)$ is a reduction factor due to focusing and walk-off effects. It can be seen that, apart from the addition of this reduction factor, (3-225) is identical to (3-70) in the case of confocal focusing.

The reduction function, $h_m(B,\xi)$, must be evaluated numerically and is plotted, for a range of walk-off parameters, in Fig. 3-24. It can be seen that in the case of zero walk off the optimum ratio of the crystal length to the confocal parameter is 2.84. While this is nearly three times the value in the confocal case (ξ=1), it can be seen that $h_m(B,\xi)$ varies quite slowly with ξ around the optimum value and the second-harmonic power obtained for optimal focusing in this case is around 1.2 times that

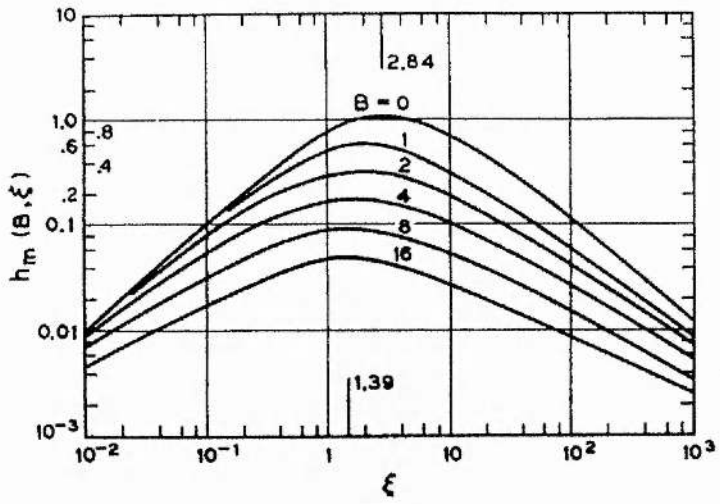

Fig. 3-24 Reduction factor for second-harmonic generation with focused Gaussian beams plotted as a function of focusing parameter ξ with for various values of walk-off parameter B [10]. Vertical lines at ξ=1.39 and ξ=2.84 indicate optimum values of ξ for values of B of 0 and 16 respectively.

predicted for confocal focusing by this analysis. The optimum value of the focusing parameter to maximise the conversion efficiency, ξ_m, is plotted as a function of walk-off parameter B in Fig. 3-25.

In the case of the doubly-resonant OPO with perfect phase-matching the equivalent expression to (3-165), giving the threshold pump power for focused Gaussian beams, is [10,22,23]:

$$P_{p,th} = \frac{4\gamma_s'\gamma_i'\pi\, c^4 \varepsilon_0 n_0^2}{d_{eff}^2 \omega_p^3 L\left(1-\delta^2\right)^2} \frac{1}{\overline{h}_m(B,\xi)} \tag{3-226}$$

where the function $\overline{h}_m(B,\xi)$ is equivalent to $h_m(B,\xi)$ in the case of SHG and is shown as a function of ξ for various walk-off parameters in Fig. 3-26. It can be seen that the results obtained are identical to those for second-harmonic generation in the case of zero walk off. For larger walk-off parameters, however, the reduction factor becomes increasingly insensitive to the degree of focusing.

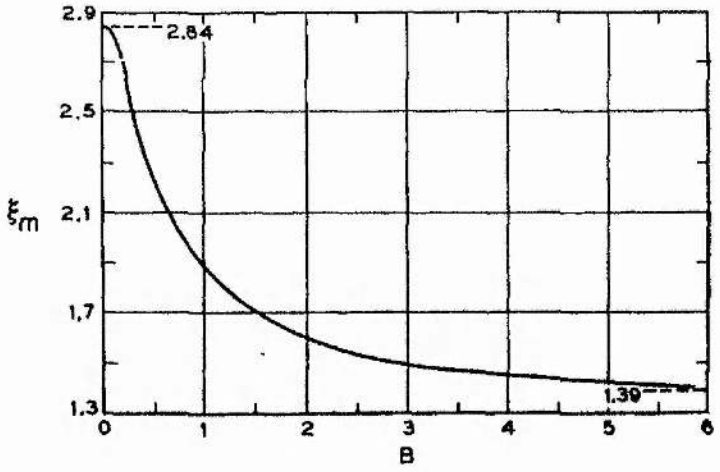

Fig. 3-25 Value of focusing parameter required to maximise second harmonic generation efficiency, ξ_m, plotted as a function of walk-off parameter, B [10].

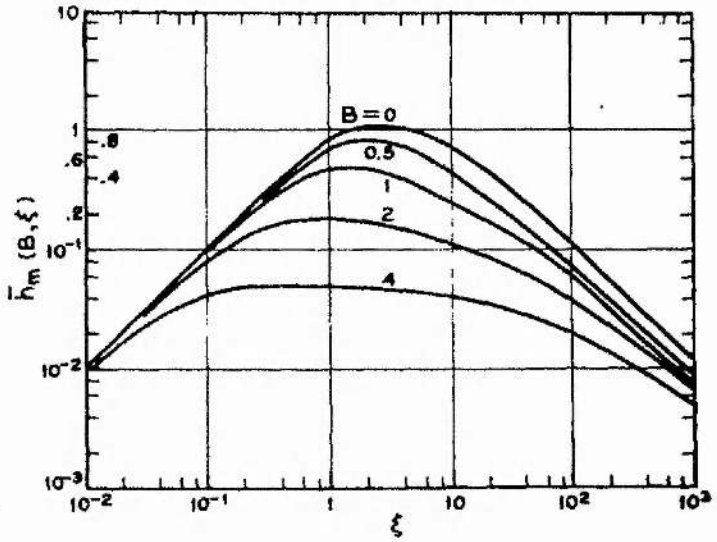

Fig. 3-26 Reduction factor for parametric oscillator threshold with focused Gaussian beams plotted as a function of focusing parameter ξ with for various values of walk-off parameter B [10].

The maximum value of the reduction factors for SHG and DRO threshold, h_{mm} and $\bar{h}_{mm}$, obtained when the focusing parameter is optimised, are plotted against the walk-off parameter, B, in Fig. 3-27. In the case of DRO threshold the value of the optimised reduction factor is approximated by the expression [10]:

$$\bar{h}_{mm}(B) = \frac{\bar{h}_{mm}(0)}{1+\left(\frac{4B^2}{\pi}\right)\bar{h}_{mm}(0)} \tag{3-227}$$

As already mentioned, the results obtained in [10] for OPO threshold are calculated for a DRO. Further, it is assumed that the signal and idler have identical confocal parameters and that the beam waist is at the centre of the crystal, i.e. a symmetric resonator design is used. In the case of a singly-resonant OPO, one of the resonant waves is unrestricted by the resonator geometry and the first of these assumptions is no longer valid. This case has been treated by Asby [171] and by Guha et al. [172], although there is some disagreement between the results with the optimum ratio of

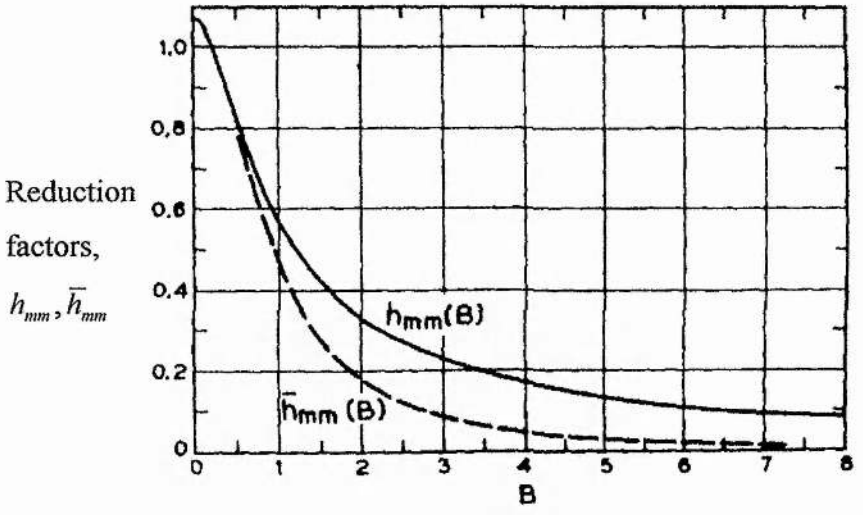

Fig. 3-27 Values of maximised reduction factors, h_{mm} and $\bar{h}_{mm}$, as functions of walk-off parameter B. The reduction factor for DRO threshold, $\bar{h}_{mm}(B)$, can be approximated by (3-227) [10].

the confocal parameters of the pump and the resonant wave being unity in the case of [171] while this is not found to be the case in [172]. The case of a DRO with unequal confocal parameters is also treated in [172], while that of a DRO employing a non-symmetric resonator has also been investigated [174,175].

3.6 Pump source requirements.

From the preceding discussion of OPO behaviour, it is now possible to determine the requirements, in terms of output power and spectral characteristics, placed on a laser if it is to be used an OPO pump source. In particular the suitability of laser diodes as pump sources can be assessed. Addressing the required power first, the common parameters given in Table 3-4 were used to calculate the minimum threshold pump powers, in the case of confocal focusing, for the principal OPO configurations. The results are shown in Fig. 3-28 as a function of effective nonlinear coefficient. The loss values used are in the range typically encountered in experimental cw OPOs, the finesses representing round-trip power losses of approximately 2.0%. For the pump-enhanced SRO and TRO cases, the enhancement factor of 30 represents the maximum enhancement attainable with parasitic losses of 3% at the pump [154]. While this is a higher loss level than could probably be attained in practice, the

Pump wavelength, λ_p.	0.8 μm
Degeneracy factor, δ.	≈ 0
Pump refractive index, n_p.	1.7
Crystal length, L.	20 mm
Cavity finesses, $\mathcal{F}_s$, $\mathcal{F}_i$.	300
Pump enhancement factor E_p	30

Table 3-4 Common OPO parameters used to calculate minimum thresholds for various OPO configurations in Fig. 3-28.

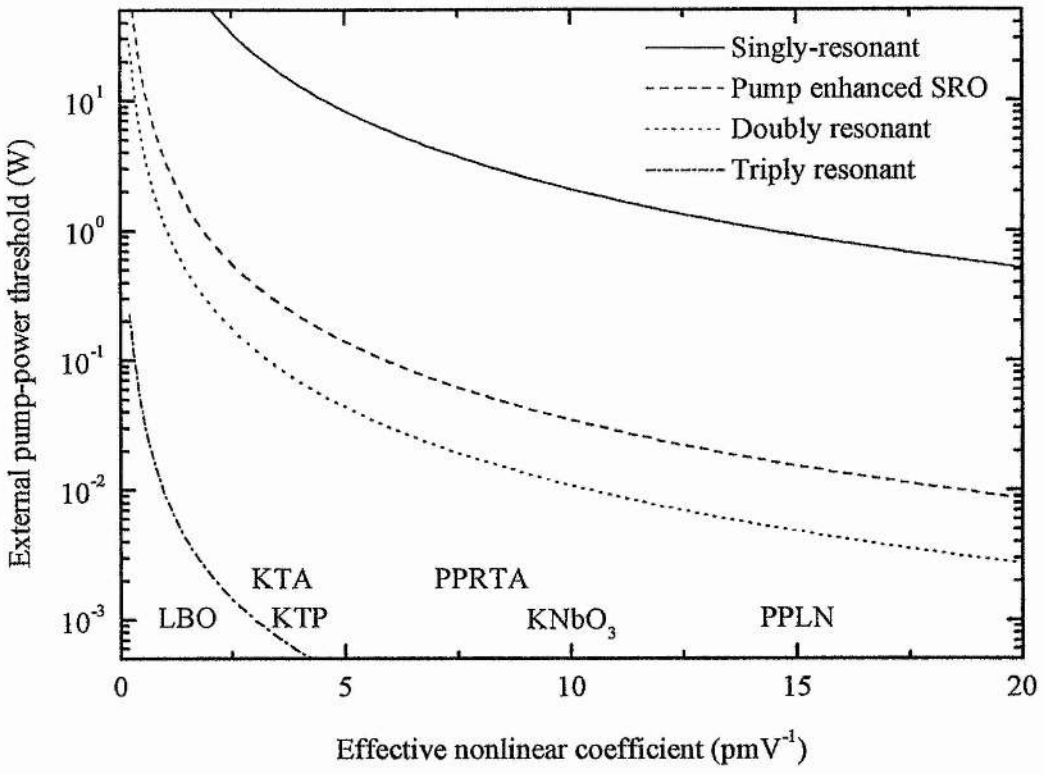

Fig. 3-28 Minimum threshold, in the case of confocal focusing, for four OPO configurations, calculated using the values given in Table 3-4. Approximate effective nonlinear coefficients obtained with various materials are indicated along the x-axis.

reduced enhancement factor also allows for imperfect impedence matching and is consistent with experimentally reported values [69].

The approximate values of the effective nonlinear coefficients, from figures consistent with experimental OPO results, are indicated along the x-axis for the materials lithium triborate (LBO, ≈1.5 pmV^{-1}) [161], potassium titanyl arsenate (KTA, ≈3.6 pmV^{-1}) [79],potassium titanyl phosphate (KTP, ≈4 pmV^{-1}) [84], potassium niobate ($KNbO_3$, ≈10 pmV^{-1}) [176], periodically-poled rubidium titanyl arsenate (PPRTA, ≈8 pmV^{-1}) [80], and periodically-poled lithium niobate (PPLN, ≈15 pmV^{-1}) [88].

When considering the data shown in Fig. 3-28, it should be born in mind that this represents the absolute minimum threshold attainable for the specified parameters and that, in practice, the actual threshold will be higher. In particular, the spatial coupling between the fields is unlikely to be perfect as is assumed in the confocal case. It is also desirable to pump the OPO several times above threshold. With these provisos in mind, it is clear that for the majority of birefringently phase-matched materials the threshold pump powers required for a singly-resonant OPO are outside the range of conventional diode-laser systems. Even with PPLN, the minimum threshold is of the order of several hundred milliwatts. A diode-pumped PPLN-based SRO has been demonstrated, with a threshold of 800 mW, using a diode tapered-amplifier pump source [89]. However, for the majority of diode-laser-based pump sources a lower threshold is required.

With pump enhancement, the external threshold of the SRO is considerably reduced. Thresholds of the order of 100mW are predicted for birefringently phase-matched materials and diode-pumped systems of this type have been demonstrated in KTP [84] and single-domain RTA [86] with thresholds in the range of 100 to 200 mW. In the case of PPLN, thresholds of a few milliwatts are predicted. A practical PPLN-based pump-enhanced SRO pumped by a Nd:YAG laser at 1064nm has been demonstrated with a threshold of 260mW [69] which scales to around 100mW at the 800nm pump wavelength considered here. Thresholds much lower than this would also appear to be possible [177].

In the case of doubly-resonant OPOs the thresholds are lower still as the enhancement factor obtained by resonating the other parametrically generated wave is, from the parameters given in Table 3-4, higher than that obtained by resonating the pump. This realistically represents practical situations, as it is generally easier to achieve a high cavity finesse for a field that does not have to be impedence-matched from an external source. The predicted thresholds in the case of birefringently phase-matched materials, of the order of 100mW, have been observed experimentally for diode-pumped systems [84]. In the case of PPLN, the predicted values of a few milliwatts have also been reflected in experimental diode-pumped systems where thresholds of around 15mW have been obtained [88]. The very low thresholds .

predicted for triply-resonant OPOs have also been seen in experimental diode-pumped systems where thresholds as low as 6mW have been observed [84].

As mentioned above, the threshold values predicted in Fig. 3-28 assume confocal focusing, and therefore optimum overlap, for all three waves. This leads to the next important criterion for a potential pump source: the spatial quality of the beam. From (3-223), it can be seen that the confocal parameter for a non-diffraction-limited beam, having a beam-quality factor M^2, is given by:

$$b = \frac{2\pi n w_0^2}{M^2 \lambda} \tag{3-228}$$

Thus, any increase in M^2 will proportionally reduce the confocal parameter, effectively limiting the interaction length for the given beam waist w_0 and thus increasing the threshold. To maintain confocal focusing w_0 can be increased. However, it can be seen from the expressions derived in section 3.4.1 that this will also result in an increased threshold. It should also be born in mind that the reduction in confocal parameter for a given beam waist implies an increased divergence of the beam. This will cause a reduction in the efficiency of the parametric interaction due to the angular acceptance bandwidth, as defined by (3-123) to (3-125), and therefore also results in an increased threshold. The degree to which this occurs will depend on the exact phase-matching geometry. Thus, as in the case of end-pumped solid-state lasers, it is desirable to have a pump source as close to diffraction limited as possible.

Given that the discussion of threshold pump powers above implies that, for diode-laser pumping, a pump-enhanced, doubly resonant or triply-resonant OPO must be used in most cases, it is clear that the pump source must have a high degree of spectral purity. In the case of the pump-enhanced SRO, the requirement that the pump frequency must correspond to a resonant mode of the cavity implies a single-mode source, preferably with a linewidth less than that of the cavity at the pump frequency. To maintain resonance, a servo system is generally used to lock the cavity length to the pump frequency, so pump instability will not generally result in significant increases in threshold. However, unless a split cavity is used, the resultant

changes in cavity length will translate any pump instability to the resonant parametric wave and therefore to the output. Thus, a high degree of pump-frequency stability is also desirable.

For the DRO, the discussion of section 3.4.3.2 clearly implies a single-mode, highly-stable pump source both to prevent the extreme frequency changes associated with mode and cluster hopping and also to minimise fluctuations in the output power. It can be seen from Fig. 3-22 and Fig. 3-23 that the degree of frequency stability required will depend on the particular parameters of the OPO, but it will clearly be less than a few tens of MHz, in some cases significantly so. The TRO will clearly have requirements on frequency stability as stringent as both the pump-enhanced SRO and the DRO.

Although this section has concentrated exclusively on the pump-source requirements of OPOs, most of the same criteria will apply in the case of second-harmonic generation or, indeed, most other nonlinear frequency-conversion processes. Clearly, SHG has no threshold requirement, however, to obtain high levels of efficiency high fundamental powers are desireable. In fact, in the case of continuous-wave diode sources, the powers required for efficient SHG usually imply the use of an enhancement cavity [51] in which case single-mode frequency requirements similar to the pump-enhanced SRO apply. Obviously the same arguments with regard to spatial quality apply to SHG as they do to OPOs.

3.7 Conclusions.

In this chapter it has been shown that nonlinear optical frequency conversion processes, by frequency-mixing or optical parametric oscillation, are flexible and useful methods for extending the spectral coverage of lasers. In the case of laser diodes, such conversion processes can be used to obtain a source with many of the attributes of diode lasers, such as efficiency, tunability, compact size and relatively low cost, at wavelengths not normally accessible to these lasers. However, the requirements placed on pump sources for nonlinear frequency conversion in terms of necessary output power, beam quality and spectral purity and stability are in many

cases very demanding and not necessarily within the performance limitations of conventional, commercially available laser diodes.

In the case of OPOs, it can be seen from Fig. 3-28, and the associated discussion, that three of the OPO configurations have power requirements that are within the range of conventional laser diodes: the pump-enhanced SRO, the DRO and the TRO. Of these, the TRO has a threshold easily within the reach of diode pumping using materials having all but the lowest effective nonlinear coefficients. With this in mind, it seems unlikely that the reduction in threshold obtained by using such a device would outweigh the disadvantages associated with trying to resonate three wavelengths simultaneously, unless the particular circumstances demanded it. Of the two remaining configurations, the DRO is the simplest, requiring a pair of identical mirrors, and will generally have the lower threshold. Against this must be weighed the complex tuning behaviour and stringent stability requirements to maintain a continuous output.

The pump-enhanced SRO, on the other hand, is less demanding of pump-frequency stability if the cavity can be servo-locked to the pump, in which case it should be relatively easy to maintain reasonable stability in the output power. As mentioned, however, the threshold is generally likely to be higher than the DRO and two different mirror coatings are required: one coated for high reflection at the pump and the other for input coupling to the resonant cavity. The transmission properties of this second mirror must be chosen with careful regard to the other losses in the cavity if optimal enhancement is to be obtained [154]: Generally, the higher the degree of enhancement required, the more difficult it will be to accurately match the level of input coupling to the parasitic losses. It can be seen that in the cases of both the DRO and pump-enhanced SRO, periodically-poled lithium niobate must be considered, by a long way, the most attractive material in view of the low pump powers likely to be available.

It should be noted that the comments made with regard to pump-frequency stability in the above discussion only consider the requirements for successful operation of the OPO. If an application is being addressed which requires a high level of frequency stability, this will be the factor which dictates the stability requirements

placed on the pump. In this case, the pump-frequency stability requirements of the pump-enhanced SRO and DRO will be very similar.

If the requirements of a particular application can be met, the directly diode-laser-pumped OPO is potentially a very attractive device for several reasons. In addition to the usual advantages of size and efficiency obtained with diode lasers, the fact that they can be rapidly temperature tuned over a large range would allow rapid tuning of the OPO outputs [161]. This would give the diode-pumped OPO a distinct advantage, in this respect, over similar devices pumped by solid-state lasers where OPO tuning would require the phase-matching conditions to be adjusted. This is generally a slower and less precise process over large ranges than temperature tuning a diode laser.

Several aspects of the applications mentioned in section 3.1 could benefit from the use of a successfully implemented diode-laser-pumped OPO. In particular, such a device would represent a highly flexible source for spectroscopic applications being multi-parameter tuneable over large ranges. Although excellent results have been achieved using difference-frequency mixing for trace-gas detection [97,98,99] the one to two orders of magnitude higher power available from a diode-pumped OPO could allow improved signal-to-noise ratios while requiring only one pump laser. In the case of frequency standards, a number of potential reference transitions exist within the wavelength range of AlGaAs diode lasers [109,178] and a diode-pumped OPO could be used to link these to other frequency standards. In addition to relatively fast tuning by varying the diode temperature, extremely fast tuning and modulation (≈tens of MHz or more) of laser diodes is possible over small ranges by varying the drive current. This feature could be particularly useful for various high-speed servo stabilisation techniques used with highly-stabilised lasers.

To summarise, continuous-wave diode-pumped doubly-resonant or pump-enhanced single-resonant optical parametric oscillators represent highly-attractive sources of tunable radiation for a number of applications. However, the requirements of relatively high output powers (of the order of 100mW or more) combined with high degrees of spatial and spectral quality represent a very demanding set of specifications in the context of the majority of commercially available laser diodes.

3.8 References.

1 P.A. Franken, A.E. Hill, C.W. Peters and G. Weinreich, "Generation of optical harmonics," Phys. Rev. Lett. **7**, 118, (1961).

2 J.A. Giordmaine, "Mixing of light beams in crystals," Phys. Rev. Lett. **8**, 19-20 (1962).

3 P.D. Maker, R.W. Terhune, M. Nisenoff and C.M. Savage, "Effects of dispersion and focusing on the production of optical harmonics," Phys. Rev. Lett. **8**, 21-22 (1962).

4 J.A. Armstrong, N. Blombergen, J. Ducuing and P.S. Pershan, "Interactions between light waves in a nonlinear dielectric," Phys. Rev. **127**, 1918-1939 (1962).

5 J.E. Geusic, H.J. Levinstein, S. Singh, R.G. Smith and L.G. Van Uitert, "Continuous 0.532-μ solid-state source using Ba_2NaNbO_5," Appl. Phys. Lett. **12**, 306-308 (1968).

6 J.A. Giordmaine and R.C. Miller, "Tunable coherent parametric oscillation in $LiNbO_3$ at optical frequencies," Phys. Rev. Lett. **14**, 973-976 (1965).

7 D.W. Faries, "Tunable far-infrared radiation generated from the difference frequency between two ruby lasers," Phys. Rev. **180**, 363-365 (1969).

8 G.D. Boyd and A. Ashkin, "Theory of parametric oscillator threshold with single-mode optical masers and observation of amplification in $LiNbO_3$," Phys. Rev. **146**, 187-198 (1966).

9 A. Yariv and W.H. Louisell, "Theory of the optical parametric oscillator," IEEE J. Quantum Electron. **QE-2**, 418-424 (1966).

10 G.D. Boyd and D.A. Kleinman, "Parametric interaction of focused Gaussian light beams," J. Appl. Phys. **39**, 3597-3639 (1968).

11 F. Zernike and J.E. Midwinter, "Applied Nonlinear Optics," John Wiley and Sons, New York (1973).

12 R.B. Chesler, M.A. Karr and J.E. Geusic, "Repetitively Q-switched Nd:YAlG-$LiIO_3$ 0.53-μ harmonic source," J. Appl. Phys. **41**, 4125-4127 (1970).

13 R.W. Wallace, "Stable, efficient optical parametric oscillations pumped with double Nd:YAG," Appl. Phys. Lett. **17**, 497-499 (1970).

14 K.F. Hulme, "Nonlinear optical crystals and their applications," Rep. Prog. Phys. **36**, 497-540 (1973).

15 E.O. Ammann, C.D. Decker and J. Falk, "High-peak-power 532-nm pumped dye laser," IEEE J. Quantum Electron. **QE-10**, 463-465 (1974).

16 R.K. Jain and T. Gustafson, "Efficient generation of continuously tunable radiation in the 2460-2650 Å spectral range," IEEE J. Quantum Electron. **QE-12** 555-556 (1976).

17 C. Gabel and M. Hercher, "A continuous tunable source of UV radiation," IEEE J. Quantum Electron. **QE-8**, 850-851 (1972).

18 A.I. Ferguson, M.H. Dunn and A. Maitland, "Tunable, continuous-wave, ultra-violet radiation around 300 nm by frequency-doubling a rhodamine 6G dye laser," Opt. Comm. **19**, 10-13 (1976).

19 R.G. Smith, J.E. Geusic, H.J. Levinstein, J.J. Rubin, S. Singh and L.G. Van Uitert, "Continuous optical parametric oscillator in $Ba_2NaNb_5O_{15}$," Appl. Phys. Lett. **12**, 308-309 (1968).

20 S.E. Harris, "Tunable optical parametric oscillators," Proc. IEEE **57**, 2096-2113 (1969).

21 D.L. Weinberg, "Tunable optical parametric amplifiers and generators," Laser Focus **5**, 35-41 (April 1969).

22 R.L. Byer, "Optical Parametric Oscillators," in "Quantum Electronics: a Treatise," ed. H. Rabin and C.L. Tang, Academic Press, New York (1975).

23 R.G. Smith, "Optical Parametric Oscillators," in "Lasers: A Series of Advances," vol. 4, ed. A.K. Levine and A.J. De Maria, Marcel Dekker, New York (1976).

24 J.A. Giordmaine and R.C. Miller, "Optical parametric oscillation in $LiNbO_3$," in "Physics of Quantum Electronics," P.L. Kelley, B. Lax and P.E. Tannenwald eds., McGraw-Hill, New York (1966).

25 J.F. Weller, T.G. Giallorenzi and R.A. Andrews, "Time-resolved spectral output of a doubly resonant cw optical parametric oscillator," J. Appl. Phys. **43**, 4650-4652 (1972).

26 R.L. Byer, M.K. Oshman, J.F. Young and S.E Harris, "Visible cw parametric oscillator," Appl. Phys. Lett. **13**, 109-111 (1968).

27 R.L. Byer, A. Kovrigin and J.F. Young, "A cw ring-cavity parametric oscillator," Appl. Phys. Lett. **15**, 136-137 (1969).

28 C. Laurence and F. Tittel, "Visible cw parametric oscillator using barium sodium niobate," J. Appl. Phys. **42**, 2137-2138 (1971).

29 J.E. Bjorkholm, "Efficient optical parametric oscillation using doubly and singly resonant cavities," Appl. Phys. Lett. **13**, 53-56 (1968).

30 L.B. Kreuzer in "Proceedings of the joint conference on lasers and Optoelectronics, University of Southampton", p.53, I.E.R.E. London (1969). "Single mode oscillation of a pulsed singly resonant optical parametric oscillator," Appl. Phys. Lett. **15**, 263-265 (1969).

31 R.W. Wallace and S.E. Harris, "Extending the tunability spectrum," Laser Focus **6**, 42-44 (November 1970).

32 T. Henningsen, M. Garbuny and R.L. Byer, "Remote detection of CO by parametric tunable laser," Appl. Phys. Lett. **24**, 242-244 (1974).

33 R.A. Baumgartner and R.L. Byer, "Remote SO_2 measurements at 4μm with a continuously tunable source," Opt. Lett. **2**, 163-165 (1978).

34 R.G. Smith, "A study of factors affecting the performance of a continuously-pumped doubly-resonant optical parametric oscillator," IEEE J. Quantum Electron. **QE-9**, 530-541 (1973).

35 C.L. Tang, W.R. Bosenberg, T. Ukachi, R.J. Lane and L.K. Cheng, "NLO materials display superior performance," Laser Focus World, September 1990, 87-97.

36 C.L. Tang, W.R. Bosenberg, T. Ukachi, R.J. Lane and L.K. Cheng, "Advanced materials aid parametric oscillator development," Laser Focus World, October 1990, 107-116.

37 T.V. Higgins, "Nonlinear crystals: where the colors of the rainbow begin," Laser Focus World, January 1992, 125-133.

38 P.F. Bordui and M.M. Fejer, "Inorganic crystals for nonlinear optical frequency conversion," Ann. Rev. Mater. Sci. **23**, 321-379 (1993).

39 T.Y. Fan and R.L. Byer, "Diode laser-pumped solid-state lasers," IEEE J. Quantum Electron. **24**, 895-912, (1988).

40 D.W. Hughes and J.R.M. Barr, "Laser diode pumped solid state lasers," J. Phys. D: Appl. Phys. **25**, 563-586, (1992).

41 B.J. Le Garrec, G.J. Razé, P.Y. Thro and M. Gilbert, "High-average-power diode-array-pumped frequency-doubled YAG laser," Opt. Lett. **21**, 1990-1992 (1996).

42 S. Konno, S. Fujikawa and K. Yasui, "Highly efficient 68-W green-beam generation by use of an intracavity frequency-doubled diode side-pumped Q-switched Nd:YAg rod laser," Appl. Opt. **37**, 6401-6404 (1998).

43 K.I. Martin, W.A. Clarkson and D.C. Hanna, "3 W of single-frequency output at 532 nm by intracavity frequency doubling of a diode-bar-pumped Nd:YAG ring laser," Opt. Lett. **21**, 875-877 (1996).

44 C. Yelland and W. Sibbett, "Stable 4 W CW solid-state green source pumped by fibre-coupled diode-laser arrays," J. Mod. Opt. **43**, 893-901 (1996).

45 P.J. Hardman, W.A. Clarkson and D.C. Hanna, "High-power diode-bar-pumped intracavity-frequency-doubled Nd:YLF ring laser," Opt. Comm. **156**, 49-52 (1998).

46 Y.K. Yap, M. Inagaki, S. Nakajima and T. Sasaki, "High-power fourth- and fifth-harmonic generation of a Nd:YAG laser by means of $CsLiB_6O_{10}$," Opt. Lett. **21**, 1348-1350 (1996).

47 A.H. Kung, L, Jr-i and P.-J. Chen, "An efficient all-solid-state ultraviolet laser source," Appl. Phys. Lett. **72**, 1542-1544 (1998).

48 M.K. Chun, L. Goldberg and J.F. Weller, "Second-harmonic generation at 421 nm using injection-locked GaAlAs laser array and $KNbO_3$," Appl. Phys. Lett. **53**, 1170-1171 (1988).

49 G.J. Dixon, C.E. Tanner and C.E. Wieman, "432-nm source based on efficient second-harmonic generation of GaAlAs diode-laser radiation in a self-locking external resonant cavity," Opt. Lett. **14**, 731-733 (1989).

50 L. Goldberg and M.K. Chun, "Efficient generation at 421 nm by resonantly enhanced doubling of GaAlAs laser diode array emission," Appl. Phys. Lett. **55**, 218-220 (1989).

51 W.J. Kozlovsky, W. Lenth, E.E. Latta, A. Moser and G.L. Bona, "Generation of 41 mW of blue radiation by frequency doubling of a GaAlAs diode laser," Appl. Phys. Lett. **56**, 2291-2292 (1990).

52 C. Tamm, "A tunable light source in the 370nm range based on an optically stabilised, frequency-doubled semiconductor laser," Appl. Phys. B **56**, 295-300 (1993).

53 C. Zimmermann, V. Vuletic, A. Hemmerich and T.W. Hänsch, "All solid state laser source for tunable blue and ultraviolet radiation," Appl. Phys. Lett. **66**, 2318-2320 (1995).

54 B. Beier, D. Woll, M. Scheidt, K.-J. Boller and R. Wallenstein, "Second harmonic generation of the output of an AlGaAs diode oscillator amplifier system in critically phase matched LiB_3O_5 and β-BaB_2O_4," Appl. Phys. Lett. **71**, 315-317 (1997).

55 D. Woll, B. Beier, K.-J. Boller and R. Wallenstein, "Generation of 1W of blue light by frequency doubling the output of a tapered InGaAs diode amplifier in critically phase-matched LBO," Conference on Lasers and Electro-Optics, May 1998, OSA Technical Digest Series 1998 vol. 6 p. 380, Optical Society of America, Washington.

56 K. Matsubara, U. Tanaka, H. Imajo, K. Hayasaka, R. Ohmukai, M. Watanabe and S. Urage, "An all-solid-state tunable 214.5-nm continuous-wave light source by using two-stage frequency doubling of a diode laser," Appl. Phys. B **67**, 1-4 (1998).

57 L.-A. Wu, H.J. Kimble, J.L. Hall and H. Wu, "Generation of squeezed states by parametric down conversion," Phys. Rev. Lett. **57**, 2520-2523 (1986).

58 L.-A. Wu, M. Xiao and H.J. Kimble, "Squeezed states of light from an optical parametric oscillatro," J. Opt. Soc. Am. B **4**, 1465-1475 (1987).

59 G. Breitenbach, S. Schiller and J. Mlynek, "Measurement of the quantum states of squeezed light," Nature **387**, 471-475 (1997).

60 E.S. Polzik, J.L. Sørensen and J. Hald, "Subthreshold tunable OPO: a source of nonclassical light for atomic physics experiments," Appl. Phys. B **66**, 759-764 (1998).

61 S. Reynaud, C. Fabre and E. Giacobino, "Quantum fluctuations in a two-mode parametric oscillator," J. Opt. Soc. Am. B **4**, 1520-1524 (1987).

62 C.D. Nabors and R.M. Shelby, "Two-colour squeezing and sub-shot-noise signal recovery in doubly resonant optical parametric oscillators," Phys. Rev. A **42**, 556-559 (1990).

63 J. Gao, F. Cui, C. Xue, C. Xie and P. Kunchi, "Generation and application of twin beams from an optical parametric oscillator including an α-cut KTP crystal," Opt. Lett. **23**, 870-872 (1998).

64 C.D. Nabors, R.C. Eckardt, W.J. Kozlovsky and R.L. Byer, "Efficient, single-axial-mode operation of a monolithic MgO:$LiNbO_3$ optical parametric oscillator," Opt. Lett. **14**, 1134-1136 (1989).

65 C.D. Nabors, S.T. Tang, T. Day and R.L. Byer, "Coherence properties of a doubly-resonant monolithic optical parametric oscillator," J. Opt. Soc. Am. B **7**, 815-820 (1990).

66 R.C. Eckardt, C.D. Nabors, W.J. Kozlovsky and R.L. Byer, "Optical parametric oscillator frequency tuning and control," J. Opt. Soc. Am. B **8**, 646-667 (1991).

67 D. Lee and N.C. Wong, "Stabilization and tuning of a doubly resonant optical parametric oscillator," J. Opt. Soc. Am. B **10**, 1659-1667 (1993).

68 A.J. Henderson, M.J. Padgett, F.G. Colville, J. Zhang and M.H. Dunn, "Doubly-resonant optical parametric oscillators: tuning behaviour and stability requirements," Opt. Comm. **119**, 256-264 (1995).

69 K. Schneider, P. Kramper, S. Schiller and J. Mlynek, "Toward an optical synthesizer: a single-frequency parametric oscillator using periodically poled $LiNbO_3$," Opt. Lett. **22**, 1293-1295 (1997).

70 K. Schneider and S. Schiller, "Narrow-linewidth, pump-enhanced singly-resonant parametric oscillator pumped at 532 nm," Appl. Phys. B **65**, 775-777 (1997).

71 M. Bode, P.K. Lam, I. Freitag, A. Tünnermann, H.-A. Bachor and H. Welling, "Continuously-tunable doubly-resonant optical parametric oscillator," Opt. Comm. **148**, 117-121 (1998).

72 R. Al-Tahtamouni, K. Bencheikh, R. Storz, K. Schneider, M. Lang, J. Mlynek and S. Schiller, "Long-term stable operation and absolute frequency stabilization of a doubly-resonant parametric oscillator," Appl. Phys. B **66**, 733-739 (1998).

73 S.T. Yang, R.C. Eckardt and R.L. Byer, "Continuous-wave singly-resonant optical parametric oscillator pumped by a single-frequency resonantly doubled Nd:YAG laser," Opt. Lett. **18**, 971-973 (1993).

74 W.R. Bosenberg, A. Drobshoff, J.I. Alexander, L.E. Myers and R.L. Byer, "Continuous-wave singly-resonant optical parametric oscillator based on periodically poled $LiNbO_3$," Opt. Lett. **21**, 713-715 (1996).

75 W.R. Bosenberg, A. Drobshoff, J.I. Alexander, L.E. Myers and R.L. Byer, "93% pump depletion, 3.5-W continuous-wave, singly resonant optical parametric oscillator," Opt. Lett. **21**, 1336-1338 (1996).

76 W.R. Bosenberg, J.I. Alexander, L.E. Myers and R.W. Wallace, "2.5-W, continuous-wave, 629-nm solid-state laser source," Opt. Lett. **23**, 207-209 (1998).

77 F.G. Colville, M.H. Dunn and M. Ebrahimzadeh, "Continuous-wave, singly resonant, intracavity parametric oscillator," Opt. Lett. **22**, 75-77 (1997).

78 L.P. Gonzalez, "Continuous wave singly resonant intracavity optical parametric oscillators using periodically poled $LiNbO_3$," MSc Thesis, School of Engineering, University of Dayton, Dayton, USA (1997).

79 T.J. Edwards, G.A. Turnbull, M.H. Dunn, M. Ebrahimzadeh and F.G. Colville "High-power, continuous-wave, singly resonant, intracavity optical parametric oscillator," Appl. Phys. Lett. **72**, 1527-1529 (1998).

80 T.J. Edwards, G.A. Turnbull, M.H. Dunn, M. Ebrahimzadeh, H. Karlsson, G. Arvidsson and F. Laurell, "Continuous-wave singly resonant optical parametric oscillator based on periodically poled $RbTiOAsO_4$," Opt. Lett. **23**, 837-839 (1998).

81 D.J.M. Stothard, M. Ebrahimzadeh and M.H. Dunn, "Low-pump-threshold, continuous-wave singly resonant optical parametric oscillator," Opt. Lett. **23**, 1895-1897 (1998).

82 F.G. Colville and B.T. McGukin, "OPOs tune solid-state CW lasers from 3 to 5 microns," Laser Focus World, November 1998, 83-87.

83 L.E. Myers, R.C. Eckardt, M.M. Fejer and R.L. Byer, "CW diode-pumped optical parametric oscillator in bulk periodically poled $LiNbO_3$," Advanced Solid State Lasers, February 1995, paper PD9, OSA Technical Digest Series 1995, Optical Society of America (Washington), 1995.

L.E. Myers, R.C. Eckardt, M.M. Fejer and R.L. Byer, "CW diode-pumped optical parametric oscillator in bulk periodically poled $LiNbO_3$," Electron. Lett. **31**, 1869-1870 (1995).

84 M. Scheidt, B. Beier, K.J. Boller and R. Wallenstein, "Diode-laser-pumped cw optical parametric oscillators of KTP," Conference on Lasers and Electro-Optics, May 1995, OSA Technical Digest Series 1995 vol. **15**, Optical Society of America, Washington.

M. Scheidt, B. Beier, R. Knappe, K.J. Boller and R. Wallenstein, "Diode-laser-pumped continuous-wave KTP optical parametric oscillator," J. Opt. Soc. Am. B **12**, 2087-2094 (1995).

85 K.J. Boller, M. Scheidt, B. Beier, C. Becher, M.E. Klein and D.H. Lee, "Diode-pumped optical parametric oscillators," Quantum Semiclass. Opt. **9**, 173-189 (1997).

86 M. Scheidt, B. Beier, K.J. Boller and R. Wallenstein, "Frequency-stable operation of a diode-pumped continuous-wave $RbTiOAsO_4$ optical parametric oscillator," Opt. Lett. **22**, 1287-1289 (1997).

87 M.E. Klein, D.-H. Lee, J.-P. Meynm B. Beier, K.-J. Boller and R. Wallenstein, "Diode-pumped continuous-wave widely tunably optical parametric oscillator based on periodically poled lithium tantalate," Opt. Lett. **23**, 831-833 (1998).

88 I.D. Lindsay, G.A. Turnbull, M.H. Dunn and M. Ebrahimzadeh, "Doubly-resonant continuous-wave optical parametric oscillator pumped by a single-mode diode laser," Opt. Lett. **23**, 1889-1891 (1998).

89 M.E. Klein, D.-H. Lee, J.-P. Meyn, B. Beier, K.-J. Boller and R. Wallenstein, "Diode-pumped continuous-wave optical parametric oscillator," Post-deadline paper CPD1.12, Conference on Lasers and Electro-Optics-Europe September 1998, OSA Technical Digest Series 1998, Optical Society of America, Washington.

90 M. Houé and P.D. Townsend, "An introduction to methods of periodic-poling for second-harmonic generation," J. Phys. D: Appl. Phys. **28**, 1747-1763 (1995).

91 M.M. Fejer, G.A. Magel, D.H. Jundt and R.L. Byer, "Quasi-phase-matched second harmonic generation: tuning and tolerances," IEEE J. Quantum Electron. **28**, 2631-2654 (1992).

92 L.E. Myers, R.C. Eckardt, M.M. Fejer, R.L. Byer, W.R. Bosenberg, J.W. Pierce, "Quasi-phase-matched optical parametric oscillators in bulk periodically poled $LiNbO_3$," J. Opt. Soc. Am. B **12**, 2102-2116 (1995).

93 L.E. Myers and W.R. Bosenberg, "Periodically poled lithium niobate and quasi-phase-matched optical parametric oscillators," IEEE J. Quantum Electron. **33**, 1663-1672 (1997).

94 J. Hecht, "Tunable mid-infrared sources entice spectroscopists," Laser Focus World, September 1993, 109-116.

95 G.M. Gibson, M.H. Dunn and M.J. Padgett, "Application of a continuously tunable, cw optical parametric oscillator for high resolution spectroscopy," Opt. Lett. **23**, 40-42 (1998).

96 F. Kühnemann, K. Schneider, A. Hecker, A.A.E. Martis, W. Urban, S. Schiller and J. Mlynek, "Photoacoustic trace-gas detection using a cw single-frequency parametric oscillator," Appl. Phys. B **66**, 741-745 (1998).

97 K.P. Petrov, S. Waltman, E.J. Dlugokencky, M. Arbore, M.M. Fejer, F.K. Tittel and L.W. Hollberg, "Precise measurement of methane in air using diode-pumped 3.4-μm difference-frequency generation in PPLN," Appl. Phys. B **64**, 567-572 (1997).

98 K.P. Petrov, R.F. Curl and F.K. Tittel, "Compact laser difference-frequency spectrometer for multicomponent trace gas detection," Appl. Phys. B **66**, 531-538 (1998).

99 For coverage of many recent results in the use of nonlinear optics for atmospheric trace-gas detection, see special issue on "Environmental trace gas detection using laser spectroscopy", Appl. Phys. B **67**, 273 (1998).

100 N.C. Wong, "Optical frequency counting from the UV to the near IR," Opt. Lett. **17**, 1155-1157 (1992).

101 K. Shimoda, "Optical frequency counters," Appl. Phys. B **63**, 507-510 (1996).

102 J.E. Bernard, L. Marmet and A.A. Madej, "A laser frequency lock referenced to a single trapped ion," Opt. Comm. **150**, 170-174 (1998).

103 S.N. Lea, G.M. Macfarlane, G. Huang and P. Gill, "Optical frequency chain at NPL: Progress and prospects," Technical digest of the National Quantum Electronics Conference QE-13, p. 53, September 1997, Institute of Physics Publishing.

104 D. Lee and N.C. Wong, "Tunable optical frequency division using a phase-locked optical parametric oscillator," Opt. Lett. **17**, 13-15 (1992).

105 N.C. Wong, "Optical-to-microwave frequency chain utilizing a two-laser-based optical parametric oscillator network," Appl. Phys. B **61**, 143-149 (1995).

106 T. Ikegami, S. Slyusarev, S. Ohshima and E. Sakuma, "Accuracy of an optical parametric oscillator as an optical frequency divider," Opt. Comm. **127**, 69-72 (1996).

107 N.C. Wong, "Proposal for a 10-THz precision optical frequency comb generator," IEEE Phot. Technol. Lett. **4**, 1166-1168 (1992).

108 O. Acef, J.J. Zondy, M. Abed, D.G. Rovera, A.H. Gérard, A. Clairon, Ph. Laurent, Y. Millerioux and P. Juncar, "A CO_2 to visible optical frequency synthesis chain: accurate measurement of the 473 THz HeNe/I_2 laser," Opt. Comm. **97**, 29-34 (1993).

109 B. Bodermann, M. Klug, H. Knöckel, E. Tiemann, T. Trebst and H.R. Telle, "Frequency measurement of I_2 lines in the NIR using Ca and CH_4 optical frequency standards," Appl. Phys. B **67**, 95-99 (1998).

110 R.W. Boyd, "Nonlinear Optics," Academic Press, Sandiego, USA, (1992).

111 D.A. Kleinman, "Nonlinear dielectric polarization in optical media," Phys. Rev. **126**, 1977-1979 (1962).

112 A. Yariv, "Quantum electronics," (second edition) John Wiley and Sons, New York (1989).

113 J.F. Nye, "Physical properties of crystals, their representation by tensors and matrices," Oxford University Press, Oxford (1957).

114 J.E. Midwinter and J. Warner, "The effects of phase matching method and of uniaxial crystal symmetry on the polar distribution of second-order non-linear optical polarisation," Brit. J. Appl. Phys. **16**, 1135-1142 (1965).

115 T. Debuisschert, A. Sizmann, E. Giacobino and C. Fabre, "Type-II continuous-wave optical parametric oscillators: oscillation and frequency-tuning characteristics," J. Opt. Soc. Am. B **10**, 1668-1680 (1993).

116 D.A. Roberts, "Simplified characterisation of uniaxial and biaxial nonlinear optical crystals: a plea for standardization of nomenclature and conventions," IEEE J. Quantum Electron. **28**, 2057-2074 (1992).

117 M.V. Hobden, "Phase-matched second-harmonic generation in biaxial crystals," J. Appl. Phys. **38**, 4365-4372 (1967).

118 B. Zysset, I. Biaggio and P. Günter, "Refractive indices of orthorombic $KNbO_3$. I. Dispersion and temperature dependence," J. Opt. Soc. Am. B **9**, 380-386 (1992).

119 I. Biaggio, P. Kerkoc, L.-S. Wu, P. Günter and B. Zysset, ", "Refractive indices of orthorombic $KNbO_3$. II. Phase-matching configurations for nonlinear-optical interactions," J. Opt. Soc. Am. B **9**, 507-517 (1992).

120 H. Ito, H. Naito and H. Inaba, "Generalized study on angular dependence of induced second-order nonlinear optical polarizations and phase matching in biaxial crystals," J. Appl. Phys. **46**, 3992-3998 (1975).

121 B. Wyncke and F. Brehat, "Calculation of the effective second-order non-linear coefficients along the phase matching directions in acentric orthorhombic biaxial crystals," J. Phys. B: At. Mol. Opt. Phys. **22**, 363-376 (1989).

122 V.G. Dmitriev and D.N. Nikogosyan, "Effective nonlinearity coefficients for three-wave interactions in biaxial crystals of mm2 point group symmetry," Opt. Comm. **95**, 173-182 (1993).

123 G.D. Boyd, A. Ashkin, J.M. Dziedzic and D.A. Kleinman, "Second-harmonic generation of light with double refraction," Phys. Rev. **128**, A1305-A1320 (1965).

124 F. Bréhat and B. Wyncke, "Calculation of double-refraction walk-off angle along the phase-matching directions in non-linear biaxial crystals," J. Phys. B: At. Mol. Opt. Phys. **22**, 1891-1898 (1989).

125 G.D. Boyd and C.K.N. Patel, "Enhancement of optical second-harmonic generation (SHG) by reflection phase matching in ZnS and GaAs," Appl. Phys. Lett. **8**, 313-315 (1966).

126 C.F. Dewey Jr. And L.O. Hocker, "Enhanced nonlinear optical effects in rotationally twinned crystals," Appl. Phys. Lett. **26**, 442-444 (1975).

127 D.E. Thompson, J.D. McMullen and D.B. Anderson, "Second-harmonic generation in GaAs "stack of plates" using high-power CO_2 laser radiation," Appl. Phys. Lett. **29**, 113-115 (1976).

128 M. Okada, K. Takizawa and S. Ieiri, "Second harmonic generation by periodic laminar structure of nonlinear optical crystal," Opt. Comm. **18**, 331-334 (1976).

129 M.S. Piltch, C.D. Cantrell and R.C. Sze, "Infrared second-harmonic generation in nonbirefringent cadmium telluride," J. Appl. Phys. **47**, 3514-3517 (1976).

130 D. Feng, N.-B. Ming, J.-F. Hong, Y.-s. Yang, J-S. Zhu, Z. Yang and Y.-N. Wang, "Enhancement of second-harmonic generation in $LiNbO_3$ crystals with periodic laminar ferroelectric domains," Appl. Phys. Lett. **37**, 607-609 (1980).

131 A. Feisst and P. Koidl, "Current induced periodic ferroelectric domain structures in $LiNbO_3$ applied for efficient nonlinear optical frequency mixing," Appl. Phys. Lett. **47**, 1125-1127 (1985).

132 D.H. Jundt, G.A. Magel, M.M. Fejer and R.L. Byer, "Periodically poled LiNbO3 for high-efficiency second-harmonic generation," Appl. Phys. Lett. **59**, 2657-2659 (1991).

133 J. Webjörn, F. Laurell and G. Arvidsson, "Blue light generated by frequency doubling of laser diode light in a lithium niobate channel waveguide," IEEE Photon. Technol. Lett. **1**, 316-318 (1989).

134 M. Fujimura, T. Suhara and N. Nishihara, "Ferroelectric-domain inversion induced by SiO_2 cladding for $LiNbO_3$ waveguide SHG," Electron. Lett. **27**, 1207-1209 (1991).

135 H. Ito, C. Takyu and H. Inaba, "Grating in LiNbO3 by electron beam writing for application of nonlinear optical processes," Electron. Lett. **27**, 1221-1222 (1991).

136 M. Yamada, N. Nada, M. Saitoh and K. Watanabe, "First-order quasi-phase matched LiNbO3 waveguide periodically poled by applying an external field for efficient blue second-harmonic generation," Appl. Phys. Lett. **62**, 435-436 (1993).

137 J. Webjörn, V. Pruneri, P.St.J. Russel, J.R.M. Barr and D.C. Hanna, "Quasi-phase-matched blue light generation in bulk lithium niobate, electrically poled via periodic liquid electrodes," Electron. Lett. **30**, 894-895 (1994).

138 Q. Chen and W.P. Risk, "Periodic poling of $KTiOPO_4$ using an applied electric field," Electron. Lett. **30**, 1516-1517 (1994).

139 G.M. Gibson, G.A. Turnbull, M. Ebrahimzadeh, M.H. Dunn, H. Karlsson, G. Arvidsson and F. Laurell, "Temperature-tuned difference-frequency mixing in periodically poled $KTiOPO_4$," Appl. Phys. B **67**, 675-677 (1998).

140 K. Mizuuchi and K. Yamamoto, "Harmonic blue light generation in bulk periodically poled $LiTaO_3$," Appl. Phys. Lett. **66**, 2943-2945 (1995).

141 J. -P. Meyn and M.M. Fejer, "Tunable ultraviolet radiation by second-harmonic generation in periodically poled lithium tantalate," Opt. Lett. **22**, 1214-1216 (1997).

142 S. Somekh and A. Yariv, "Phase matching by periodic modulation of the nonlinear optical properties," Opt. Comm. **6**, 301-304 (1972).

143 Y. Yacoby, R.L. Aggarwal and B. Lax, "Phase matching by periodic variation of nonlinear coefficients," J. Appl. Phys. **44**, 3180-3181 (1973).

144 J.D. McMullen, "Optical parametric interactions in isotropic materials using a phase-corrected stack of nonlinear dielectric plates," J. Appl. Phys. **46**, 3076-3081 (1975).

145 A. Szilagyi, A. Hordvik and H. Schlossberg, "A quasi-phase-matching technique for efficient optical mixing and frequency doubling," J. Appl. Phys. **47**, 2025-2032 (1976).

146 K.C. Rustagi, S.C. Mehendale and S. Meenakshi, "Optical frequency conversion in quasi-phase-matched stacks of nonlinear crystals," IEEE J. Quantum Electron. **QE-18**, 1029-1041 (1982).

147 C.R. Wylie and L.C. Barrett, "Advanced engineering mathematics," fifth edition, McGraw-Hill, London (1985).

148 P.E. Powers, T.J. Kulp and S.E. Bisson, "Continuous tuning of a continuous-wave periodically poled lithium niobate optical parametric oscillator by use of a fan-out grating design," Opt. Lett. **23**, 159-161 (1998).

149 P.T. Nee and N.C. Wong, "Optical frequency division by 3 of 532 nm in periodically poled lithium niobate with a double grating," Opt. Lett. **23**, 46-48 (1998).

150 L.A. Eyres, C.B. Ebert, M.M. Feyer and J.S. Harris, "MBE growth of laterally anti-phase patterned GaAs films using thin Ge layers for waveguide mixing," Conference on Lasers and Electro-Optics, May 1998, OSA Technical Digest Series 1998 vol. **6** p. 276, Optical Society of America, Washington.

151 M.J. Missey, V. Dominic, L.E. Myers and R.C. Eckardt, "Diffusion-bonded stacks of periodically poled lithium niobate," Opt. Lett. **23**, 664-666 (1998).

152 N.P. Barnes and V.J. Corcoran, "Parametric generation processes: spectral bandwidth and acceptance angles," Appl. Opt. **15**, 696-699 (1976).

153 F.G. Colville, "An analysis of the performance characteristics of continuous-wave optical parametric oscillators," PhD thesis, University of St Andrews, 1994.

154 A.E. Siegman, "Lasers," University Science Books, Mill Valley, California (1986).

155 J.E. Bjorkholm, A. Ashkin and R.G. Smith, "Improvement of optical parametric oscillators by nonresonant pump reflection," IEEE J. Quantum Electron. **QE-6**, 797-799 (1970).

156 G. Robertson, M.J. Padgett and M.H. Dunn, "Continuous-wave, singly resonant pump-enhanced type II LiB_3O_5 optical parametric oscillator," Opt. Lett. **19**, 1735-1737 (1994).

157 S.T. Yang, R.C. Eckardt and R.L. Byer, "Power and spectral characteristics of continuous-wave parametric oscillators: the doubly to singly resonant transition," J. Opt. Soc. Am. B **10**, 1684-1695 (1993).

158 D. Chen, D. Hinkley, J. Pyo, J. Swenson and R. Fields, "Single-frequency low-threshold continuous-wave 3-μm periodically poled lithium niobate optical parametric oscillator," J. Opt. Soc. Am. B **15**, 1693-1697 (1998).

159 A.E. Siegman, "Nonlinear optical effects: an optical power limiter," Appl. Opt. **1**, 739-744 (1962).

160 J.E. Bjorkholm, "Analysis of the doubly-resonant optical parametric oscillator without power-dependent reflections," IEEE J. Quantum Electron. **QE-5**, 293-295 (1969).

161 F.G. Colville, M. Ebrahimzadeh, W. Sibbett and M.H. Dunn, "Continuous-wave LiB_3O_5 optical parametric oscillator pumped by a tunable Ti:sapphire laser," Appl. Phys. Lett. **64**, 1765-1767 (1994).

162 A.I. Kovrigin and R.L. Byer, "Stability factor for optical parametric oscillators," IEEE J. Quantum Electron. **QE-5**, 384 (1969).

163 F.G. Colville, M.J. Padgett and M.H. Dunn, "Smooth frequency tuning from optical parametric oscillators: the transition from single- to dual-cavity oscillators," in "Advanced solid-state lasers," T.Y. Fan and B.H.T. Chai eds., OSA Proceedings vol. 20 p. 438-442, Optical Society of America, Washington (1994).

164 A.J. Henderson, M.J. Padgett, J. Zhang, W. Sibbett and M.H. Dunn, "Continuous frequency tuning of a cw optical parametric oscillator through tuning of its pump source," Opt. Lett. **20**, 1029-1031 (1995).

165 F.G. Colville, M.J. Padgett and M.H. Dunn, "Continuous-wave, dual-cavity, doubly-resonant, optical parametric oscillator," Appl. Phys. Lett. **64**, 1490-1492 (1994).

166 T. Ikegami, S. Slyusarev, T. Kurosu, Y. Fukuyama and S. Ohshima, "Characteristics of a cw monolithic $KTiOPO_4$ optical parametric oscillator," Appl. Phys. B **66**, 719-725 (1998).

167 M.J. Padgett, F.G. Colville and M.H. Dunn, "Mode selection in doubly-resonant optical parametric oscillators," IEEE J. Quantum Electron. **30**, 2979-2985 (1994).

168 F.G. Colville, A.J. Henderson, M.J. Padgett, J. Zhang and M.H. Dunn, "Continuous-wave parametric oscillation in lithium triborate," Opt. Lett. **18**, 205-207 (1993).

169 S. Lin, B. Wu, F. Xie and C. Chen, "Phase-retracing behaviour: New features in LiB_3O_5," Appl. Phys. Lett. **59**, 1541-1543 (1991).

170 S.P. Velsko, M. Webb, L. Davis and C. Huang, "Phase-matched harmonic generation in lithium triborate (LBO)," IEEE J. Quantum Electron. **27**, 2182-2192 (1991).

171 R. Asby, "Theory of optical parametric amplification from a focused Gaussian beam," Phys. Rev. B. **2**, 4273-4282 (1970).

172 S. Guha, F.-J. Wu and J. Falk, "The effects of focusing on parametric oscillation," IEEE J. Quantum Electron. **QE-18**, 907-912 (1982).

173 D.A. Kleinman, A. Ashkin and G.D. Boyd, "The second harmonic generation of light by focussed laser beams," IEEE J. Quantum Electron. **QE-2**, 425-429 (1966).

174 E. O. Ammann and P.C. Montgomery, "Threshold calculation for an optical parametric oscillator employing a hemispherical resonator," J. Appl. Phys. **41**, 5270-5274 (1970).

175 G.D. Boyd and F.R. Nash, "Parametric oscillator thresholds in symmetric and half-symmetric configurations in the absence of double refraction," J. Appl. Phys. **42**, 2815-2817 (1971).

176 W.R. Bosenberg and R.A. Jarman, "Type-II phase-matched KNbO3 optical parametric oscillator," Opt. Lett. **18**, 1323-1325 (1993).

177 G.A. Turnbull, I.D. Lindsay, D.G. Mc Gloin, M. Ebrahimzadeh and M.H. Dunn, unpublished.

178 Y. Millerioux, D. Youahri, L. Hilico, A. Clairon, R. Felder, F. Biraben and B. de Beauvoir, "Towards an accurate frequency standard at λ=778nm using a laser diode stabilized on a hyperfine component of the Doppler-free two-photon transitions in rubidium," Opt. Comm.. **108**, 91-96 (1994).

4. High-Power, High-Quality Diode-Laser-Based Pump Sources.

4.1 Introduction.

It was shown in chapter 2 that three main requirements are placed on a pump source for solid-state lasers if low-threshold, efficient, end-pumped operation at useful power levels is required. These are relatively high (>100mW) output powers, near diffraction-limited beam quality and, less significantly, a spectrally-narrow output. In the case of optical parametric oscillators it can be seen from chapter 3 that these requirements not only also exist, but do so to a far more exacting extent than in the case of end-pumped solid-state lasers. In particular, there is little tolerance for beam quality significantly worse than the diffraction limit. In the case of low-threshold continuous-wave (cw) OPOs, which typically have multiply-resonant cavities, the pump source must exhibit stable single longitudinal-mode performance if stable OPO operation is to be achieved.

Simultaneous achievement of all the above-mentioned criteria has long been the goal of research in the field of semiconductor lasers. It was recognised early on in development of laser diodes that confinement of the optical field in the plane of the junction, to an active region of a width similar to its thickness perpendicular to the junction, was necessary to obtain single transverse-mode operation [1]. The small active-region thickness, typically ≈1μm, perpendicular to the junction plane usually results in fundamental transverse mode operation in this direction. However, an active area considerably wider than its thickness resulted in laser operation occurring in higher transverse modes and/or random and uncoupled "filaments" across the junction plane [1]. Reduction of the transverse dimension of the active region, to around 50μm wide against 1μm thick, resulted in single-filament operation on

higher-order transverse modes with Hermite-Gaussian profiles [2]. Further reduction of the active-area width resulted in lowest-order transverse mode operation [3].

One of the early methods used to attempt this narrowing was to increase the resistivity of the layers above the active region except in a narrow strip down the length of the device creating a "stripe" electrode and confining current flow to a narrow transverse region. This had the effect of making areas outside this region lossy thereby discouraging operation on transverse modes falling outside the narrow region of current flow - so called gain guiding. One of the most successful methods of achieving this was to bombard the device with protons except along the narrow stripe required [4], a method still used today to restrict current flow to narrow regions.

Gain guiding did not provide especially reliable confinement of the optical field. In particular, reproducibility of the transverse mode pattern between devices was poor and also tended to vary with current for a given device [2]. To obtain stronger confinement the active volume, with a width ≈1-5μm, was surrounded with lower-index material on all sides in the first buried-heterostructure (BH) device [5], essentially resulting in the formation of a waveguide in the active region. Combining this tight optical confinement with stripe-contact current confinement resulted in the lowest thresholds reported up to that point.

Fabrication of the buried heterostructure was, however, fairly complex requiring multiple stages of epitaxial growth and etching. A simpler method of producing the required transverse refractive-index profile was the channelled-substrate planar (CSP) structure [6,7]. It was noted in [7] that single longitudinal-mode operation was also obtained from these lasers when operated well above threshold, as would be expected from a homogeneously-broadened transition, and the authors suggested that stable, single transverse-mode operation also resulted in this improved spectral purity. Similar confinement methods to that of the CSP laser and the inverted equivalent, shown in Fig. 4-1 [8], are still widely used today in single-mode laser diodes.

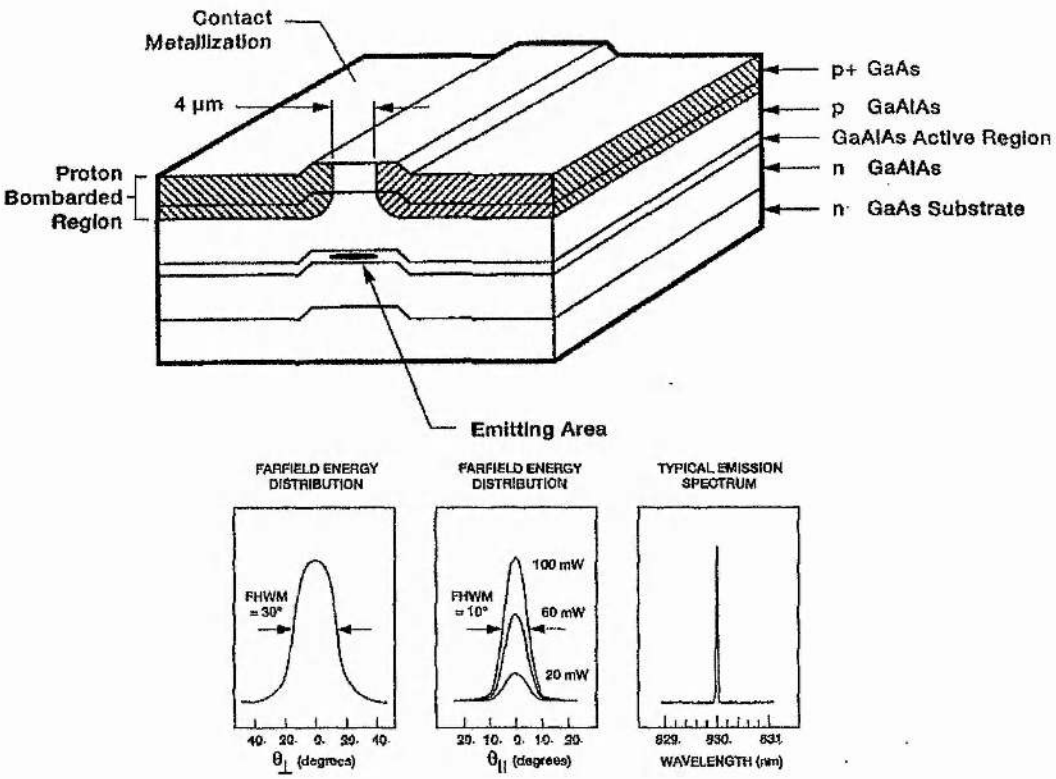

Fig. 4-1 Typical single-mode laser diode (SDL-5400 series c.1994) structure and emission characteristics (left to right, far-field power distributions perpendicular to and parallel to the junction and emission spectrum). [8].

Experimental studies by a number of workers arrive at typical catastrophic-damage intensities for AlGaAs laser diodes of a few $\times 10^6$ W cm^{-2} [5,9,10,11]. Clearly this means that the requirement discussed above, for an emitting region which is narrow in the plane of the junction, places an upper limit on the output power. In the typical case of an emitting region cross section of 3×1µm this limit is around 100mW. In recent years, single-mode diode lasers have been demonstrated with output powers significantly higher than this [12,13]. However, the specified maximum output of commercially available devices continues to be limited to around 100mW although even these devices have been shown to operate reliably at significantly higher powers than that at which they are nominally rated in some cases [14].

Coherent arrays of diode-laser emitters [15] were developed in an attempt to increase the total output power of laser diodes while maintaining a diffraction-limited, single longitudinal mode output. Research into these devices was motivated by the belief that a series of narrow emitters, each producing a diffraction-limited beam, could be made to emit in phase with each other, if caused to couple together, resulting in a far-field interference pattern consisting of a single, diffraction-limited lobe. While individual emitters could produce output powers within the limitation of catastrophic facet damage, the total output power was expected to scale with the number of emitters.

When considering such devices it is important to distinguish between the two forms of optical confinement that can exist in waveguide-type devices having a variable refractive-index profile. The most familiar form of optical confinement is that where a region of high refractive index is surrounded by a lower index material as in optical fibres or the single-mode diode lasers described above. In this case, often described as a positive-index guide, total internal reflection results in strong confinement of the optical modes of the waveguide structure with a small evanescent field leaking into the surrounding low-index material. In the opposite situation the optical mode propagates in a low-index region surrounded by higher-index material. In this case the confinement is much weaker and, while some of the field is reflected at the boundary, much larger leakage of the field occurs than in the evanescent case. Such confinement is usually described as antiguiding and the confined fields as leaky modes.

The first attempt to produce a coherent diode array used a conventional broad-area double heterostructure with five stripe electrodes defined by proton bombardment on the top contact to form a series of gain-guided emitters [16]. Such devices are inherently of the antiguided type with high leakage from, and consequently strong coupling between, adjacent emitters as the refractive index in the regions of high gain is reduced by the increased carrier concentration, although this was not realised until some years later [17,18]. Although such devices were investigated for several years [19,20,21] diffraction-limited output powers achieved were not significantly higher than those obtained from narrow-stripe single-mode devices. It was also found

that these devices, being weakly guided, could exhibit a marked susceptibility to thermal or gain induced perturbations in the active region resulting in instabilities in the far-field beam profile.

These devices had previously been modelled using simple diffraction theory under the assumption that evanescent coupling occurred between the stripes [22]. It was subsequently realised, however, that the emitters were, in fact, strongly coupled [17] and the device was better modelled as a broad-area laser with a periodic gain perturbation [18,23]. This explained why high diffraction-limited powers were difficult to obtain and why attempts to, as it was thought, improve coupling by linking the proton-defined contacts [24,25] had little beneficial effect on beam quality. Research into these devices as sources of diffraction-limited radiation was largely abandoned as a result of the various problems encountered and interest concentrated on devices with stronger confinement resulting from the definition of the array elements by real refractive index variations fabricated into the device structure.

The use of positive index guides, it was thought, would solve many of these problem. Coupled-mode analysis [26,27] indicated that in-phase operation of the elements of such an array would result in a single-lobed far field and it was thought that strong index-guiding would result in stable, well-defined modes for individual emitters while evanescent coupling would ensure in-phase operation of the array. A number of methods were used to fabricate such arrays [28,29,30,31] with the regions of high gain coinciding with those of high index. Unfortunately, with a few exceptions at low powers [29,30], most operated with the adjacent array elements in antiphase when significantly above threshold, resulting in a non diffraction-limited dual-lobed far field, as this mode of operation resulted in better overlap with the gain distribution [32,33].

Although real-index antiguided structures, where the high gain regions correspond to those of low refractive index, had been fabricated early on in the development of laser diode arrays [34] their development was not at first widely pursued since leaky-mode solutions were not predicted by coupled-mode theory and were recognised to be very lossy for only a few elements. However, for a larger number of elements the

high leakage results in strong coupling between elements rather than increased losses [35]. Furthermore, it was shown that the in-phase array mode could be favoured over the out of phase one [36,37]. In addition, larger refractive index steps could be used to define the waveguides, thus making the structure less susceptible to perturbations in temperature than in the evanescent case where an increased index step reduces the coupling [37]. A number of such devices have been demonstrated [35,38,39,40] yielding powers of up to 10W, with 60% of this in a 2×diffraction limited peak, under pulsed operation [41] and around 1 W, with 75% in a 1.7×diffraction limited peak, in cw operation [42].

Despite these recent successes, array devices offering diffraction limited performance tend to have complex structures, do not appear to be commercially available at the time of this work and are therefore not particularly practical for most purposes. As a result, the above review has been quite brief although more in-depth coverage of the field can be found in reference [15].

It is interesting to note that, despite lack of success as difraction-limited devices, gain guided arrays, using simple proton implanted stripe arrays of electrodes, continued to be used as high brightness, non diffraction-limited sources until quite recently. Such a device is shown in Fig. 4-2 (a) [43]. The preference of these devices over simpler broad-area laser diodes appears to have been due to the controlled current distribution afforded by the array electrode which resulted in less power-dependent instability in the far-field emission pattern. Indeed, a theoretical study in 1991 concluded that the width of the far-field pattern from a broad area device was related to the uniformity of the gain distribution and that improved epitaxial methods could result in higher quality broad-area devices with far-fields comparable to those of gain-guided arrays [44]. This prediction seems to have been fulfilled in recent years as commercial suppliers appear to have replaced gain-guided arrays with broad area devices such as that shown in Fig. 4-2 (b) [8] for high-power, high-brightness applications.

Although a much research has been carried out on the array-type devices described so far, the results obtained in terms of achieving single-mode diffraction-limited

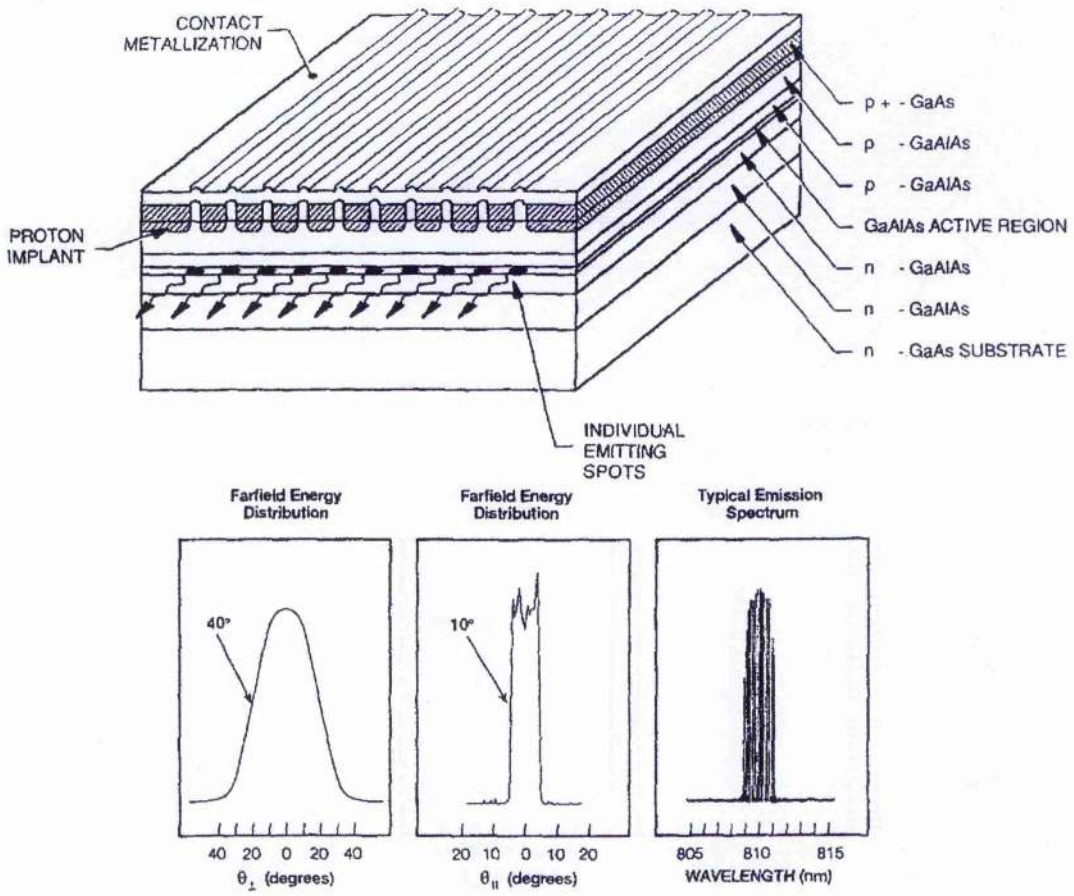

Fig. 4-2 Typical commercial gain-guided laser-diode array (SDL 2400 series c.1990) structure and emission characteristics (left to right, far-field power distributions perpendicular to and parallel to the junction and emission spectrum) [43].

emission have been largely disappointing. Most of the successful developments in this direction have been achieved using alternative schemes.

Nearly 4W, with 50% of the power in a 1.7×diffraction-limited output, has been obtained from an unstable resonator based on a tapered diode-amplifier [45]. An output power of 1W in a diffraction-limited beam was obtained from a similar device with an external-grating [46]. A more recent development has been the angled-grating distributed-feedback laser, or α-DFB [47,48,49]. These are essentially

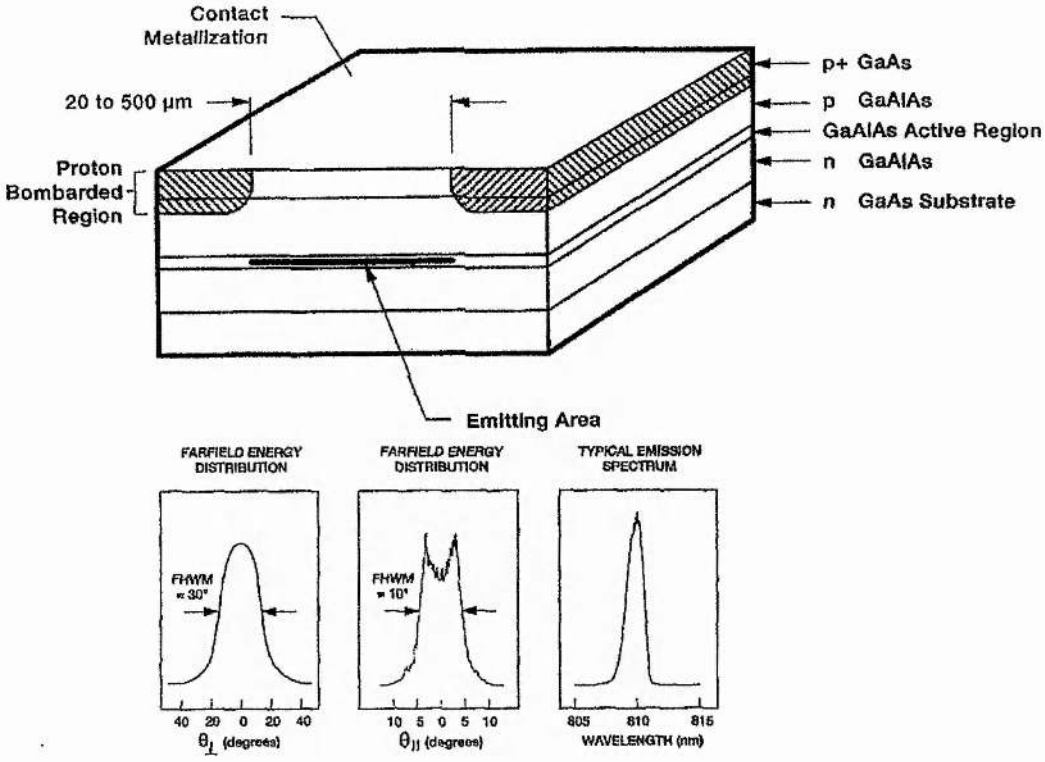

Fig. 4-3 Typical commercial broad-area laser-diode (SDL 2300 series c.1994) structure and emission characteristics (left to right, far-field power distributions perpendicular to and parallel to the junction and emission spectrum) [8].

broad-area devices which use an angled gain stripe and angled Bragg-grating across the area of the device to provide single transverse- and longitudinal-mode operation [50]. Diffraction-limited output powers of up to 1W have been démonstrated [47] and 500-mW commercial devices are currently available [51].

Another particularly successful approach to obtaining high single-mode diffraction-limited powers has been to use one of a number of amplification schemes. In these cases the low-power high, spatial- and spectral-quality emission of a single-mode laser diode such as that shown in Fig. 4-1, acting as a master laser, is amplified to higher powers using another laser-diode type gain element while retaining most of

the spatial and spectral properties of the master laser. These schemes are discussed in the next section.

4.2 Optically-injected diode laser systems.

Systems using a high power semiconductor laser or amplifier under external optical injection to produce a diffraction-limited single-longitudinal-mode output can be divided into two categories. In so-called "injection locked" systems the input beam is resonantly amplified within a normal diode laser to produce several coherent output beams which superpose in the far field to produce a single, near-diffraction-limited lobe. In travelling wave systems only one output beam is produced by the injected beam making either a single or a double (one round trip) pass through the amplifier.

4.2.1 Travelling-wave amplifiers.

The first method of amplifying the output from a low-power master laser to be considered here are the class of devices where no resonance effects are present. Such devices can be categorised as travelling-wave amplifiers and are used in three main configurations. The amplifier can be either of a broad area type, the active area essentially taking the form of a rectangular slab, or of a flared or tapered type where the width of the active area increases from the input end to the output end. In addition, broad area amplifiers offer two potential modes of operation - single pass, where the input and output are from opposite facets, and double pass, where the injected beam enters and leaves by the same facet undergoing reflection from the back facet of the device. These configurations are shown in Fig. 4-4.

Early demonstrations of broad area travelling wave amplifiers made use of arrays [52,53] and broad stripes [54] very similar to the commercially available broad area and array lasers used in multiple pass systems. The main adaptation for travelling wave amplifier use was the antireflection coating of either one or both facets depending on whether a single or double pass configuration was required. Systems demonstrated under cw operation include a single pass arrangement producing 100mW for 1.7mW injected power [52] and a double pass system giving 425mW for

70 mW injected power [53]. A double pass system was also demonstrated driven by a pulsed current source (0.5-5μs pulses with a 10% duty cycle) to allow the use of higher currents without excessive heating occurring [54]. This device produced

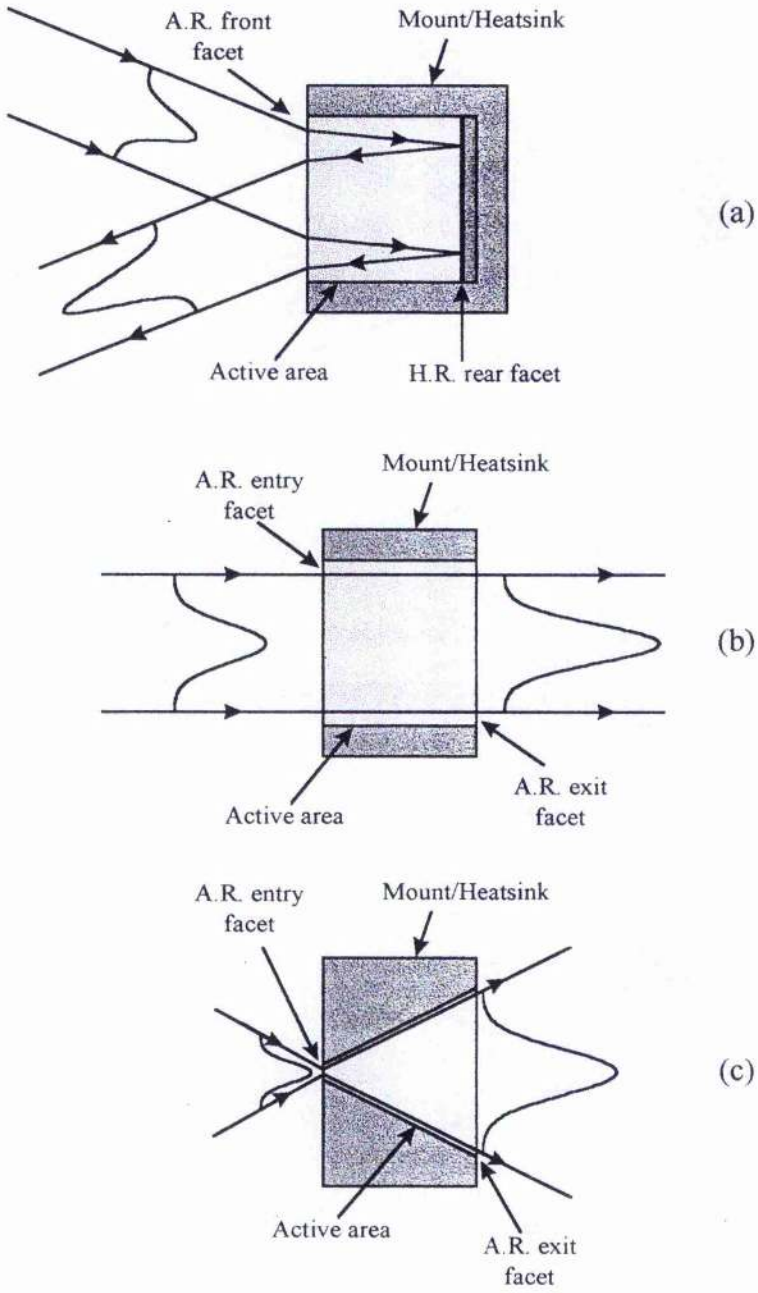

Fig. 4-4 The three principal diode-laser travelling-wave amplifier configurations: (a) Broad-area double pass. (b) Broad-area single pass. (c) Tapered.

output powers of up to 2.5W with input powers of the order of 100mW.

Broad area amplifiers specifically intended for use as travelling wave amplifiers generally have a longer active area than those used as broad area lasers (typically 500-2000μm compared to 250-500μm) and a 400-600μm stripe width. Using such devices operating cw, output powers of 1.1W for 100mW input in a double pass configuration [55] and 3.3W for 400 mW input in a single pass configuration [55,56] have been achieved. Again, higher powers have been obtained by using a pulsed current source to avoid the build up of thermal effects, with outputs of 12W for 500mW input to a double pass system [57] and 21W for 500mW input to a single pass system [58] having been reported, both using a Ti:Sapphire master laser. Using a semiconductor master laser, 11.6W of output for 100mW input has been achieved in a single pass configuration [59]. All used current pulses of 0.3-1μs duration and a 1% duty cycle.

Although the antireflection coatings applied to the facets of such amplifiers typically result in reflectivities of less than 1%, and in many cases less than 0.5%, the high gains achievable in semiconductor devices mean that laser operation is still possible at even relatively low injection currents. This is especially true in the case of double pass devices which have a significantly lower round trip loss than single pass devices due to the high reflectivity of the back facet. Even if lasing does not occur, a round-trip cavity loss approaching unity can result in resonant effects and wavelength dependence in the amplifier gain [54]. To avoid such effects, the amplifier can be operated below threshold with low injected powers of the order of a few milliwatts [52] or (more commonly) operated with high injected powers, of the order of a hundred milliwatts, resulting in strong gain saturation [54-59] which also achieves maximum power extraction from the amplifier. Small signal gains of the order of >20dB have been measured in a double pass system with a front facet reflectivity of around 0.5%, which implies a round trip gain of unity[54]. The same device showed a saturated gain of 10dB with an input power of 250mW resulting in a round trip loss of 13dB and effective suppression of resonant effects. The reduction of Fabry-Perot resonances was further aided by the fact that the beam was injected at an angle of ≈5° to allow separation of the input and output beams. This resulted in any

subsequent passes through the amplifier moving progressively further into the unpumped regions at the sides of the active area and rapidly being absorbed.

The properties of single and double pass travelling wave amplifiers have been studied and compared, both theoretically and experimentally, in some detail and the relative merits of the two configurations assessed [55]. Some of these findings are summarised here. From a practical point of view double pass systems are easier to manufacture and mount since access to only one facet is required whereas in the case of single pass systems the mount and heatsink must be matched to the length of the device to allow both facets to be accessed as shown in Fig. 4-4. The fact that the heatsink does not have to be matched to the device length in the double pass case also allows improved heat dissipation, which is particularly important under cw operating conditions, as the heatsink can extend beyond the device at the high reflectivity end.

In terms of performance, double pass amplifiers also offer a number of advantages over single pass systems. In a single pass system the intensity of the injected beam just after the input facet is relatively low as it has undergone little amplification at this point. This results in the amplifier gain being unsaturated or only weakly saturated leading to reduced power extraction efficiency. In addition, the absence of strong gain saturation by the forward propagating beam in this initial section of the amplifier leads to the availability of residual gain which can amplify the weak reverse propagating beam resulting from the non zero reflectivity of the output facet. Modelling [55] shows that in this region the parasitic reverse propagating beam is able to saturate the gain, thus reducing the gain available to the forward beam.

In the case of a double pass system the reverse propagating beam is simply the second pass through the amplifier. In the region where the gain is only weakly saturated by the forward propagating beam, the reverse beam has a high intensity and saturates the residual gain, achieving efficient power extraction. The combination of the parasitic reverse propagating beam and the region of incomplete gain saturation reduced the output power to 13W for the modelled single pass amplifier as opposed to 16W for a double pass device with conditions otherwise identical. For relatively

low injection powers (100mW) the modelling predicted 30% greater output power for the double pass amplifier than the single pass device.

Several mechanisms are present in both single and double pass amplifiers which can cause degradation of the beam quality. Phase-front distortion can be caused by two lensing mechanisms within the amplifier - one due to transverse variations in the carrier concentration, and therefore refractive index, caused by differing levels of gain saturation and the other due to thermal effects.

Saturation induced lensing, which occurs as a result of the Gaussian nature of the injected beam, has been investigated by measuring the amount of phase front curvature that has to be introduced into the injected beam using an external lens to compensate for the lensing in the amplifier [55]. It was observed that below transparency (ie. with low injection currents when the amplifier does not have gain) absorption at the centre of the beam profile, where the intensity is highest, resulted in higher carrier concentrations, and therefore a lower refractive index, than at the edges. Thus, an effective negative lens was formed. At higher currents gain saturation at the centre of the beam resulted in a lower carrier concentration here and therefore a higher refractive index than at the edges, forming an effective positive lens.

Since the gain saturates at the centre of the Gaussian profile before it does so in the wings, the wings effectively experience higher gain than the centre resulting in a profile which is flattened with respect to the injected beam. This reduces the difference in intensity and therefore in induced carrier concentration between the centre and edge of the beam and causes the lensing effect to saturate at higher gains. It is interesting to note that this saturation induced transverse gain variation and resultant flattening of the beam profile has been observed to result in an amplified beam having a lower angular divergence than the injected beam [54], as it effectively increases the beam-width between the $1/e^2$ points. Although saturation induced lateral variations in carrier density can be reduced by injecting a beam which is broader and therefore more uniform across the aperture of the amplifier this results in a larger discontinuity in amplitude at the edges of the amplifier causing increased diffraction into side lobes in the far field [55].

The other phase-front distortion mechanism, thermal lensing, occurs due to the current heating effects in the amplifier resulting in a temperature gradient from the centre of the device to the edges. This has been shown to lead to a quadratic refractive index profile across the amplifier, forming an effective positive lens [60]. Again, the effect can be compensated by introducing an opposing phase front curvature in the injected beam using external optics [60] and the required extent of this compensation can be used to measure the strength of the thermal lens [55,60].

Comparing the level of compensation required in the cases of short, low duty cycle pulsed current operation, where significant thermal effects are assumed not to occur, and cw operation, a refractive index gradient five times larger in the cw case was observed in a 250×100μm device [60] indicating significant thermal lensing. Another study using a 600×1100μm device showed no significant difference between the pulsed and cw case implying that thermal lensing was small [55]. It seems likely therefore that the extent of thermal lensing depends strongly on the structure and dimensions of the particular device.

Another effect detrimental to beam quality commonly observed in semiconductor amplifiers is filamentation. As mentioned in Section 4.1, this effect has long been known to occur in broad-area laser diodes taking the form of intensity "hotspots" in the transverse near-field profile. It is usually attributed to nonlinear interactions between the carriers and the optical field (i.e. gain depletion by high field intensities results in a local refractive index increase) initiated by small inhomogeneities in the device structure or current density [1,44,61]. Similar effects also occur in travelling-wave diode amplifiers taking the form of a high contrast periodic intensity variation in the near field.

Filamentation in amplifiers was first observed in double pass devices operating at near normal incidence and was seen to be accompanied by a far field change from a single lobe to several peaks of much lower intensity [62]. Theoretical analysis has shown that the phenomenon is caused by a nonlinear interaction between the forward and reverse propagating beams at the device facet [63]. Perturbations in the forward propagating beam are amplified to give a significant spatial variation in the reverse beam. This causes a periodic index variation at the front facet of the device due to

thermal and saturation effects which in turn imposes a spatial variation on the injected forward propagating beam, thus establishing feedback between the input and output beams and allowing the effect to become self sustaining.

Experimental work [62] shows good agreement with the theoretical predictions for double pass structures in terms of filament period as a function of amplifier length. The observed multilobed far field [55,62] is explained as a result of the spatial modulation of the near field, the filaments acting as a series of coherent emitters which interfere in the far field as in the multiple-pass amplifier case. Although the theoretical study does not predict filamentation for single-pass amplifiers, it assumes zero facet reflectivities. Experimental work using single-pass devices with realistic reflectivities of the order of 0.5% has shown filamentation to occur in single-pass structures at normal incidence but at much higher output powers than double-pass devices. Typically, filamentation is seen to occur at output powers of a few hundred mW in double-pass structures [55,62] but only at ≈4W in a single-pass device [55].

Although filamentation is only reported for devices operating around normal incidence (typically ±0.75° [55]) it has been suggested that it negates the advantages of double-pass devices discussed previously. This makes single-pass devices preferable [55], despite the fact that double-pass systems are usually operated at off-normal incidence to allow for the separation of input and output beams. It is possible that filamentation occurs at off normal incidence for higher output powers, making the presence of a strong backward propagating beam undesirable in high power devices. This has been suggested as the reason for the maximum reported powers achieved with single-pass amplifiers being greater than those for double-pass devices, despite the advantages offered by double-pass systems in terms of gain saturation efficiency [63].

Many of the problems associated with broad area amplifiers can be avoided to a large extent by the use of flared or tapered amplifier structures. These devices have a gain region which is narrower in the plane of the junction at the input facet than at the output facet. The angle at which broadening takes place is chosen to allow free diffraction of the beam entering through the aperture formed by the input facet. The main advantages offered by tapered amplifiers are a lower injected power required to

achieve saturation and an increased resistance to most of the beam degradation mechanisms described above.

Typical dimensions for the active area of tapered amplifiers include 10μm at the input facet broadening to 160μm at the output over a length of 1500μm [55,64], 215μm broadening to 450μm over 1500μm [55,65] and 250μm broadening to 500μm again over 1500μm [66]. As can be seen from these dimensions, the width of the input facet is in all cases much less than that of the broad area amplifiers described above (typically 400-600μm). This allows saturation in the region of the input facet across the whole device width to be achieved using lower injected powers than for broad area devices. Published results for the above devices include an output of 2W for 25mW injected power [64], 4.5W for 150mW injected power[65] and 5.25W for 200mW injected power [66] all operating cw, compared to a maximum reported cw output of 3.3W for 400mW injected for a broad area amplifier [55,56].

The lower powers required for saturation allow single transverse- and longitudinal-mode laser diodes to be used as the master laser. Even for low injected powers, reduced saturation levels are an advantage as the reduction in required input power for saturation also allows stabilised, narrow-linewidth external cavity diode lasers to be used as the master laser. These often have output powers of only a few milliwatts but, when combined with a tapered amplifier, yield a source of high-power, near-diffraction-limited beam quality, spectrally pure radiation [67].

Tapering the active region results in a relatively constant power density and level of gain saturation along the length of the amplifier. In addition, the fact that the beam is diverging results in a significant reduction in the power reaching the input facet from the parasitic reverse propagating beam and therefore increases resistance to filament formation [55]. Tapered devices have also shown greater slope efficiencies than broad area amplifiers, a typical example being a differential quantum efficiency of 72% which is claimed to be 20% higher than broad area structures of the same length when strongly injected with 500mW and 40% higher than weakly (100mW) injected broad area devices [55].

To date, tapered amplifiers have been the most successful method for obtaining high, near-diffraction-limited output powers with high spectral purity from all-diode systems. In an amplifier configuration, over 5W has been obtained from both AlGaAs [66] and InGaAs devices [68]. AlGaInP devices have also been demonstrated producing visible powers of over 1.5W [69]. Tapered gain elements have also been used in various external cavity configurations [70,71,72] providing near-diffraction-limited output powers of up to 1W [70].

As a result of their good high-power spatial and spectral properties, tapered-amplifier based systems have been employed in a number of applications. As pump sources for frequency upconversion, they have been used to generate light in the visible [73,74] and ultra-violet [75,76,77,78] regions of the spectrum. Frequency down-conversion has been demonstrated by the use of tapered-amplifier based systems as pump sources for optical parametric oscillators [79,80,81] including the first example of a diode-pumped, continuous, singly-resonant OPO [82]. Amplification of the output of mode-locked diode lasers has allowed high peak powers to be produced in pulses on a picosecond timescale [83,84]. The near-diffraction-limited nature of the output has also allowed tapered-amplifier based systems to be used as pumps for Kerr-lens mode-locked solid-state lasers [85].

The main drawback of tapered amplifiers is their limited availability. As far as can be ascertained, at present only one range of such devices covering a variety of wavelengths is available commercially [86] with a rated output power of 500mW cw. In addition, these devices are considerably more expensive than many other types of diode laser costing 10 to 15 times the price of a typical 100mW single-mode device of the type shown in Fig. 4-1 at the time of this work [87].

4.2.2 Monolithic Master-Oscillator/Power Amplifiers.

When under external injection from a master laser, the above amplifiers together with the master laser form a master oscillator power amplifier (MOPA) system. Clearly, the fact that tapered amplifiers can produce high output powers when injected with power levels readily available from a single mode semiconductor

lasers, and the fact that both can be manufactured using the same materials system (typically GaAs/AlGaAs or InGaAs), makes the monolithic integration of such a MOPA system highly attractive. Several such monolithic MOPAs have been demonstrated [88,89,90,91] and diffraction limited cw output powers of up to 3W in InGaAs [89] and 2.2W in AlGaAs [92] have been achieved. A 1W device operating at 980nm is commercially available [93].

It has been noted, however, that the coupling of the master laser directly to the amplifier with no intervening isolation makes these devices particularly susceptible to even small amounts of feedback. Any optical feedback entering the device passes first through the amplifier section before entering the master laser, thus even small levels of feedback into the device as a whole can result in large levels reaching the master laser. All the above monolithic MOPA systems for which details have been published use distributed Bragg reflector (DBR) master lasers, which are less sensitive to feedback than Fabry-Perot devices, and have amplifier section facet reflectivities of 0.05% as opposed to typically 0.1-0.5% for amplifiers used in discrete MOPA systems. Both these facts would seem to indicate that feedback sensitivity is a significant problem in such devices.

Reports of experimental use of a monolithic MOPA have highlighted the susceptibility to feedback, noting that instabilities were introduced by feedback from the beam shaping optics supplied in the MOPA packaging and even from the antireflection coated input surface of a Faraday isolator used to reduce feedback from subsequent optics [94]. Experimental studies of discrete MOPA systems with a passively mode-locked master laser have noted that isolation is required between the master laser and amplifier sections to achieve mode-locking [95].Without isolation, mode-locking is prevented by amplified spontaneous emission from the amplifier section interfering with the recovery of the saturable absorber used to mode-lock the master laser. The authors point out that this could prevent the implementation of a mode-locked monolithic MOPA.

4.2.3 Injection-Locked High-Power Diode Lasers.

The final amplification scheme to be considered is that commonly described as injection-locking [96]. In this case, the injected beam is focused into a standard broad stripe semiconductor laser or gain-guided array through the front facet. This generally results in the far-field of the slave laser becoming single-lobed in the plane of the junction with the majority of the power falling in a single near-diffraction-limited peak. In addition, the slave laser adopts the spectral properties of the master laser and generally operates on a single longitudinal mode.

Early demonstrations of such systems used multiple emitter coupled semiconductor laser arrays as the amplifier section [96,97,98,99]. The output powers achieved ranged from 105mW for a 3mW injected beam, using a 10 element array [96] to 510 mW for an 11mW injected beam with a 40 element array [99]. More recent demonstrations of injection-locked diode systems have used broad area single stripe lasers as the amplifier element [100,101,102,103] with near-diffraction-limited output powers of up to 400mW being achieved for an injected power of 12mW [102], and a reported 700mW for 15mW injected [103]. However, the published beam profiles of [103] would seem to indicate that the claimed fraction of the output power in the diffraction-limited lobe is somewhat exaggerated. In all cases, for arrays and broad stripes, the output was observed to have the majority of the power concentrated in a single longitudinal mode when under external injection, spectrally matching the output of the master laser.

Injection-locked systems show high sensitivity to beam injection angle and wavelength, exhibiting variation in the angular position of the single far field lobe with changes in the injected wavelength. With one exception [97], where no strong dependence on injection angle was observed, most published work seems to agree on an optimum injection angle to achieve single lobe output of around 4° for both arrays and broad stripe lasers. Variation of the angular position of the single far field lobe with injection wavelength is widely reported as occurring, with more detailed studies of the phenomenon indicating a linear dependence of angle on frequency detuning [97,104]. It has also been observed that for optimum injection locking the injected beam in the plane of the slave-laser junction should be around half to one times the

dimension of the slave-laser facet in this plane and that the injection point should be towards one end of the facet [98,99,100].

Early attempts to explain the behaviour, observed in gain-guided arrays, suffered from the same misconceptions, mentioned in Section 4.1, as studies of the arrays themselves in assuming that these devices could be treated as individual, evanescently-coupled emitters. Thus, early studies considered array supermodes locked in phase and frequency [96], injection into a single "element" of the array [97] and eigenmode analysis of arrays of coupled waveguides [105]. Although several numerical models were developed which showed reasonable agreement with experimental results [106,107,108], these did not provide a great deal of insight into the physical processes involved. The realisation that a more accurate picture of gain-guided arrays was as perturbed broad-area devices [23], along with the fact almost identical results were obtained with broad-area devices [100,101,102], largely resulted in the evanescent-coupling and array-supermode pictures being abandoned. Since these early attempts, two analytical models have been developed which explain the behaviour of injection-locked arrays and broad-area lasers in terms of physical processes and show excellent agreement with experimental results. However, the two physical interpretations are quite different.

The first model to be proposed was that of Abbas et al. [101]. This takes a simple Fabry-Perot view of the broad-area device and assumes that after injection from the master laser the beam then makes several passes through the broad-area laser, being amplified and generating an output beam on each pass. The focusing of the injected beam at the injection point results in the output beams being divergent and overlapping in the far field. This far field superposition results in an interference pattern, similar to that produced by a diffraction grating, consisting of principal maxima interspersed with secondary maxima of much lower intensity. The intensity of the interference pattern is modulated spatially by a Gaussian envelope representing the intensity profile of the injected master beam. It is by limiting the width of this envelope to include only one principal maximum of the interference pattern that the desired single far field lobe is obtained. Although the model was based on a broad stripe system, it is argued that the perturbed-broad-area picture of

gain-guided arrays mentioned above, and the fact that broad stripe and coupled array systems appear to show identical behaviour, indicate that the same processes take place in both and that under relatively strong injection, the perturbation due to gain guiding in arrays becomes relatively insignificant.

The widely observed optimum injection angle of 3-5° is explained by the need for the injected beam to fill the cavity, saturating the gain throughout the device and thus preventing the laser from operating on any free running modes of its own. At larger angles the successive passes of the injected beam cease to overlap leaving areas of unsaturated gain. At smaller angles it is argued that the resulting large overlap between the successive passes makes the system more sensitive to phase front curvature across the beam and to phase variations across the device, resulting in instabilities. It is also pointed out that at smaller angles the successive passes all propagate close to the axis of the device and this may result in unsaturated gain at the edges. This cavity-filling argument also explains the observed requirement for the injection point to be towards one end of the array.

As mentioned above, the injected spot size must be chosen so that its divergence envelope in the far field includes one principal maximum of the interference pattern. For best coupling efficiency of the output into the single lobe, the model predicts that the Gaussian divergence envelope should not be much larger than the interference maximum although close matching of the two results in a high sensitivity to injection angle, i.e. the maximum of the envelope must coincide accurately with the interference maximum. It is interesting to note that in the only paper which reported no dependence of single lobe intensity on injection angle [97] a very small injected beam waist (<5μm in the plane of the junction) was used in an attempt to couple into only one element of the array used in the experiment. This would clearly have resulted in a very broad Gaussian envelope in the far field and variations of a few degrees in the injection angle would not have caused significant changes in the peak intensity.

As previously mentioned, the behaviour commonly observed in multiple pass broad stripe and array systems was usually attributed to in-phase coupled array emitters or superposition of coupled array supermodes. Abbas et al. assert that this is not the

case and demonstrated this (for broad stripes at least) by injecting a broad stripe laser at the centre of the front facet. The angle of injection results in the injected beam making multiple passes through half of the laser, which displayed the usual behaviour of an injected system. The other half of the laser with which the injected beam did not interact displayed normal free running behaviour. From the physical picture proposed by this model, it is clear why some early numerical models, which considered the array as a series of in-phase emitters, showed good agreement with experiment [106].

Another model, published three years later by Verdiell et al. [109], also assumes that arrays behave in essentially the same way as broad-area devices with a perturbation due to gain-guiding effects. However, in this case it is assumed argued that in a free running array the transverse modes are perturbed broad area modes and that under external injection, these modes are locked in phase and frequency and the far field pattern formed by their coherent summation is the observed single lobe. Using this model to investigate the effect of varying the injection beam parameters such as waist dimensions and angle, and comparing the predicted results with experiment [104], similar behaviour to that predicted by the model of Abbas et al. [101], including the optimum injection angle of 4-5° and the variation of angle of the far field maximum with injection wavelength, is observed.

In this case, the various experimentally observed phenomena are explained as follows: Injection at one end of the array results in more efficient locking because overlap with the injected beam is more likely for a greater number of transverse modes. The emission angle of the diffraction-limited lobe steers with injection-frequency as different frequencies couple to different transverse broad-area modes, with higher-order modes resulting in an emission peak at larger angles. The injection-angle must also be appropriate, corresponding to a reflection of the peak emission angle, to couple into the correct set of transverse modes for the injected frequency if a single-lobed output is to be obtained. Effects related to the size of the injected spot are also explained in terms of angular coupling into the transverse modes. A small, divergent spot has a large angular spread and thus couples into many modes inefficiently, but will generally be coupled into some of the modes over

a large frequency range. On the other hand, a large spot will result in a smaller range of angles, thus coupling into only a few modes, and therefore maintaining efficient locking but over only a small frequency range.

Since both models accurately predict the same phenomena, it is difficult to reach any conclusions about which physical picture is the correct one and it is possible that both interpretations are valid under different circumstances. The variation of the locked output power with injected power, both in the case of gain-guided arrays [98] and broad-area devices [101,102], tends to show a rapid increase with low injected powers followed by saturation and little variation at higher injected powers. This behaviour would seem to suggest operation as a saturable amplifier favouring the interpretation of Abbas et al. [101]. However, it could also be argued that this behaviour occurs as an increasing number of broad area modes are phase locked, saturation occurring when all the modes are locked in phase, which would maintain the validity of the model of Verdiell et al. [109].

It might be expected that the near-field distributions in the two cases would show a marked difference, that resulting from a series of coherently emitting beams being different from that caused by a superposition of broad-area modes. Abbas et al. [101] compare experimental and calculated near field profiles, obtaining good agreement for large injection angles but less exact agreement at smaller angles of injection. Verdiell et al. [109] do not carry out any comparison of experimental and theoretical near fields, so it is difficult to comment in this case. It might also be possible to carry out spectrally-resolved studies of near- and far-field patterns to determine whether a superposition of transverse modes or resonant amplification is occurring. Abbas et al. [101] did this in a limited way, resolving only emission at the injected wavelength for some near-field measurements. However, it is difficult to draw any firm conclusions from the results. Verdiell et al. [109] carried out no spectrally-resolved measurements.

It should be noted that neither the experimental results nor the models exhibit behaviour which would be considered injection locking in the conventional sense and, as has been pointed out [101], this makes the term somewhat inaccurate when

applied to such systems. However, the term remains widely used in the literature in this context and is used here for consistency.

Typical injection-locked systems have a configuration similar to that shown in Fig. 4-5. The collimated output from the master laser passes through an optical isolator to prevent feedback from the high-power laser destabilising the master laser. A cylindrical lens, acting in the plane of the diode junctions, in combination with a spherical collimating lens shapes the beam to give the correct injected waist and angle at the broad-area laser facet. The spherical collimating lens also collimates the highly divergent output of the broad-area laser perpendicular to the junction plane. The off-axis injection results in an angular separation of the input and output beams in the junction plane, allowing a mirror to be used to separate the output.

In addition to master-laser injected systems similar to that shown in Fig. 4-5, a number of systems have been demonstrated where the injected power is provided by the output of the injection-locked array or broad-area laser itself. These have included external-cavity configurations which preferentially feed back from the injection-locked far field profile of the device using narrow-stripe mirrors or slits [110,111,112,113], angled-mirror cavities [114,115,116], or optical fibre rings [117]. Phase-conjugate-mirror systems have also been used to injection-lock broad-area lasers and arrays both in master-laser systems [118,119,120] and external cavities

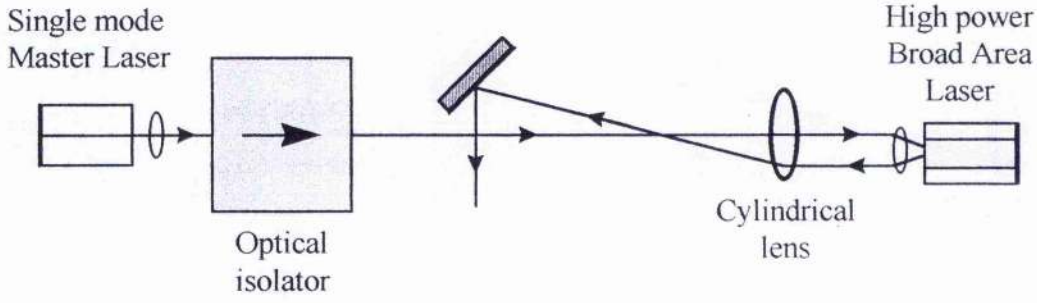

Fig. 4-5 Typical injection-locked diode laser system viewed in the plane of the diode junctions.

[121,122]. Such systems have the advantage that the phase-conjugate feedback automatically couples into the high-gain region of the array making the system self-aligning [118,121]

Injection-locked systems have been used in a number of applications including second-harmonic generation [123] and the pumping of optical parametric oscillators [124,125] and solid-state lasers [126,127,128,129]. However, in recent years the complexity of their alignment and operation has largely resulted in their being superseded by simpler tapered-amplifier systems.

4.3 Modelling of injection-locked broad-area diode lasers.

The model described by Abbas et al. [101] is useful for investigating and demonstrating the properties of an injection-locked broad area laser. The basis for this model is shown schematically in Fig. 4-6. The injected Gaussian beam is incident on the front facet of the device, which has a width d and a depth L, at an injection angle θ_o (highly exaggerated in the diagram) and at a point (x_{in}, z_{in}). It undergoes refraction into the device resulting in an internal injection angle θ_i. The minimum beam waist is assumed to occur at the injection point on the front facet. Upon entering the device, the beam undergoes multiple reflections, resulting in an output beam exiting the front facet on each round trip (for clarity, only two round trips are shown in this case).

For each output beam, the apparent location of the beam waist in free space is at some point behind the device having coordinates (x_a, z_a) in the standard coordinate system shown which has its origin at the centre of the front facet . By making this virtual waist the origin of an alternative coordinate system having its z-axis aligned with the direction of propagation, and considering the divergence in the x-z plane (ie. as viewed in Fig. 4-6), the Gaussian beam parameters, and thus the amplitude of the E-field disturbance, can be calculated at any point in space using standard Gaussian beam propagation theory.

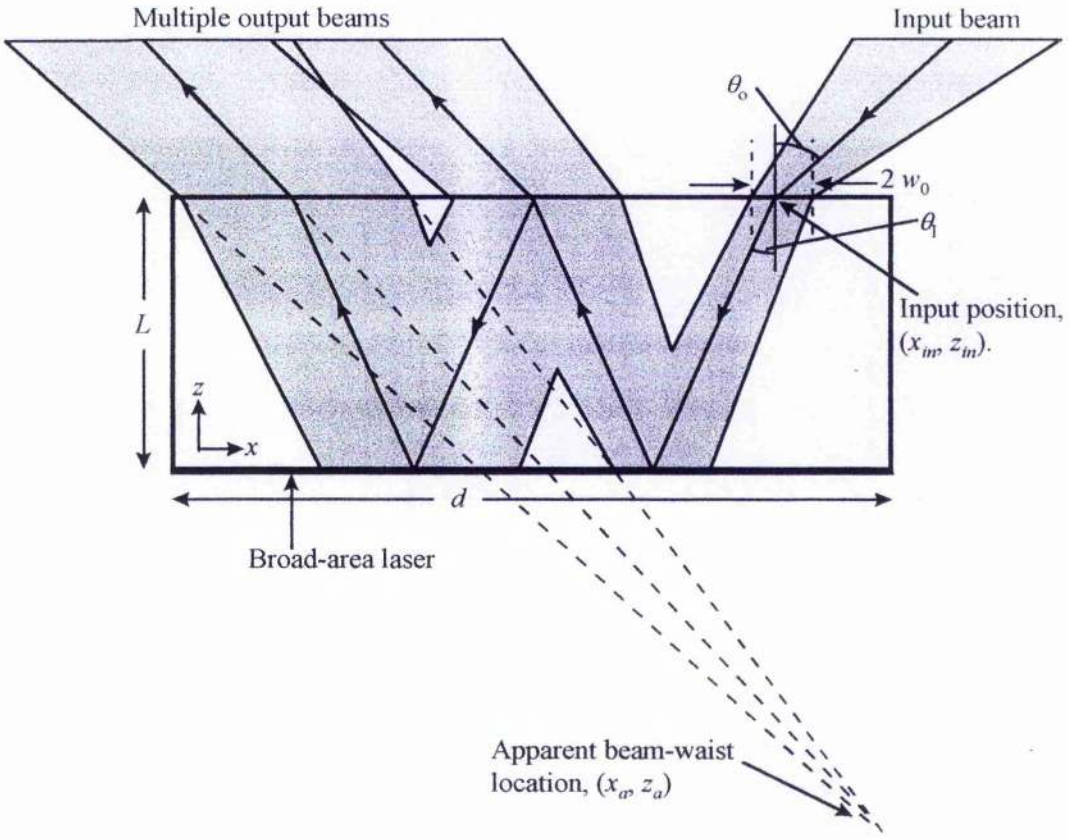

Fig. 4-6 Schematic diagram of injection-locked broad-area laser used in modelling calculations.

Although the higher refractive index of the amplifier medium reduces the rate at which the beam diverges within it, thus causing the beam to appear to have propagated over an equivalent free space distance less than the physical distance it has travelled from the beam waist (and resulting in the virtual beam waist at (x_a, z_a)) the higher index medium implies a greater optical path length. As a result, from the point of view of phase, the beam waist appears to occur at a point (x_p, z_p), which is different from (x_a, z_a). Thus another coordinate system, with its origin at (x_p, z_p), must be used to calculate the phase of the output beam at any point along its path. For the jth output beam, the co-ordinates of the amplitude (divergence) and phase origins, respectively, are given by:

$$x_{aj} = x_{in} + j\left(\frac{L'}{n}\sin\theta_o - 2L\tan\theta_I\right) \quad (4\text{-}1\ a)$$

$$z_{aj} = -j\frac{L'}{n}\cos\theta_o \quad (4\text{-}1\ b)$$

$$x_{pj} = x_{in} + j\left(L'n\sin\theta_o - 2L\tan\theta_I\right) \quad (4\text{-}2\ a)$$

$$z_{pj} = -jL'n\cos\theta_o \quad (4\text{-}2\ b)$$

where L' is the physical path length of a double pass through the broad-area laser and is given by:

$$L' = \frac{2L}{\cos\theta_I} \quad (4\text{-}3)$$

To obtain the E-field due to a single output beam at a given point in space, the co-ordinates of the point (x, z) are transformed into the alternative co-ordinate system for that beam, giving new coordinates (x'_{aj}, z'_{aj}) for the Gaussian beam properties and (x'_{pj}, z'_{pj}) for the phase.

These coordinates are then used to calculate the E-field using the standard Gaussian-wave equation [130]:

$$E_j(x,z) = E_o\frac{w_o}{w}\exp\left(-i\left[k_o z'_{pj} - \eta\right] - (x'_{aj})^2\left(\frac{1}{w^2} + \frac{ik_o}{2R}\right)\right) \quad (4\text{-}4)$$

where:

$$w^2 = w_o^2\left[1 + \left(\frac{\lambda\, z'_{aj}}{\pi\, w_o^2}\right)^2\right] \quad (4\text{-}5\ a)$$

$$\eta = \tan^{-1}\left(\frac{\lambda\, z'_{aj}}{\pi\, w_o^2}\right) \quad (4\text{-}5\ b)$$

$$R = z'_{aj}\left[1 + \left(\frac{\pi\, w_o^2}{\lambda\, z'_{aj}}\right)^2\right] \quad (4\text{-}5\ c)$$

$$k_o = \frac{2\pi}{\lambda} \tag{4-5 d}$$

and w_0 is the half width of the beam between the e^{-2} power points in the x-z plane.

The above formulation is slightly different from that used by Abbas et al. [101] in several respects. Firstly, the factor w_o/w in equation (4-4) replaces $\sqrt{w_o/w}$ used by in [101]. Secondly, Abbas et al. [101] introduce a factor of 1/2 before the inverse tangent term in equation(4-5 b). The equations in the forms given above emerge directly from the derivation of the Gaussian wave equation and are of the form used by most other authors including the source of equation (4-4) [130], as cited by Abbas et al. [101]. In fact these changes have no qualitative effect (e.g. number, positions or relative magnitude of maxima) on the far field patterns obtained using the model, although they do produce significantly different near field results. In addition, in equation (4-4) the peak amplitude of the distribution, E_o, is normalised for the modelling carried out here so that ratio of E_o to w_o remains constant. This is equivalent to using a constant injected power with all beam waists.

The total resultant E-field amplitude at a given point is obtained by adding the contributions from each of the output beams. Thus for N beams:

$$E_T(x,y) = \sum_{j=0}^{N} E_j(x,y) \tag{4-6}$$

The intensity is then calculated by squaring the modulus of the total E-field amplitude:

$$I(x,y) = \left|E_T(x,y)\right|^2 \tag{4-7}$$

The number of emitted beams, N, is obtained by calculating the number of round trips necessary to traverse the device from the injection point using:

$$N = \frac{x_{in} + \frac{d}{2}}{2L\tan(\theta_i)} \tag{4-8}$$

and then taking the integer part of this result as the number of beams.

Apart from dictating the number of beams, the effects of interaction with the sides of the device (e.g. partial clipping of a beam, waveguiding effects, etc.) are ignored. The round trip gain for each beam is assumed to be unity and the refractive index is assumed to be constant throughout the device (a value of n=3.6 is assumed).

The resultant far field intensity profile is calculated as a function of angle from the normal to the device facet. The x and z coordinates for a given angle and radial distance from the device, r, are calculated using:

$$x_\theta = r\sin\theta \tag{4-9}$$

$$y_\theta = r\cos\theta \tag{4-9}$$

The radial distance used must be large enough to ensure full overlap of all the emitted beams. This will be the case if the angle subtended by the front facet at a distance r from the facet is small compared to the diffraction angle of a beam having a waist which fills the facet. In practice, the criterion used was that the angle subtended by the facet of width d at distance r should be 10% of the diffraction angle. This results in a value for r given by:

$$r = 10\frac{\pi d^2}{4\lambda} \tag{4-10}$$

which was used throughout the modelling.

The far field intensity distributions obtained by Abbas et al. [101] using the model agree very well with his experimental results. The conditions used in the paper (injection angle, beam waist diameter, wavelength and device dimensions) to obtain various results were put into the model and the resultant far field profiles compared with those obtained by Abbas et al. [101] to verify that the model was working

correctly. Once this had been done, modelling was carried out for a Spectra Diode Labs (SDL-2362) device having a stripe width of d=100μm and operating at a wavelength of 810nm. Although the length, L, was not supplied in the device specifications, the published description of a similar device [131] gave a length of 250μm and this value was used in the calculations.

The interference pattern generated by a series of coherent emitters is familiar (e.g. from a diffraction grating) as a series of principal maxima interspersed with much less intense secondary maxima. In the case of the output from a multiple pass externally injected broad area laser, this interference pattern is modulated by the Gaussian intensity envelope of the divergent injected beam. This is illustrated by Fig. 4-7 which shows the far field pattern produced by the model for a beam injected at 3° and having a 5μm beam waist (i.e. w_0=2.5μm).

Increasing the injected beam waist diameter results in a narrower Gaussian envelope,

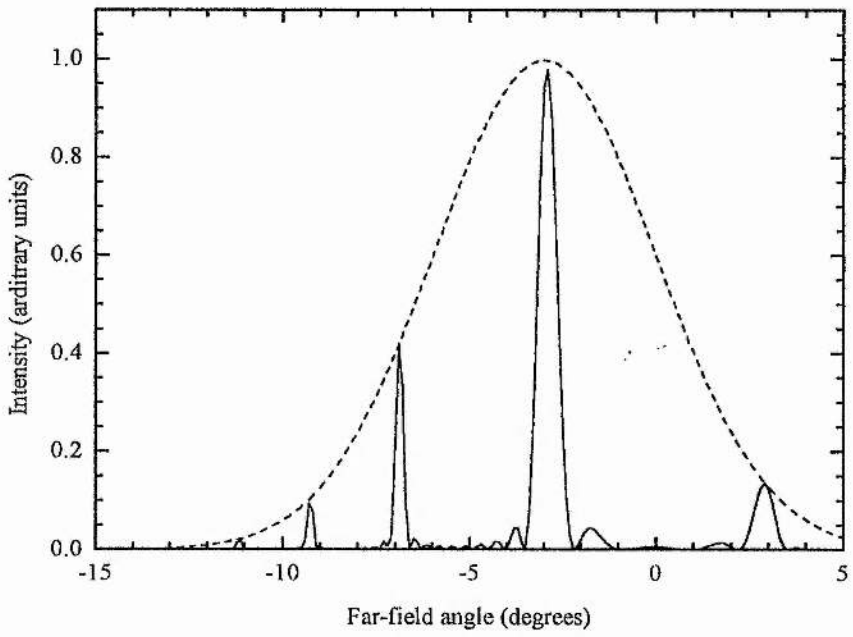

Fig. 4-7 Calculated far-field pattern for a 5-μm diameter beam waist injected at 3° to the facet normal.

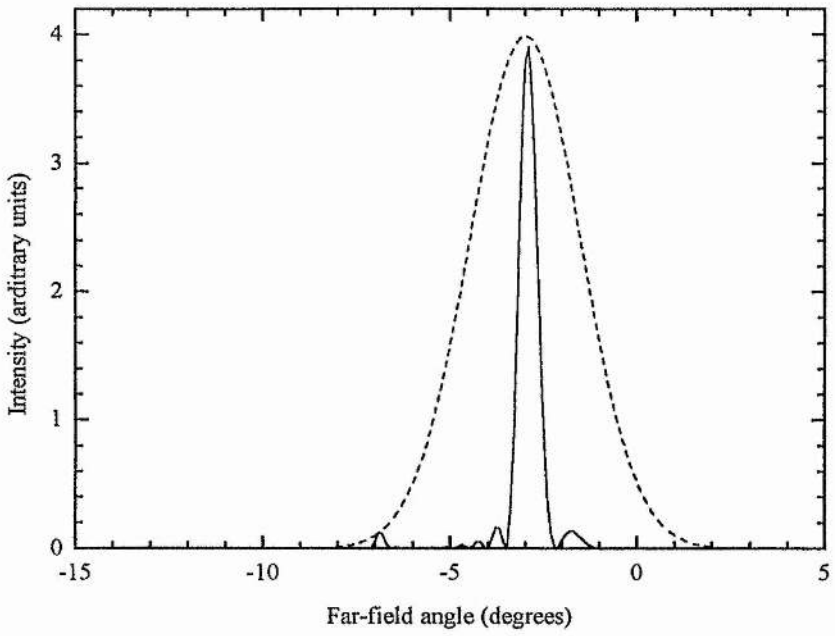

Fig. 4-8 Calculated far-field pattern for a 10-μm diameter beam waist injected at 3° to the facet normal.

as shown in Fig. 4-8. In this case, a 10μm beam waist was used with all other conditions unchanged. Although the envelope now only includes one principal maximum, it is still much broader than this intensity peak. It would, therefore, be expected that much of the output power would fall outside this main peak. It should be remembered that the calculations carried out here only represent the interference effects resulting from the injection-locked output of the broad-area laser and do not make any predictions about the free-running (i.e. unlocked) output of the device. In the case where a significant fraction of the output falls outside one of the principal interference maxima it would be expected that this would couple into the free-running output power of the device and would, therefore, not be of use as a near-diffraction-limited source.

To improve the efficiency of coupling into the required single lobe, the width of the envelope can be further reduced by increasing the injected beam waist still more. Fig. 4-9 shows the far field intensity profile for an injected beam having a 25μm

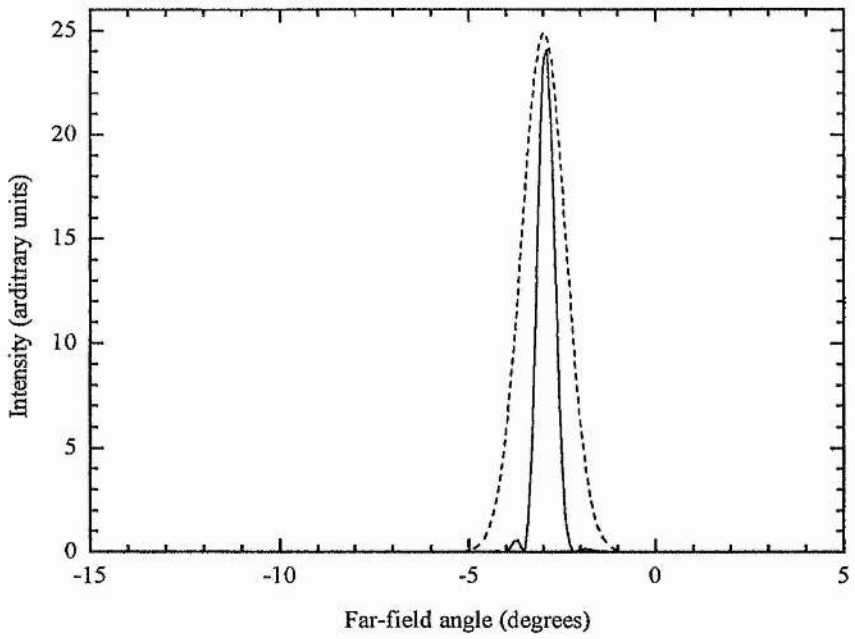

Fig. 4-9 Calculated far-field pattern for a 25-μm diameter beam waist injected at 3° to the facet normal.

waist diameter with all other conditions as before. In this, case the Gaussian envelope is approximately twice the width of the interference pattern maximum and virtually all of the pattern, but the required single lobe, is suppressed. Obviously, the best coupling of the output into a single lobe would be obtained if the width of the Gaussian envelope were closely matched to the width of the interference pattern maximum. This situation is shown Fig. 4-10, where a 50μm beam waist was used. All side-lobes have now been suppressed and virtually all of the output contributes constructively to the single central lobe.

In all the modelling results presented so far, the injection point on the front facet was at a point on the front facet x_{in}=25μm or a distance of 25μm from the right hand side of the device, as shown in Fig. 4-6. This is as far to the right as the injection point can be without clipping the injected beam for the largest beam waist diameter illustrated here (25μm) although an injection point further to the right could have been used for the smaller beam waists. However, by using the same injection point

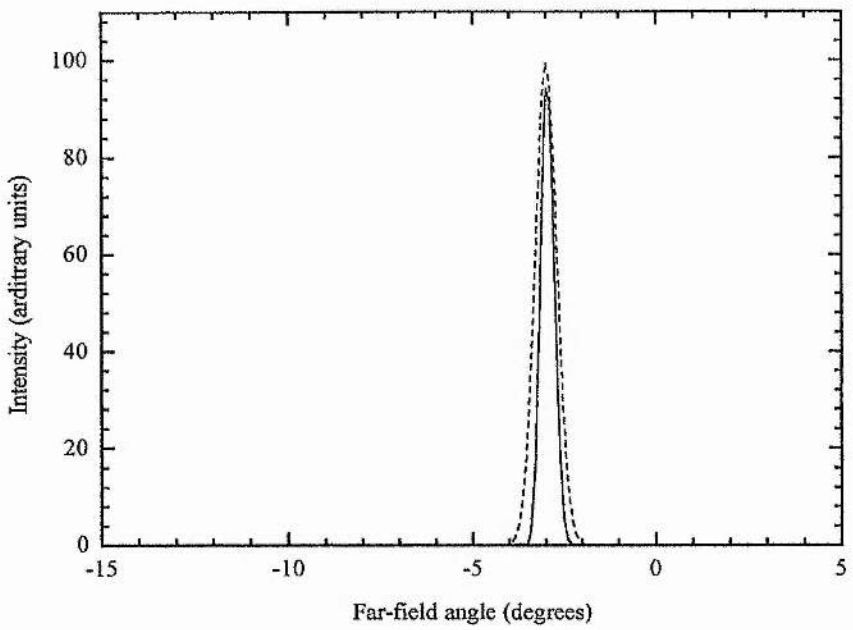

Fig. 4-10 Calculated far-field pattern for a 50-μm diameter beam waist injected at 3° to the facet normal.

for all beam waists the number of round trips, and therefore the number of output beams, remains constant (in this case 10). Due to the normalisation of E_o in equation (4-4) mentioned above, this results in the same total output power in all cases making the relative intensity scale on all the far field patterns illustrated directly comparable.

This direct comparability allows interesting contrasts to be made between the results for various beam waist diameters in terms of the peak intensity that is achieved. Obviously, for the 5μm and 10μm beam waist cases (Fig. 4-7 and Fig. 4-8) where the Gaussian envelope covers a much larger angular range than the interference pattern maximum, the peak intensity is much lower than in the case of narrower envelopes (Fig. 4-9 and Fig. 4-10). Perhaps more significant is the difference between the 25μm beam waist case (Fig. 4-9) and the 50μm case (Fig. 4-10). Although there is little qualitative difference between the two, it can be seen that the closer matching of the Gaussian envelope shown in Fig. 4-10 results in a significant increase in the peak intensity. Clearly maximum coupling will be achieved with an envelope having a

width less than or equal to that of the interference maximum. It would therefore seem desirable to have as large a beam waist diameter, and therefore as narrow a Gaussian envelope, as possible. However, as will be shown, this is not necessarily the case.

Although Abbas et al. [101] note that angular steering of the far field intensity maximum occurs as the operating wavelength of the device is varied, and demonstrate this experimentally, they do not use the model to demonstrate this effect. Obviously, from the point of view of developing a practical tunable source based on an injection-locked system, the extent of the angular variation of the output beam with changes in wavelength is an important consideration. Modelling of this effect gives a useful insight into the possible limitations of such a system.

Fig. 4-11 shows the tuning characteristics for a 10μm diameter injected beam at an angle of 3° and a central wavelength of 810nm (i.e. the same conditions as Fig. 4-8). The solid plot shows the variation in angular position of the intensity maximum as

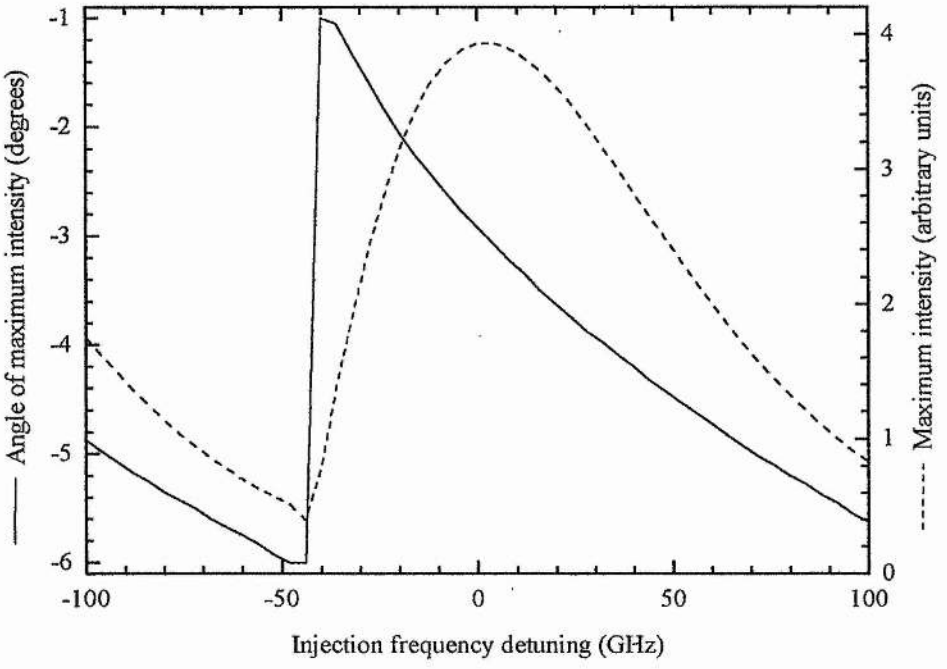

Fig. 4-11 Tuning characteristics for beam injected at 3° with 10 μm waist.

the wavelength is varied and the dashed plot shows the peak intensity of this maximum.

In effect tuning causes the interference pattern to move across the window formed by the Gaussian envelope. This can be seen to occur in Fig. 4-11, where the angular position of the maximum varies smoothly as one of the interference pattern maxima is swept across the Gaussian envelope. At a frequency detuning of around -45GHz, the position of the intensity maximum makes a sudden change in angular position as another maximum of the interference pattern moves out of the wing of the Gaussian envelope and takes over as the most intense point in the distribution. As the tuning continues further, the position of this new peak is seen to sweep smoothly across the Gaussian envelope in the first plot, its intensity tracing out the angular variation of the envelope's intensity, as can be seen in the second plot.

If a larger beam waist is used, the reduced angular width of the Gaussian envelope becomes less than the separation of the principal maxima of the interference pattern.

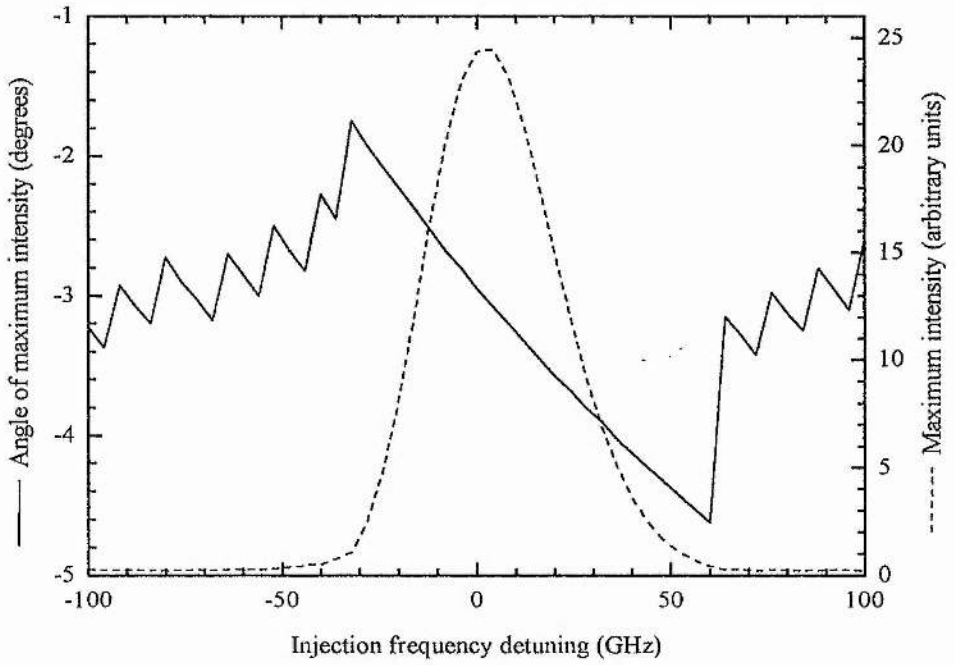

Fig. 4-12 Tuning characteristics for beam injected at 3° with 25μm waist.

This is shown in Fig. 4-12, where a 25μm beam waist was used (same conditions as Fig. 4-9). The initial rapid variation, with many discontinuities, in the angular position of the maximum intensity is due to secondary peaks in the interference pattern moving across the Gaussian envelope.

It can be seen from Fig. 4-12 that these are all of very low intensity. At a detuning of approximately -30GHz one of the principal maxima of the interference pattern falls within the envelope and tunes smoothly across it. Again, the second plot shows the maximum following the intensity profile of the envelope as it moves.

Increasing the beam waist to 50μm (i.e. the same conditions as the far field distribution of Fig. 4-10) results in the tuning characteristics shown in Fig. 4-13. Clearly, these results are very similar to those shown in Fig. 4-12, the various features occurring for the same reasons. However, it can be seen that the narrower Gaussian envelope has reduced the range over which smooth tuning occurs from around 90 GHz in Fig. 4-12 to approximately 40 GHz in Fig. 4-13.

The locking bandwidth of a multiple pass system is defined by Goldberg [96] as the

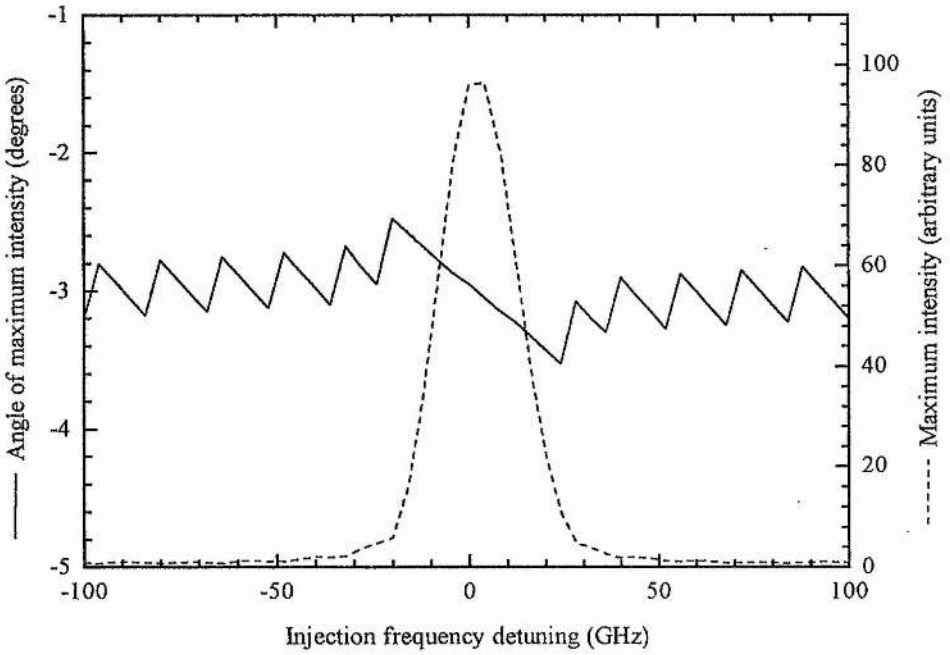

Fig. 4-13 Tuning characteristics for beam injected at 3° with 50μm waist.

frequency range over which the single lobe height is at least 50% of its maximum value. This definition results in locking bandwidths of approximately 100 GHz for the 10μm beam waist, 50 GHz for the 25μm waist and 25 GHz for the 50μm waist.

The above results show that the requirements for achieving efficient coupling of the broad area laser output into a single lobe, and those for allowing a large continuously tunable range, are to some extent mutually incompatible. While the former requires as narrow a Gaussian envelope, and therefore as broad an injected beam waist, as possible, the opposite is true in the latter case. However, most applications requiring broad tuning would be unlikely to tolerate the angular variation (and therefore translation) of the beam that this implies. Thus, in practice, the tuning range would be limited by the tolerable angular variation and the beam waist would be chosen to give the narrowest Gaussian envelope which would accommodate this range without introducing too large a variation in intensity with wavelength.

The tuning range in Fig. 4-11 to Fig. 4-13 of ±100 GHz corresponds to a change in

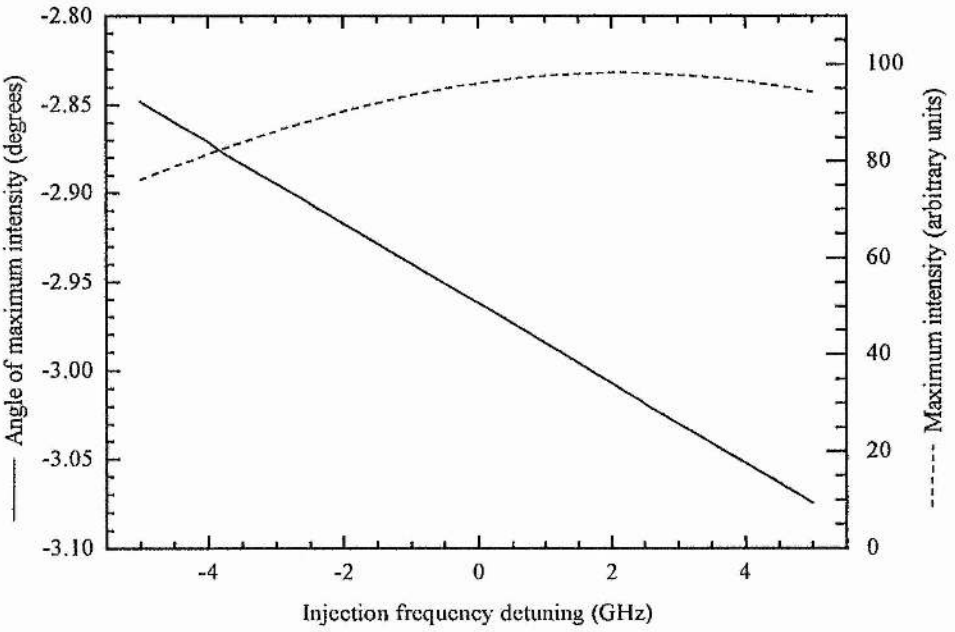

Fig. 4-14 Tuning characteristics over 10 GHz for a 50 micron beam waist injected at 3°.

wavelength of ±0.2 nm at 810 nm. In terms of a practical example, this is relatively large compared to the tolerable pump-frequency tuning range for a typical doubly resonant OPO. Fig. 4-14 shows the tuning characteristics for the 50μm beam waist over a more realistically useful tuning range of ±5 GHz, which is similar to the pump tuning range of ± 4.5 GHz reported for a servo locked DRO [132]. The asymmetry of the intensity variation curve is due to the chosen injection angle of 3° not coinciding exactly with the centre of one of the principal maxima of the interference pattern for the central wavelength of 810nm. The angular variation across the tuning range of approximately 0.2° represents a beam translation of 3.5 mm per metre of propagation and the intensity shows a variation of 20% over this tuning range.

The implications of the modelling can be summarized as follows:

To obtain maximum coupling of the output power into a single far field lobe at a fixed wavelength, the Gaussian divergence envelope of the input beam would ideally be matched as closely as possible in angular position and width to the principal maximum of the interference pattern. Doing this, however, will make even a nominally fixed frequency system highly sensitive to small variations in both wavelength and input beam angle, thus in practice a slightly wider Gaussian envelope than required for optimal coupling into the single lobe should be used.

If tuning of the system is necessary, the width of the Gaussian envelope (and therefore the input beam waist) will be determined by the smooth tuning range required, a broader envelope (and therefore narrower beam waist) being necessary for a greater tuning range. This will result in a reduction in the maximum intensity achievable when compared to the fixed frequency case. The useful smooth tuning range will probably be limited by the tolerance of subsequent devices (e.g. an OPO) to the angular variation and translation of the beam caused by tuning.

For greater wavelength coverage, the centre wavelength of the smooth tuning range could be varied. This would require the injection angle to be adjusted to match the centre of the Gaussian envelope with the new position of the interference maximum. Subsequent optical systems or devices would have to be realigned to compensate for the significant changes in beam angle and position this larger wavelength change

would produce. Fig. 4-11 to Fig. 4-13 show that tuning through a few tens of GHz can cause angular variations of 1°, corresponding to a beam translation of approximately 17mm per metre of propagation length.

4.4 Conclusions.

Of the various methods for obtaining high spatial and spectral quality output from laser-diode based sources discussed in this chapter, tapered-amplifier systems are clearly the most attractive from a technical point of view. Compared to injection-locked systems they are relatively simple and amplify the output of the master laser without any injection-angle or wavelength related variations in output power or angle. In addition, the cw output powers achieved with tapered-amplifier systems are significantly larger than those obtained from injection-locked devices.

By contrast, injection-locked devices require complex optical systems and careful control of the master-laser beam parameters to reliably obtain high-power near-diffraction-limited output. As a result, they are not generally robust systems and are therefore unsuitable for most practical applications. In one important practical respect, however, injection-locked systems have a clear advantage. Both the laser diodes required for an injection-locked system are commercially available at relatively low cost while, as mentioned in Section 4.2.1, the only commercially available tapered amplifiers are considerably more expensive and not specified for significantly higher output powers than those typical produced by injection-locked systems.

As a result, it was decided to use an injection-locked system for the work described in this thesis. While not necessarily practical for the development of robust and reliable diode-pumped devices, an injection-locked system represents a useful laboratory source of several hundred milliwatts of single-frequency, near-diffraction-limited output. As such it makes a useful test-bed system for the investigation of solid-state lasers and optical parametric oscillators pumped directly by diode-laser based sources having high spatial and spectral quality.

4.5 References.

1 G.H.B. Thompson, "A Theory for filamentation in semiconductor lasers including the dependence of dielectric constant on injected carrier density," Opto-electronics **4**, 257-310 (1972).

2 J.C. Dyment, "Hermite-Gaussian mode patterns in GaAs junction lasers," Appl. Phys. Lett. **10**, 84-86 (1967).

3 T.H. Zachos, "Gaussian beams from GaAs junctions," Appl. Phys. Lett. **12**, 318-320 (1968).

4 J.C. Dyment, L.A. D'Asaro, J.C. North, B.I. Miller and J.E. Ripper, "Proton-bombardment formation of stripe-geometry heterostructure lasers for 300 K CW operation," Proc. IEEE **60**, 726-728 (1972).

5 T. Tsukada, "GaAs-$Ga_{1-x}Al_xAs$ buried-heterostructure injection lasers," J. Appl. Phys. **45**, 4899-4906 (1974).

6 K. Aiki, M. Nakamura, T. Kuroda and J. Umeda, "Channeled-substrate planar structure (AlGa)As injection lasers," Appl. Phys. Lett. **30**, 649-651 (1977).

7 K. Aiki, M. Nakamura, T. Kuroda, J. Umeda, R. Ito, N. Chinone and M. Maeda, "Transverse mode stabilized $Al_xGa_{1-x}As$ injection lasers with channeled-substrate-planar structure," IEEE J. Quantum Electron. **QE-14**, 89-94 (1978).

8 SDL laser diode operators manual and technical notes, SDL Inc,. San Jose, California (1994).

9 C.H. Henry, P.M. Petroff, R.A. Logan and F.R. Merritt, "Catastrophic damage of $Al_xGa_{1-x}As$ double-heterostructure laser material," J. Appl. Phys. **50**, 3721-3732 (1979).

10 K. Wakao, N. Takagi, K. Shima, K. Hanamitsu, K.-I. Hori and M. Takusagawa, "Catastrophic degradation level of visible and infrared GaAlAs lasers," Appl. Phys. Lett. **41**, 1113-1115 (1982).

11 T. Shibutani, M. Kume, K. Hamada, H. Shimizu, K. Itoh, G. Kano and I. Teramoto, "A novel high-power laser structure with current-blocked regions near cavity facets," IEEE J. Quantum Electron. **QE-23**, 760-763 (1987).

12 H. Jaeckel, G.-L. Bona, P. Buchmann, H.P. Meier, P. Vettiger, W.J. Kozlovsky and W. Lenth, "Very high-power (425mW) AlGaAs SQW-GRINSCH ridge laser with frequency-doubled output (41mW at 428 nm)," IEEE J. Quantum Electron **27**, 1560-1567 (1991).

13 O. Imafuji, T. Takayama, H. Sugiura, M. Yuri, H. Naito, M. Kume and K. Itoh, "600 mW single-mode GaAlAs triple-quantum-well laser with a new index-guided structure," IEEE J. Quantum Electron. **29**, 1889-1894 (1993).

14 D. Welch, R. Craig, W Streifer and D. Scifres, "High reliability, high power, single mode laser diodes," Electron. Lett. **26**, 1481-1483 (1990).

15 D. Botez and D.R. Scifres, "Diode laser arrays," Cambridge Studies in Modern Optics, Cambridge University Press, Cambridge, UK (1994).

16 D.R. Scifres, R.D. Burnham and W. Streifer, "Phase-locked semiconductor laser array," Appl. Phys. Lett. **33**, 1015-1017 (1979).

17 E. Kapon, C. Lindsay, J. Katz, S. Margalit and A. Yariv, "Coupling mechanism of gain-guided integrated semiconductor laser arrays," Appl. Phys. Lett. **44**, 389-391 (1984).

18 G.R. Hadley, J.P. Hohimer and A. Owyoung, "High-order (v>10) eigenmodes in ten-stripe gain-guided diode laser arrays," Appl. Phys. Lett. **49**, 684-686 (1986).

19 D. Scifres, R.D. Burnham, W. Streifer and M. Bernstein, "Lateral beam collimation of a phased array semiconductor laser," Appl. Phys. Lett. **41**, 614-616 (1982).

20 D.R. Scifres, C. Lindström, R.D. Burnham, W. Streifer and T.L. Paoli, "Phase-locked (GaAl)As laser diode emitting 2.6 W CW from a single mirror," Electron. Lett. **19**, 169-171 (1983).

21 D.R. Scifres, R.D. Burnham, C. Lindström, W. Streifer and T.L. Paoli, "Phase-locked (GaAl)As laser emitting 1.5 W CW per mirror," Appl. Phys. Lett. **42**, 645-647 (1983).

22 D.R. Scifres, W. Streifer and R.D. Burnham, "Experimental and analytical studies of coupled multiple stripe diode lasers," IEEE J. Quantum Electron. **QE-15**, 917-922 (1979).

23 J.P. Hohimer, G.R. Hadley and A. Owyoung, "Interelement coupling in gain-guided diode laser arrays," Appl. Phys. Lett. **48**, 1504-1506 (1986).

24 D.R. Scifres, W. Streifer and R.D. Burnham, "High-power coupled-multiple-stripe phase-locked injection laser," Appl. Phys. Lett. **34**, 259-261 (1979).

25 D.R. Scifres, W. Streifer and R.D. Burnham, "High-power coupled multiple stripe quantum well injection lasers," Appl. Phys. Lett. **41**, 118-120 (1982).

26 J.K. Butler, D.E. Ackley and D. Botez, "Coupled-mode analysis of phase-locked injection laser arrays," Appl. Phys. Lett. **44**, 293-295 (1984).

27 E. Kapon, J. Katz and A. Yariv, "Supermode analysis of phase-locked arrays of semiconductor lasers," Opt. Lett. **10**, 125-127 (1984).

28 D.E. Ackley, "Single longitudinal mode operation of high power multiple-stripe injection lasers," Appl. Phys. Lett. **42**, 152-154 (1983).

29 Y. Twu, A. Dienes, S. Wang and J.R. Whinnery, "High power coupled ridge waveguide semiconductor laser arrays," Appl. Phys. Lett. **45**, 709-711 (1984).

30 S. Mukai, C. Lindsey, J. Katz, E. Kapon, Z. Rav-Noy, S. Margalit and A. Yariv, "Fundamental mode oscillation of a buried ridge waveguide laser array," Appl. Phys. Lett. **45**, 834-835 (1984).

31 E. Kapon, L.T. Lu, Z. Rav-Noy, M. Yi, S. Margalit and A. Yariv, "Phased arrays of buried-ridge InP/InGaAsP diode lasers," Appl. Phys. Lett. **46**, 136-138 (1985).

32 S.R. Chinn and R.J. Spiers, "Modal gain in coupled-stripe lasers," IEEE J. Quantum Electron. **QE-20**, 358-363 (1984).

33 W. Streifer, A. Hardy, R.D. Burnham and D. Scrifes, "Single-lobe phased-array diode lasers," Electron. Lett. **21**, 118-119 (1985).

34 D.E. Ackley and R.W.H. Englemann, "High-power leaky-mode multiple-stripe laser," Appl. Phys. Lett. **39**, 27-29 (1981).

35 D. Botez, L. Mawst, P. Hayashida, G. Peterson and T.J. Roth, "High-power, diffraction-limited-beam operation from phase-locked diode-laser arrays of closely spaced "leaky" waveguides (antiguides)," Appl. Phys. Lett. **53**, 464-466 (1988).

36 D. Botez and G. Peterson, "Modes of phase-locked diode-laser arrays of closely spaced antiguides," Electron. Lett. **24**, 1042-1044 (1988).

37 G.R. Hadley, "Index-guided arrays with a large index step," Opt. Lett. **14**, 308-310 (1989).

38 T.H. Shiau, S. Sun, C.F. Schaus, K. Zheng and G.R. Hadley, "Highly stable strained layer leaky-mode diode laser arrays," IEEE Photon. Technol. Lett. **2**, 534-536 (1990).

39 J.S. Major Jr., D. Mehuys, D.F. Welch and D.R. Scifres, "High power, high efficiency antiguide laser arrays," Appl. Phys. Lett. **59**, 2210-2212 (1991).

40 L.J. Mawst, D. Botez, C. Zmudzinski, M. Jansen, C. Tu, T.J. Roth and J. Yun, "Resonant self-aligned-stripe antiguided diode laser array," Appl. Phys. Lett. **60**, 668-670 (1992).

41 H. Yang, L.J. Mawst, M. Nesnidal, J. Lopez, A. Bhattacharya and D. Botez, "10 W near-diffraction-limited peak pulsed power from Al-free, 0.98μm-emitting phase-locked antiguided arrays," Electron. Lett. **33**, 136-137 (1997).

42 C. Zmudzinski, D. Botez, L.J. Mawst, C. Tu and L. Frantz, "Coherent 1W continuous wave operation of large-aperture resonant arrays of antiguided diode lasers," Appl. Phys. Lett. **62**, 2914-2916 (1993).

43 SDL laser diode operators manual and technical notes, SDL Inc,. San Jose, California (1990).

44 R.J. Lang, A.G. Larsson and J.G. Cody, "Lateral modes of broad-area semiconductor lasers: theory and experiment," IEEE J. Quantum Electron. **27**, 312-320 (1991).

45 E.S. Kintzer, J.N. Walpole, S.R. Chinn, C.A. Wong and L.J. Missaggia, "High-power, strained-layer amplifiers and lasers with tapered gain regions," IEEE Photon. Technol. Lett. **5**, 605-608 (1993).

46 D. Mehuys, D. Welch and D. Scifres, "1W CW, diffraction-limited, tunable external-cavity semiconductor laser," Electron. Lett. **29**, 1254-1255 (1993).

47 S.D. DeMars, K.M. Dzurko, R.J. Lang, D.F. Welch, D.R. Scifres and A. Hardy, "Angled-grating distributed feedback laser with 1W cw single-mode diffraction-limited output at 980 nm," Conference on Lasers and Electro-Optics 1996, OSA 1996 Technical Digest Series volume 9, p. 77, Optical Society of America, Washington (1996).

48 S.D. DeMars, T. Oleskevich, A. Schoenfelder and R.J. Lang, "400-mW single-mode fibre-coupled DFB laser at 980 nm," Conference on Lasers and Electro-Optics 1997, OSA 1997 Technical Digest Series volume 11, p. 1, Optical Society of America, Washington (1997).

49 S. Siala, J. Webjorn, S. DeMars, V. Wong, A. Schoenfelder, R. Waarts and R.J. Lang, "Compact visible laser sources based on frequency-doubled α-DFB laser diode," Conference on Lasers and Electro-Optics 1998, OSA 1998 Technical Digest Series volume 6, p. 381, Optical Society of America, Washington (1998).

50 R.J. Lang, K. Dzurko, A.A. Hardy, S. Demars, A. Schoenfelder and D.F. Welch, "Theory of grating-confined broad-area lasers," IEEE J. Quantum Electron. **34**, 2196-2210 (1998).

51 SDL Inc. SDL-XC10 series, SDL 1998 Semiconductor Laser Product Catalog (supplement).

52 J.R. Andrews, "Traveling-wave amplifier made from a laser diode array," Appl. Phys. Lett. **48**, 1331-1333 (1986).

53 J.R. Andrews and G.L. Schuster, "High-power and high-spatial-coherence broad-area power amplifier," Opt. Lett. **16**, 913-915 (1991).

54 L. Goldberg and J.F. Weller, "Broad-area high-power semiconductor optical amplifier," Appl. Phys. Lett. **58**, 1357-1359 (1991).

55 L. Goldberg, D. Mehuys, M.R. Surette and D.C. Hall, "High-power, near-diffraction-limited large-area travelling-wave semiconductor amplifiers," IEEE J. Quantum Electron. **29**, 2028-2043 (1993).

56 L. Goldberg, D. Mehuys and D.C. Hall, "3.3W CW diffraction limited broad area semiconductor amplifier," Electron Lett. **28**, 1082-1084 (1992).

57 L. Goldberg, J.F. Weller, D. Mehuys, D.F. Welch, D.R. Scifres, "12W broad area semiconductor amplifier with diffraction limited optical output," Electron. Lett. **27**, 927-929 (1991).

58 L. Goldberg and D. Mehuys, "21W broad area near-diffraction-limited semiconductor amplifier," Appl. Phys. Lett. **61**, 633-635 (1992).

59 D. Mehuys, D.F. Welch, L. Goldberg and J.F. Weller, "11.6 W peak power, diffraction-limited diode-to-diode optical amplifier," Appl. Phys. Lett. **62**, 544-546 (1993).

60 J.R. Andrews, "Variable focusing due to refractive-index gradients in a diode-array travelling-wave amplifier," J. Appl. Phys. **64**, 2134-2137 (1988).

61 O. Hess, S.W. Koch and J.V. Moloney, "Filamentation and beam propagation in broad-area semiconductor lasers," IEEE J. Quantum Electron. **31**, 35-43 (1995).

62 M.Tamburrini, L. Goldberg, D. Mehuys, "Periodic filaments in reflective broad area semiconductor optical amplifiers," Appl. Phys. Lett. **60**, 1292-1294 (1992).

63 R.J. Lang, D. Mehuys, D.F. Welch and L. Goldberg, "Spontaneous filamentation in broad-area diode laser amplifiers," IEEE J. Quant. Electron. **30**, 685-694 (1994).

64 D. Mehuys, D.F. Welch and L. Goldberg, "2.0W CW, diffraction-limited tapered amplifier with diode injection," Electron. Lett. **28**, 1944-1946 (1992)

65 D. Mehuys, L. Goldberg, R. Waarts and D.F. Welch, "4.5W CW, near-diffraction-limited tapered-stripe semiconductor optical amplifier," Electron. Lett. **29**, 219-221 (1993).

66 D. Mehuys, L. Goldberg and D.F. Welch, "5.25-W near-diffraction-limited tapered-stripe semiconductor optical amplifier," IEEE Photon. Technol. Lett. **5**, 1179-1182 (1993).

67 A.C. Wilson, J.C. Sharpe, C.R. McKenzie, P.J. Manson and D.M. Warrington, "Narrow-linewidth master-oscillator power amplifier based on a semiconductor tapered amplifier," Appl. Opt. **37**, 4871-4875 (1998).

68 S. O'Brien, A. Schoenfelder and R.J. Lang, "5-W diffraction-limited InGaAs broad-area flared amplifier at 970 nm," IEEE Photon. Technol. Lett. **9**, 1217-1219 (1997).

69 D. Mehuys, R.S. Geels, W.E. Plano and D.F. Welch, "1.5W visible, near-diffraction-limited, tapered-stripe optical amplifier," Electron. Lett. **30**, 961-962 (1994).

70 D. Mehuys, D. Welch and D. Scifres, "1W CW, diffraction-limited, tunable external-cavity semiconductor laser," Electron. Lett. **29**, 1254-1255 (1993).

71 D.M. Cornwell Jr. And H.J. Thomas, "High-power (>0.9 W cw) diffraction-limited semiconductor laser based on a fiber Bragg grating external cavity," Appl. Phys. Lett. **70**, 694-695 (1997).

72 A.K. Goyal, P. Gavrilovic and H. Po, "Stable single-frequency operation of a high-power external cavity tapered diode laser at 780 nm," Appl. Phys. Lett. **71**, 1296-1298 (1997).

73 B. Beier, D. Woll, M. Scheidt, K.-J. Boller and R. Wallenstein, "Second harmonic generation of the output of an AlGaAs diode oscillator amplifier system in critically phase matched LiB_3O_5 and β-BaB_2O_4," Appl. Phys. Lett. **71**, 315-317 (1997).

74 D. Woll, B. Beier, K.-J. Boller and R. Wallenstein, "Generation of 1W of blue light by frequency doubling the output of a tapered InGaAs diode amplifier in critically phase-matched LBO," Conference on Lasers and Electro-Optics, May 1998, OSA Technical Digest Series 1998 vol. **6**, p. 380, Optical Society of America, Washington.

75 D.A.V. Kliner, J.P. Koplow and L. Goldberg, "Narrow-band, tunable, semiconductor-laser-based source for deep-UV absorption spectroscopy," Opt. Lett. **22**, 1418-1420 (1997).

76 K. Matsubara, U. Tanaka, H. Imajo, K. Hayasaka, R. Ohmukai, M. Watanabe and S. Urage, "An all-solid-state tunable 214.5-nm continuous-wave light source by using two-stage frequency doubling of a diode laser," Appl. Phys. B **67**, 1-4 (1998).

77 R. Knappe, C.K. Laue and R. Wallenstein, "Tunable UV-source based of frequency-doubled red diode laser oscillator-amplifier system," Electron. Lett. **34**, 1233-1234 (1998).

78 J.P. Koplow, D.A.V. Kleiner and L. Goldberg, "Development of a narrow-band, tunable, frequency-quadrupled diode laser for UV absorption spectroscopy," Appl. Opt. **37**, 3954-3960 (1998).

79 K.J. Boller, M. Scheidt, B. Beier, C. Becher, M.E. Klein and D.H. Lee, "Diode-pumped optical parametric oscillators," Quantum Semiclass. Opt. **9**, 173-189 (1997).

80 M. Scheidt, B. Beier, K.J. Boller and R. Wallenstein, "Frequency-stable operation of a diode-pumped continuous-wave $RbTiOAsO_4$ optical parametric oscillator," Opt. Lett. **22**, 1287-1289 (1997).

81 M.E. Klein, D.-H. Lee, J.-P. Meynm B. Beier, K.-J. Boller and R. Wallenstein, "Diode-pumped continuous-wave widely tunably optical parametric oscillator based on periodically poled lithium tantalate," Opt. Lett. **23**, 831-833 (1998).

82 M.E. Klein, D.-H. Lee, J.-P. Meyn, B. Beier, K.-J. Boller and R. Wallenstein, "Diode-pumped continuous-wave optical parametric oscillator," Post-deadline paper CPD1.12, Conference on Lasers and Electro-Optics-Europe, September 1998, OSA Technical Digest Series 1998, Optical Society of America, Washington.

83 L. Goldberg and D. Mehuys, "Blue light generation using a high power tapered amplifier mode-locked laser," Appl. Phys. Lett. **65**, 522-524 (1994).

84 L. Goldberg and D.A.V. Kliner, "Tunable UV generation at 286 nm by frequency tripling of a high-power mode-locked semiconductor laser," Opt. Lett. **20**, 1640-1642 (1995).

85 A. Robertson, R. Knappe and R. Wallenstein, "Kerr-lens mode-locked Cr:LiSAF femtosecond laser pumped by the diffraction-limited output of a 672-nm diode-laser master-oscillator power-amplifier system," J. Opt. Soc. Am. B **14**, 672-675 (1997).

86 SDL Inc. SDL-TC30 series (formerly SDL-8630), SDL Semiconductor Laser Product Catalog, 1998.

87 Quotation from AMS Electronic (SDL Inc. UK distributor), April 1999: SDL-5410-H1 single-mode 100mW diode laser: £700 approx, SDL-TC30 external-cavity tapered-amplifier laser system £12,500 approx, additional tapered gain elements £8,300 approx if purchased in addition to external cavity system.

88 D.F. Welch, R. Parke, D. Mehuys, A. Hardy, R. Lang, S. O'Brien and S. Scifres, "1.1W CW, diffraction-limited operation of a monolithically integrated flared-amplifier master oscillator power amplifier," Electron. Lett. **28**, 2011-2013 (1992)

89 R. Parke, D.F. Welch, S. O'Brien, R. Lang, "3.0-W cw diffraction-limited performance from a monolithically integrated master oscillator power amplifier," Talk CTu14, Conference on Lasers and Electro-Optics 1993, OSA 1993 Technical Digest Series, Optical Society of America, Washington (1993).

90 S. O'Brien, D.F. Welch, R. Parke, D. Mehuys, K. Dzurko, R.J. Lang, R. Waarts and D. Scifres, "Operating characteristics of a high-power monolithically integrated flared amplifier master oscillator power amplifier," IEEE J. Quantum Electron. **29**, 2052-2057 (1993).

91 S. O'Brien, D. Mehuys, J. Major, R.J. Lang, R. Parke, D.F. Welch and D. Scifres, "1.3 W CW, diffraction-limited monolithically integrated master oscillator flared amplifier at 863 nm," Electron. Lett. **29**, 2109-2110 (1993).

Botez, "Comment: 1.3W CW diffraction-limited monolithically integrated master oscillator flared amplifier at 863nm," Electron. Lett. **30**, 1053-1054 (1994).

Errata: S. O'Brien, "Reply: 1.3W CW diffraction-limited monolithically integrated master oscillator flared amplifier at 863 nm," Electron. Lett. **30**, 1552 (1994).

92 S. O'Brien, R. Lang, R. Parke, J. Major, D.F. Welch and D. Mehuys, "2.2-W continuous-wave diffraction-limited monolithically integrated master oscillator power amplifier at 854 nm," IEEE Photon. Tech. Lett. **9**, 440-442 (1997).

93 SDL Inc., Model 5760-A6.

94 C. Zimmermann, V. Vuletic, A. Hemmerich and T.W. Hänsch, "All solid state laser source for tunable blue and ultraviolet radiation," Appl. Phys. Lett. **66**, 2318-2320 (1995).

95 A. Mar, R. Helkey, J. Bowers, D. Mehuys and D. Welch, "Mode-locked operation of a master oscillator power amplifier," IEEE Photon. Technol. Lett. **6**, 1067-1069 (1994).

96 L. Goldberg, H.F. Taylor, J.F. Weller and D.R. Scifres, "Injection-locking of coupled-stripe diode laser arrays," Appl. Phys. Lett. **46**, 236-238 (1985).

97 J.P. Hohimer, A. Owyoung and G.R. Hadley, "Single-channel injection locking of a diode-laser array with a cw dye laser," Appl. Phys. Lett. **47**, 1244-1246 (1985).

98 L. Goldberg and J.F. Weller, "Injection-locked operation of a 20-element coupled-stripe laser array," Electr. Lett. **22**, 858-859 (1986).

99 L. Goldberg and J.F. Weller, "Injection locking and single-mode fibre coupling of a 40-element laser diode array," Appl. Phys. Lett. **50**, 1713-1715 (1987).

100 G.L. Abbas, S. Yang, V.W.S. Chan, J.G. Fujimoto, "Injection behaviour of high-power broad-area diode lasers," Opt. Lett. **12**, 605-607 (1987).

101 G.L. Abbas, S. Yang, V.W.S. Chan, J.G. Fujimoto, "Injection behaviour and modeling of 100 mW broad area diode lasers," IEEE J. Quantum Electron. **24**, 609-617 (1988).

102 L. Goldberg and M.K. Chun, "Injection-locking characteristics of a 1 W broad stripe laser diode," Appl. Phys. Lett. **53**, 1900-1902 (1988).

103 H. Tsuchida, "Tunable, narrow-linewidth output from an injection-locked high-power AlGaAs laser diode array," Opt. Lett. **19**, 1741-1743 (1994).

104 J. Verdiell, H. Rajbenbach, and J. Huignard, "Injection-locking of gain guided diode laser arrays: influence of the master beam shape," Appl. Opt. **31**, 1992-1997 (1992).

105 J.-P. Weber and S. Wang, "Analysis of the far-field output angle scanning by injection locking of a diode laser array," Appl. Phys. Lett. **48**, 1719-1721 (1986).

106 G.R. Hadley, A. Owyoung and J.P. Hohimer, "Modeling of injection-locking phenomena in diode-laser arrays," Opt. Lett. **11**, 144-146 91986).

107 M.K. Chun, T.L. Whitman and D.G. Soenksen, "Far-field behaviour of injection-locked semiconductor laser arrays," Appl. Opt. **26**, 4518-4521 (1987).

108 M.K. Chun, L. Goldberg and J.F. Weller, "Injection-beam parameter optimization of an injection-locked diode-laser array," Opt. Lett. **14**, 272-274 (1989).

109 J.-M. Verdiell, R. Frey, and J.-P. Huignard, "Analysis of injection-locked gain-guided diode laser arrays," IEEE J. Quant. Electron. **27**, 396-401 (1991).

110 J. Yaeli, W. Streifer, D.R. Scifres and P.S. Cross, "Array mode selection utilizing an external cavity configuration," Appl. Phys. Lett. **47**, 89-91 (1985).

111 C. Chang-Hasnain, D.F. Welch, D.R. Scifres, J.R. Whinnery, A. Dienes and R.D. Burnham, "Diffraction-limited emission from a diode laser array in an apertured graded-index external cavity," Appl. Phys. Lett. **49**, 614-616 (1986).

112 C.J. Chang-Hasnain, J. Berger, D.R. Scifres, W. Streifer, J.R. Whinnery and A. Dienes, "High-power with high efficiency in a narrow single-lobed beam from a diode laser array in an external cavity," Appl. Phys. Lett. **50**, 1465-1467 (1987).

113 R. Pillai and E. Garmine, "External-cavity semiconductor-laser array insensitive to paraxial misalignment," Opt. Lett. **20**, 2108-2110 (1995).

114 L. Goldberg and J.F. Weller, "Narrow lobe emission of high power broad stripe laser in external resonator cavity," Electron. Lett. **25**, 112-114 (1989).

115 A. Barthelemy, F. Louradour and V. Couderc, "Wavelength-tunable diffraction-limited operation of a standard high-power diode-laser array using an off-centred extended cavity," Electron. Lett. **28**, 2038-2040 (1992).

116 A.V. Chelnokov, J.-M. Lourtioz and P. Gavrilovic, "Ultrashort pulses in diffraction-limited beam from diode laser arrays with external cavity," Electron. Lett. **29**, 861-862 (1993).

117 L. Goldberg and J.F. Weller, "Single lobe operation of a 40-element laser array in an external ring laser cavity," Appl. Phys. Lett. **51**, 871-873 (1987).

118 S. MacCormack and R.W. Easton, "Near-diffraction-limited single-lobe emission from a high-power diode-laser array coupled to a photorefractive self-pumped phase-conjugate mirror," Opt. Lett. **16**, 705-707 (1991).

119 S. MacCormack, J. Feinberg and M.H. Garrett, "Injection-locking a laser-diode array with a phase-conjugate beam," Opt. Lett. **19**, 120-122 (1994).

120 K. Iida, H. Horiuchi, O. Matoba, T. Omatsu, T. Shimura and K. Kuroda, "Injection locking of a broad-area diode laser through a double phase-conjugate mirror," Opt. Comm. **146**, 6-10 (1998).

121 S. MacCormack and J. Feinberg, "High-brightness output from a laser-diode array coupled to a phase-conjugating mirror," Opt. Lett. **18**, 211-213 (1993).

122 M. Løbel, P.M. Petersen and P.M. Johansen, "Tunable single-mode operation of a high-power laser-diode array by use of an external cavity with a grating and a photorefractive phase-conjugate mirror," J. Opt. Soc. Am. B **15**, 2000-2005 (1998).

123 M.K. Chun, L. Goldberg and J.F. Weller, "Second-harmonic generation at 421 nm using injection-locked GaAlAs laser array and $KNbO_3$," Appl. Phys. Lett. **53**, 1170-1171 (1988).

124 M. Scheidt, B. Beier, K.J. Boller and R. Wallenstein, "Diode-laser-pumped cw optical parametric oscillators of KTP," Conference on Lasers and Electro-Optics, May 1995, OSA Technical Digest Series 1995 vol. 15, Optical Society of America, Washington.

M. Scheidt, B. Beier, R. Knappe, K.J. Boller and R. Wallenstein, "Diode-laser-pumped continuous-wave KTP optical parametric oscillator," J. Opt. Soc. Am. B **12**, 2087-2094 (1995).

125 I.D. Lindsay, G.A. Turnbull, M.H. Dunn and M. Ebrahimzadeh, "Doubly-resonant continuous-wave optical parametric oscillator pumped by a single-mode diode laser," Opt. Lett. **23**, 1889-1891 (1998).

126 B. Beier, J.-P. Meyn, R. Knappe, K.-J. Boller, G. Huber and R. Wallenstein," A 180 mW Nd:$LaSc_3(BO_3)_4$ single-frequency TEM_{00} microchip laser pumped by an injection-locked diode-laser array," Appl. Phys. B **58**, 381-388 (1994).

127 R. Knappe, K.-J. Boller and R. Wallenstein, "Single-mode continuous-wave Cr^{3+}:LiSAF ring laser pumped by an injection-locked 670-nm broad-area diode laser," Opt. Lett. **20**, 1988-1990 (1995).

128 D. Burns, M.P. Critten and W. Sibbett, "Low-threshold diode-pumped femtosecond Cr^{3+}:$LiSrAlF_6$ laser," Opt. Lett. **21**, 477-479 (1996).

129 I.D. Lindsay and M. Ebrahimzadeh, "Efficient continuous-wave and Q-switched operation of a 946-nm Nd:YAG laser pumped by an injection-locked broad-area diode laser," Appl. Opt. **37**, 3961-3970 (1998).

130 A. Yariv, "Quantum electronics," (second edition) John Wiley and Sons, New York (1989).

131 C. Lindström, R.D. Burnham, D.R. Scifres, T.L. Paoli, W. Streifer, "One watt CW visible single-quantum-well lasers," Electron. Lett. **19**, 80-81 (1983).

132 A.J. Henderson, M.J. Padgett, F.G. Colville, J. Zhang and M.H. Dunn, "Doubly-resonant optical parametric oscillators: tuning behaviour and stability requirements," Opt. Comm. **119**, 256-264 (1995).

5. Injection-Locked Broad-Area Diode Laser System: Design and Characterisation.

5.1 Introduction.

Having decided to develop an injection-locked system for the reasons outlined in section 4.4, the design of this system is now described and its operation characterised. The basic design for all such systems is generally similar to that shown in Fig. 4-5, using a cylindrical lens operating in the plane of the diode junctions to shape the injected beam. The main issue to address is a detailed analysis of the optical system enabling an optical design, which allows injection-locking, to be developed. To carry out this design, the beam parameters of the diode lasers must be first determined and these, together with the other diode-laser characteristics, are described in the next section.

5.2 Characterisation of diode lasers.

The initial stage in the development of the injection-locked system was the investigation of the operating characteristics of the two diode lasers used. The results obtained for each laser are now discussed.

5.2.1 Single-mode master laser.

The master laser used was an SDL-5412-H1 device with an emission region measuring 1μm perpendicular to and 3μm parallel to the plane of the junction. The maximum output power was around 100mW in a single longitudinal mode and a single transverse mode in both junction planes. The operating wavelength was

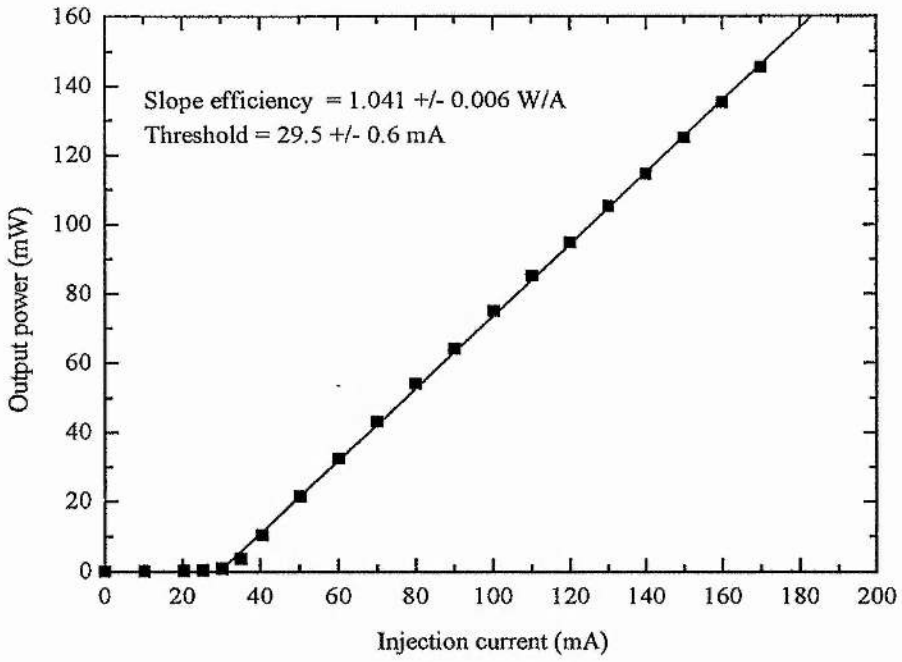

Fig. 5-1 Output power vs. Current characteristic for SDL-5412-H1 single-mode diode laser operating at 25°C.

around 813 nm and the facets were coated to provide reflectivities of approximately 95% on the back facet and 5% on the front (output) facet. A low-noise current source (ILX-Lightwave LDX-3620) was used to drive the laser and could maintain constant drive current or constant laser output power, with a photodiode integral to the laser package providing feedback in the latter case. The temperature of the laser was controlled using a thermoelectric cooler (TEC) and monitored using a thermistor, both of which were contained within the laser packaging. The TEC and thermistor were connected to a temperature controller (ILX-Lightwave LDT-5412) to provide closed-loop control.

The variation of the master laser output power with current, measured at a temperature of 25°C, is shown in Fig. 5-1. The performance is significantly better than specified by the manufacture, giving an output power of 145mW (as opposed to the 100mW) at the specified typical operating current of 170mA [1]. The temperature tuning characteristics are shown in Fig. 5-2. These results were taken

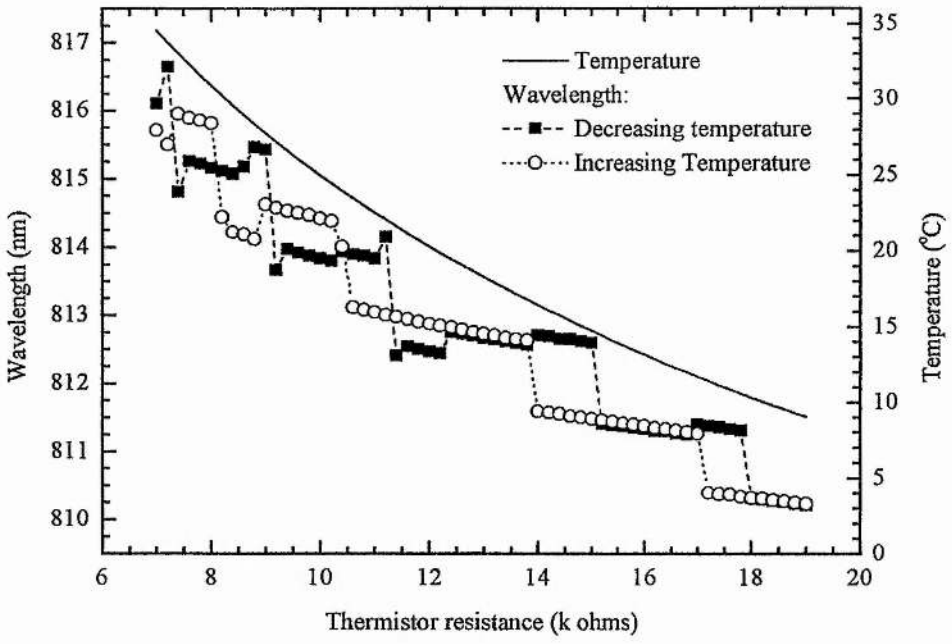

Fig. 5-2 Temperature-tuning data for single-mode laser taken in constant-power mode at an output power of 120mW.

with the diode-driver operating in constant output-power mode at an output power of 120mW. The diode temperature, calculated from the Steinhart-Hart coefficients supplied by the manufacturer for the integral thermistor, is also shown.

It can be seen that a temperature change of approximately 25°C results in a change in wavelength of around 6.5nm. Both increasing and decreasing the temperature produce the stepped tuning behaviour, due to mode hopping, typical of diode lasers. However, additional small steps appear in the case of decreasing temperature and hysterisis in wavelength with temperature occurs at the mode-hop points. This behaviour is predicted by the manufacturer and is attributed to wavelength-stabilisation techniques used in the diode-laser construction [1].

Since, in an injection-locked system, the injection-locked output adopts essentially the same frequency characteristics as those of the master laser, it is important to determine what these are. The longitudinal mode structure of the master laser was observed using a scanning confocal Fabry-Perot interferometer. Initial measurements

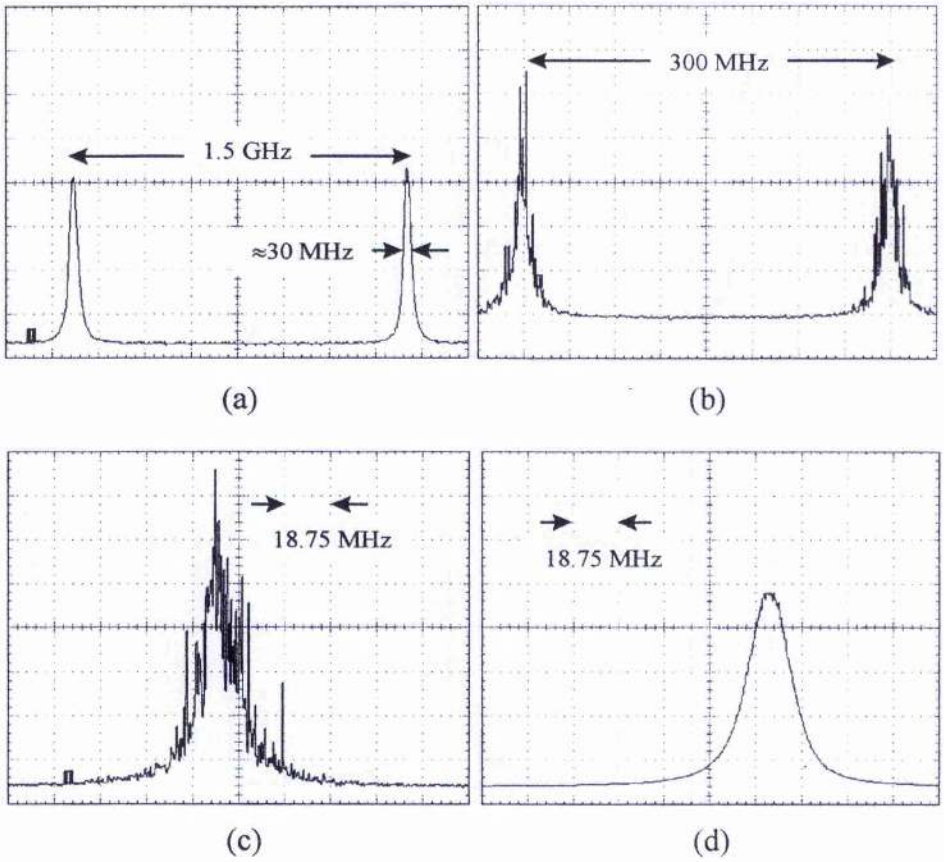

Fig. 5-3 Scanning interferometer mode-structure measurements on single-mode diode laser: (a) 1.5GHz FSR, 30MHz resolution interferometer, (b) 300MHz FSR, <1MHz resolution interferometer, (c) magnified single peak of (b), (d) same as (c) but averaged over ≈10 seconds.

used an interferometer with a free spectral range (FSR) of 1.5 GHz and a resolution of around 30 MHz. These results are shown in Fig. 5-3 (a). It can be seen that the laser operated on a single longitudinal mode and that the linewidth measurement is limited by the resolution of the interferometer. Higher resolution measurements were made with an interferometer having a free spectral range of 300 MHz and a resolution of less than 1 MHz. These measurements are shown in Fig. 5-3 (b) and (c). It can be seen that the full-width at half-maximum of the laser emission is around 15 MHz.

From the structure of the peak, it appears that the instantaneous linewidth is considerably narrower than this value, but rapid fluctuations broaden the apparent width of the emission to the level measured. To gauge the effects of longer-term fluctuations, an average linewidth measured over approximately 10 seconds was also measured and is shown in Fig. 5-3 (d). It can be seen that this results in an averaged width of around 20 MHz.

The frequency stability of the single-mode laser was also gauged by tuning the laser to the side of a resonance of the 1.5 GHz FSR interferometer and observing the transmitted intensity. These results are shown in Fig. 5-4. To obtain an approximate relationship between frequency stability and transmitted power the interferometer was operated in its normal scanning mode, as shown in Fig. 5-4 (a). If the variation

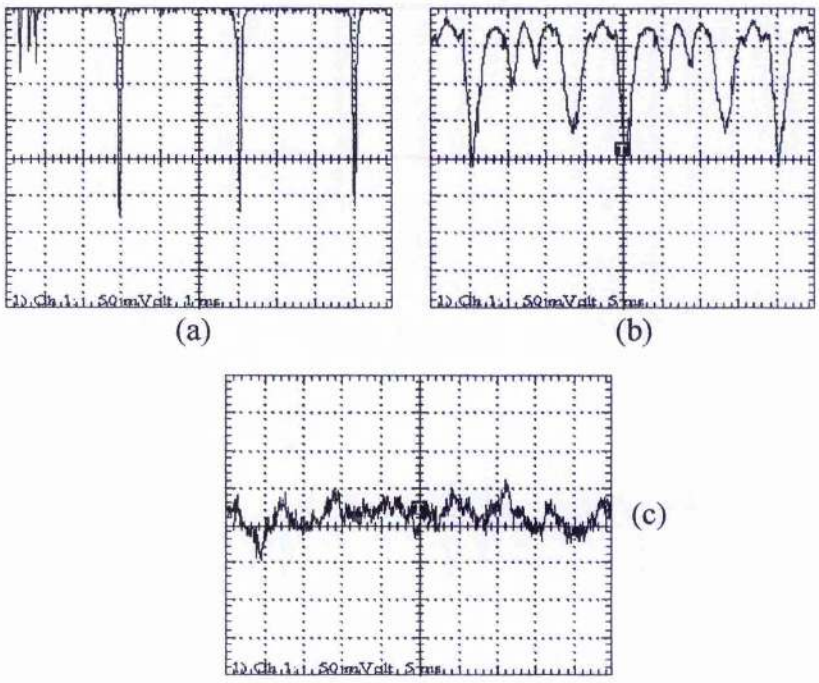

Fig. 5-4 Single-mode laser power transmitted by fixed confocal interferometer with laser tuned to side of fringe: (a) interferometer transmission as length is scanned, (b) transmission for fixed interferometer length with laser running on mains power, (c) same as (b) but with laser running on battery power.

of transmitted power with frequency is assumed to be linear while on one side of the transmission peak, it can be seen from Fig. 5-4 (a) and the known resolution of the interferometer (approximately 30 MHz) that the rate of change of frequency with photodetector voltage is approximately 55 kHz/mV.

The current source used to drive the single-mode laser could be operated either using mains power or internal batteries. The fixed-length interferometer transmission, with the laser tuned to the side of a transmission fringe, when using mains power is shown in Fig. 5-4 (b). As the transmission does not reach the peak value seen in Fig. 5-4 (a), it is assumed that the laser frequency remained on the same side of the fringe and did not cross the peak for the duration of the measurement. It can be seen that the amplitude of the voltage fluctuations is around 180mV, implying a frequency stability of +/- 5 MHz. It is interesting to note that the fluctuations are periodic with a period of 20 ms, indicating that 50Hz noise from the mains supply is manifesting itself as frequency instability in the laser. Fig. 5-4 (c) shows the same measurement made with the battery power supply. It can be seen that the frequency fluctuations are reduced to approximately +/- 2.75 MHz and that there is no periodicity. On the basis of these results it was determined that the single-mode laser should be operated from the battery supply whenever frequency stability was critical.

Another source of frequency instability in diode lasers is unwanted optical feedback. It is well known that the very high gains available in diode lasers make them extremely sensitive to even small levels of unwanted feedback from reflective optical components. Since the front-facet reflectivity of the single-mode laser was approximately 5%, it can be seen that even extremely low feedback levels will be significant. As a result, an optical isolator providing around 60dB of isolation (Gsänger DLI 1) was used directly after the lens collimating the single-mode laser output. The isolator had a micrometer adjustment to allow the maximum isolation to be optimised for a given wavelength. This also allowed the effects of varying levels of feedback to be investigated. The adjustment was calibrated for the level of isolation by directing the laser output through the isolator in the reverse direction and measuring the fraction of power transmitted.

After calibration, the isolator was set up in the normal mode of operation, i.e. with the laser output passing through it in the forward direction, and a highly reflecting mirror was then used to return light through the isolator in the direction of the laser, providing feedback. An uncoated glass slide after the isolator was used to direct a small fraction of the light into a scanning interferometer and the output spectrum was monitored while the level of isolation was adjusted. Significant levels of feedback were observed to cause the laser to operate on several longitudinal modes or to mode hop frequently. The results of the calibration for two wavelengths are shown in Fig. 5-5, together with the range of isolation over which single-mode operation was observed. It can be seen that reverse transmissions greater than -53dB, or approximately 5×10^{-6}, resulted in obvious multimode operation and extreme frequency instability.

For higher levels of isolation than this, single-mode operation was observed. However, even at the maximum level of isolation, it was noticed that blocking and

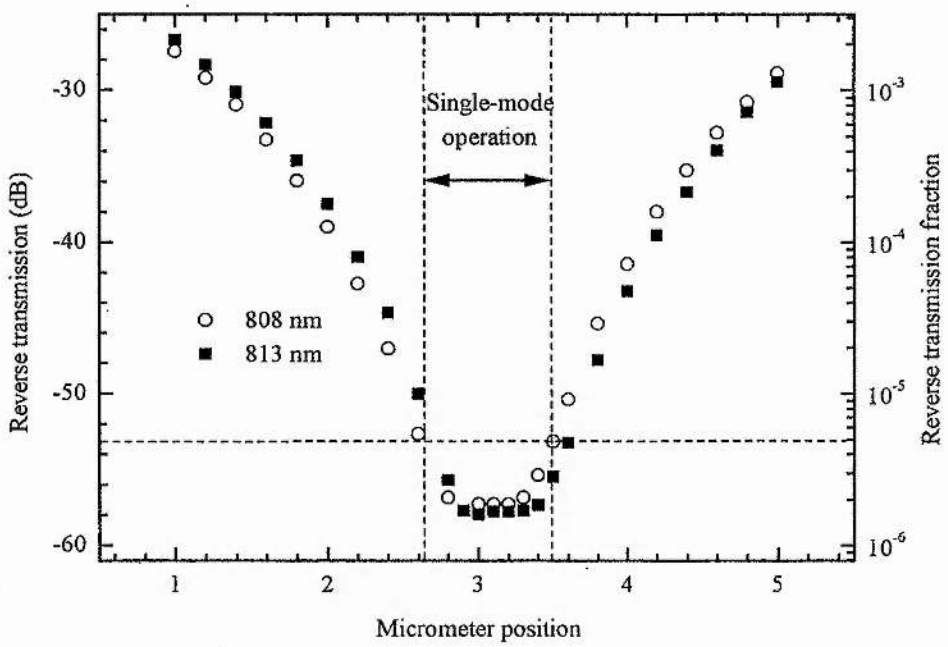

Fig. 5-5 Calibration of optical isolator adjustment at 808 and 813 nm and single-mode operating range of laser.

unblocking the feedback path resulted in small frequency shifts in the single-mode operating point observed using the interferometer. This indicated that, even with the maximum attainable isolation, weak feedback effects were still present although not strong enough to seriously disrupt the laser. Obviously, in practice, the entire transmitted output would not be returned to the isolator in most cases. However, these results demonstrate the extreme sensitivity of the single-mode laser to unwanted optical feedback.

Clearly, when designing the optical system for injection locking, the spatial properties of the laser output are particularly important. Typical vertical (perpendicular to the junction plane) and horizontal (in the junction plane) far-field profiles of the uncollimated laser, taken using a photodiode array, are shown in Fig. 5-6. To characterise the beam quality of the laser, the output was collimated then brought to a focus. The width within which 95.4% of the power was contained, corresponding to the $1/e^2$ diameter in the case of a Gaussian distribution, was measured for a range of longitudinal positions through the focus, using a translating knife edge as described in appendix A1. The results of these measurements are

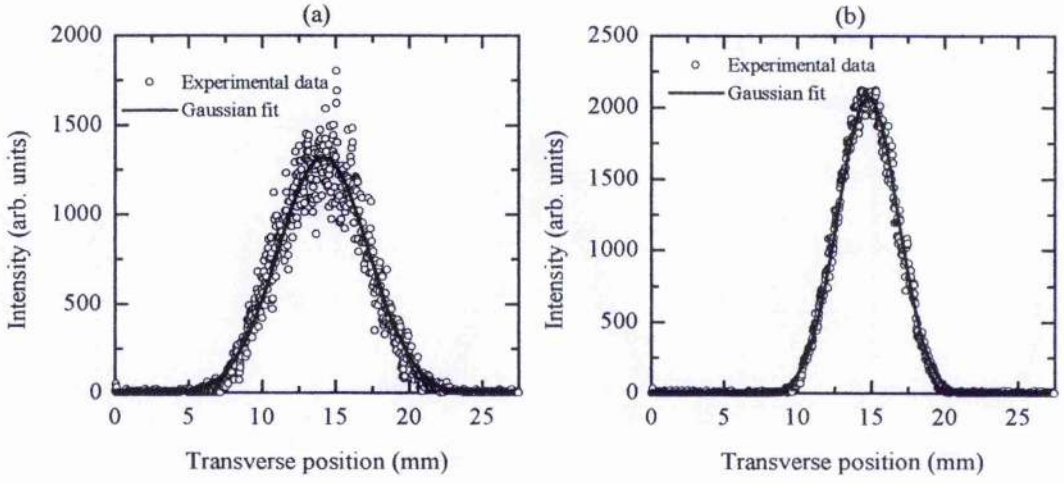

Fig. 5-6 Typical far-field profiles of the single-mode laser output: (a) vertical (perpendicular to the junction plane), (b) horizontal (parallel to the junction plane).

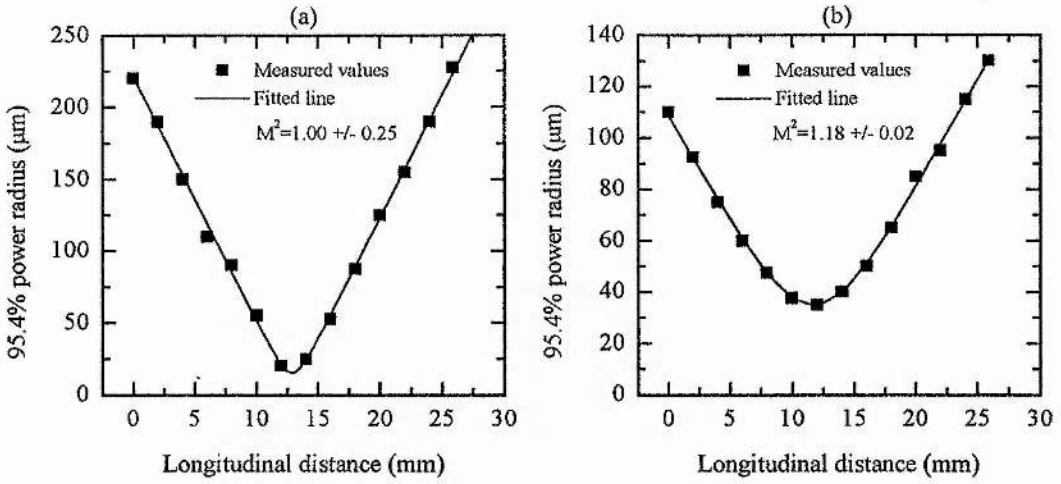

Fig. 5-7 95.4% power radius of single-mode laser beam through focus in (a) vertical and (b) horizontal directions. Note that the results shown in (a) and (b) are not for the same focus.

shown in Fig. 5-7, although not for the same focus. Fitting a function of the form of equation **(A1-7)**, given in appendix A1, gives a value of $M^2 \approx 1$, implying diffraction-limited performance, in both directions.

5.2.2 High-power broad-area laser.

The high-power slave laser used in the injection-locked system was an SDL-2362-P1 broad-area device with a 1×100μm active area cross-section, a rated maximum output power of 1.2 W [2], and a nominal operating wavelength of 808 nm. As with the single-mode device, the broad-area laser was packaged with an integral thermoelectric cooler and monitor photodiode and the specified facet reflectivities were approximately 95% and 5% for the back and front facets, respectively. The output power vs. current characteristic, measured at 25°C, for this device is shown in Fig. 5-8.

The temperature tuning behaviour, measured at a current of 1.5 A, is shown in Fig. 5-9. The output of the laser was spectrally broad and the values plotted in Fig. 5-9

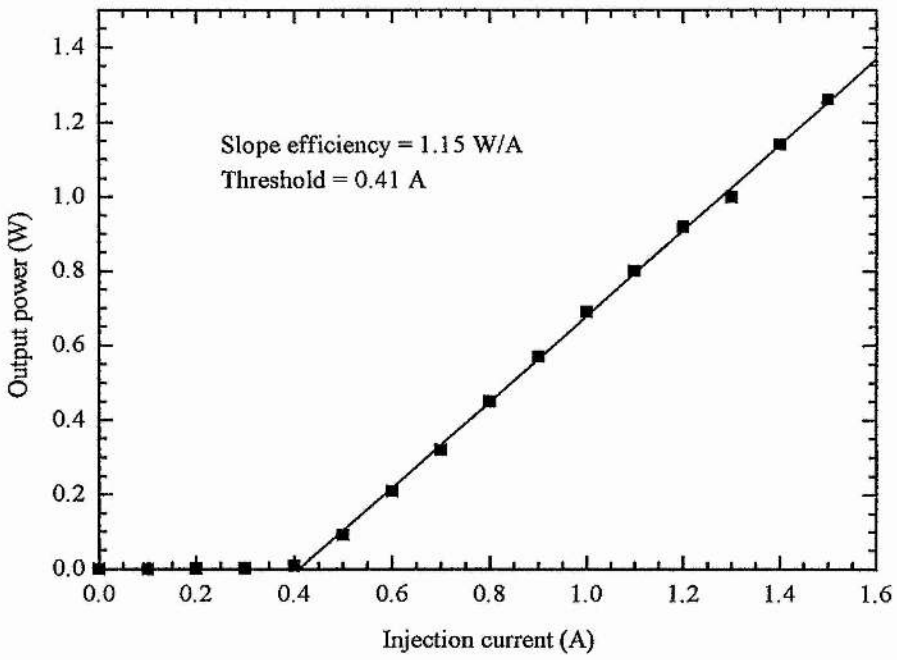

Fig. 5-8 Output power vs. Current characteristic for SDL-2362-P1 broad-area diode laser operating at 25°C.

represent the central wavelength. A typical emission spectrum is shown in Fig. 5-10. It can be seen that the full width at half maximum of the emission is around 2 nm.

The far-field beam profiles of the uncollimated laser in both directions, measured using a photodiode array, are shown in Fig. 5-11. It can be seen that while the emission perpendicular to the plane of the junction is Gaussian, that parallel to the junction has a two-lobed profile typical of such devices. To explicitly determine the beam quality in both directions, the radius defining the 95.4% power width was measured through a focus, as for the single-mode laser. The results of these measurements are shown in Fig. 5-12. It can be seen that although the output is near diffraction limited in the direction perpendicular to the junction plane, the output parallel to the junction plane is around 24× diffraction limited. Note that, again, the measurements in the two planes are for different foci.

It is clear from the characteristics described in this section that, in particular, the spatial properties of the free-running broad-area laser are unsatisfactory when

considered in the context of a pump source for end-pumped solid-state lasers which fully exploits the potential of this geometry. As a pump source for optical parametric oscillators, both the spatial and spectral qualities are highly unsuitable.

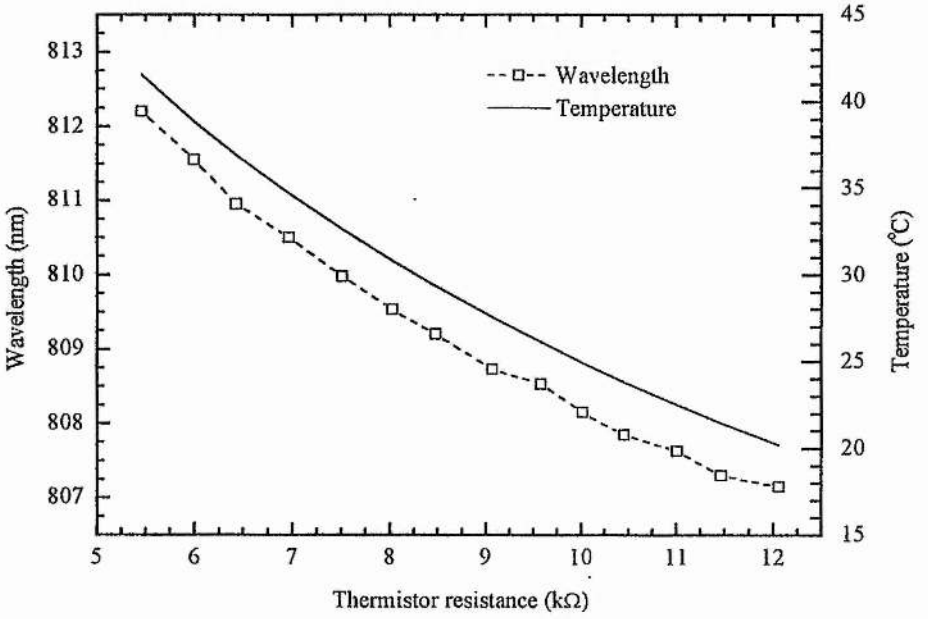

Fig. 5-9 Temperature tuning characteristics of broad-area diode laser at a current of 1.5A.

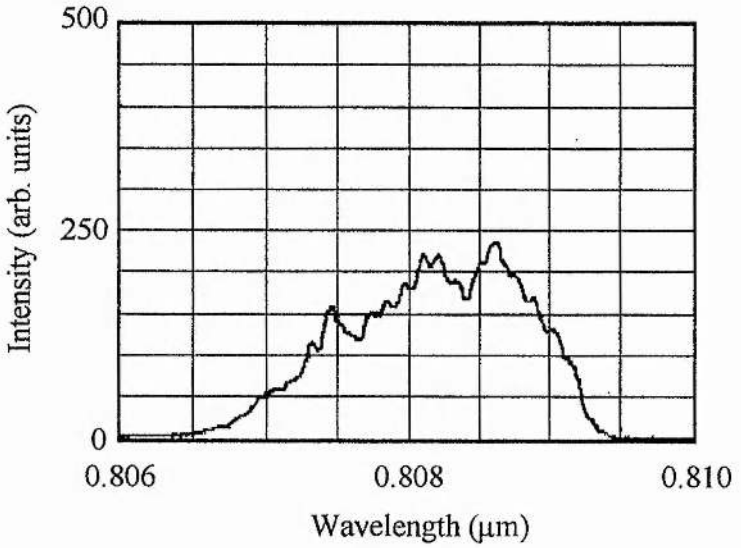

Fig. 5-10 Typical emission spectrum of the broad-area diode laser.

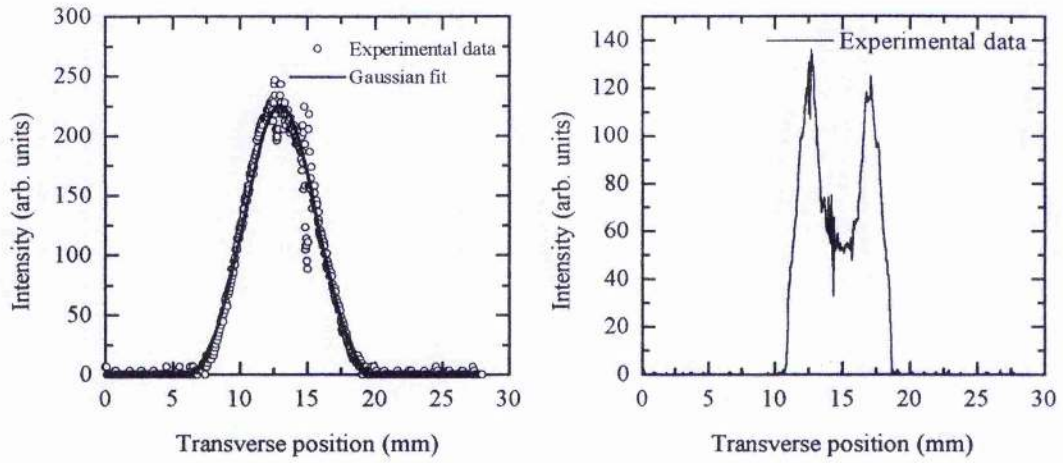

Fig. 5-11 Typical far-field profiles of the broad-area laser output: (a) vertical (perpendicular to the junction plane), (b) horizontal (parallel to the junction plane).

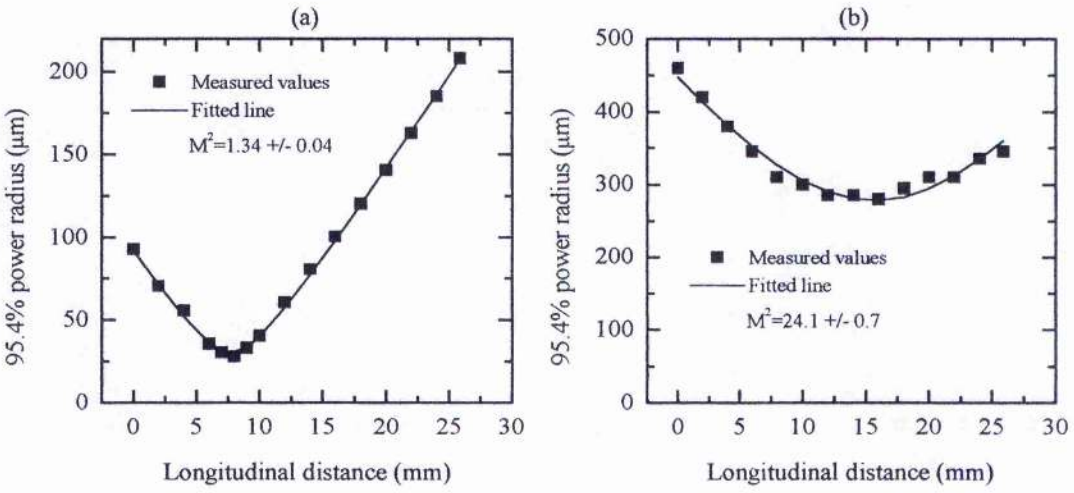

Fig. 5-12 95.4% power radius of broad-area laser beam through focus in (a) vertical and (b) horizontal directions. Note that the results shown in (a) and (b) are not for the same focus.

5.3 Optical system design.

It is clear that the optical system used to injection lock the broad-area laser must fulfil two functions. Firstly, it must create a waist in the injected master-laser beam having appropriate position and dimensions to obtain injection-locked output, based on the criteria discussed in section 4.3. Secondly, it must allow the injection-locked far-field peak of the output to be extracted.

The small emitting apertures of diode lasers result in very high divergence angles, especially in the direction perpendicular to the junction, and short-focal-length, high-numerical-aperture lenses must be used to collect the output. The majority of experimentally demonstrated injection-locked systems use an additional cylindrical lens, acting in the plane of the junction, to shape the master-laser beam for injection into the broad-area laser [3,4,5]. The two main variations are systems where the injected beam is brought to a focus between the master laser and the cylindrical lens by the short-focal-length "collimating" lens[3,4] and those where the injected beam is collimated [5]. It was decided to use a collimated master-laser beam in the system developed here, similar to the configuration shown in Fig. 4-5 as it was anticipated that this would be easier to set up reproducibly.

Considering first the shaping and positioning of the injected beam at the high-power laser, a paraxial ray-tracing calculation was used to calculate the injection angle and position. This was used initially, as opposed to an ABCD matrix calculation, as the paraxial optics approach more easily allows analytical expressions describing the approximate system behaviour to be developed. A numerical ABCD matrix calculation is, however, necessary to more exactly determine the beam dimensions and waist positions and such a calculation was used at a later stage.

The paraxial optics calculation uses two variables to describe a ray at any given point, these being the angle from the axis u and the perpendicular distance from the axis h. Conventionally distances measured upwards from the axis, and angles measured anti-clockwise from the ray to the axis are positive. The two variables h and u are essentially equivalent to the two ray-matrix elements used in the ABCD matrix treatment of paraxial ray optics [6]. The two key expressions describing the

transformation of the ray variables by a lens of power K and propagation over a distance d, respectively, are:

$$u' - u = hK \tag{5-1 a}$$

$$h' = h - du \tag{5-1 b}$$

where unprimed values are those before transformation by the optical element and primed values are those after.

The cylindrical lens and broad-area laser collimating lens are shown schematically, using this notation, in Fig. 5-13, viewed in the plane of the diode-laser junctions. The cylindrical lens is designated L_1, having a power $K_1=1/f_1$, and is assumed to be centred on the axis of the master-laser beam in the transverse direction. The spherical collimating lens is designated L_2, has power $K_2=1/f_2$, and is allowed to be translated by a transverse distance δ from the axis on which the input beam and

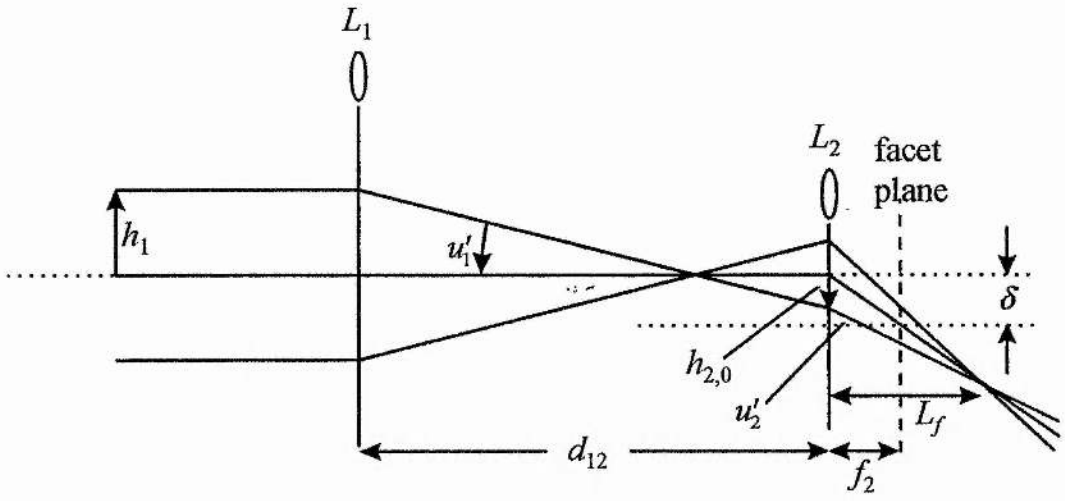

Fig. 5-13 Schematic diagram of injection-locking optics viewed in the plane of the diode junctions. L_1 is the cylindrical lens and L_2 is the broad-area laser collimating lens displaced by transverse distance δ from the axis of the optical system.

cylindrical lens are centred. The distance separating the two lenses is indicated by the quantity d_{12}. Since L_2 must also collimate the broad-area laser output in the direction perpendicular to the junction it is assumed that the distance from L_2 to the facet plane is the focal length of L_2, namely f_2. Considering transformation by the first lens:

$$u_1' = h_1 K_1 \tag{5-2}$$

after transfer to L_2, using (5-1 b), the height at the second lens, measured from the main optical axis, is given by:

$$h_{2,0} = h_1\left(1 - d_{12}K_1\right) \tag{5-3}$$

Given the translation δ of L_2 from the main axis, as shown in Fig. 5-13, the ray height of (5-3), measured from the axis of L_2 rather than the main axis, is given by:

$$h_2 = h_1\left(1 - d_{12}K_1\right) - \delta \tag{5-4}$$

Considering the operation of the second lens, the incident angle $u_2 = u_1'$ is transformed according to (5-1 a), and using (5-2) and (5-4), to give the exit angle:

$$u_2' = h_1\left(K_1 + K_2 - d_{12}K_1K_2\right) - \delta K_2 \tag{5-5}$$

This expression can be used, together with (5-4), in (5-1 b) to obtain the ray height at the broad-area laser facet, h_f, by assuming the distance from L_2 to the facet to be f_2, as previously mentioned:

$$h_f = h_1\left(1 - d_{12}K_1\right) - \delta - f_2\left[h_1\left(K_1 + K_2 - d_{12}K_1K_2\right) - \delta K_2\right] \tag{5-6}$$

Since f_2=1/K_2, it can be seen that this expression reduces to:

$$h_f = -h_1\frac{K_1}{K_2} \tag{5-7}$$

From (5-5), it can be seen that the exit angle from L_2, and therefore the angle of incidence at the broad-area laser facet, shows a linear variation with the transverse displacement, δ, of L_2. The position at the facet can be seen from (5-7) to be invariant with δ, when measured relative to the axis of L_2. The implication of these two observations is that translation of L_2, with the broad-area laser position fixed, results in a variation of both the injection position at the laser facet and the injection angle. On the other hand, the simultaneous translation of L_2 and the broad-area laser results in a variation in the injection angle alone. Thus, mounting the collimating lens L_2 and the broad-area laser in such a way that both can be translated together, in addition to independent translation of the lens, allows independent control of the injection position and angle.

To determine the distance d_f from L_2 to the plane where the beam is brought to a focus after L_2, it is assumed that δ=0, to allow the plane to be identified as that where the ray intersects the axis. Then:

$$L_f = \frac{h_2}{u_2'} \tag{5-8}$$

From (5-4) and (5-5), with δ=0, we obtain:

$$L_f = \left(\frac{K_1}{1 - d_{12} K_1} + K_2 \right)^{-1} \tag{5-9}$$

It can be seen that setting $d_{12}=f_1$ results in $L_f=0$, placing the focus at L_2, and setting $d_{12}=f_1+f_2$ gives $L_f=\infty$, implying a collimated output, as would be expected. L_f is plotted as a function of d_{12} in Fig. 5-14, where the abscissa is the difference between the lens separation d_{12} and the focal length of L_1, (i.e. f_1), normalised to f_1. Thus, a value of zero represents the focal point of L_1 being at L_2, and a value of 1 represents the lenses being spaced confocally. The ordinate shows the distance from L_2 to the focal point, normalised in terms of f_2.

In section 4.3 the focal point of the injected beam was assumed to be at the facet of the broad-area laser. Clearly, this will correspond to a value of L_f/f_2 =1 in Fig. 5-14.

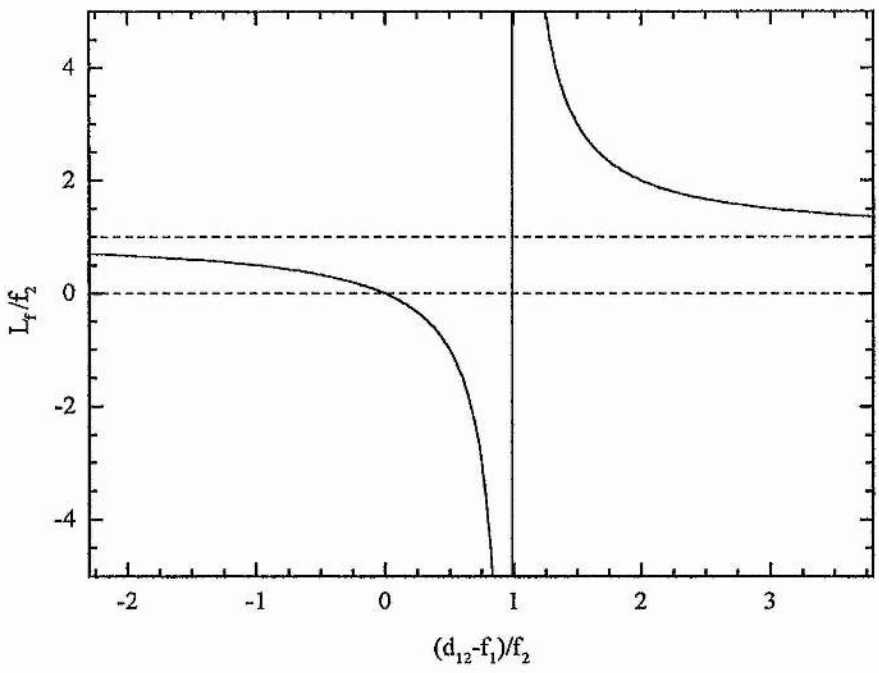

Fig. 5-14 Variation of L_f (distance to focal point from lens L_2) with lens separation d_{12}. L_f is normalised to focal length f_2, and d_{12} is represented as the difference between lens separation and focal length f_1, normalised to f_2.

The calculated position can be seen from Fig. 5-14 to approach this value in an asymptotic way, so this situation cannot be achieved in practice. A value of $L_f/f_2 = 0$ corresponds to a focal point at L_2. Clearly, it is desirable to achieve a value of L_f/f_2 somewhere between these values, resulting in a focal point falling somewhere between the collimating lens L_2 and the broad-area laser facet. The focal position can be varied over this range by varying the lens spacing d_{12} over the range of values where d_{12} is smaller than f_1 by a few times f_2, as can be seen from Fig. 5-14.

Although (5-9) and Fig. 5-14 give an indication of the variation of focal position with lens separation, obtaining exact values requires a Gaussian-beam ABCD matrix calculation for the particular lens combination involved. This is carried out later in this section, after the extraction of the injection-locked output has been studied from a paraxial ray-tracing point of view.

As mentioned earlier, the second function of the optical system is to extract the injection-locked output. The schematic representation of the optical system used to investigate this behaviour from a paraxial optics point of view is shown in Fig. 5-15. This is essentially the same as the system shown in Fig. 5-13, but reversed to consider propagation from the broad-area laser. Additionally, the displacement of L_2, δ, is set to zero, as this simplifies the calculation of the positions of the various planes which are the main values of interest here and are not affected by the value of δ. The output of the system is considered at an imaging plane a distance d_{img} from the cylindrical lens L_1. This might be the position of a detector used to observe the injection-locked output or of a pick-off mirror, such as that shown in Fig. 4-5 used to extract the injection-locked output power.

Transfer from the facet plane through L_2, L_1 and the intervening spaces, gives the ray height and angle after L_1:

$$h_1' = h_0\left(1 - K_2 d_{12}\right) - \frac{u_0}{K_2} \tag{5-10 a}$$

$$u_1' = h_0 K_1\left(1 - d_{12} K_2\right) - u_0 \frac{K_1}{K_2} + h_0 K_2 \tag{5-10 b}$$

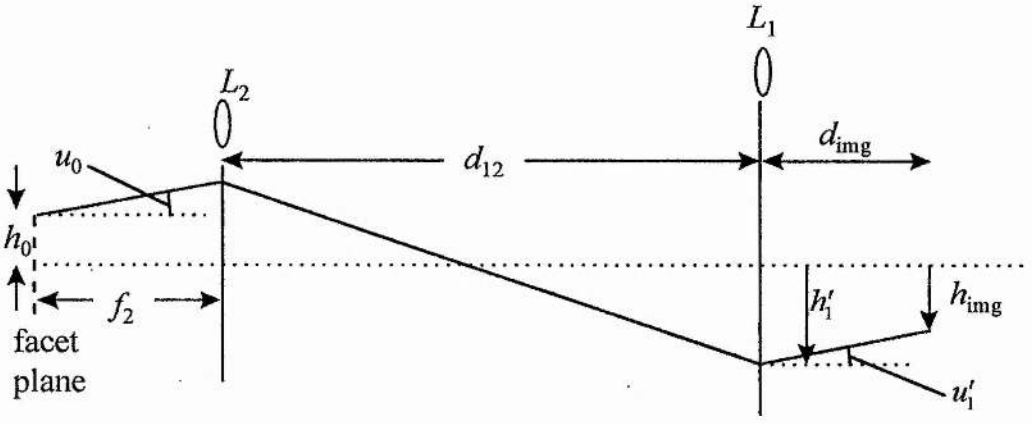

Fig. 5-15 Schematic diagram of injection-locking optics viewed in the plane of the diode junctions as considered for paraxial ray-tracing treatment of the extraction of the injection-locked output.

Using these expressions and (5-1 b) to transfer to the image plane, gives the ray height here as:

$$h_{img} = h_0\left[1+d_{img}K_1\left(K_2d_{12}-1\right)-K_2\left(d_{img}+d_{12}\right)\right]-u_0\left(\frac{1}{K_2}-d_{img}\frac{K_1}{K_2}\right) \tag{5-11}$$

This expression can be rearranged to take the form:

$$h_{img} = M\left(h_0 - d_{obj}u_0\right) \tag{5-12}$$

with:

$$M = 1+d_{img}K_1\left(K_2d_{12}-1\right)-K_2\left(d_{img}+d_{12}\right) \tag{5-13 a}$$

$$d_{obj} = \frac{\left(\frac{1}{K_2}-d_{img}\frac{K_1}{K_2}\right)}{\left[1+d_{img}K_1\left(K_2d_{12}-1\right)-K_2\left(d_{img}+d_{12}\right)\right]} \tag{5-13 b}$$

The form of (5-12) indicates that the output obtained at the imaging plane is an image of the distribution at an object plane, d_{obj} from the facet, which is produced by the divergence from the facet over the distance d_{obj} at an angle u_0. The distribution at the image plane is magnified by a factor M relative to that at the object plane.

The results of (5-12) and (5-13) have important implications for the design of the optical system. As was shown in chapter 4, the injection-locked output can be considered as resulting from the far-field interference pattern of the multiple output beams from the injected broad-area laser. Clearly, this implies that the plane imaged by the output of the optical system must be sufficiently far from the facet of the broad-area laser for the far field to have formed. While it was ensured in the modelling of section 4.3 that this was the case by making the observation distance significantly larger than the facet dimension, the minimum distance for far-field formation must be determined more accurately for the purposes of designing the optical system.

To do this, a point P lying in a plane parallel to the facet and a perpendicular distance d_{obj} from the facet was considered. If the points at the opposite ends of the facet are designated P_1 and P_2, then the far field can be considered to have formed when the phase difference due to the difference in the distances P_1P and P_2P shows little variation with d_{obj}. These two distances are given by:

$$P_1P = \left[d_{obj}^2 + \left(w_f + d_{obj} \tan\theta \right)^2 \right]^{\frac{1}{2}} \tag{5-14 a}$$

$$P_2P = \left[d_{obj}^2 + \left(w_f - d_{obj} \tan\theta \right)^2 \right]^{\frac{1}{2}} \tag{5-14 b}$$

resulting in a phase difference of:

$$\Delta\phi_{obj} = 2\pi \left(\frac{P_1P - P_2P}{\lambda} \right) \tag{5-15}$$

where $2w_f$ is the width of the facet and θ is the angle of the line joining the centre of the facet to the point P from the perpendicular to the facet. For the broad area laser used, the width of the facet was $2w_f$=100μm and plots of $\Delta\phi_{obj}$ with distance for various angles θ and a wavelength of 810nm are shown in Fig. 5-16. It can be seen that a phase shift which is stable with distance, and hence the far field, is obtained for distances greater than approximately 2-3mm, the necessary distance increasing with far-field angle. Clearly, the optical system must be designed so that d_{obj} as defined by (5-13 b) is no smaller than this value.

To determine the suitability of various focal-length combinations for L_1 and L_2, d_{obj} was calculated using (5-13 b) for a number of combinations of commercially available cylindrical and diode-laser collimating lenses. Since it was shown in Fig. 5-14 that the separation of the lenses, d_{12}, must be less than or equal to the focal length of L_1, if the focal point is to lie between L_2 and the facet, d_{obj} was calculated for two lens separations: d_{12}=f_1 and d_{12}=f_1-f_2. The results of these calculations are shown in Fig. 5-17 as a function of imaging-plane distance, d_{img}, as shown in Fig. 5-15. Clearly, it is desirable that a sufficiently large value of d_{obj} for the far field to be

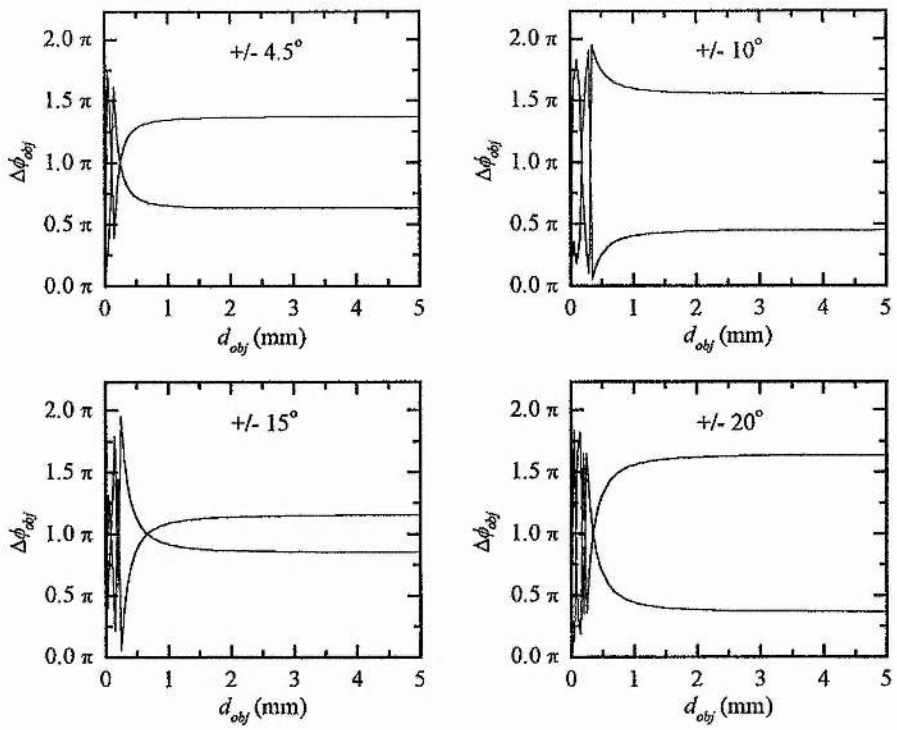

Fig. 5-16 Variation of phase shift between points at opposite ends of 100μm facet with distance from facet to imaging plane for various imaging angles and a wavelength of 810 nm.

formed is achieved for small values of d_{img}, if the system is to remain physically compact.

It was shown above that the object distance, d_{obj}, should be greater than around 2mm. It can be seen from Fig. 5-17 that if this is to be achieved with an imaging distance, d_{img}, less than ≈500mm, only the 6.5mm and 4.5mm collimating lenses can be used. Even in these cases, the cylindrical lens must have a focal length less than ≈80mm with the 6.5mm collimating lens and ≈40mm with the 4.5mm collimating lens. Reducing the lens separation, d_{12}, moves the object plane closer to the broad-area laser facet, resulting in only the 6.5mm/63mm lens combination giving practical values of d_{img}<500mm. Thus, it is clearly desirable to keep d_{12} as close to f_1 as possible.

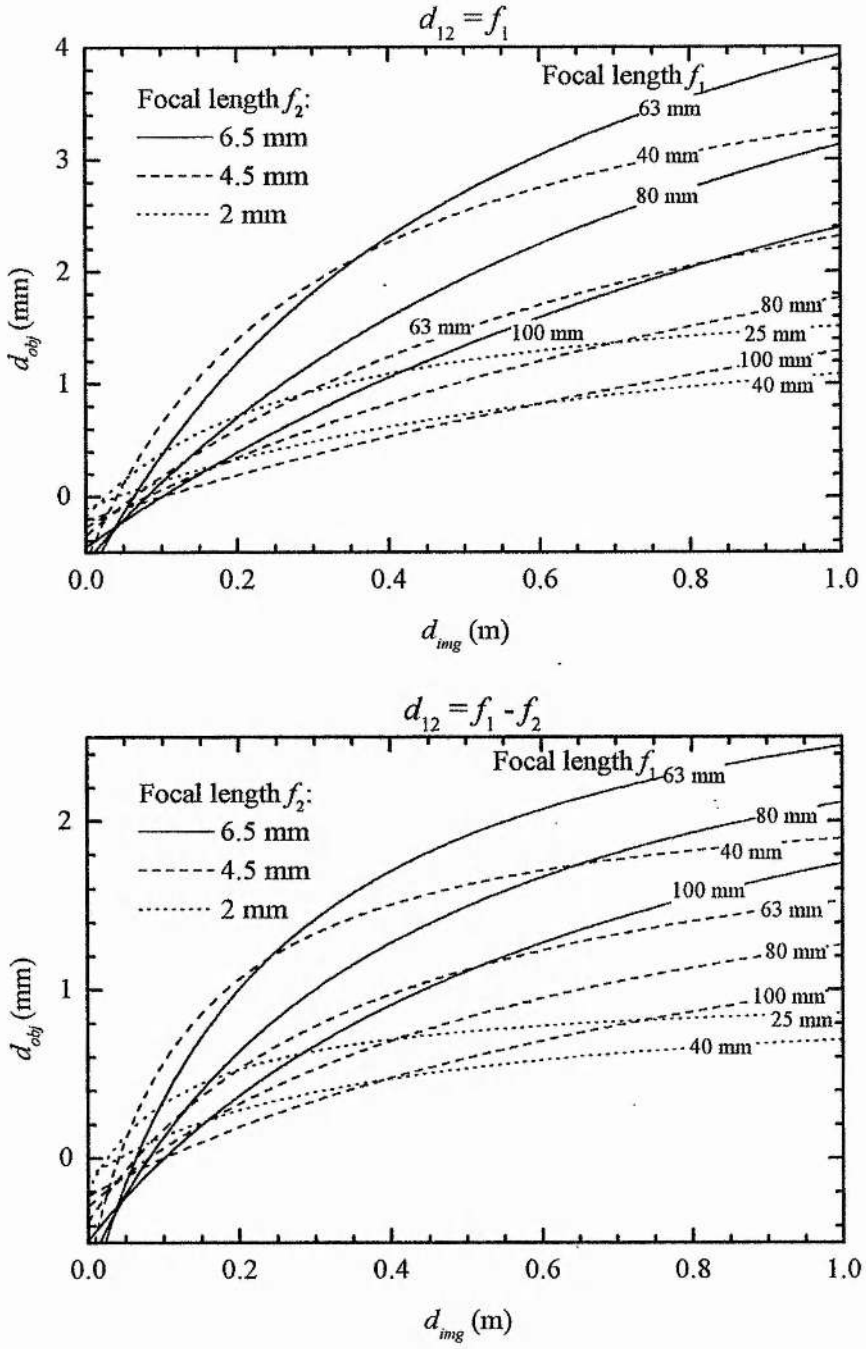

Fig. 5-17 Variation of object-plane distance, d_{obj}, from broad-area laser facet with imaging-plane distance, d_{img}, for a range of collimating-lens focal lengths, f_2, and cylindrical-lens focal lengths, f_1. Results are calculated for lens separations $d_{12}=f_1$ (top) and $d_{12}=f_1-f_2$ (bottom).

The other aspect of output extraction which can be treated using paraxial ray optics is the issue of the distance required to allow separation of the input and output beams. This can be determined from Fig. 5-18 where it is assumed that the emission angle of the injection-locked far-field peak is of the same magnitude as the injection angle, and that the facet dimension is small compared to the distance f_2, allowing injection and emission to be considered as occurring at the same point. It can be seen from Fig. 5-18 and equations (5-1) that the distance, d_{img}, required to achieve a separation h'_{sep} of the input and output beams, as shown when injecting at an angle of u'_2, will be given by:

$$d_{img} = f_1\left(1 - \frac{h'_{sep}}{2u'_2 f_2}\right) \tag{5-16}$$

Having investigated the general properties of the system using the paraxial ray optics approach above, and identified some suitable lens combinations from the point of view of extracting the injection-locked output, the Gaussian-beam performance of specific optical systems was calculated using ABCD matrix propagation methods.

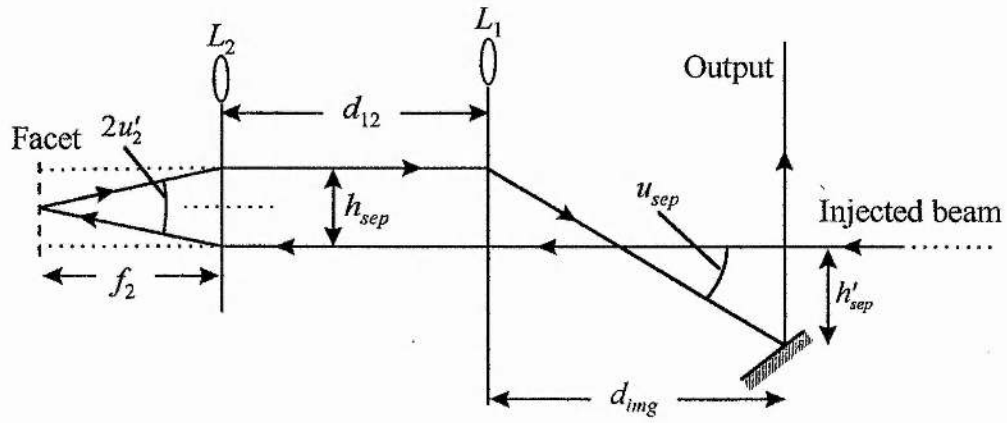

Fig. 5-18 Schematic diagram of lens system used to calculate propagation distance required to separate the injected and output beams.

The initial optical element to be chosen was the lens collimating the single-mode master laser. It was decided to use the collimating lenses of both lasers to collimate the output in the direction perpendicular to the junction plane. Due to the difference in emitter dimensions perpendicular and parallel to the junction, this resulted in imperfect collimation of the master laser output parallel to the junction. However, the effect was minor and would be expected to become insignificant after focusing by the cylindrical lens.

In the direction perpendicular to the junction, it would be preferable to use identical focal length collimating lenses for both lasers. This is due to the fact that the emitter dimensions of both lasers were the same in this direction. As a result, collimation and refocusing by lenses of the same focal length would maximise the coupling into the broad-area laser in this direction. It can be seen from Fig. 5-17 that the 6.5 mm collimating lens is most attractive from the point of view of extracting the injection-locked output. However, in terms of collimating the master laser, a 6.5 mm focal length lens was calculated to give a 6.7-mm $1/e^2$ collimated beam diameter perpendicular to the junction. This would have suffered severe clipping by the 5 mm clear aperture of the optical isolator used. As a result, a 2 mm focal length lens was used to collimate the master laser which gave a collimated diameter of 2.1 mm perpendicular to the junction. It was estimated that this would approximately halve the coupling efficiency into the broad-area laser.

Having determined the focal length of the collimating lens, the ABCD matrix transfer of the master laser output to the broad-area laser was calculated in the plane of the junctions. Both collimating lens positions were set to be one focal length from their respective laser facets and the distance, d_{12}, from the cylindrical lens, L_1, to the broad-area laser collimating lens, L_2, was varied around the cylindrical-lens focal length, f_1. All the lenses were treated as single-element thin lenses for the purposes of the calculation, and the additional space in the system was adjusted so that the distance between the two laser facets was one metre. This was judged to be a realistic distance to allow for the optical isolator, output extraction mirror and any other additional elements required.

The calculated waist radius and position for a number of the lens combinations of Fig. 5-17 resulting in suitable object-plane distances are shown in Fig. 5-19. The injected-beam radius at the broad-area laser facet is also shown. Comparing the results shown here to those calculated using paraxial ray optics, shown in Fig. 5-14, it can be seen that the calculated equivalent waist locations occur for slightly larger lens separations using the ABCD matrix/Gaussian beam treatment. From the

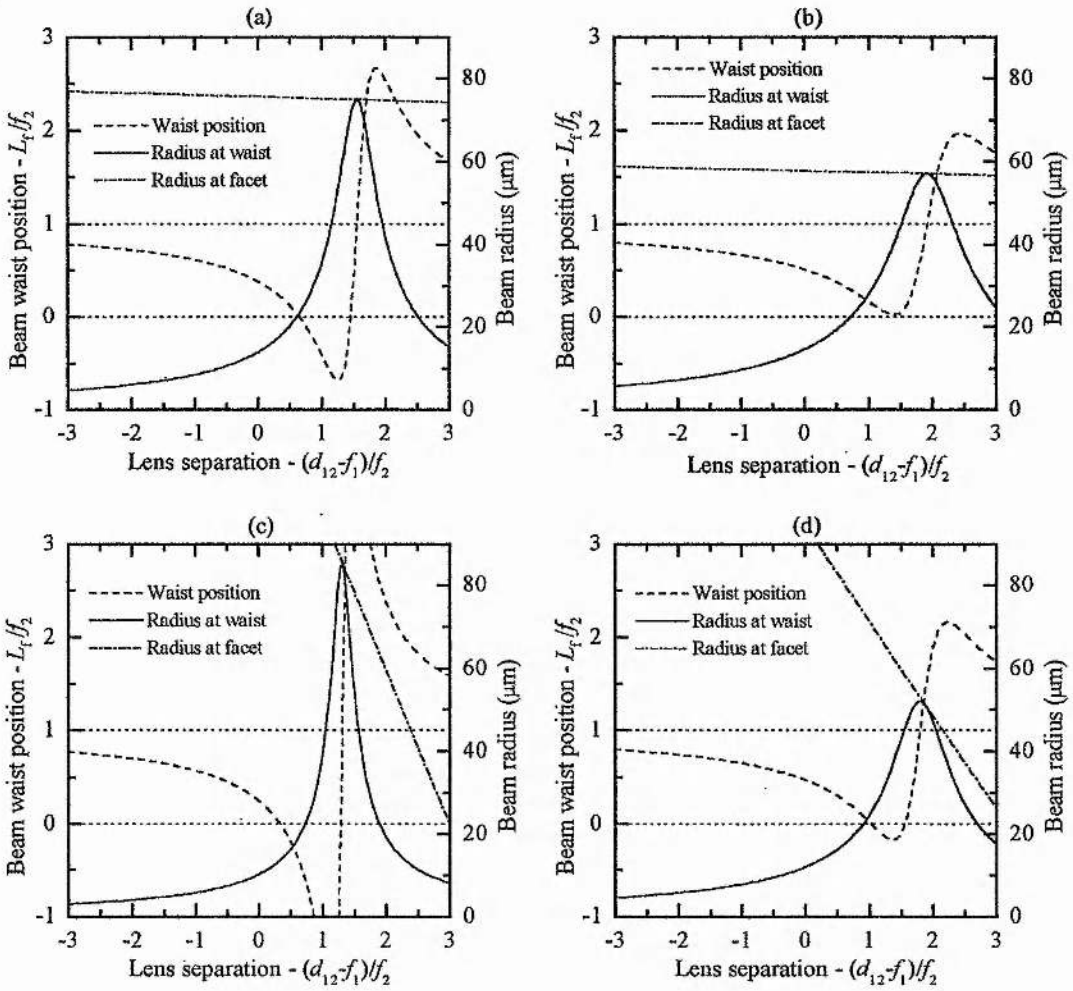

Fig. 5-19 Injected beam waist position (measured from lens L_2 towards broad-area laser facet), beam waist radius and beam radius at facet, calculated for lens L_1 and L_2 focal lengths: (a) f_1=63mm, f_2=6.5mm, (b) f_1=80mm, f_2=6.5mm, (c) f_1=40mm, f_2=4.5mm, (d) f_1=63mm, f_2=4.5mm. Master laser collimating lens was f=2mm, λ=810nm, distance between laser facets 1m.

modelling described in section 4.3, it was shown that the key to obtaining good injection-locked performance is control of the divergence produced by the master-laser beam waist. It was seen that it is desirable to have an injected-beam waist diameter around half that of the broad-area laser facet in the junction plane , corresponding to a waist radius of approximately 25μm in the case of the broad-area laser used here.

In addition to the beam-waist size requirement, the waist position must be located between lens L_2 and the broad-area laser facet. This region is indicated by the dotted lines of the graphs in Fig. 5-19. It can be seen in all cases that obtaining the required waist radius results in a waist location close to L_2 and approximately f_2 from the facet. With f_2=4.5mm, it can be seen that the beam waist obtained with f_1=40mm is significantly smaller than the required value for suitable waist positions, making this solution unsuitable. Although the f_2=4.5mm, f_1=63mm combination gives more suitable waist dimensions, it can be seen from Fig. 5-17 that this results in a object plane far closer to the facet than with the f_2=6.5mm solutions, and thus requires the imaging plane to be far further away if the far-field output is to be obtained.

Both solutions with f_2=6.5mm give waist radii close to the required values although the solution with f_1=80mm gives the required waist at positions slightly closer to the facet than with f_1=63mm. This results in a smaller beam radius at the facet than in the f_1=63mm case and thus improves the degree of overlap. It should be noted that all the solutions result in a beam diameter larger than the facet diameter in the plane of the junction. This is a result of the beam waist being at a distance from the facet in the optical system used. Although this results in a reduction in overlap and coupling efficiency, it was anticipated that this could be compensated by increasing the injected power. Although the f_2=6.5mm, f_1=63mm solution results in a poorer overlap, it can be seen from Fig. 5-17 that this lens combination reduces the imaging-plane distance required to obtain a far-field image when compared to the f_2=6.5mm, f_1=80mm combination. As a result, it was decided to use focal lengths of f_2=6.5mm and f_1=63mm in the final injection-locked system design.

Having decided upon a suitable optical design for injection into the broad-area laser, and confirmed that it fulfils the imaging requirements for output extraction discussed

above, the extraction of the injection-locked output using this system of lenses can now be investigated. If it is assumed that an h'_{sep} value of ≈5mm is required to extract the output in the manner shown in Fig. 5-18, then, from (5-16) for the chosen lenses, a separation distance of d_{img}=400mm is required for an injection angle of 3°, falling to d_{img}=214mm for a 5° injection angle. This latter value, however, can be seen from Fig. 5-17 to be insufficient for reliable far-field imaging of the broad-area laser output, so a d_{img} value of approximately 400mm was used.

When considering the extraction of the output from a Gaussian beam/ABCD-matrix point of view, it is useful to consider the nature of the initial emitter. It was seen, from equation (5-12) in the paraxial-ray treatment of output extraction, that the output can be considered as the magnified image of the far field pattern at a plane a distance d_{obj} from the emitter. It is also evident from (5-12) that the intensity distribution at this plane results from divergence at an angle u_0 from an emitter of dimension h_0. Since, when successfully injection locked, the far-field pattern would be expected to be the same as that for diffraction-limited emission from the broad-area laser, it can be assumed that h_0 represents the $1/e^2$ dimension of the emitter and u_0 the diffraction-limited divergence angle. Thus, as long as the optics fulfil the far-field imaging criteria detailed above, the system can be treated using standard ABCD matrix formalism and the source can be considered to be a diffraction-limited emitter with the same dimensions as the emitting aperture of the broad-area laser.

This technique was used to determine a suitable optical system for shaping the output after extraction from the injection-locked system. The unshaped output had different dimensions and divergences in the two planes, due both to the different emitter dimensions of the broad-area laser and the cylindrical lens L_1 acting in the junction plane only. The broad-area laser was considered as a diffraction-limited emitter in both planes and the propagation through the optical system was calculated using ABCD matrices. The extraction point was set to 400mm from the cylindrical lens L_1 and an additional 200mm was allowed beyond this before the effects of beam-shaping optics were calculated. To equalise the dimensions and divergences in both planes a cylindrical lens was used in each plane, both being arranged confocally with a common spherical lens. The calculated beam radius through the system is

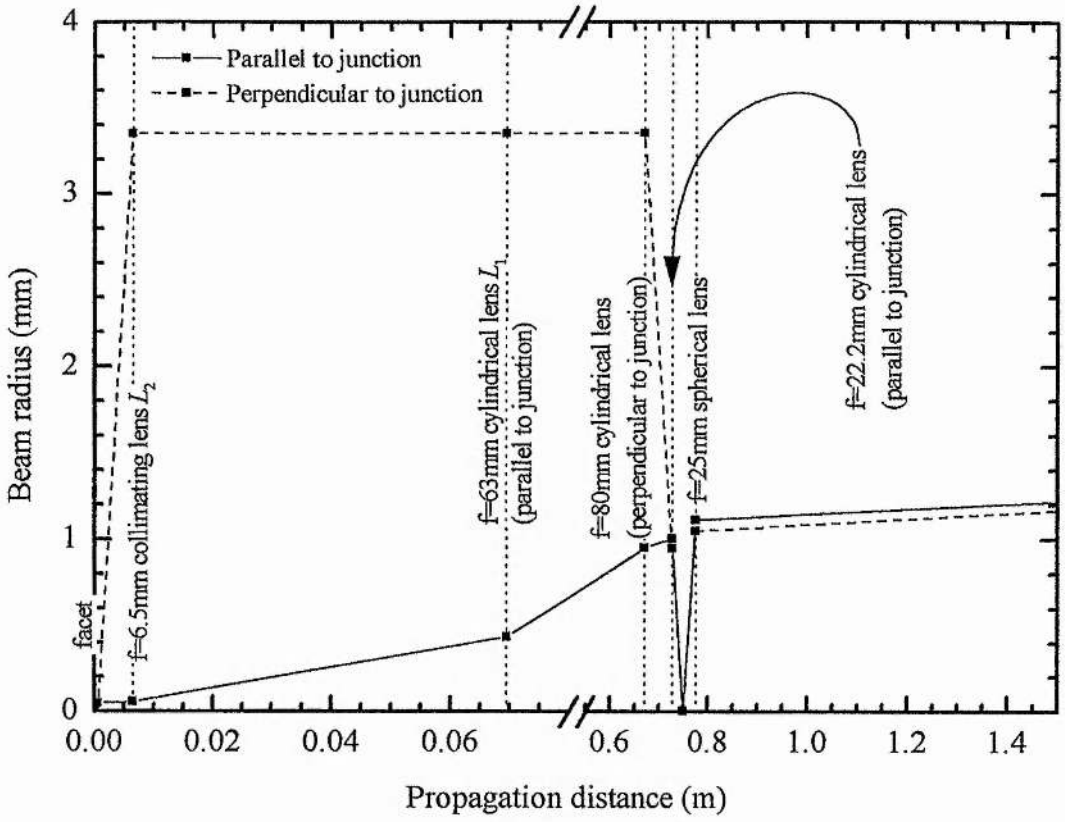

Fig. 5-20 Beam radius of the injection-locked broad-area laser output, calculated parallel and perpendicular to the junction plane, as it propagates through the optical system including the final output-shaping optics.

shown in Fig. 5-20. It can be seen that an f=80mm cylindrical lens acting perpendicular to the junction plane and an f=22.2mm cylindrical lens acting parallel to the junction plane, when both arranged confocally with an f=25mm spherical lens, result in an output beam having almost identical dimensions (approximately 1.1mm radius) and divergences in both planes. In addition, the output is close to collimated and the small divergence is the same in both planes. This allows a single spherical lens to be used for subsequent focusing.

Having designed a suitable optical system, the injection-locked broad-area laser system was implemented experimentally and characterised.

5.4 Experimental implementation.

The final design of the injection-locked broad-area diode laser system is shown in Fig. 5-21, viewed in the plane of the diode-laser junctions. The output of the single-mode master laser was collimated by the f=2mm lens and then passed through an optical isolator giving 60dB of isolation. A combination of a half-wave plate and a polarising beamsplitter allowed the injected power (polarised in the plane of the junctions) to be varied continuously, while picking off the remainder (polarised perpendicular to the junction plane) for wavelength measurement, by a fibre-coupled optical spectrum analyser, and spectral monitoring, by a scanning Fabry-Perot

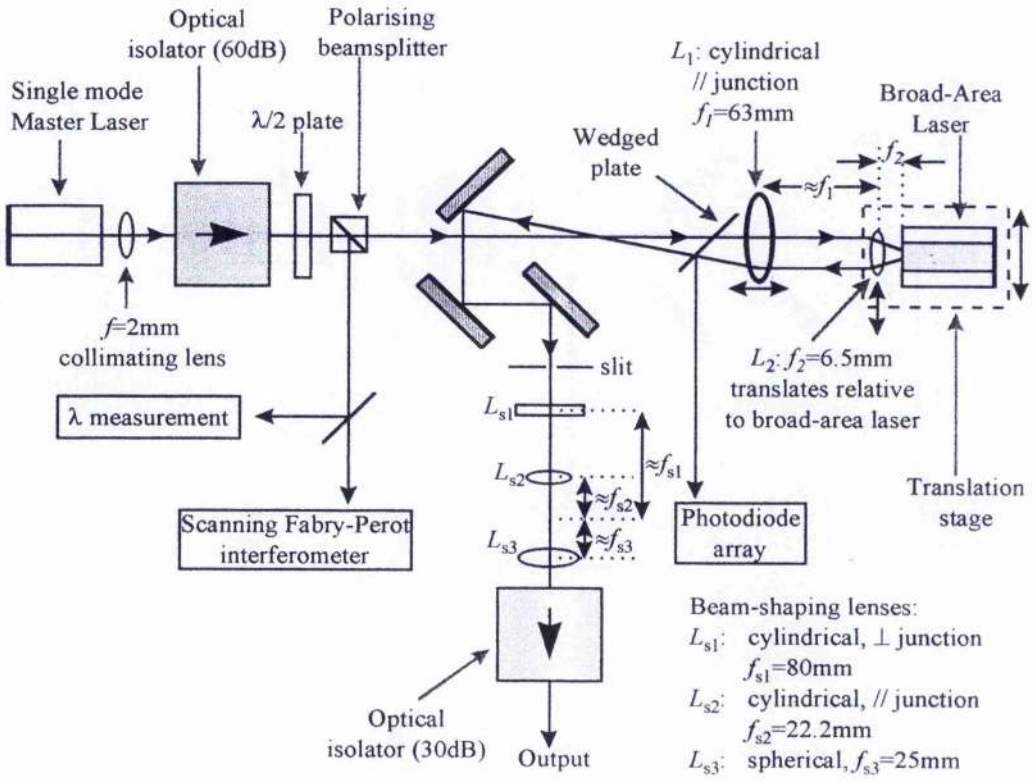

Fig. 5-21 Experimental implementation of the injection-locked broad-area diode laser system, viewed in the plane of the diode-laser junctions. The distance between the diode facets was ≈1m, between L_1 and the pick-off mirror ≈400mm and between the pick-off mirror and L_{s1}≈200mm.

interferometer. Following the polarising beamsplitter, the master-laser output went on to enter the injection optics, as detailed in the previous section. The transverse position of the cylindrical lens, L_1, was fixed to be centred on the master-laser beam, while its longitudinal position could be adjusted using a translation stage. The stage on which the collimating lens, L_2, was mounted was in turn mounted with the broad-area laser on a large translation stage. This arrangement allowed the injection position and angle to be varied independently, as described in the previous section.

Upon exiting the injection optics, the injection-locked output passed through an uncoated, wedged glass plate. This split off a small fraction of the output, which was then directed to a photodiode array allowing the intensity distribution to be monitored. The small wedge on the glass plate allowed the separation of the reflection from the front and back surfaces, thus avoiding ambiguity in the measured beam profile. The main injection-locked output passed through the wedged plate and continued on to the pick-off mirror which directed the principal maximum of the output, when injection locked, out of the system. A pair of beam-steering mirrors were used to compensate for any changes in output angle and ensure the beam remained on axis through the subsequent optics. An adjustable slit after these mirrors was used to block output outside the injection-locked peak. Beam shaping was carried out by two cylindrical lenses acting in orthogonal planes and arranged confocally with a common spherical lens, as described in the previous section, to give a near-collimated, near-circular output beam with a radius of around 1.1mm. Finally, an optical isolator giving 30dB of isolation was used to prevent back reflections into the injection-locked system from subsequent optics, as it was found this could seriously impair injection-locked performance. Since the lasers were mounted with their junctions in the plane of the optical table, the direction parallel to the junctions is referred to as horizontal and that perpendicular to the junctions as vertical.

Due to the relatively small aperture of the broad-area laser, into which the master-laser beam had to be injected, a reliable method of aligning the system had to be devised. This was achieved by using the photo-voltaic response of the broad-area laser to position both it and the injection optics. Although reverse biasing of the

broad-area laser for use as a detector was considered, it was not known whether this would result in damage. As a result, a unity-gain operational amplifier circuit, providing no biasing, was simply connected between the anode and cathode of the device and the amplifier output directed to a voltmeter.

The procedure developed to align the system is shown as a flowchart in Fig. 5-22. The master-laser collimating lens was adjusted to give a beam collimated in the vertical direction, propagating parallel to the surface of the table and perpendicular to the plane of the broad-area laser facet. The injected master-laser power was then set to around 20mW and the broad-area laser was translated horizontally across the beam until the photo-voltage was maximised. Although the lasers were nominally at the same height, a slight correction to the position of the master-laser collimating lens was usually necessary to maximise the photo-voltage in this direction. Since, at this stage, the dimensions of the master-laser beam at the broad-area laser were much larger than the active region of the broad-area laser itself, this only represented an approximate alignment.

The broad-area laser collimating lens was now inserted and its horizontal, vertical and longitudinal adjustments were used to roughly maximise the photo-voltage. Since the photo-voltaic response of the broad-area laser was found to saturate for very low focused master-laser powers, the power was set to 0.5mW for this and subsequent alignment. The transverse response (obtained by translating the collimating lens across the facet of the broad-area laser) is shown in Fig. 5-23. It can be seen that the central region of maximum voltage is around 100μm wide, corresponding to the active area. The lens was positioned half way between the two maxima at the edges of this region which, it was assumed, centred it on the facet, and this position was noted. The vertical and longitudinal adjustments were now modified to maximise the voltage for this transverse position. It was found that, for an incident power of 0.5mW, the voltages shown in Fig. 5-23, of 1.2-1.3V for the side peaks of the central region, usually indicated good alignment. It was noticed that the longitudinal position of the broad-area collimating lens which maximised the photo-voltage also resulted in the broad-area laser output being collimated in the vertical direction, as would be expected.

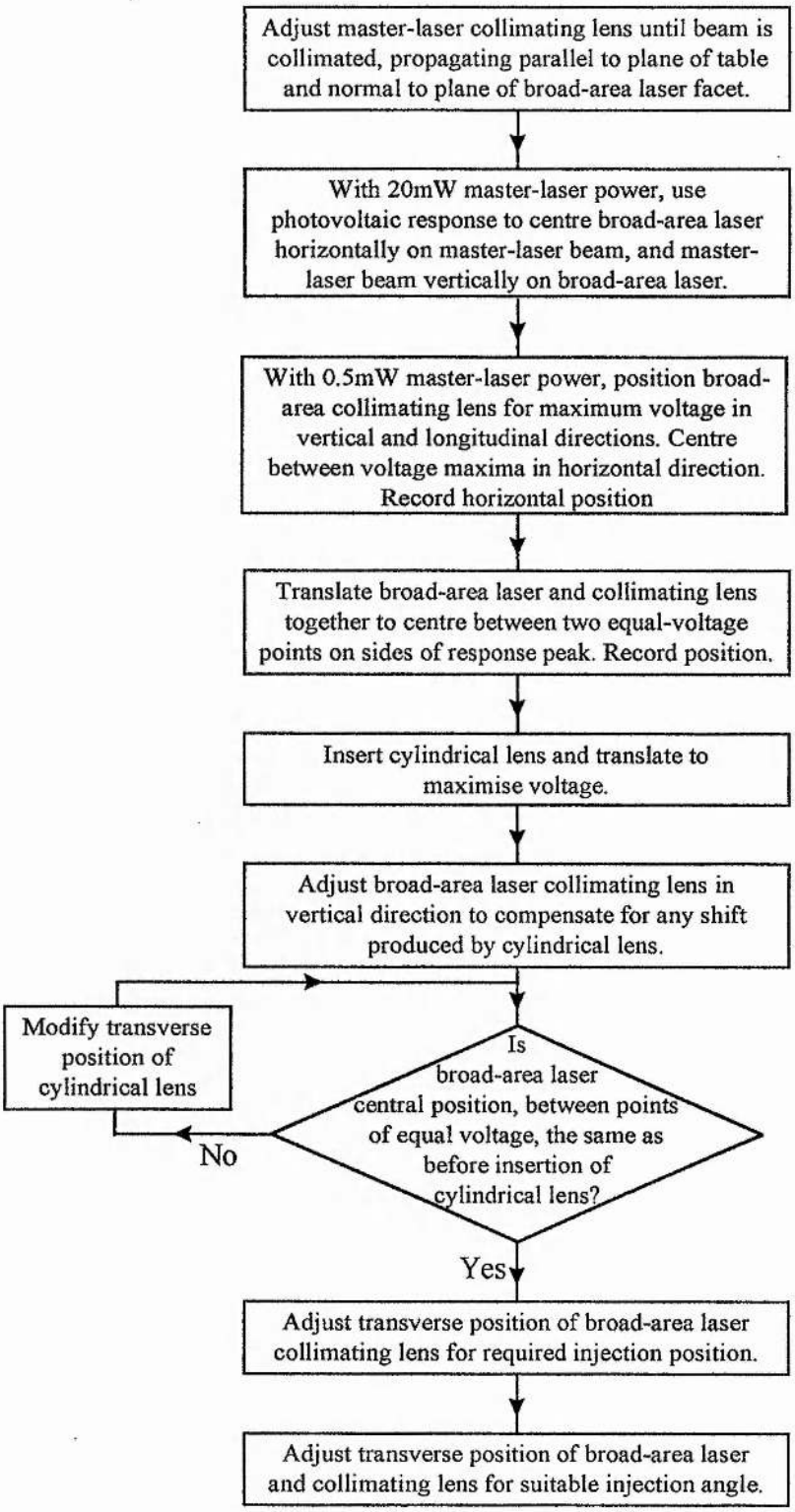

Fig. 5-22 Procedure for alignment of injection-locked broad-area laser system.

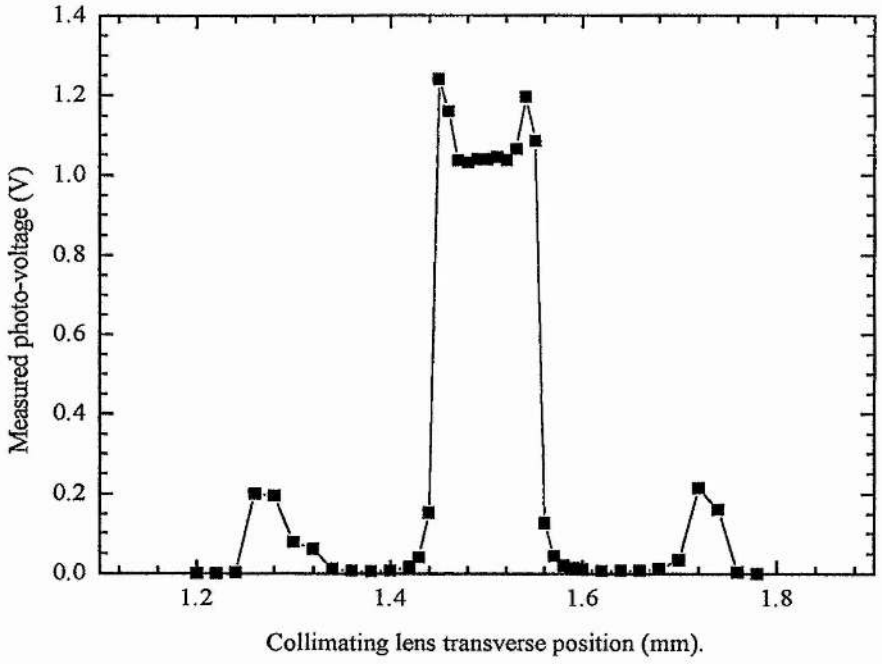

Fig. 5-23 Photo-voltaic response of broad-area laser to translation of the collimating lens, L_2, for a master-laser power of 0.5mW.

The broad-area laser and its collimating lens were next translated together across the master-laser beam. As discussed previously, this was expected to result in a variation in the injection angle only. This would appear to be the case from the results of a typical translation, as shown in Fig. 5-24 (a). It can be seen that the response has a flat central region, consistent with little or no significant change in the injection position, before falling off at the sides.

This fall-off was, in fact, mainly due to aperturing of the master-laser beam by the edges of the collimating-lens mount. It was found, however, that when the collimating lens had been accurately centred on the laser facet using the procedure described above, the fall-off was symmetrical about the centre of the response. It was thus possible to use two points of equal voltage either side of the central flat region to determine the central position. Typically, the points where the response fell to 0.8V were used and the central position was taken to be half way between these. The

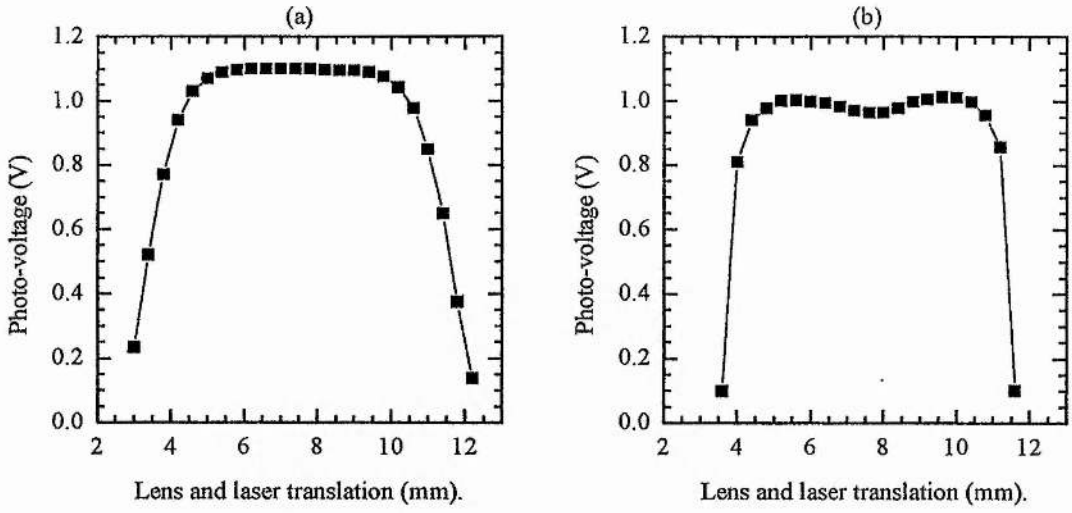

Fig. 5-24 Photo-voltaic response of broad-area laser to simultaneous translation of the laser and collimating lens for a master-laser power of 0.5mW: (a) collimating lens, L_2, alone, (b) cylindrical lens, L_1, in place.

translation-stage micrometer reading for this position was recorded and used as the central reference position for this translation.

Having determined the central reference positions for both the individual translation of the collimating-lens, L_2, and the combined L_2 and broad-area-laser translation, the cylindrical lens, L_1, was now inserted. With the laser and collimating lens both in their centred positions, the cylindrical lens was translated to maximise the photo-voltage, thus providing an approximate central alignment. Although this lens did not act in the vertical direction, it usually introduced some small translation in the beam in this direction and the broad-area laser collimating lens was adjusted vertically to compensate for this.

To accurately centre the cylindrical lens on the beam, the broad-area laser and collimating lens were again translated together. A typical response in this case is shown in Fig. 5-24 (b). It can be seen to be very similar to Fig. 5-24 (a), except that there is now a slight variation over the, previously flat, central region and the fall-off at the sides is more rapid. Again, the 0.8V points on the fall-off were used to

determine the central position and the transverse position of the cylindrical lens was then adjusted to obtain the same central position as that obtained before the cylindrical lens was inserted. Once this had been done, the transverse position of the cylindrical lens was not changed.

Once the alignment procedure had been carried out, and all the components were centred on the master-laser beam, the broad-area laser was re-connected to its controller and switched on and the master laser power was reset to the required operating level. The broad-area laser collimating lens, L_2, was translated from its central position to the required transverse injection point (a point typically 25-30μm from the central position was used) and the laser and collimating lens were translated together, to vary the injection angle, until a single-lobed injection-locked output was observed on the photodiode array.

Once injection-locking had initially been achieved, the injection parameters could be fine-tuned to maximise the injection-locked output power. Fine tuning was carried out by adjustments to the injection point (by translating the collimating lens), the injection angle (by translating the lens and laser together) and the injected beam waist (by longitudinal translation of the cylindrical lens). The transverse position of the cylindrical lens was not changed. For fixed lens and laser positions, the master-laser wavelength was varied for maximum injection-locked output.

Once aligned in this way, it was found that the system remained fairly well aligned in the short term, and if injection-locked output ceased to be produced, this was usually due to a shift in wavelength of the master laser. In the longer term, of the order of a few hours, it was found that mechanical drift resulted in misalignment, particularly in the vertical direction, which was most sensitive due to the small dimension of the broad-area laser in this direction. This was not generally serious and could be corrected by adjusting the vertical position of the broad-area laser collimating lens until injection-locked output was obtained. Drift also occurred in the position of the master-laser collimating lens, which usually had to be repositioned on a daily basis. To avoid having to carry out the alignment procedure of Fig. 5-22 on each occasion, an iris diaphragm was placed just before the wedged plate and centred on the master-laser beam when well aligned. This provided a sufficiently accurate point of

reference for repositioning of the master-laser beam for injection-locked operation to be achieved by small adjustments to the injection optics. When performance became seriously degraded, and high injection-locked powers could not be obtained, the system had to be realigned again, following the procedure of Fig. 5-22.

To convert the transverse profile, measured by the photodiode array, to a far-field angular distribution equations, (5-12) and (5-13) were used. The same far-field imaging criteria apply to the positioning of the photodiode array as to that of the pick-off mirror. Thus, the distance from the cylindrical lens, L_1, to the array must be sufficiently large that the position of the resulting object plane given by (5-13 b) is in the far field. If this requirement is satisfied, then (5-12) can be used to give:

$$u_0 = -\frac{h_{arr}}{Md_{obj}} \tag{5-17}$$

where the dimension at the array, h_{arr}, has replaced h_{img} of (5-12) and it has been assumed that the dimension at the array, h_0 in (5-12), is much less than the object-plane distance, d_{obj}. The values of M and d_{obj} are determined from (5-13), with the distance from the cylindrical lens to the array, d_{arr}, replacing the image-plane distance, d_{img}. In the experimental arrangement used, the distance from L_1 to the array, d_{arr}, was 495mm. If the distance from the cylindrical lens to the collimating lens is assumed to be equal to the focal length of the cylindrical lens, i.e. $d_{12}=f_1$, this gives values of M=-16.55 (the minus sign simply indicates an image inversion) and d_{obj}=2.69mm. From (5-17), this gives a conversion expression:

$$u_0 = \frac{h_{arr}}{0.0445} \tag{5-18}$$

Since the position of the cylindrical lens is in fact variable, it is important to determine how the conversion factor of (5-18) varies over the range of likely lens positions. The value of the conversion factor, $1/Md_{obj}$, is shown in Fig. 5-25 for a lens spacing of d_{12} varying from f_1-f_2 to f_1+f_2, with f_1=63mm and f_2=6.5mm. It can be seen that the conversion factor varies by only 3% of the central value over the range

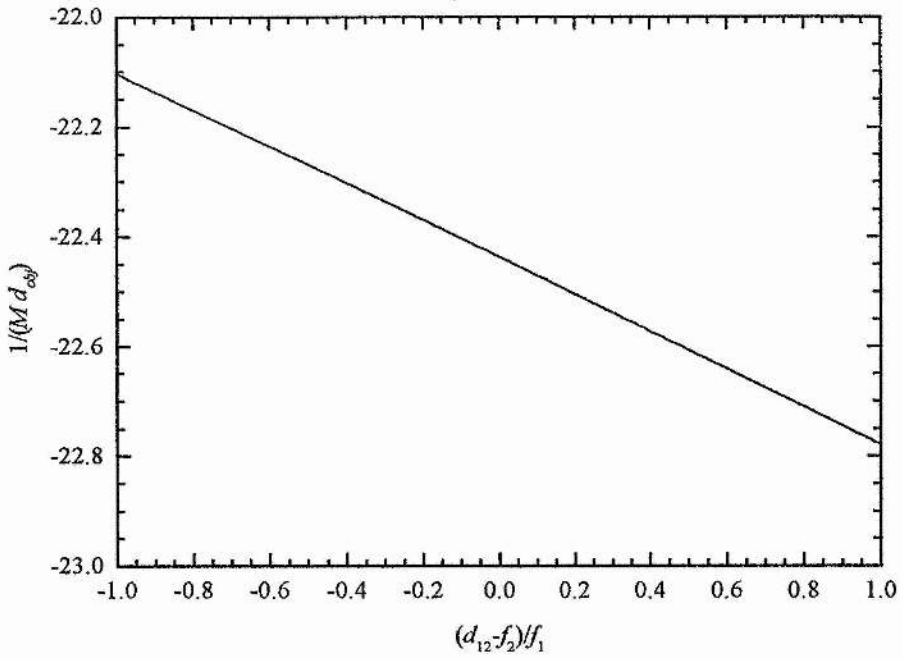

Fig. 5-25 Variation with lens spacing, d_{12}, of conversion factor to obtain far-field angle from photodiode array distance for f_1=63mm, f_2=6.5mm and distance from L_1 to array, d_{arr}=495mm.

shown. As a result, it was decided that the central value of the conversion factor could be used for all likely positions of the cylindrical lens.

5.5 Operating characteristics.

Having described the construction and operation of the injection-locked broad-area laser system, its performance is now described. The most obvious indication of successful injection-locking was the change in the broad-area laser far-field beam profile in the horizontal plane. Typical profiles obtained with the laser free-running and injection-locked are shown in Fig. 5-26. It can be seen that the free-running profile at an output of 1.2W has a full-width at half-maximum of approximately 11°, showing good agreement with the specified value of 12° [2] and confirming the imaging calculations.

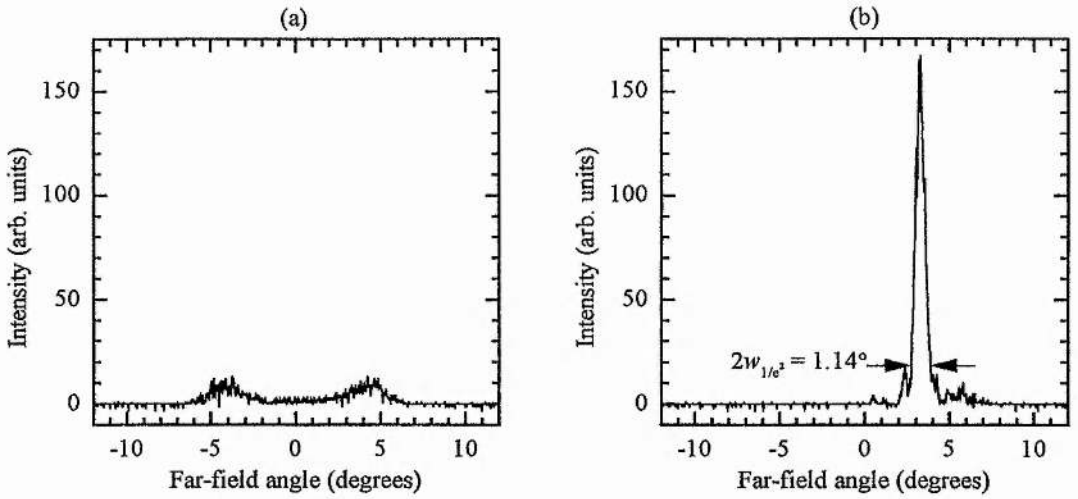

Fig. 5-26 Far-field profiles of the broad area in the plane of the junction: (a) free running, (b) injection-locked. Free-running output power was 1.2W, master laser power was 75mW.

When injection-locked with a master-laser power of 75mW entering the injection optics, the majority of the output power is seen to be concentrated in a single peak having a $1/e^2$ divergence half-angle of 0.57°. This is larger than the far-field divergence of a Gaussian beam from a 100μm diameter waist (a half angle of 0.3° would be expected), but is closer to the 0.46° diffraction angle expected from a 100μm rectangular aperture illuminated by a plane wave. It can be seen that although the free-running output power was 1.2W and the power contained in the injection-locked peak (determined using the adjustable slit) was only 450mW, the integrated area contained within the injection-locked peak of Fig. 5-26 (b) appears much larger than that under the free-running profile of Fig. 5-26 (a). In general, it was found that the injection-locked profile obtained with the photodiode array did not give a good indication of the power contained in the injection-locked peak which was usually much less than it would appear from this observation alone.

To make an unambiguous measurement of the injection-locked beam quality in the plane of the junction, the beam radius was measured through a focus using the techniques described in appendix A1 and the M^2 value was calculated. The results of

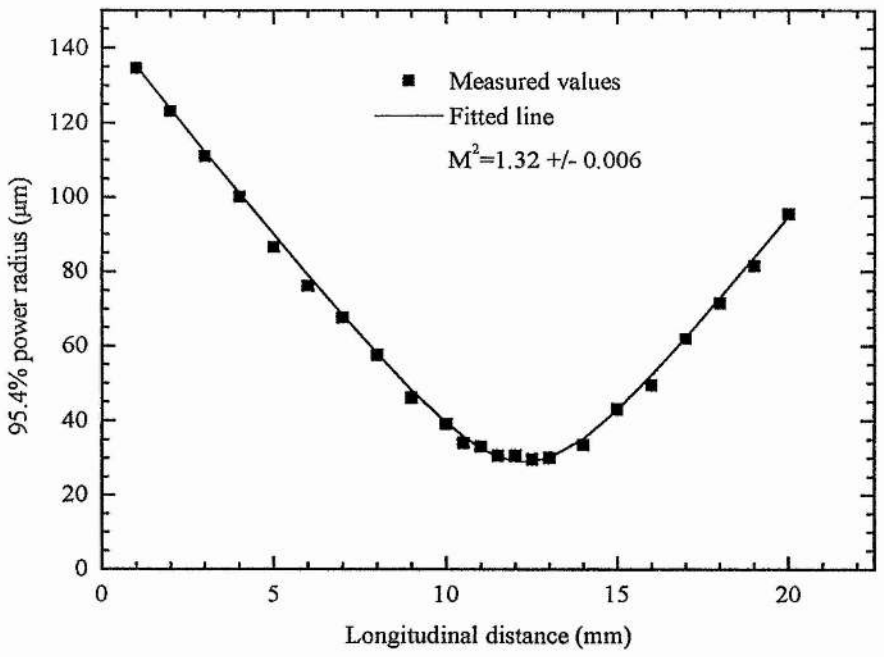

Fig. 5-27 Beam-waist measurement in plane of junction for injection-locked broad-area laser for an injection-locked output power of 360mW after the optical isolator.

these measurements are shown in Fig. 5-27. These measurements were made after the optical isolator, at a power of 360mW. This corresponded to ≈400mW before the isolator. It can be seen that the beam has an M^2 of 1.3, which is a considerable improvement over the value of 24.1 obtained from the data shown in Fig. 5-11 (b).

In addition to this improvement in spatial quality, the broad-area laser also showed considerable improvement in spectral quality when injection-locked. The scanning Fabry-Perot spectra of the free-running and injection-locked outputs are shown in Fig. 5-28. In the free-running case, the output spectrum is similar to that shown in Fig. 5-10 and is, therefore, actually much broader than the free-spectral-range of the interferometer used. Thus, Fig. 5-28 (a) does not represent the exact output spectrum but rather demonstrates the highly multi-mode nature of the output. Fig. 5-28 (b) shows that, once injection-locked, the output is essentially the same as that of the master laser shown in Fig. 5-3 (a). It was found that the output wavelength of the

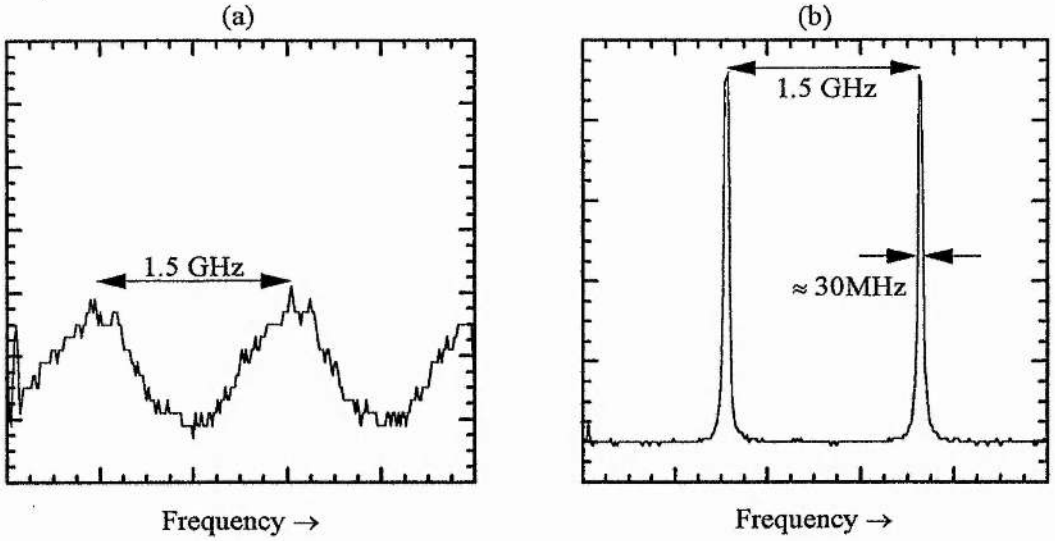

Fig. 5-28 Scanning Fabry-Perot interferometer spectrum of broad-area laser: (a) free-running, (b) injection-locked. Note that (a) corresponds to the situation shown in Fig. 5-10 and the spectral width is actually much greater than the free spectral range of the interferometer.

injection-locked laser was generally the same as that of the master laser, if the free-running wavelength was similar. Although the broad-area laser would tend to adopt the master-laser wavelength if the two were different, it was found that the injection-locking became less effective, and more power remained in the free-running portion of the output, as the wavelength separation increased. As a result, the system was generally operated with the free-running broad-area laser wavelength matched to that of the master laser.

To investigate the variation of output power with injected power, the injected power was varied using the half-wave plate/polariser combination and the injection-locked output power was measured for a range of broad-area laser injection currents. This measurement was made after the beam-shaping optics, but before the second optical isolator, which had a transmission loss of around 11%. The total output power was also determined. Since this could not be measured directly while injection locked, the power reflected by the wedged-plate beam-splitter used to obtain the far-field

profile was measured. The total free-running output power, which could be measured directly, was compared to that measured from the beam-splitter to provide a calibration factor for subsequent measurements from the beam-splitter.

The variation of the output power in the injection-locked peak with injected power is shown in Fig. 5-29 for a range of broad-area laser currents. It can be seen that up to 426mW of injection-locked output was obtained. The behaviour appears similar to that of an amplifier, increasing rapidly for low injected powers and saturating as the injected power is increased. The variations in the injection-locked output at higher broad-area laser currents were somewhat erratic, but were found to be entirely

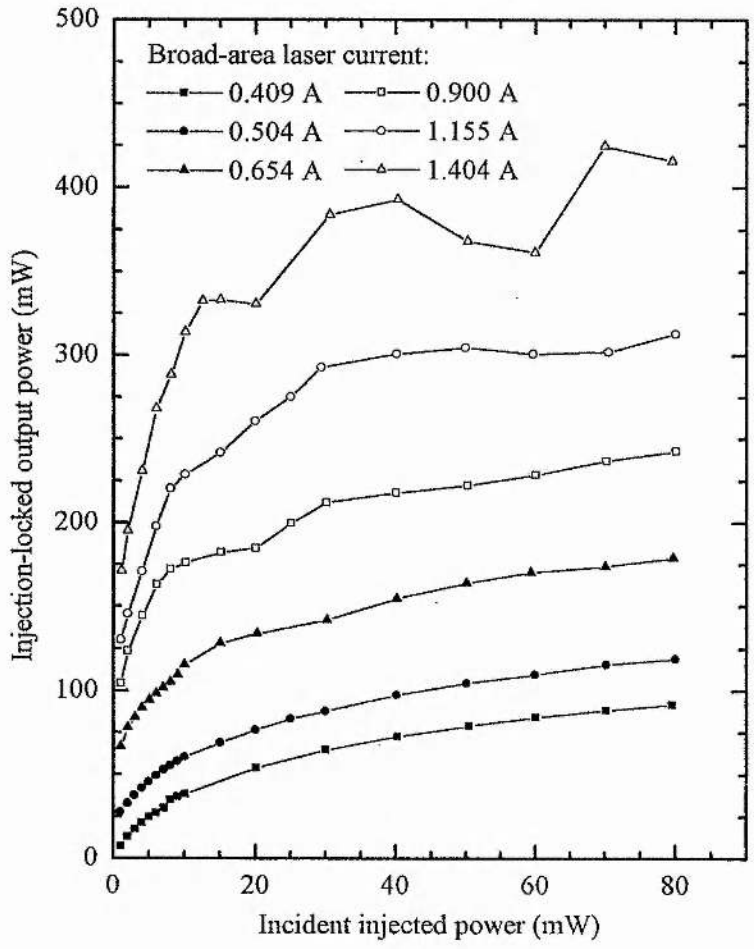

Fig. 5-29 Variation of power in injection-locked peak with incident master-laser power for a range of broad-area laser currents.

reproducible if only the injected power was changed. It was found that, even when operating in the saturated region, the injection-locked output power at these higher currents varied erratically and by substantial amounts with small changes in injected power, wavelength and injection position and angle. This was the case even for injection-locked outputs having very similar far-field profiles. Subsequent to the measurements of Fig. 5-29, and with slightly higher broad-area laser currents, injection-locked output powers of up to 450mW were observed after the second optical isolator, implying around 500mW of injection-locked output

The variation in the total output power and the fraction on this in the injection-locked peak are shown in Fig. 5-30. It can be seen from Fig. 5-30 (a) that there is little variation in the total output power with injected power, indicating that the injection-locking process simply transfers power from the free-running output into

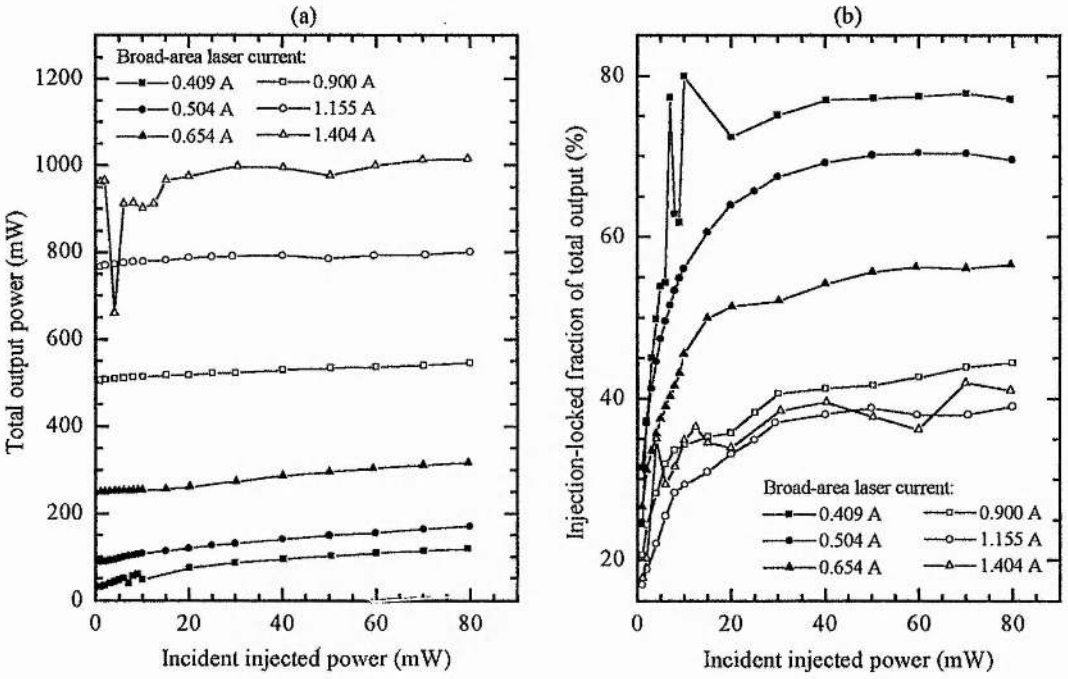

Fig. 5-30 Variation in total broad-area laser output power (a) and fraction of this in injection-locked peak (b) with incident injected power for a range of broad-area laser currents.

the injection-locked peak. The change in total power between 0mW and 80mW of injected power varies from 88.5mW for a broad-area laser current of 0.409A decreasing to 34.9mW for a current of 1.155A before increasing again to 53.4mW for 1.404A. These increases in total power were thought to be largely due to the power coupled in from the injected beam, with some contribution from the below-threshold gain of the broad-area laser being extracted by the injected beam.

From the injection beam dimensions at the facet, calculated in section 5.3, it was estimated that around 41% of the incident injected power in the vertical direction and 82% in the horizontal direction actually overlapped with the facet. Combined with the facet reflectivity of 5%, this would suggest around 32% of the incident injection power actually entered the broad-area device. For the maximum incident power of 80mW this would correspond to an injected power of 25mW which, although less than the increases in total power observed experimentally, is of a similar order to that seen at higher broad-area laser currents.

Fig. 5-30 (b) shows that the fraction of the total output which can be injection-locked, i.e. the locking efficiency, decreases with broad-area laser current. This is thought to be due to it being increasingly difficult for the injected beam to saturate the majority of the gain, and thus to suppress free-running output, as the current increases. It is possible that regions of unsaturated gain, resulting in free-running operation of parts of the broad-area laser, contribute to the erratic variation in injection-locked output power seen in Fig. 5-29. The gain saturation behaviour [5,7,8,9], near-constant total power [5,7] and fall in locking efficiency for increased broad-area laser gain [10] are consistent with the observations of others.

5.6 Conclusions.

To put the performance of the system described here in context, it is compared to published results from similar systems in Table 5-1. It can be seen that the performance compares well with the results of others. With the exception of [11], the injection-locked output powers achieved are significantly higher than those reported for other broad-area or array devices of the same active area width.

It is apparent from Table 5-1 that higher powers are, in general, obtained from wider active-region devices. This would be expected from the results shown in Fig. 5-30 (b), where it can be seen that increasing the broad-area laser current results in reduced locking efficiency, due to increased difficulty in saturating the gain. Increasing the broad-area laser width would allow a lower current to be used,

Incident injection power	Injection coupling efficiency	Broad-area laser / array width	Locked single-lobe output power (mW)	Comments and year	Ref.
15 mW	-	100 μm	700 mW	Claimed locked fraction appears doubtful from results. (1994)	[11]
45 mW	-	200 μm	640 mW	(1994)	[12]
10.4 mW	-	160 μm	450 mW	(1988)	[8]
70 mW	≈ 32%	100 μm	425 mW	This work, see Fig. 5-29. (1996)	
11 mW	-	400 μm	357 mW	(1987)	[4]
12.5 mW	≈ 32%	100 μm	330 mW	This work, see Fig. 5-29. (1996)	
15 mW	-	250 μm	235 mW	670 nm diodes. (1995)	[13]
3.9 mW	-	200 μm	189 mW	(1986)	[7]
10 mW	15 %	100 μm	119 mW	(1992)	[10]
12 mW	20 %	100 μm	<100 mW	(1985)	[14]
12 mW	10-20 %	100 μm	80 mW	(1988)	[5]
3 mW	10-20 %	100 μm	63-74 mW	First injection-locked diode demonstration. (1985)	[3]

Table 5-1 Results of this work compared to significant injection-locked diode laser results.

resulting in improved efficiency, and compensating for the reduced gain by increasing the gain volume. Commercial broad-area devices up to 200μm wide are available in the same range as the 100μm device used here and this could potentially be a means of increasing the output power.

The question of coupling efficiency was raised earlier and it was pointed out that re-design of the optical system to allow better overlap between the injected beam and the broad-area laser facet would improve this. However, it an be seen from Table 5-1 that the estimated coupling efficiency compares favourably with that of others. In addition to this, it can be seen from Fig. 5-29 that, once operating in the saturated region, the increases in injected power necessary to obtain significantly more output power are large. Therefore, with the power available from the master laser used, there is little to be achieved by improving the coupling efficiency, especially when the likely increase in the complexity of aligning the optical system is considered.

Although the simple model described in section 4.3 provided sufficient understanding of the injection-locking process for the optical desgin described in this chapter to be carried out, the behaviour of the injection-locked broad-area laser is likely to be considerably more complex in practice. This would appear to be the case from the results shown in Fig. 5-29 and Fig. 5-30 where, particularly at high powers, reproducible behaviour occurs which is not consistent with the simple treatment. More rigorous modeling, adressing issues such as local gain variations and interaction between beams passing through the broad-area laser, could potentially explain this behaviour. Such a study is, however, outside the scope of this thesis.

To conclude, the results presented in this chapter demonstrate the successful development and operation of an injection-locked broad-area diode laser system. Power levels of over 400mW were obtained with spatial and spectral properties similar to those of a single-mode diode laser. Although the injection-locked system should be viewed as, essentially, a laboratory-based pump source suitable for test and characterisation, the performance observed makes it a useful high-power diode-laser-based system for the pumping of solid-state lasers and optical parametric oscillators. The use of the injection-locked system in these two applications is described in the following chapters.

5.7 References.

1 SDL 5400 series data sheet, SDL Inc. (1995).

2 SDL 2300 series data sheet, SDL Inc. (1995).

3 L. Goldberg, H.F. Taylor, J.F. Weller and D.R. Scifres, "Injection-locking of coupled-stripe diode laser arrays," Appl. Phys. Lett. **46,** 236-238 (1985).

4 L. Goldberg and J.F. Weller, "Injection locking and single-mode fibre coupling of a 40-element laser diode array," Appl. Phys. Lett. **50**, 1713-1715 (1987).

5 G.L. Abbas, S. Yang, V.W.S. Chan, J.G. Fujimoto, "Injection behaviour and modeling of 100 mw broad area diode lasers," IEEE J. Quantum Electron. **24**, 609-617 (1988).

6 A.E. Siegman, "Lasers," University Science Books, Mill Valley, California, USA (1986).

7 L. Goldberg and J.F. Weller, "Injection-locked operation of a 20-element coupled-stripe laser array," Electr. Lett. **22**, 858-859 (1986).

8 L. Goldberg and M.K. Chun, "Injection-locking characteristics of a 1 W broad stripe laser diode," Appl. Phys. Lett. **53**, 1900-1902 (1988).

9 M.K. Chun, L. Goldberg and J.F. Weller, "Injection-beam parameter optimization of an injection-locked diode-laser array," Opt. Lett. 14, 272-274 (1989).

10 J. Verdiell, H. Rajbenbach, and J. Huignard, "Injection-locking of gain guided diode laser arrays: influence of the master beam shape," Appl. Opt. **31**, 1992-1997 (1992).

11 H. Tsuchida, "Tunable, narrow-linewidth output from an injection-locked high-power AlGaAs laser diode array," Opt. Lett. **19**, 1741-1743 (1994).

12 B. Beier, J.-P. Meyn, R. Knappe, K.-J. Boller, G. Huber and R. Wallenstein," A 180 mW Nd:$LaSc_3(BO_3)_4$ single-frequency TEM_{00} microchip laser pumped by an injection-locked diode-laser array," Appl. Phys. B **58**, 381-388 (1994).

13 R. Knappe, K.-J. Boller and R. Wallenstein, "Single-mode continuous-wave Cr^{3+}:LiSAF ring laser pumped by an injection-locked 670-nm broad-area diode laser," Opt. Lett. **20**, 1988-1990 (1995).

14 J.P. Hohimer, A. Owyoung and G.R. Hadley, "Single-channel injection locking of a diode-laser array with a cw dye laser," Appl. Phys. Lett, **47**, 1244-1246 (1985).

6. Injection-Locked Broad-Area Diode Laser Pumped 946-nm Nd:YAG Laser.

6.1 Introduction.

To initially investigate the performance of the injection-locked broad-area diode laser as a high spatial and spectral-quality pump source, it was used to pump a small, quasi-three-level, Nd:YAG laser operating at 946 nm. This allowed comparison not only with the performance predicted by the theoretical model developed in chapter 2 but also with the results obtained from an otherwise identical laser pumped by a low-quality, gain-guided diode laser array [1,2]. In this chapter, the optimisation of this laser according to the criteria discussed in chapter 2 is described and the results of cw and Q-switched operation are presented. Single-pass frequency-doubling of the Q-switched laser is also described.

6.2 CW operation.

Initial investigations of the 946-nm Nd:YAG laser were carried out in the cw regime to which the majority of the analysis of chapter 2 applies. As mentioned above, comparison with a previously demonstrated system [1,2] was desired and largely identical components were used to construct the laser described here.

6.2.1 System design and projected performance.

A simple near-hemispherical cavity, as analysed in chapter 2, was used for the 946-nm Nd:YAG laser. The Nd:YAG rod was 3mm in diameter, 2mm long and doped at ≈1.1%. The plane external face of the rod was coated for ≈99.7% reflectivity at

946nm and had ≈84% transmission at 808nm. The surface internal to the cavity was antireflection coated (R<0.35%) at 946nm. A number of output coupling mirrors were available having a radius of curvature of 50mm and transmissions at 946nm between 97.5% and >99%. The output couplers all had a reflectivity of R<30% at 1064nm to suppress parasitic oscillation at this wavelength. No attempt was made to control the temperature of the laser rod.

As was pointed out in chapter 2, the pump absorption coefficient depends on the degree of spectral overlap between the emission bandwidth of the pump and the absorption bandwidth of the laser medium. Values as diverse as $5.2cm^{-1}$ [3], $9.5cm^{-1}$ [3] and $12cm^{-1}$ [4] have been quoted for 1.1% doped material, depending on the spectral properties of the pump source. To measure the absorption coefficient for the pump source and laser crystal combination used here, the master laser was used to carry out absorption measurements on the crystal. The peak of the absorption bandwidth was found to occur at 808.5nm and an absorption coefficient of $8cm^{-1}$ was measured at this wavelength. From the results obtained in chapter 5, the injection-locked system was found to have an M^2 value of 1.3 both in the plane of the junction when locked and perpendicular to the junction plane. This value was used in (2-35) to obtain an optimum pump beam waist radius. The predicted operational characteristics of the laser were calculated using the parameters given above, in addition to those given in Table 2-1. These parameters are summarised in Table 6-1.

An optimisation diagram, similar to those shown in Fig. 2-11 to Fig. 2-13, was calculated to determine the optimum crystal length and level of output coupling. This was calculated for a pump power of 320mW, which was arrived at by correcting the maximum power of 380mW, incident on the Nd:YAG rod, for the input face reflectivity of 16% at the pump wavelength. The other parameters used in the calculation were as given in Table 6-1, the pump beam waist was set to the optimum value for the given crystal length, and the average laser mode radius was set equal to that for the pump beam. The results of this calculation are shown in Fig. 6-1. It can be seen that, for the given pump power and beam quality, the optimum crystal length and level of output coupling are 3mm and 6.5%, respectively. This optimum crystal

Parameter.	Symbol.	Value.
Nd^{3+} ion concentration (1.1 at.% doping).	N_0	1.518×10^{20} cm^{-3}
Upper state manifold fluorescence lifetime.	τ	230μs
Absorption/stimulated emission cross section.	σ	4×10^{-20} cm^2
Fractional population of upper laser level (300K).	f_b	0.602
Fractional population of lower laser level (300K).	f_a	0.0078
Reabsorption coefficient (300K).	α_l	0.0474 cm^{-1}
Distributed crystal losses.	α_i	0.002 cm^{-1}
Pump absorption coefficient (λ_p=808.5nm).	α	8 cm^{-1}
Pumping efficiency.	η_p	1
Refractive index.	n	1.82
Crystal length.	L	2 mm
Pump beam quality factor.	M^2	1.3
Parasitic surface losses.	δ_p	1%
Cavity length.	L_{cav}	≈50 mm

Table 6-1 Parameters used in the modelling of end-pumped Nd:YAG lasers.

length is somewhat larger than the 2mm length of the crystal used here. Similarly, the maximum level of output coupling, used in the work described here, of 2.5% is considerably smaller than the optimum value predicted by the results shown in Fig. 6-1. It would be expected that approximately 135mW of 946-nm output would be obtained with the values used experimentally here, as opposed to 160mW with the optimum values.

For the 2mm crystal length used experimentally and the pump M^2 value of 1.3, equation (2-35) gives an optimum pump beam waist radius of 15μm at the input face of the crystal. Although, in Fig. 6-1, the laser mode waist radius was set to give an average value equal to that of the pump, this is not necessarily the optimum value. To determine the optimum laser waist, the output power was calculated by solving

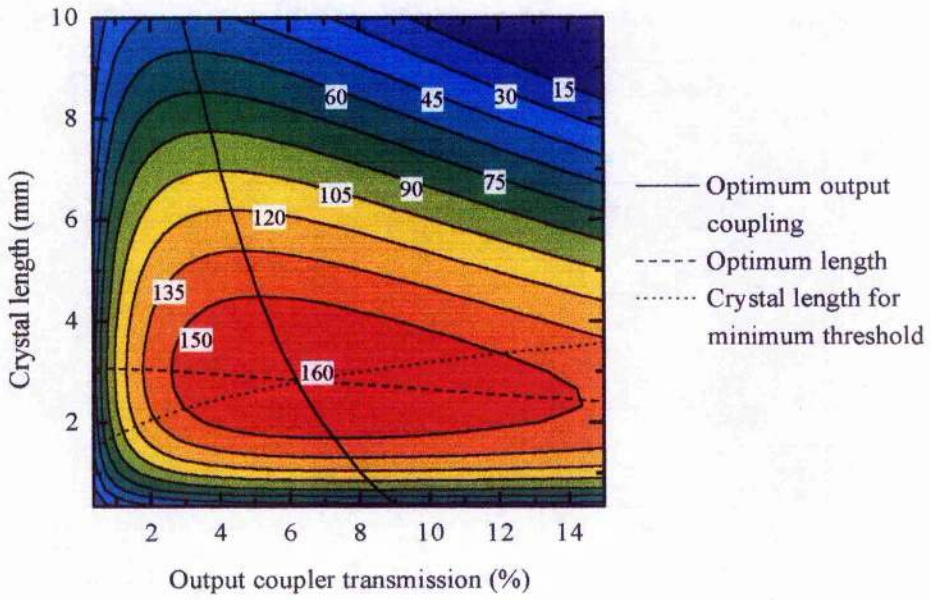

Fig. 6-1 Calculated output power (mW), as a function of crystal length and output coupling, for experimentally investigated configuration of the 946-nm Nd:YAG laser. Pump power entering the laser crystal was set to 320mW, $w_P = w_{P,opt}$, $\overline{w}_L = \overline{w}_P$ and all other parameters were as given in Table 6-1.

equation (2-28) numerically for a pump waist fixed at the optimum value of 15μm and various laser mode waist radii. The input pump power was set, as before, to 320mW and the values of other parameters were as given in Table 6-1. The results of these calculations are shown in Fig. 6-2. It can be seen that two output-power maxima occur at $w_L/w_P = 0.65$ and $w_L/w_P = 1.3$. The first of these, however, is not a true maximum but occurs because the same average mode waist, as calculated by equation (2-34), can be arrived at from two different waist radii. In practice, however, values of $w_L/w_P < 1$ will result in poor overlap and lower output power than predicted by Fig. 6-2. Solutions in this region are shown by a dashed line.

The optimum value of the waist radius ratio, w_L/w_P is thus 1.3, corresponding to a laser mode waist of $w_L = 20\mu m$. The ratio of the average mode radii, $\overline{w}_L/\overline{w}_P$, is also plotted in Fig. 6-2. It can be seen that this has a value of $\overline{w}_L/\overline{w}_P \approx 1$ for the optimum laser mode radius which was the assumption made in the calculations of Fig. 6-1.

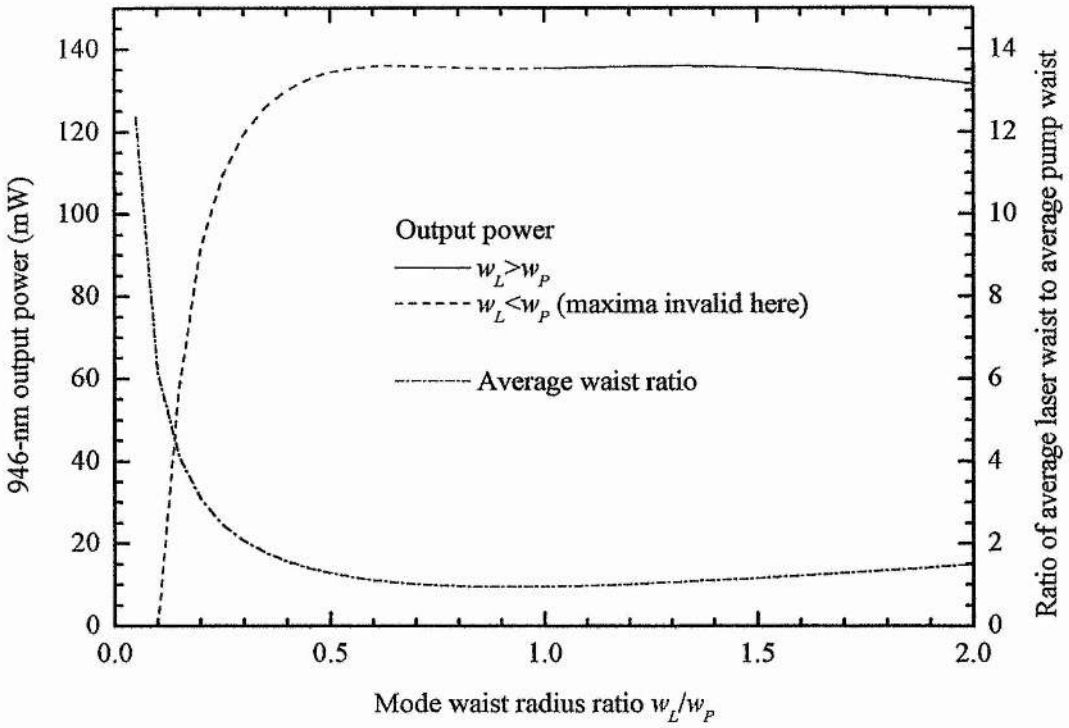

Fig. 6-2 Variation of output power of 946-nm Nd:YAG laser and average mode waist ratio, $\overline{w}_L/\overline{w}_P$, with laser mode waist ratio w_L/w_P for a fixed pump waist of 15μm. Input pump power was 320mW and all other parameters were as given in Table 2-1.

Continuing the ABCD ray tracing calculation shown in Fig. 5-20, it was calculated that a 63mm focal length lens, placed one focal length from the input face of the laser crystal, would result in waist radii of 14μm and 14.7μm in the horizontal and vertical planes, respectively. The laser mode waist, calculated by ABCD matrix analysis, is plotted as a function of cavity length in Fig. 6-3. It can be seen that the required 20μm mode radius is obtained with an overall cavity length of ≈51mm and that, at this point, the stability of the cavity is highly marginal. In practice, the pump beam was focused into the crystal using the 63mm lens as described and the cavity length was varied to maximise the output power.

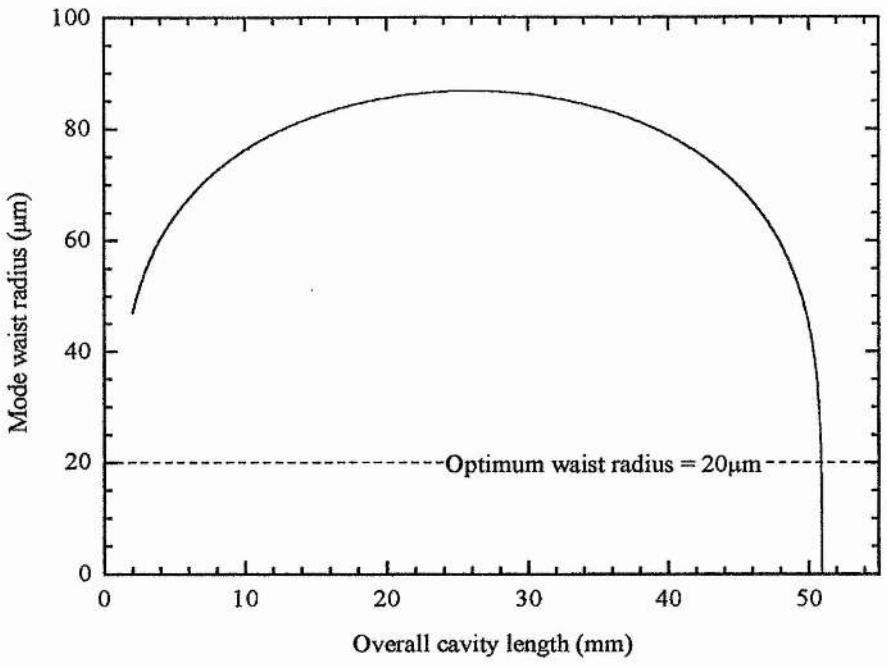

Fig. 6-3 Variation of laser mode waist in near-hemispherical cavity of 946-nm Nd:YAG laser. Mirror radius of curvature was 50mm and Nd:YAG crystal length was 2mm.

The experimental configuration used in practice is shown in Fig. 6-4. The circularised output of the injection-locked system passed through a variable neutral-density filter, to allow variation of the pump power, before being focused by the 63mm lens onto the end of the Nd:YAG rod. The focusing lens, laser crystal and spherical mirror could all be translated along the axis of the laser and the crystal and mirror could both be rotated in the horizontal and vertical plane. The incident pump power and output power at 946nm were measured with an optical power meter calibrated for each wavelength. An RG850 filter was used to block any residual pump light passing through the laser and 946-nm measurements were corrected for the 89% transmission of the filter at this wavelength. Due to the small mode waist used in the laser, the output at 946 nm was highly divergent and a 100mm lens was used to refocus this onto the detector.

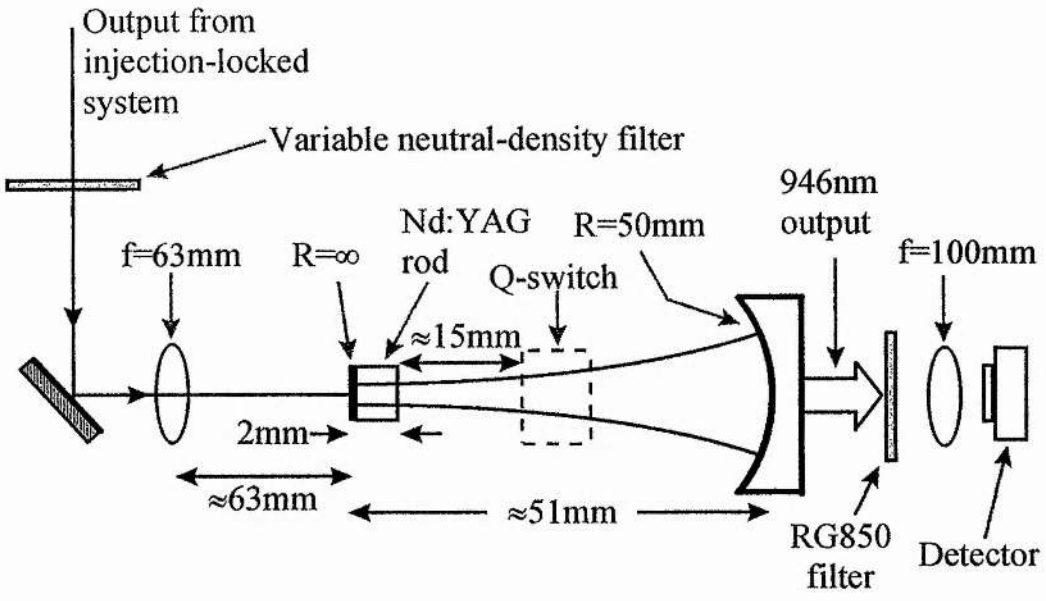

Fig. 6-4 Experimental configuration used for investigation of the 946-nm Nd:YAG laser. Q-switch was removed from cavity for cw operation.

6.2.2 Results and discussion.

The measured output power, as a function of the input pump power (pump power entering the laser crystal) is shown in Fig. 6-5. The threshold was observed to be 52mW and the average slope efficiency, obtained by a linear fit to the data, was 48% of input pump power. Results of this type, especially slope efficiency, are frequently reported in terms of absorbed pump power. This is shown along the upper axis of Fig. 6-5, having been calculated using the known absorption coefficient of $8cm^{-1}$. In these terms, the threshold is 42mW and the slope efficiency is 60%.

Also shown in Fig. 6-5 is the theoretical performance calculated using (2-28) with the parameters of the experimental system. These calculated results predict a threshold of 26mW and slope efficiency of 46% in terms of input pump power. It is clear that, although the experimental slope efficiency is slightly better than that predicted by theory, the experimental threshold is considerably higher than would be

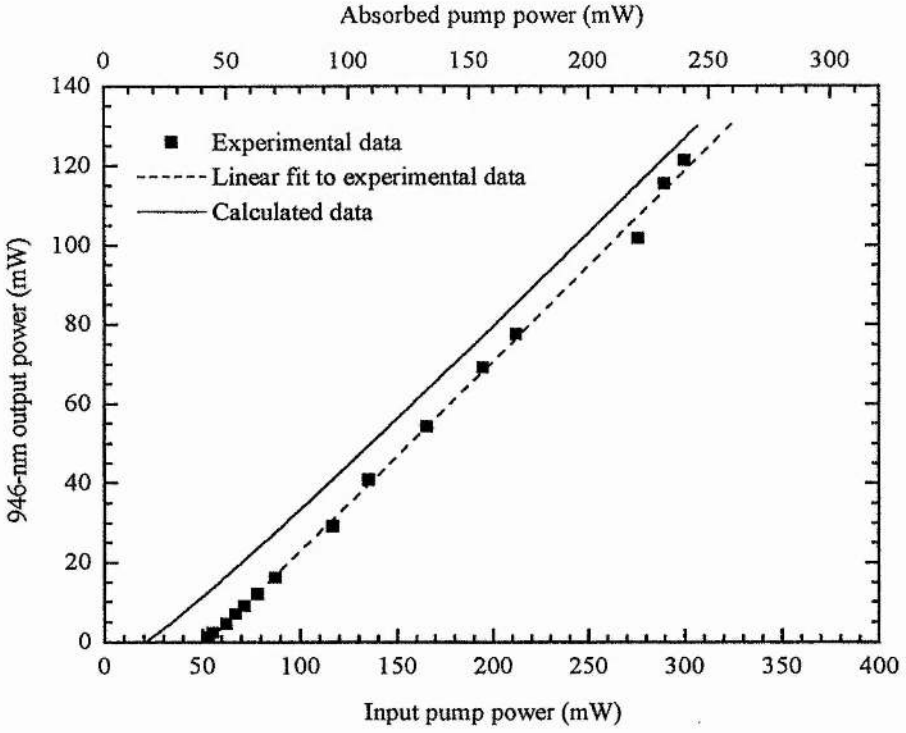

Fig. 6-5 Output power of 946-nm Nd:YAG laser as a function of input pump power with 2.5% output coupler. Fitted line gives a threshold of 52mW and average slope efficiency of 48% for input pump power, threshold of 42mW and average slope efficiency of 60% with absorbed pump power. Calculated data has threshold of 26mW and slope efficiency of 46% in terms of input pump power.

expected. At higher pump powers, however, the agreement between theory and experiment is considerably better.

The improved agreement at higher powers, together with the slightly higher efficiency observed experimentally, seems likely to result from the effects on the laser mode of the pump-induced thermal lens in the Nd:YAG crystal. During the experiment the cavity was adjusted to maximise the output power at maximum pump power. It would, therefore, be expected that cavity adjustment would compensate for any thermal lens present at these higher powers. At low powers, however, any

thermal-lensing effects would be considerably weaker and the cavity would be over compensated, resulting in an increased threshold.

To illustrate this effect, the expression for the equivalent focal length of a thermal lens derived by Innocenzi et al. [5] was used:

$$f = \frac{\pi K_c w_P^2}{P_{ph} \frac{dn}{dT}} \left(\frac{1}{1 - \exp(-\alpha L)} \right) \tag{6-1}$$

where K_c is the thermal conductivity of the material (13 $Wm^{-1}K^{-1}$ for Nd:YAG [6]), P_{ph} is the input pump power which contributes to heating of the rod and dn/dT describes the temperature dependence of the refractive index (7.3×10^{-6} K^{-1} for Nd:YAG [6]). The derivation used in [6] assumes the thermal lens to be due to a quadratic refractive index variation with the radial distance, r, of the form:

$$n(r) = n_0 - \frac{n_2}{2} r^2 \tag{6-2}$$

where n_0 is the on-axis refractive index at $r = 0$. This can be related to the equivalent focal length by the expression [6]:

$$f \approx \frac{1}{n_2 L} \tag{6-3}$$

This allows the quadratic gradient of the index variation, n_2, to be calculated from (6-1). The resulting value can then be used to obtain the ABCD matrix for the Nd:YAG rod which is given by [7]:

$$\begin{bmatrix} \cos\left(L\sqrt{\frac{n_2}{n_0}}\right) & \frac{1}{\sqrt{n_0 n_2}} \sin\left(L\sqrt{\frac{n_2}{n_0}}\right) \\ -\sqrt{n_0 n_2} \sin\left(L\sqrt{\frac{n_2}{n_0}}\right) & \cos\left(L\sqrt{\frac{n_2}{n_0}}\right) \end{bmatrix} \tag{6-4}$$

As was shown in Fig. 6-3, to obtain the small mode waist required, the laser cavity was operated close to the hemispherical limit where the resulting mode waist varies rapidly with effective cavity length. This results in the mode waist radius in the crystal being highly sensitive to thermal lensing effects. To estimate the effect of thermal lensing on threshold, equation (6-1) was used to estimate the thermal lens at 320mW of input pump power and 120mW of laser output as having an equivalent focal length of around 13mm. Equations (6-2) to (6-4) were then used to obtain the ABCD matrix for the Nd:YAG rod in the presence of this thermal lens, making the approximation $n_0 = n = 1.82$. This matrix was then used to replace that of the simple Nd:YAG rod in the cavity stability calculations. The overall cavity length in the stability calculation was then adjusted to give the required 20μm mode radius in the presence of the thermal lens at 320mW of input pump power. With the cavity length fixed at this value, as would be the case for a laser optimised at maximum pump power, the thermal lens and overall ABCD matrix for one round trip was calculated for a range of pump power levels. Using the ABCD matrices thus obtained, the waist radius at each pump power level was calculated. This was then used in (2-20) to calculate the threshold.

The results of these calculations are shown in Fig. 6-6. The solid curves correspond to above threshold operation and the dashed curves to that below threshold. It can be seen that as the pump power falls, the thermal lens becomes weaker, causing the laser mode waist radius to increase thus increasing the threshold. At an input pump power level of around 43mW, the threshold power input and pump power are equal, and laser operation would be expected to cease at pump powers below this level. It can, therefore, be seen that the threshold would be expected to be higher than that calculated assuming the mode waist radius to be optimum at all pump power levels.

The calculated results shown in Fig. 6-6 should, however, be viewed with some degree of caution for a number of reasons. Firstly, the model described in [5] assumes that, above threshold, the difference between absorbed pump power and laser output power contributes to the heating of the crystal. Below threshold, a significant fraction of the absorbed power is re-emitted as fluorescence and a different set of assumptions need to be made about the thermal loading of the crystal

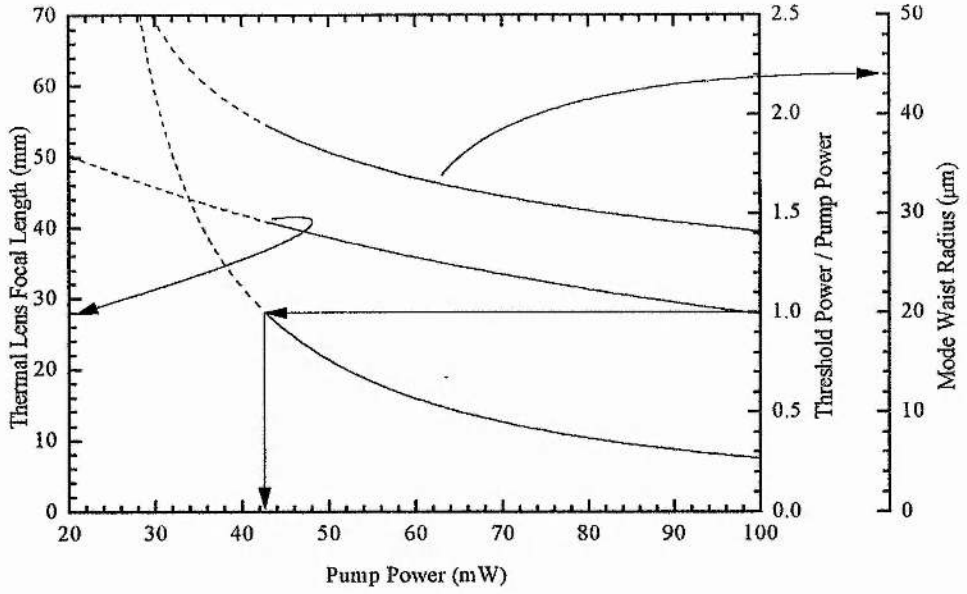

Fig. 6-6 Calculated thermal lens focal length for a range of pump powers and corresponding laser-mode waist radius and threshold-to-pump-power ratio. The laser cavity length was set, in the calculation, to compensate the thermal lens induced at maximum pump power.

based on the fluorescence branching ratios and absorption coefficients at the main fluorescent wavelengths. While the results below the predicted threshold value are marked with dashed lines to indicate this, it should also be noted that, for the same reasons, the model starts to become less valid at lower powers in the above-threshold region.

The second limitation arising from the model of [5] is the assumption, in the derivation of (6-1), that solely radial heat flow occurs in the crystal. While this assumption is largely valid in the case of long crystals, in our case, where the crystal length and radius are similar, significant heat flow would be expected through the end faces. Finally, as already mentioned, the near-hemispherical cavity is highly sensitive to changes in its effective length, causing small changes in the input parameters of the calculations used to produce Fig. 6-6 to result in large changes in the results. As a result of these limitations, the results shown in Fig. 6-6 should be

regarded as a qualitative illustration of the process leading to increased threshold rather than an accurate quantitative model of the situation under consideration here.

6.3 Q-switched operation.

For applications in nonlinear optics, it is often desirable to increase the maximum instantaneous output power of a laser by operating it in a pulsed regime. To investigate pulsed operation of the 946-nm Nd:YAG laser, an acousto-optic Q-switch fabricated from a Brewster-angled lead molybdate crystal was inserted into the cavity. The length of the Q-switch crystal along the optical path was 14mm and its refractive index was 2.35. As the cavity was operated in a near-hemispherical configuration, and therefore close to the stability limit, insertion of the Brewster-angled element resulted in a large disparity in mode radii between the tangential and saggittal planes.

The equivalent diagram to Fig. 6-3, showing the mode waist radii as a function of cavity length, with the Q-switch in place is shown in Fig. 6-7. It can be seen that when the optimum laser mode waist radius of 20μm, calculated for the cw case, is achieved in the tangential plane, the mode has a waist radius of ≈65μm in the sagittal plane. Clearly, the pump beam should ideally be shaped to match this ellipicity to some extent. In practice, however, the same optical system was used to shape the output of the injection-locked pump source as in the cw case. Once the laser cavity length had been adjusted for optimised Q-switched operation, it was found that some improvement in performance could be achieved by slight longitudinal repositioning of the cylindrical lenses in the output beam-shaping system of the injection-locked laser, thus introducing a slight ellipicity in the pump beam.

The cw threshold and slope efficiency were measured with the Q-switch in place for the cases of the cavity adjusted for maximum cw output and maximum peak power when Q-switched. The results of these measurements are shown in Fig. 6-8. It can be seen that the cw optimised cavity had a threshold of 85.4mW of input power and a slope efficiency of 31%, while the Q-switch optimised cavity had a similar threshold at 85.1mW but a reduced slope efficiency of 25%. The difference in slope efficiency

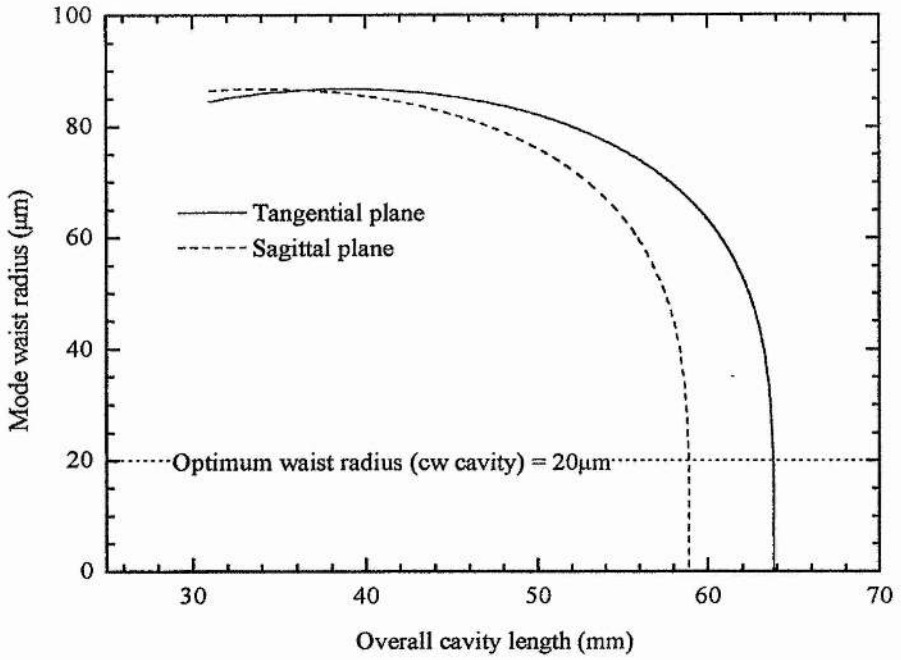

Fig. 6-7 Variation of laser mode waist in astigmatic near-hemispherical cavity of Q-switched 946-nm Nd:YAG laser. Mirror radius of curvature was 50mm and Nd:YAG crystal length was 2mm. Brewster-angled Q-switch had a path length of 14mm and refractive index of 2.35 and was located ≈15mm from intra-cavity face of laser crystal.

is attributed, again, to thermal lensing effects at higher powers, the thermal loading under Q-switched operation being different from that under cw operation. The increase in threshold and reduction in slope efficiency for both cases compared to the cavity without the Q-switch would appear to be caused by a combination of losses introduced by the Q-switch and reduced mode overlap due to the astigmatic laser mode.

For pulsed operation the high-frequency output of the Q-switch driver was modulated using the pulse train from a signal generator. The maximum duty cycle (ratio of low-Q to high-Q period) that could be obtained in this way was 95%. Even at high repetition rates, this resulted in the cavity being in a high-Q state for considerably longer than the pulse duration. The Q-switched pulses were observed

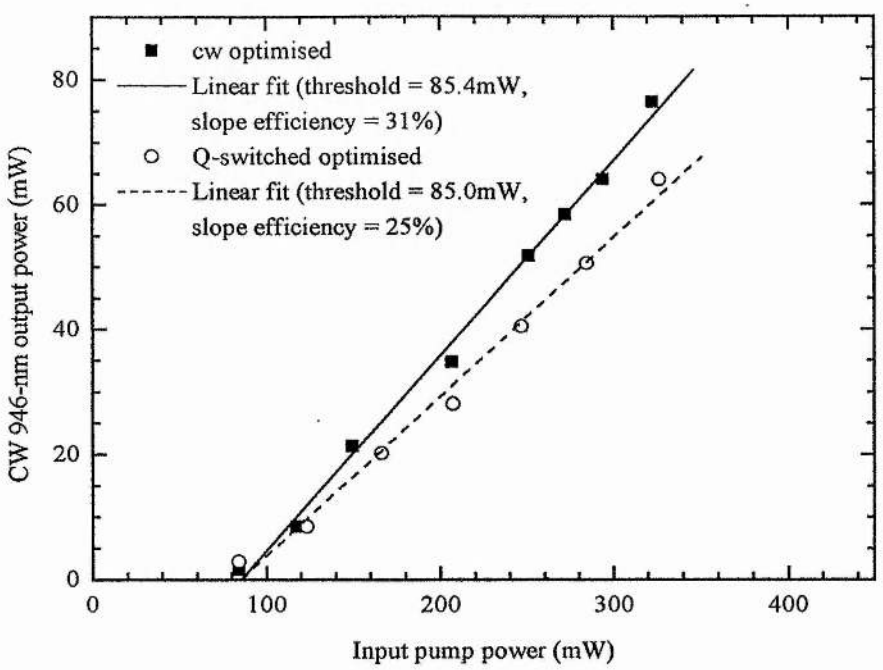

Fig. 6-8 CW output power variation with pump power for 946-nm Nd:YAG laser with intra-cavity Q-switch. Two sets of results shown are for cavity optimised for maximum cw output and cavity optimised for maximum peak power when Q-switched.

using a calibrated, fast photodiode (BPX65) and a set of calibrated neutral-density filters to avoid detector saturation. The average output powers were measured using an optical power meter with a calibrated RG850 filter to block any residual pump light.

The variation of peak power with repetition rate was measured to determine a suitable maximum repetition rate for laser operation. It would not be expected that there would be any major advantage in having low-Q periods significantly longer than the upper-state lifetime of 230μs. The results of these measurements, which were taken with an incident pump power ≈400mW (input pump power ≈336mW), are shown in Fig. 6-9. The peak power was both measured directly using the calibrated photodiode and calculated from the average power using the repetition rate and pulse duration (≈27ns) and assuming a Gaussian pulse profile. The results

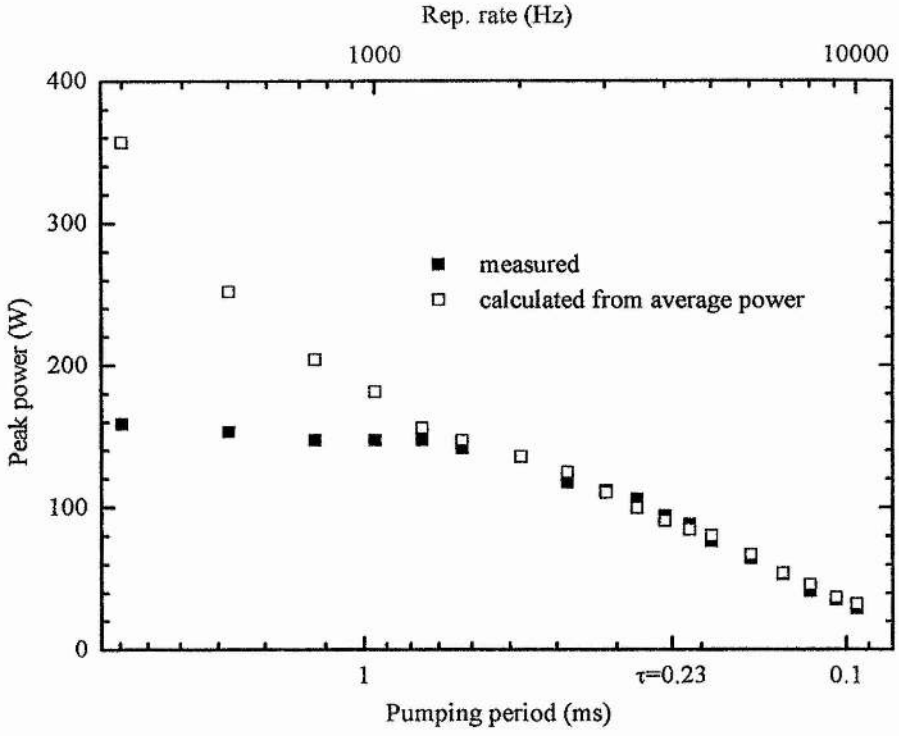

Fig. 6-9 Variation of peak Q-switched power, both measured directly and calculated from the average power, with repetition rate. Incident pump power was 400mW (input power 336mW), low-Q period of duty cycle was 95%. Pumping period was calculated as $0.95\times(\text{rep. rate})^{-1}$.

are plotted against both the repetition rate and the pumping period. This was defined as the duration of the low-Q state between pulses and was calculated as $0.95\times(\text{rep. rate})^{-1}$, the maximum 95% duty cycle being used in all cases.

There are several features to note in these results. Firstly, it can be seen that there is little to gain in peak power by having a repetition rate significantly lower than 1.5kHz. This corresponds to a pumping period of 0.63 ms or 2.7× the upper-state lifetime. It can also be seen that while the directly measured peak power value and that calculated from the average power show good agreement at high repetition rates they deviate significantly at lower frequencies. This was attributed to the fact that the duty-cycle limit resulted in the cavity being in a high-Q state for considerably longer than the duration of the main pulse. This would allow multiple pulsing and/or cw

operation within the duration of the high-Q period thus increasing the average power while the peak power remained the same. As a result of these measurements, the Q-switched laser was operated at a repetition rate of 1.5kHz with a 95% duty cycle for all subsequent work.

The observed Q-switched pulses, for a range of input pump powers, are shown in Fig. 6-10. The maximum peak power obtained can be seen to be 180W for an input pump power of 335mW (incident pump power of 400mW), the pulse width at half-maximum being 27ns in this case. These values result in a calculated pulse energy of 5.2μJ if a Gaussian pulse profile is assumed. Given the 1.5kHz repetition rate, this pulse energy implies an average output power of 7.8mW, although in practice the average output power was measured to be 11.5mW, implying a 7.7μJ pulse energy. This discrepancy was, again, attributed to the duty-cycle limit on the Q-switch drive signal as described above.

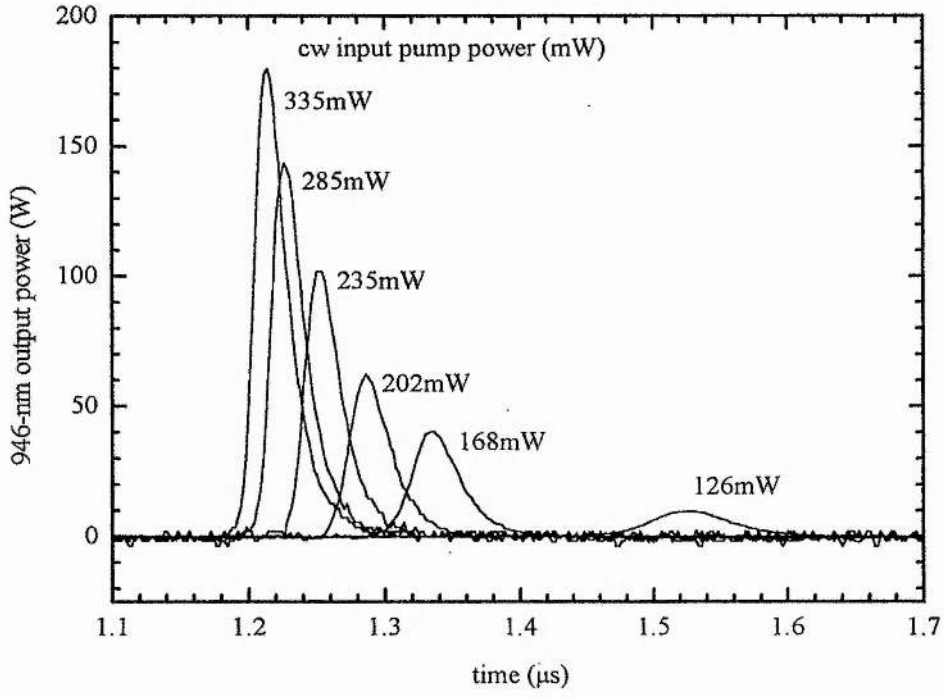

Fig. 6-10 Q-switched pulses obtained from the 946-nm Nd:YAG laser for a range of input pump powers. Repetition rate was 1.5kHz with a 95% low-Q duty cycle.

It has been shown that the standard methods of modelling Q-switched lasers can be simply extended to the quasi three-level case to give expressions for the pulse build-up time t_b, pulse width Δt, and peak power P_{pk} of the form [1,2]:

$$t_b = \frac{A\tau_c}{(r-1)} \tag{6-5 a}$$

$$\Delta t = \frac{r\eta(r)}{r-1-\ln r}\tau_c \tag{6-5 b}$$

$$P_{pk} = \frac{ch\nu_L n_{th}}{(f_a+f_b)2L_{cav}}(r-1-\ln r)T \tag{6-5 c}$$

where τ_c is the cavity lifetime determined by all losses other than reabsorption, n_{th} is the threshold population inversion, L_{cav} is the cavity length, T is the output coupler transmission and $h\nu_L$ is the laser photon energy. The parameter r is the ratio of the population inversion to that at threshold for the cavity in the high-Q state. This is equivalent to the ratio of pump power to that at threshold, allowing r to be easily determined from experimentally measured quantities. The energy extraction efficiency $\eta(r)$ is the same as that for a four-level system and is widely published as a function of r in standard treatments of Q-switching [7]. The quantity A is given by $\ln(S_{ss}/S_i)$, where S_{ss} is the steady-state (i.e. cw) intra-cavity photon number at the pump level concerned and S_i is the initial photon number which can be approximated to unity [7]. From the measured cw data for the Q-switch optimised cavity shown in Fig. 6-8, A is seen to have a value of around 22 in this case.

It can be seen from equations (6-5) that all three pulse parameters will vary linearly if plotted against suitable functions of r, as is done in Fig. 9. The gradients of the fitted lines for the pulse width and build-up time imply cavity lifetimes of 5.8 ± 0.4 ns and 8.2 ± 0.1ns, respectively. For 2.5% output coupling and the estimated 1% additional round-trip loss assumed earlier, these figures imply single-pass losses due to the Q-switch of 1.1 ± 0.2% and 0.3 ± 0.004%. The measured single-pass loss of the Q-switch was somewhere between these two figures at around 0.7%. The significant discrepancy between the two values obtained from the Q-switched results is probably due to the difficulty in estimating the values of r and $\eta(r)$ from the

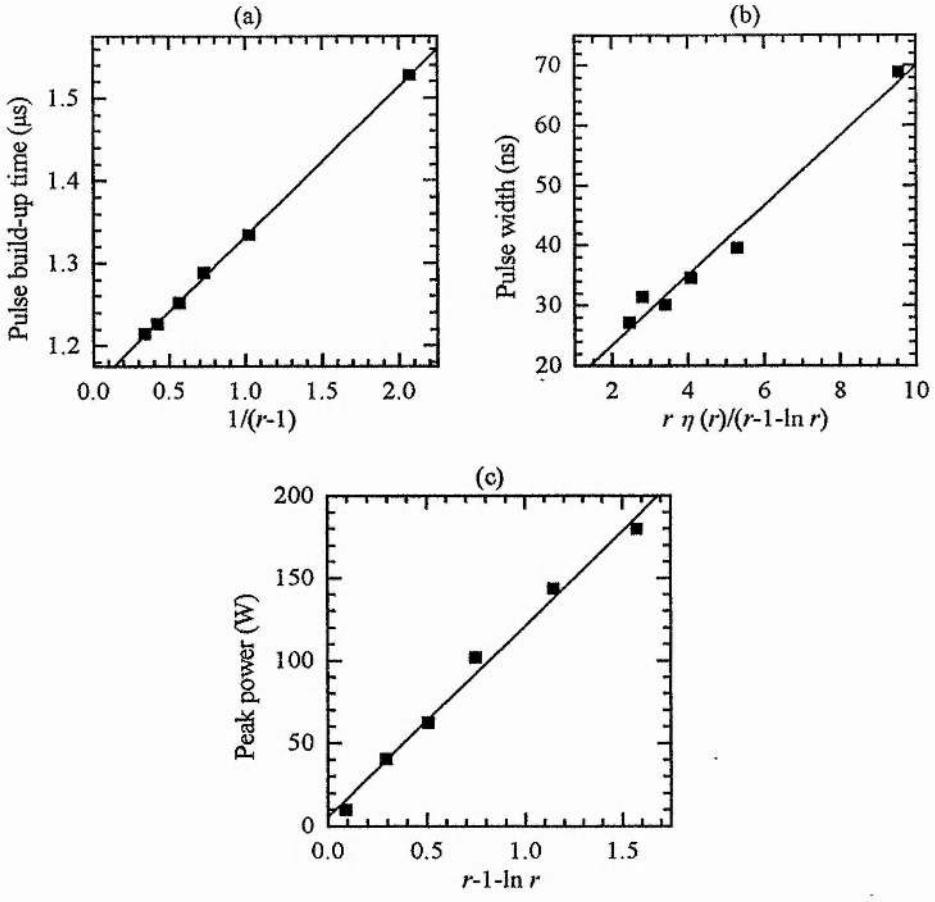

Fig. 6-11 Q-switched pulse parameters (a) build-up time, (b) width and (c) peak power plotted against appropriate functions of r, the pump-rate relative to that at threshold.

measured threshold which, as has been shown, is mainly determined by the pump induced thermal lens.

6.4 Second harmonic generation.

As was mentioned in chapter 2, the 946-nm transition in Nd:YAG has attracted much interest as it can be frequency doubled to produce blue light at 473nm. To demonstrate this with the laser described here, single-pass frequency doubling of the Q-switched output was carried out in potassium niobate.

It was shown in Fig. 3-8 that type-I second-harmonic generation of 946-nm light in potassium niobate could be phase-matched at room temperature with the second harmonic polarised along the dielectric x-axis and the fundamental polarised in the y-z plane. A number of parameters are of interest when considering this interaction, including the phase-matching angle, effective nonlinear coefficient, walk-off angle and temperature acceptance bandwidth. Since room-temperature operation, with no temperature control of the potassium niobate crystal, was used, the effects of uncertainties in the absolute temperature of the crystal must be considered. While the Sellmeier equations used to produce the data shown in Fig. 3-8 [8] were specific for 295K, temperature-dependent versions of these equations have also been published [9] and were used in the calculations described here. These equations have the form, for each polarisation direction:

$$n^2(\lambda,T) = 1 + \frac{(A_1 + A_2F)\lambda^2}{\lambda^2 - (A_3 + A_4F)^2} + \frac{(B_1 - B_2F - B_3G)\lambda^2}{\lambda^2 - (B_4 + B_5F - B_6G)^2} \qquad (6\text{-}6)$$

$$-(C_1 - C_2F)\lambda^2 - DF\lambda^4$$

where the temperature-dependence functions are given by:

$$F(T) = T^2 - 295.15^2 \qquad (6\text{-}7\ a)$$

$$G(T) = T - 293.15 \qquad (6\text{-}7\ b)$$

In (6-6) and (6-7), λ is given in μm and T in K. The coefficients for each polarisation direction are given in Table 6-2, where the axis definitions commonly used in the literature, and summarised in Table 3-2, have been used.

Given the refractive indices obtained from (6-6) and (6-7), the phase-matching angle was calculated using equation (3-82) for a range of temperatures around room temperature. For each of the angles thus obtained, the effective nonlinear coefficient was calculated using equation (3-87) and nonlinear coefficient values of d_{31}=15.8pmV^{-1} and d_{32}=18.3pmV^{-1} [10]. The walk-off angle, ρ, was calculated using

	Polarisation direction		
Coefficient	x (c,Z,3)	y (a,X,1)	z (b,Y,2)
A_1	2.370517	2.6386669	2.5389409
A_2	2.8373545×10^{-6}	1.6708469	3.8636303×10^{-6}
A_3	0.1194071	0.1361248	0.1371639
A_4	1.75×10^{-7}	0.796×10^{-7}	1.767×10^{-7}
B_1	1.048952	1.1948477	1.4451842
B_2	2.1303781×10^{-6}	1.3872635×10^{-6}	3.909336×10^{-6}
B_3	1.8258521×10^{-4}	0.90742707×10^{-4}	1.2256136×10^{-4}
B_4	0.2553605	0.2621917	0.2725429
B_5	1.89×10^{-7}	1.231×10^{-7}	2.38×10^{-7}
B_6	2.48×10^{-5}	1.82×10^{-5}	6.78×10^{-5}
C_1	1.939×10^{-2}	2.513×10^{-2}	2.837×10^{-2}
C_2	0.27×10^{-8}	0.558×10^{-8}	1.22×10^{-8}
D	5.7×10^{-10}	4.4×10^{-10}	3.3×10^{-10}

Table 6-2 Temperature-dependent Sellmeier-equation coefficients for use in equation (6-6) [9].

the equivalent expression to equation (3-94) for this case and the temperature acceptance bandwidth calculated using equation (3-122) with a 3mm crystal length.

The results of these calculations are shown in Fig. 6-12. The phase-matching angle, φ, is seen to be $\approx60°$, measured from the dielectric y-axis and the effective nonlinear coefficient $\approx16.4\text{pmV}^{-1}$. The walk-off angle, ρ, can be seen to be $\approx0.85°$. While the

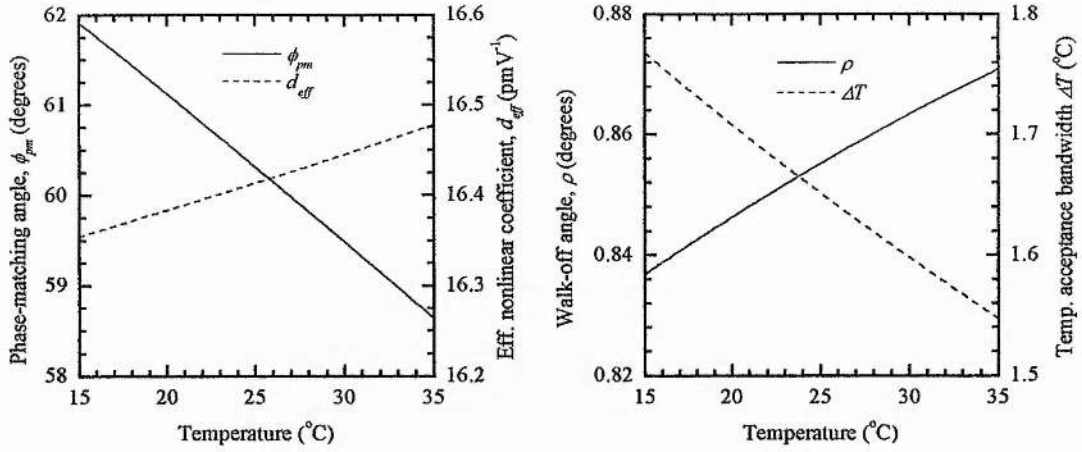

Fig. 6-12 Calculated parameters for room-temperature SHG of 946-nm light in $KNbO_3$. Second harmonic is polarised along dielectric x-axis and fundamental is polarised in dielectric y-z plane. Phase-matching angle, φ, is measured from the dielectric y-axis. Axis definitions used follow the literature convention given in Table 3-2. A crystal length of 3mm was used in the acceptance-bandwidth calculation.

temperature acceptance bandwidth of ≈1.65 K implies the conversion efficiency will have a high degree of sensitivity to fluctuations in temperature at a given angle, it can be seen that small rotations of the crystal in the y-z plane, thus adjusting the phase-matching angle, can be used to compensate for this.

A 3mm long potassium niobate crystal, cut for phase-matching as described above, with faces anti-reflection coated at 946nm and 473nm was used to carry out the second-harmonic generation. Given the calculated walk-off angle, the Boyd-Kleinman walk-off parameter B [11], as defined by equation (3-224), has a value of B=1.55. It can be seen from Fig. 3-25 that, for this value of B, the conversion efficiency will be maximised when the focusing parameter has a value of $\xi \approx 1.7$. From Fig. 3-24 it can be seen that, in this case, the reduction factor will take a value of $h_m(B,\xi) \approx 0.4$. Given the refractive index of ≈2.2, equation (3-223) indicates that the appropriate value of $\xi \approx 1.7$ will be obtained with a beam waist radius of 11μm in the crystal. Given these parameter values, a power-dependent conversion efficiency

figure in the absence of depletion of the fundamental is obtained from equation (3-225) of:

$$\eta_{0.p} = \frac{P_{2\omega}}{P_{\omega}^2} = 0.00213 \qquad (6\text{-}8)$$

In practice, it was found to be difficult to focus the 946-nm fundamental to the required 11μm radius spot due to the highly astigmatic nature of the beam caused by the intracavity Q-switch. The best results were obtained using an f=80mm spherical lens to focus the fundamental to an estimated 6μm×24μm waist in the crystal. This results in a waist area ≈1.2× that in the case of optimum focusing.

The pulses generated at the second harmonic were monitored using a fast photodiode with a BG38 filter blocking residual fundamental light. The photodiode was uncalibrated at 473nm, although the average power could be measured using an optical power meter. This average measurement was used to calculate the peak powers, given the measured pulse width and assuming a Gaussian profile.

The pulse at the second harmonic generated by a 180W peak-power pulse at the fundamental is shown in Fig. 6-13. The pulse at the second harmonic would be expected to show a narrowing by a factor of $\sqrt{2}$ when compared to the pulse at the fundamental, due to the quadratic power dependence of the second harmonic and this can be seen to be the case in Fig. 6-13. The average power at the second harmonic in this case was 1.62mW and the repetition rate was 1.5kHz. These values imply a peak power of ≈50W, given the 20ns pulse width shown in Fig. 6-13 and assuming a Gaussian pulse shape. This results in a peak conversion efficiency of 28%.

From equation (6-8), a peak conversion efficiency of 38% would be expected in this case in the absence of fundamental depletion. At the high peak powers involved, however, depletion must be considered and a peak conversion efficiency of 30% is calculated using the correction of equation (3-71). This is slightly larger than the observed value, possibly due to the imperfect focusing in the doubling crystal.

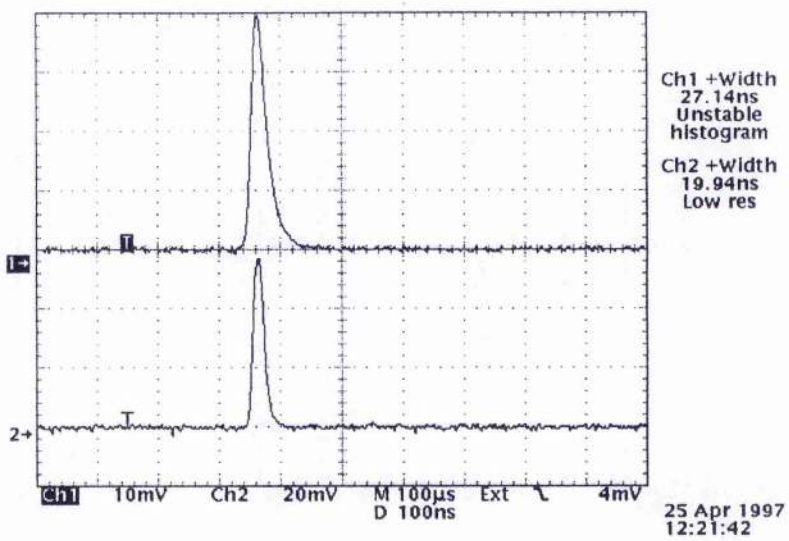

Fig. 6-13 Observed pulse at 946 nm (upper trace, vertical scale 4.5WmV^{-1}) and second-harmonic pulse at 473nm (lower trace, no vertical calibration). Pulse widths are shown at right hand side. Average power at second harmonic was 1.62mW and the repetition rate was 1.5kHz.

6.5 Conclusions.

The primary objective of the work contained in this chapter was the evaluation of the performance of the injection-locked broad-area diode laser as a near diffraction-limited, spectrally-narrow pump source. The calculated cw performance shows good agreement, given the probable thermal-lensing effects around threshold, with that calculated for the near diffraction-limited output of the injection-locked diode laser. It is, however, useful to make a comparison between the results presented here and those obtained by others with a variety of pump sources of varying spatial and spectral quality.

A number of such results are shown in Fig. 6-14 where the threshold pump power and slope efficiency of 946-nm Nd:YAG lasers with a variety of pump sources are plotted. It can be seen that the results achieved with the injection-locked broad-area

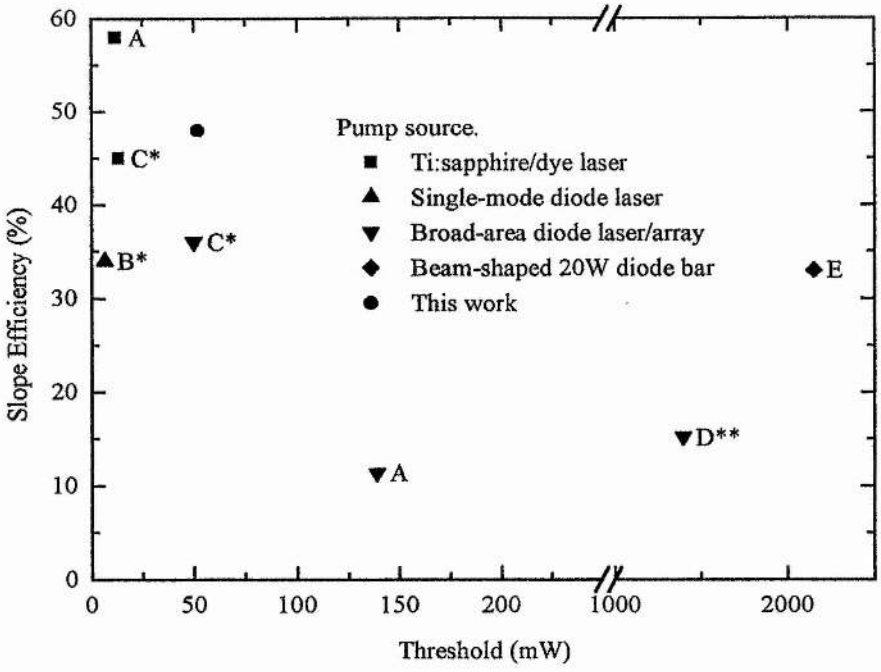

Fig. 6-14 Slope efficiency and threshold for cw 946-nm Nd:YAG lasers pumped by a variety of sources. Threshold and slope efficiency are in terms of absorbed pump power except for points marked * where absorbed pump power is used. Point marked ** indicates quasi-cw operation. References: A [1], B [12], C [13], D [14], E [15].

diode are comparable in threshold and slope efficiency to those obtained with high-quality Ti:sapphire and dye lasers and significantly better than those typically achieved with broad-area diode lasers or diode-laser arrays. It is likely that the slope efficiency would be further improved had an output coupler of optimum transmission and crystal of optimum length, as predicted by the calculations shown in Fig. 6-1, been available.

The Q-switched performance also shows considerable improvement over a virtually identical system pumped by diode-laser arrays [1,2]. In this case, 344mW of incident pump power (≈302mW input) produced a peak Q-switched power of 60W when operating with the Nd:YAG crystal at room temperature. This compares to a peak

power of 180W for 335mW of input pump power when pumping with the injection-locked broad-area diode laser system.

This improvement in Q-switched performance resulted in enhanced second-harmonic generation. While the average second-harmonic power of 1.62mW obtained with the injection-locked pump source is only slightly better than that of 1.55mW obtained with the diode-array pump [1,2], it should be noted that the narrower pulses obtained here (20ns) resulted in a significantly higher peak second-harmonic power of ≈50W, as compared to ≈22W in the diode-array pumped case for 42ns pulses. It should also be pointed out that while the room-temperature doubling carried out here was critically phase-matched, the results of [1,2] were obtained using non-critical phase matching at ≈185°C, utilising the d_{32} coefficient alone to provide a d_{eff}≈10% greater than that at room temperature. In addition, the doubling crystal used in [1,2] was, at 5mm, 67% longer than that used here.

The injection-locked broad-area diode laser does not necessarily represent a practical pump source for the routine pumping of solid-state lasers. In particular, the potential for power-scaling is somewhat limited and the poor efficiency of low-quality diode pump sources can often be countered by the high powers available from them [15]. However, the results presented here demonstrate that as a high spatial and spectral quality pump source for laboratory use the injection-locked broad-area diode laser is capable of performance comparable to that of Ti:sapphire and dye lasers, enabling solid-state lasers to be end-pumped with high efficiencies and low thresholds. For applications in nonlinear optics, such as the pumping of optical parametric oscillators, where even high-power sources are unsuitable if their spatial and spectral quality are poor, these attributes of the injection-locked system are considerably more important. The use of the injection-locked system in such an application is investigated in the next chapter.

6.6 References.

1 J. Hong, "Diode laser pumped Nd:YAG laser for 946-nm and its frequency doubling," PhD thesis, University of St Andrews (1992).

2 J. Hong, B.D. Sinclair, W. Sibbett and M.H. Dunn, "Frequency-doubled and Q-switched 946-nm Nd:YAG laser pumped by a diode-laser array," Appl. Opt. **31**, 1318-1321, (1992).

3 W.P. Risk and W. Lenth, "Room-temperature, continuous-wave, 946-nm Nd:YAG laser pumped by laser-diode arrays and intracavity frequency doubling to 473nm," Opt. Lett. **12**, 993-995, (1987).

4 J.J. Zayhowski and J. Harrison, "Minature Solid-State Lasers," in Handbook of Photonics, CRC Press, New York, 1997.

5 M.E. Innocenzi, H.T. Yura, C.L. Fincher and R.A. Fields, "Thermal modeling of continuous-wave end-pumped solid-state lasers," Appl. Phys. Lett. **56**, 1831-1833 (1992).

6 W. Koechner, "Solid-State Laser Engineering" (third edition), Springer-Verlag, Berlin, (1992).

7 A.E. Siegman, "Lasers," University Science Books, Mill Valley, California (1986).

8 B. Zysset, I. Biaggio and P. Günter, "Refractive indices of orthorombic $KNbO_3$. I. Dispersion and temperature dependence," J. Opt. Soc. Am. B **9**, 380-386 (1992).

9 D.H. Jundt, P. Günter and B. Zysset, "A temperature-dependent dispersion equation for $KNbO_3$," Nonlinear Opt. **4**, 341-345 (1993). (Referenced in: V.G. Dimitriev, G.G. Garzadyan and D.N. Nikogosyan, "Handbook of Nonlinear Optical Crystals," 2nd edition, Springer-Verlag, Berlin (1997).

10 I. Biaggio, P. Kerkoc, L.-S. Wu, P. Günter and B. Zysset, ", "Refractive indices of orthorombic $KNb0_3$. II. Phase-matching configurations for nonlinear-optical interactions," J. Opt. Soc. Am. B **9**, 507-517 (1992).

11 G.D. Boyd and D.A. Kleinman, "Parametric interaction of focused Gaussian light beams," J. Appl. Phys. **39**, 3597-3639 (1968).

12 T.Y. Fan and R.L. Byer, "Continuous-wave operation of a room-temperature, diode-laser-pumped, 946-nm Nd:YAG laser," Opt. Lett. **12**, 809-811, (1987).

13 W.P. Risk and W. Lenth, "Room-temperature, continuous-wave, 946-nm Nd:YAG laser pumped by laser-diode arrays and intracavity frequency doubling to 473nm," Opt. Lett. **12**, 993-995, (1987).

14 F. Hanson, "Efficient operation of a room-temperature Nd:YAG 946-nm laser pumped with multiple diode arrays," Opt. Lett. **20**, 148-150 (1995).

15 W.A. Clarkson, R. Koch and D.C. Hanna, "Room-temperature diode-bar-pumped Nd:YAG laser at 946nm," Opt. Lett. **21**, 737-739, (1996).

7. Diode-Laser Pumped Doubly-Resonant Optical Parametric Oscillator.

7.1 Introduction.

It can be seen from Fig. 3-28 that a doubly-resonant OPO (DRO) based on periodically-poled lithium niobate (PPLN) represents a highly attractive option for diode-laser pumping. While having a threshold well within the range of diode-laser based pump sources, the DRO does not have any of the impedance-matching requirements of the pump-enhanced SRO. When compared to the triply-resonant OPO, the DRO also offers a simpler solution as it avoids many of the problems associated with TROs while still maintaining a low threshold when PPLN is used. As a result, it was decided to develop a PPLN DRO to investigate diode-laser pumping.

7.2 System design.

From Fig. 3-28 it can be seen that an ≈20mm long PPLN crystal would be expected to give a minimum threshold of the order of milliwatts with typical cavity parameters. It was thus decided to use a 19mm long PPLN crystal in the OPO. A set of DRO mirrors coated for ≈810nm pumping were already available having high-reflectivity signal and idler bands at 1.12-1.24μm and 2.43-2.7μm, respectively, and the OPO was designed to operate at these wavelengths. At the time this work was carried out, PPLN with suitable grating periods to phase-match OPO interactions pumped at ≈800nm was not available as a standard stock item and an appropriate grating set had to be designed. The various elements of the DRO are described in the following sections.

7.2.1 PPLN design.

The PPLN was configured, in the usual manner, for propagation along the optical x-axis with all three interacting waves polarised along the z-axis (extraordinarily polarised) and poling carried out in the z direction. This allowed access to the highest nonlinear coefficient, d_{33}. The x,y and z dimensions of the crystal were 19mm, 11.5mm and 0.5mm, respectively. The manufacturer's standard configuration allowed eight different grating periods to be poled adjacently along the y-axis. As mentioned above, the periods of these gratings had to be specified as no suitable standard periods were available at the time of this work.

The quasi-phase-matched tuning behaviour of the PPLN can be calculated using equation (3-106) which, in the case of perfect first-order quasi-phase-matching, can be rewritten:

$$\Delta k_Q = 2\pi\left(\frac{n_p}{\lambda_p} - \frac{n_s}{\lambda_s} - \frac{n_i}{\lambda_i} - \frac{1}{\Lambda}\right) = 0 \tag{7-1}$$

The refractive indices for the three waves were calculated using a published Sellmeier equation for extraordinarily-polarised waves in lithium niobate [1]:

$$n_e^2(\lambda) = a_1 + b_1 f(T) + \frac{a_2 + b_2 f(T)}{\lambda^2 - \left(a_3 + b_3 f(T)\right)^2} + \frac{a_4 + b_4 f(T)}{\lambda^2 - a_5^2} - a_6\lambda^2 \tag{7-2 a}$$

$$f(T) = \left(T - T_0\right)\left(T + T_0 + 2\times 273.16\right) \tag{7-2 b}$$

where T is measured in °C, T_0=24.5°C, λ is measured in microns and the Sellmeier coefficients of equation (7-2 a) are given in Table 7-1.

When calculating the temperature tuning characteristics of a quasi-phase-matched material it is important to take account of the change in grating period resulting from thermal expansion. This can be calculated using the relationship [1]:

$$l = l_{25°C}\left[1 + \alpha\left(T - 25°C\right) + \beta\left(T - 25°C\right)^2\right] \tag{7-3}$$

a_1	5.35583	b_1	4.629×10^{-7}
a_2	0.100473	b_2	3.862×10^{-8}
a_3	0.20692	b_3	-0.89×10^{-8}
a_4	100	b_4	2.657×10^{-5}
a_5	11.34927		
a_6	1.5334×10^{-2}		

Table 7-1 Sellmeier coefficients used in equation (7-2 a) [1].

where T is in °C and the values of the thermal expansion coefficients are $\alpha = 1.54\times10^{-5}\ K^{-1}$ and $\beta = 5.3\times10^{-9}\ K^{-2}$.

Although photorefractive scattering effects are not as strong in PPLN as in single-domain lithium niobate, such effects are known to degrade the performance of PPLN OPOs unless the crystal is held at elevated temperatures [2]. However, it was also desirable to retain the option of room-temperature operation. With this in mind, it was decided to design the PPLN grating periods to enable phase-matching of the required interactions between room temperature and 200°C.

The phase-matched signal and idler wavelengths at 25°C and 200°C, calculated for a pump wavelength of 810nm using (7-2) and (7-3), are plotted against grating period in Fig. 7-1. It can be seen that, at this pump wavelength, the phase-matching curve is two-branched. This, potentially, allows idler wavelengths between degeneracy and 5μm (well into the strong infrared absorption region for the material) to be phase-matched by a relatively small range of grating periods. It was decided to specify the PPLN slab with eight gratings having periods ranging from 21μm to 22.4μm in 0.2μm steps. It can be seen from Fig. 7-1 that this range of grating periods, in conjunction with temperature tuning, will allow phase-matching of OPO interactions throughout the transparency range of the material for this pump wavelength.

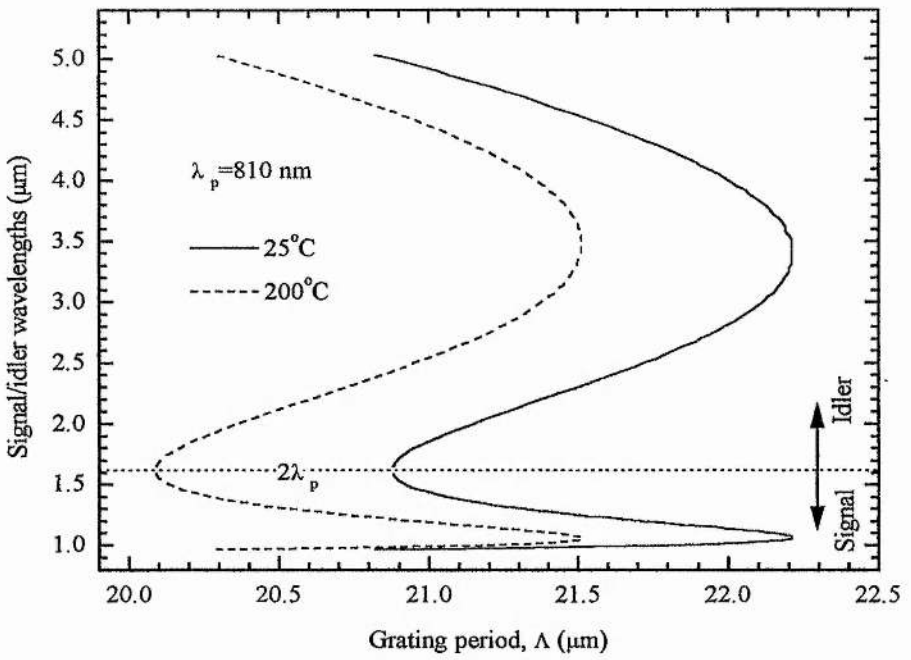

Fig. 7-1 Phase-matched signal and idler wavelengths, plotted against grating period, for a pump wavelength of 810nm and temperatures of 25°C and 200°C.

To obtain a more accurate picture of the tuning properties in the wavelength regions of interest, the temperature tuning characteristics were calculated for the chosen grating periods and for pump wavelengths approximately defining the limits of the tuning range of the single-mode diode laser. The results of these calculations are shown in Fig. 7-2. It can be seen that, depending on the pump wavelength, a number of the chosen grating periods would be expected to phase-match within the mirror bandwidths. Furthermore, adjustment of the temperature enables the OPO to be tuned throughout the mirror bands with a single, appropriate, grating period.

As mentioned in section 3.7, a particularly attractive feature of diode-laser-based pump sources for OPOs is their wavelength tuneability, which allows more rapid tuning of the signal and idler wavelengths than varying the OPO crystal temperature. The pump-wavelength tuning behaviour, with the grating periods specified, is shown in Fig. 7-3, for temperatures of 25°C and 200°C.

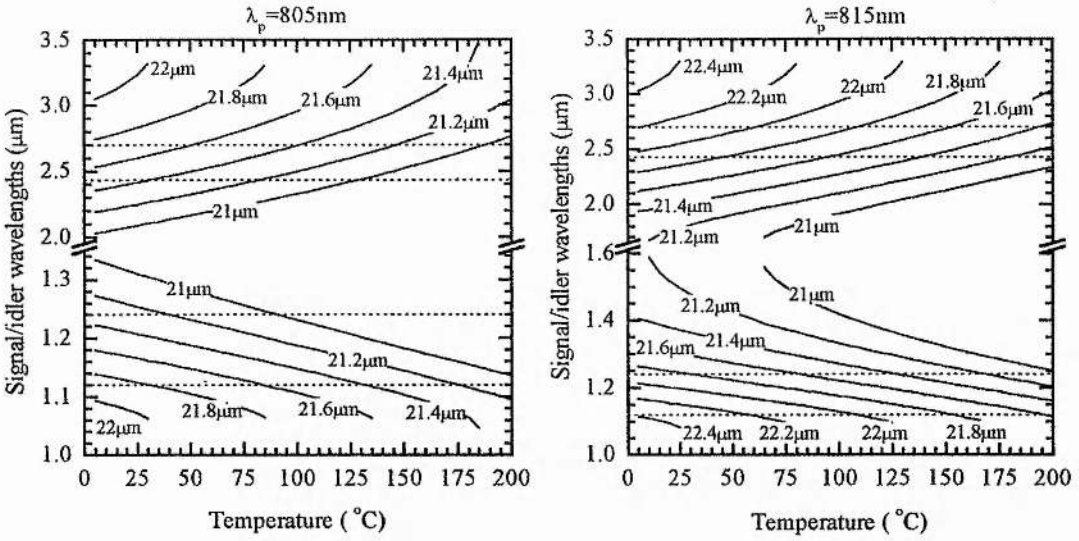

Fig. 7-2 Temperature tuning characteristics of the PPLN at pump wavelengths of 805nm and 815nm. Dotted lines represent approximate limits of the mirror high-reflectivity bands. Values marked on curves indicate grating periods.

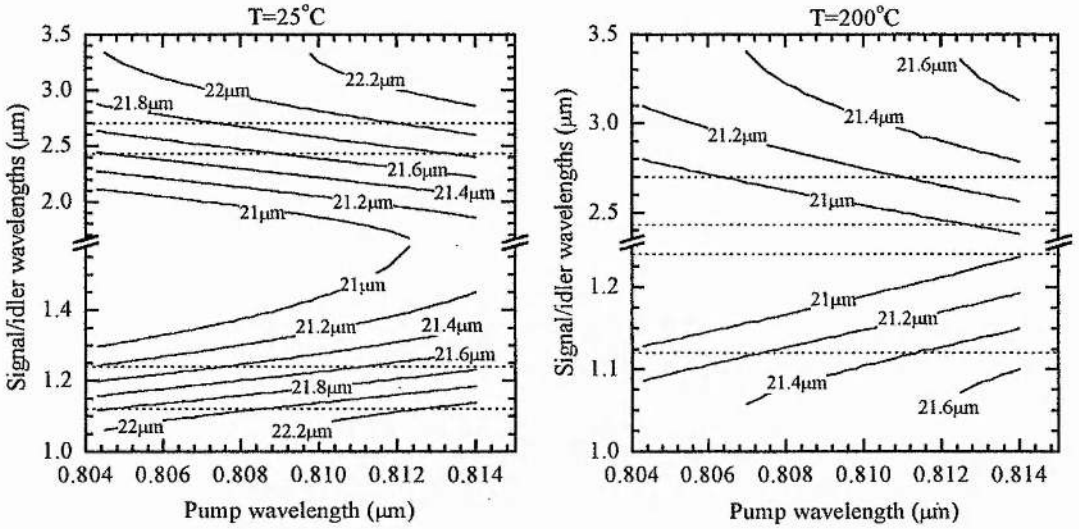

Fig. 7-3 Pump-wavelength tuning characteristics of the PPLN at temperatures of 25°C and 200°C. Dotted lines represent approximate limits of the mirror high-reflectivity bands. Values marked on curves indicate grating periods.

It can be seen that appropriate choice of grating period and temperature allows the signal and idler wavelengths to be tuned throughout the mirror high-reflectivity bands through variation of the pump wavelength by around 10nm.

Fig. 7-2 and Fig. 7-3 show that the diode-laser pumped PPLN DRO has a high degree of tuning flexibility. Both the crystal temperature and pump wavelength can be used to tune the outputs over the ranges defined by the mirror coatings. With these two parameters fixed, the quasi-phase-matching (QPM) grating period can be changed to generate several different wavelength combinations. Since high temperature (≈100°C or more) operation is required to avoid photorefractive effects, and at temperatures this high the crystal and heating system will take some time to stabilise after any variation, the most practical mode of operation is probably to leave the temperature fixed and use a combination of grating-period and pump-wavelength variation to tune the OPO outputs.

When calculating the effective quasi-phase-matched nonlinear coefficient, equation (3-112) is applied for the case of first-order QPM (m =1) to give:

$$d_Q = \frac{2d_{eff}}{\pi} \tag{7-4}$$

In this case, d_{eff} is the d_{33} coefficient of lithium niobate. To determine the value of d_{33} at the wavelengths of interest, the dispersion in the second-order susceptibility must be taken into account. This can be done using a Miller's rule expression similar to that given by Roberts [3] which, in our case, can be expressed as:

$$d_{eff} = d_{eff,0}\frac{\left[n_p^2(\lambda_p)-1\right]\cdot\left[n_s^2(\lambda_s)-1\right]\cdot\left[n_i^2(\lambda_i)-1\right]}{\left[n_p^2(\Lambda_p)-1\right]\cdot\left[n_s^2(\Lambda_s)-1\right]\cdot\left[n_i^2(\Lambda_i)-1\right]} \tag{7-5}$$

Here, $d_{eff,0}$ is a measured reference value, the measurement having been made by the interaction of the wavelengths Λ_p, Λ_s and Λ_i. The refractive indices $n_p(\Lambda_p)$, $n_s(\Lambda_s)$ and $n_i(\Lambda_i)$ are those for these wavelengths. The interaction for which d_{eff} is to be calculated is that between λ_p, λ_s and λ_i, which are assumed to have the same polarisation as their corresponding wavelengths in the reference interaction. In the

case of PPLN, d_{33} has been measured for an all extraordinary-wave QPM interaction by the frequency doubling of 1.064μm light, giving a value of d_{33}=27pmV^{-1} [3]. With $\Lambda_p=\Lambda_s$=1.064μm, Λ_i=0.532μm, λ_p=0.810μm, λ_s=1.184μm, λ_i=2.565μm and calculating the corresponding refractive indices from (7-2) and (7-3) at 150°C, (7-5) gives a value of d_{33}=23.4pmV^{-1} for the interaction of interest here. This results in a corresponding first-order QPM nonlinear coefficient of d_Q=14.9pmV^{-1}.

7.2.2 Mirrors and cavity configuration.

It was seen in sections 3.4.1 and 3.5 that the OPO threshold is minimised when the interacting waves are focused close to the confocal condition in the crystal. The signal and idler waists are obviously determined by the mirror curvatures and separation. Mirror curvatures of 10, 20, 30 and 50mm were available with the coatings described. The minimum mirror separation was limited to approximately 40mm by the dimensions of the oven containing the PPLN.crystal.

Fig. 7-4 shows the variation of the mode-waist radii at the centre of the PPLN crystal calculated for a range of cavity lengths, using the ABCD matrix method [4]. It is assumed that the mirrors are spaced symmetrically on either side of the crystal and that the signal and idler wavelengths are 1.184μm and 2.565μm, respectively, these being the approximate centres of the mirror-coating high reflectivity bands. The refractive indices at these wavelengths were calculated from (7-1) and (7-2), assuming a temperature of 150°C. It can be seen from equation (3-221) that, to maximise the tolerance of the DRO to pump frequency fluctuations, it is desirable to maximise the free-spectral-range (FSR) and therefore to minimise the cavity length. As a result, the 50mm radius of curvature mirrors were not used and calculations were only carried out for radii of curvature (ROC) of 10, 20 and 30mm.

The vertical dotted line in Fig. 7-4 indicates the minimum cavity length attainable experimentally (limited by the size of the crystal oven) and the horizontal lines show the optimum mode-waist radii. These are determined by the confocal condition of equation (3-145) (crystal length ≈ confocal parameter), resulting in signal and idler wasit radii of 40.7μm and 60.6μm, and the results of Boyd and Kleinman [5] (crystal

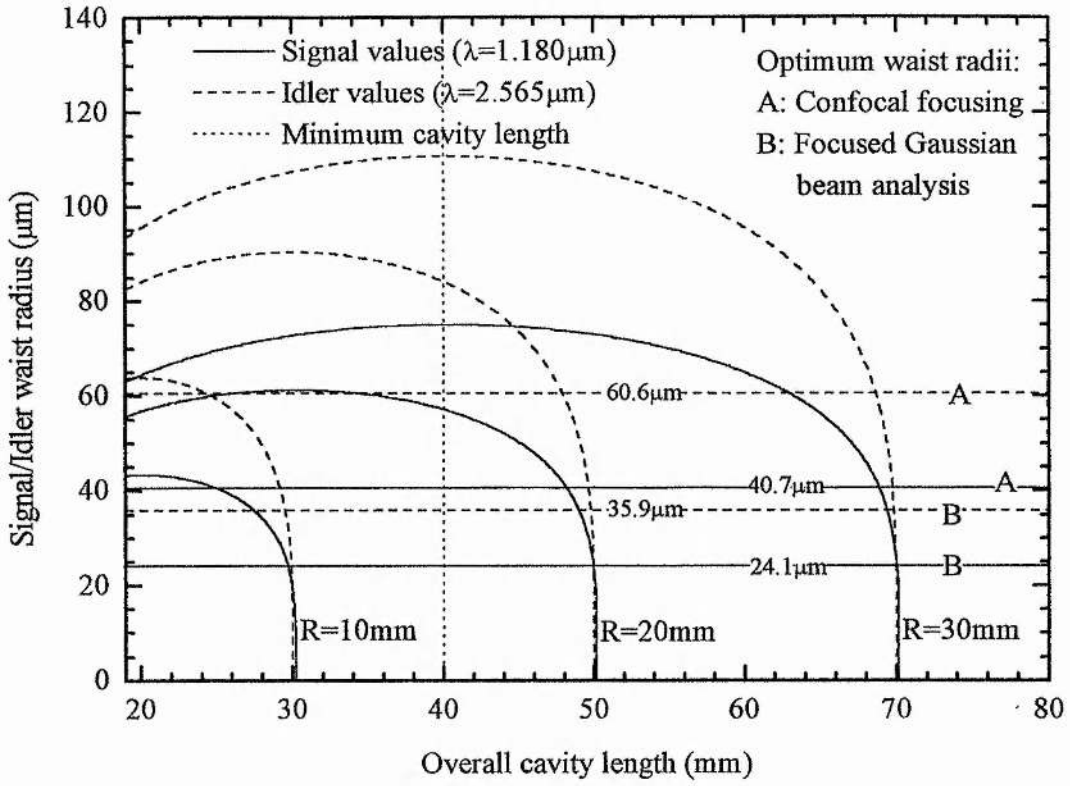

Fig. 7-4 Variation of signal and idler cavity mode-waist radii with overall cavity length calculated for a symmetric cavity with mirror radii of curvature of 10, 20 and 30mm. Minimum experimentally practicable cavity length is shown by the vertical dotted line. Horizontal lines show optimum signal and idler mode waists determined by the confocal condition (A) and focused Gaussian beam analysis (B) [5].

length = 2.84×confocal parameter) discussed in section 3.5, resulting in signal and idler waist radii of 24.1μm and 35.9μm, respectively. Note that, since the difference in refractive index between the signal and idler wavelengths is relatively small, it is possible to obtain near-optimum focusing at both wavelengths with the same cavity lengths.

It can be seen from Fig. 7-4 that, while it can accommodate the 19mm long crystal, a cavity formed by the 10mm ROC mirrors cannot contain the crystal oven. As a result, the 20mm and 30mm ROC mirrors were used for the subsequent experimental

work. Fig. 7-4 shows that both these cavity configurations allow the mode waists to be varied through the optimum values obtained by both calculation methods.

Having determined suitable cavity configurations defining the signal and idler mode waists, matching of the input pump beam to these must also be considered. For a pump wavelength of 810nm, the confocal condition indicates an optimum pump-mode radius of 33.5μm at the centre of the crystal, while the focused Gaussian beam results of Boyd and Kleinman determine the optimum waist radius to be 19.9μm. To determine an appropriate focal length and position for the focusing lens, the ABCD beam trace analysis of the injection-locked broad-area diode-laser output shown in Fig. 5-20 was extended to the OPO. The effects of the focusing lens on the pump beam waist in the PPLN crystal were then calculated, taking into account transmission through the concave input mirror of the OPO. The distance from the final component of the injection-locked system beam-shaping optics to the lens focusing into the OPO was set to 1.5m, which was approximately equal to the distance in the experimental arrangement used, although the near-collimated nature of the injection-locked system output meant that this distance had little effect on the final results.

The results of these calculations are shown in Fig. 7-5. The radius and position of the pump beam waist in the PPLN crystal are plotted as a function of focusing-lens position for three typical lens focal lengths. The crystal is assumed to be at the centre of the cavity and results are calculated for cavities formed by mirrors with 20mm (Fig. 7-5 (a)) and 30mm (Fig. 7-5 (b)) ROC. In both cases the cavity length is set for confocal focusing, corresponding to overall lengths of 48mm and 68.8mm, respectively. As was seen in Fig. 7-4, these lengths are only slightly shorter than those for optimum waist radii in the focused Gaussian beam case and the difference between the two cases had little effect on the results of Fig. 7-5. The optimum waist radii for both cases are indicated in Fig. 7-5. Beam parameters calculated in the horizontal plane (in the plane of the diode-laser junctions and the x-z plane of the PPLN crystal) are shown in black and those in the vertical plane (normal to the plane of the diode-laser junctions and in the y-z plane of the PPLN crystal) are shown in

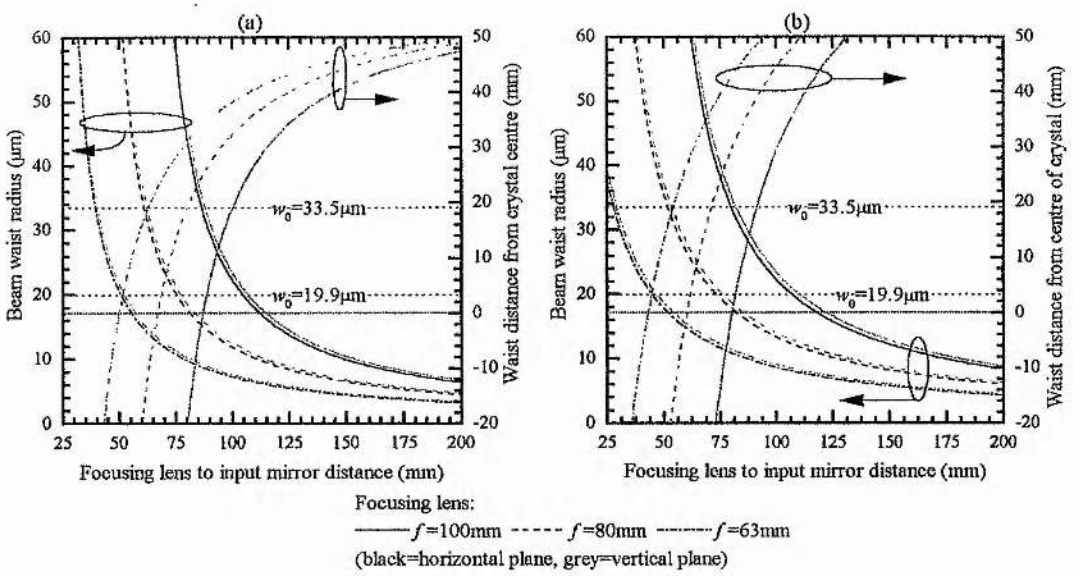

Fig. 7-5 Variation of pump beam-waist radius and position with distance of focusing lens from OPO input mirror. (a) mirror ROC=20mm, 48mm overall cavity length. (b) mirror ROC=30mm, 68.8mm overall cavity length. Black lines represent beam properties in horizontal direction (in plane of diode-laser junctions, in x-z plane of PPLN crystal), grey lines represent properties in vertical direction (normal to junction plane, in x-y plane of PPLN crystal).

grey. It can be seen that the differences between the two planes are largely insignificant.

Clearly, it is desirable to determine the combination of lens focal length and position which results in an appropriate waist radius at the same time as locating the waist at the centre of the crystal. It can be seen from Fig. 7-5 that for both OPO cavity configurations a lens focal length of 63mm fulfils this requirement for the focused-Gaussian beam waist, while a 100mm focal length does so for the confocal beam waist. In practice, it was decided to use an 80mm focal-length lens which can be seen to result in a waist radius of ≈25μm when placed ≈68mm from the 20mm ROC cavity mirror, and ≈28μm when placed ≈61mm from the 30mm ROC cavity mirror. The corresponding signal and idler mode radii, fulfilling equation (3-143), are 31 and

34μm, and 46 and 51μm, respectively. It can be seen from Fig. 7-4 that operating with these slightly larger signal and idler waist radii, rather than those predicted as optimum by the focused Gaussian beam model, results in a cavity with less marginal stability. These mode-waist values result in values of the focusing parameter, as defined by equation (3-223), of ξ=1.7 to 1.5. It can be estimated from Fig. 3-26 that the resulting increase in threshold is around 10-15%.

The final configuration for the DRO is shown in Fig. 7-6. Both 20mm and 30mm ROC mirrors were used with the overall cavity lengths and lens-to-mirror distances, as described above for each case, to obtain near-confocal focusing. The PPLN crystal was mounted in an oven, allowing its temperature to be varied between room temperature and 200°C. The oven was held in a mount providing three translational and three rotational degrees of freedom. The translational controls allowed grating-period selection in addition to placement of the PPLN within the cavity, while the rotational controls allowed alignment of the crystal along the cavity axis. This was particularly important, given the 0.5mm aperture in the z-direction. The output

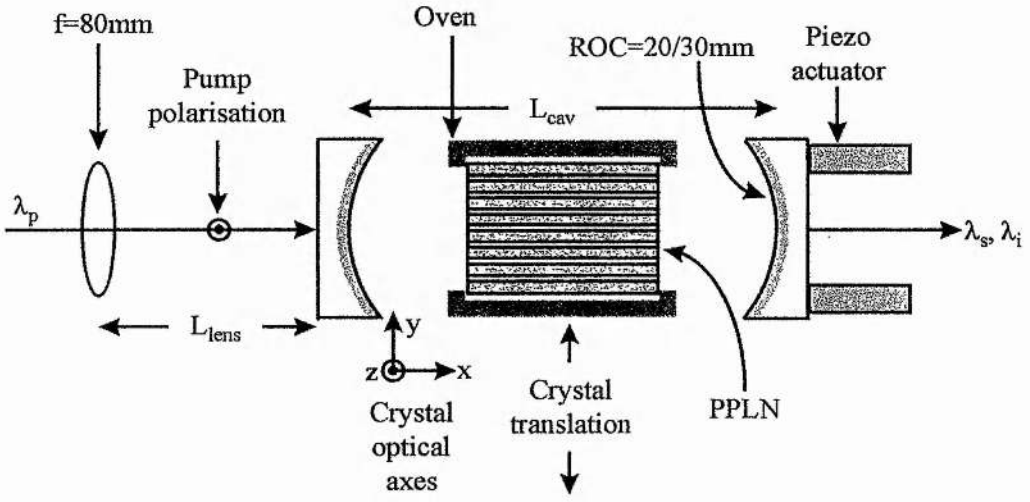

Fig. 7-6 Diode-laser pumped DRO experimental configuration (side view). L_{cav} typically ≈48mm for 20mm ROC mirrors and ≈69mm for 30mm ROC mirrors. L_{lens} typically 68mm for 20mm ROC mirrors and 61mm for 30mm ROC mirrors.

mirror was mounted on a piezo-electric actuator, allowing the cavity length to be scanned over a range of approximately 1μm.

A dichroic beamsplitter, reflecting at the signal wavelength while transmitting at the pump, was used to separate the output at the signal from the pump light transmitted by the OPO. The signal output was then monitored using either a germanium-detector power meter, if absolute power measurements were required, or an InGaAs photodiode. An RG1000 filter was used before the signal detector to block any residual pump light not removed by the beamsplitter. While the beamsplitter was found to be ≈100% reflective at the signal, calibration of the RG1000 filter showed a signal transmission of 80% and this value was used to calibrate signal-power measurements. The transmitted pump, separated by the beamsplitter, was directed onto a silicon detector for monitoring. The input pump power to the OPO was controlled by the use of a half-wave plate and polarising beamsplitter before the focusing lens.

7.2.3 Threshold calculations.

Having determined a suitable cavity configuration, the OPO threshold can now be estimated. This can be done in the confocal case using equation (3-164):

$$P_{p,th,o}^{in} = \frac{\gamma_s'\gamma_i'\pi n_p n_s n_i \varepsilon_0 c^3}{4L^2\omega_s\omega_i\chi_{eff}^2}\frac{1}{m^2} \tag{7-6}$$

where γ_s' and γ_i' are the single-pass losses at the signal and idler, m is the spatial coupling factor as defined in equation (3-58), and all other parameters are as previously defined. Optimum phase-matching (Δk=0) is also assumed. In the focused Gaussian beam case, expression (3-226) is used:

$$P_{p,th} = \frac{4\gamma_s'\gamma_i'\pi\, c^4\varepsilon_0 n_0^2}{d_{eff}^2\omega_p^3 L\left(1-\delta^2\right)^2}\frac{1}{\bar{h}_m(B,\xi)} \tag{7-7}$$

where γ_s' and γ_i' are, again, the single-pass losses, δ is the degeneracy factor, as defined in equation (3-147), $\overline{h}_m(B,\xi)$ is the focusing factor of Fig. 3-26 and all other parameters are as previously defined. Obviously, in addition to the focusing, effective nonlinear coefficient and crystal length, the major factor in determining the threshold of the OPO is the level of loss at the signal and idler wavelengths. The majority of the losses in such a device are due to reflections at mirror and crystal surfaces. The OPO mirrors, as already mentioned, had dielectric coatings with high-reflecting bands at wavelengths of 1.12-1.24μm and 2.43-2.7μm, thus defining the signal and idler ranges, respectively. The end faces of the PPLN crystal were anti-reflection coated over similar ranges.

The performance of these coatings is shown in Fig. 7-7. The round-trip losses due to the crystal-face coatings and the mirror coatings are shown separately. Also shown are the combined total round-trip losses. All the data shown were obtained from the test curves supplied with the coated optics by the coating manufacturers. As can be seen from (7-6) and (7-7), the product of the signal and idler losses determines the threshold. In view of this, Fig. 7-7 also shows, for a given wavelength, the loss at the corresponding parametric wavelength, if a pump wavelength of 810nm is assumed.

The threshold pump powers calculated using (7-6) and (7-7) are shown, as a function of round-trip loss, in Fig. 7-8. The loss figure along the x-axis is the value used for both the signal and idler losses in the calculation and is therefore equal to $2\gamma_s'$ and $2\gamma_i'$ in (7-6) and (7-7), respectively. Although the losses at the signal and idler will generally be different, it can be seen from the form of (7-6) and (7-7) that the x-axis value of Fig. 7-8 represents the geometric mean of the round-trip power losses at the signal and idler. In calculating the results shown in Fig. 7-8, the various parameters were assigned values as described above, that is L=19mm, $d_{eff}=d_Q$=14.9pmV^{-1}, λ_p=0.810μm, λ_s=1.184μm and λ_i=2.565μm, the refractive indices being calculated for these wavelengths using (7-2). For the focused Gaussian (Boyd and Kleinman) analysis, the focusing parameter was set to ξ=1.5, yielding a reduction factor of $\overline{h}_m(B,\xi) = 0.9$. In the confocal case, the confocal parameter was set equal to the crystal length for all three waves. In fact, as already mentioned, the waist radii were

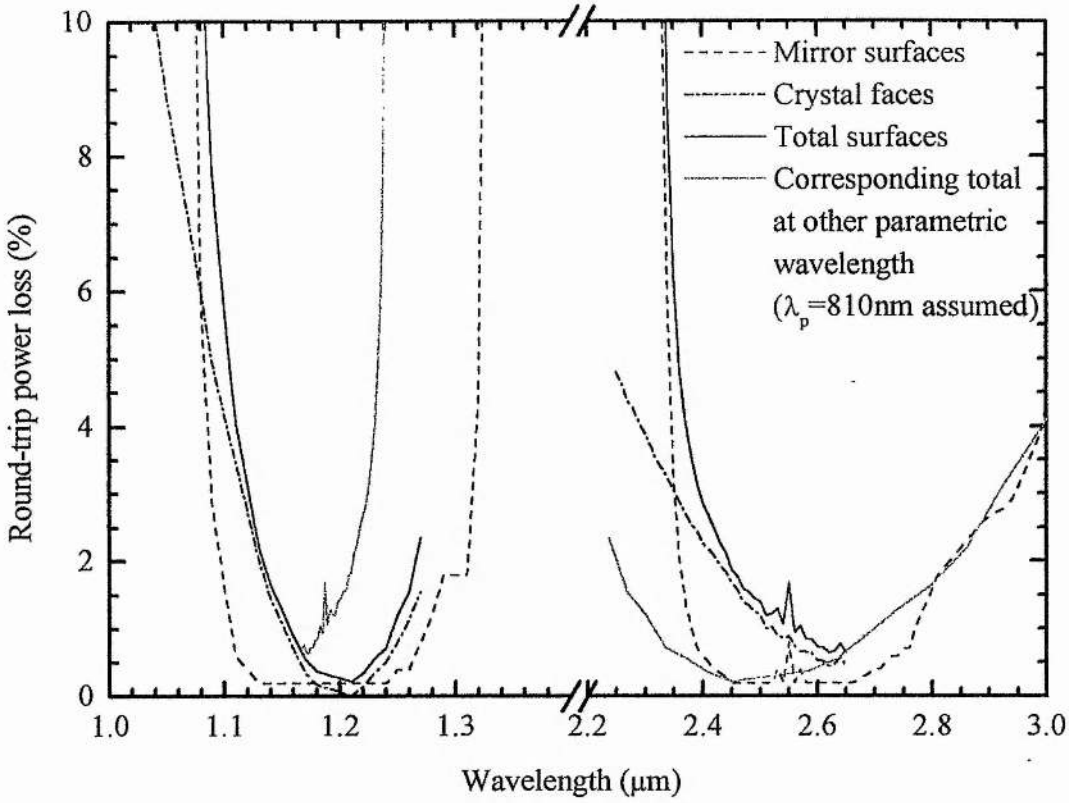

Fig. 7-7 Round-trip losses due to coated surfaces in the PPLN DRO. Total losses are sum of crystal and mirror losses. Losses at other parametric wavelength are those for that wavelength corresponding to the x-axis value if a pump wavelength of 810nm is assumed. Note that absorption losses within the crystal are not included here.

slightly smaller than in this case. However, reducing the waist radii below the confocal condition results in unrealistically low threshold when using this analysis.

It can be seen from Fig. 7-7 that the minimum signal-idler loss product occurs when both round-trip losses are approximately 0.6% and this value is marked in Fig. 7-8, corresponding to a threshold value of around 1mW. As previously mentioned, the losses shown in Fig. 7-7 represent those from surfaces only and do not take account of absorption in the PPLN crystal. The manufacturers specify absorption in the crystal as being a maximum of $0.0015cm^{-1}$ at 1.064μm [6], which results in a round-

trip power loss of 0.57% in our case of a 19mm long crystal. As losses are minimal for the extraordinary polarisation in lithium niobate below approximately 4μm [2], it was assumed that this value could also be applied to the signal and idler in this case. The overall loss, including this maximum absorption value, is also indicated in Fig. 7-8 and can be seen to result in a threshold of around 4mW. From the calculations shown in Fig. 7-8, the OPO would, therefore, be expected to have a pump-power threshold of less than 4mW when operating at the wavelengths resulting in minimum losses as indicated by coating characteristics shown in Fig. 7-7.

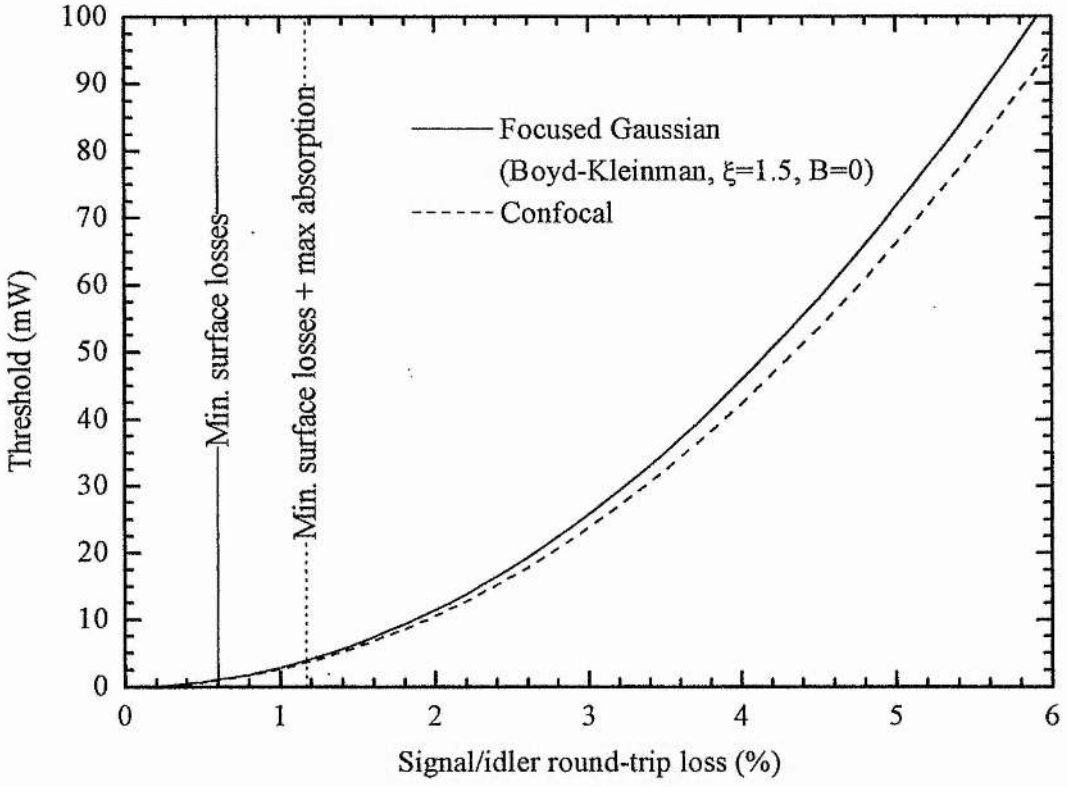

Fig. 7-8 Pump power thresholds calculated using the near-field analysis (equation (7-6) with confocal parameters equal to crystal length) and focused Gaussian case ξ=1.5, B=0 giving $\bar{h}_m(B,\xi) = 0.9$. Loss values along x-axis represent geometric mean of signal and idler round-trip losses. Minimum surface loss value of Fig. 7-7 is marked as is this value plus maximum crystal absorption.

7.2.4 Stability calculations.

As was seen in section 3.4.3.2, the principal properties of the DRO cavity affecting its tuning behaviour and stability are the difference in the signal and idler FSRs and the signal and idler finesses. The stability and mode-hop properties of the PPLN DRO, calculated using the expressions derived in section 3.4.3.2, are shown in Table 7-2 for various cavity and wavelength configurations of the OPO.

Signal / idler wavelengths	λ_s=1.215μm λ_i=2.430μm			λ_s=1.184μm λ_i=2.565μm			λ_s=1.157μm λ_i=2.700μm		
Temp. (°C)	134.0			164.8			191.33		
Signal / idler r-t losses	$2\gamma_s' = 0.89\%$ $2\gamma_i' = 2.81\%$			$2\gamma_s' = 0.94\%$ $2\gamma_i' = 1.54\%$			$2\gamma_s' = 1.85\%$ $2\gamma_i' = 1.77\%$		
Cavity length (mm)	68.8	48.0	40.0	68.8	48.0	40.0	68.8	48.0	40.0
FSR_s (GHz)	1.652	2.143	2.42	1.651	2.142	2.419	1.651	2.142	2.418
FSR_i (GHz)	1.665	2.164	2.447	1.666	2.166	2.450	1.667	2.169	2.453
ΔFSR (MHz) ($= \Delta\nu_{p,hop}$)	12.37	20.86	26.63	14.21	23.97	30.6	16.06	27.1	34.6
$\Delta\nu_{p,stab}$ (MHz)	4.89	6.36	7.19	3.28	4.26	4.81	4.78	6.20	7.02
Δl_{hop} (nm)	3.02	3.92	4.43	3.47	4.51	5.09	3.92	5.09	5.75
Δl_{stab} (nm)	1.19	1.19	1.19	0.80	0.80	0.80	1.17	1.17	1.17

Table 7-2 Calculated mode-hop and stability tolerances for pump frequency and cavity length. In all cases, λ_p=810nm and Λ=21.2μm, with crystal temperatures as indicated. Wavelengths represent approximate limits and centre of mirror bands. Losses obtained from data of Fig. 7-7 with additional 0.57% absorption loss at both signal and idler. Cavity lengths are confocal values for 30 and 20mm ROC mirrors and minimum value.

The cavity lengths in Table 7-2 represent the confocal conditions for the two mirror curvatures used and the minimum cavity length defined by the crystal oven. The wavelength combinations represent the approximate limits and the centre of the tuning range defined by the mirror coatings. The round-trip loss values used are obtained from the data of Fig. 7-7 with an additional crystal-absorption loss, assumed to be the maximum value of 0.57% as discussed above, at both the signal and idler.

As would be expected, increasing the difference between the signal and idler wavelengths results in a larger FSR difference, ΔFSR, due to the dispersion of the PPLN crystal. Reducing the cavity length also increases ΔFSR as the dispersive element (the crystal) becomes an increasingly significant fraction of the overall cavity length. These increases in ΔFSR result in an increased tolerance to mode-hopping, both for pump frequency and cavity length, as the cavity length is reduced and the wavelength separation increased. These changes also result in the stability within a given signal-idler mode pair to changes in pump frequency, $\Delta\nu_{p,stab}$, increasing. The stability to changes in cavity length, Δl_{stab}, can be seen from equation (3-220) to be independent of FSR and varies with wavelength only as a result of changes in losses and therefore cavity finesses.

As was discussed in section 3.4.3.2, the expressions derived to calculate the mode hopping and stability behaviour of the DRO do not give any indication of the effects of hopping between signal-idler mode-pair clusters. These effects can, however, be gauged by numerical mode-selection calculations such as those shown in Fig. 3-22 and Fig. 3-23. The results of such calculations for the PPLN DRO are shown in Fig. 7-9. Calculations were carried out for the two extreme situations of those summarised in Table 7-2, these being minimum signal-idler wavelength separation (λ_s=1.215μm, λ_i=2.430μm) with maximum cavity length (68.8mm) and maximum signal-idler wavelength separation (λ_s=1.157μm, λ_i=2.700μm) with minimum cavity length (40mm). All other parameters used in the calculations were as given in Table 7-2 for these two cases. In both, cases the cavity length was adjusted from the nominal value to position one cluster at the centre of the phase-matching band, and the magnitudes of these length adjustments are indicated in Fig. 7-9.

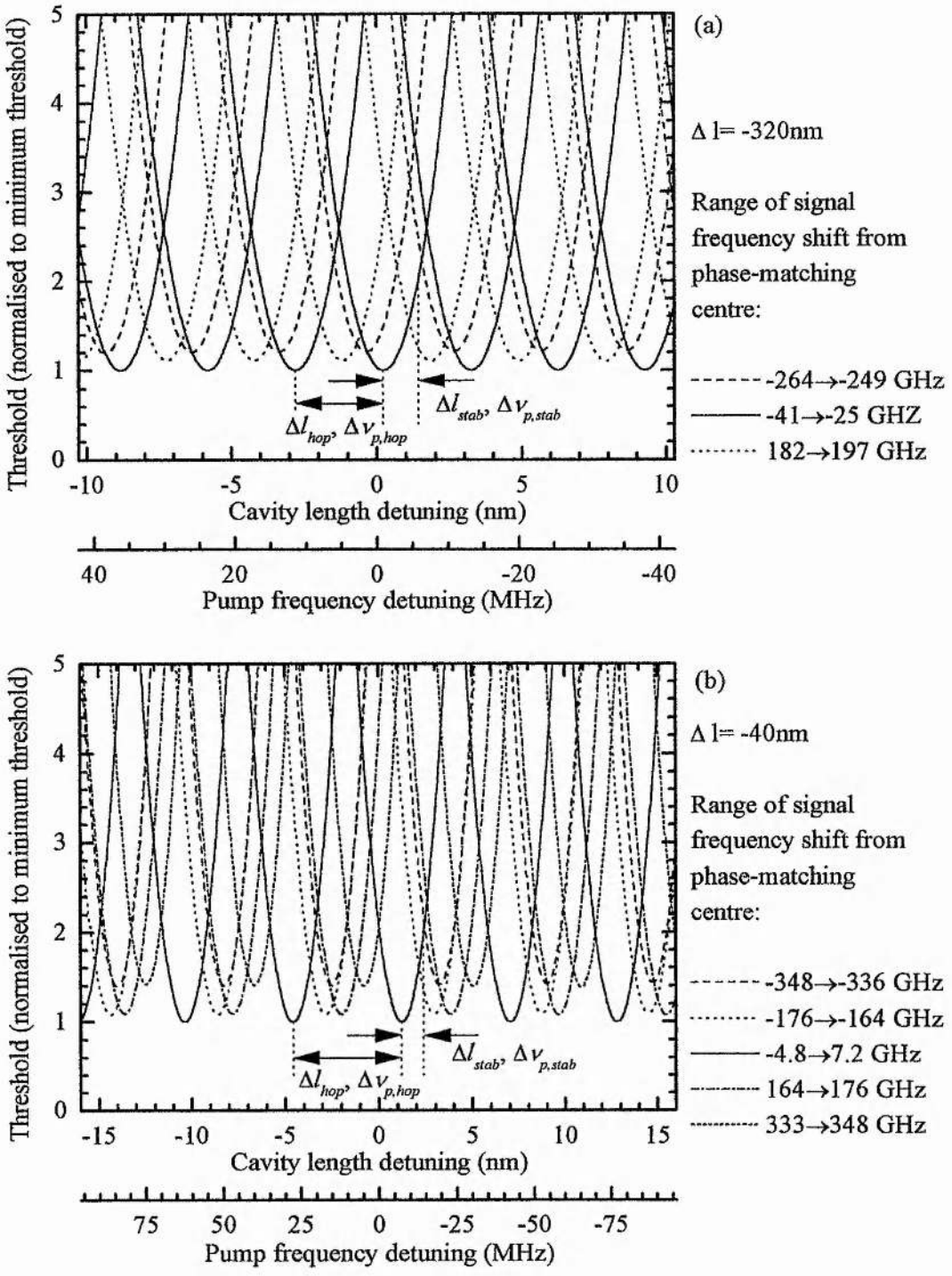

Fig. 7-9 Mode-selection diagrams for PPLN DRO. (a) 68.8mm nominal cavity length, λ_s=1.215μm, λ_i=2.430μm. (b) 40mm nominal cavity length, λ_s=1.157μm, λ_i=2.700μm. Nominal cavity lengths modified by Δl as indicated. All other parameters are as given in Table 7-2 for each case.

Examining Fig. 7-9, it is clear that the values of Δl_{hop}, Δl_{stab}, $\Delta \nu_{p,hop}$ and $\Delta \nu_{p,stab}$ obtained from these numerically calculated results show good agreement with those in Table 7-2 obtained analytically. The intra-cluster mode-hop stability figures given in Table 7-2 appear to indicate a significant improvement in the tolerance to mode hopping can be achieved by shortening the cavity and increasing the signal-idler wavelength separation. It can be seen from Fig. 7-9, however, that while this is the case when only one cluster is considered, inter-cluster mode hopping results in the two situations displaying very similar performance in practice.

Using equation (3-119) to calculate the phase-matching bandwidth by setting $\lambda_3=\lambda_s$ and $\lambda_2=\lambda_i$ results in a value at the signal of $\Delta\lambda_{pm,s}\approx$5nm or $\Delta\nu_{pm,s}\approx$1.067 THz for the wavelength ranges under consideration. As the cluster spacing, in terms of mode numbers, is given by the ratio of the average FSR to the FSR difference, ΔFSR, it can be seen from the values given in Table 7-2 that approximately 5 or 6 clusters will fall within the phase-matching bandwidth in the two situations under consideration. Since this bandwidth defines the region where the OPO threshold is less than ≈2.5 times that for perfect phase-matching, more clusters would be expected to be above threshold at high pump powers.

As a result of the relatively large phase-matching bandwidth, when compared to the cluster spacing, the increase in threshold seen by clusters adjacent to the central one is minimal. Thus, while shortening the cavity and increasing the signal-idler wavelength separation results in a significant improvement in the tolerance to mode-hops within a cluster, it can be seen from Fig. 7-9 (b) that between the central-cluster coincidences the DRO will operate in other clusters with only a small increase in threshold. Although increasing the FSR difference, ΔFSR, improves the intra-cluster mode-hop stability, Δl_{hop} and $\Delta \nu_{p,hop}$, it also reduces the cluster spacing and thus increases the degree of inter-cluster mode-hopping. It is clear, therefore, that while the PPLN DRO will probably show slightly better definition of the signal-idler coincidences as the cavity length is varied than the Type-I DRO near degeneracy shown in Fig. 3-22, the degree of definition obtained from the TYPE-II DRO as shown in Fig. 3-23 is unlikely to be achieved. This behaviour, resulting in a lack of well-defined resonance points, appears likely to make the active stabilisation of the

PPLN DRO more difficult than is the case for DROs having well-defined signal-idler resonance coincidences.

7.3 Experimental results.

The experimental configuration shown in Fig. 7-6 was used to investigate the performance of the PPLN DRO. As no attempt was made, initially, to actively stabilise the cavity length, it was expected, from the discussion in section 7.2.4, that the output power would show significant variation. In view of this, a ramp signal was applied to the piezo-electric element, on which the output mirror was mounted, to scan the cavity length continuously and the pump transmission and signal output were monitored. As mentioned in section 7.2.2, a calibrated detector was used to monitor the signal output, allowing absolute output power measurements to be made.

7.3.1 Injection-locked broad-area diode laser pumping.

Initial characterisation of the PPLN DRO was carried out with the injection-locked broad-area diode laser as the pump source. A typical result showing output at the signal, and corresponding depletion of the transmitted pump, as the OPO cavity length was varied is shown in Fig. 7-10. This result was obtained with a near-confocal cavity configuration using 30mm ROC mirrors. The pump wavelength was 808nm, the grating period 21.2μm and the temperature 150°C, corresponding to signal and idler wavelengths of ≈1.20μm and ≈2.47μm, respectively. The pump power was 365mW and the signal detector response $100mWV^{-1}$. The undepleted pump transmission, corresponding to the situation where the OPO was not operating, can be seen as the top trace shown in Fig. 7-10. This shows a slight modulation with varying cavity length due to the small residual reflectivity(<10%) of the mirrors at this wavelength. The zero point for both the pump transmission and signal output is shown as the bottom trace. It can be seen that a pump depletion of over 50% and signal output of ≈14mW was observed.

To measure the variation of output power with pump power, the peak signal output power occurring as the cavity length was scanned was measured for a range of input

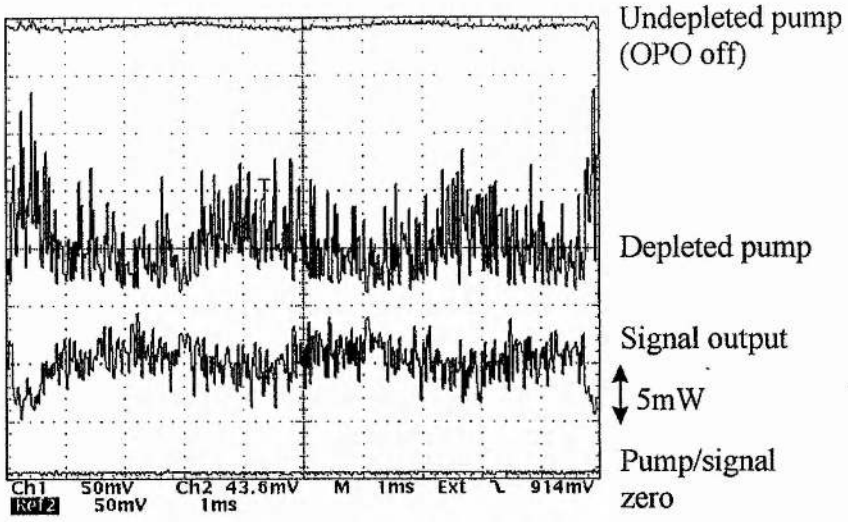

Fig. 7-10 Signal output and corresponding pump depletion of from the PPLN DRO pumped by the injection-locked broad-area diode laser. $\lambda_s \approx 1.20\mu m$, $\lambda_i \approx 2.47\mu m$. Pump power: 365mW. Signal detector response: $100mWV^{-1}$.

pump powers with a near-confocal cavity formed by 20mm ROC mirrors. The minimum DRO threshold was observed to occur for λ_p=0.8105μm, λ_s=1.222μm and λ_i=2.407μm, phase matching of this interaction being achieved using the 21.2μm grating period at 150°C. At these wavelengths, the round-trip surface losses can be seen from Fig. 7-7 to be 0.4% and 2.75% for the signal and idler, respectively. Assuming the manufacturers specified maximum round-trip absorption loss at 1.064μm in the crystal of 0.57% for both signal and idler, losses of $2\gamma_s' = 0.97\%$ and $2\gamma_i' = 3.32\%$ are obtained. These values give a geometric-mean loss of 1.79%, which can be seen from Fig. 7-8 to imply a threshold of ≈9mW in the case of near-confocal focusing.

The results of these measurements are shown in Fig. 7-11. It can be seen that an external threshold pump power of 25mW is achieved. Approximately 92% of this external pump power entered the crystal. Above threshold, it can be seen from equations (3-186) that the down-converted power would be expected to show a dependence upon the pump power of the form:

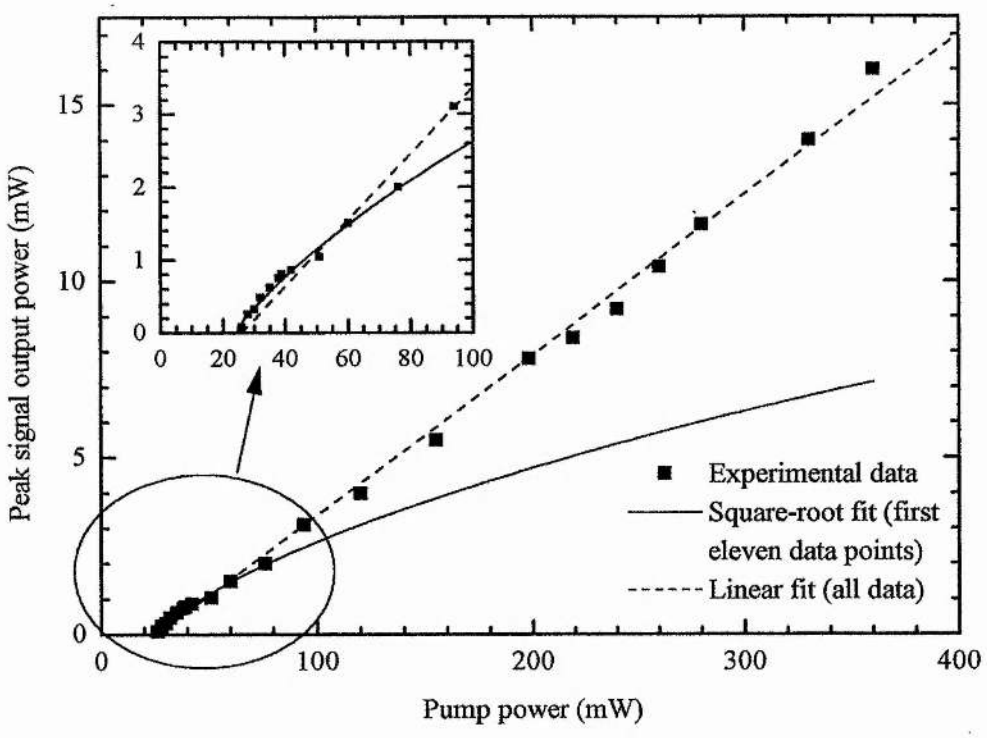

Fig. 7-11 Variation of signal output power for PPLN DRO with near-confocal cavity formed by 20mm ROC mirrors pumped by injection-locked broad-area diode laser. Operating wavelengths: λ_s=1.222μm, λ_i=2.407μm.

$$P_s \propto \sqrt{P_p P_{p,th}} - P_{p,th} \tag{7-8}$$

with P_s, P_p and $P_{p,th}$ being the signal, pump and threshold pump power, respectively. Thus, the output power at the signal would be expected to vary as the square-root of the pump power for a given pump power threshold. The results in Fig. 7-11 show such a dependence at low pump powers levels, but deviate from this at higher pump powers as a result of the measurement method.

As was seen in Fig. 7-9, it would be expected that output would be produced by many different signal-idler mode pairs throughout the phase-matching bandwidth as the cavity length is varied. All these mode pairs will have slightly different levels of output coupling due to small variations in the mirror transmission across the phase

matching bandwidth. The maximum output power during a cavity length scan will always be produced by the signal-idler mode pair having the closest to optimal level of output coupling for the given pump power. Close to the OPO threshold, this will also be the mode pair with the lowest threshold. However, as the pump power increases, the maximum output power will tend to result from mode pairs having higher levels of output coupling and thus higher thresholds. As a result, $P_{p,th}$ in equation (7-8) can only be regarded as a constant for pump powers close to threshold and at higher pump powers a square-root dependence will not be observed.

It is not clear why the lowest threshold occurred for a wavelength combination which, especially at the idler, appears from Fig. 7-7 to show significantly higher surface losses than the minimum values. Taking into account the ≈8% loss at the pump between the measured value and the power entering the crystal, the internal threshold of 23mW is still significantly higher than the value of 9mW calculated from the losses.

The OPO was also operated at a signal wavelength close to the edge of the mirror high-reflectivity band, where the level of output coupling at the signal was higher. This was achieved with a pump wavelength of 808nm, a PPLN grating period of 21.0μm and a temperature of 150°C, to give a signal and idler wavelengths of ≈1.245μm and ≈2.302μm, respectively. The corresponding variation of maximum signal output power with incident pump power is shown in Fig. 7-12. It can be seen that the threshold, in this case, has been increased to ≈75mW and over 35mW of output at the signal are obtained. It should be pointed out that the measured signal output powers, shown in both Fig. 7-11 and Fig. 7-12, are from one OPO mirror only. Similar power levels would be expected to be emitted from the other mirror back in the direction of the pump beam. While it can be seen from Fig. 7-7 that the round-trip surface losses at the signal are around 1% at this wavelength, those at the idler appear to be considerably greater than 10%. This result would appear to cast some doubt on the accuracy of the loss data, as specified by the coating manufacturers, shown in Fig. 7-7.

To investigate the temperature-tuning behaviour, the pump and signal spectra were monitored, as the cavity length was scanned, using an optical spectrum analyser and

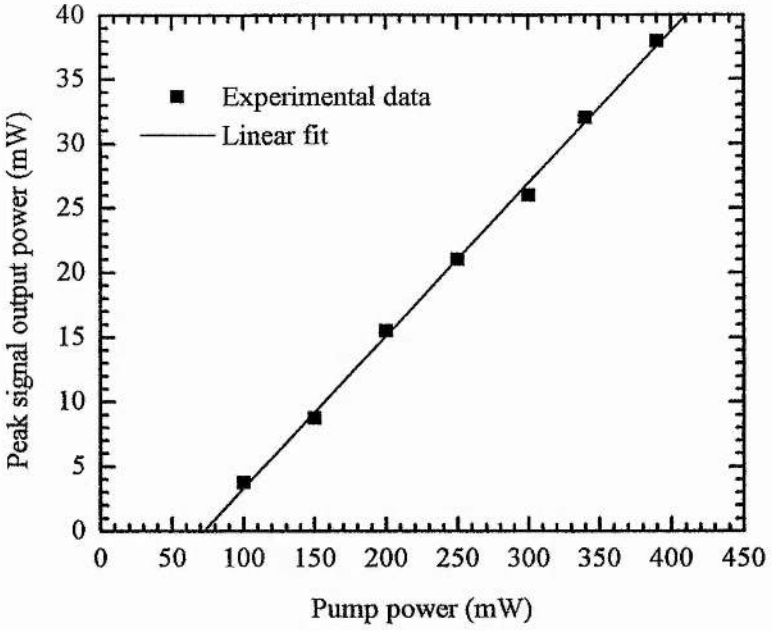

Fig. 7-12 Variation of signal output power for PPLN DRO with near-confocal cavity formed by 20mm ROC mirrors pumped by injection-locked broad-area diode laser. Operating wavelengths of λ_s=1.245μm, λ_i=2.302μm result in increased output coupling at the signal and idler.

the idler wavelength inferred from these measurements. In the case of the signal, the output spectrum was generally over a band of ≈5nm, corresponding to the calculated phase matching bandwidth, and the centre wavelength was recorded. Temperature tuning was carried out between room temperature and 190°C, with a pump wavelength of 808.7nm, for five grating periods ranging from 21.0μm to 21.8μm. The results obtained are shown in Fig. 7-13.

The tuning range at signal can be seen to be 1.16-1.24μm and that at the idler 2.31-2.66μm. The signal tuning range can be seen from Fig. 7-7 to correspond well with the region of minimum loss. However, the short-wavelength limit of the idler tuning range appears from Fig. 7-7 to extend into a region where the round-trip losses are well over 10%. This result, therefore, again casts some doubt on the manufacturers loss data shown in Fig. 7-7.

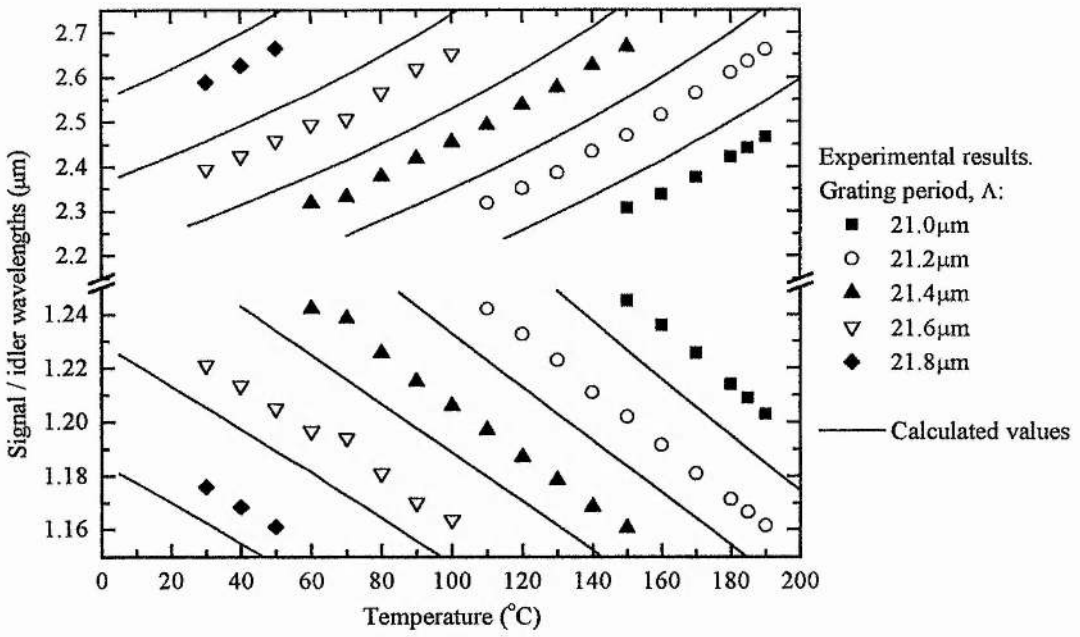

Fig. 7-13 Temperature tuning behaviour of the PPLN DRO pumped by the injection-locked broad-area diode laser. The pump wavelength was λ_p=808.7nm. The calculated values were obtained using equations (7-2) and (7-3).

As already mentioned, PPLN is usually operated at elevated temperatures to avoid photorefractive effects which, in the case of infra-red pumped OPOs, are generally attributed to visible light generated through non-phase-matched mixing processes [2,7]. Although room-temperature operation was observed here, significant levels of visible light were generated by frequency doubling of the signal. Scattering effects, resulting in impaired OPO performance, were observed after 20-30 minutes of room temperature operation in the same area of the crystal. These effects were easily removed by re-heating.

The experimental data shown in Fig. 7-13 can be seen to show an offset from the calculated values corresponding to a temperature shift of ≈20°C. Temperature offsets in the same direction, although of different magnitudes, have been observed by others in PPLN OPOs pumped at similar wavelengths [8,9]. It is interesting to note

that the Sellmeier coefficients given in Table 7-1 are largely derived from data obtained with ≈1μm-pumped OPOs [1]. At this pump wavelength, the tuning characteristics are significantly different and do not show the two-branched behaviour seen in Fig. 7-1. It appears likely, therefore, that the observed offset is a result of inaccuracies in the Sellmeier equations at the pump wavelengths used here.

As was pointed out in section 3.7, diode-laser pumped OPOs have the significant advantage of broad pump-wavelength tuning when compared to OPOs pumped by fixed-wavelength sources. To investigate the pump-wavelength tuning behaviour of the PPLN DRO, the output wavelength of the injection-locked broad-area diode laser system was varied by variation of the master laser wavelength, while the OPO grating period and crystal temperature remained fixed at Λ=21.2μm and T=150°C, respectively.

The results of these measurements are shown in Fig. 7-14. It can be seen that the tuning ranges are identical to those obtained by varying the crystal temperature, confirming that the entire tuning range of the OPO, as defined by the coating bandwidths, can be exploited by pump-wavelength tuning alone. It can also be seen that a similar offset exists between the calculated and experimental values to that observed when temperature tuning.

7.3.2 Single-mode diode laser pumping.

In view of the threshold of 25mW, it was decided to attempt direct pumping of the OPO by the single-mode master laser without amplification by injection-locking the broad-area diode laser. This was done using the experimental configuration shown in Fig. 7-15. The f=80mm focusing lens was retained for mode-matching into the OPO and the output of the collimated single-mode laser was reshaped in the plane of the junction to give a near-circular beam of similar dimensions to the shaped output of the injection-locked system. This reshaping was carried out by a cylindrical telescope, acting in the plane of the diode-laser junction, consisting of an f=80mm lens followed by a 100mm lens with an approximately confocal separation.

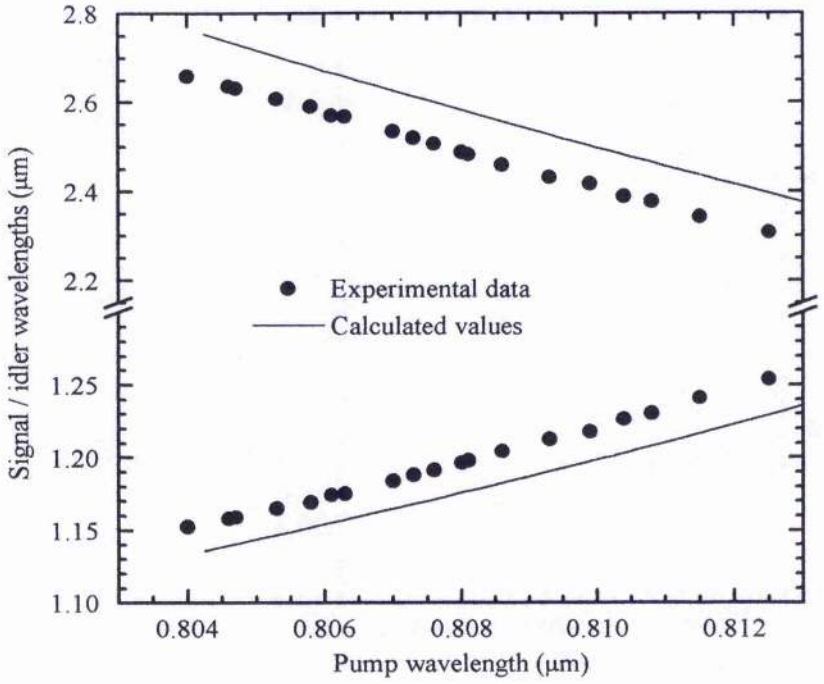

Fig. 7-14 Pump-wavelength tuning behaviour of the PPLN DRO pumped by the injection-locked broad-area diode laser. Grating period was Λ=21.2μm, and temperature was 150°C. Calculated values were obtained using equations (7-2) and (7-3).

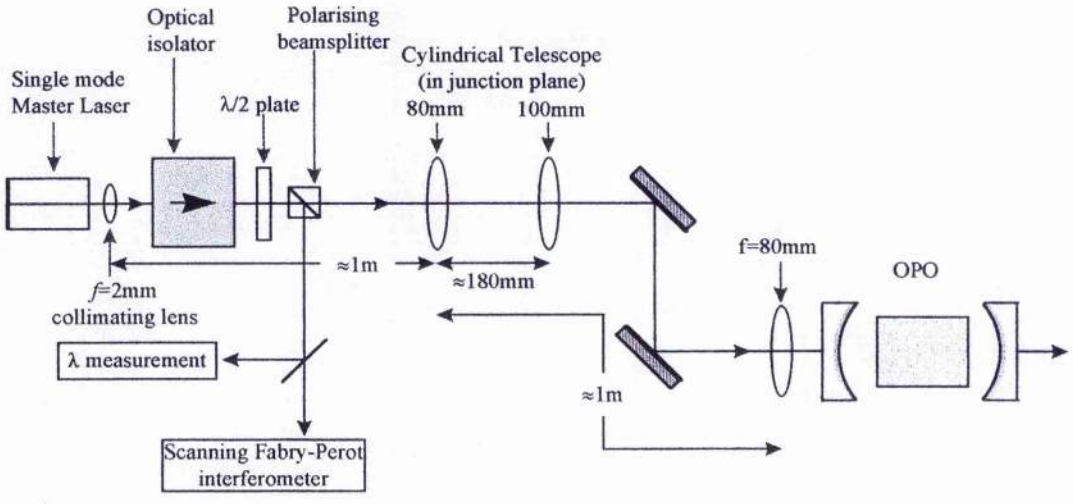

Fig. 7-15 Experimental arrangement for single-mode diode-laser pumping of the PPLN DRO.

The overall distance from the single-mode diode laser to the OPO was approximately two metres and the beam-shaping telescope was located approximately half way between the two. The calculated beam-waist radii and positions within the PPLN crystal, as the position of the mode-matching lens is varied, are shown in Fig. 7-16 for 20mm and 30mm ROC mirrors in a near-confocal configuration. It can be seen that similar beam waist radii are obtained at the centre of the crystal to those obtained with the injection-locked system as shown in Fig. 7-5 and similar threshold values would, therefore, be expected.

The variation of maximum output power with input pump power, obtained in a similar manner to the results shown in Fig. 7-11, are shown in Fig. 7-17. It can be seen that in this case the threshold pump power was 16mW and up to 5mW of output

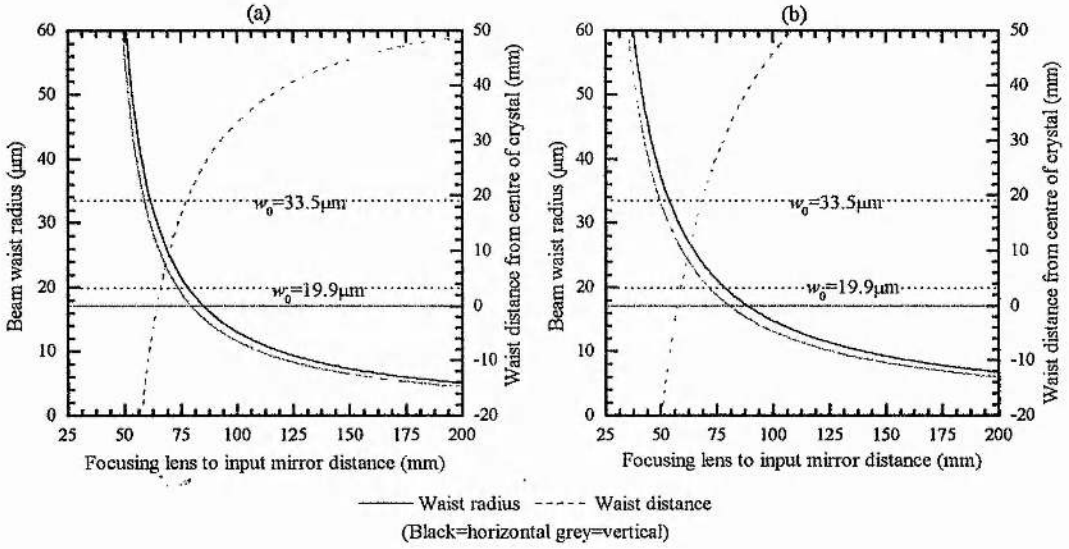

Fig. 7-16 Variation of pump beam waist radius and position with distance of f=80mm focusing lens from OPO input mirror for reshaped single-mode diode laser beam. (a) mirror ROC=20mm, 48mm overall cavity length. (b) mirror ROC=30mm, 68.8mm overall cavity length. Black lines represent beam properties in horizontal direction (in plane of diode-laser junctions, in x-z plane of PPLN crystal), grey lines represent properties in vertical direction (normal to junction plane, in x-y plane of PPLN crystal).

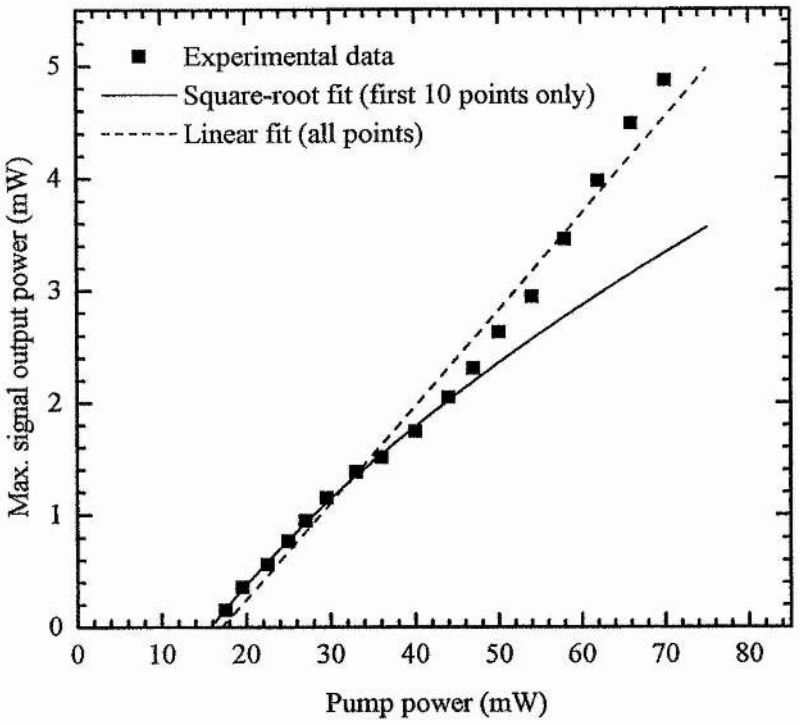

Fig. 7-17 Variation of signal output power for PPLN DRO with near-confocal cavity formed by 20mm ROC mirrors pumped by single-mode diode laser. Operating wavelengths: λ_s=1.222μm, λ_i=2.407μm.

at the signal was obtained. As with the injection-locked pump source, the output shows a square-root variation with pump power initially from which the results deviate at higher powers, as a result of the measurement method, for the reasons described above. It is not clear why a reduction in threshold was observed, when pumping with the single-mode diode, compared to that obtained with the injection-locked pump. It is possible that in the case of the injection-locked system some residual free-running output was present which did not couple into the OPO and therefore did not contribute to the pumping.

Despite the reduction in threshold, when compared to the injection-locked pump source, the measured threshold value is still significantly larger than the value of ≈9mW calculated from the estimated losses. As has already been pointed out, however, other aspects of the OPO performance are not entirely consistent with the

loss data shown in Fig. 7-7 and it is possible that actual the losses are greater than those estimated.

To investigate the OPO tuning behaviour when pumped by the single-mode diode, pump-wavelength tuning was carried out. As was seen with the injection-locked pump source, the tuning range obtained by this method is identical to that achieved through temperature tuning and therefore this measurement should give a good indication of the tuning limits with the single-mode diode pump source. As with the injection-locked pump source, pump-wavelength tuning was carried out with the 21.2μm grating period at a temperature of 150°C.

The results obtained are shown in Fig. 7-18, along with those obtained with the injection-locked pump source for comparison. It can be seen that the tuning behaviour when pumping with the single-mode diode is similar to that seen when pumping with the injection-locked system. The range over which the OPO can be tuned is, however, slightly smaller, being limited to a shorter maximum idler wavelength as the lower pump power available restricts operation at the edge of the coating bandwidth.

7.3.3 Active cavity length control.

Up to this point, all the results presented were obtained without any attempt to maintain operation of the DRO on a single signal-idler mode pair. As was seen in section 3.4.3.2, and is clear from Fig. 7-9 in this chapter, small changes in cavity length or pump frequency can result in the DRO mode-hopping. Single-mode operation can be maintained by the use of electronic servo techniques which can, not only, compensate for fluctuations in cavity length, but also for those in pump frequency, as the two have equivalent effects in the opposite sense. A number of servo techniques have been used to stabilise DROs in this way [10,11,12,13]. One of the simplest methods to implement is side-of-fringe locking, where the output power at the signal is monitored by the servo electronics which aim to maintain this output power at a constant level [11,14,15]. It was decided to use this technique here.

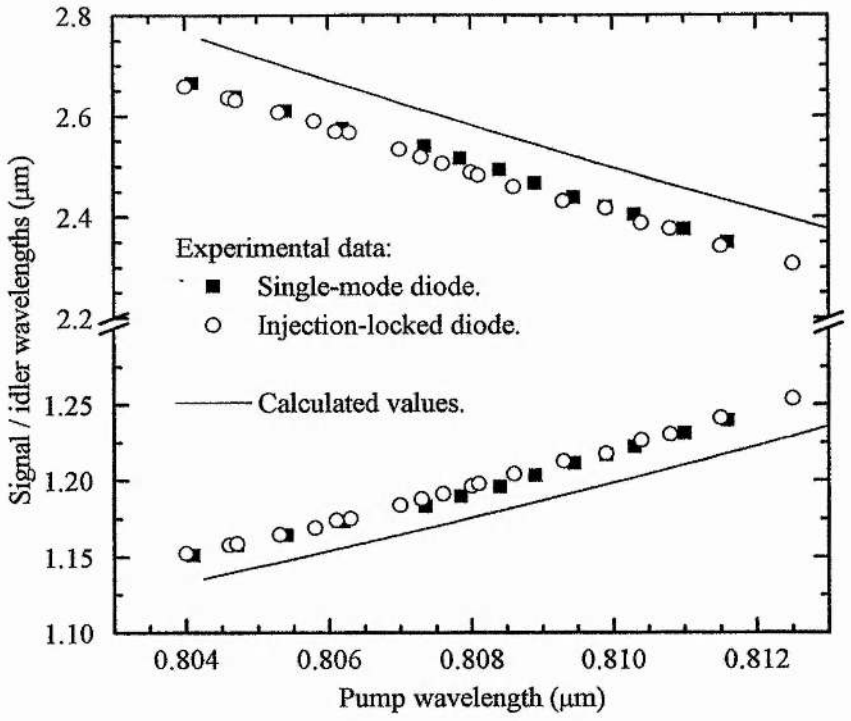

Fig. 7-18 Pump-wavelength tuning behaviour of the PPLN DRO pumped by the single-mode diode laser with data obtained using the injection-locked system included for comparison. Grating period was Λ=21.2μm and temperature was 150°C. Calculated values were obtained using equations (7-2) and (7-3).

One of the disadvantages of the side-of-fringe technique is that well-defined signal-idler resonance peaks, as the cavity length varies, are required to give a clear locking region on the side of each resonance. The majority of previous experimental implementations of this technique have made use of type-II birefringently phase-matched DROs operating near degeneracy. As was seen in Fig. 3-23, these devices generally exhibit better discrimination between the mode-pairs in a given cluster and better cluster selectivity than those for the PPLN DRO shown in Fig. 7-9. It was seen in Fig. 7-9 and Table 7-2 that the definition of individual mode-pair resonances would be expected to show some slight improvement by shortening the cavity and increasing the wavelength separation. It would also be expected that reducing the

pump power or increasing the threshold by, for example, misaligning the cavity slightly, would reduce the number of mode pairs able to reach threshold and thus improve the definition of the resonances for the remaining lowest-threshold modes.

To experimentally investigate the effects of signal/idler wavelength separation and cavity length on the definition of individual resonances the output at the signal was monitored, as the cavity length was varied, for different wavelength combinations and cavity lengths. Such results are shown in Fig. 7-19 for three different wavelength combinations and two different cavity lengths. To ensure that approximately the same number of mode pairs were above threshold in each case, the pump power was adjusted to give approximately similar average output powers at the signal. With a cavity length of approximately 68mm (30mm ROC mirrors), results were taken for three wavelength combinations (obtained by changing the grating period with temperature and pump wavelength fixed) with progressively greater wavelength separations between the signal and idler. These results are shown in Fig. 7-19 (a)-(c). It can be seen that the depth of modulation increases slightly, indicating better definition of the resonances, as the wavelength separation increases.

Fig. 7-19 (d) shows results obtained with a combination of wavelengths between those of Fig. 7-19 (a) and (b), but with a considerably shorter cavity length of 40mm (limited by the dimensions of the crystal oven) using 20mm ROC mirrors. It can be seen that the shortening of the cavity also results in a slight improvement in definition of the signal-idler resonances. Despite this, however, the individual resonances are still not particularly well defined.

All the results of Fig. 7-19 were obtained with the OPO approximately two times above threshold. It can be seen from Fig. 7-9 that reducing the pump power should reduce the number of signal-idler mode-pair combinations which can achieve threshold and hence improve the definition of the remaining resonances. The signal output and transmitted pump power, as the cavity length was varied, are shown for four pump-power levels in Fig. 7-20. These results were all obtained with a cavity length of 40mm using 20mm ROC mirrors and utilising the Λ=21.6μm grating at room temperature. This resulted in signal and idler wavelengths of approximately 1.22μm and 2.39μm, respectively, when pumping at 808nm.

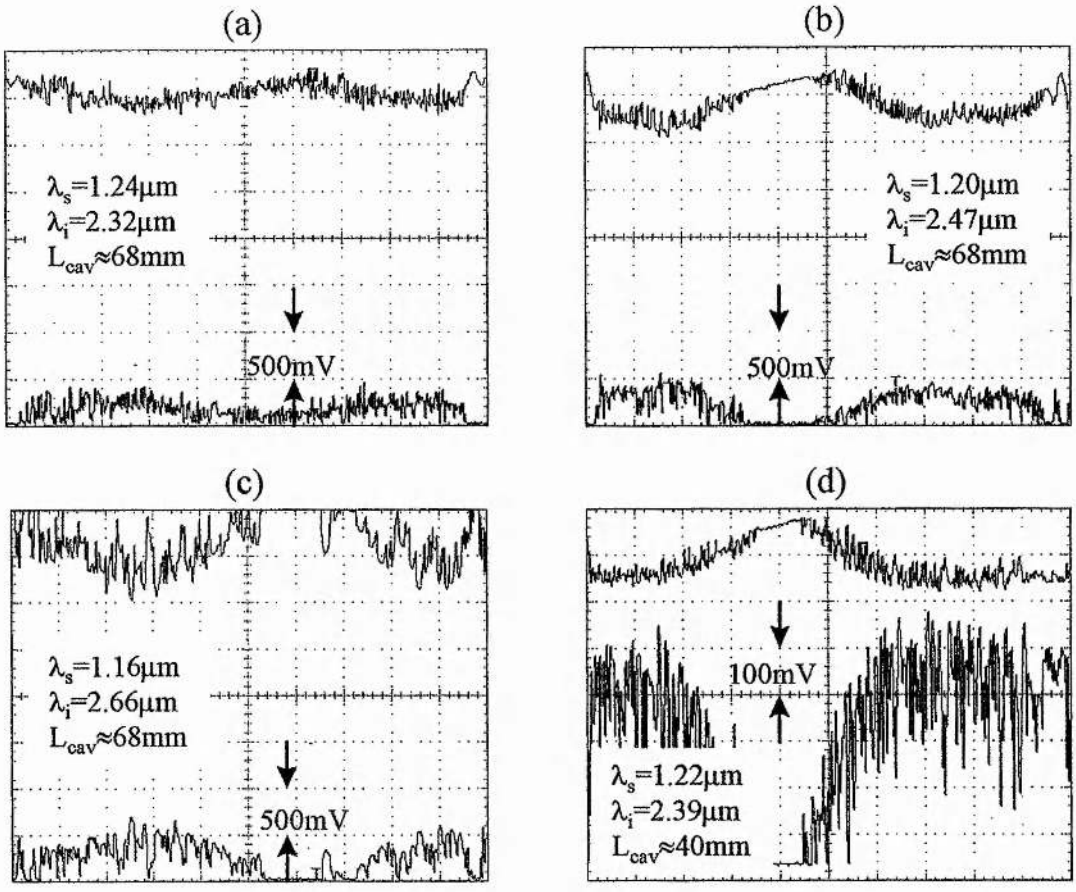

Fig. 7-19 Variation in PPLN DRO signal output and pump depletion as cavity length was scanned: (a) λ_s=1.24μm, λ_i=2.32μm (Λ=21.0μm, T≈150°C), (b) λ_s=1.20μm, λ_i=2.47μm (Λ=21.2μm, T≈150°C), λ_s=1.16μm, λ_i=2.66μm (Λ=21.4μm, T≈150°C), (d) λ_s=1.22μm, λ_i=2.39μm (Λ=21.6μm, T≈25°C). Overall cavity length: (a), (b), (c) L_{cav}≈68mm, (d) L_{cav}≈40mm. Vertical scale indications refer to the signal. Note change of scale in (d).

Examining the results shown in Fig. 7-20, it can be seen that as the pump power is increased beyond ≈1.5×threshold, the individual resonances become increasingly difficult to resolve, although there is still a reasonably high level of modulation in the signal output power at ≈2×threshold. By ≈4×threshold, however, the OPO is continually operating as the cavity length is varied and there is a smaller degree of

modulation than at lower pump powers, indicating that large numbers of individual signal-idler resonances are merging into one another.

In practice, when active stabilisation of the cavity length was attempted, the OPO was generally operated in a situation giving results with an appearance somewhere between those at 1.5× and 2×threshold in Fig. 7-20. For practical purposes, rather

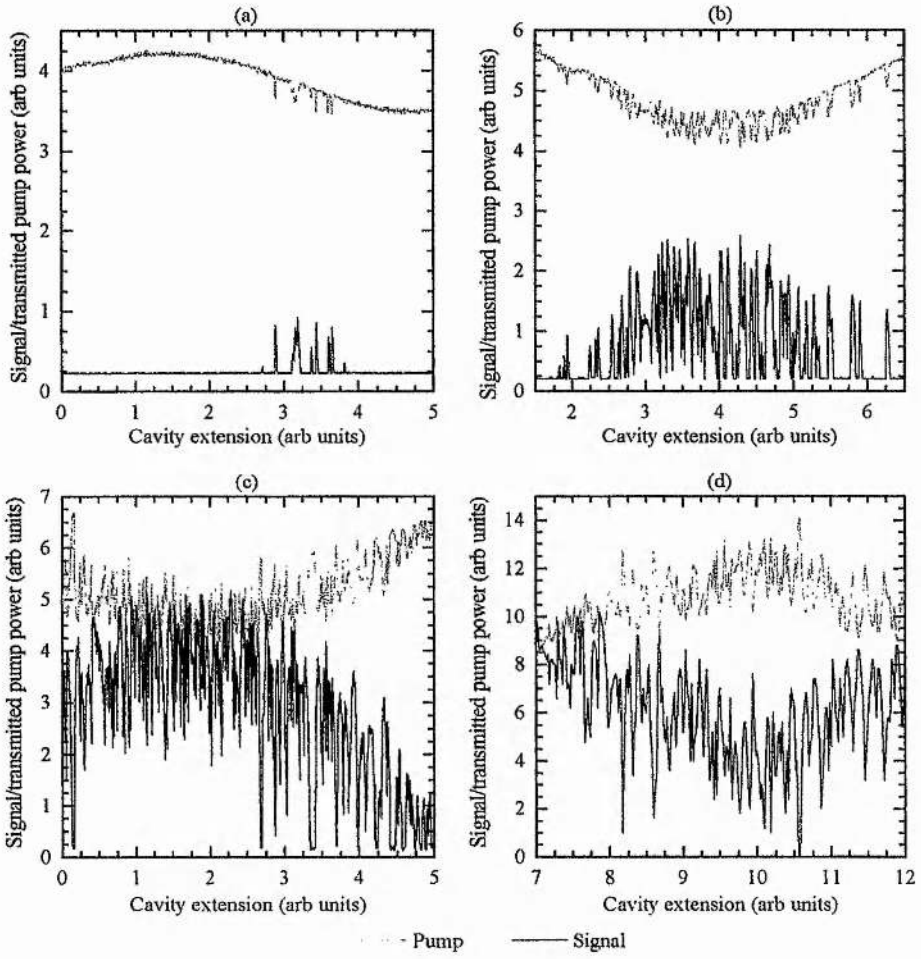

Fig. 7-20 Signal output and corresponding pump depletion when pumping OPO at approximately (a) threshold, (b) 1.5×threshold, (c) 2×threshold and (d) 4×threshold. Pump, signal and idler wavelengths were λ_p=808nm, $\lambda_s \approx 1.22\mu m$ and $\lambda_i \approx 2.39\mu m$, respectively. Grating period was Λ=21.6μm and temperature was ≈25°C.

than varying the pump power, this was generally achieved by slightly misaligning one of the cavity mirrors.

As mentioned above, all the results shown in Fig. 7-20 were taken at room temperature. It had been noted, since the initial operation of the OPO, that the output at the signal and the transmission at the pump showed a large modulation, with a period of several seconds, in addition to that due to OPO effects. This was found to be due to thermal effects induced by the temperature controller operating the crystal oven. This device was based on an industrial process controller (Eurotherm 818) which was found to supply current to the heating element in discrete bursts rather than continuously. The period of these bursts was determined by the controller's programmed cycle time, variable between 0.3 and 10 seconds, and coincided with the period of the observed fluctuations in output power and pump transmission. The cycle time was initially set to 10s (the default value) and reduction to 0.3s improved the situation considerably as the same power was supplied in many small bursts rather than one large one.

Operating the controller with a 0.3s cycle time avoided the large thermal modulation of the outputs and allowed all the results so far, taken with the cavity length continuously scanned by the piezo mirror-mount, to be obtained as the period of the remaining thermal fluctuations was much larger than that of the cavity length scan. However, significant modulation of the signal output, with the 0.3s period of the controller cycle time, remained and disrupted the servo electronics when cavity-length stabilisation was attempted. As a result, all servo stabilisation was carried out at room temperature with the oven switched off. Although this led to photorefractive effects occurring in the PPLN crystal, the low pump powers used to obtain well-defined signal-idler resonances meant that these effects took many hours to develop and several days of room-temperature operation could be obtained, by repeatedly moving to unaffected parts of the crystal, before reheating was required to remove the photorefractive damage.

The servo-stabilisation system is shown schematically in Fig. 7-21. An uncoated glass slide was used to pick off a small fraction of the signal output (in practice this was placed after the dichroic beamsplitter used to separate the signal output from the

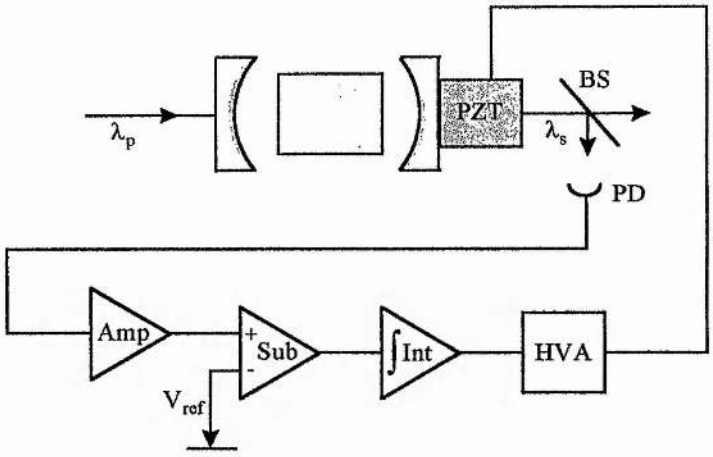

Fig. 7-21 Schematic diagram of servo-locking system for cavity length control of the PPLN DRO. Labelled components are BS: glass-slide beamsplitter, PD: InGaAs photodiode, Amp: amplifier, Sub: op-amp subtractor, Int: integrator, HVA: high-voltage amplifier, PZT: piezo-electric mirror mount.

transmitted pump). This small fraction of the signal output was then incident on an InGaAs photodiode which was used in preference to the germanium detector, as it had a greater bandwidth. The photodiode output was amplified and a reference voltage, equal in magnitude to the required amplified-photodiode output at the lock point, subtracted from it. As a result, the output of the subtraction circuit was zero only when the OPO was operating at the required lock point. Either side of this point the output was a non-zero positive or negative voltage. The subtractor output therefore acted as an error signal.

The output of the subtraction circuit was integrated with the result that a non-zero output from the subtraction circuit (indicating the OPO was not at the lock point) produced a voltage of continually increasing magnitude from the integrator. The integrator output was then amplified in a high-voltage amplifier before being applied to the piezo-electric mirror transducer. As a result, any deviation of the OPO from the lock point resulted in a voltage of increasing magnitude being applied to the

piezo-electric transducer, adjusting the cavity length until the error signal was returned to zero.

The results of servo stabilisation of the DRO cavity length are shown in Fig. 7-22. The OPO output power, recorded over 100s, is shown in Fig. 7-22 (a) without stabilisation. It can be seen that there are a number of large fluctuations in the output power, corresponding to DRO mode hops, as well as higher-frequency fluctuations in the output power between these hops. The spectral properties of the unlocked OPO, monitored by observing the signal output over 60s with a scanning interferometer,

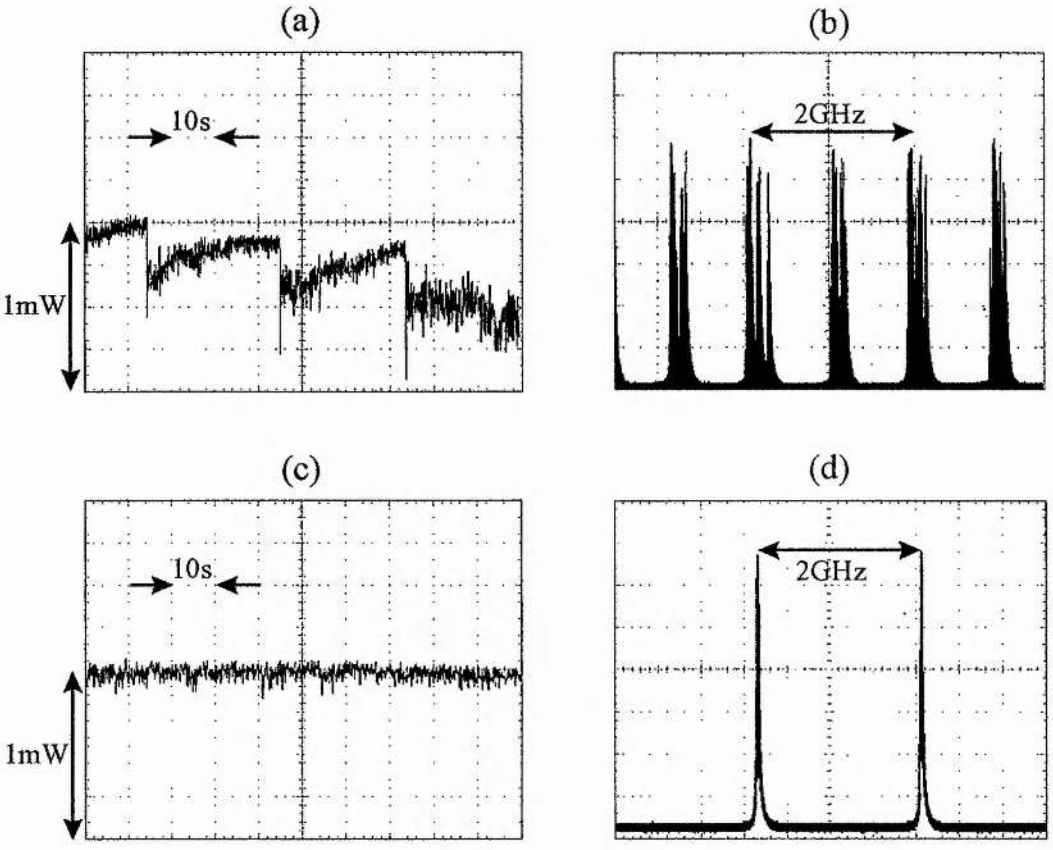

Fig. 7-22 Effects of servo stabilisation of DRO cavity length on output power and signal spectrum. (a) unstabilised output power over 100s, (b) unstabilised signal spectrum integrated over 60s, (c) servo-stabilised output power over 100s, (d) servo-stabilised signal spectrum integrated over 60s.

are shown in Fig. 7-22 (b). It can be seen that many mode-hops occur within the monitoring period.

With servo-stabilisation of the cavity length, it can be seen from Fig. 7-22 (c) that the large fluctuations in output power are eliminated as the servo system adjusts the DRO cavity length to compensate for the variations in cavity length and / or pump frequency which caused the mode-hops to occur. It can also be seen that some reduction in the high-frequency fluctuations is also obtained through the stabilisation of cavity length. Single signal-idler mode pair operation, when stabilised by the servo system, is confirmed by the results shown in Fig. 7-22 (d), where it can be seen that no mode-hops occur within the same period in which many occurred when unstabilised.

While the servo-stabilisation system could compensate for drifts in the DRO cavity length or pump frequency, it obviously could not maintain single mode-pair operation if the pump laser underwent a mode-hop. As was mentioned in section 5.2.1, simple Fabry-Perot diode lasers are highly susceptible to optical feedback, which can cause general instability and mode-hopping. The ≈60dB of optical isolation used for the single-mode master laser in the injection-locked system was found to be sufficient to obtain most of the results observed when pumping directly with the single-mode laser. However, it was found that ≈90dB of isolation, obtained using two optical isolators, was required for successful stabilisation with the servo system. Even with this high level of isolation, the single-mode laser suffered mode hops on the time-scale of minutes and it was ultimately this factor which limited the duration for which servo-locked operation could be maintained.

7.4 Conclusions.

The design and characterisation of the PPLN DRO has demonstrated the suitability of such devices for direct pumping by diode lasers. Use of the injection-locked broad-area diode laser as a pump source proved useful in initial characterisation of the device, providing pump powers considerably higher than the ultimate minimum threshold. Perhaps more significant, however, is the demonstration of direct pumping

by the single-mode diode laser. While the DRO pumped by the injection-locked system does not necessarily represent a convenient practical method of generating near-to-mid infrared wavelengths, a single-mode diode pumped DRO could form the basis of a highly compact and practical infrared source for various applications. The results presented here have shown that such a device can generate infra-red powers of several milliwatts, can be tuned over wide wavelength ranges by the variation of multiple parameters and has the potential for frequency-stable operation.

The main limitations to the practical use of the single-mode-diode pumped DRO are associated with the implementation of stabilised operation. Although short-term stabilisation was demonstrated using the simple side-of-fringe technique, several problems with this mode of operation were highlighted. The first of these was the requirement to operate at room temperature due to the thermal instabilities introduced by the crystal oven. While possible in the short term, this situation is unsatisfactory for long term operation due to the photorefractive effects occurring in the PPLN. These stability problems, however, were only a feature of the particular oven controller unit used and should be simply eliminated by the use of an improved temperature control unit.

While even the simple side-of-fringe technique was able to provide short-term stabilised OPO operation against small fluctuations in cavity length and pump frequency, no method of stabilising the OPO alone could be expected to cope with the mode-hopping of the pump laser, which ultimately limited the level of stabilisation which could be achieved here. High sensitivity to mode-hopping is an inherent feature of simple Fabry-Perot diode lasers, but can be avoided using external-grating feedback methods. An external-cavity diode would also have the advantage of improved overall frequency stability and considerably reduced linewidth compared to the unstabilised diode. Such devices have been shown to produce output powers well in excess of the threshold for the PPLN DRO [16].

The operational characteristics of the DRO itself also limit the stabilised performance. As was seen, to obtain the reasonably well-defined signal-idler resonances required for side-of-fringe locking, the OPO could not be operated significantly above threshold due to operation on the large number of mode-pairs

within the phase-matching bandwidth. A reduced phase-matching bandwidth would help to address this problem, and could be implemented due to the potential for control of the phase-matching profile afforded by quasi-phase-matching [17]. Simpler solutions to the problem might be the use of an intracavity etalon to introduce a narrow low-loss bandwidth (although this would be likely to increase the threshold considerably), or the use of more sophisticated stabilisation technique to lock to the peaks of the resonances rather than the sides. Such locking techniques have been used to stabilise type-I birefringently phase-matched DROs near degeneracy and would also have the advantage of allowing the maximum on-resonance output power to be extracted.

In spite of these limitations, all of which could be addressed by further development, the PPLN DRO described here has been a useful device to prove the principles of low-threshold diode-pumped operation of an OPO. As far as can be ascertained, the initial demonstration of this device [18] represented the first reported operation of a DRO pumped directly by a single-mode diode laser, the first non-degenerate diode-pumped PPLN OPO and the first PPLN OPO diode-pumped at AlGaAs wavelengths.

7.5 References.

1 D.H. Jundt, "Temperature-dependent Sellmeier equation for the index of refraction, n_e, in congruent lithium niobate," Opt. Lett. **22**, 1553-1555 (1997).

2 L.E. Myers and W.R. Bosenberg, "Periodically poled lithium niobate and quasi-phase-matched optical parametric oscillators," IEEE J. Quantum Electron. **33**, 1663-1672 (1997).

3 D.A. Roberts, "Simplified characterisation of uniaxial and biaxial nonlinear optical crystals: a plea for standardization of nomenclature and conventions," IEEE J. Quantum Electron. **28**, 2057-2074 (1992).

4 H. Kogelnik and T. Li, "Laser beams and resonators," Proc. IEEE **54**, 1312-1329 (1966).

5 G.D. Boyd and D.A. Kleinman, "Parametric interaction of focused Gaussian light beams," J. Appl. Phys. **39**, 3597-3639 (1968).

6 Lithium Niobate data sheet, Crystal Technology Inc., Palo Alto, California.

7 L.E. Myers, R.C. Eckardt, M.M. Fejer, R.L. Byer, W.R. Bosenberg, J.W. Pierce, "Quasi-phase-matched optical parametric oscillators in bulk periodically poled $LiNbO_3$," J. Opt. Soc. Am. B **12**, 2102-2116 (1995).

8 G.A. Turnbull, T.J. Edwards, M.H. Dunn and M. Ebrahimzadeh, "Continuous-wave singly-resonant intracavity optical parametric oscillator based on periodically-poled $LiNbO_3$," Electron. Lett. **33**, 1817-1818 (1997).

9 M.E. Klein, Universität Kaiserslautern, Private communication (1998).

10 C.D. Nabors, S.T. Tang, T. Day and R.L. Byer, "Coherence properties of a doubly-resonant monolithic optical parametric oscillator," J. Opt. Soc. Am. B **7**, 815-820 (1990).

11 A.J. Henderson, M.J. Padgett, F.G. Colville, J. Zhang and M.H. Dunn, "Doubly-resonant optical parametric oscillators: tuning behaviour and stability requirements," Opt. Comm. **119**, 256-264 (1995).

12 M. Bode, P.K. Lam, I. Freitag, A. Tünnermann, H.-A. Bachor and H. Welling, "Continuously-tunable doubly-resonant optical parametric oscillator," Opt. Comm. **148**, 117-121 (1998).

13 R. Al-Tahtamouni, K. Bencheikh, R. Storz, K. Schneider, M. Lang, J. Mlynek and S. Schiller, "Long-term stable operation and absolute frequency stabilization of a doubly-resonant parametric oscillator," Appl. Phys. B **66**, 733-739 (1998).

14 A.J. Henderson, M.J. Padgett, J. Zhang, W. Sibbett and M.H. Dunn, "Continuous frequency tuning of a cw optical parametric oscillator through tuning of its pump source," Opt. Lett. **20**, 1029-1031 (1995).

15 G.M. Gibson, M.H. Dunn and M.J. Padgett, "Application of a continuously tunable, cw optical parametric oscillator for high resolution spectroscopy," Opt. Lett. **23**, 40-42 (1998).

16 A.S. Arnold, J.S. Wilson and M.G. Boshier, "A simple extended-cavity diode laser," Rev. Sci. Instrum. **69**, 1236-1239 (1998).

17 M.M. Fejer, G.A. Magel, D.H. Jundt and R.L. Byer, "Quasi-phase-matched second harmonic generation: tuning and tolerances," IEEE J. Quantum Electron. **28**, 2631-2654 (1992).

18 I.D. Lindsay, G.A. Turnbull, M.H. Dunn and M. Ebrahimzadeh, "Doubly-resonant continuous-wave optical parametric oscillator pumped by a single-mode diode laser," Opt. Lett. **23**, 1889-1891 (1998).

8. Conclusions.

In this chapter, the work described in this thesis will be summarised and its implications will be discussed. Other developments in the fields relevant to this thesis, which have occurred within the same time-frame, will also be discussed in the context of the work presented here. Finally, possible directions for future research in the fields of interest will be outlined.

The development of the injection-locked broad-area diode laser pump source was, on the whole, highly successful, satisfying the requirements of generating a narrow-band, near-diffraction-limited, output of several hundred mW. This source was demonstrated to show similar performance to Ti:sapphire and dye lasers when pumping the 946-nm Nd:YAG laser and was found to have adequate spatial and spectral qualities with more than sufficient output power when pumping the PPLN doubly-resonant OPO (DRO). Effective optical design criteria have been identified for the development of such systems and it is probable that a similar system producing higher output powers could be implemented if a broad-area diode laser with a larger stripe width were used.

There are, however, a number of reasons why further development of such systems is unlikely to be justified. Both of the main reasons for this are developments which have occurred largely within the same period of time as the work presented here. As was mentioned in section 4.4, tapered diode-amplifiers represent the current state-of-the-art in high-power, diffraction-limited diode systems. Their main attraction is their relative simplicity when, by contrast, the injection-locked system has many components, requires careful alignment and displays complex tuning behaviour. While these disadvantages are not uncommon in many laser systems, two of the main justifications for developing diode-laser based sources are simplicity and compact size.

Although when the work presented here was started tapered-amplifier systems were largely experimental, such systems have, in recent years, been more routinely used as pump sources for OPOs [1,2,3], other nonlinear optical frequency conversion processes [4,5,6] and solid-state lasers [7]. As a result, injection-locked systems appear to have been rendered largely obsolete. It must be born in mind, however, that while tapered-amplifier devices appear technologically well developed, and in routine use in certain laboratories, their general availability remains extremely limited. While this fact, alone, justifies the adoption of the injection-locked approach in the work described here, it seems likely that tapered diode-amplifiers must enter more widespread use in the near future, where high-power diffraction-limited diode-based sources are required

The second recent development which has made pursuing further work on the injection-locked system less attractive is the widespread availability of quasi-phase-matched nonlinear materials, particularly periodically-poled lithium niobate (PPLN). While the output powers available from the injection-locked system would be necessary for pumping typical birefringently phase-matched DROs, where thresholds from several tens to a few hundred mW might be expected, the results of chapter 7 demonstrated that DROs based on PPLN can have threshold powers well within the capabilities of low-power single-mode diode lasers. Indeed, the use of PPLN has made possible the demonstration of a singly-resonant OPO (SRO) pumped by a diode laser (albeit a tapered-amplifier system) [8], a development which only a few years ago would have seemed highly unlikely. A DRO or pump-enhanced SRO pumped by a single-mode diode laser has the potential to form the basis of a highly practical, compact source of tuneable radiation. Thus, while the injection-locked system was instrumental in the development of the DRO described in chapter 7, the single-mode-diode pumped approach seems a considerably more important route for future research into OPOs of this type.

Pumping of the 946-nm Nd:YAG laser with the injection-locked system was largely intended as a demonstration of the capabilities of the pump source. As such, the results achieved represented a useful proof-of-principle demonstrating that, given a high-quality pump, even low-gain transitions exhibiting reabsorption loss can yield

efficient, low threshold laser action when used in an end-pumped configuration. The results confirmed that the injection-locked system represented such a high-quality source. When compared to results obtained by others with broad-area diode lasers or diode-laser arrays, the results obtained here demonstrated the advantages of a near-diffraction-limited pump in the end-pumped configuration.

Although useful as a laboratory tool, the injection-locked system clearly does not represent a practical pump source for routine use with end-pumped solid-state lasers, where a simpler pump system would be more appropriate. For low-threshold, high-efficiency operation at moderate power levels, two single-mode laser diodes could be polarisation combined to yield output powers approximately half that of the injection-locked system in a diffraction-limited beam. It should be noted, however, that this method is not applicable to all solid-state laser materials. For high-power operation, threshold and efficiency can be sacrificed in favour of pump power and non-diffraction-limited sources such as fibre-coupled high-power diode lasers [9] or beam-shaped diode bars [10] utilised in the end-pumped geometry.

The criteria developed in section 2.3.4 for the optimisation of end-pumped lasers given a pump source with arbitrary M^2 were, primarily, intended as an illustration of the effects of pump beam quality on laser performance. The near-diffraction-limited nature of the injection-locked system did not afford an opportunity to test these criteria experimentally. Such optimisation techniques could, however, prove extremely useful in the future development of end-pumped lasers with a variety of pump sources. It would, therefore, be interesting to experimentally investigate the optimisation of an end-pumped laser with pump sources having a range of beam quality factors and compare the results to predictions based on the criteria developed in section 2.3.4.

When considering the development of the PPLN-based DRO described in chapter 7 and the results obtained, conclusions must be drawn in the light of the fact that the widespread availability of PPLN, which occurred within the time-scale of the work presented here, has had a dramatic effect on the field of nonlinear optics in general, and cw OPOs in particular. The demonstration of direct pumping of a DRO by a single-mode diode described in section 7.3.2, the first such demonstration to our

knowledge, showed that injection-locked or amplified diode systems are no longer a prerequisite for diode-laser pumping of OPOs. Given the recent level of interest in compact, tuneable sources in the near-to-mid infrared for applications such as atmospheric trace-gas detection [11,12,13], development of single-mode-diode pumped OPOs appears likely to prove a worthwhile and active area of research.

In the case of immediate development of the DRO demonstrated here, improved stabilisation is the most obvious requirement. The first stage in achieving this is improved temperature control of the PPLN crystal to allow stabilised operation at the elevated temperatures required to avoid photorefractive effects. This requires the development of an oven and temperature controller providing stability of the order of a few mK, without the large fluctuations introduced by the temperature controller used presently.

The other immediate requirement for achieving long-term stable operation is improvement of the frequency stability of the single-mode diode laser pump source. The results in section 7.3.3 were obtained with no attempt to stabilise the single-mode diode. This resulted in the high degree of susceptibility to mode hops, typical of free-running Fabry-Perot diode lasers, and mode-hopping by the pump laser proved to be the factor limiting the duration for which stabilisation could be maintained. The performance of the single-mode diode in this respect could be improved considerably by operating it in an external cavity with grating feedback. This would also result in a reduction in linewidth. External-cavity single-mode diode lasers have been demonstrated with output powers as high as 80mW [14], which would be quite sufficient given the 16mW threshold observed for the DRO. The development of an external-cavity grating-stabilised single-mode diode laser having an output power of ≈100mW should thus be regarded as a high priority for the further advancement of this work.

Although the work presented in this thesis has mainly concentrated on DROs, the availability of PPLN has also resulted in advances in the development of pump-enhanced SROs (PE-SROs) [15,16,17]. Although these devices have all had thresholds of a few hundred mW, the calculations shown in Fig. 3-28 would appear to indicate that, given a sufficient degree of pump enhancement, sub-100mW

thresholds should be achievable. This would appear to be born out by preliminary results obtained with a Ti:sapphire laser [18]. The pump-enhanced configuration has considerably less complex tuning behaviour than the DRO, although the mode-hop-free tuning range is typically limited to one free-spectral-range of the OPO cavity. It is interesting, however, to consider the possibility that the higher parametric gains available using PPLN when compared to other materials may make the level of intracavity losses in such devices less critical. This could allow the use of frequency-selection elements conventionally used in tuneable lasers, such as intracavity etalons, to extend the mode-hop-free tuning range.

The side-of-fringe locking technique used in 7.3.3 was chosen mainly for reasons of simplicity and is certainly not the best method available. In the case of PE-SROs the method is completely unsuitable, as it cannot lock the cavity to the peak of the pump resonances where enhancement is maximised. In these devices, the FM-based Pound-Drever locking technique is generally used. This technique has also been successfully applied to the stabilisation of DROs [19,20]. It can be seen that a stabilisation technique which locked to a resonance peak would be particularly advantageous in the case of the PPLN DRO developed here, as it would avoid many of the problems associated with obtaining the well-defined peaks necessary for side-of-fringe locking. This was shown to be the case in [19], where a near-degenerate DRO using type-I birefringent phase-matching, which would be expected to have many overlapping signal-idler resonances, was stabilised using the Pound-Drever technique. Thus, the development of more advanced servo-locking and stabilisation methods would benefit both the further development of the PPLN DRO and the implementation of PE-SROs pumped by a stabilised single-mode diode laser.

The fact that all the PE-SROs described above were pumped by miniature diode-pumped Nd:YAG ring lasers operating at 1.064μm raises the question of whether such lasers represent more suitable pump sources than diode-based systems. These lasers are generally constructed as monolithic non-planar ring oscillators (NPROs), resulting in significantly better frequency stability and narrower linewidth (≈kHz) than even grating-stabilised diode lasers (≈100s kHz typical linewidth). Such lasers have output powers typically of the order of several hundred mW. They are,

therefore, attractive sources for OPO pumping, especially in applications where highly-stable narrow-linewidth operation is required such as frequency standards and metrology. The principal advantages of diode-based systems, as OPO pump sources, over such lasers are cost (especially if a single-mode diode laser is used directly) and tuneability. The tuning range of typical Nd:YAG NPROs is ≈10GHz, whereas, as was seen in chapter 7, diode lasers can typically be tuned over several nm or several THz. It was shown that this can result in wide tuning of the OPO without having to change the crystal temperature or grating period. This large tuning range represents a distinct advantage for diode-laser pumps in spectroscopic applications, where extremely narrow linewidths are not required, such as trace-gas detection in which only relatively broad spectral features are required to be resolved [11].

While PPLN was the material which formed the basis of all the OPO development described in this thesis, and has been instrumental in a number of advances in the field of cw OPOs in recent years, other nonlinear materials should not be completely discounted. The principal advantages of PPLN are flexibility in phase-matching and effective nonlinear coefficients significantly higher than the majority of other materials in common use. However, as has been mentioned a number of times, PPLN suffers from photorefractive effects, which necessitate operation at elevated temperatures typically >100°C. This requirement is clearly undesireable in many applications and materials offering room-temperature operation while having similar performance in other respects would be preferable. While quasi-phase-matching has been demonstrated in a number of other nonlinear materials, notably KTP [21], RTA [22] and lithium tantalate [23], none of these have yet reached the same level of development as PPLN. It is likely, however, that such materials will enter wider use in the near future and may allow room-temperature operation of quasi-phase-matched OPOs.

Birefringently phase-matched materials should certainly not be completely discounted and are likely to remain more appropriate in certain situations than quasi-phase-matched materials. If, for example, the first-order QPM grating period required would be shorter than that which can be successfully fabricated or nonlinear optical interaction between waves of orthogonal polarisation is necessary,

birefringently-phase-matched materials may still have an advantage. The highest effective nonlinear coefficients are, however, always going to be offered by quasi-phase-matched materials. Thus, such materials in general and, in the short term, PPLN in particular, will remain the materials of choice for single-mode-diode pumped OPOs.

To conclude, the work presented in this thesis has demonstrated that diode-laser-based sources can be developed which generate high spatial- and spectral-quality output at power levels higher than those attainable with single-mode diode lasers alone. The near-diffraction-limited performance of such a source has allowed the efficient, low-threshold operation of an end-pumped solid-state laser, despite the chosen laser transition having a low emission cross-section and exhibiting significant reabsorption losses. Finally, the high effective nonlinear coefficient available from a quasi-phase-matched material has enabled the demonstration of a low-threshold doubly-resonant optical parametric oscillator, having versatile tuning characteristics, pumped both by the injection-locked source and, directly, by a single-mode diode laser alone. This final result has highlighted the potential of single-mode diode-laser pumped OPOs as practical sources of tunable radiation in the near- to mid-infrared. The further development, demonstration and application of single-mode diode-laser pumped OPOs, whether doubly-resonant or pump-enhanced devices, appears likely to become an active and widespread field of future research.

8.1 References.

1 K.J. Boller, M. Scheidt, B. Beier, C. Becher, M.E. Klein and D.H. Lee, "Diode-pumped optical parametric oscillators," Quantum Semiclass. Opt. **9**, 173-189 (1997).

2 M. Scheidt, B. Beier, K.J. Boller and R. Wallenstein, "Frequency-stable operation of a diode-pumped continuous-wave $RbTiOAsO_4$ optical parametric oscillator," Opt. Lett. **22**, 1287-1289 (1997).

3 M.E. Klein, D.-H. Lee, J.-P. Meynm B. Beier, K.-J. Boller and R. Wallenstein, "Diode-pumped continuous-wave widely tunably optical parametric oscillator based on periodically poled lithium tantalate," Opt. Lett. **23**, 831-833 (1998).

4 K. Matsubara, U. Tanaka, H. Imajo, K. Hayasaka, R. Ohmukai, M. Watanabe and S. Urage, "An all-solid-state tunable 214.5-nm continuous-wave light source by using two-stage frequency doubling of a diode laser," Appl. Phys. B **67**, 1-4 (1998).

5 R. Knappe, C.K. Laue and R. Wallenstein, "Tunable UV-source based of frequency-doubled red diode laser oscillator-amplifier system," Electron. Lett. **34**, 1233-1234 (1998).

6 D. Woll, B. Beier, K.-J. Boller and R. Wallenstein, "Generation of 1W of blue light by frequency doubling the output of a tapered InGaAs diode amplifier in critically phase-matched LBO," Conference on Lasers and Electro-Optics, May 1998, OSA Technical Digest Series 1998 vol. **6** p. 380, Optical Society of America, Washington.

7 A. Robertson, R. Knappe and R. Wallenstein, "Kerr-lens mode-locked Cr:LiSAF femtosecond laser pumped by the diffraction-limited output of a 672-nm diode-laser master-oscillator power-amplifier system," J. Opt. Soc. Am. B **14**, 672-675 (1997).

8 M.E. Klein, D.-H. Lee, J.-P. Meyn, B. Beier, K.-J. Boller and R. Wallenstein, "Diode-pumped continuous-wave optical parametric oscillator," Post-deadline paper CPD1.12, Conference on Lasers and Electro-Optics-Europe September 1998, OSA Technical Digest Series 1998, Optical Society of America, Washington.

9 Y. Kaneda, M. Oka, H. Masuda and S. Kubota, "7.6W of continuous-wave radiation in a TEM00 mode from a laser-diode end-pumped Nd:YAG laser," Opt. Lett. **14**, 1003-1005, (1992).

10 W.A. Clarkson and D.C. Hanna, "Efficient Nd:YAG laser end pumped by a 20-W diode-laser bar," Opt. Lett. **21**, 869-871, (1996).

11 K.P. Petrov, S. Waltman, E.J. Dlugokencky, M. Arbore, M.M. Fejer, F.K. Tittel and L.W. Hollberg, "Precise measurement of methane in air using diode-pumped 3.4-mm difference-frequency generation in PPLN," Appl. Phys. B 64, 567-572 (1997).

12 K.P. Petrov, R.F. Curl and F.K. Tittel, "Compact laser difference-frequency spectrometer for multicomponent trace gas detection," Appl. Phys. B 66, 531-538 (1998).

13 For coverage of many recent results in the use of nonlinear optics for atmospheric trace-gas detection, see special issue on "Environmental trace gas detection using laser spectroscopy", Appl. Phys. B **67**, 273 (1998).

14 A.S. Arnold, J.S. Wilson and M.G. Boshier, "A simple extended-cavity diode laser," Rev. Sci. Instr. **69**, 1236- 1239 (1998).

15 K. Schneider, P. Kramper, S. Schiller and J. Mlynek, "Toward an optical synthesizer: a single-frequency parametric oscillator using periodically poled $LiNbO_3$," Opt. Lett. **22**, 1293-1295 (1997).

16 K. Schneider and S. Schiller, "Narrow-linewidth, pump-enhanced singly-resonant parametric oscillator pumped at 532 nm," Appl. Phys. B **65**, 775-777 (1997).

17 D. Chen, D. Hinkley, J. Pyo, J. Swenson and R. Fields, "Single-frequency low-threshold continuous-wave 3-μm periodically poled lithium niobate optical parametric oscillator," J. Opt. Soc. Am. B **15**, 1693-1697 (1998).

18 G.A. Turnbull, I.D. Lindsay, D.G. Mc Gloin, M. Ebrahimzadeh and M.H. Dunn, unpublished.

19 M. Bode, P.K. Lam, I. Freitag, A. Tünnermann, H.-A. Bachor and H. Welling, "Continuously-tunable doubly-resonant optical parametric oscillator," Opt. Comm. **148**, 117-121 (1998).

20 R. Al-Tahtamouni, K. Bencheikh, R. Storz, K. Schneider, M. Lang, J. Mlynek and S. Schiller, "Long-term stable operation and absolute frequency stabilization of a doubly-resonant parametric oscillator," Appl. Phys. B **66**, 733-739 (1998).

21 G.M. Gibson, G.A. Turnbull, M. Ebrahimzadeh, M.H. Dunn, H. Karlsson, G. Arvidsson and F. Laurell, "Temperature-tuned difference-frequency mixing in periodically poled $KTiOPO_4$," Appl. Phys. B **67**, 675-677 (1998).

22 T.J. Edwards, G.A. Turnbull, M.H. Dunn, M. Ebrahimzadeh, H. Karlsson, G. Arvidsson and F. Laurell, "Continuous-wave singly resonant optical parametric oscillator based on periodically poled $RbTiOAsO_4$," Opt. Lett. **23**, 837-839 (1998).

23 M.E. Klein, D.-H. Lee, J.-P. Meynm B. Beier, K.-J. Boller and R. Wallenstein, "Diode-pumped continuous-wave widely tunably optical parametric oscillator based on periodically poled lithium tantalate," Opt. Lett. **23**, 831-833 (1998).

A1. Spatial Beam Quality and M^2.

The beam quality of a pump source is a central theme throughout this thesis. In this appendix, the definition of the quality of a laser beam and the parameter used to characterise it, M^2, are described. Methods of measuring this parameter are also discussed.

A1.1 Propagation of non-diffraction-limited beams.

The intensity distribution of a lowest-order transverse-mode laser beam,

$$I(r) = I_0 e^{-2\left(\frac{r}{w}\right)^2} \tag{A1-1}$$

has a characteristic radius, w, defining the point where the intensity falls to $1/e^2$ of its maximum value. The well-known expression [1], arising from Gaussian beam propagation theory, describing the variation of this characteristic radius with distance is:

$$w^2(z) = w_0^2\left(1+\left(\frac{\lambda z}{\pi w_0^2}\right)^2\right) \tag{A1-2}$$

The extent of the focal region is generally described as the confocal parameter, z_c, and defined as that distance over which the beam area is less than or equal to twice that at the waist, i.e. between the points where $w = \sqrt{2}w_0$. The distance between the waist and one of these points is generally described as the Rayleigh range, z_R, being half the confocal parameter:

$$z_c = 2z_R = \frac{2\pi w_0^2}{\lambda} \tag{A1-3}$$

In the limit of large z ($z >> w_0$), (A1-2) can be approximated by the linear relationship:

$$w(z) \approx \frac{\lambda z}{\pi w_0} \tag{A1-4}$$

This leads to an expression for the far-field divergence half-angle:

$$\theta_{1/2} = \frac{\lambda}{\pi w_0} \tag{A1-5}$$

Using a similar far-field assumption, the radius of the focal spot obtained when a lens of focal length f is used to focus a collimated beam of radius w_c can be determined from:

$$w_0 = \frac{\lambda f}{\pi w_c} \tag{A1-6}$$

It should again be emphasised that all the expressions derived above apply to the fundamental transverse mode only and divergences conforming to (A1-2) are usually described as diffraction-limited and represent the best possible performance in terms of minimising the divergence for a given waist radius, maximising the confocal parameter and minimising the focused spot size.

For beams which do not have this idealised performance, a factor M^2 can be introduced to allow for non-diffraction-limited behaviour. This appears to have first been done to account for multiple transverse-mode operation [2], and has since been discussed both in the context of both multiple transverse modes and beam-degradation processes in general [3,4,5].

The concept of the M^2 parameter is best introduced by considering the transverse modes of a resonant cavity. In this case, the higher-order transverse mode will at all positions have a radius M times larger than that of the fundamental mode at the same position for the same resonator geometry. Thus, the waist radius of the higher-order

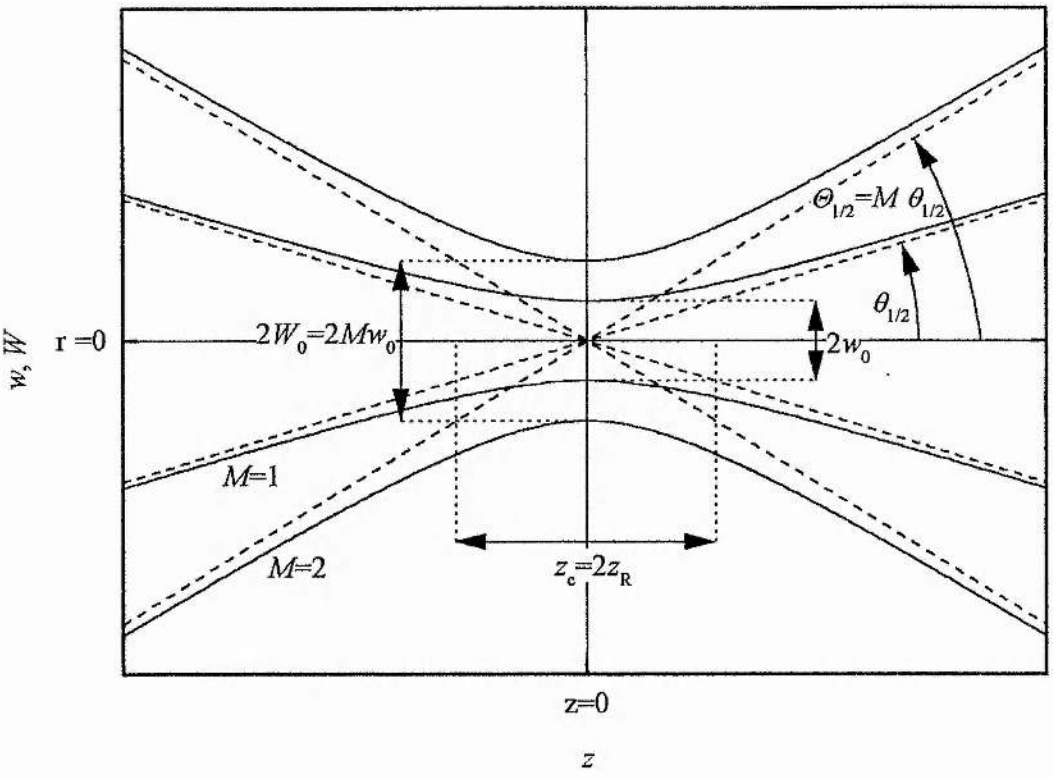

Fig. A1-1 Beam behaviour through focus for fundamental transverse mode (M^2=1) and higher order mode (M^2=4 in this case).

mode will have a value W_0, defined as $W_0=Mw_0$, and the far-field divergence will be defined as $\Theta=M\theta$, where θ is as defined by (A1-4). This situation is summarised in Fig. A1-1 where a higher-order mode having M=2 is shown in addition to the fundamental mode. Note that, as the ratio of radii is constant at all points, the two modes necessarily have the same confocal parameter. The fundamental mode in a situation such as this is often described as the "embedded Gaussian". It is important to note that this does not represent the diffraction-limited version of the higher-order mode but rather the diffraction-limited mode that would be obtained for the same resonator geometry and wavelength.

In most practical situations it is more useful to know how a non-diffraction-limited beam will behave when compared to a diffraction-limited beam having the same waist or, conversely, the waist radius obtained with a non-diffraction-limited beam

when focused from a given collimated radius as compared to a diffraction-limited beam of the same initial collimated radius. From the discussion above and Fig. A1-1, it can be seen that the substitutions $w=W/M$ and $w_0=W_0/M$ can be made in (A1-2) to obtain, after re-arrangement, the equivalent expression in terms of the non diffraction-limited beam:

$$W^2(z) = W_0^2\left(1+\left(\frac{M^2\lambda\, z}{\pi\, W_0^2}\right)^2\right) \tag{A1-7}$$

Since this expression is directly equivalent to (A1-2), it is convenient to equate $W=w$ and $W_0=w_0$, i.e. allow w and w_0 to represent all modes rather than just the diffraction-limited one, to obtain the general version of (A1-2):

$$w^2(z) = w_0^2\left(1+\left(\frac{M^2\lambda\, z}{\pi\, w_0^2}\right)^2\right) \tag{A1-8}$$

which is valid for any beam of a given M^2 and becomes the diffraction-limited expression of (A1-2) when $M^2=1$. It can be seen from this expression that the M^2 formulation is extremely convenient in that by simply replacing λ with $M^2\lambda$ in the standard expressions for fundamental-mode Gaussian beam propagation these expressions can be applied to beams of arbitrary quality. Thus, the expressions (A1-3) to (A1-5) become:

$$z_c = 2z_R = \frac{2\pi\, w_0^2}{M^2\lambda} \tag{A1-9 a}$$

$$\theta_{1/2} = \frac{M^2\lambda}{\pi\, w_0} \tag{A1-9 b}$$

$$w_0 = \frac{M^2\lambda f}{\pi\, w_c} \tag{A1-9 c}$$

It can thus be seen that for a beam with $M^2>1$ and a waist radius w_0, the confocal parameter will be smaller, and the far-field divergence larger, by a factor M^2 compared to a diffraction-limited beam having the same waist radius. Conversely,

for the same collimated radius w_c, the focal spot obtained from a non-diffraction-limited beam will be a factor M^2 larger than that from a diffraction-limited beam. The parameter M^2 is thus directly equivalent to the number of, "times diffraction limited," of the beam. It should be noted that the discussion so far has assumed a beam having radial symmetry. It is, of course, possible to consider propagation in different planes using the Gaussian beam expressions and a beam can thus have different M^2 values in different planes. This is especially true in the case of diode lasers.

A1.2 Measurement of beam radius and M^2.

The idea of the embedded Gaussian illustrated in Fig. A1-1, and described above, is rather an abstract concept constructed mainly for the formal derivation of the M^2 parameter and has little bearing on practical situations. In practice, it is not necessary to have any knowledge of the exact modal content of the beam to determine its M^2 value. It can be seen from expressions (A1-8) and (A1-9) that it is simply necessary to characterise the divergence behaviour and compare this to that expected for the diffraction limited case to determine the value of M^2. Clearly, this measurement will involve the determination of the waist radius and of the radius at (at least) one other point, a known longitudinal distance from the waist. The problem then arises of how the radius should be defined for a beam of arbitrary M^2 and how it can be measured.

Several definitions of the beam radius and methods of measuring it have been proposed and demonstrated [6,7]. Imaging devices such as CCDs or photodiode arrays are often unsuitable for measuring waist radii, as a large number of individual detector elements must fall within the beam to obtain an accurate profile. The finite element dimensions thus prevent accurate profiles of even moderately small waists (<100μm) from being made. In addition, the high intensities occurring at the beam waist are many times greater than the saturation intensities of most such detectors necessitating the use of neutral-density filters which introduce additional aberrations and reductions in beam quality of their own.

Scanning pinholes and slits can be used, with the transmitted power being measured by a single element detector, to build up an intensity map of the beam. This method avoids detector saturation problems, as neutral-density filters can be introduced after the scanning aperture where additional aberrations do not affect the measurement. These methods, however, also suffer from resolution problems and the transmitting aperture must be very much smaller than the dimensions of the beam to reduce these effects. If this is not the case the resulting profile is a convolution of the beam intensity distribution and the transmission function of the aperture.

The use of a single knife edge, as opposed to a slit, avoids most of these problems. For any position of the knife edge within the beam, the transmitted power will clearly be the transverse integral across the intensity distribution up to the position of the knife edge, as shown in Fig. A1-2 for a fundamental-mode Gaussian distribution. Thus by translating the knife edge across the beam and differentiating the resulting

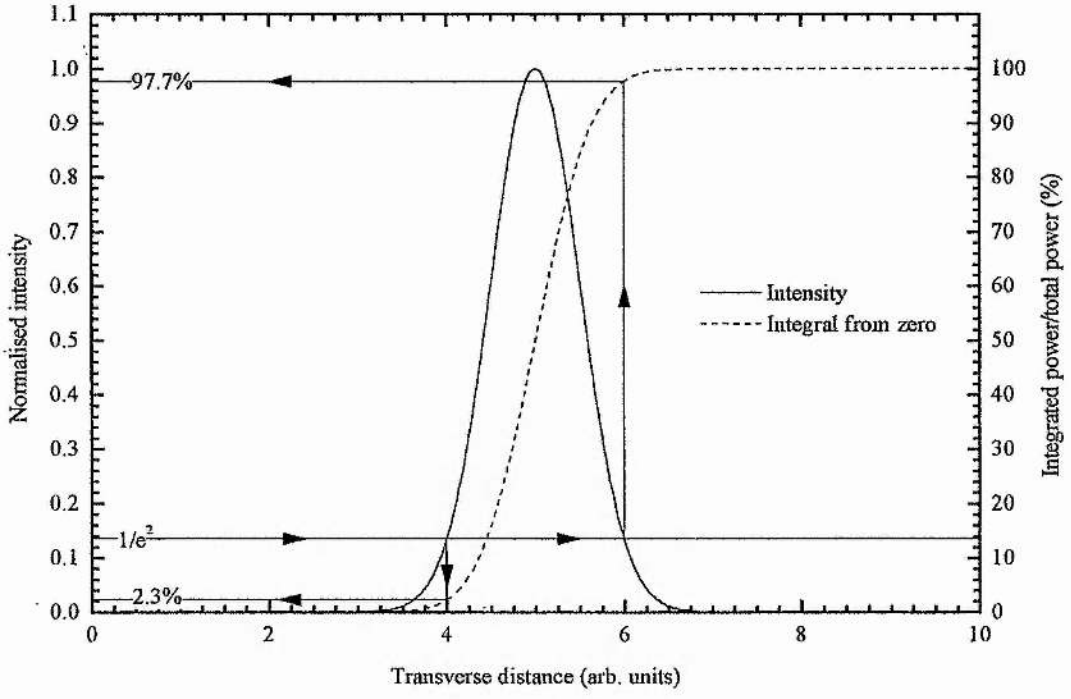

Fig. A1-2 Gaussian intensity distribution and fraction of integrated power to total power with transverse distance.

variation of transmitted power with position the intensity profile can be obtained. The resolution of this method is limited only by the accuracy with which the knife edge can be positioned and, as with the slit and aperture methods, neutral density filters can be inserted after the knife edge, where their aberrating effects are not important, allowing high-power beams to be profiled. This method is used as the basis for a number of commercial beam-profiling and M^2-measurement devices [8].

In the case of the Gaussian fundamental-mode distribution shown in Fig. A1-2, the mode diameter is clearly defined using the standard definition of the distance between the points having intensities $1/e^2$ of the maximum. However, in the case of non-diffraction-limited beams, this definition is not so easily applied. A number of generalised definitions applying to arbitrary intensity distributions have been proposed [3,7]. The definition of the $1/e^2$ width of the maximum peak intensity gives increasingly inconsistent results for higher-order Hermite-Gaussian modes and therefore cannot really be used as a general definition. More consistent results are obtained using the $1/e^2$ points of the outermost peaks [3] for Hermite-Gaussian distributiuons, but this technique is not so easily applied to more arbitrary intensity distributions. The most generalised measurement involves the calculation of the second moment of the intensity distribution. However, this method is computationally complex and lends itself best to measurement techniques producing a large array of intensity values such as CCD detectors.

If a fundamental Gaussian distribution, such as that shown in Fig. A1-2, is assumed to have circular symmetry, cylindrical integration to the $1/e^2$ radius gives a value of 86.5% of the total power. A consistent diameter for non-diffraction-limited beams can thus be defined as that of an aperture transmitting 86.5% of the total power. This definition has been widely applied to beams having circular symmetry, but is inaccurate for cases such as that of diode lasers where the beam is highly asymmetric. The alternative to this definition in the asymmetric case is to integrate across the beam in one direction and use this measurement to determine the radius along the axis thus defined. This has been done in Fig. A1-2 and it can be seen that 95.4% of the total power is contained between the $1/e^2$ points in the case of a Gaussian distribution.

This definition, i.e. the transverse distance within which 95.4% of the power is contained, is commonly used for beam diameter measurements along one axis of beams having arbitrary intensity distributions. The definition particularly lends itself to the scanning knife edge measurement method as only two measurements, the knife edge positions where 2.3% and 97.7% of the total power are transmitted, need to be made to obtain the diameter.

The M^2 value of the beam can be measured using this method to examine the divergence from a waist produced by simply focusing the beam with a lens. It is, in principle, only necessary to measure the diameter at the waist and at one other position, as already mentioned. In practice, however, the waist location is not usually exactly known and a more practical method is to measure the 95.4% power diameters for a range of longitudinal positions through the waist location and then fit a function having the form of (A1-8) to this data. This also serves to reduce random experimental errors.

There are a number of aspects to making measurements using this method where care must be taken. Firstly, the waist produced must be small enough to obtain significant divergence (i.e. several confocal parameters) over the longitudinal distance over which measurements are taken. However, the waist must not be too small to be resolved by whatever method is used to translate the knife edge, such as a micrometer-driven stage. When taking measurements, it is vital to determine the radius of the beam within the confocal range of the waist, as data taken outside this range will tend to show a linear divergence which could correspond to a many beam waist/M^2 combinations. Thus, unless an explicit measurement of the waist within the nonlinear confocal region is obtained, M^2 cannot be determined accurately. Care must also be taken when fitting an expression of the form of (A1-8) to the data. Obviously, the wavelength must be a fixed parameter but care must also be taken to ensure that the fitting process does not reduce w_0 significantly below the measured value, to accommodate a large measured divergence, instead of increasing M^2.

All the M^2 measurements described in this thesis were taken by measuring the 95.4% power diameter of the beam with the scanning knife-edge method using a razor blade as the knife edge and micrometer-driven translation stages to provide

longitudinal and transverse positioning. M^2 values were obtained by fitting to the experimental data using the nonlinear least-squares fitting module of Microcal Origin 5.0.

A1.3 References.

1 H. Kogelnik and T. Li, "Laser beams and resonators," Proc. IEEE **54**, 1312-1329 (1966).

2 L. Marshall, "Applications a la mode," Laser Focus **4**, 26-28 (April 1971).

3 M.W. Sasnett, "Propagation of multimode laser beams - the M^2 factor," in "the physics and technology of laser resonators," ed. D.R. Hall and P.E. Jackson, Adam Hilger, Bristol (1989).

4 T.F. Johnston Jr., "M^2 concept characterises beam quality," Laser Focus World **26** No. 5, 173-183 (May 1990).

5 A.E. Siegman and S.W. Townsend, "Output beam propagation and beam quality from a multimode stable-cavity laser," IEEE J. Quantum Electron. **29**, 1212-1217 (1993).

6 D.K. Cohen, B. Little and F.S. Luecke, "Techniques for measuring 1-μm diam Gaussian beams," Appl. Opt. 23, 637-640 (1984).

7 D. Wright, "Beamwidths of a diffracted laser using four proposed methods," Opt Quantum Electron. **24**, S1129-S1135 (1992).

8 "Meter charts multimode laser beams," Laser Focus World **26** No. 5, 29-32 (May 1990).

A2. Publications and Conference Proceedings.

A2.1 Publications.

I.D. Lindsay and M. Ebrahimzadeh, "Efficient continuous-wave and Q-switched operation of a 946-nm Nd:YAG laser pumped by an injection-locked broad-area diode laser," Appl. Opt. **37**, 3961-3970 (1998).

I.D. Lindsay, G.A. Turnbull, M.H. Dunn and M. Ebrahimzadeh, "Doubly-resonant continuous-wave optical parametric oscillator pumped by a single-mode diode laser," Opt. Lett. **23**, 1889-1891 (1998).

A2.2 Conference proceedings.

I.D. Lindsay, M.H. Dunn and M. Ebrahimzadeh, "Efficient 946-nm Nd:YAG laser pumped by an injection-locked broad area diode laser," Conference on Lasers and Electro-Optics 1997, OSA 1997 Technical Digest Series volume 11, talk CFE8, p. 482, Optical Society of America, Washington (1997).

I.D. Lindsay, M.H. Dunn and M. Ebrahimzadeh, "Efficient cw and Q-switched operation of a 946nm Nd:YAG laser pumped by an injection-locked broad area semiconductor laser," Technical digest of the National Quantum Electronics Conference QE-13, p. 31, September 1997, Institute of Physics Publishing.

I.D. Lindsay, G.A. Turnbull, M.H. Dunn and M. Ebrahimzadeh, "Doubly resonant cw PPLN optical parametric oscillator pumped by injection-locked broad-area diode laser," Conference on Lasers and Electro-Optics 1998, OSA 1998 Technical Digest Series volume 6, talk CMK3, p. 43, Optical Society of America, Washington (1998).

I.D. Lindsay, G.A. Turnbull, M.H. Dunn and M. Ebrahimzadeh, "Doubly-resonant continuous-wave PPLN optical parametric oscillator pumped by injection-locked broad area diode laser," Conference on Lasers and Electro-Optics-Europe September 1998, OSA 1998 Technical Digest Series, talk JTuA2, p. 136, Optical Society of America, Washington (1998).

I.D. Lindsay, G.A. Turnbull, M.H. Dunn and M. Ebrahimzadeh, "Low-threshold, diode-laser pumped optical parametric oscillators," Rank Prize Funds Symposium on Optical Parametric Processes and their Applications, July 1999.

I.D. Lindsay, G.A. Turnbull, C. Petridis, M.H. Dunn and M. Ebrahimzadeh, "Low-threshold, diode-laser pumped continuous-wave optical parametric oscillators," National Quantum Electronics Conference QE-14, September 1999, Manchester, U.K. (accepted for presentation)

Acknowledgements.

There are many people to whom I owe a real debt of gratitude for their support while this work was carried out. First and foremost, thanks are due to my supervisor, Dr. Majid Ebrahimzadeh, both for initiating and securing funding for the project, and for providing patient guidance, encouragement and advice throughout. Special thanks must also go to Prof. Malcolm Dunn and the other members of the cw OPO group, present and departed, Graham Turnbull, Tom Edwards, Dave Stothard and Finlay Colville who, for some or all of my time here, have been around to offer help, advice or sympathy as required.

Other members of the department who were always happy to offer assistance, loan equipment, show interest or help me have some semblance of a social life have been much appreciated. Thanks then, particularly, to Richard Conroy, Mark Holden, Neil Simpson, Jim Hyland, Graham Friel, Cameron Rae, Alan Kemp, Colin Trueman, James Boon, Dave Fulton, Gordon Kennedy and everyone else who has lent me a mirror or bought me a drink in the last four years. Thanks, also, go to the technical and administrative staff, without whose efforts few of us would get anything done at all.

Of course, there is life outside work and those who have reminded me of this once in a while deserve special praise, particularly Alan, Graham, Jim, Ian, Gaitee and Rob, in St Andrews, and all those friends from previous lives who have helped me to escape the place every now and then.

Finally, I would particularly like to thank all the members of my family, especially Mum, Dad, Anne and Jeanette, for supporting and encouraging me in this and everything else I have chosen to do.